Summer 2017

Application of millimeter-wave differential probe for crack detection on riveted structures

Kuang Ping Ying

Department:

APPLICATION OF MILLIMETER-WAVE DIFFERENTIAL PROBE FOR CRACK DETECTION ON RIVETED STRUCTURES

by

KUANG PING YING

A THESIS

Presented to the Faculty of the Graduate School of the

MISSOURI UNIVERSITY OF SCIENCE AND TECHNOLOGY

In Partial Fulfillment of the Requirements for the Degree

MASTER OF SCIENCE IN ELECTRICAL ENGINEERING

2017

Approved by

Reza Zoughi, Advisor
Mohammad Tayeb Ghasr
Donald Palmer
Joseph Newkirk

ABSTRACT

This thesis proposes the use of a W-band wideband differential probe for crack detection on riveted structures, such as aircraft fuselage lap joints. Detection of crack at its early stage (surface-breaking) is particularly important to prevent the development of a fatigue crack. This probe utilizing millimeter-wave frequencies serves as a viable candidate on detecting surface-breaking cracks, as it can be employed in measurements in a non-contact fashion, while allowing for high spatial-resolution images and the abilities to penetrate through dielectric materials (paint), making it attractive for detecting small cracks. In previous works, a V-band differential probe has shown promise for detecting surface breaking crack near a fastener head. This work is extended in this thesis by investigating the surface crack detection capability of the W-band differential probe. The W-band probe is tested with various intentional misalignments of the probe, as well as a paint layer covering the crack, the variations in its crack detection capability are then observed. The measurement results indicate that this fabricated probe is capable of detecting a surface crack at a length of 1.27 mm (adjacent to a fastener head), and the detection is not significantly affected by a slight misalignment, although consequently some undesired signals may also be registered. In addition, a layer of thick paint over crack introduces uncertainties to the detection signals and complicates the evaluations. To reduce the significance of these undesired signals, SAR filter is applied to the results. The outcome demonstrates an enhanced crack detection and weakened undesired signals, but the influence of a thick paint layer cannot be completely removed. A more in-depth analysis regarding the influence of paint on crack detection may be desired to fully understand the crack detection capabilities of the W-band differential probe.

ACKNOWLEDGMENTS

First of all, thank you to my advisor, Dr. Reza Zoughi, for all his guidance, encouragement, and support throughout my master's degree. I would also like to thank my committee members, Dr. Donald D. Palmer, Dr. Joseph Newkirk and especially Dr. Mohammad Tayeb Ghasr for their advice and valuable time and effort spent serving on my committee.

Special thanks to my friends and colleagues at the Applied Microwave Nondestructive Testing Laboratory (*amntl*), in particular Matthew Dvorsky and Katelyn Brinker, for their valuable help and collaboration in this project. Also special thanks to Jeffrey Birt from the ECE department for setting up the measurement system and fabricating the probe used in this project.

I would like to thank my family and friends, without whom I could not have accomplished this work. Thank you to my wife, Meiyu Xing, for the constant encouragement that she has continued to provide.

In addition, thank you to everyone who I've had the pleasure of getting to know or worked with throughout my graduate degree.

This work was supported by The Boeing Company, St. Louis, MO.

TABLE OF CONTENTS

LIST OF ILLUSTRATIONS

Page

1. INTRODUCTION

1.1. FATIGUE CRACKS IN RIVETED STRUCTURES – AN OVERVIEW

Critical aeronautical structural components, such as aircraft wings and riveted fuselage lap joints, are exposed to harsh environments and undergo fatigue damage around fastener holes due to severe mechanical stresses. Detection of fatigue cracks is particularly important in lap joints, where the surfaces of two fuselage panels overlap longitudinally and are joined together using rivets. The presence of fatigue cracks around rivets reduces the mechanical integrity of a lap joint causing the two plates to come apart when under stress.

The development of a fatigue crack begins with initiation of a surface-breaking crack, which can become larger (in all directions) if it is not detected early on, and can eventually lead to structural failures. In most cases, a surface crack is only visible when under mechanical stress (i.e., during flight), and otherwise appears closed. Additionally, cracks initiated on aircraft structures are typically hidden under paint, making it more difficult to visually detect them. Figure 1.1 represents an example of a riveted fuselage skin from a pressure bulkhead [1]. The forward force represents the mechanical stress experienced during the flight, which pressurizes the upper portion of the fuselage skin, and initiates surface-breaking cracks.

The simultaneous presence of several closely-spaced fatigue cracks (of sufficient sizes) forms what is known as widespread fatigue damage (WFD) [1]. The presence of WFD often leads to structural failure. The development of WFD in an airplane structure is a critical concern for older aircraft. Figure 1.2 depicts an example of a riveted fuselage structure with fatigue cracks near the joining fastener heads. This is a very clear example of WFD [1].

Fatigue cracks near riveted fuselage lap joints are thought to have been responsible for the Aloha Airline flight 243 accident which occurred on April 28th, 1988 [1], [2]. In this accident, the 19-year old Boeing 737 aircraft (manufactured in 1969) experienced an explosive decompression and structural failure at 24,000 feet above ground. This caused approximately 18 feet of the fuselage skin and structure to separate from the aircraft body in mid-flight. The National Transportation Safety Board (NTSB)

concluded that the probable cause of this accident was rooted in the failure of the Aloha Airlines maintenance program which led to not detecting the presence of fatigue cracks near the fastener heads on the fuselage skin [2]. This eventually led to failure of the lap joints and the separation of the upper fuselage skin panel, resulting in the separation and explosive decompression of the fuselage.

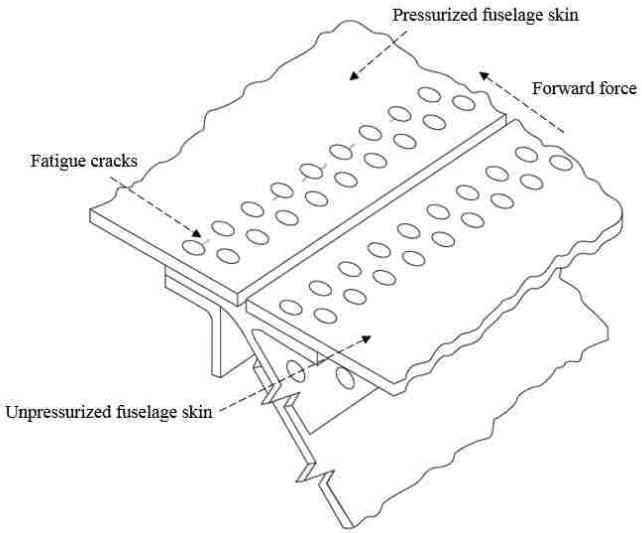

Figure 1.1. Example of structure susceptible to WFD [1].

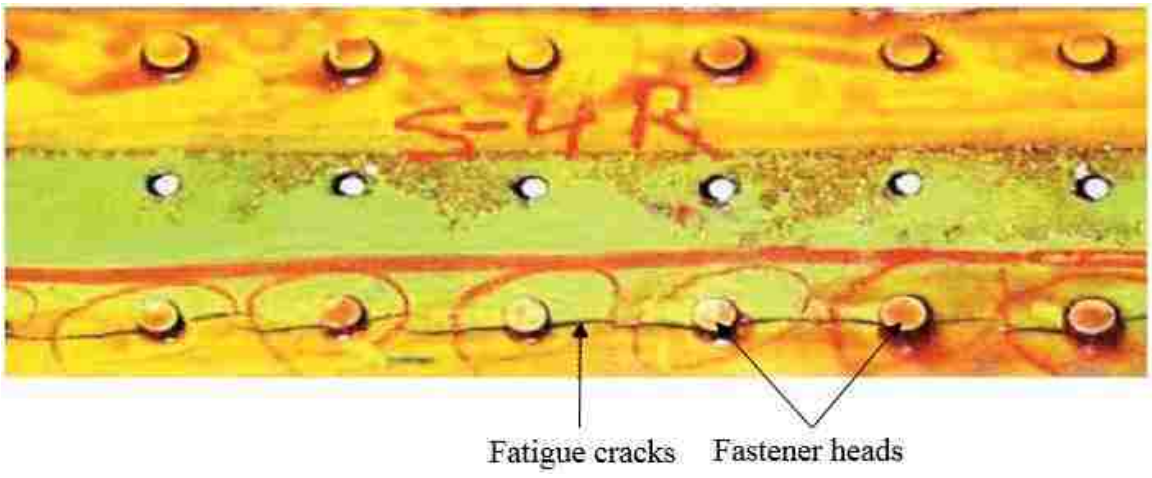

Figure 1.2. Real life fatigue cracks near fastener heads [1].

By 1988, aircraft fleets were inspected regularly with eddy-current (EC) probe and visual inspection. EC probe had proved successful in accurately detecting surface cracks [3]. However, the use of an EC probe and the analysis requires a trained technician. According to the maintenance schedule of Aloha Airlines [2], moderate inspections were conducted after every 175 accumulated flight hours, and substantial inspections were conducted after every 3,000 or more flight hours. Moderate inspections refer to inspections that are conducted to determine the general condition (for instance, evidences of damages or corrosions) of the aircraft, and substantial inspections are to check for serviceability of individual components, therefore are more extensive [2].

This accident raised significant concerns about the safety of commercial air carriers. The U.S. Federal Aviation Administration (FAA) then changed the maintenance practices for old aircraft, and more efficient inspection methods have been developed since. To this end, inspection methods that can detect surface-breaking crack (at the early stage of development), are able to do so through thin coatings such as paint (without the need to remove), and require little need for operator expertise with shorter inspection time are desirable and sought after.

1.2. CURRENT WORK

Currently, there are several well-established nondestructive testing and evaluation (NDT&E) techniques for detecting surface-breaking cracks in conducting materials. NDT&E is a practical field of engineering and science where measurement techniques are developed in order to inspect materials and structures without altering their physical properties and usefulness [4], [5]. Examples include but are not limited to: acoustic emission testing, liquid penetrant testing, eddy-current (EC) testing, ultrasonic testing (UT), and radiographic testing [4]. However, these techniques each have their own advantages and disadvantages when used for detecting surface cracks. For instance, the performance of these techniques can be greatly reduced due to the presence of paints or other coatings, therefore, hidden surface cracks may not always be reliably detected. Additionally, for detecting a crack near a fastener head, the techniques listed above could potentially result in false indications (where a crack does not exist) due to signal interaction with fastener head.

Conventional EC and UT techniques have been commonly used for detecting the stress-induced cracks in riveted structures [3], [6]-[12]. These methods commonly require that the transducer be placed in close proximity of the sample under test (SUT). Additionally, most UT methods require a couplant (if not air-coupled) to be placed in contact with the SUT to permit the transmission of acoustic signals from the transducer to the test specimen [11]-[13]. Furthermore, to obtain optimal results when using EC or UT methods, paint coatings on the fuselage skin may need to be removed. Consequently, a significant amount of time and resources are required to perform the inspection. An alternative technique that can overcome these issues is microwave and millimeter-wave NDT. Since microwave and millimeter-wave signals can propagate in air and do not require a couplant [13], they may offer significant advantage over UT. Microwave and millimeter-wave signals also penetrate through paint, allowing for inspection without the need to remove it.

1.3. BACKGROUND ON MICROWAVE NDT/SURFACE CRACK SCANNING

Microwaves and millimeter-waves cover the portion of the electromagnetic spectrum with frequency range from ~300 MHz – 30 GHz and 30 – 300 GHz, respectively [14]. The utility of microwave signals for nondestructive testing (NDT) was first demonstrated in the 1950s and over time have become a significant component of the NDT toolbox. A class of techniques based on microwave and millimeter-wave technology for detecting sub-millimeter size cracks were then developed [15]-[25]. Near-field microwave and millimeter-wave NDT techniques using open-ended probes offer many advantages when used for inspection [5]:

- measurements can be conducted in non-contact fashion as mentioned earlier, and the standoff distance between the detection probe and the SUT may be optimized to increase measurement sensitivity,
- near-field probes are usually relatively small in dimensions at microwave and millimeter-wave frequencies, this allows for high spatial-resolution measurements and images (the spatial-resolution in the near-field of a probe is a function of the probe dimensions not wavelength) and make them very attractive for detecting small cracks,

- there are several different types of near-field probes other than open-ended rectangular waveguides that may be used (open-ended circular waveguides, open-ended coaxial lines, microstrip patches, cavity resonators, etc.) each providing its own unique advantageous features for a specific application, and
- there is no requirement for a bulky antenna and near-field measurement systems are commonly small, handheld, portable, operator friendly and require low microwave power [5].

Among these developed techniques are those that employ open-ended rectangular waveguides [5], [15]-[20]. These probes, when operated in their near-field region, are sensitive to surface discontinuities in conducting materials. At millimeter-wave frequencies the skin depth (which is inversely proportional to the frequency of operation) associated with the SUT is very small (< 1 μm) and can be considered zero for all practical purposes. Therefore, only surface-breaking cracks can be detected using these probes. However, these signals penetrate through dielectric materials, such as paint [26], and therefore can interrogate paint-covered conducting materials for crack detections.

In principle, millimeter-wave crack detection technique is based on detecting the scattered (or reflected) electromagnetic waves by surface cracks, which are the results of induced surface current perturbation due to presences of cracks. Similarly, the presence of other scatterers on the surface (e.g., edges of fastener heads) also interact with the impinging electromagnetic waves. The additional scattered signal from the fastener head can potentially mask the indication of small cracks or create false indications, greatly influence the detection capability.

Millimeter-wave differential probes have demonstrated the ability to detect small flaws such as surface cracks and corrosion precursor pitting on conducting surfaces, particularly under thin coatings of paint [26]-[29]. The ability of such probe to compensate for unwanted common effects such as variations in standoff distance and scattered signals from the fastener head edges, makes it a viable candidate in many applications, especially riveted structure inspections.

1.4. PRINCIPLE OF DIFFERENTIAL PROBE & WIDEBAND SCANNING

The differential probe measurement system [26] (shown in Figure 1.3) consists of a source, a magic tee (hybrid coupler), two open-ended rectangular waveguides, and a diode detector. Each waveguide aperture is selected to match the desire frequency band standard (e.g., for a standard V-band (WR-15) aperture, the dimensions of the waveguides are 3.8 mm x 1.9 mm). The source consists of a Gunn oscillator and an isolator to prevent unwanted reflected signals entering into and damaging the oscillator.

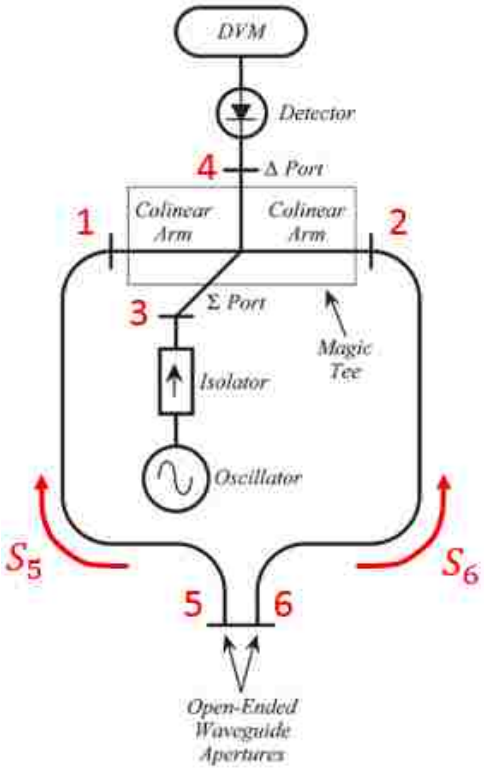

Figure 1.3. Schematic of differential probe.

The signal generated by the oscillator is fed to the summation (Σ) port (port 3) of the magic tee, the magic tee then divides the original signal into two identical (in both phase and magnitude) signals at its collinear arms (ports 1 and 2). The signals are transmitted through the open-ended waveguide apertures (ports 5 and 6), irradiate the

localized SUT and are reflected by the surface. These reflected signals are collected through the apertures and travel back to the magic tee, which sums and differentiates the signals. If the two reflected signals (represented by its transmission/reflection coefficients, or S-parameters) from each waveguide aperture are labeled S_5 and S_6, the magic tee will generate $0.5(S_5 + S_6)$ at its Σ port and $0.5(S_5 - S_6)$ at its difference (Δ) port (port 4), as will be explained later. The summed signal is outputted through the Σ port and absorbed by the isolator, and the coherently differentiated signal is outputted through the Δ port, and picked up by the diode detector, resulting in a DC voltage measured by a digital voltmeter (DVM). The probe output $|\Delta V|^2$ is calculated using the following set of equations [30]:

$$S_5 = S_{55} + S_{56} \tag{1}$$

$$S_6 = S_{66} + S_{65} \tag{2}$$

$$S = S_{43} + S_{41}\frac{S_{13}S_{51}^2S_5 + S_{12}S_{23}S_{62}^2S_6}{1 - S_{12}^2} + S_{42}\frac{S_{23}S_{62}^2S_6 + S_{12}S_{13}S_{51}^2S_5}{1 - S_{12}^2} \tag{3}$$

$$|\Delta V|^2 = P_S\,|S|^2 \tag{4}$$

S_{55}, S_{56}, S_{66}, and S_{65} are the S-parameters at the waveguide aperture of the differential probe, the other S-parameters represent the probe characteristics, and P_s is the power of the source which is assumed to be unity ($P_s = 1$). To simplify the calculations, the probe is assumed to be ideal in the sense that all ports are matched and the probe is reciprocal, symmetrical, and balanced, namely:

$$S_{43} = S_{12} = 0 \tag{5}$$

$$S_{13} = S_{23} = 0.707 = 3\ dB \tag{6}$$

$$S_{41} = -S_{42} = 0.707 = 3\ dB \tag{7}$$

$$S_{51} = S_{62} = 1 = 0\ dB \tag{8}$$

From (1) – (8), the expression for the differential probe output with respect to reflected signals can be obtained, as shown in (9). This corresponds to the output to the Δ port discussed earlier.

$$|\Delta V^2| = |0.5(S_5 - S_6)|^2 \quad (9)$$

Since the two waveguide apertures of the differential probe are adjacent to each other, the differential probe is sensitive to local changes. Ideally, when both the waveguide apertures are inspecting identical surfaces, the two reflected signals will be identical in both phase and magnitudes, which ultimately results in a differential output of zero at the detector. When one of the apertures senses a localized target such as crack, the coherent difference between the two reflected signals will no longer be zero and is registered on the detector. The two cases are illustrated in Figure 1.4, when used for fastener head scanning.

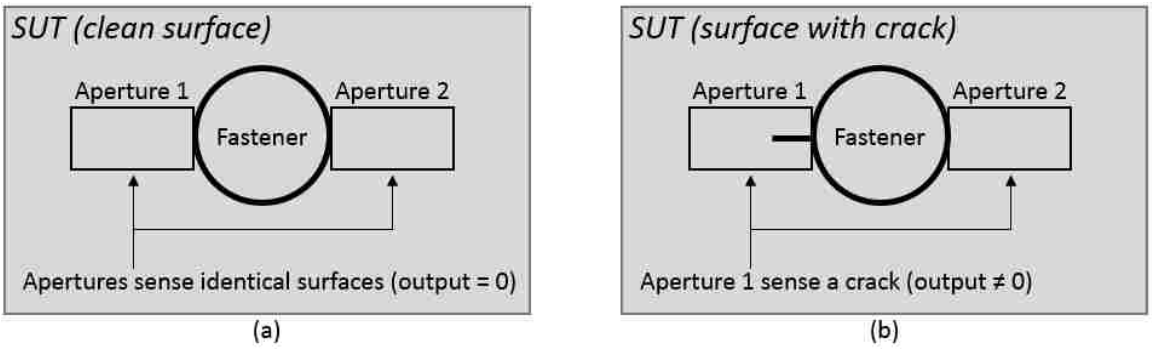

Figure 1.4. Positioning of the differential probe on inspecting: (a) a clean surface, (b) a surface with crack next to the fastener head.

Therefore, a differential probe can be utilized to detect surface cracks near a fastener head, where the scattered signals from the fastener head are coherently subtracted, and the presence of crack registers in the output of the probe. Additionally, the differential probe can overcome the adverse effect of standoff distance variation due to curved surfaces (i.e., aircraft fuselage skins are normally curved), the ability of a differential probe on removing the standoff distance variation had been demonstrated in [26]. Finally, as described, differential probes are inherently sensitive to detecting the presence of small flaws.

The differential probes presented in this thesis operated at V-band (50 – 75 GHz) and W-band (75 – 110 GHz). The V-band differential probe has been introduced in [29] and will be revisited here. This thesis will primarily focus on the crack detection capabilities of the W-band differential probe. The benefits of inspecting riveted structures with high frequency signals are that tiny cracks will appear larger in higher frequencies due to the smaller aperture. Therefore, the practice of using high frequency signals on detecting stress-induced surface cracks (that are normally tiny) increase the probability of detection. Furthermore, since signals of different frequencies (thus different wavelengths) interact with the edges of fastener heads and cracks (if present) differently, multi-frequency measurements were conducted to observe the variations in the probe output due to change in frequencies. In additional, Synthetic Aperture Radar (SAR) filter is applied onto the multi-frequency signals to investigate the efficacy and benefits of such signal processing for improving detection capability, the details of which will be discussed in Section 5. The design process for the optimal W-band differential probe and the finished measurement system will be discussed in Section 2.

1.5. SUMMARY OF SECTIONS

In order to thoroughly investigate the surface crack detection capability of the millimeter-wave differential probe near fastener heads, both numerical simulations and measurements were conducted. The investigation was performed by simulating various scenarios using CST Microwave Studio®, a commercial full wave 3D electromagnetic simulation tool [31]. Furthermore, number of experiments were performed on a skin sample with several fastener heads to illustrate the utility and limitations of this technique for detecting real surface cracks. The simulation results are presented in detail in Section 3, and the measurement results are presented in Section 4 to verify the simulation data. Section 5 represents the results of synthetic aperture processing applied to the multi-frequency data and the corresponding enhancement in crack detection. Section 6 contains some additional numerical simulations to further investigate the potential of differential probe crack detection with a non-uniform paint layer, and Section 7 gives a summary and discussion of the entire investigation and suggestions for future consideration.

2. DIFFERENTIAL PROBE DESIGN & SCANNING SYSTEM

2.1. DIFFERENTIAL PROBE ASSEMBLY & PERFORMANCE

The design of a differential probe requires two collinear waveguides of the magic tee to be transformed into two parallel and side-by-side waveguides. This requires the use of several waveguide sections including: straight sections, 45° bends, and 90° bends, as illustrated in Figure 2.1. The differential probe can be made in two distinct configurations where the millimeter-wave components can either be placed above the dual-waveguide section or within its geometry (Figure 2.2).

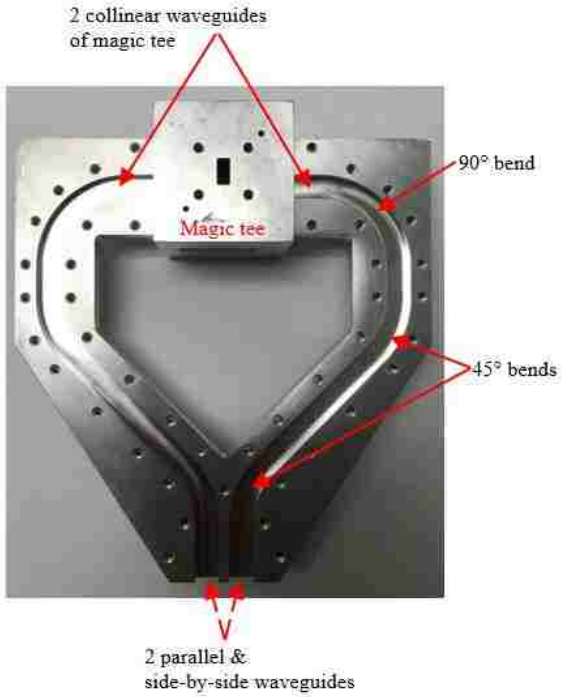

Figure 2.1. Illustration of a machined differential probe.

While electromagnetically the two designs are the same, from mechanical stability point-of-view (while operating the probe as part of an automated measurement system), they are not. Since using either of these two cases requires a different set of

waveguide sections and bends, it is important to investigate the shortest possible length of a bend section while keeping its transmission and reflections performances (S-parameters) acceptable and the overall assembly dimensions as small as possible. Consequently, the electromagnetic properties of the W-band rectangular waveguide straight sections, bends, and the combined structure are simulated using CST, and the results are presented in Sections 2.1.1 through 2.1.3.

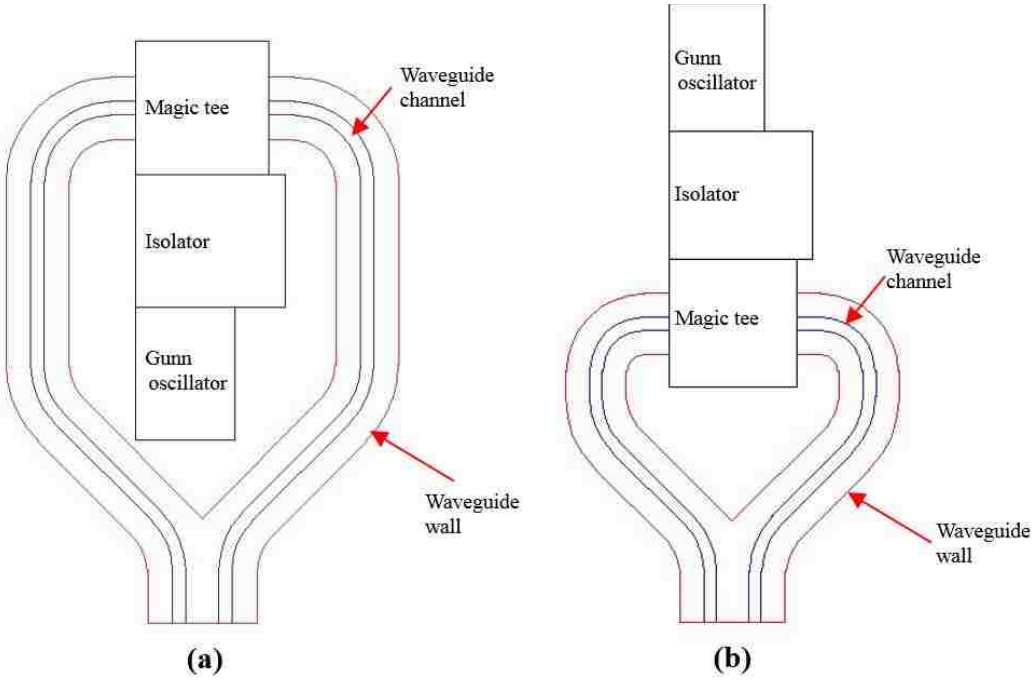

Figure 2.2. Differential probe configurations: millimeter-wave components are: (a) within the waveguide assembly, and (b) above the waveguide assembly.

2.1.1. W-band Rectangular Waveguide. An ideal rectangular waveguide is a transmission line that propagates electromagnetic waves without energy losses, namely, the numerical representations of transmission coefficients (S_{12} and S_{21}) of this 2-port device are 1 (or 0 dB, lossless transmission), and the reflection coefficients (S_{11} and S_{22}) are 0 (-∞ dB, no reflections) [14]. However, real rectangular waveguide transmissions involve losses due to conductor and signal attenuations. To evaluate the performance of a

real W-band (WR-10, operating frequencies from 75 to 110 GHz) rectangular waveguide (with dimensions of $a = 2.54$ mm and $b = 1.27$ mm), the S-parameters of a 10 mm-long W-band rectangular waveguide (Figure 2.3) are simulated and the results are presented in Figure 2.4.

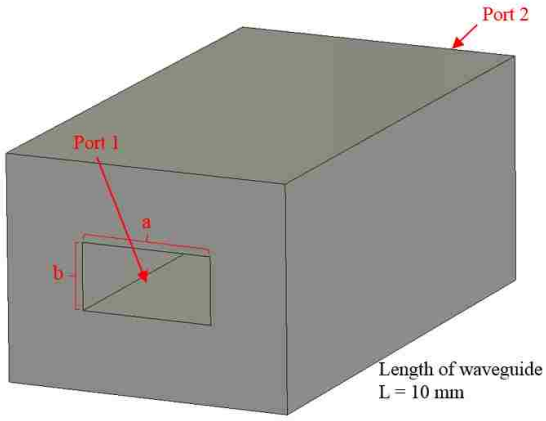

Figure 2.3. Straight W-band rectangular waveguide model.

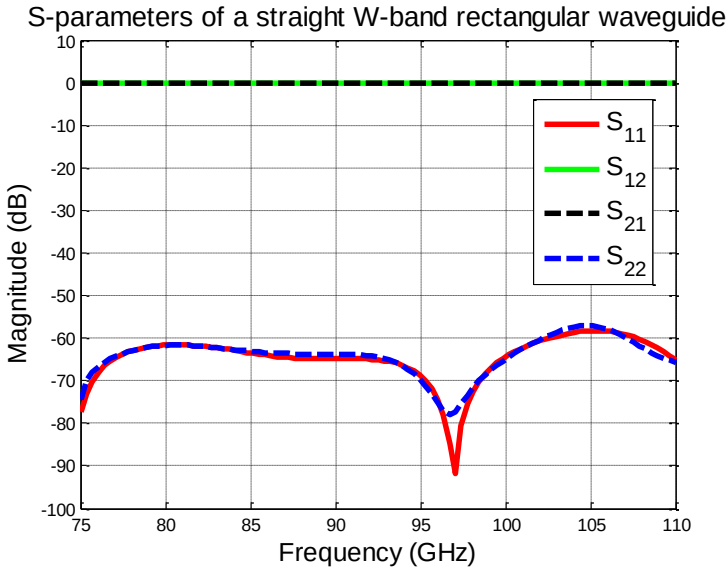

Figure 2.4. Simulated reflection and transmission performances of a straight W-band rectangular waveguide.

The results show that for a straight W-band waveguide, its reflection coefficients average at approximately -60 dB across the frequency band, which implies a very low amount of the reflections back to the source. Consequently, most signals will transmit through the waveguide coincides with transmission coefficients of ~0 dB. The dips in the reflection coefficients at ~97 GHz are due to numerical errors in the simulation. These S-parameter performances will be desired for the complete W-band differential probe assembly.

2.1.2. Waveguide Bend Sections. Waveguide components are commonly designed in a way such that their dimensions (i.e., lengths, widths, and radius of curvatures) are functions of the wavelength (λ) of the operating frequency. In general, λ represents the wavelength of the mid-band frequency of a specific band (for instance, the mid-band frequency of W-band is 92.5 GHz, with corresponding λ of ~3.24 mm). The mid-band frequency is chosen because it represents the average frequency (and wavelength) across a frequency band. By making the waveguide dimensions functions of λ, it allows for a design to be remodeled to operate in other frequency bands easily. For instance, if the complete W-band differential probe is to be redesigned to operate in V-band, the only parameter that needs to be modified is λ, and λ in this case represents the wavelength of the mid-band frequency of V-band. Since the other waveguide dimensions are all relative to λ, the S-parameter performance will be similar. Consequently, the radius of curvatures of both 45° (Figure 2.5) and 90° (Figure 2.6) waveguide bends are defined as a function of the mid-band wavelength of W-band. Each waveguide bend will have straight sections extend out to minimize the phase error produced by the bends.

Shown in Figure 2.7 are the average magnitude of reflection and transmission coefficients for both 45° and 90° waveguide bends, with respect to different values of radius of curvature (with unit of λ). The results show that for both bends, a radius of curvature as small as 0.5λ provides an average reflection coefficient below -40 dB and transmission coefficient of ~0 dB, which constitutes an acceptable performance. Furthermore, a radius of curvature of 2λ or larger provides an average reflection coefficient below -60 dB, which makes the performances comparable to that of a straight W-band rectangular waveguide (Figure 2.4).

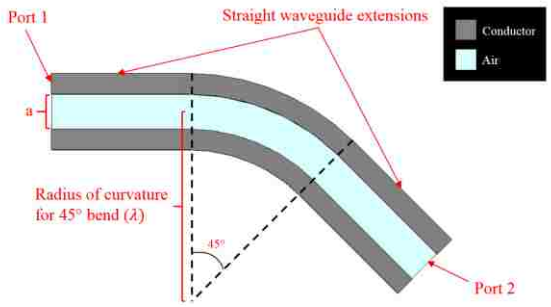

Figure 2.5. Schematic of 45° waveguide bend.

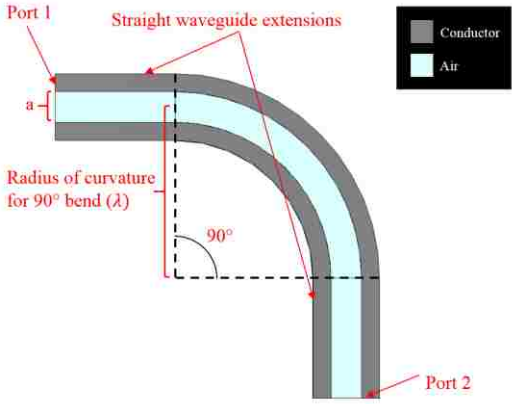

Figure 2.6. Schematic of 90° waveguide bend.

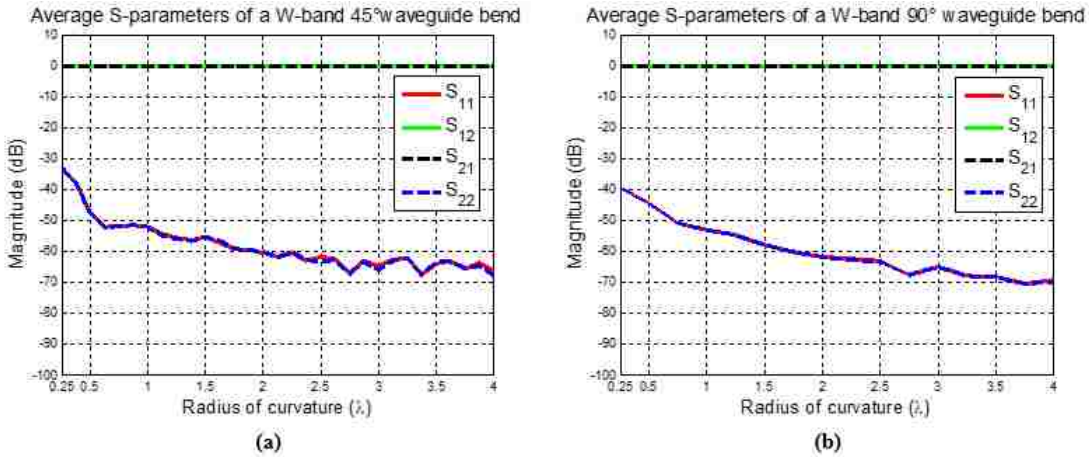

Figure 2.7. Simulated reflection and transmission performances of a W-band: (a) 45° waveguide bend, (b) 90° waveguide bend.

As previously mentioned, two designs were originally considered for the differential probe (Figure 2.2). The first design incorporates the relatively heavy Gunn oscillator and isolator in the middle of the probe assembly, providing for a (mechanically) stable probe. In the second design, the oscillator is placed above the dual-waveguide assembly, making the differential probe top-heavy and (mechanically) moderately unstable and problematic to scan over a sample. Although the latter design provides a smaller overall differential probe assembly, the former design has a much more balanced weight distribution and is preferred for inspection purposes (i.e., where stability of the measurement system is required). The source (Gunn oscillator), isolator, and the magic tee are obtained commercially. Therefore, only the dual waveguide assembly is designed and optimized in this effort.

2.1.3. Waveguide Arm of W-Band Differential Probe. The choice of the waveguide bend radii also needs to be considered given the desire to minimize the overall assembly size. As a result, a bend with a radius of curvature of ~4.1λ (~14.66 mm) and ~4.5λ (~13.97 mm) are selected for the 45° and 90° waveguide bends, respectively. These bend radii result in desired S-parameter performances of the differential probe and optimally encloses the millimeter-wave components. Figure 2.8 shows the schematic of a complete waveguide arm, and its S-parameter performances are simulated and presented in Figure 2.9.

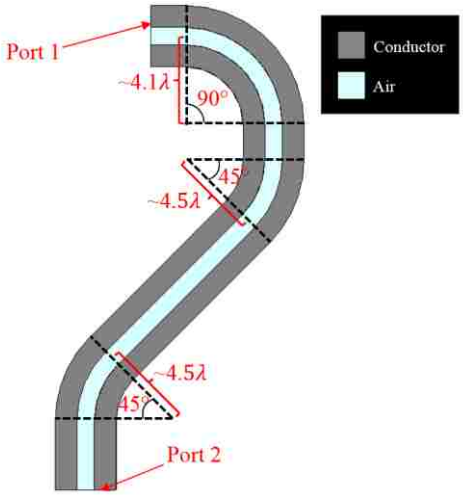

Figure 2.8. Schematic of a complete waveguide arm.

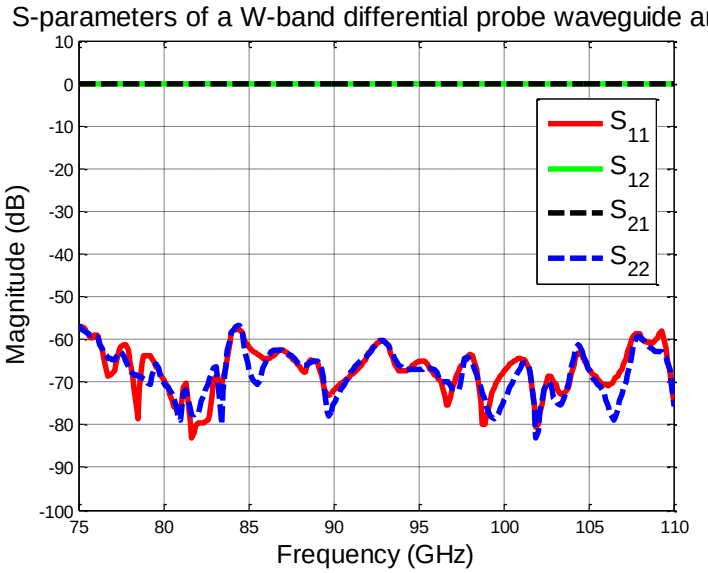

Figure 2.9. Simulated reflection and transmission performances of the designed W-band waveguide arm.

With reflection coefficients average at approximately -60 dB and transmission coefficients at ~0 dB, this design fulfills the electrical and mechanical design requirements. Since the desired performances of the waveguide arms are reached, two waveguide arms are put together (Figure 2.10) with an aperture spacing of 6.35 mm (0.25") between the two waveguide channels, which corresponds to the diameter of a fastener head that will be measured in this investigation. The intention is that by properly aligning the differential probe with the fastener head, the scattered signals from the fastener head can be optimally removed, and the remaining signals will be an indication of surface-breaking cracks (if present). The dual W-band waveguide assembly is simulated and its S-parameter performances are shown in Figure 2.11.

As discussed earlier in Section 1.4, the differential probe signal output is related to the difference between the reflected signals (S_{11} and S_{22}) traveling back to the magic tee. The results in Figure 2.11 suggest that the magnitude of S_{11} and S_{22} are nearly identical when the differential probe is probing the same environment (free-space in this case), therefore the differential probe signal output is ~0. Additionally, the transmission coefficients are low indicating that proper isolations between the two waveguides are

achieved (i.e., the majority of the reflected signals return to the waveguide aperture that transmits the original signal).

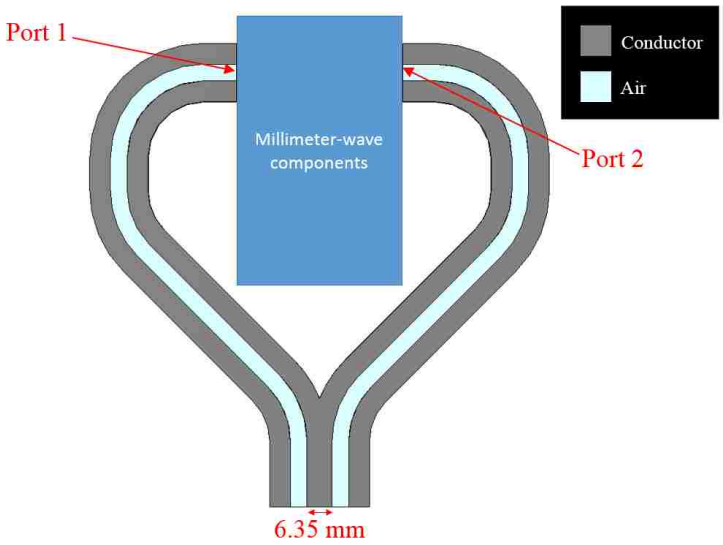

Figure 2.10. Schematic of a complete W-band differential probe.

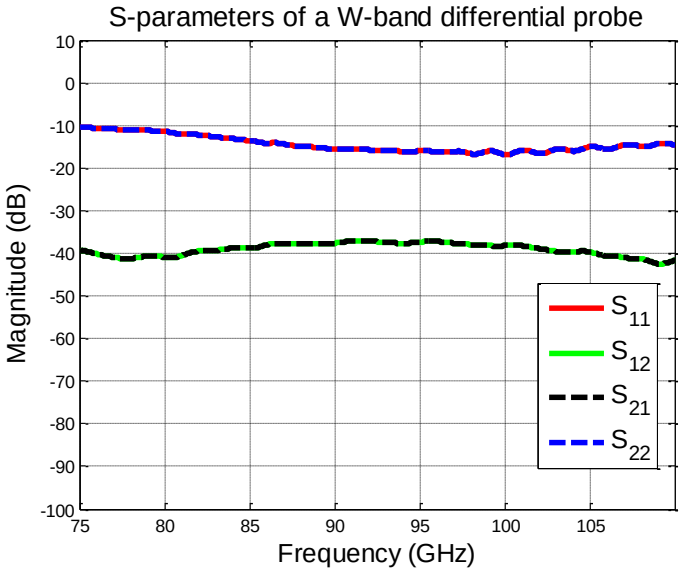

Figure 2.11. Simulated reflection and transmission coefficients of the complete W-band differential probe.

2.2. MEASUREMENT SYSTEM & W-BAND DIFFERENTIAL PROBE

To evaluate the efficacy of the designed and manufactured differential probes for detecting cracks around fastener heads, various measurements were conducted on a 127 mm (5") by 381 mm (15") test panel (Figure 2.12).

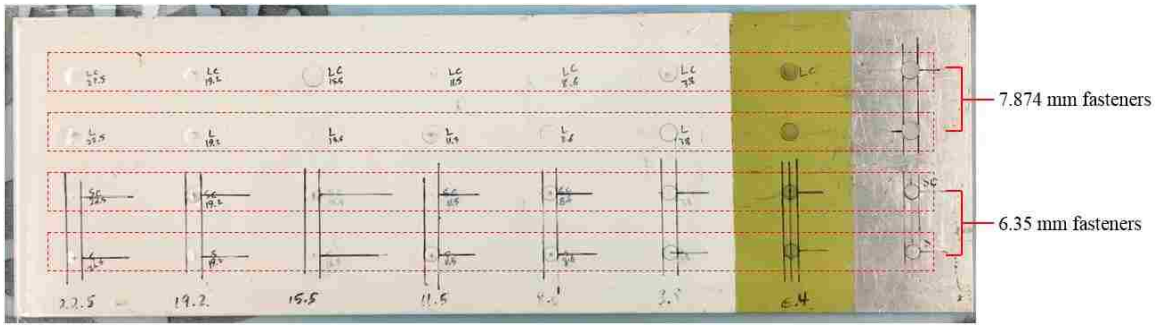

Figure 2.12. Test panel with cracked & un-cracked fastener heads.

This test panel was supplied by the sponsor and has four rows of fastener heads with two different sizes, namely: a small size of 6.35 mm (0.25") in diameter and large size of 7.87 mm (0.31") in diameter. Two of the rows have 1.27 mm (0.05") long surface-breaking notches (created by electrical discharge machining (EDM), Figure 2.13) that could be used to compare to an un-cracked fastener heads. Additionally, this sample has eight sections, distinguished by the thicknesses of paint applied, varying from 0 to 0.572 mm (0" to 0.0225").

Measurements are conducted with an automated 1-D scanner. The scanner is equipped with fixtures for holding both the V-band and W-band differential probes, as shown in Figure 2.14. The differential probe shown in this figure is the W-band probe. Figures 2.15 and 2.16 show the details of the fabricated V-band [29] and W-band differential probe that will be employed for measurements. The spacing between the two waveguide channels is also 6.35 mm for the V-band differential probe, with same reason previously mentioned.

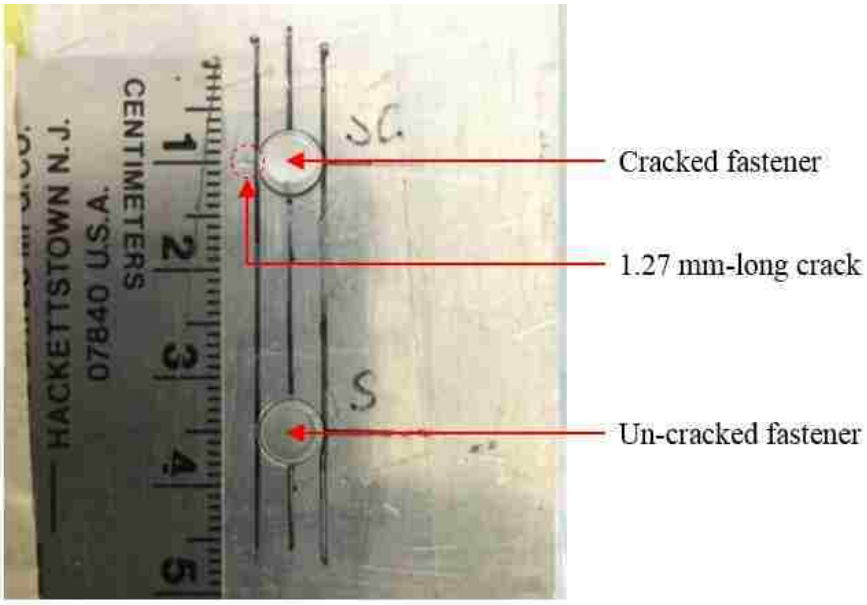

Figure 2.13. Close-up look of 1.27 mm-long surface-breaking crack initiated around a fastener head of 6.35 mm in diameter.

Figure 2.14. Measurement system that incorporates an automated 1-D scanner, and fixtures for holding the differential probes.

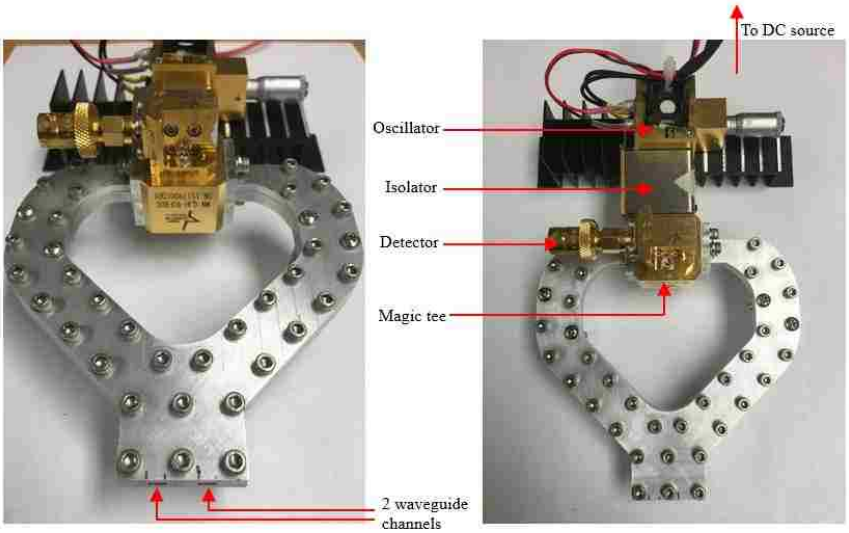

Figure 2.15. V-band differential probe, in slanted (left) and top (right) view.

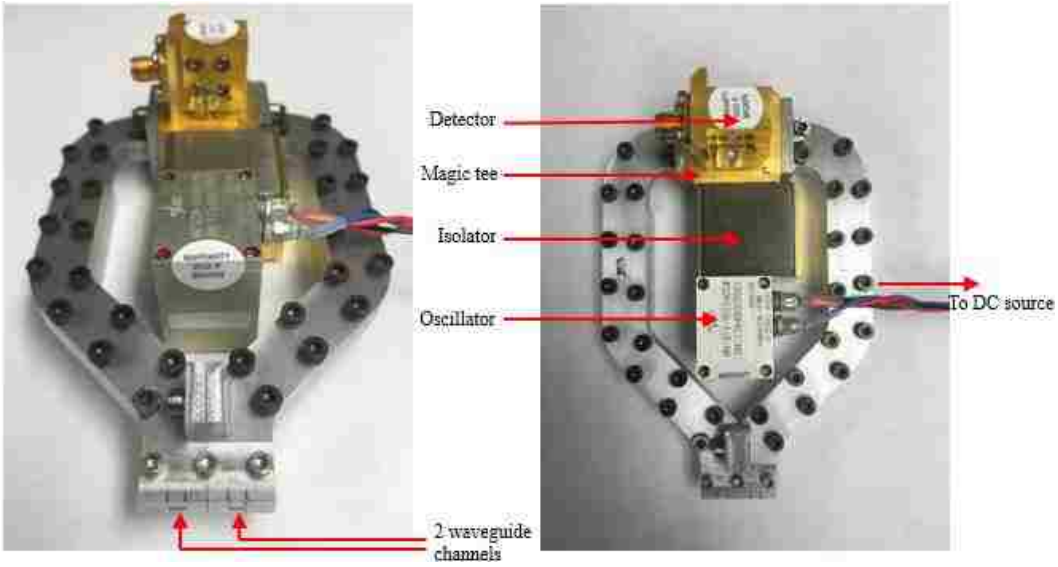

Figure 2.16. W-band differential probe, in slanted (left) and top (right) view.

The measurement system is capable of performing measurements with various adjustments to the probe, allowing for different orientation of the probe. The system is capable of up to five adjustments (degrees of freedom) or relative orientation between the SUT and the probe aperture, namely: three rotational movements and two linear

movements. Shown in Figures 2.17 through 2.19 are the three types of rotational movements that can be applied to the probe. Figure 2.17 shows the rotations of the probe to its sides, this rotation creates an unequal standoff distance between the two waveguide apertures (Aperture Offset). Figure 2.18 shows the rotation of the differential probe with respect to the fastener axis (Probe Offset), this rotation illustrates cases when the probe is not properly aligned with respect to the SUT. Figure 19 illustrates the vertical tilt applied onto the probe which creates un-parallel surfaces between the SUT and probe aperture, this type of rotation is not simulated nor applied onto measurements due to the nature of differential probe for removing standoff variations [26]. The two linear movements describe the ability of adjusting standoff distances and horizontal adjustments of the probe.

These available adjustments and the combinations allow for an extensive set of simulations and measurements with respect to several factors. This fixture will be used to experimentally investigate the effect of various misalignments on detecting cracks near fastener heads at both V-band and W-band frequencies. The results will be discussed in later sections.

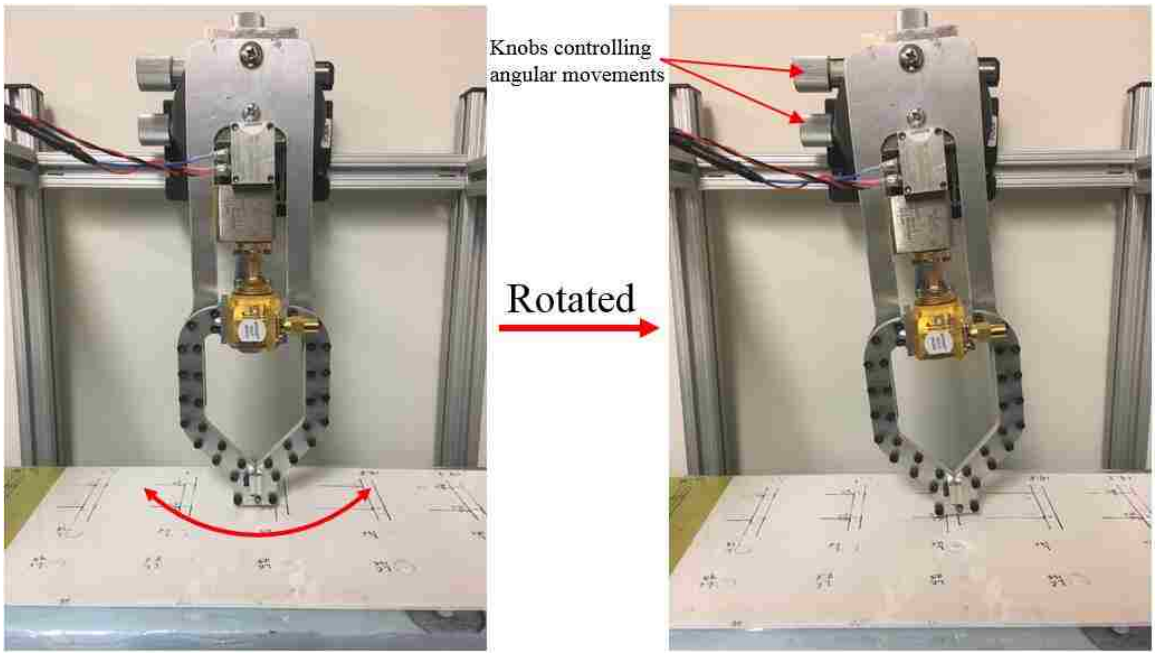

Figure 2.17. Rotational adjustment - aperture offset (type 1).

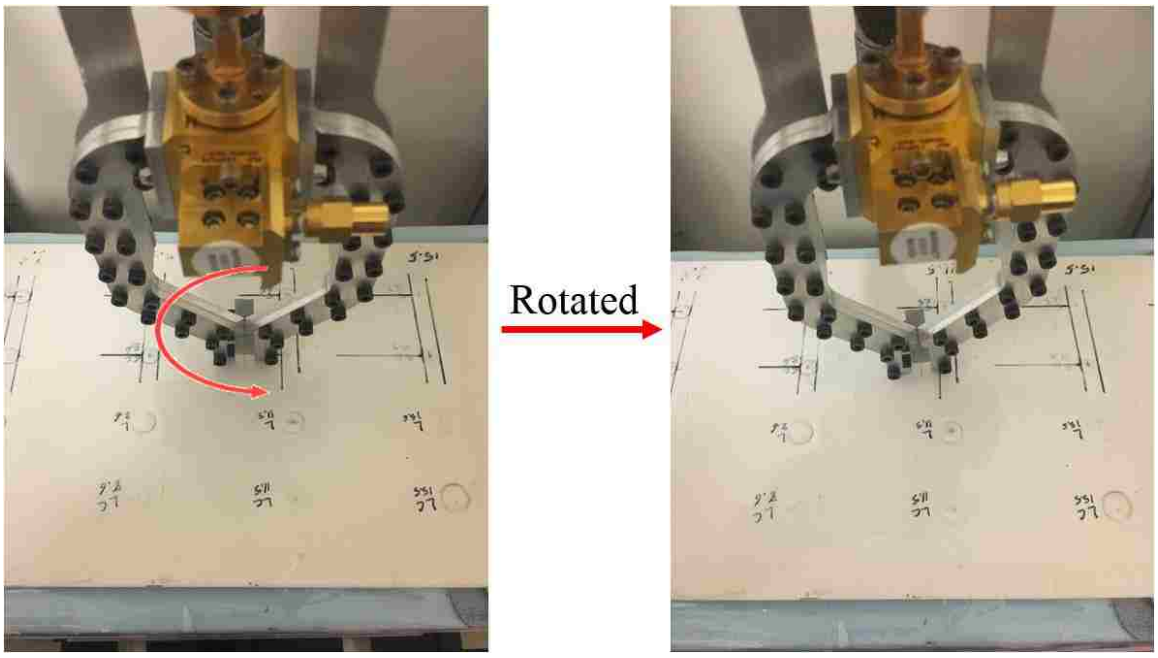

Figure 2.18. Rotational adjustment – probe offset (type 2).

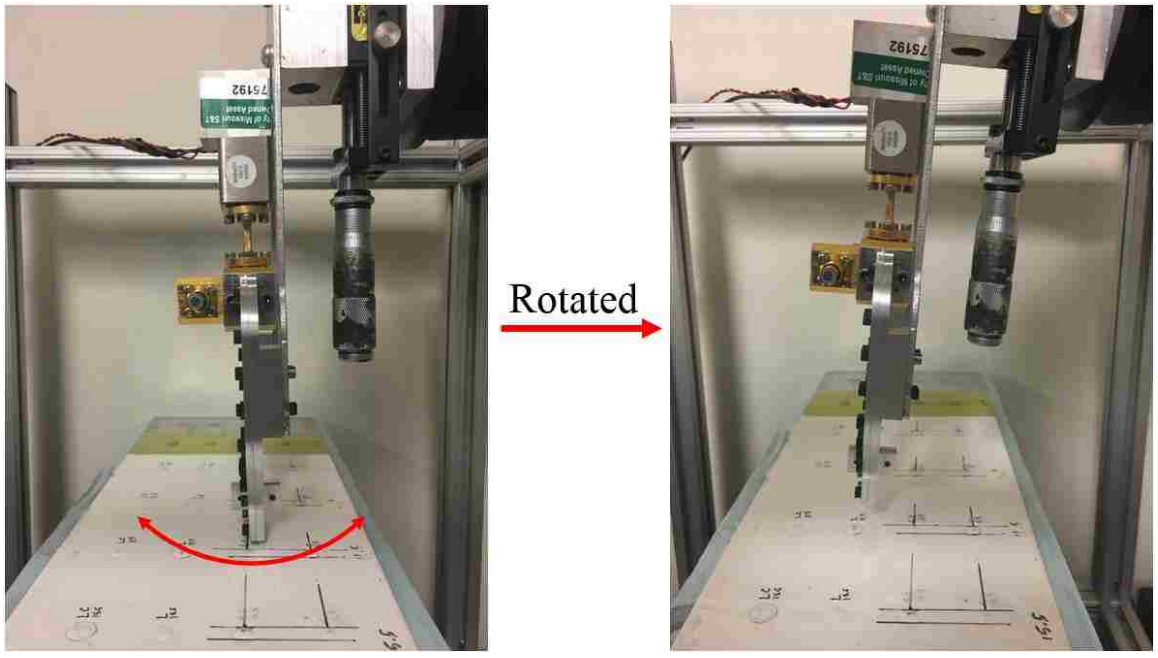

Figure 2.19. Rotational adjustment (type 3).

3. NUMERICAL ANALYSES

Simulations were performed to investigate the effect of potential misalignments of the differential probe, such as standoff distance (Section 3.1), aperture offset (Section 3.2), fastener head tilt (Section 3.3), probe misalignment (Section 3.5) and probe offset (Section 3.6), as well as paint covering the fastener heads and cracks (Section 3.4). The pertinent illustrations of these misalignments can be found in the corresponding sections, respectively. When evaluating the effect of standoff distance for fastener head crack detection capabilities, both W-band and V-band frequencies were considered.

Figure 3.1 shows the models used to simulate 1-D scans of a 1 mm-deep and 0.05 mm-wide surface-breaking crack (with variable crack length) near a fastener head. The sample surface is made of Aluminum with conductivity (σ) of $3.56 \cdot 10^7$ S/m, and the fastener head is made of a conductivity material with (σ) of $3 \cdot 10^7$ S/m, simulating a fastener head made of other materials (e.g., stainless steel, brass, etc.). However, in general millimeter-wave crack detection techniques are not sensitive to variations in the conductivity of the material due to the small skin depths at these frequencies. Therefore, the probe output signal is independent of the conductivities of SUT [29].

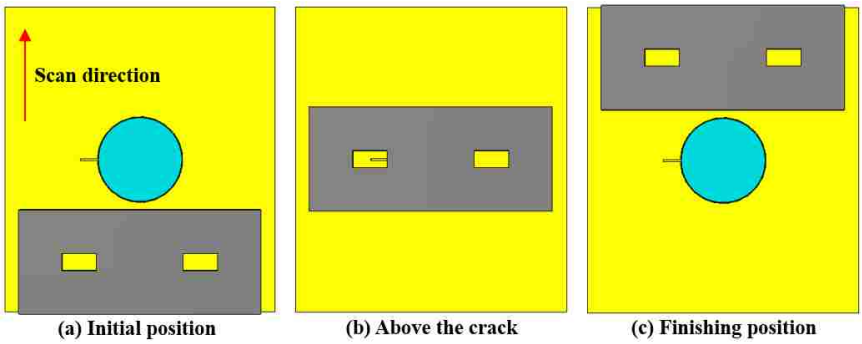

Figure 3.1. Schematic of simulation models.

As illustrated in Figure 3.1, when the probe is at the initial position both waveguide apertures are probing identical surfaces, thus the probe output is ideally zero,

as described earlier. As the probe continues its 1-D movement towards the fastener head, both apertures detect equal scattered signals from the fastener head due to symmetry, which also leads to an ideal probe output of zero. When the probe begins to detect the presence of a crack, the scattered signals from the crack are mostly collected through the aperture shown on the left of Figure 3.1 (b). This leads to a non-zero probe output which represents a detection of surface-breaking crack. Lastly, as the probe moves away from the fastener head (Figure 3.1 (c)), both apertures continue to detect equal scattered signals from the environment (fastener head and sample surface), resulting in a probe output of zero.

3.1. EFFECT OF STANDOFF DISTANCE

The sensitivity of a near-field probe in detecting cracks is highly influenced by standoff distance (and its variation) and frequency of operation. Simulations were performed to investigate the influence of these parameters on the sensitivity of the probe for detecting a crack on the side of a fastener head. Figure 3.2 illustrates the definition of standoff distance, the separation between the SUT and waveguide aperture.

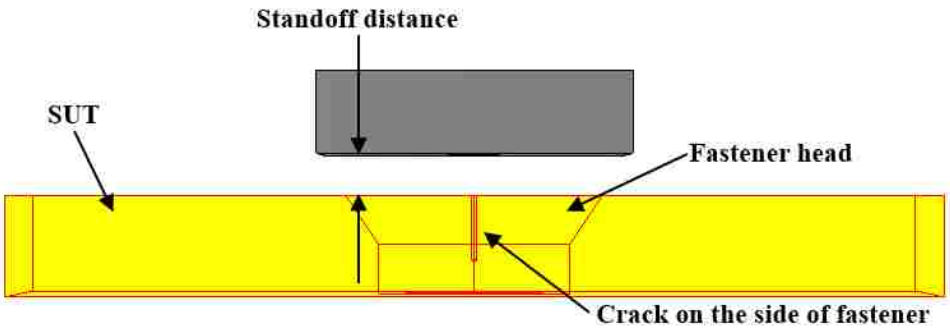

Figure 3.2. Definition of standoff distance (mm).

In the simulations, standoff distances of 0.25, 0.5, 0.75 and 1 mm were considered along with several crack lengths varying from 0 to 2.54 mm (0, 0.635, 1.27, 1.905, 2.54 mm). Twenty-one different frequencies equally spaced within the 75 – 110 GHz range for

W-band probe and within the 50 – 75 GHz range for V-band probe were use in the simulations. Since signals of different frequencies interact with the structure differently due to variation in wavelengths, both the single-frequency and wideband probe responses are investigated. Sections 3.1.1 and 3.1.2 show the results for W-band fastener head scanning while Sections 3.1.3 and 3.1.4 are for V-band results.

3.1.1. W-band Single-Frequency Response. Selected single-frequency results at a fixed standoff distance of 1 mm are shown in Figures 3.3 through 3.6. Results for other standoff distances are provided in Appendix A. The results are provided in both linear and logarithmic scales for a better understanding of correlation between signal responses and crack lengths.

The profiles of the probe output signals on fastener head scanning in these figures match the expectations made earlier, where the probe output is near zero at the starting (-7.5 mm location) and finishing (+7.5 mm location) positions, and a peak signal which represents the presence of a crack shows up around the 0 mm position (where cracks are located).

From Figures 3.3 to 3.6, it can be noticed that the peak signal level is not linearly proportional to crack length at W-band frequencies. In fact, the longest crack (2.54 mm) does not produce the strongest indication. Similar trends can be observed from results at other standoff distances provided in Appendix A.

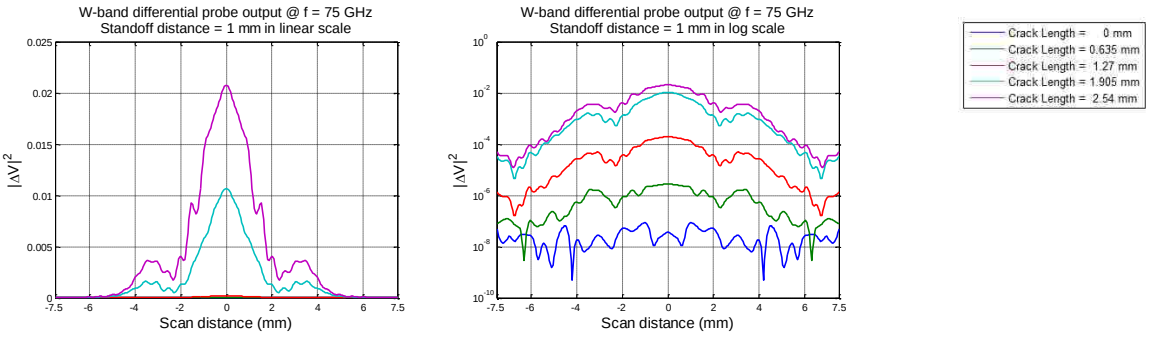

Figure 3.3. Simulated W-band differential probe output signals with various crack lengths, at a standoff distance of 1 mm and frequency of 75 GHz in linear scale (left), and in logarithmic scale (right).

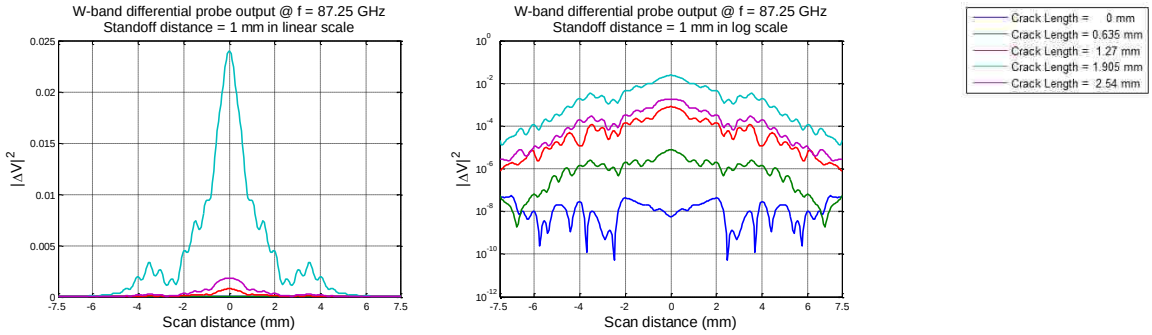

Figure 3.4. Simulated W-band differential probe output signals with various crack lengths, at a standoff distance of 1 mm and frequency of 87.25 GHz in linear scale (left), and in logarithmic scale (right).

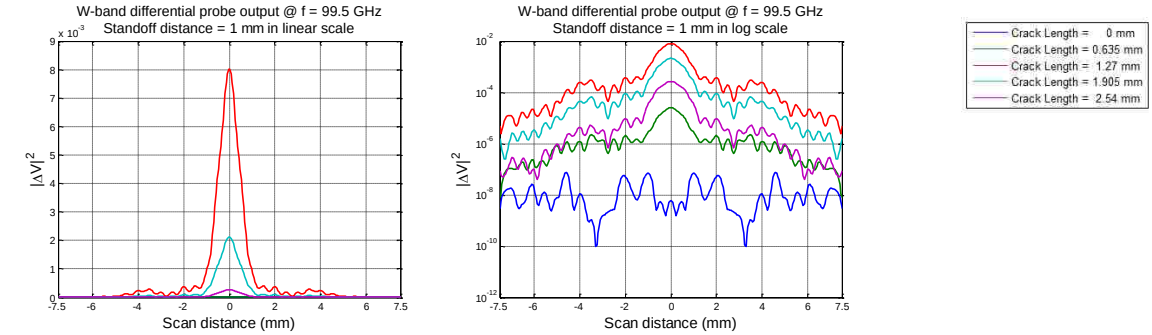

Figure 3.5. Simulated W-band differential probe output signals with various crack lengths, at a standoff distance of 1 mm and frequency of 99.5 GHz in linear scale (left), and in logarithmic scale (right).

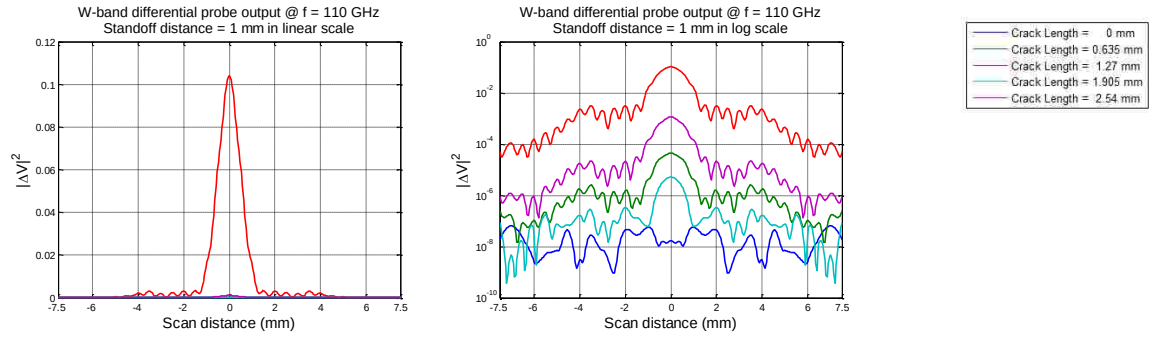

Figure 3.6. Simulated W-band differential probe output signals with various crack lengths, at a standoff distance of 1 mm and frequency of 110 GHz in linear scale (left), and in logarithmic scale (right).

This effect is most likely due to the crack length being near the half-wavelength of operating frequencies and therefore the scattered signals becomes frequency dependent and causes the cracks to resonate. For the frequency of 75 GHz (the lowest frequency in W-band), the signal level is monotonically increasing with the crack length. However, at other frequencies (e.g., 99.5 GHz, Figure 3.5), cracks shorter than 2.54 mm can produce significantly larger crack output signal level. A quick look at the cracks that produce a large signal at a particular frequency shows that crack length is approximately equal to the half-wavelength of that frequency. For instance, in the 110 GHz results shown in Figure 3.6, the 1.27 mm-long crack produces the largest signal and this specific length is very close to the half-wavelength (1.36 mm) at that frequency. These results suggest that W-band frequencies may be useful for detecting cracks of small sizes due to smaller wavelengths. This will be further discussed in later sections.

3.1.2. W-band Wideband Response. The wideband responses of the W-band probe on fastener head scanning with 1 mm standoff distance are shown in Figure 3.7. The purpose of summing up all the single-frequency responses across the bandwidth is that the frequency dependency of the probe output can be averaged, and it also provides a clearer view on the applicability of W-band frequencies for fastener head crack detection.

Figure 3.7 suggests that at this specific standoff distance (1 mm), the W-band probe is sensitive to cracks of lengths approximately between 1.27 and 1.905 mm, for the reasons stated above (the crack lengths are near the half-wavelengths of operating frequencies). Similar observations can be made on results at other standoff distances shown in Appendix A.

Figure 3.8 summarizes the effect of standoff distance on the W-band wideband differential probe crack output signal level. The signal levels in this figure represent the crack responses when the probe is directly above the cracks (i.e., maximum interaction between the transmitted signals and crack occurs).

As expected, the output signal level (associated with a fixed crack length) decreases with respect to increase in standoff distance, due to the increase in traveling distance and the associated radiation losses of the transmitted signals. The only exception is that the longest crack does not produce the strongest indications as discussed earlier. While the higher W-band frequencies provide higher sensitivity to shorter cracks, their

response becomes non-monotonic with crack length. This figure also suggests that W-band frequencies are more sensitive in detecting cracks with dimensions near the half-wavelength in the band.

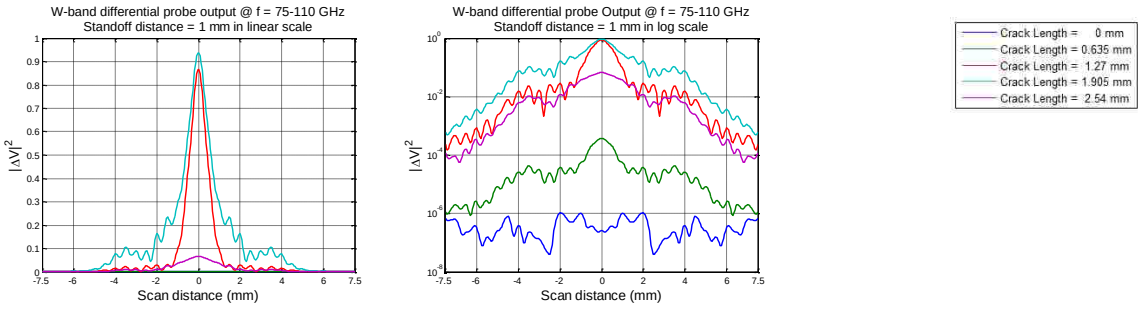

Figure 3.7. Simulated W-band wideband differential probe output signal with various crack lengths, at a standoff distance of 1 mm in linear scale (left), and in logarithmic scale (right).

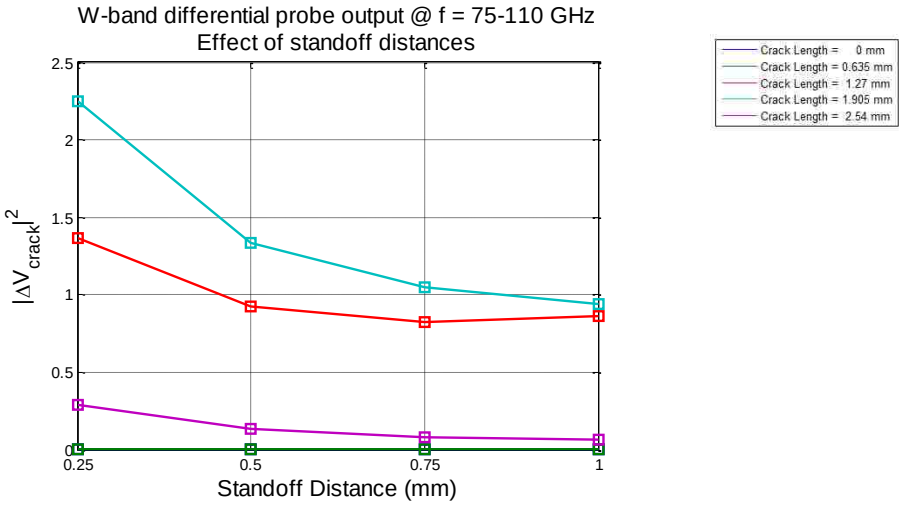

Figure 3.8. Effect of standoff distance on the W-band wideband differential probe crack output signal level.

To better illustrate the effect of standoff distance on the W-band wideband differential probe crack output signal level, the percentages of decreases in the crack

output signal levels versus standoff distance are investigated. To do this, the signals with respect to the different combinations of crack lengths and standoff distances are normalized to the largest (in magnitude) value among them. The results are presented in Figure 3.9, which suggests the same observation, but with percentage of decreases clearly marked.

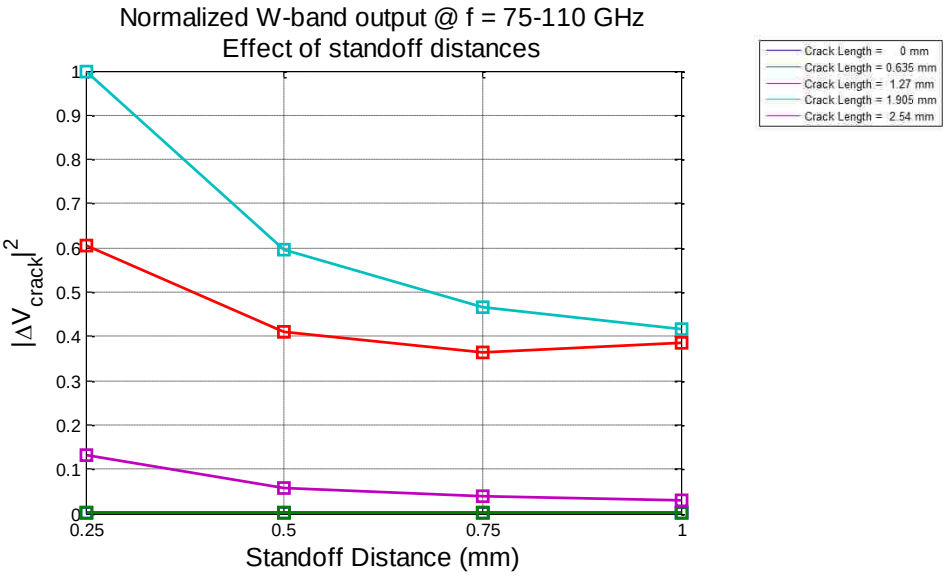

Figure 3.9. Normalized W-band wideband differential probe crack output signal level on effect of standoff distance.

3.1.3. V-band Single-Frequency Response. With the similar setup (but using waveguide dimensions of $\boldsymbol{a}$ = 3.8 mm and $\boldsymbol{b}$ = 1.9 mm for V-band), the simulations were repeated for a V-band probe. Selected single-frequency results at a fixed standoff distance of 1 mm are shown in Figures 3.10 through 3.13. Results for other standoff distances are provided in Appendix A along with the W-band results. The results are provided in both linear and logarithmic scales.

The simulation results demonstrate the capability of V-band probe for fastener head crack detection. The profiles of the V-band probe output signal on fastener head scanning also match expectations, as shown in Sections 3.1.1 and 3.1.2. However, since

the half-wavelength of V-band frequencies is beyond 2 mm, this frequency band likely causes the cracks of lengths of 2 mm or longer to resonate, based on the observations made earlier.

The results from Figures 3.10 through 3.13 confirm that the 2.54-mm long crack now produces the strongest indication, and in fact the crack output signal level is monotonically increasing with the crack length. In addition, the two smaller peaks at around ±4 mm locations are likely due to the edge effects from the probe flange. Similar conclusions can be observed from other standoff distances shown in Appendix A.

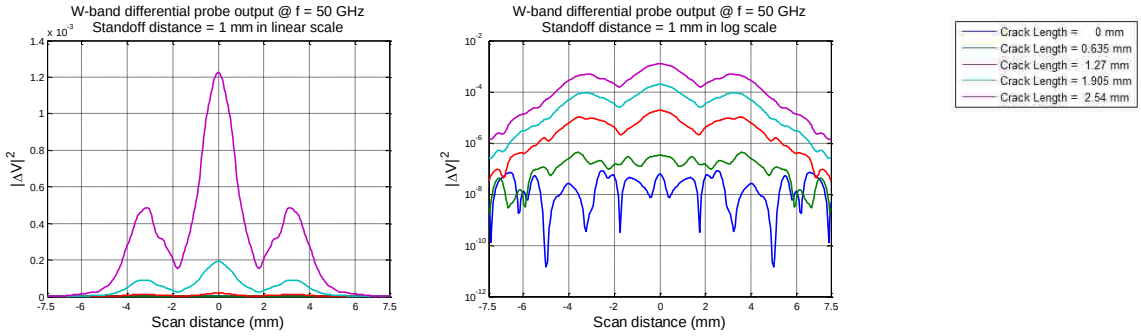

Figure 3.10. Simulated V-band differential probe output signal with various crack lengths, at a standoff distance of 1 mm and frequency of 50 GHz in linear scale (left), and in logarithmic scale (right).

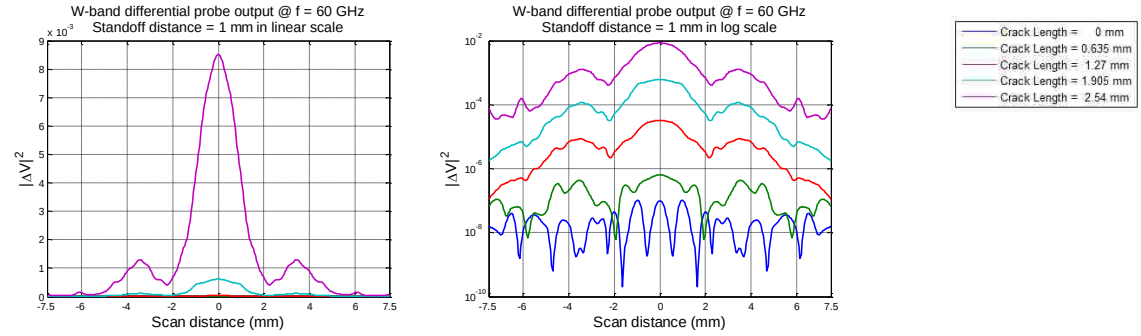

Figure 3.11. Simulated V-band differential probe output signal with various crack lengths, at a standoff distance of 1 mm and frequency of 60 GHz in linear scale (left), and in logarithmic scale (right).

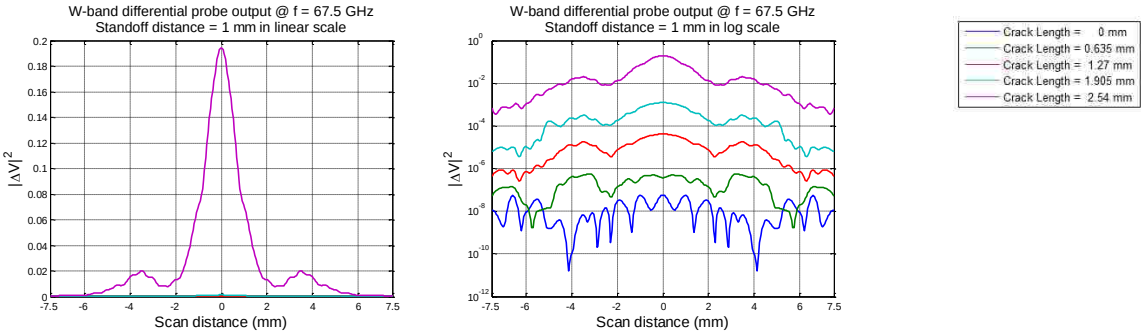

Figure 3.12. Simulated V-band differential probe output signal with various crack lengths, at a standoff distance of 1 mm and frequency of 67.5 GHz in linear scale (left), and in logarithmic scale (right).

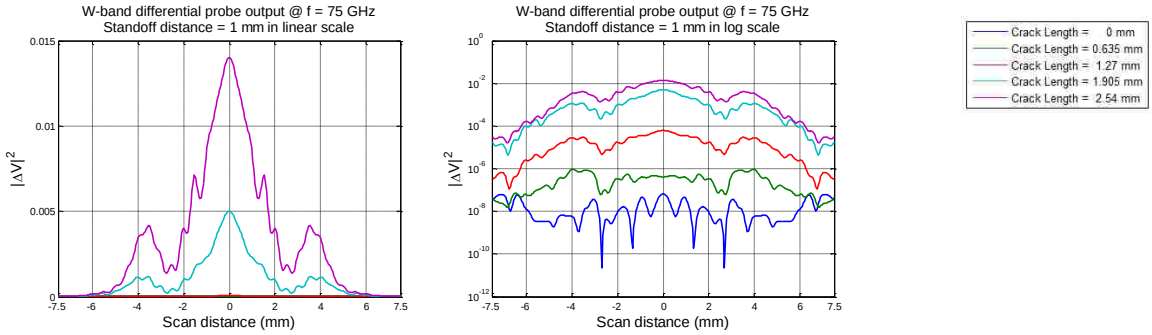

Figure 3.13. Simulated V-band differential probe output signal with various crack lengths, at a standoff distance of 1 mm and frequency of 75 GHz in linear scale (left), and in logarithmic scale (right).

3.1.4. V-band Wideband Response. The wideband responses of the V-band probe on fastener head scanning with 1 mm standoff distance are shown in Figure 3.14. The purpose of summing up all the single-frequency responses across the bandwidth was stated earlier.

Figure 3.14 suggests that at this specific standoff distance (1 mm), the V-band probe is sensitive to crack of length of 2.54 mm, it is also capable of detecting cracks of smaller dimensions but the indications are much weaker. The same observations can be made for other standoff distances and are shown in Appendix A.

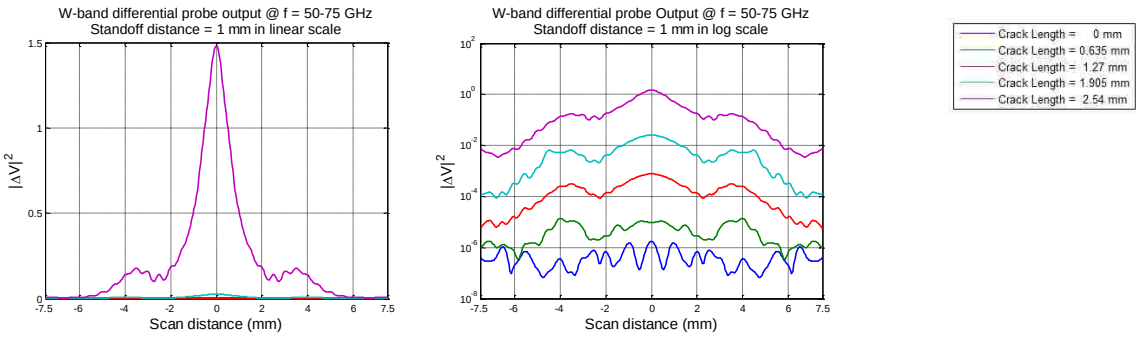

Figure 3.14. Simulated V-band wideband differential probe output signal with various crack lengths, at a standoff distance of 1 mm in linear scale (left), and in logarithmic scale (right).

Figure 3.15 summarizes the effect of standoff distance on the V-band wideband probe crack output signal level. The signal levels in this figure represent the crack responses when the probe is directly above the cracks. As expected, the output signal levels decrease as a function of an increase in standoff distance, similar to the W-band results (Section 3.1.2), and the magnitude increases monotonically with crack length. This figure also suggests that the V-band probe is more sensitive to cracks of longer lengths (greater than ~2 mm).

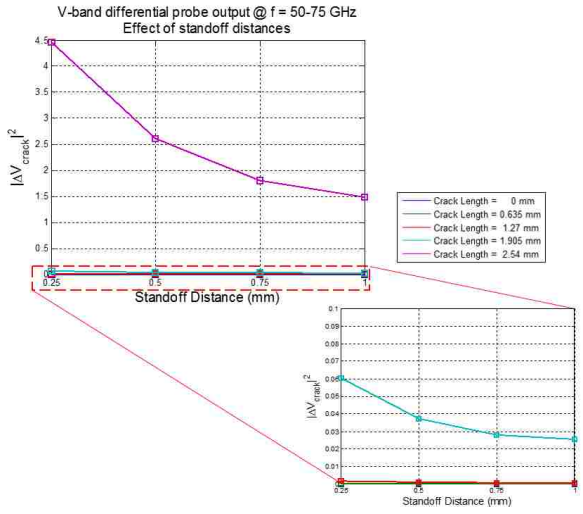

Figure 3.15. Effect of standoff distance on the V-band wideband differential probe crack output signal level.

To better illustrate the effect of standoff distance on the V-band wideband probe crack output signal level, the percentages of decreases in the crack output signal levels versus standoff distance are investigated. To do this, the signals with respect to the different combinations of crack lengths and standoff distances are normalized to the largest (in magnitude) value among them. The results are presented in Figure 3.16, which suggests the same observation, but with percentage of decreases clearly marked.

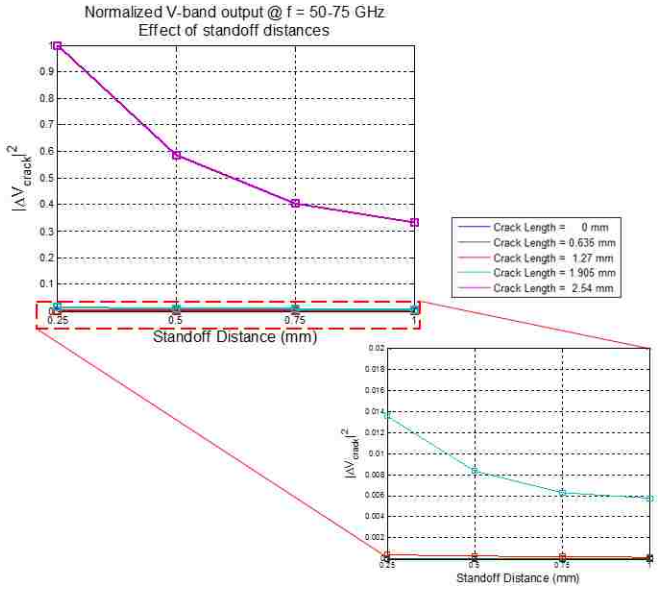

Figure 3.16. Normalized V-band wideband differential probe crack output signal level on effect of standoff distance.

3.2. EFFECT OF APERTURE OFFSET

Occasionally during the measurements, the probe is not optimally aligned with respect to the fastener head, which leads to imperfect cancelation of the scattered signals from the fastener heads and interferes with the signals from the crack, adversely affecting the crack detection capability. This section describes a possible tilt in the probe with respect to the sample surface, or aperture offset. Influences of other types of misalignments will be discussed in later sections.

Aperture offset is defined as the difference in the standoff distance of each probe aperture to the sample surface. A negative aperture offset is when the probe aperture is tilted closer to the crack, and a positive aperture offset is when the probe is tilted away from the crack, as shown in Figure 3.17. In order to reduce simulation time, the actual aperture offsets defined in simulations are as shown in Figure 3.18. The difference between the two models is that the aperture offsets are defined by the angle of rotation (°) on the probe in Figure 3.17, while Figure 3.18 uses distance (mm) instead.

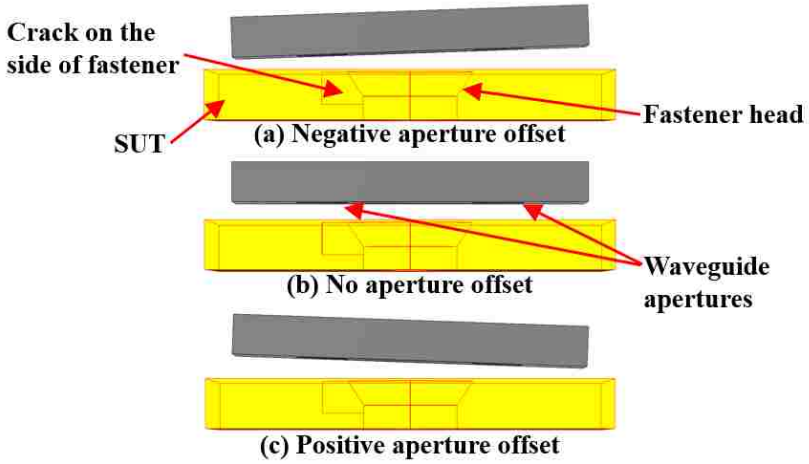

Figure 3.17. Illustration of aperture offsets on differential probe operation.

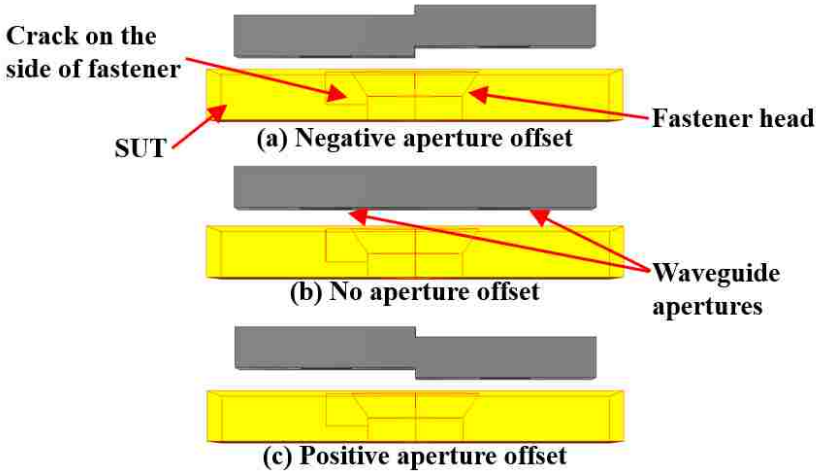

Figure 3.18. Illustrations of aperture offsets used in simulations.

When an aperture offset is applied to a probe, two waveguide apertures are at different standoff distances relative to the sample surface. As discussed in Section 3.1, a higher standoff distance has the likelihood of reducing the magnitude of crack output signal levels due to additional signal losses. Therefore, when a negative aperture offset occurs, the crack output signal level becomes stronger as opposed to when there is no aperture offset, consider the standoff distance being fixed. Similarly, when a positive aperture offset occurs, the crack signal becomes weaker as opposed when no aperture offset occurs. In the simulations, aperture offsets of ±0.5, ±0.25 and 0 mm were considered, as well as standoff distances of 0.5 and 1 mm, with the same crack lengths and frequencies of operation previously mentioned. Both the single-frequency (Section 3.2.1) and wideband (Section 3.2.2) responses are investigated.

3.2.1. Single-Frequency Response. Selected single-frequency results at a fixed standoff distance of 1 mm, and probe aperture offsets of ±0.5 and 0 mm are shown in Figures 3.19 through 3.21. The complete results (standoff distance of 0.5 mm and other aperture offsets) are provided in Appendix B.

These results indicate that an aperture offset (either positive or negative) creates a significant DC bias because of the unequal standoff distances of the two probe apertures, which can interfere with the crack signal and distort it. The non-monotonically correlation between the crack lengths and crack output signal levels is also confirmed here, where the strongest crack output signal levels are from those with lengths approximately between 1.27 and 1.905 mm, close to the half-wavelength of W-band frequencies. For instance, in the 83.75 GHz results (Figure 3.20), the 1.905 mm-long crack produced the largest signal (in magnitude) and that length is close to the half-wavelength at that frequency (1.79 mm). Another example is at the frequency of 110 GHz (Figure 3.21), where the largest signal is due to the 1.27 mm-long crack, which is close to the half-wavelength at that frequency (1.36 mm).

These single-frequency responses show that the signal levels are highly influenced by the bias caused by the aperture offset. The signal peaks that are near the edges of the scans (±7.5 mm location) are due to edge effects.

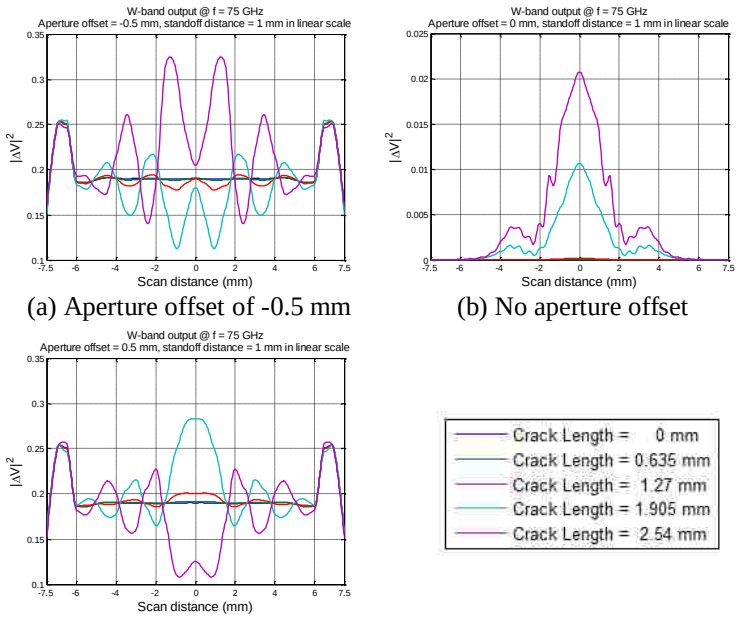

(a) Aperture offset of -0.5 mm (b) No aperture offset

(c) Aperture offset of +0.5 mm

Figure 3.19. Simulated W-band differential probe output signals with various crack lengths, at a standoff distance of 1 mm, frequency of 75 GHz, and aperture offset of (from (a) to (c)): -0.5 mm, 0, and +0.5 mm.

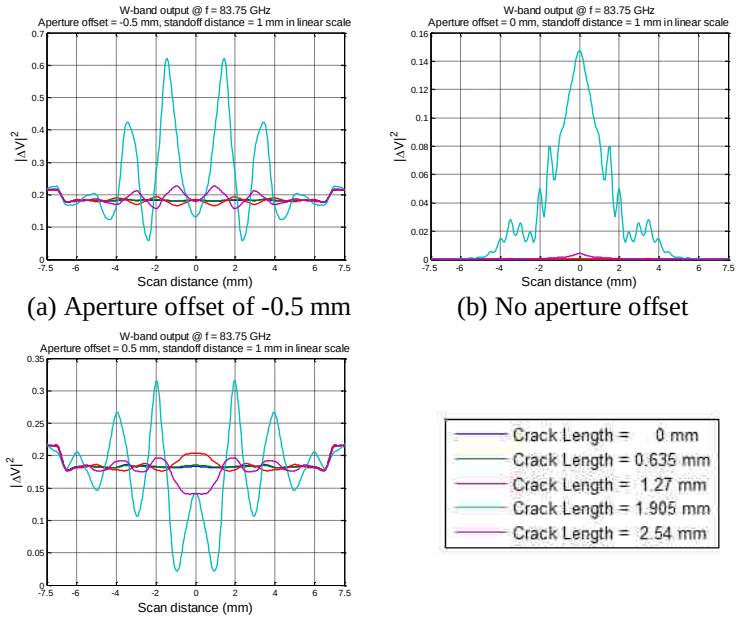

(a) Aperture offset of -0.5 mm (b) No aperture offset

(c) Aperture offset of +0.5 mm

Figure 3.20. Simulated W-band differential probe output signals with various crack lengths, at a standoff distance of 1 mm, frequency of 83.75 GHz, and aperture offset of (from (a) to (c)): -0.5 mm, 0, and +0.5 mm.

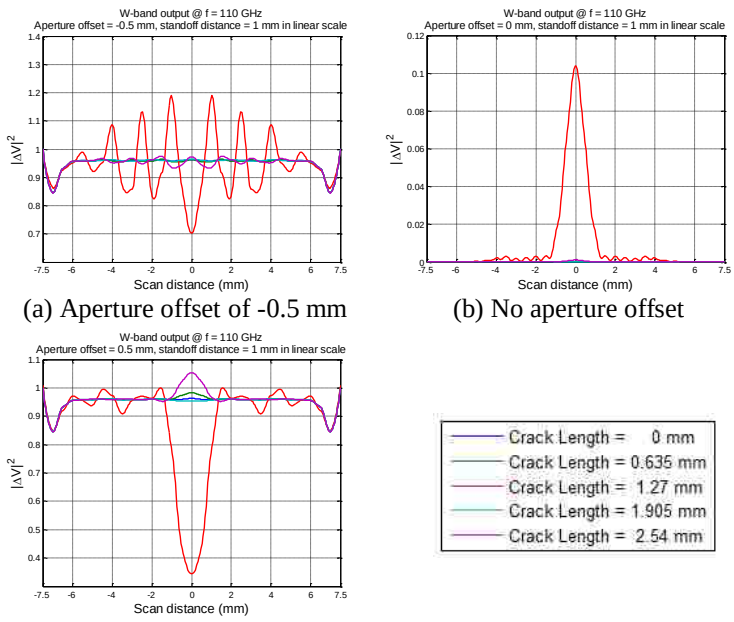

(a) Aperture offset of -0.5 mm (b) No aperture offset

(c) Aperture offset of +0.5 mm

Figure 3.21. Simulated W-band differential probe output signals with various crack lengths, at a standoff distance of 1 mm, frequency of 110 GHz, and aperture offset of (from (a) to (c)): -0.5 mm, 0, and +0.5 mm.

In an attempt to observe a correlation between crack output signal levels and aperture offsets, the DC bias is estimated (the probe output signal levels without the presence of a crack) and removed from other crack output signal levels. Therefore, the crack output signal levels are now referenced (all the common factors are removed, in this case the DC bias), as shown in Figures 3.22 through 3.24.

The referenced probe output signals are clearer when it comes to evaluating the relationship between aperture offsets and crack output signal levels. These results indicate that a negative aperture offset causes the largest crack output signal levels and a broader main lobe. This can be expected as the probe is tilted towards the crack, effectively decreases the distance between the probe aperture and the crack. The crack output signal levels reduce as the aperture is tilted away from the crack.

3.2.2. Wideband Response. The wideband responses (with DC bias removed) of the W-band probe on fastener head scanning with 1 mm standoff distance and aperture offsets of ±0.5 and 0 mm are shown in Figure 3.25.

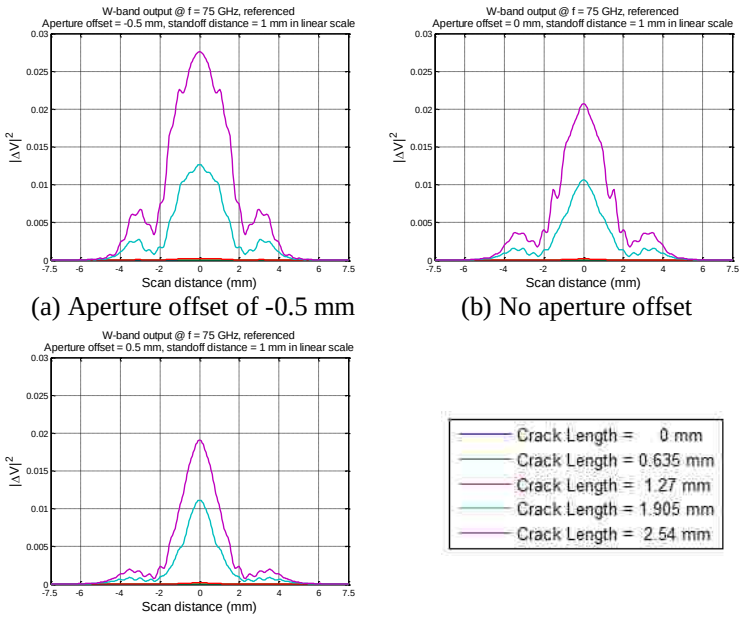

(a) Aperture offset of -0.5 mm (b) No aperture offset

(c) Aperture offset of +0.5 mm

Figure 3.22. Simulated W-band differential probe output signals (referenced) with various crack lengths, at a standoff distance of 1 mm, frequency of 75 GHz, and aperture offset of (from (a) to (c)): -0.5 mm, 0, and +0.5 mm.

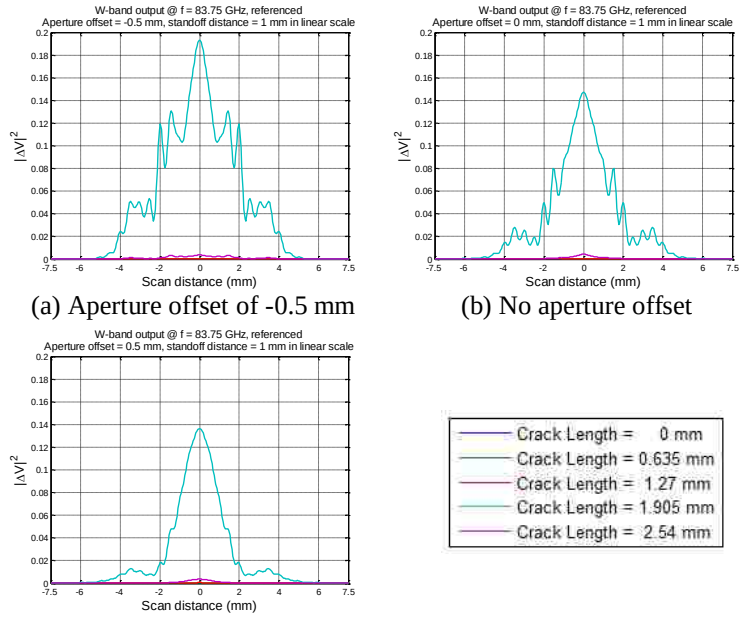

(a) Aperture offset of -0.5 mm (b) No aperture offset

(c) Aperture offset of +0.5 mm

Figure 3.23. Simulated W-band differential probe output signals (referenced) with various crack lengths, at a standoff distance of 1 mm, frequency of 83.75 GHz, and aperture offset of (from (a) to (c)): -0.5 mm, 0, and +0.5 mm.

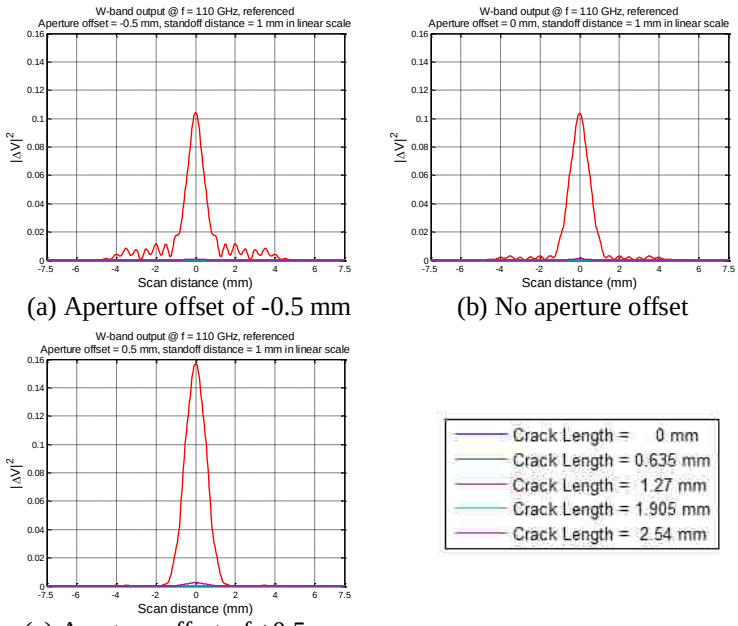

(a) Aperture offset of -0.5 mm

(b) No aperture offset

(c) Aperture offset of +0.5 mm

Figure 3.24. Simulated W-band differential probe output signals (referenced) with various crack lengths, at a standoff distance of 1 mm, frequency of 110 GHz, and aperture offset of (from (a) to (c)): -0.5 mm, 0, and +0.5 mm.

Figure 3.25 suggests that at this specific standoff distance (1 mm), the W-band probe is sensitive to cracks of lengths approximately between 1.27 and 1.905 mm as observed earlier. Also, if the DC bias can be removed from the output signals, the presence of an aperture offset has minimal effect on fastener head crack detection. Similar conclusions can be observed for other standoff distances and aperture offsets shown in Appendix B.

Figures 3.26 and 3.27 summarize the effect of aperture offset on the W-band wideband differential probe crack output signal level, at standoff distances of 0.5 and 1 mm, respectively. The signal levels in these figures represent the crack responses when the probe is directly above the cracks.

Figures 3.26 and 3.27 suggest that the variations in crack signal levels that are due to aperture offsets are almost as significant as to variations due to changes in standoff distance. But, the presence of aperture offsets is not critical in terms of crack detection capabilities. When the standoff distance is small (0.5 mm), the crack output signal levels

reduce with respect to increasing aperture offsets, which is expected because of the increasing distance between the crack and the probe aperture.

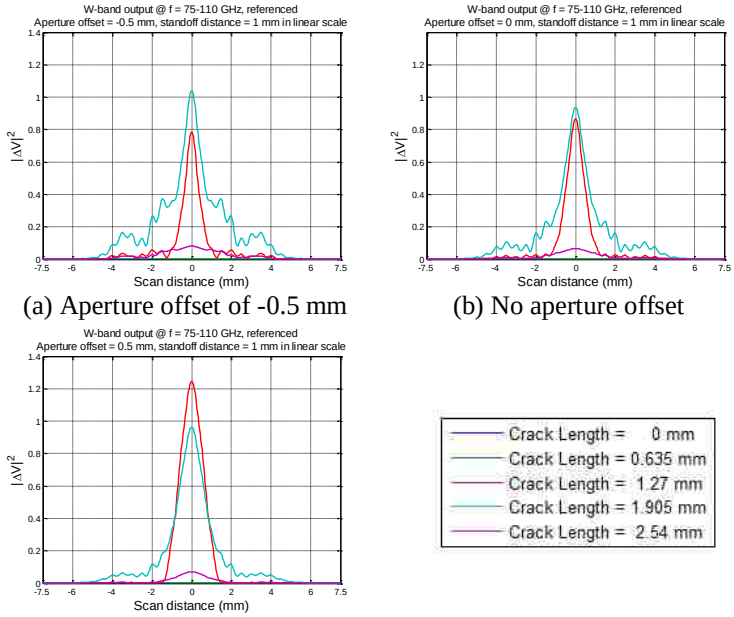

(a) Aperture offset of -0.5 mm (b) No aperture offset

(c) Aperture offset of +0.5 mm

Figure 3.25. Simulated W-band wideband differential probe output signal (referenced) with various crack lengths, at a standoff distance of 1 mm, and aperture offset of (from (a) to (c)): -0.5 mm, 0, and +0.5 mm.

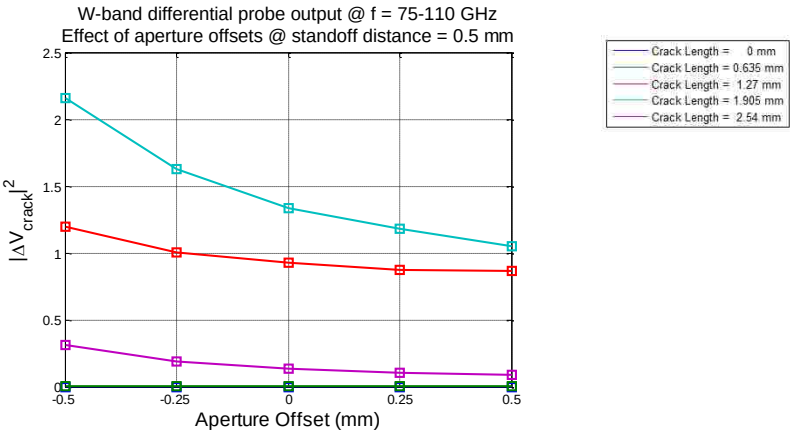

Figure 3.26. Effect of aperture offset on the W-band wideband differential probe crack output signal level (referenced), at standoff distance of 0.5 mm.

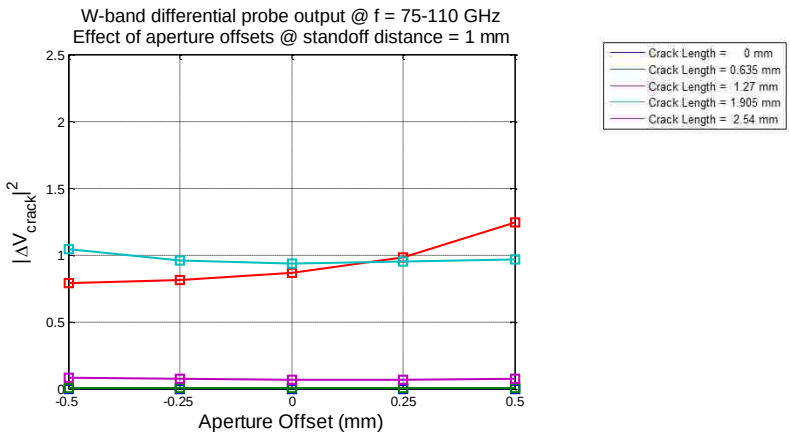

Figure 3.27. Effect of aperture offset on the W-band wideband differential probe crack output signal level (referenced), at standoff distance of 1 mm.

To better illustrate the effect of aperture offset on the W-band wideband differential probe crack output signal level, the percentages of decreases in the crack output signal levels versus aperture offsets, and standoff distances of 0.5 and 1 mm are investigated. To do this, the signals with respect to the different combinations of crack lengths, standoff distances, and aperture offsets are normalized to the largest (in magnitude) value among them. The results are presented in Figures 3.28 and 3.29.

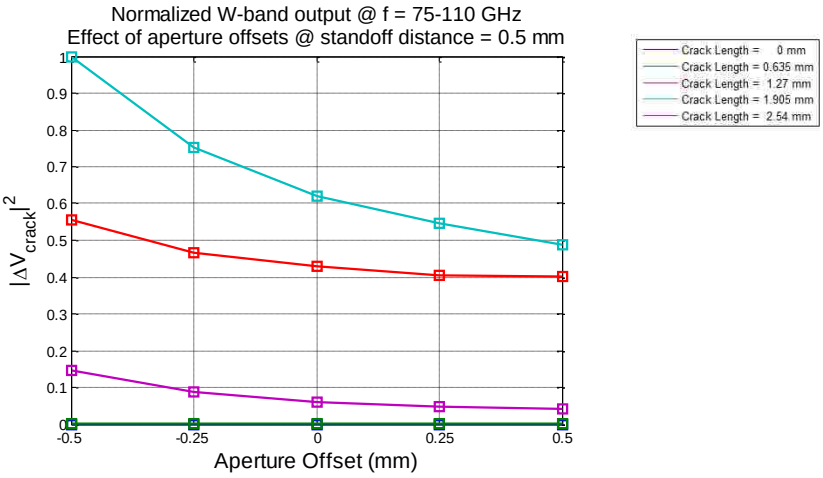

Figure 3.28. Normalized W-band wideband differential probe crack output signal level (referenced) on effect of aperture offset, at standoff distance of 0.5 mm.

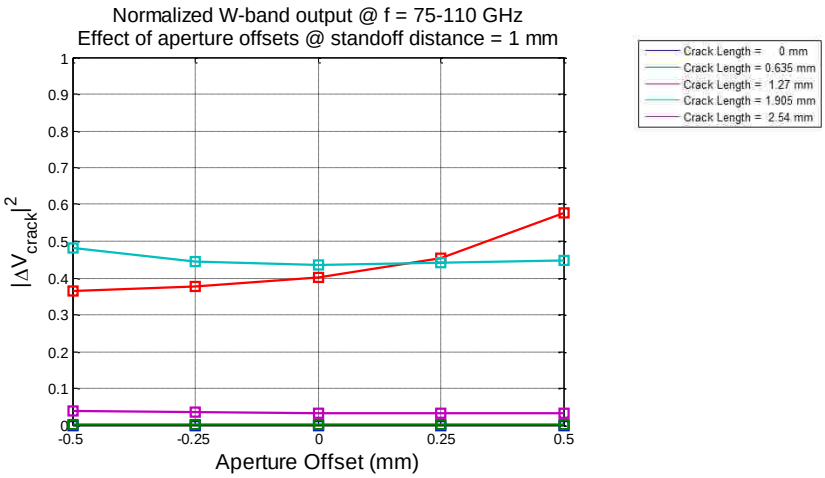

Figure 3.29. Normalized W-band wideband differential probe crack output signal level (referenced) on effect of aperture offset, at standoff distance of 1 mm.

These results suggest that at W-band the strongest crack signals occur for a 1.905 mm-long crack with an aperture offset of -0.5 mm, when the aperture is closer to the crack (i.e., relatively shorter standoff distance compared to another aperture). The results also show that the presence of an aperture offset only impacts the crack signals significantly when inspecting cracks in a close distance. Otherwise the signal drops with respect to standoff distance are more significant.

3.3. EFFECT OF FASTENER HEAD TILT

This section describes a potential tilt in the fastener head with respect to the sample surface, or fastener head tilt. Fastener head tilt is defined as the angular displacement (in degrees) between the edge of the sample surface (on the side where crack exists) and the adjacent edge of fastener head, causing one side of the fastener head to be raised above the sample surface and the other side to be embedded inside the skin sample. A negative fastener head tilt is when the fastener head is tilted below the sample surface, and a positive fastener head tilt is when the fastener head is tilted above the sample surface, as shown in Figure 3.30.

The occurrence of a fastener head tilt is similar to an aperture offset, where the two probe apertures are at different standoff distances relative to the fastener head.

However, the presence of a fastener head tilt may have a much more significant effect on crack signals since the fastener head edge is expected to create a relatively strong scattered signals and therefore an undesired effect on the probe output signal. When a positive fastener head tilt occurs, for which the fastener head edge is higher than the crack, the probe becomes more sensitive to the fastener head than to a crack, and this may lead to distortion in probe output signal potentially resulting in missing the crack.

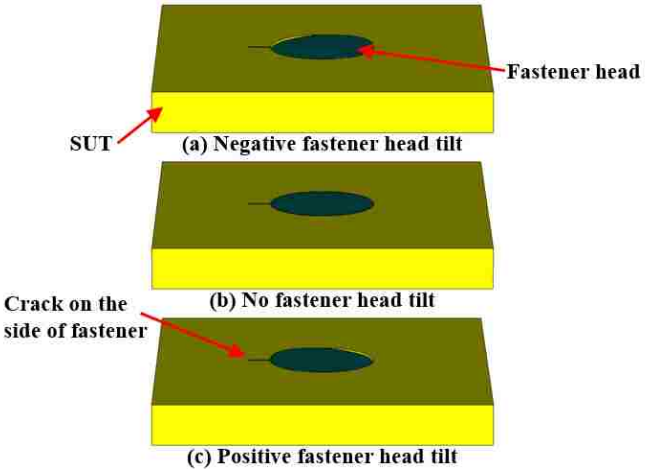

Figure 3.30. Definition of fastener head tilt.

In the simulations, fastener head tilts of ±3°, ±1.5° and 0° were considered, as well as standoff distances of 0.5 and 1 mm, with the same crack lengths and frequencies of operations previously mentioned. Both the single-frequency (Section 3.3.1) and wideband (Section 3.3.2) responses are investigated.

3.3.1. Single-Frequency Response. Selected single-frequency results at a fixed standoff distance of 1 mm, and fastener head tilts of ±3° and 0° are shown in Figures 3.31 through 3.33. The complete results (standoff distance of 0.5 mm and other fastener head tilts) are provided in Appendix C.

These results indicate that when the fastener head is negatively tilted, the probe output signal is not significantly affected when compared to the no-tilt case. However, when the fastener head is positively tilted, the scattered signals from the fastener head

edge causes significant scattered signals and overwhelms the probe response. These single-frequency results confirm that a positively tilted faster head influences the capability of the probe for crack detection as the probe becomes more sensitive to the fastener head edges.

3.3.2. Wideband Response. The wideband responses of the W-band probe on fastener head scanning with 1 mm standoff distance, and fastener head tilts of ±3°and 0° are shown in Figure 3.34.

Figure 3.34 suggests that at this specific standoff distance (1 mm), the W-band probe is sensitive to cracks of lengths approximately between 1.27 and 1.905 mm as observed earlier. The wideband responses also show that a positive fastener head tilt has more of an effect on the probe output signal variations than a negative fastener head tilt, and a negative fastener head tilt actually enhances the crack output signal levels. Similar observations can be made on the results for a standoff distance of 0.5 mm provided in Appendix C.

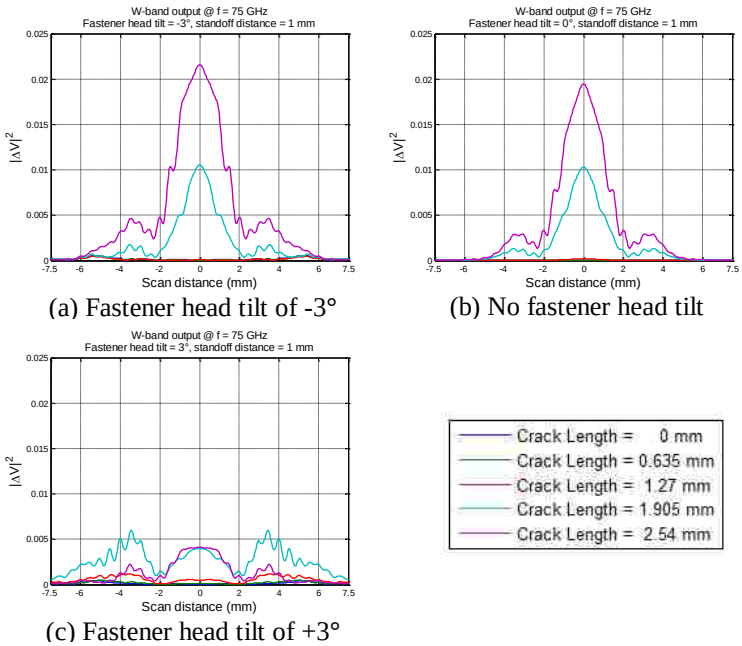

(a) Fastener head tilt of -3°

(b) No fastener head tilt

(c) Fastener head tilt of +3°

Figure 3.31. Simulated W-band differential probe output signals with various crack lengths, at a standoff distance of 1 mm, frequency of 75 GHz, and fastener head tilt of (from (a) to (c)): -3°, 0°, and +3°.

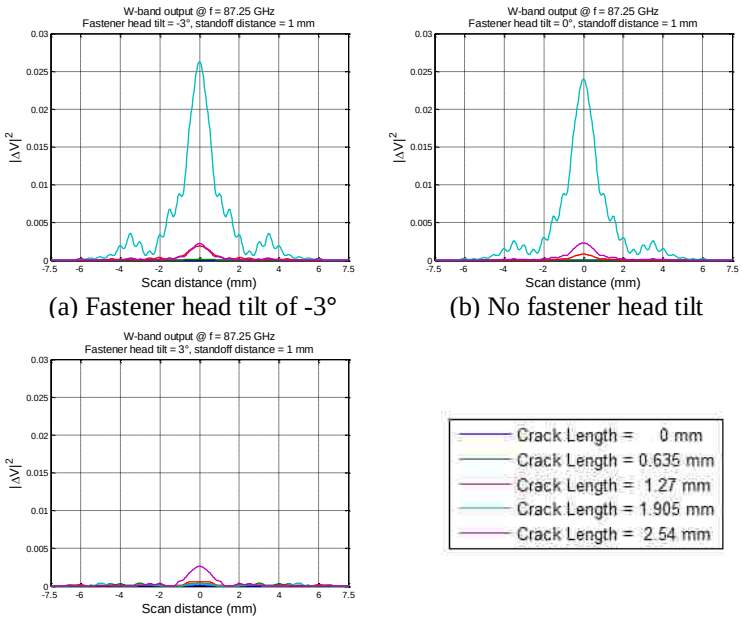

(a) Fastener head tilt of -3°

(b) No fastener head tilt

(c) Fastener head tilt of +3°

Figure 3.32. Simulated W-band differential probe output signals with various crack lengths, at a standoff distance of 1 mm, frequency of 87.25 GHz, and fastener head tilt of (from (a) to (c)): -3°, 0°, and +3°.

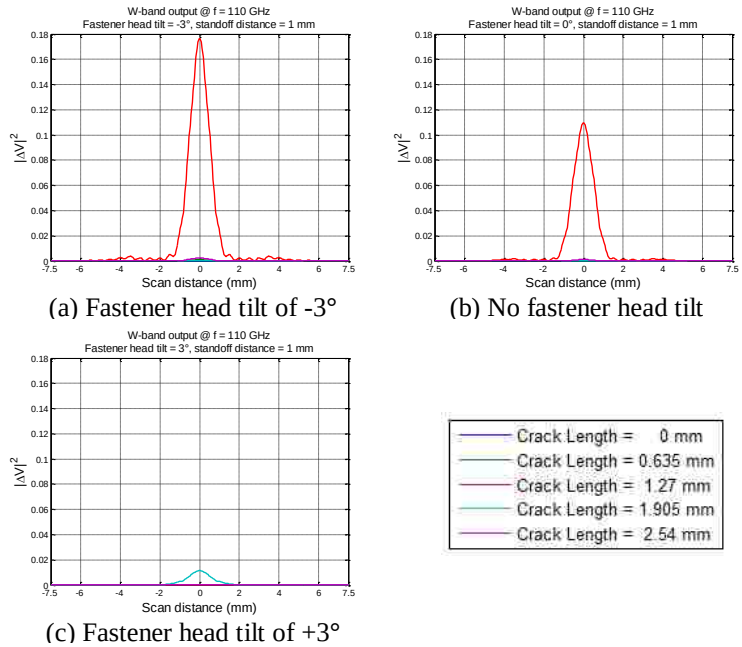

(a) Fastener head tilt of -3°

(b) No fastener head tilt

(c) Fastener head tilt of +3°

Figure 3.33. Simulated W-band differential probe output signals with various crack lengths, at a standoff distance of 1 mm, frequency of 110 GHz, and fastener head tilt of (from (a) to (c)): -3°, 0°, and +3°.

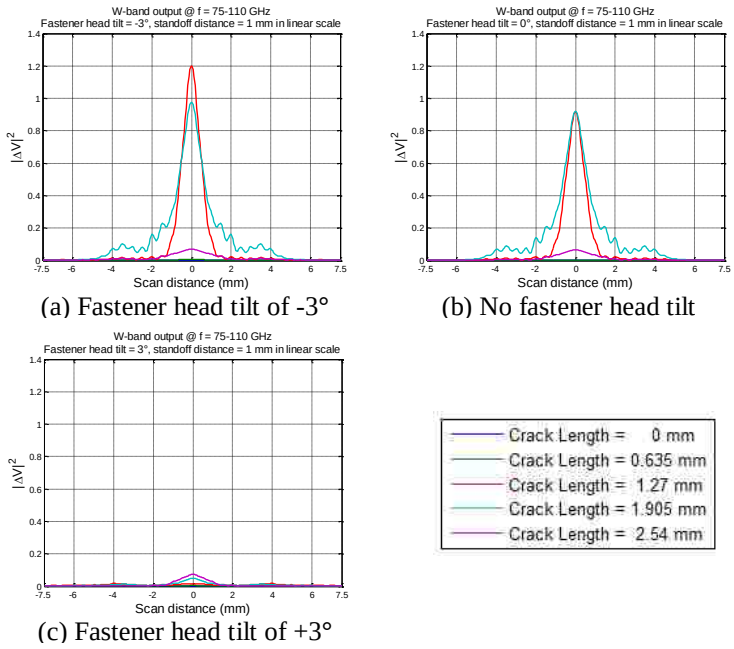

(a) Fastener head tilt of -3° (b) No fastener head tilt

(c) Fastener head tilt of +3°

Figure 3.34. Simulated W-band wideband differential probe output signals with various crack lengths, at a standoff distance of 1 mm, and fastener head tilt of (from (a) to (c)): -3°, 0°, and +3°.

Figures 3.35 and 3.36 summarize the effect of fastener head tilt on the W-band wideband differential probe crack output signal level, at standoff distances of 0.5 and 1 mm, respectively. The signal levels in these figures represent the combinations of the crack responses and scattered signals from the edge of fastener head, when the probe is directly above the crack.

Figures 3.35 and 3.36 confirm that a negatively tilted fastener head does not influence the crack detection capabilities of the W-band probe significantly. However, with a positively tilted fastener head, the probe no longer causes cracks of lengths between 1.27 and 1.905 mm to resonate. Instead, the presence of a crack, regardless of its length, results in the probe output signal to be at approximately the same level.

To better illustrate the effect of fastener head tilt on the W-band wideband differential probe crack output signal level, the percentages of decreases in the crack output signal level versus fastener head tilt, at standoff distances of 0.5 and 1 mm are investigated. To do this, the signals with respect to the different combinations of crack

lengths, standoff distances, and fastener head tilts are normalized to the largest (in magnitude) value among them. The results are presented in Figures 3.37 and 3.38.

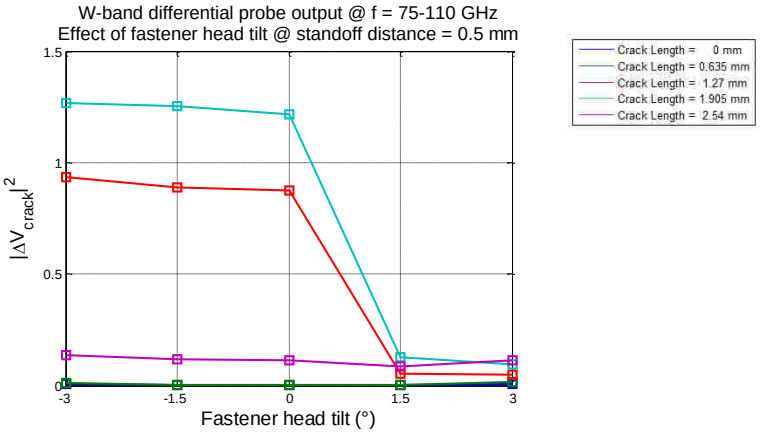

Figure 3.35. Effect of fastener head tilt on the W-band wideband differential probe crack output signal level, at standoff distance of 0.5 mm.

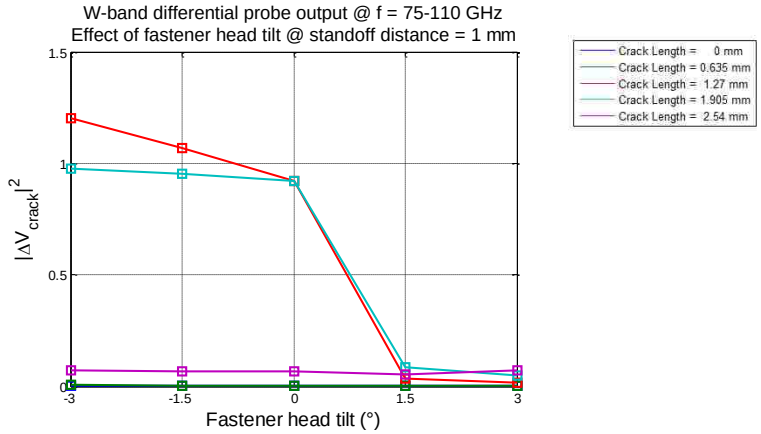

Figure 3.36. Effect of fastener head tilt on the W-band wideband differential probe crack output signal level, at standoff distance of 1 mm.

These results demonstrate again that, in general, as the standoff distance increases, the crack output signal level decreases. The results also confirm that with a positively tilted fastener head, the W-band probe is no longer sensitive to cracks with

lengths near the half-wavelength of W-band frequencies, and the sensitivity of the probe becomes independent of crack length. Lastly, the results show that a fastener head tilt can contribute to a non-zero probe output signal when inspecting an un-cracked fastener head. For instance, a non-zero output signal is generated when the W-band probe inspects an un-cracked fastener head with a -3° tilt, at a standoff distance of 0.5 mm. This signal level may be sufficient to result in false indication of cracks (where a crack does not exist).

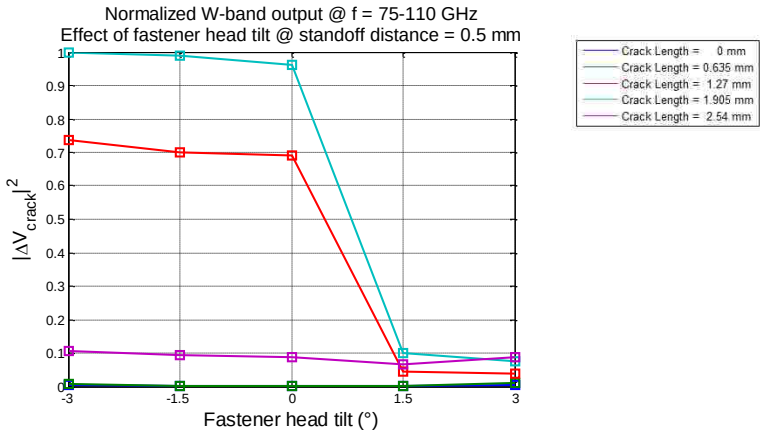

Figure 3.37. Normalized W-band wideband differential probe crack output signal level on effect of fastener head tilt, at standoff distance of 0.5 mm.

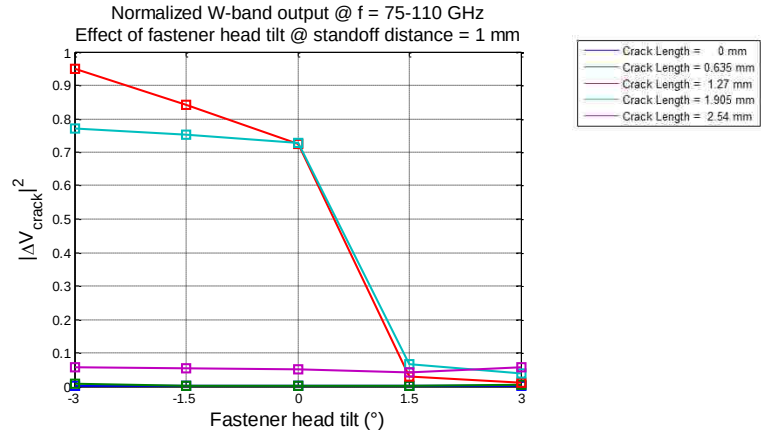

Figure 3.38. Normalized W-band wideband differential probe crack output signal level on effect of fastener head tilt, at standoff distance of 1 mm.

3.4. EFFECT OF PAINT THICKNESS

Simulations were performed to illustrate the effect of a paint layer covering the fastener head and crack on crack detection capabilities of the W-band probe. Figure 3.39 illustrated the schematic used for the model when a layer of paint is uniformly applied onto the sample surface. The paint material chosen in the simulation is Rogers 4350 which has relative permittivity (ϵ_r) of 3.66, which is similar to the actual paint permittivity (ϵ_r of ~3).

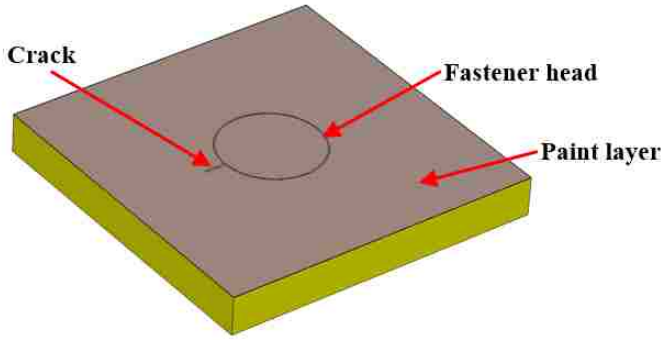

Figure 3.39. Illustration of paint layer covering the fastener head and crack.

Paint thickness has a similar effect on the probe output signal as does the standoff distance, since the presence of paint acts as a dielectric layer between the probe and sample surface. Therefore, the electrical distance between the probe and the sample surface increases. Also, due to the higher permittivity of the paint compared to air, the paint layer tends to concentrate the electric field in the localized area in front of the probe aperture [29], while making the cracks (if present) appearing electrically larger. The paint layer also causes internal reflections between itself and sample surface, making the signal behavior less straightforward to predict.

In the simulations, paint thicknesses in the range of 0 to 0.51 mm (0, 0.08, 0.13, 0.25, 0.38, and 0.51 mm) were considered, as well as standoff distances of 0.5 and 1 mm, with the same crack lengths and frequencies of operation previously mentioned. Both the single-frequency (Section 3.4.1) and wideband (Section 3.4.2) responses are investigated.

3.4.1. Single-Frequency Response. Selected single-frequency results at a fixed standoff distance of 1 mm, and paint thicknesses of 0, 0.08 and 0.51 mm (simulating cases of no paint, a thin layer of paint, and a thick layer of paint) are shown in Figures 3.40 through 3.42. The complete results (standoff distance of 0.5 mm and other paint thicknesses) are provided in Appendix D. Note that the figures are not in the same scales.

These results indicate that the probe output signals become more distorted if a thicker layer of paint is applied. For instance, at operating frequencies of 75 GHz (Figure 3.40), without the presence of a paint layer, the 1.905 mm-long crack results in a probe output signal of ~0.01 V, when a thin layer (0.08 mm) of paint is applied, the output signal dramatically increases to ~ 0.4 V, and slightly reduces to ~ 0.35 V when the paint layer becomes thick (0.51 mm). However, at other operating frequencies, similar patterns are not observed. To further understand the relationship between paint thicknesses and W-band probe output signals, the wideband responses are studied.

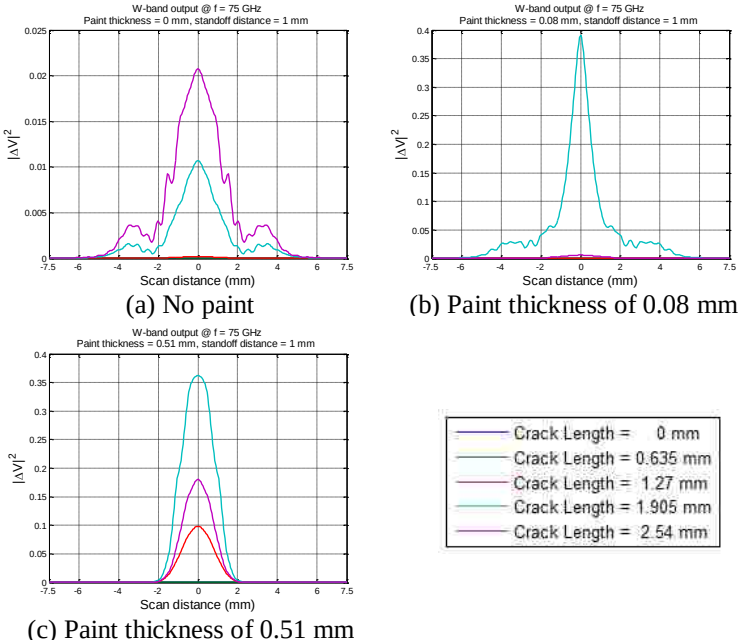

(a) No paint

(b) Paint thickness of 0.08 mm

(c) Paint thickness of 0.51 mm

Figure 3.40. Simulated W-band differential probe output signals with various crack lengths, at a standoff distance of 1 mm, frequency of 75 GHz, and paint thickness of (from (a) to (c)): 0, 0.08 mm, and 0.51 mm.

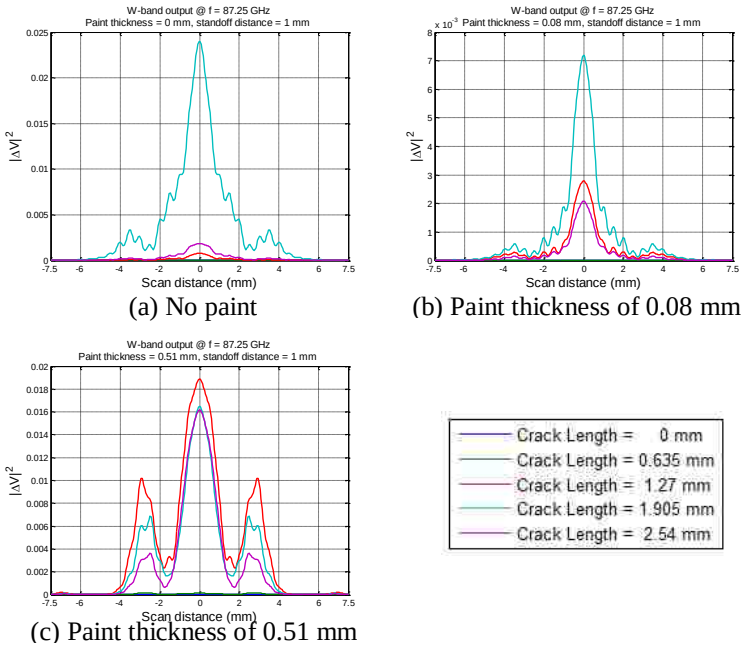

(a) No paint

(b) Paint thickness of 0.08 mm

(c) Paint thickness of 0.51 mm

Figure 3.41. Simulated W-band differential probe output signals with various crack lengths, at a standoff distance of 1 mm, frequency of 87.25 GHz, and paint thickness of (from (a) to (c)): 0, 0.08 mm, and 0.51 mm.

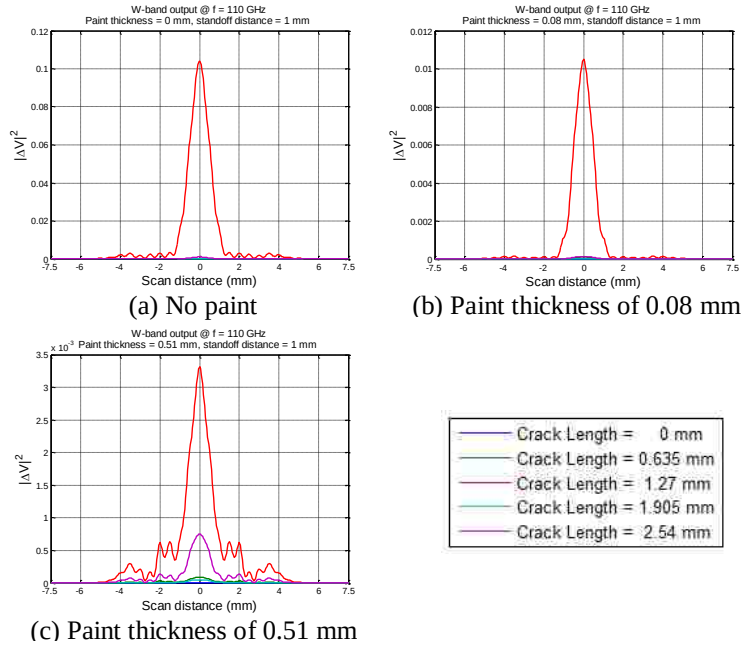

(a) No paint

(b) Paint thickness of 0.08 mm

(c) Paint thickness of 0.51 mm

Figure 3.42. Simulated W-band differential probe output signals with various crack lengths, at a standoff distance of 1 mm, frequency of 110 GHz, and paint thickness of (from (a) to (c)): 0, 0.08 mm, and 0.51 mm.

3.4.2. Wideband Response. Shown in Figure 3.43 are the wideband responses of the W-band probe on fastener head scanning with 1 mm standoff distance and a layer of paint of thicknesses 0, 0.08 and 0.51 mm.

In the previous results, the W-band probe is sensitive to cracks of lengths between 1.27 and 1.905 mm only, however, this result is no longer true when a layer of paint is applied. Figure 3.43 suggests that at this specific standoff distance (1 mm), the W-band probe is sensitive to cracks of other dimensions (0.635 and 2.54 mm) as well. This is due to the presence of a paint layer which makes the crack appear electrically larger, and change the resonance properties of the crack. It can be assumed that under a thick layer of paint, the 0.635 mm-long crack is approximately equal to (electrically) the half-wavelength of the operating frequency, making the W-band probe capable of detecting cracks of smaller sizes. Similarly, the 2.54 mm-long crack can be assumed approximately equal to (electrically) a full-wavelength (or multiples of a half-wavelength).

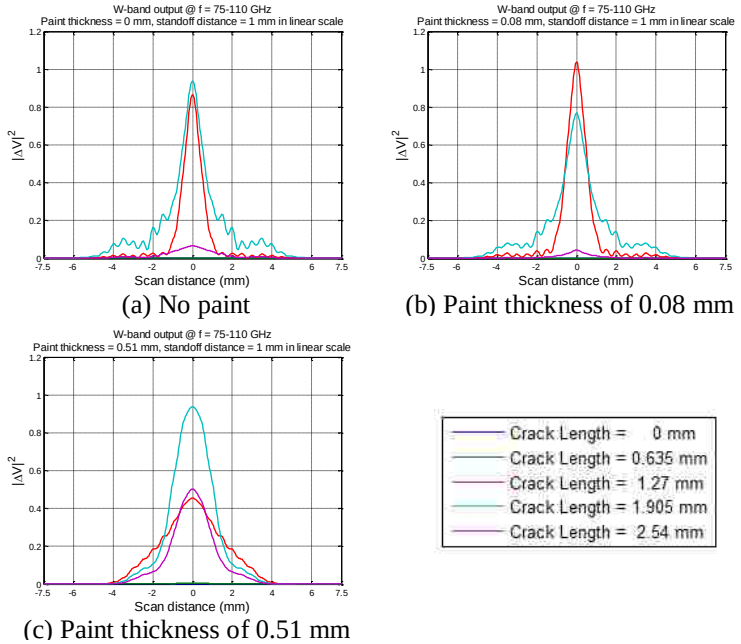

(a) No paint (b) Paint thickness of 0.08 mm

(c) Paint thickness of 0.51 mm

Figure 3.43. Simulated W-band wideband differential probe output signals with various crack lengths, at a standoff distance of 1 mm, and paint thicknesses of (from (a) to (c)): 0, 0.08 mm, and 0.51 mm.

Figures 3.44 and 3.45 summarize the effect of paint thickness on the W-band wideband differential probe crack output signal level, at standoff distances of 0.5 and 1 mm, respectively. The signal levels in these figures represent the combinations of the crack responses and influences in output signals due to paint layers of various thicknesses, when the probe is directly above the crack.

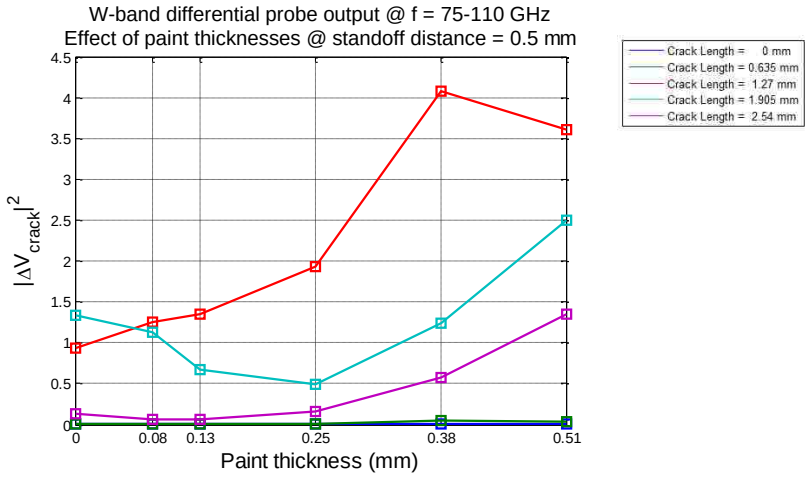

Figure 3.44. Effect of paint thickness on the W-band wideband differential probe crack output signal level, at standoff distance of 0.5 mm.

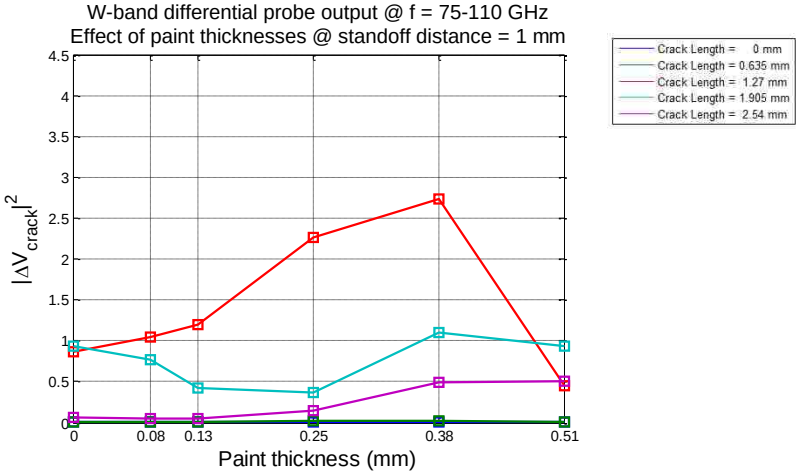

Figure 3.45. Effect of paint thickness on the W-band wideband differential probe crack output signal level, at standoff distance of 1 mm.

Both Figures 3.44 and 3.45 suggest that the crack output signal levels are not proportional to paint thicknesses, instead the tendency of paint to concentrate the electric field within the paint substrate changes the signal levels in an unpredictable way. Although in general the presence of a paint layer enhances the signal levels, except for some cases (e.g., 1.905 mm-long crack under 0.25 mm-think paint).

To better illustrate the effect of paint thickness on the W-band wideband differential probe crack output signal levels, the percentages of decreases in the crack output signal levels versus paint thicknesses, and standoff distances of 0.5 and 1 mm are investigated. To do this, the signals with respect to the different combinations of crack lengths, standoff distances, and paint thicknesses are normalized to the largest (in magnitude) value among them. The results are presented in Figures 3.46 and 3.47.

These normalized results confirm that the presence of a paint layer generally enhances the capability of the W-band probe for crack detection, especially when a thin layer (e.g., 0.0762 mm) is applied. However, the paint layer on an actual aircraft skin may take on other shapes (instead of a uniform layer, e.g., paint filling the crack, excess paint forming a clump, etc.), influencing the crack detection capability. Such effect will be discussed in later sections.

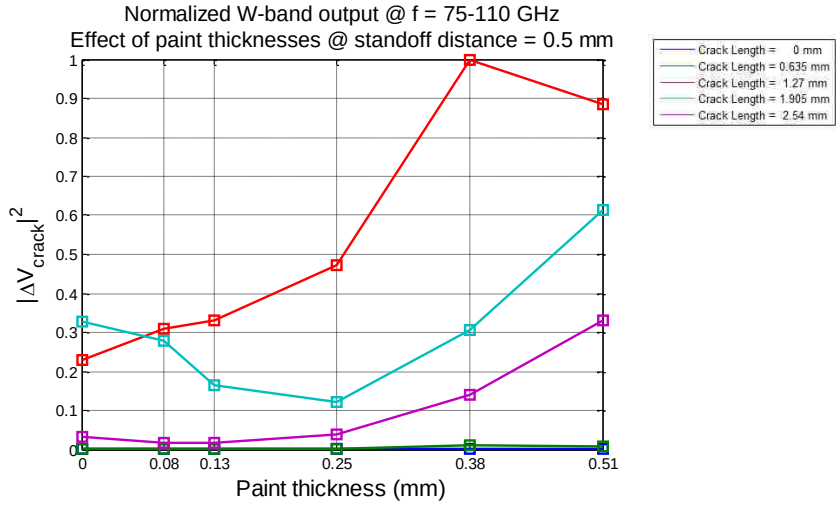

Figure 3.46. Normalized W-band wideband differential probe crack output signal level on effect of paint thickness, at standoff distance of 0.5 mm.

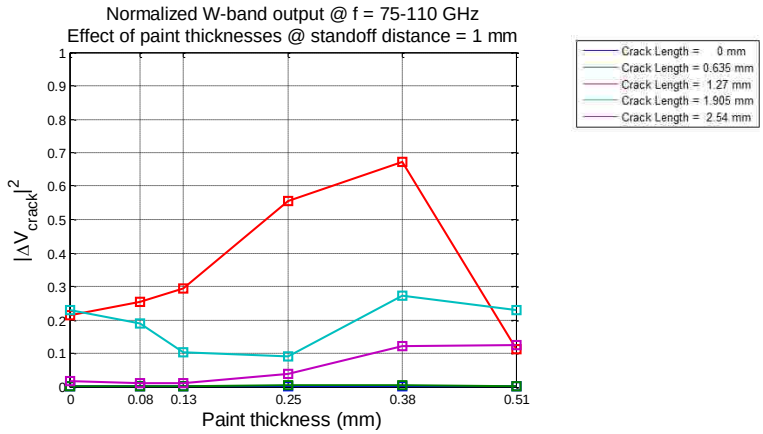

Figure 3.47. Normalized W-band wideband differential probe crack output signal level on effect of paint thickness, at standoff distance of 1 mm.

3.5. EFFECT OF PROBE MISALIGNMENT

This section describes the potential misalignment between the probe and the fastener head, or probe misalignment. Probe misalignment is defined as the displacement between the center points of the fastener head and the probe aperture. A negative probe misalignment is when the probe is shifting towards the crack, and a positive probe misalignment is when the probe is shifting away from the crack, as shown in Figure 3.48.

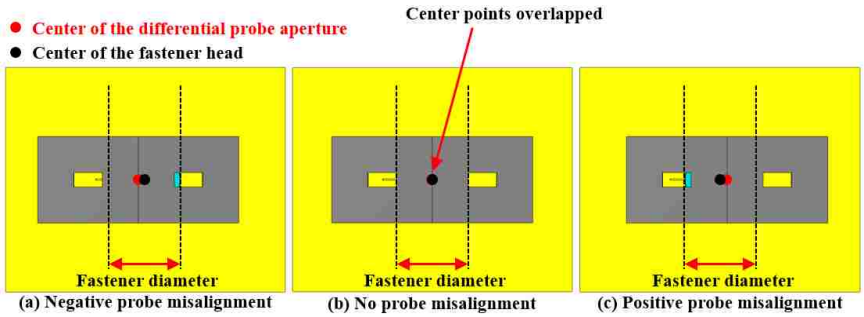

Figure 3.48. Definition of probe misalignment.

Probe misalignment results in an imperfectly canceled scattered signals from the fastener head. When a negative probe misalignment is applied, the probe does not cancel

the scattered signals from the fastener head completely. Therefore, the combination of scattered signals from the fastener head and crack results in a weaker peak signal level at crack locations, and potential signal peaks near the edge of the fastener heads. These issues would become less significant if the probe is positively misaligned, as the un-eliminated scattered signals from the fastener head is collected through the same probe aperture collecting the scattered signals from the crack. Both cases of probe misalignments may lead to false indications of cracks.

In simulations, probe misalignments of ±1.27, ±0.635, and 0 mm were considered, as well as standoff distances of 0.5 and 1 mm, with the same crack lengths and frequencies of operation previously mentioned. Both the single-frequency (Section 3.5.1) and wideband (Section 3.5.2) responses are investigated.

3.5.1. Single-Frequency Response. Selected single-frequency results at a fixed standoff distance of 1 mm, and probe misalignments of ±1.27 and 0 mm are shown in Figures 3.49 through 3.52. The complete results (standoff distance of 0.5 mm and other probe misalignments) are provided in Appendix E. Note that the figures are not in the same scales.

These results indicate that when the probe is negatively misaligned, the combination of additional scattered signals from the fastener head and crack signals results in a weaker peak signal level at crack locations, and additional signal peaks near the edge of the fastener head are generated. This effect is also frequency dependent as shown.

These additional signal peaks could contribute to false indications in real-world applications. Also, these issues become less significant if the probe is positively misaligned as expected, except for a few cases. However, under positive probe misalignments, the scattered signals from cracks become weaker when the displacement becomes large, as scattered signals from the crack is not fully captured by the probe aperture.

3.5.2. Wideband Response. Shown in Figure 3.53 are the wideband responses of the W-band probe on fastener head scanning with 1 mm standoff distance, and probe misalignments of ±1.27 and 0 mm.

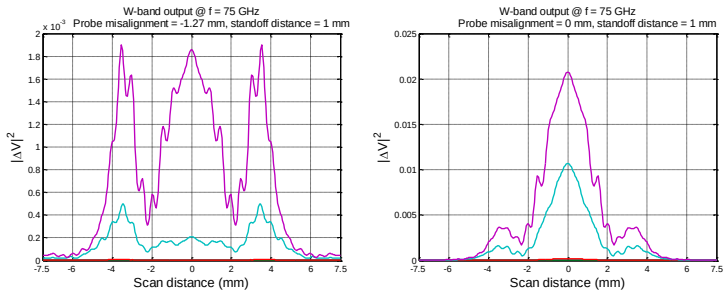

(a) Probe misalignment of -1.27 mm (b) No probe misalignment

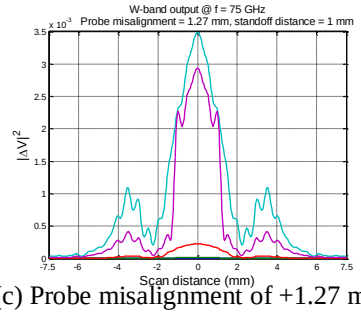

(c) Probe misalignment of +1.27 mm

Figure 3.49. Simulated W-band differential probe output signals with various crack lengths, at a standoff distance of 1 mm, frequency of 75 GHz, and probe misalignments of (from (a) to (c)): -1.27 mm, 0 mm, and +1.27 mm.

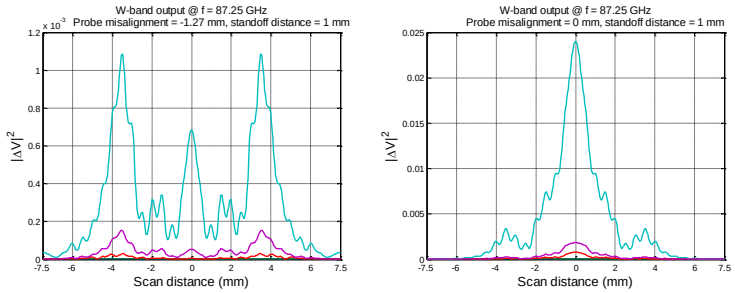

(a) Probe misalignment of -1.27 mm (b) No probe misalignment

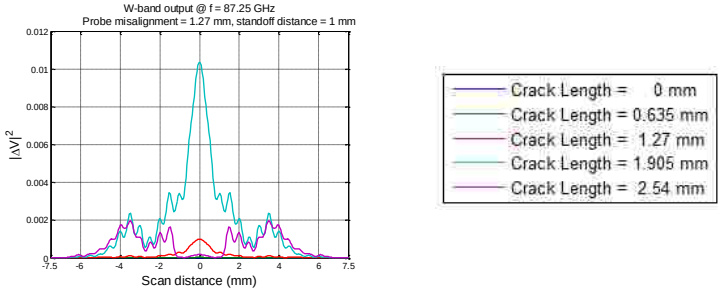

(c) Probe misalignment of +1.27 mm

Figure 3.50. Simulated W-band differential probe output signals with various crack lengths, at a standoff distance of 1 mm, frequency of 87.25 GHz, and probe misalignments of (from (a) to (c)): -1.27 mm, 0 mm, and +1.27 mm.

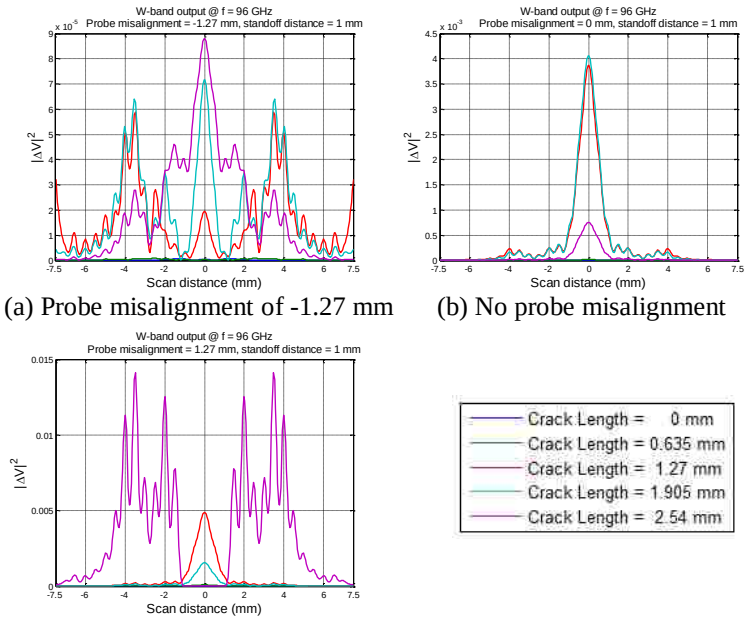

(a) Probe misalignment of -1.27 mm (b) No probe misalignment

(c) Probe misalignment of +1.27 mm

Figure 3.51. Simulated W-band differential probe output signals with various crack lengths, at a standoff distance of 1 mm, frequency of 96 GHz, and probe misalignments of (from (a) to (c)): -1.27 mm, 0 mm, and +1.27 mm.

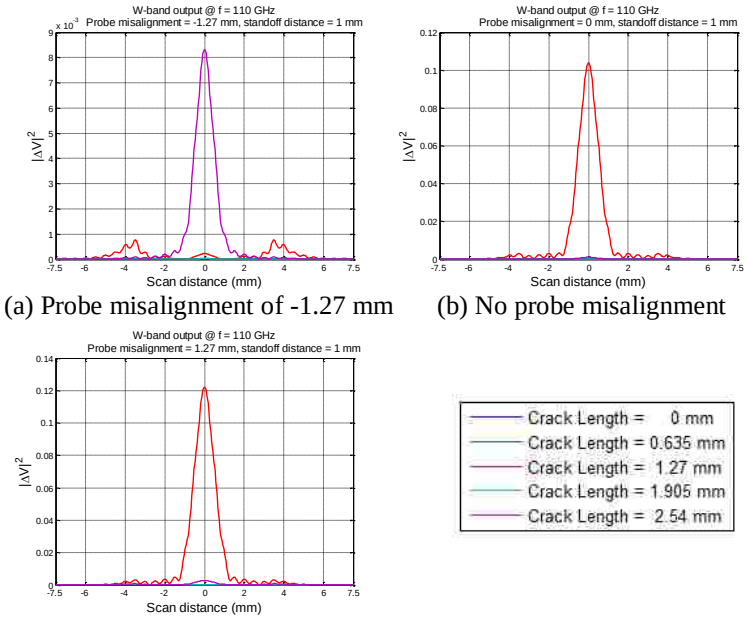

(a) Probe misalignment of -1.27 mm (b) No probe misalignment

(c) Probe misalignment of +1.27 mm

Figure 3.52. Simulated W-band differential probe output signals with various crack lengths, at a standoff distance of 1 mm, frequency of 110 GHz, and probe misalignments of (from (a) to (c)): -1.27 mm, 0 mm, and +1.27 mm.

Figure 3.53 also suggests that when a negative probe misalignment is present, the unwanted scattered signals from the fastener head decrease the probe output signal at the crack location, and additional signal peaks are formed. On the other hand, a positive probe misalignment has minimal effect on the crack output signal levels, but for longer cracks (1.905 and 2.54 mm-long cracks), since the scattered signals from the crack is not fully captured, the corresponding crack output signal levels reduce. The same pattern can be observed for standoff distance of 0.5 mm shown in Appendix E.

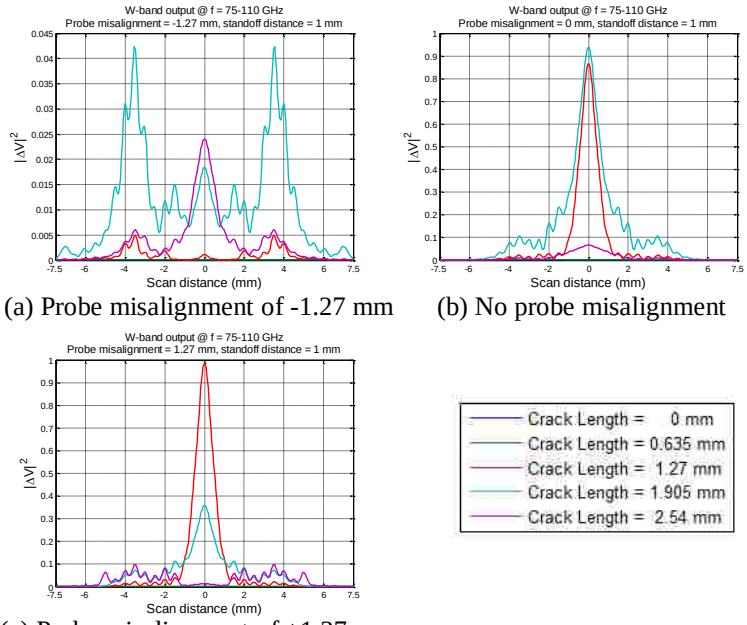

(a) Probe misalignment of -1.27 mm (b) No probe misalignment

(c) Probe misalignment of +1.27 mm

Figure 3.53. Simulated W-band wideband differential probe output signals with various crack lengths, at a standoff distance of 1 mm, and probe misalignments of (from (a) to (c)): -1.27 mm, 0, and +1.27 mm.

Figures 3.54 and 3.55 summarize the effect of probe misalignment on the W-band wideband differential probe crack output signal level, at standoff distances of 0.5 and 1 mm, respectively. The signal levels in these figures represent the combinations of the crack responses and the unwanted scattered signals from the fastener head due to misalignments, when the probe is directly above the crack.

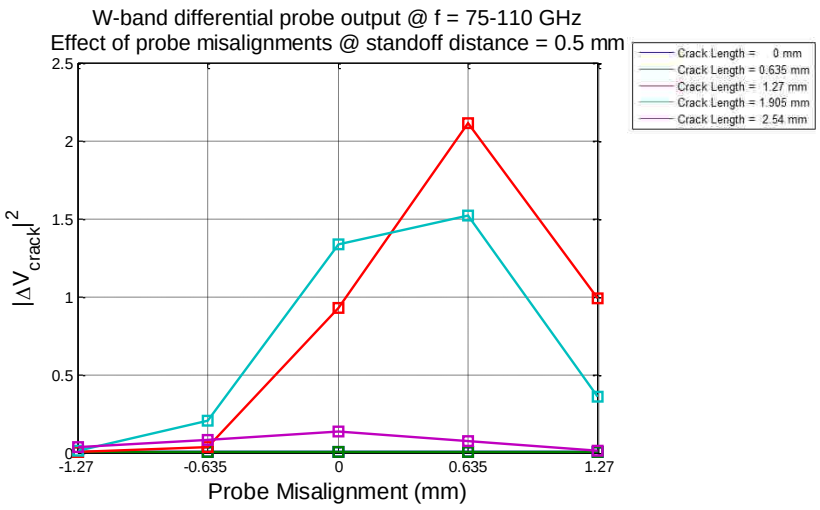

Figure 3.54. Effect of probe misalignment on the W-band wideband differential probe crack output signal level, at standoff distance of 0.5 mm.

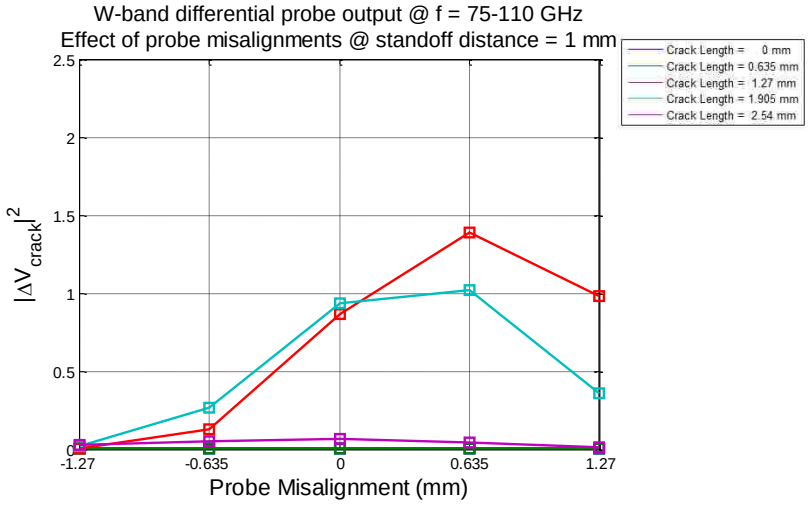

Figure 3.55. Effect of probe misalignment on the W-band wideband differential probe crack output signal level, at standoff distance of 1 mm.

Both Figures 3.54 and 3.55 confirm the observations earlier, where the crack output signal levels are significantly weaker if the probe is negatively misaligned, and the effects are less critical if the probe is positively misaligned. In real-world applications,

the direction of a crack (if present) is normally unknown. Therefore the direction of probe misalignments cannot actually be defined.

In general, to get accurate results, the tolerance on the probe misalignments should be less than the length of the crack wanted to detect. For instance, if it is desired to detect cracks with lengths 0.5 mm or longer, the value of probe misalignments should not exceed 0.5 mm, otherwise the scattered signals from the cracks may not be completely detected (e.g., Figure 3.56).

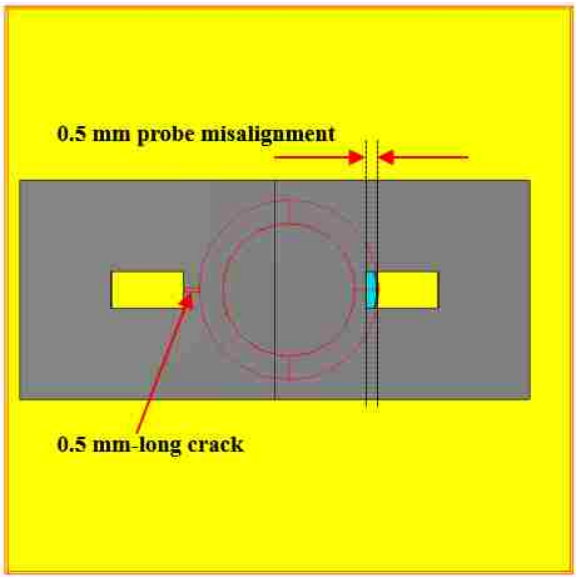

Figure 3.56. Illustration of when probe misalignment is larger than or equal to cracks in lengths.

To better illustrate the effect of probe misalignment on the W-band wideband differential probe crack output signal level, the percentages of decreases in the crack output signal levels versus probe misalignments, and standoff distances of 0.5 and 1 mm are investigated. To do this, the signals with respect to the different combinations of crack lengths, standoff distances, and probe misalignments are normalized to the largest (in magnitude) value among them. The results are shown in Figures 3.57 and 3.58.

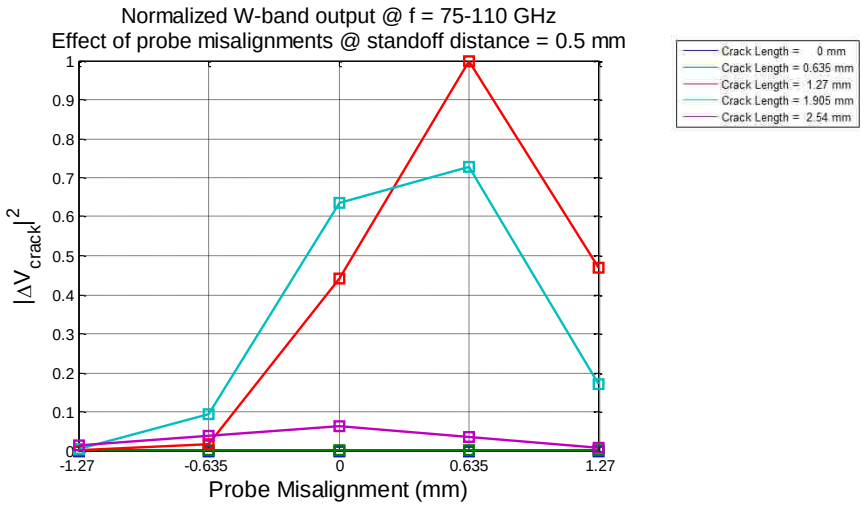

Figure 3.57. Effect of probe misalignment on the W-band wideband differential probe crack output signal level, at standoff distance of 0.5 mm.

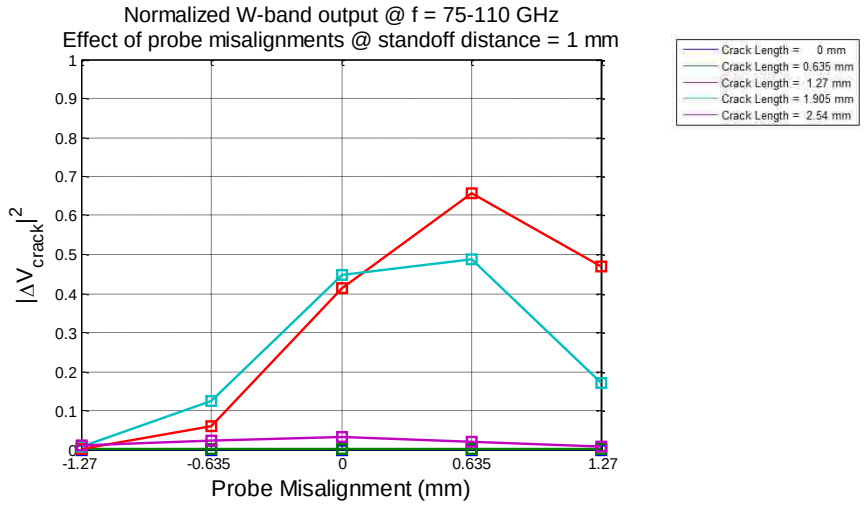

Figure 3.58. Effect of probe misalignment on the W-band wideband differential probe crack output signal level, at standoff distance of 1 mm.

These results suggest that at 1 mm standoff distance, a negative probe misalignment can cause the crack output signal levels for the 1.27 and 1.905 mm-long cracks to be at the level as if there are no cracks present, while a positive probe

misalignment has less an effect. Similar patterns can be observed from the results of 0.5 mm standoff distance.

3.6. EFFECT OF PROBE OFFSET

This section describes a possible rotation of the probe with respect to the fastener axis, or probe offset. Probe offset is defined as the angle of rotation of the probe centered at the fastener head. This rotation can lead to undesired consequences where the scattered signals from the fastener head cannot be completely removed as a result of non-symmetrical configuration of the structure, similar to several situations discussed earlier (e.g., probe misalignments). The illustration of probe offsets is shown in Figure 3.59.

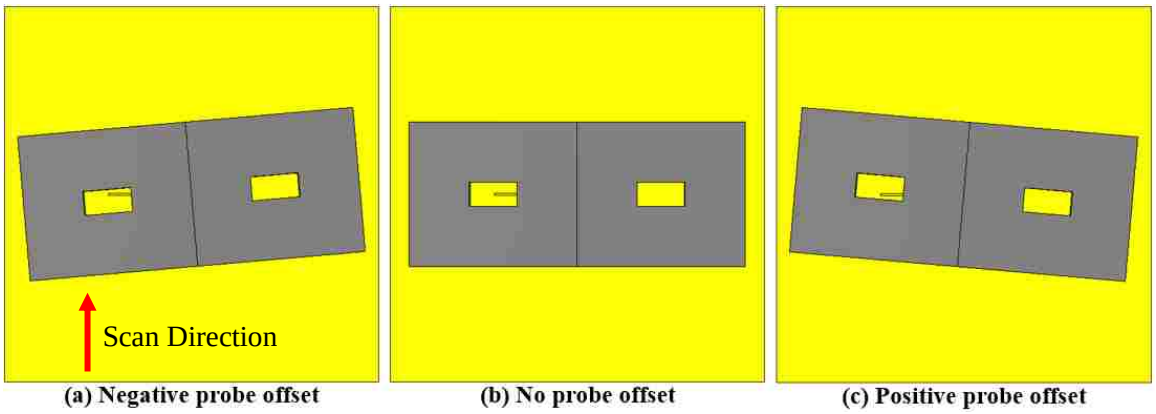

Figure 3.59. Definition of probe offsets.

The presence of a probe offset is considered an error in measurement system setup. Instead of having both probe apertures sensing the edges of fastener head simultaneously, a negative probe offset results in a situation where the detection of the crack is delayed in distance because the aperture on the crack side arrives at the crack location later compared to when no probe offset is present. On the other hand, a positive probe offset will advance the detection of the crack because the aperture on the crack side arrives at the crack location earlier. Therefore, a probe offset is expected to change the

location of the actual crack signals, and the unwanted scattered signals from the fastener head may reduce the crack output signal levels.

In the simulations, probe offsets of ±5°, ±2.5° and 0° were considered, as well as standoff distances of 0.5 and 1 mm, with the same crack lengths and frequencies previously mentioned. Both the single-frequency (Section 3.6.1) and wideband (Section 3.6.2) responses are investigated.

3.6.1. Single-Frequency Response. Selected single-frequency results at a fixed standoff distance of 1 mm, and probe offsets of ±5° and 0° are shown in Figures 3.60 through 3.62. The complete results (standoff distance of 0.5 mm and other probe offsets) are provided in Appendix F.

These results indicate that a probe offset (both positive and negative) does not significantly influence the probe output signal, but it shifts the location of the peak signals away from the actual crack location (e.g., the peak signals are located at ~ +0.5 mm, 0, and ~ -0.5 mm locations in Figure 3.62).

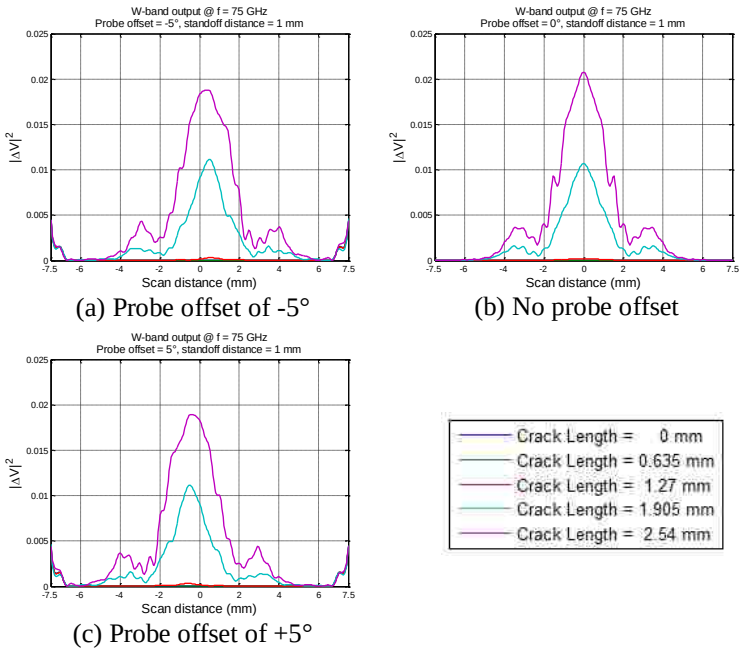

(a) Probe offset of -5°

(b) No probe offset

(c) Probe offset of +5°

Figure 3.60. Simulated W-band differential probe output signals with various crack lengths, at a standoff distance of 1 mm, frequency of 75 GHz, and probe offsets of (from (a) to (c)): -5°, 0°, and +5°.

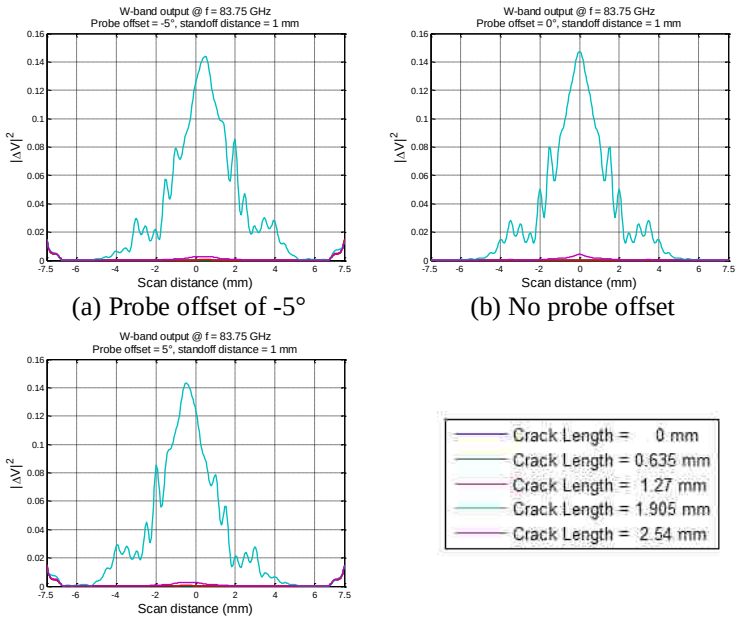

(a) Probe offset of -5°

(b) No probe offset

(c) Probe offset of +5°

Figure 3.61. Simulated W-band differential probe output signals with various crack lengths, at a standoff distance of 1 mm, frequency of 83.75 GHz, and probe offsets of (from (a) to (c)): -5°, 0°, and +5°.

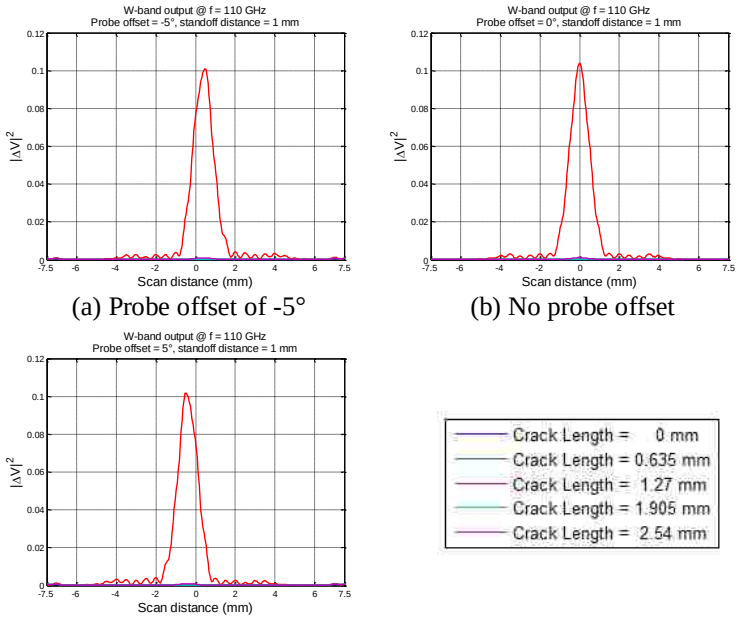

(a) Probe offset of -5°

(b) No probe offset

(c) Probe offset of +5°

Figure 3.62. Simulated W-band differential probe output signals with various crack lengths, at a standoff distance of 1 mm, frequency of 110 GHz, and probe offsets of (from (a) to (c)): -5°, 0°, and +5°.

Therefore, a probe offset does not significantly influence the capability of W-band probe for fastener head crack detection. For some single-frequency responses (e.g., 75 GHz), there are signal peaks generated at the edge of the scan section, and those are due to one probe aperture becoming too close to the edge of the sample surface.

3.6.2. Wideband Response. Shown in Figure 3.63 is the wideband responses of the W-band probe on fastener head scanning with 1 mm standoff distance, and probe offsets of ±5° and 0°.

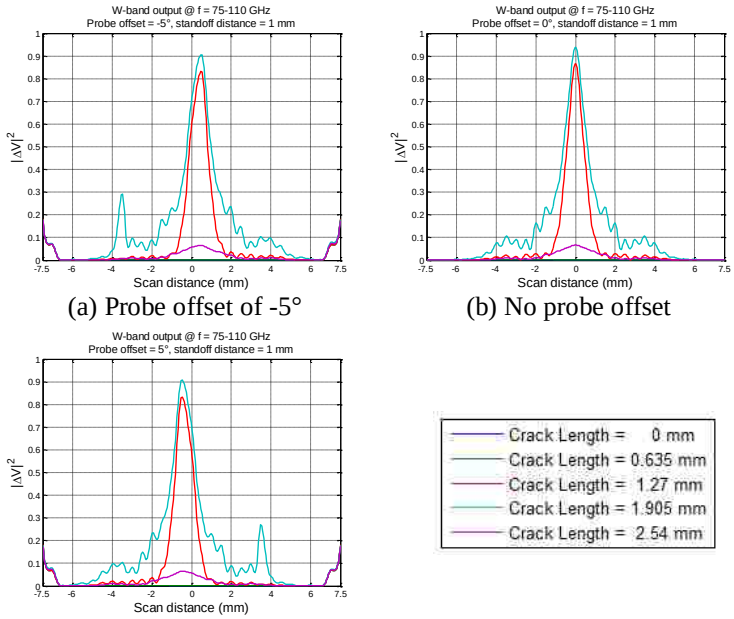

(a) Probe offset of -5°

(b) No probe offset

(c) Probe offset of +5°

Figure 3.63. Simulated W-band wideband differential probe output signals with various crack lengths, at a standoff distance of 1 mm, and probe offsets of (from (a) to (c)): -5°, 0°, and +5°.

The wideband responses also suggest that either a positive or negative probe offset has a significant effect on probe output signal level. The only attribute is that the location of the signal peaks shifted away from the actual location of crack, which is expected. In addition, a probe offset makes a crack to appear electrically smaller because

the side of the waveguide and the cracks are no longer parallel, effectively reduces the magnitude of crack output signals (as will be shown clearer later).

Figures 3.64 and 3.65 summarize the effect of probe offset on the W-band wideband differential probe crack output signal level, at standoff distances of 0.5 and 1 mm, respectively. The signal levels in these figures represent the combination of the crack responses and the unwanted scattered signals from the fastener head (which is minor, according the simulations), when the probe is directly above the crack.

Both Figures 3.64 and 3.65 confirm the observations made earlier, as the crack output signal levels are not significantly affected by the occurrence of a probe offset, and the only consequences are the location shift in the signal peaks, which would provide for false information on crack locations, and slightly reduced magnitudes of crack signals. However, this kind of errors is less an issue compared to situations discussed previously.

To better illustrate the effect of probe offset on the W-band wideband differential probe crack output signal level, the percentages of decreases in the crack output signal levels versus probe offsets, and standoff distances of 0.5 and 1 mm are investigated. To do this, the signals with respect to the different combinations of crack lengths, standoff distances, and probe offsets are normalized to the largest (in magnitude) among them. The results are presented in Figures 3.66 and 3.67.

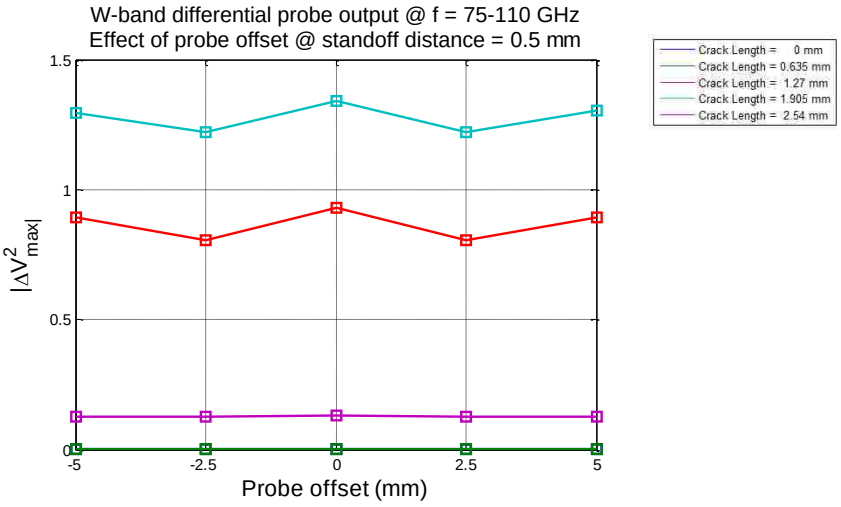

Figure 3.64. Effect of probe offset on the W-band wideband differential probe crack output signal level, at standoff distance of 0.5 mm.

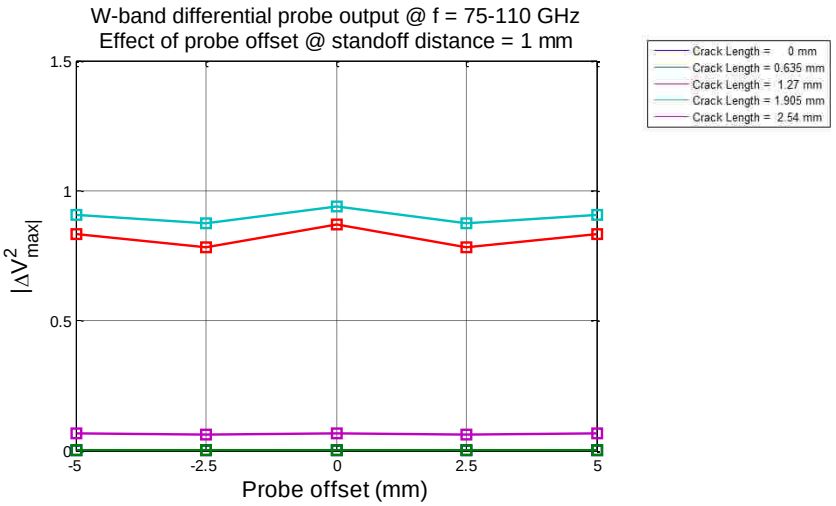

Figure 3.65. Effect of probe offset on the W-band wideband differential probe crack output signal level, at standoff distance of 1 mm.

These normalized results also suggest the same conclusion, where the reduction in crack output signal levels is less than 15% at all times (between probe offsets of -5° and 5°), and are the consequences of crack appearing electrically smaller and some imperfectly canceled scattered signals from fastener heads.

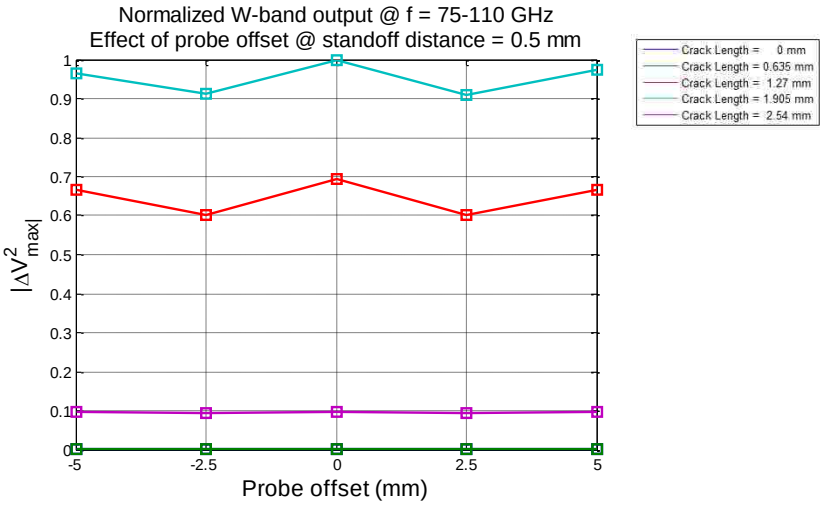

Figure 3.66. Normalized W-band wideband differential probe crack output signal level on effect of probe offset, at standoff distance of 0.5 mm.

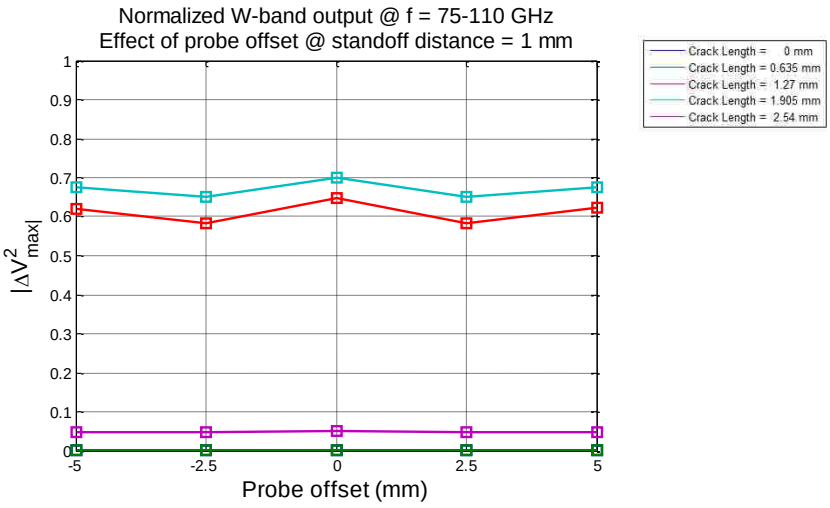

Figure 3.67. Normalized W-band wideband differential probe crack output signal level on effect of probe offset, at standoff distance of 1 mm.

3.7. SUMMARY

In this section, the effects of various positing of the differential probe and variations of sample surfaces were evaluated. The considerations are:

- standoff distances (at both W-band and V-band frequencies),
- aperture offsets,
- probe misalignments,
- probe offsets,
- paint thicknesses, and
- fastener head tilts.

In those considerations, the first four are integrated into the setup of measurement systems and are avoidable, and the last two are constraints on the sample which would be harder to accommodate with. It is found, through simulations, the parameters listed above contribute to the probe output signals as follows:

- W-band frequencies have the tendency to cause cracks of lengths approximately equal to the half-wavelengths (which are cracks of 1.27 and 1.905 mm-long in the simulations) to resonate, resulting in a stronger scattered signal compared to scattered signals by cracks of other dimensions.

However, as the operating frequencies reduce to V-band (increasing wavelength), the 2.54 mm-long crack (longest crack in the sample set) becomes the crack that resonates (the half-wavelengths of V-band frequencies are beyond 2 mm).

- The higher the standoff distance, the weaker the probe output signals due to higher radiation losses. However, a high standoff distance can be intentionally applied to reduce the effects caused by a misalignment in the measurement system. For instance, a high standoff distance can reduce the magnitudes of the additional signal peaks that are formed due to probe misalignments (Section 3.5), or reduce the probe sensitivity on the edge of fastener head when the fastener head is tilted (Section 3.3).
- The consequences of an aperture offset is essentially a DC bias due to unequal standoff distances between the two probe apertures. However, as demonstrated in Section 3.2, the DC bias line can potentially be estimated and removed from the probe output signals, leaving the effect of aperture offset at minimum.
- A probe misalignments have a direction dependency. If the probe is shifted towards the crack, the unwanted scattered signals from the fastener head is sufficiently strong that it may mask out the scattered signals from the crack. On the other hand, if the probe is shifted away from the crack, the probe may be limited in the sizes of cracks it can detect (Figure 3.56), as a small crack may be missed if the misalignment is large. Although in general, the directions of the cracks on the side of fastener heads are not known, multiple measurements may be required to identify whether a signal peak in the probe output signal is the result of a crack, or the presence of a probe misalignment.
- Probe offset, as shown in Section 3.6, do not interfere with the probe output signals significantly (the signal levels reduce by less than 15% for probe offsets between -5° and 5°), but a potential false information on the crack location is given. However, as introduced in Section 1, the surface-breaking cracks that formed on the aircraft skins are due to mechanical stresses in two directions (up and down). Therefore, it is possible for the location of a

potential crack to be predicted. Thus the occurrence of probe offsets is less critical.

- As shown in Section 3.3, a fastener head tilt affects the crack detection capabilities of the W-band probe if the edge of the fastener head is tilted below the crack (a negative fastener head tilt). Since in general the fastener head orientation (whether it has tilts) and location of the crack (if present) are not known, multiple measurements may be required to recognize and confirm the presence of a crack.
- A layer of paint introduces uncertainties to the probe output signals, not only the paint may not be uniformly spread onto the surface (variable standoff distances), but also the behaviors of the electric field near the aperture and the paint around it becomes difficult to predict. The investigations on effects of non-uniform paint thickness will be discussed in Section 6.

In conclusion, the parameters that are generally critical are related to the sample conditions (fastener head tilts and paint thickness). Other parameters relating to setup errors either have minimal effects on the probe output signals, or can be adjusted through post processing (e.g., removing the DC bias caused by aperture offsets). Measurements using the instruments and samples described in Section 2 will be conducted to verify the findings from these numerical analyses.

4. MEASUREMENT VERIFICATIONS

Measurements were conducted using the optimal W-band differential probe and the previously-built (as described in Section 2) V-band differential probe to verify the simulated results discussed in Section 3. As previously described, the test panel has fastener heads with two different diameters (6.35 mm and 7.87 mm), the measurement results presented in this section correlate to the scanned results of the 6.35 mm fastener head.

Due to limited availability of samples, the investigations on the effect of fastener head tilt cannot be verified through measurements, instead the experimental investigations on effect of standoff distance (Section 4.1), aperture offset (Section 4.2), paint thickness (Section 4.3), probe misalignment (Section 4.4) and probe offset (Section 4.5) were conducted. Variations in probe output signals with respect to different crack lengths cannot be repeated either, due to the availability of only one crack with a length 1.27 mm. Therefore, this section provides a one-to-one comparison between the simulation and measurement results on scanning a 1.27 mm-long crack only. Similar to the simulations, both W-band and V-band frequencies were applied onto evaluating the effect of standoff distance.

The W-band wideband voltage-controlled Gunn oscillator (VCO) is used for measurements. The W-band varactor-tuned oscillator is capable of generating signals at a frequency range of 87.734 – 92.265 GHz by sweeping the DC bias voltage input to its varactor. A close estimate of frequencies used for the measurements are listed in Appendix G. Also listed in Appendix G are the frequencies used in the simulations, a comparison between the two sets of frequencies is conducted to ensure that the results can be optimally compared one-to-one (e.g., simulated results @ 89 GHz is compared to scanned results @ 88.9755 GHz). On the other hand, V-band frequencies are generated by a wideband Gunn mechanically-tuned oscillator which is capable of generating signals at a frequency range of 68.8 – 71.3 GHz, and the frequency is controlled using a micrometer-controlled tuning rod.

Figure 4.1 illustrates the measurement setup with the W-band probe. Markings on the sample surface and the probe were used to ensure proper alignment. A pair of fastener

heads (of 6.35 mm diameter in this case) are inspected during each scan (with a scan step size of 0.25 mm). One of the fastener heads has a surface crack of ~0.127 mm (~0.005") by 1.27 mm (0.05") in dimension on its side, as shown in the figure. The center of the cracked fastener head (and also the crack) are positioned to be 10 mm away from the initial probe position, while the center of the un-cracked fastener head is positioned to be 35 mm away. Similar measurement setup is applied with the V-band probe.

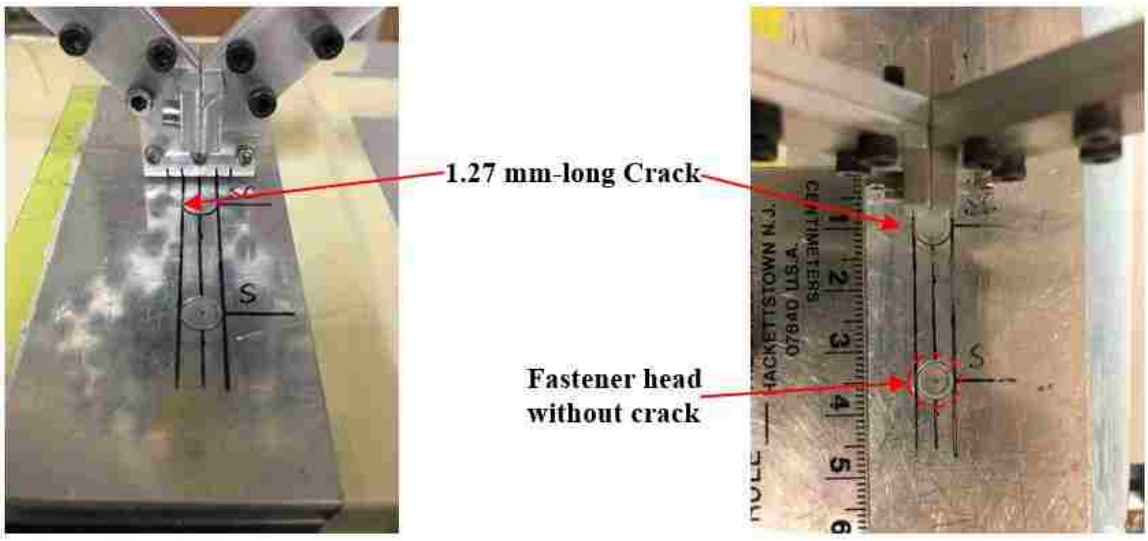

Figure 4.1. W-band measurement setup for 6.35 mm fastener heads.

Figure 4.2 represents an example of the W-band differential probe output signals when scanned over a pair of fastener heads, at a standoff distance of 1 mm, and at the frequency of ~91.02 GHz. Figure 4.3 represents an example of the V-band (~69.6 GHz) probe output signal. These figures represent the variations in differential probe output signals when a crack is present (10 mm location) as opposed to when no crack is present (35 mm location).

Theoretically, the differential probe output is zero if both apertures of the probe are inspecting an identical surface (e.g., the edges of a fastener head), as previously described. However, due to the inherent internal mismatches in the probe component characteristics (e.g., the magic-tee), and also the imperfect alignments between the probe

and sample surface, the output is not exactly zero and is biased to a certain output voltage level. In the example shown in Figure 4.2, the bias level can be approximated at 235 mV.

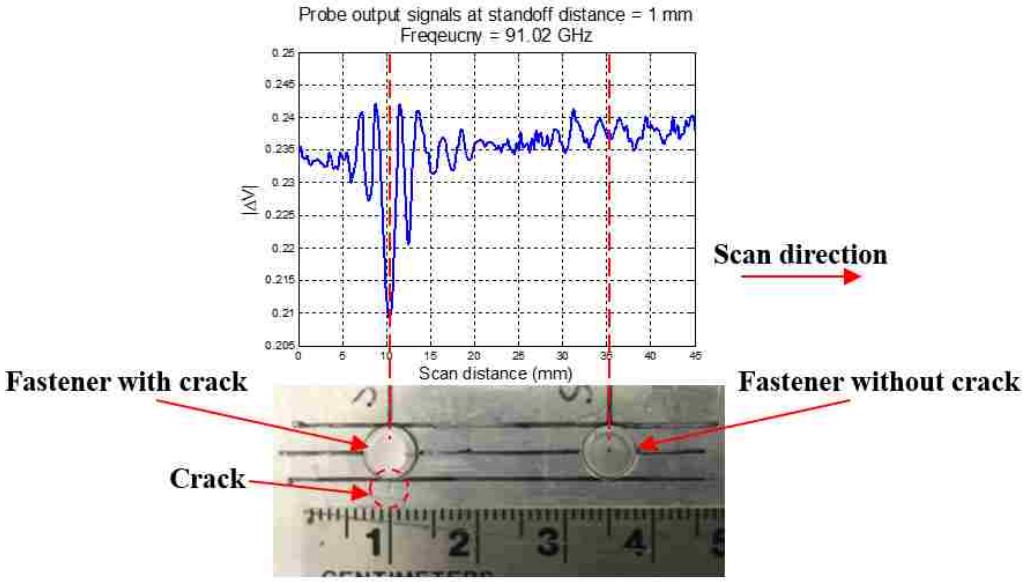

Figure 4.2. Example of W-band (~91.02 GHz) differential probe output signals over a pair of fastener heads.

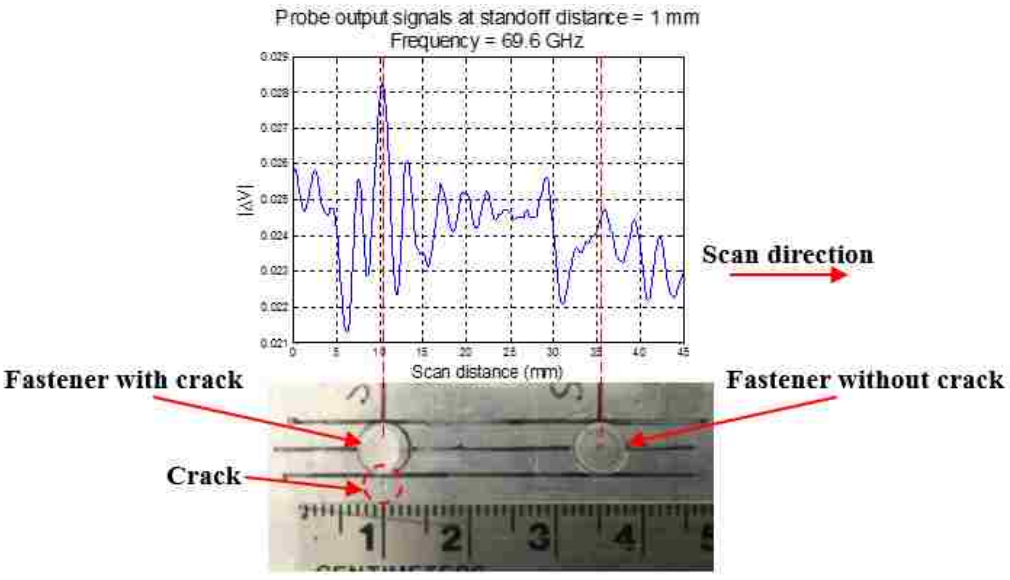

Figure 4.3. Example of V-band (~69.6 GHz) differential probe output signals over a pair of fastener heads.

To eliminate the effect of this bias voltage, the bias voltage is estimated and subtracted from the probe output signals. This is achieved by taking the average voltage value of the probe output signals in the scan region that does not include a fastener head (i.e., 20 – 25 mm region shown in Figure 4.2 and 4.3), and subtract it from the probe output signals. This procedure gives an indication of potential self-calibration capability of the probe. Figure 4.4 represents the referenced W-band probe output signals after the bias voltage (of the signal in Figure 4.2) is removed, and Figure 4.5 represents the referenced V-band results. The reference bias voltage levels are now at approximately zero volts.

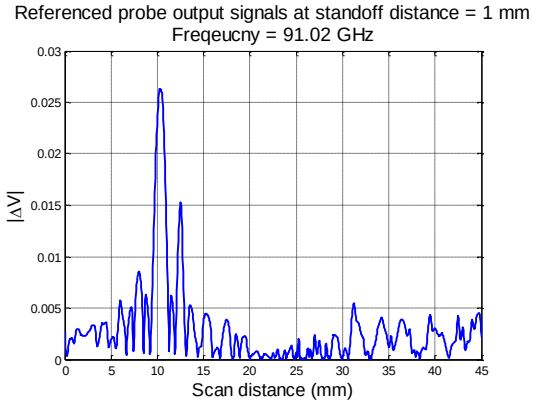

Figure 4.4. W-band probe output signals after the bias voltage is removed.

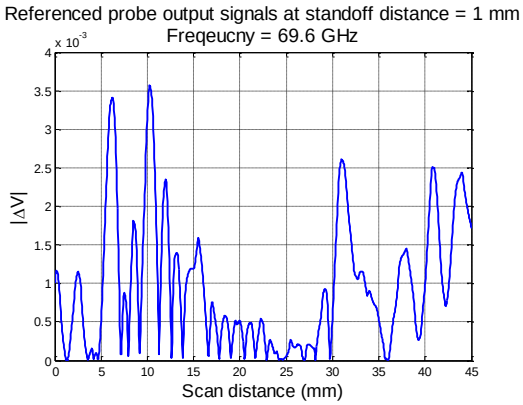

Figure 4.5. V-band probe output signals after the bias voltage is removed.

The referenced results provide for a better representation of variations in probe output signal when the probe is at different locations (e.g., above cracked versus un-cracked fastener heads). For instance, in Figure 4.4, the indication of crack at the 10 mm position clearly dominates probe output signal at other locations, demonstrating the capability of crack detection with the W-band probe.

In Sections 3.1.3 and 3.1.4, the V-band simulations were evaluated to be suitable for fastener head crack scanning, as the V-band differential probe also has the capability of eliminating the scattered signals from fastener heads. However, the measured V-band probe output signal (Figure 4.5) shows that in measurements it is more difficult to eliminate the effect of fastener heads as opposed to when scanned with W-band frequencies, potentially due to the longer wavelengths. Similar observations can be made on V-band measurement results presented in Section 4.1.2.

4.1. EFFECT OF STANDOFF DISTANCE

To evaluate the effect of standoff distance on both W-band and V-band differential probe output signals, scans were performed at probe standoff distance of 0.25, 0.5, 0.75, and 1 mm, identical to values used in the previously-reported numerical simulations. For the measurement results, only the wideband results are evaluated, where the probe output signals from all frequencies are added. Section 4.1.1 represents the W-band scanned results, while Section 4.1.2 represents the V-band results.

4.1.1. W-band Wideband Response. Figures 4.6 through 4.9 represent the W-band measurement results at varying standoff distances between 0.25 and 1 mm.

The results suggest an indication of crack near the 10 mm position, also, in the region without fastener heads (20 – 25 mm), the probe output signals are relatively consistent. In addition, when the probe is near the un-cracked fastener head (~35 mm), the resulting signal variations are much weaker than ones from the cracked fastener head. The imperfect cancellation of scattered signals from the fastener head is primarily thought to be the result of imperfect misalignments of the probe. The variations in signals are better represented when the bias voltages are removed, as demonstrated in Figures 4.10 through 4.13.

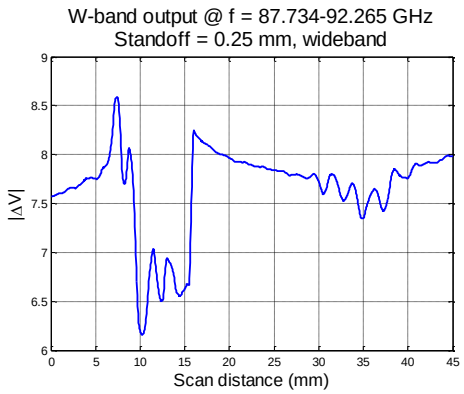

Figure 4.6. W-band wideband probe output signals at standoff distance of 0.25 mm.

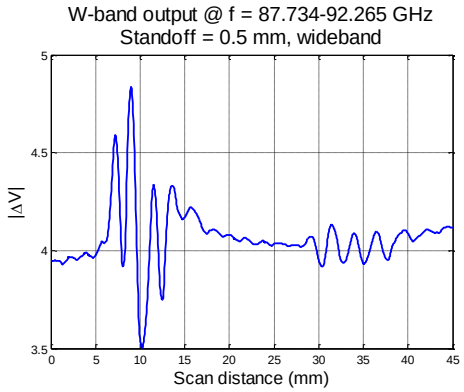

Figure 4.7. W-band wideband probe output signals at standoff distance of 0.5 mm.

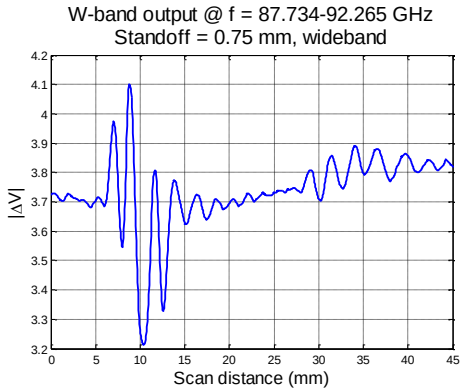

Figure 4.8. W-band wideband probe output signals at standoff distance of 0.75 mm.

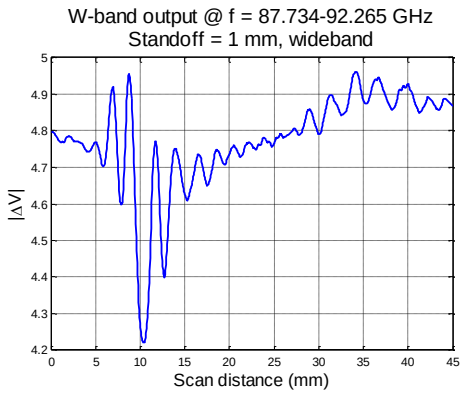

Figure 4.9. W-band wideband probe output signals at standoff distance of 1 mm.

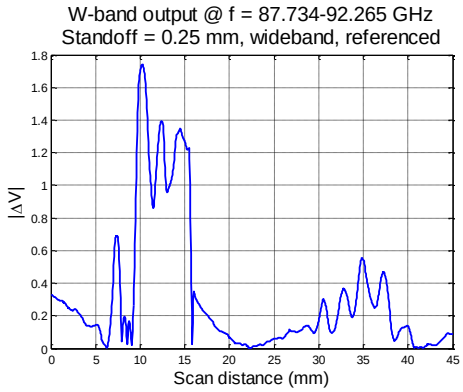

Figure 4.10. Referenced W-band wideband probe output signals at standoff distance of 0.25 mm.

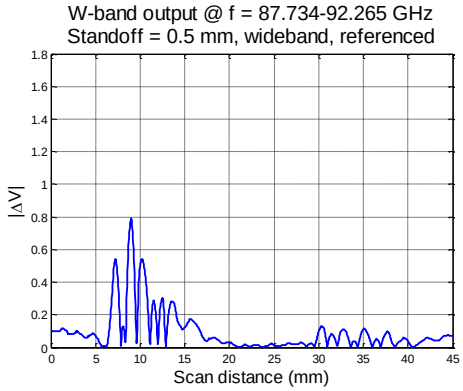

Figure 4.11. Referenced W-band wideband probe output signals at standoff distance of 0.5 mm.

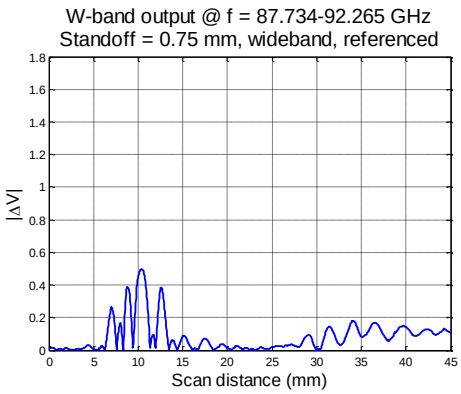

Figure 4.12. Referenced W-band wideband probe output signals at standoff distance of 0.75 mm.

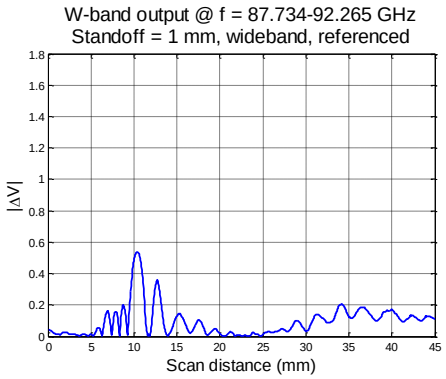

Figure 4.13. Referenced W-band wideband probe output signals at standoff distance of 1 mm.

Similar observations are found with the referenced data, where the probe output signal is composed of an indication of crack near the 10 mm position, and a relatively weaker response near the un-cracked fastener head. In addition, if only the signal peaks due to presence of cracks are considered, the output signal level reduces with respect to increase in standoff distances. Which is similar to the observation from the numerical simulations (Section 3.1).

Appendix G shows that there are four frequencies that are similar between the simulated and measured W-band frequencies. Thus, the measured and simulated data (with a 1.27 mm-long crack) at these four frequencies are compared. The comparisons

are shown in Figures 4.14 through 4.17. The results presented are referenced wideband data. Both the measurement and simulation results are referenced to case when the SUT is a clean surface (i.e., no fastener heads.).

These figures illustrate the comparison between ideal scanned results and actual measurements. The simulation shows that the differential probe output is only non-zero when a crack is present, but this is difficult to achieve in measurements due to potential imperfect alignments between the probe and fastener heads, and a non-flat surface (which can be expected in real world applications, e.g., curvatures on aircraft structures) causing a slightly unequal standoff distance (between the two apertures) throughout the scan.

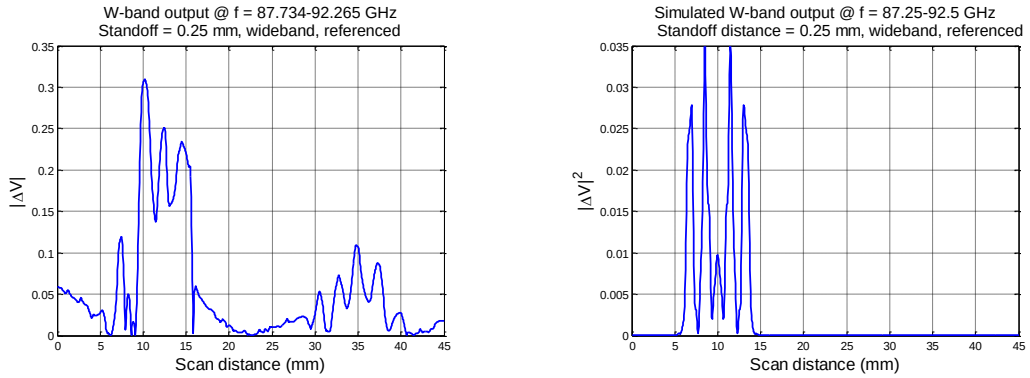

Figure 4.14. Measured (left) and simulated (right) W-band results of 1.27 mm-long crack, at standoff distance of 0.25 mm.

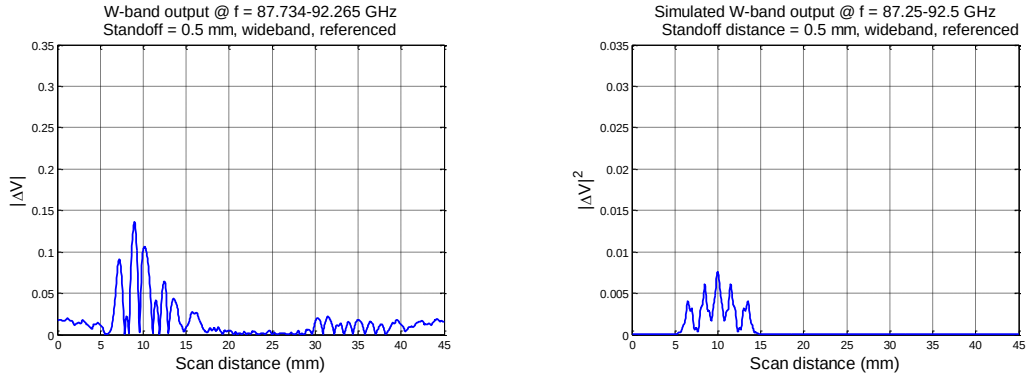

Figure 4.15. Measured (left) and simulated (right) W-band results of 1.27 mm-long crack, at standoff distance of 0.5 mm.

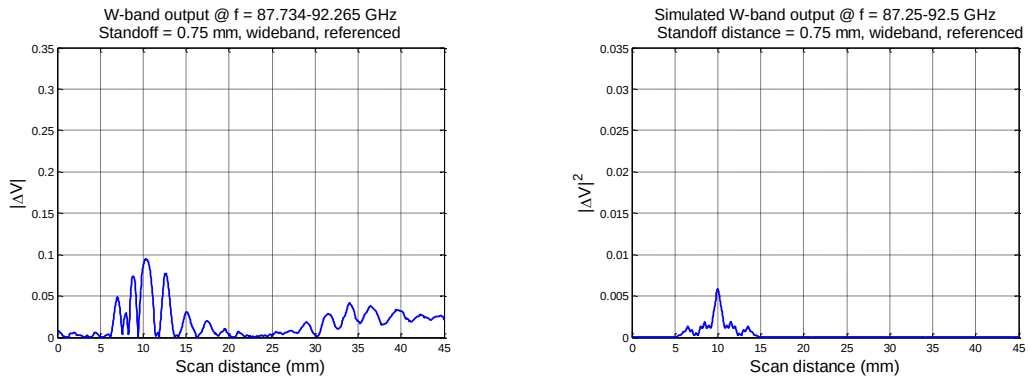

Figure 4.16. Measured (left) and simulated (right) W-band results of 1.27 mm-long crack, at standoff distance of 0.75 mm.

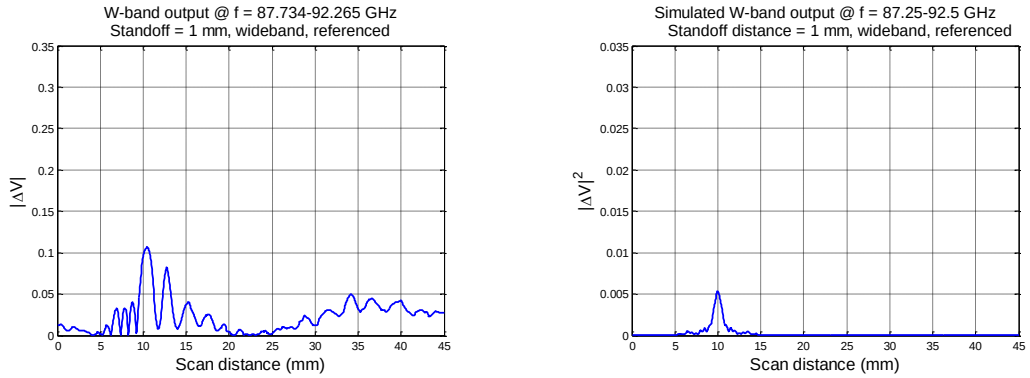

Figure 4.17. Measured (left) and simulated (right) W-band results of 1.27 mm-long crack, at standoff distance of 1 mm.

Figure 4.14 shows that at this frequency range, a small standoff distance (0.25 mm) results in a "sidelobe" (combination of scattered signals from both the fastener head and crack) that surpasses the crack signal in magnitude, and a strong probe output signals in the region of un-cracked fastener head (in measurements), which is potentially a false indication of crack. However, a higher standoff distance reduces the significances of these issues, because the effect of misalignments (which potentially causes the unwanted scattered signals) reduces with respect to increase in travel distance of the transmitted signal.

Figure 4.18 summarizes the effect of standoff distance on W-band wideband differential probe output signal levels. The signal levels presented in this figure are the peak values of the probe output signals when the probe is above the crack, in the region without fastener heads, and above the un-cracked fastener head. Both measurement and simulation results are presented.

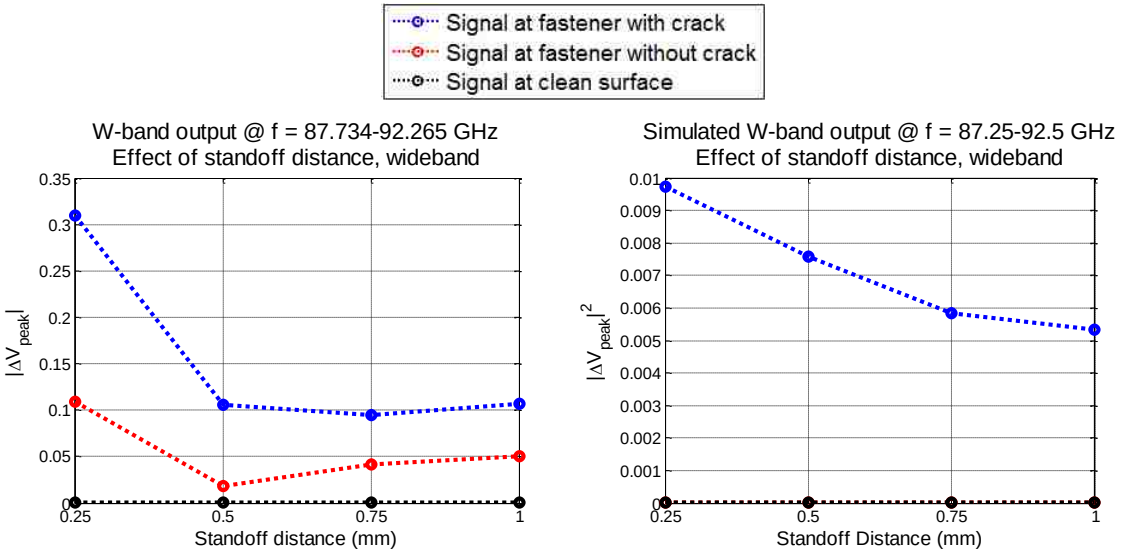

Figure 4.18. Investigation on effect of standoff distance with W-band differential probe. Presented are measurement (left) and simulation results (right).

The simulated results demonstrate that an ideal scan results in zero output when the probe is in the region without fastener heads (black curve), a non-zero output when the probe is near the crack (blue curve), and a much smaller output (close to zero) when the probe is above the un-cracked fastener head (red curve, not visible in the figure showing simulation results). The measurement results show non-zero outputs at both fastener heads that are likely due to imperfect misalignments of the probe. Trends can be observed from both measurement and simulation results that a higher standoff distance results in a generally lower probe output signals. To better illustrate the effect of standoff distance on the W-band wideband differential probe crack output signal level with the selected measured and simulated data (at the four common frequencies), the percentages

of decreases in the probe output signal levels versus standoff distances are investigated. To do this, the signals with respect to different standoff distances are normalized to the largest (in magnitude) value among them. The normalized results provide a one-to-one comparison between the measured and simulated data (e.g., comparison in the amount of signal reduction under the same condition), as shown in Figure 4.19.

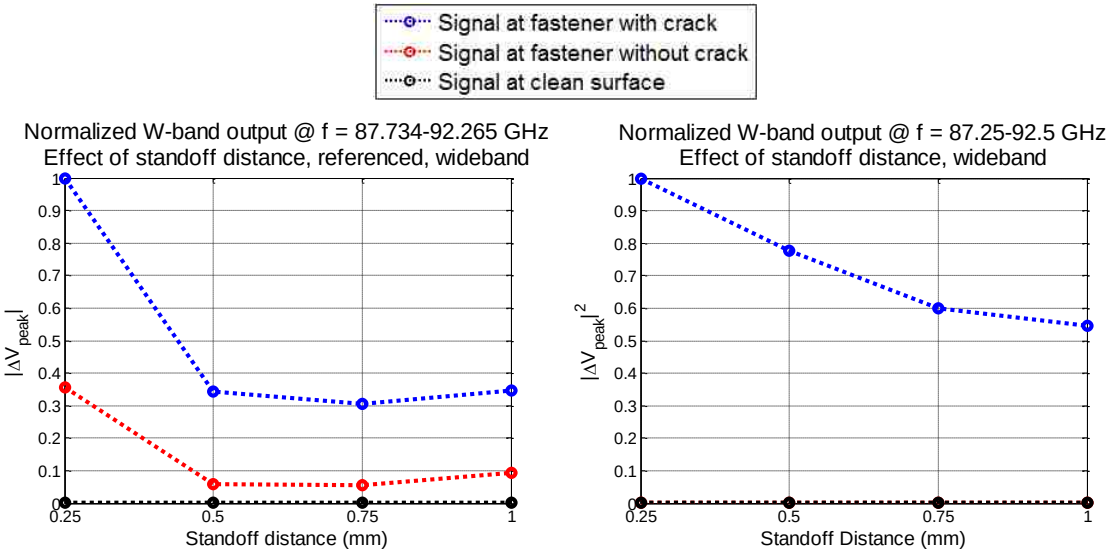

Figure 4.19. Normalized W-band results on effect of standoff distance with W-band differential probe. Presented are measurement (left) and simulation results (right).

The normalized comparisons also suggest that the crack signal level reduces with respect to increase in standoff distance, and a higher standoff distance reduces the effect of combined scattered signals from fastener head and crack on the crack signal level, because of the increase in traveling distance and the associated radiation losses of the transmitted signals.

4.1.2. V-band Wideband Response. Figures 4.20 through 4.23 represent the V-band measurement results at varying standoff distances between 0.25 and 1 mm. The results suggest the similar observations as of W-band measurements, as there are indications of crack near the 10 mm position, also, in the region without fastener heads (20 – 25 mm) the probe output signals are relatively consistent.

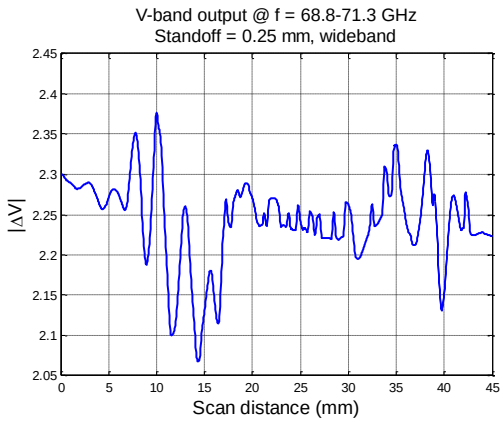

Figure 4.20. V-band wideband probe output signals at standoff distance of 0.25 mm.

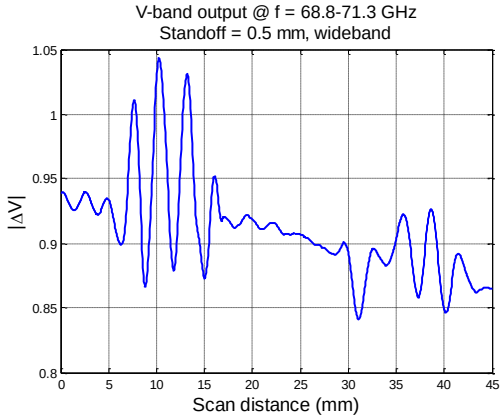

Figure 4.21. V-band wideband probe output signals at standoff distance of 0.5 mm.

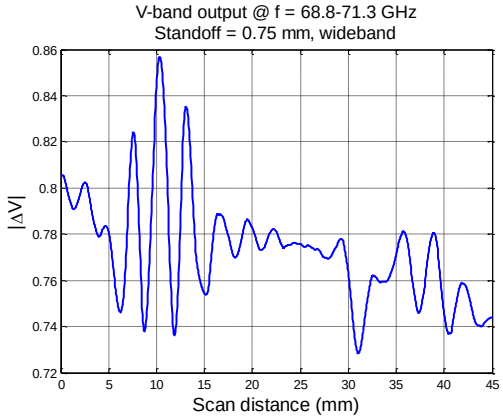

Figure 4.22. V-band wideband probe output signals at standoff distance of 0.75 mm.

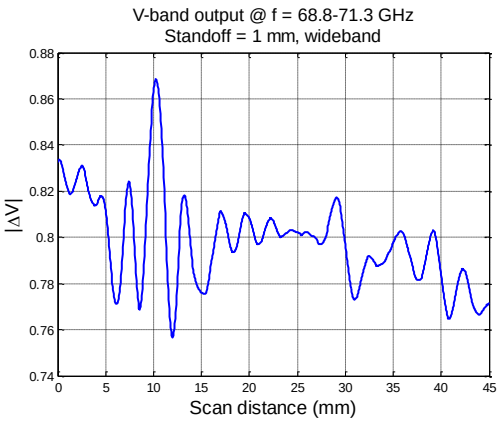

Figure 4.23. V-band wideband probe output signals at standoff distance of 1 mm.

In addition, when the probe is near the un-cracked fastener head (~35 mm), the resulted signal variations are weaker than ones from the cracked fastener head. However, the signal variations around the peaks (i.e., magnitude of "sidelobe") are stronger than ones of W-band measurements, and it is due to the longer wavelengths of V-band frequencies. The effect of "sidelobe" become significant when the standoff distance is small (i.e., standoff distance of 0.25 mm, Figure 4.20). The variations in signals are better represented when the bias voltages are removed, as demonstrated in Figures 4.24 through 4.27.

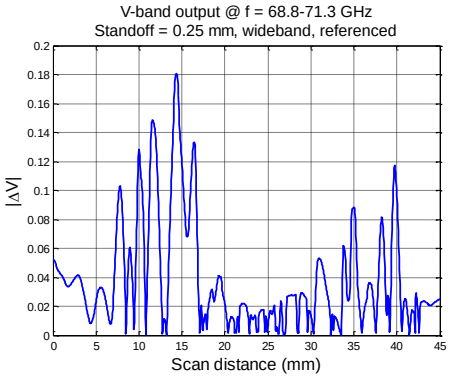

Figure 4.24. Referenced V-band wideband probe output signals at standoff distance of 0.25 mm.

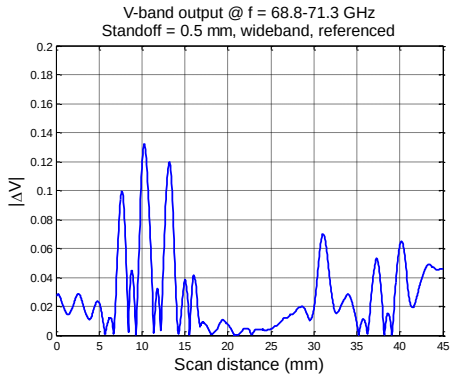

Figure 4.25. Referenced V-band wideband probe output signals at standoff distance of 0.5 mm.

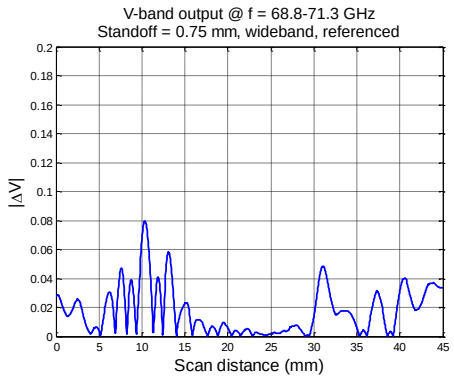

Figure 4.26. Referenced V-band wideband probe output signals at standoff distance of 0.75 mm.

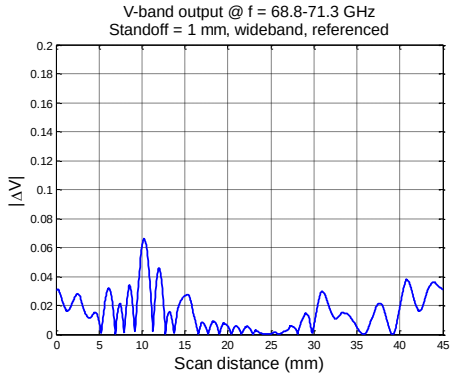

Figure 4.27. Referenced V-band wideband probe output signals at standoff distance of 1 mm.

Similar observations are found with the referenced data, where the probe output signal is composed of an indication of crack near the 10 mm position, a slightly weaker (but substantial) response near the un-cracked fastener head, and "sidelobe" that can potentially result in a false indication of crack, especially when the standoff distance is small. If only the signal peaks due to presence of cracks are considered, the output signal level reduces with respect to increase in standoff distances. Which is similar to the observation from the numerical simulations (Section 3.1).

Appendix G shows that there are three frequencies that are similar between the simulated and measured V-band frequencies. Thus, the measured and simulated data (with a 1.27 mm-long crack) at these three frequencies are compared. The comparisons are shown in Figures 4.28 through 4.31. The results presented are referenced wideband data. Both the measurement and simulation results are referenced to the probe output signals over the scanned region without fastener heads as previously described.

These figures illustrate the comparison between ideal scan results and actual measurements. The simulation shows that the differential probe output is only non-zero when a crack is present, but this is difficult to achieve in measurements due to reasons previously mentioned, and the magnitude of "sidelobe" (of crack signals) become stronger due to the longer wavelengths (of V-band).

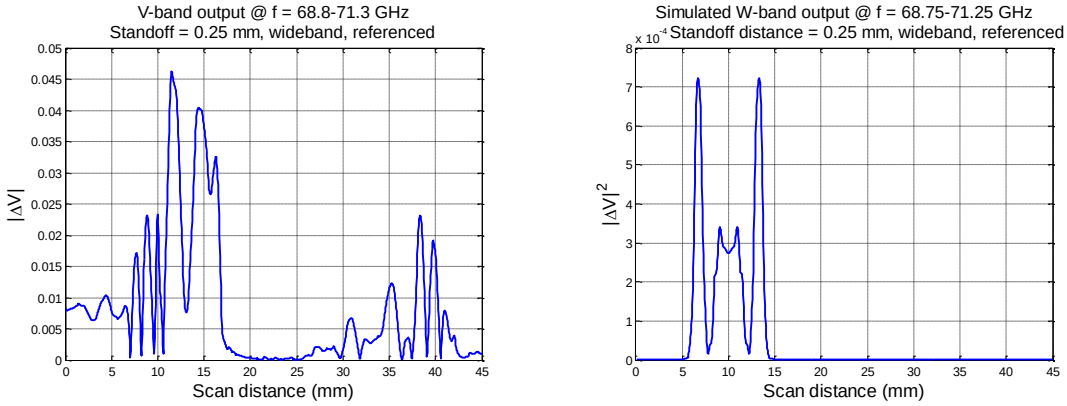

Figure 4.28. Measured (left) and simulated (right) V-band results of 1.27 mm-long crack, at standoff distance of 0.25 mm.

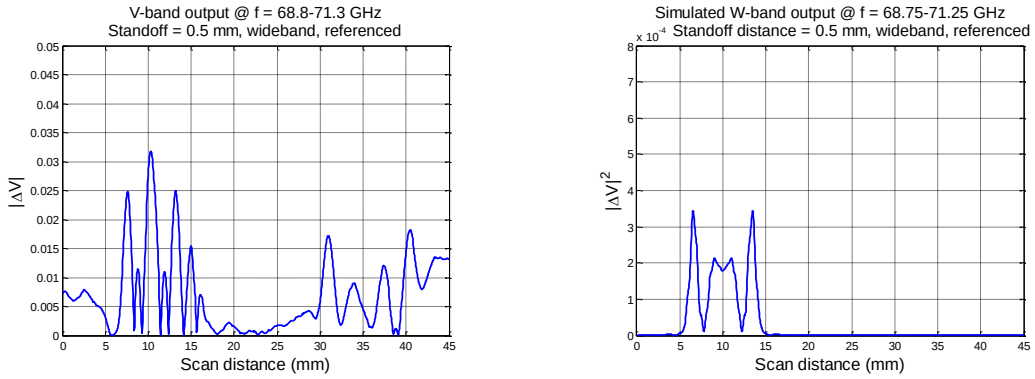

Figure 4.29. Measured (left) and simulated (right) V-band results of 1.27 mm-long crack, at standoff distance of 0.5 mm.

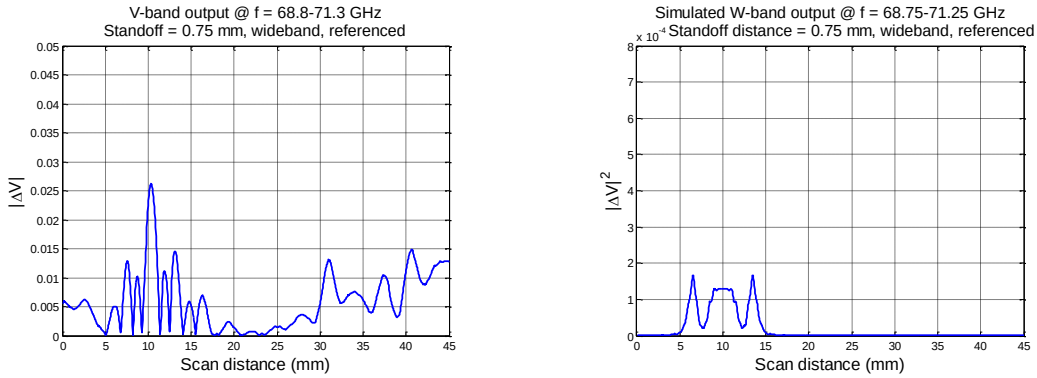

Figure 4.30. Measured (left) and simulated (right) V-band results of 1.27 mm-long crack, at standoff distance of 0.75 mm.

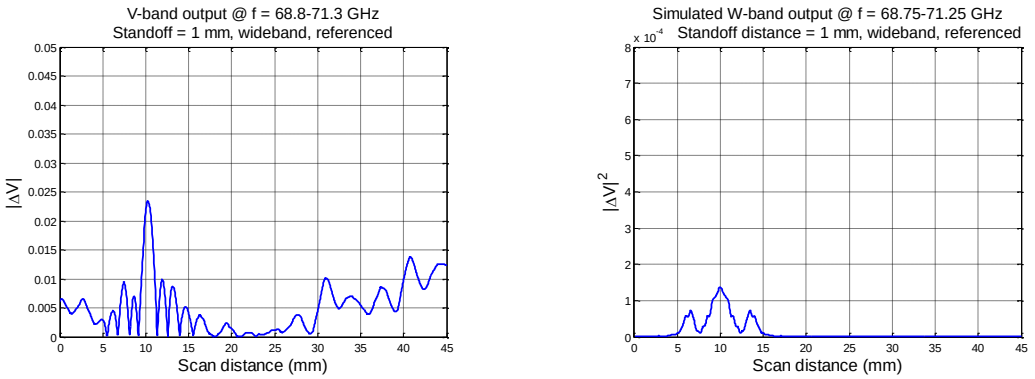

Figure 4.31. Measured (left) and simulated (right) V-band results of 1.27 mm-long crack, at standoff distance of 1 mm.

The measurement results show that V-band frequencies are applicable for fastener head crack detection, but the signals are composed of more unwanted components compared to W-band measurements.

Figure 4.32 summarizes the effect of standoff distance on V-band wideband differential probe output signal levels. The signal levels presented in this figure are the peak values of the probe output signals when the probe is above the crack, in the region without fastener heads, and above the un-cracked fastener head. Both measurement and simulation results are presented.

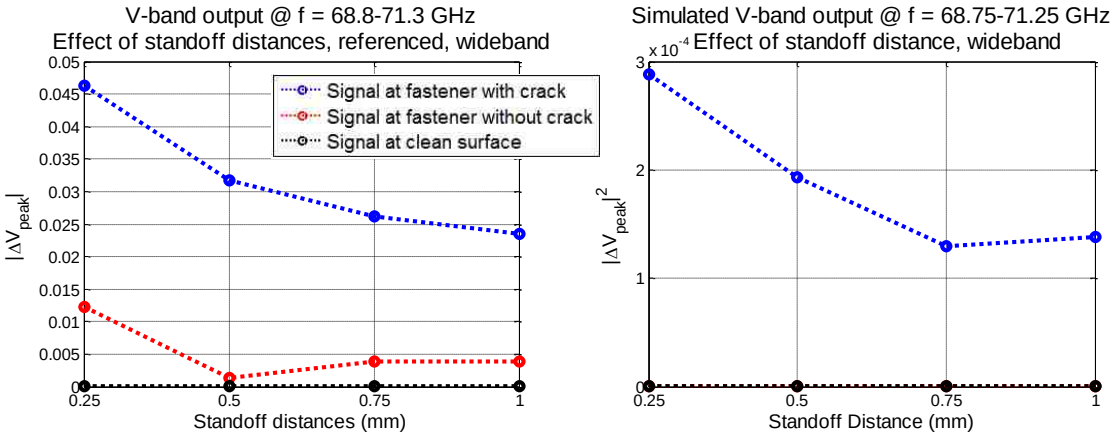

Figure 4.32. Investigation on effect of standoff distance with V-band differential probe. Presented are measurement (left) and simulation results (right).

The simulated results demonstrate again that an ideal scan results in zero output when the probe is in the region without fastener heads (black curve), a non-zero output when the probe is near the crack (blue curve), and a much smaller output (close to zero) when the probe is above the un-cracked fastener head (red curve, not visible in the figure showing simulation results). The measurement results show non-zero outputs at both fastener heads that are likely due to imperfect misalignments of the probe. Similar to the W-band measurements on investigations of effect of standoff distance, trends can be observed from both measurement and simulation results that a higher standoff distance results in a generally lower probe output signals. To better illustrate the effect of standoff

distance on the V-band wideband differential probe crack output signal level with the selected measured and simulated data (at the three common frequencies), the percentages of decreases in the probe output signal levels versus standoff distances are investigated. To do this, the signals with respect to different standoff distances are normalized to the largest (in magnitude) value among them. The normalized results provide a one-to-one comparison between the measured and simulated data, as shown in Figure 4.33.

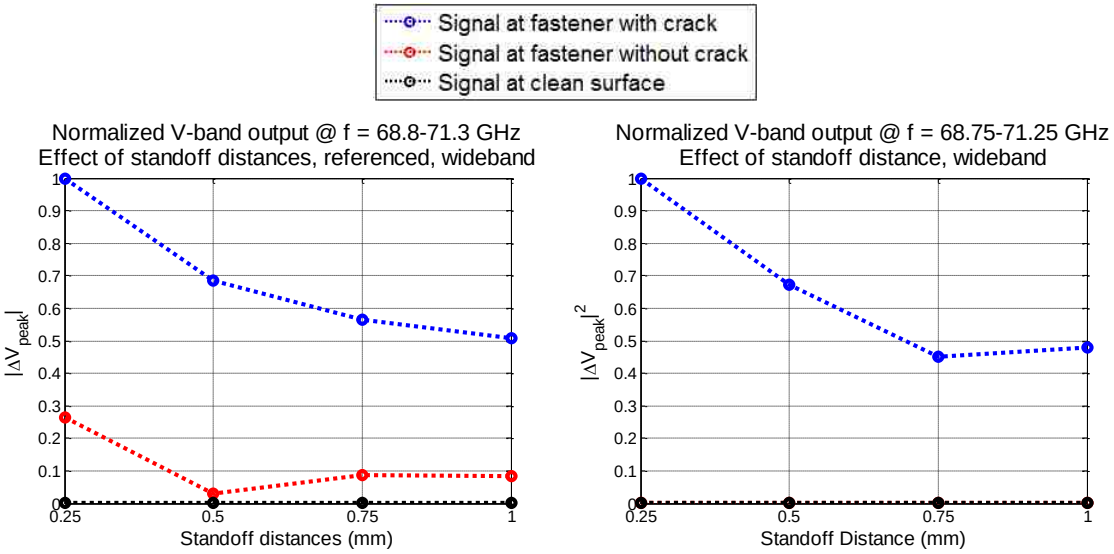

Figure 4.33. Normalized V-band results on effect of standoff distance. Presented are measurement (left) and simulation results (right).

These normalized results also suggest that the crack signal level reduces with respect to increase in standoff distance. In the end, a comparison between the W-band and V-band measurement results is conducted to study the effect of frequencies (e.g., different sensitivities) with respect to change in standoff distance. The comparison is shown in Figure 4.34.

Figure 4.34 suggests that in comparison, V-band frequencies are less sensitive to change in standoff distance compared to W-band frequencies. This is due to the longer wavelengths of V-band frequencies and essentially a relative shorter electrical length between the SUT and probe aperture.

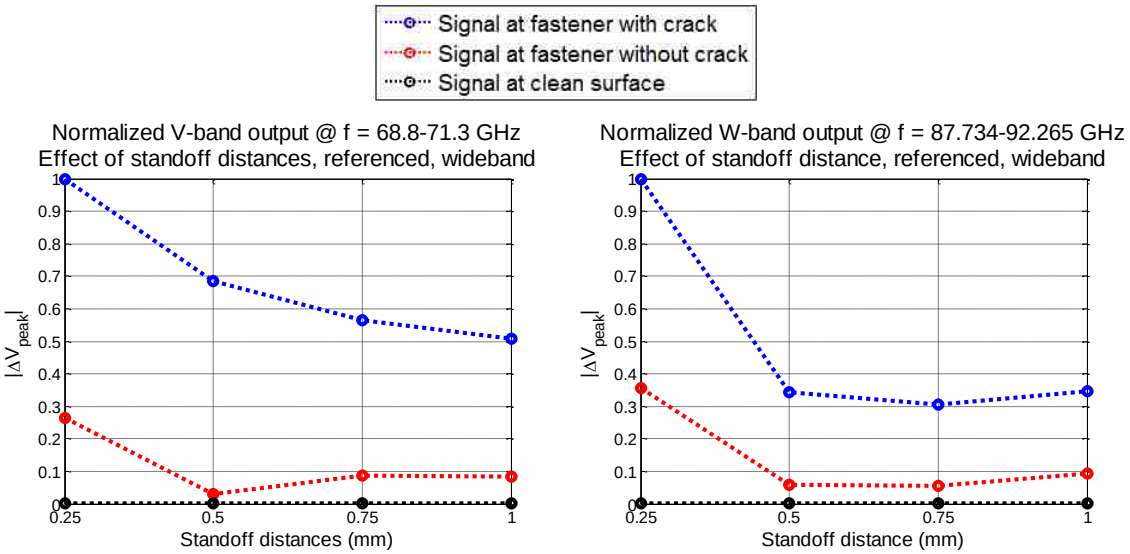

Figure 4.34. Effect of frequencies on fastener head crack scanning (in measurements).

4.2. EFFECT OF APERTURE OFFSET

The aperture offsets represent a tilt in the differential probe with respect to the sample surface. Unlike simulations, the aperture offsets cannot be translated into numerical values (e.g., aperture offsets of ±0.5 mm applied in simulations) in measurements. Therefore, in measurements, the aperture offset is defined by the number of complete rotations (of the knob controlling angular movements, Figure 2.17). A negative aperture offset is when the probe aperture is closer to the crack, and a positive aperture offset is when the probe is farther away from the crack. It is approximated that one complete rotation of the knob is equivalent to 0.1 mm of offset. Therefore, an aperture offset of -2 rotations is approximately equal to -0.2 mm of offset, which means that one aperture is 0.2 mm higher than another.

For the measurements, aperture offsets of ±2, ±1 and 0 rotations (approximately ±0.2, ±0.1 and 0 mm) were applied, along with standoff distances of 0.5 and 1 mm. The results from 1 mm standoff distance, and aperture offsets of ±2 and 0 rotations are presented in the following figures, while the complete results (standoff distance of 0.5 mm and other aperture offsets) are provided in Appendix H. Figure 4.35 shows the

relative position between the probe and sample surface when aperture offsets of ±2 rotations are applied.

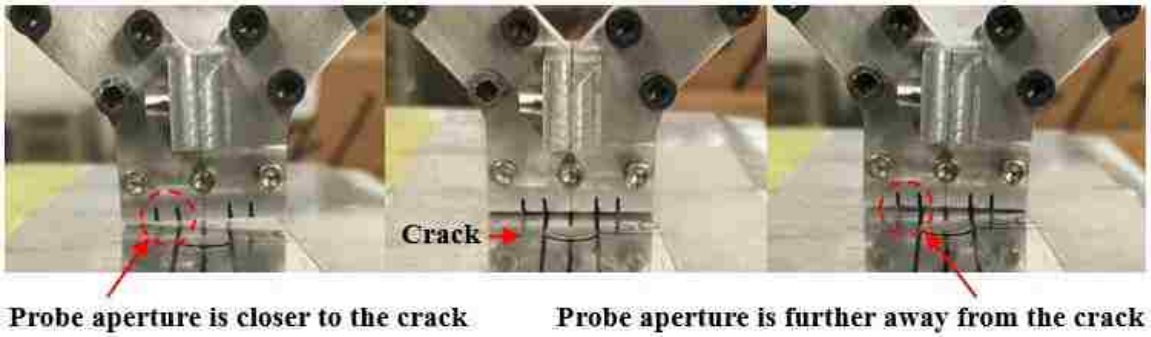

Figure 4.35. Aperture offsets of (from left to right): -2 rotations, no rotation, and +2 rotations.

Similar to previous sections, only the wideband measurement results are evaluated. Figures 4.36 through 4.38 represent the W-band measurement results at standoff distance of 1 mm, and aperture offset of -2, 0, and +2 rotations, respectively.

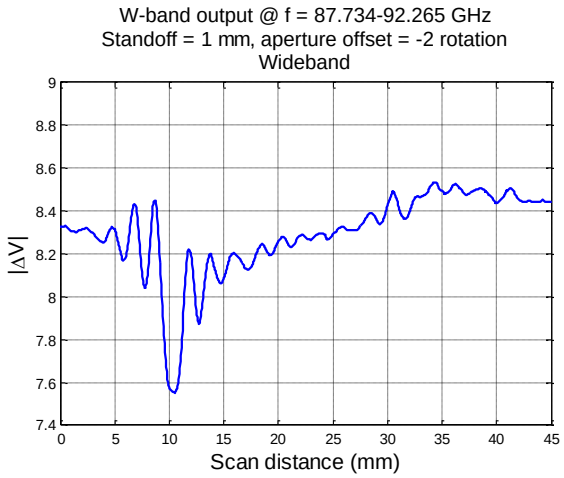

Figure 4.36. W-band wideband probe output signals at standoff distance of 1 mm, and aperture offset of -2 rotations.

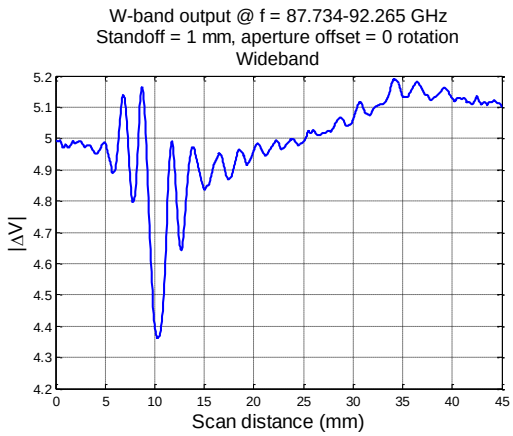

Figure 4.37. W-band wideband probe output signals at standoff distance of 1 mm, and no aperture offset.

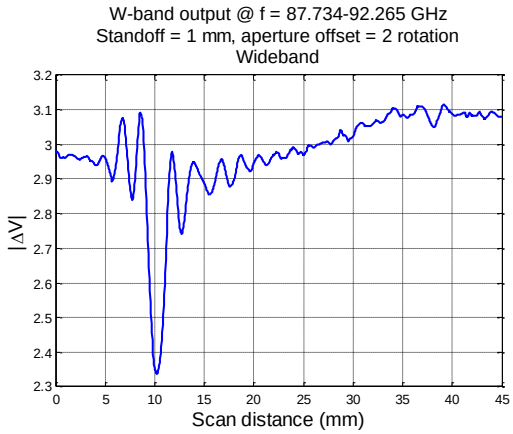

Figure 4.38. W-band wideband probe output signals at standoff distance of 1 mm, and aperture offset of +2 rotations.

The results suggest the similar observations as of previous measurements, as there are indications of crack near the 10 mm position, also, in the region without fastener heads the probe output signals are relatively consistent. In addition, when the probe is near the un-cracked fastener head, the resulted signal variations are weaker than ones from the cracked fastener head. The variations in signals are better represented when the bias voltages are removed, as demonstrated in Figures 4.39 through 4.41.

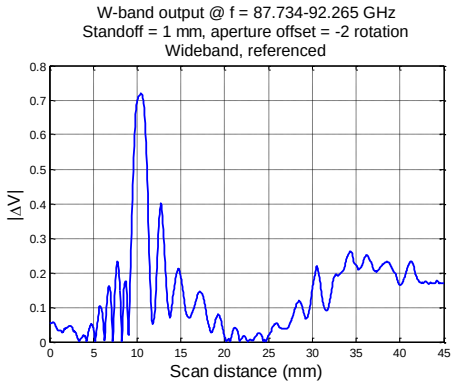

Figure 4.39. Referenced W-band wideband probe output signals at standoff distance of 1 mm, and aperture offset of -2 rotations.

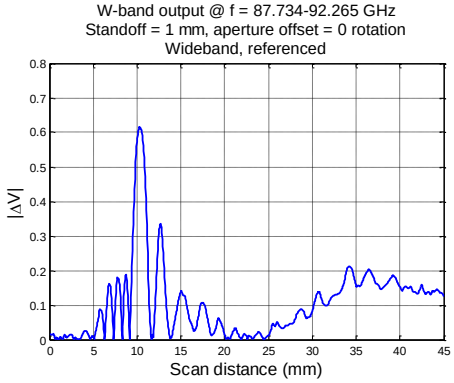

Figure 4.40. Referenced W-band wideband probe output signals at standoff distance of 1 mm, and no aperture offset.

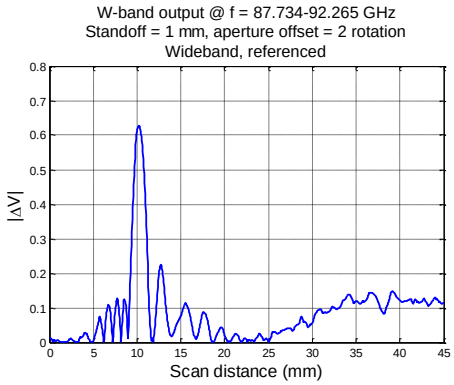

Figure 4.41. Referenced W-band wideband probe output signals at standoff distance of 1 mm, and aperture offset of +2 rotations.

Similar observations are found with the referenced data, where the probe output signal is composed of an indication of crack near the 10 mm position, and a relatively weaker response near the un-cracked fastener head.

The simulation results from Section 3.2 suggested that the presence of an aperture offset is not significantly critical with regard to crack detection capabilities. An aperture offset creates a DC bias to the probe output signals due to unequal standoff distances between the two probe apertures, which in measurements this DC bias is combined with the bias voltage due to inherent mismatches, and is removed (Figures 4.39 through 4.41). Therefore, the effect of aperture offset is relatively insignificant after the DC bias is removed, as it can also be observed that the probe output signals presented in Figures 4.39 through 4.41 are almost identical. Similar observations can be made on results at standoff distance of 0.5 mm provided in Appendix H.

It was mentioned earlier that a rotation of an aperture offset is approximately equal to 0.1 mm in offset. Therefore, the measurement results at aperture offset of ±2 rotations (~ ±0.2 mm) are compared to simulation results at aperture offset of ±0.25 mm. The measured and simulated data (with a 1.27 mm-long crack) at the four common frequencies (listed in Appendix G) are compared. The comparisons are shown in Figures 4.42 through 4.44. The results presented are referenced wideband data. As before, both the measurement and simulation results are referenced to the case of a clean surface (i.e., the DC bias caused by the aperture offset is removed).

These figures illustrate the comparison between ideal scan results and actual measurements. The simulation shows that the differential probe output is only non-zero when a crack is present, but this is difficult to achieve in measurements for reasons previously mentioned, thus a non-zero output (but much smaller compared to crack signal) is also generated around the un-cracked fastener head in the measurements.

The results verify the conclusions observed from the simulations where the effect of aperture offset is minimal if the DC bias is removed. However, if the standoff distance is small (0.5 mm), the crack output signal reduces with respect to increase in aperture offset (Figure 4.45), as the result of imperfect cancelation of scattered signals from fastener heads. This becomes less of a concern at higher standoff distances because of the

additional traveled distance of the transmitted signals which reduces the significance of the unwanted scattered signals.

Figures 4.45 and 4.46 summarize the effect of aperture offset on W-band wideband differential probe output signal levels, at standoff distances of 0.5 and 1 mm. The signal levels presented in these figures are the peak values of the probe output signals when the probe is above the crack, in the region without fastener heads, and above the un-cracked fastener head.

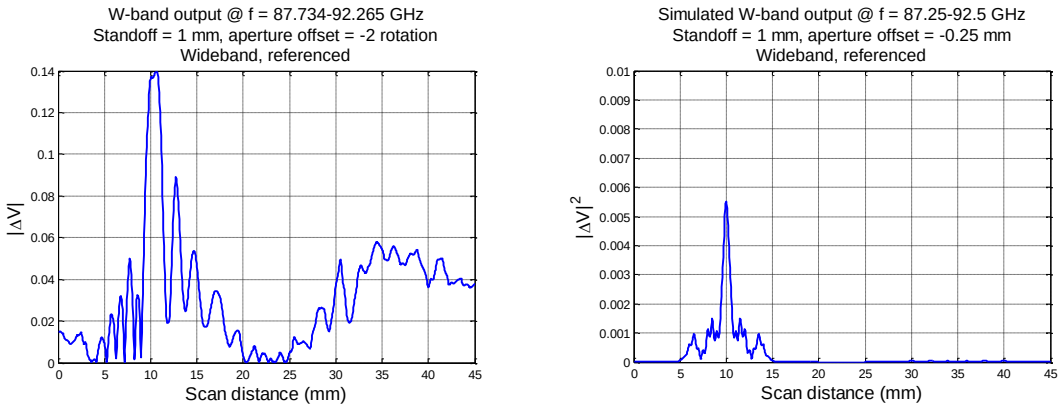

Figure 4.42. Measured (left) and simulated (right) W-band results of 1.27 mm-long crack, at standoff distance of 1 mm, and aperture offset of -2 rotations (measurements) and -0.25 mm (simulations).

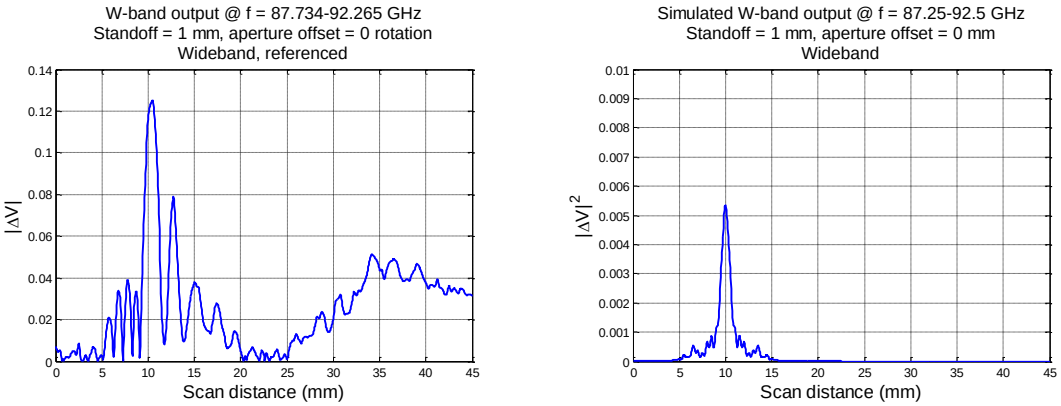

Figure 4.43. Measured (left) and simulated (right) W-band results of 1.27 mm-long crack, at standoff distance of 1 mm, and no aperture offset.

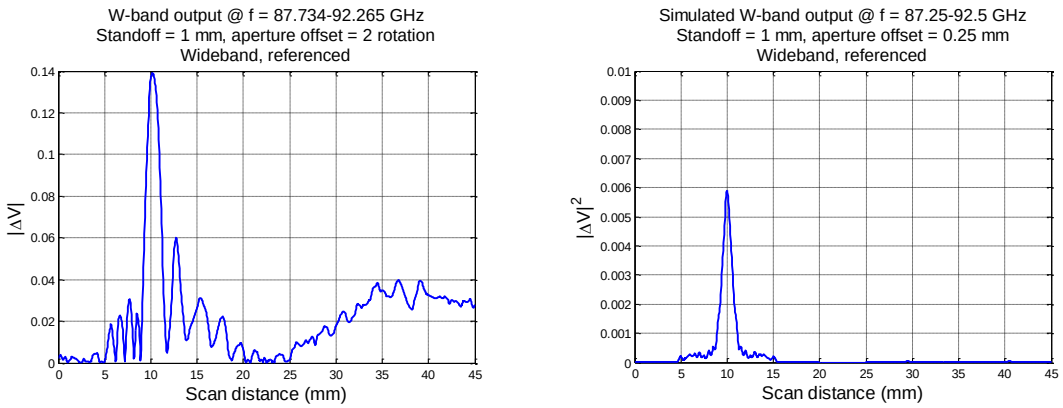

Figure 4.44. Measured (left) and simulated (right) W-band results of 1.27 mm-long crack, at standoff distance of 1 mm, and aperture offset of +2 rotations (measurements) and +0.25 mm (simulations).

The simulated results demonstrate again that an ideal scan results in zero output when the probe is in the region without fastener heads (black curve), a non-zero output when the probe is near the crack (blue curve), and a much smaller output (close to zero) when the probe is above the un-cracked fastener head (red curve, not visible in the figure).

The measurement results show non-zero outputs at both fastener heads, similar to measurement results presented in previous sections. Both the measurement and simulation results have the same trends in crack output signal levels as a function of varying aperture offsets. At a lower standoff distance, a negative aperture offset on the probe results in a higher probe output signal level, and reduces with respect to increase in aperture offset, due to varying amount of unwanted scattered signals from the fastener head. This issue can be minimized by increasing the standoff distance, as demonstrated in Figure 4.46.

To better illustrate the effect of aperture offset on the W-band wideband differential probe crack output signal level with the selected measured and simulated data (at the four common frequencies), the percentages of decreases in the probe output signal levels versus aperture offsets are investigated. To do this, the signals with respect to the different combination of aperture offsets and standoff distances are normalized to the largest (in magnitude) value among them. The normalized results provide a one-to-one

comparison between the measured and simulated data (e.g., comparison in the amount of signal reduction under the same condition), as shown in Figures 4.47 and 4.48.

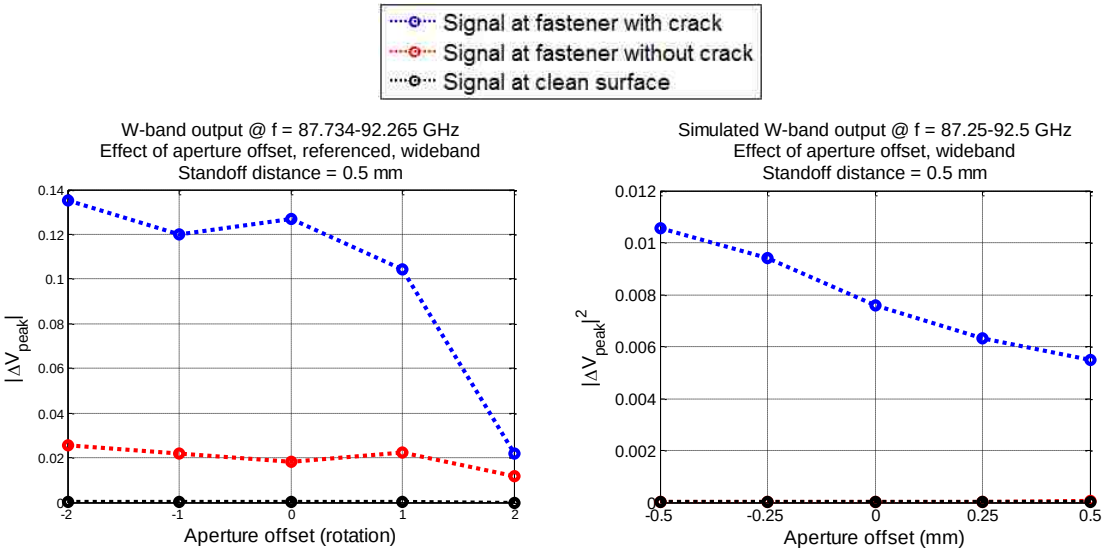

Figure 4.45. Investigation on effect of aperture offset with W-band differential probe. Presented are measurement (left) and simulation results (right), at standoff distance of 0.5 mm.

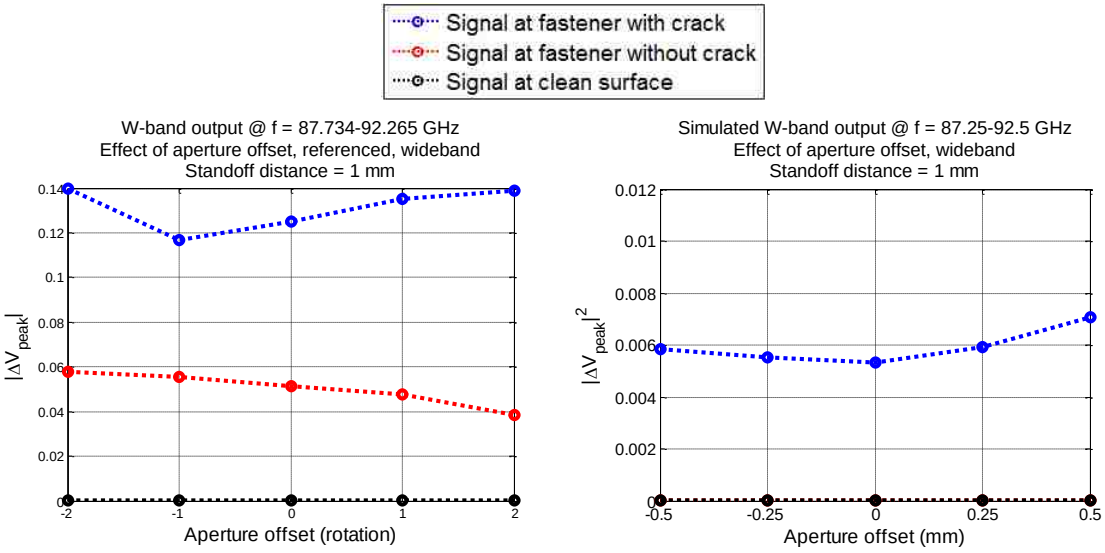

Figure 4.46. Investigation on effect of aperture offset with W-band differential probe. Presented are measurement (left) and simulation results (right), at standoff distance of 1 mm.

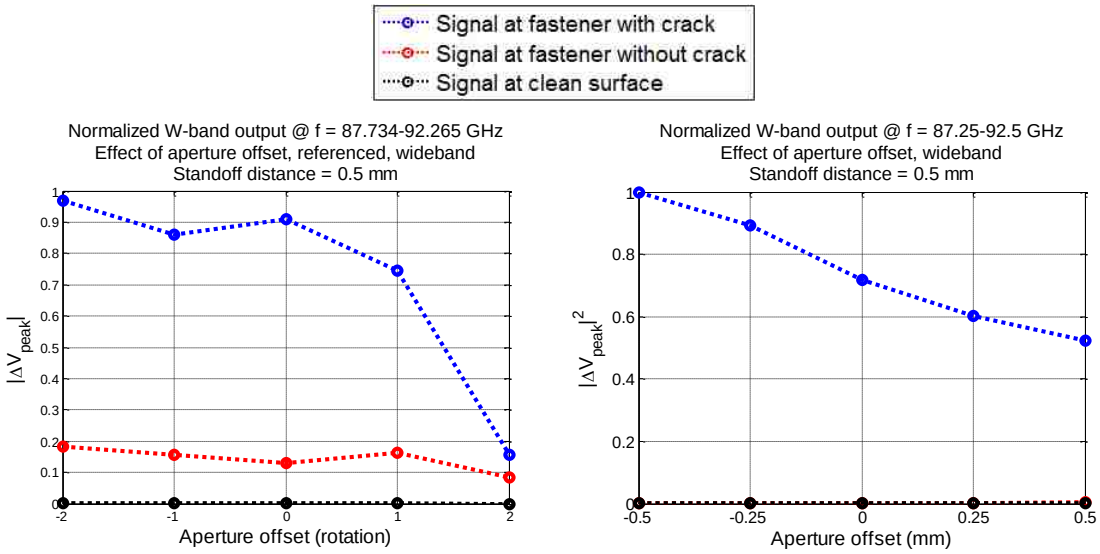

Figure 4.47. Normalized W-band results on effect of aperture offset. Presented are measurement (left) and simulation results (right), at standoff distance of 0.5 mm.

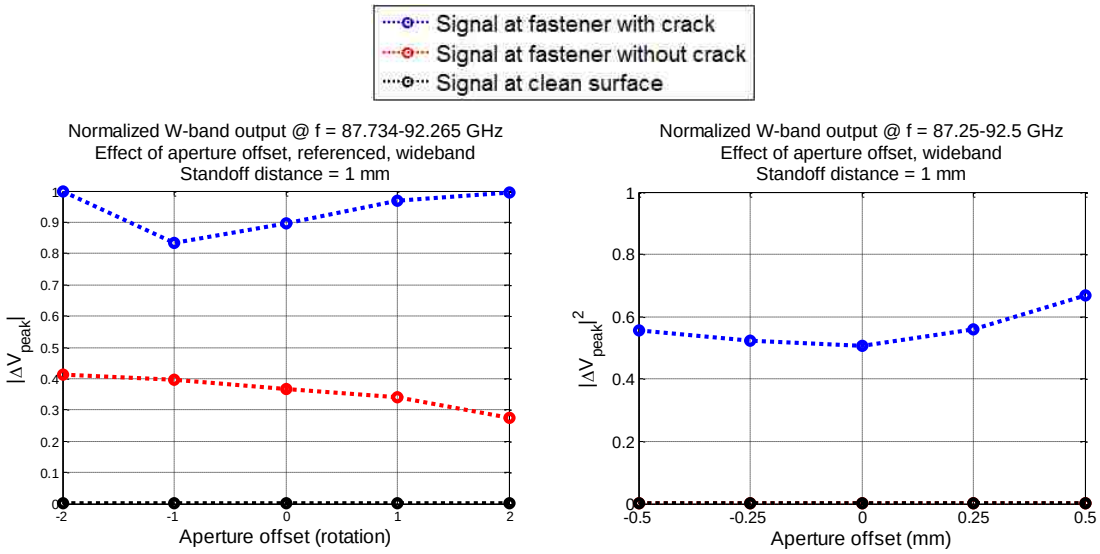

Figure 4.48. Normalized W-band results on effect of aperture offset. Presented are measurement (left) and simulation results (right), at standoff distance of 1 mm.

These normalized results also suggest that at 0.5 mm standoff distance, the magnitude of both crack signals and signals from un-cracked fastener head reduce with respect to increase in aperture offset. While at 1 mm standoff distance, the variations in

signals are less significant, because of the additional traveled distance of the transmitted signals which reduces the significance of the unwanted scattered signals. However, a high standoff distance raises the probe output signal levels of the un-cracked fastener head (Figure 4.48 (a)).

4.3. EFFECT OF PAINT THICKNESS

Measurements were conducted to evaluate the effect of paint on fastener head crack detection. The presence of paint acts as a dielectric layer between the probe and sample surface. Therefore, the electrical distance between the probe and the sample surface increases.

For the measurements, all the paint layers with varying thicknesses (from 0 to 0.57 mm, 7 total) were inspected, along with standoff distances of 0.5 and 1 mm. For the case with paint thickness of 0.49 mm, due to the paint clumps accumulated on the fastener head that is more than 0.5 mm in height, the standoff distance of 0.5 mm cannot be applied onto the measurement.

The results from 1 mm standoff distance, and paint thicknesses of 0, 0.1, 0.39 and 0.51 mm are presented, while the complete results (standoff distance of 0.5 mm and other paint thicknesses) are provided in Appendix I. Fastener heads covering by different paint thicknesses can be found in Figure 2.12.

Similar to previous sections, only the wideband measurement results are evaluated. Figures 4.49 through 4.52 represent the W-band measurement results at standoff distance of 1 mm, and paint thicknesses of 0, 0.1, 0.39, and 0.49 mm, respectively.

The results suggest that when the paint layer is relatively thin (less than 0.1 mm), a clear indication of crack near the 10 mm position can still be found, but for thicker paints (0.39 and 0.49 mm of paint), due to the presence of paint that is not uniformly formed around the fastener head (e.g., Figure 4.53), some variations in the probe output signals are also observed due to the imperfectly canceled scattered signals from paint (i.e., a peak signal near the 35 mm position, or additional signal peaks near the actual crack signals).

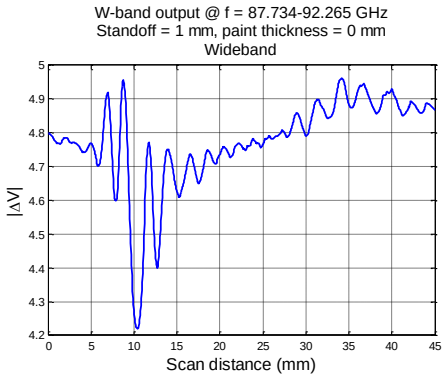

Figure 4.49. W-band wideband probe output signals at standoff distance of 1 mm, and without paint.

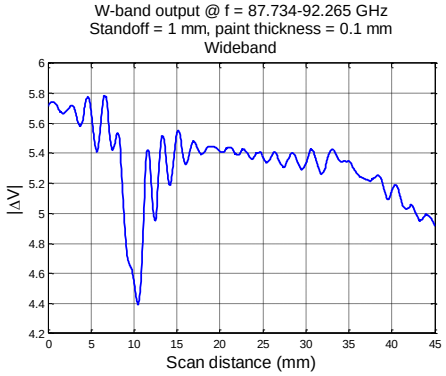

Figure 4.50. W-band wideband probe output signals at standoff distance of 1 mm, and paint thickness of 0.1 mm.

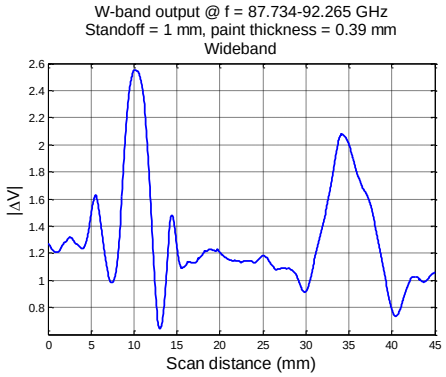

Figure 4.51. W-band wideband probe output signals at standoff distance of 1 mm, and paint thickness of 0.39 mm.

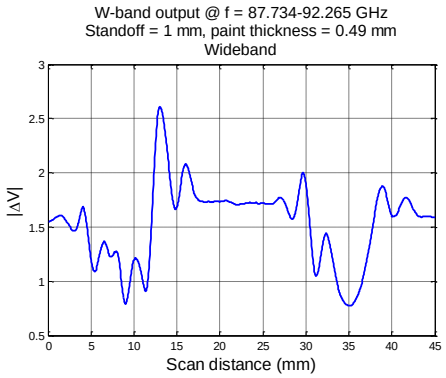

Figure 4.52. W-band wideband probe output signals at standoff distance of 1 mm, and paint thickness of 0.49 mm.

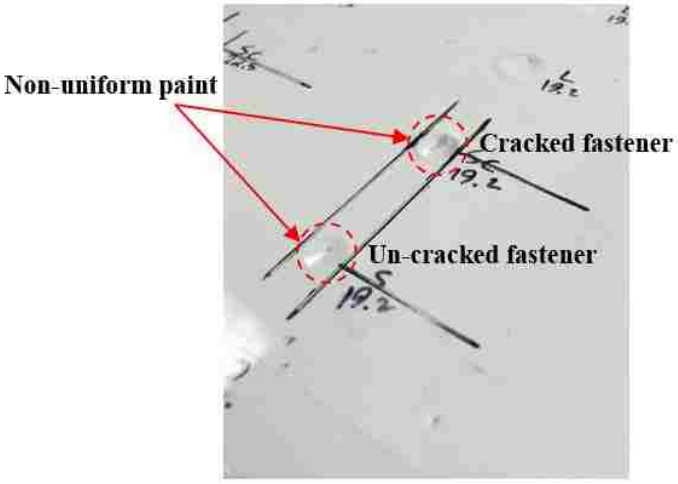

Figure 4.53. Non-uniform paint around fastener heads potentially causing signal variations.

The variations in signals are better represented when the bias voltages are removed, as demonstrated in Figures 4.54 through 4.57.

Similar observations are found with the referenced data, where the probe output signal is composed of a clear indication of crack near the 10 mm position when the paint is thin, but additional signal peaks are formed due to the presence of a thick paint layer (that is likely not uniformly spread).

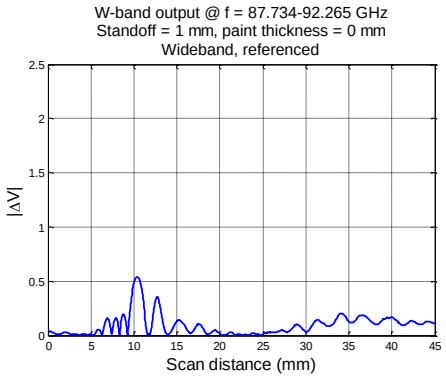

Figure 4.54. Referenced W-band wideband probe output signals at standoff distance of 1 mm, and without paint.

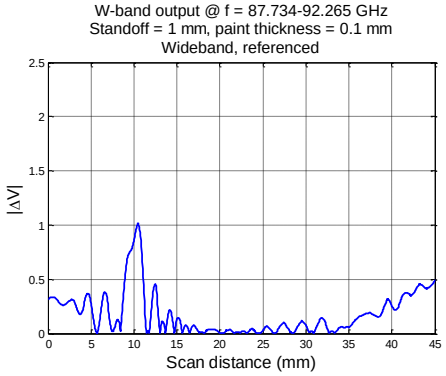

Figure 4.55. Referenced W-band wideband probe output signals at standoff distance of 1 mm, and paint thickness of 0.1 mm.

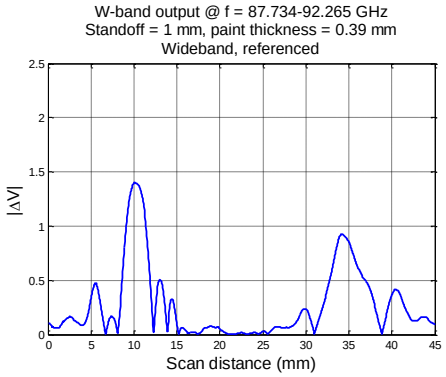

Figure 4.56. Referenced W-band wideband probe output signals at standoff distance of 1 mm, and paint thickness of 0.39 mm.

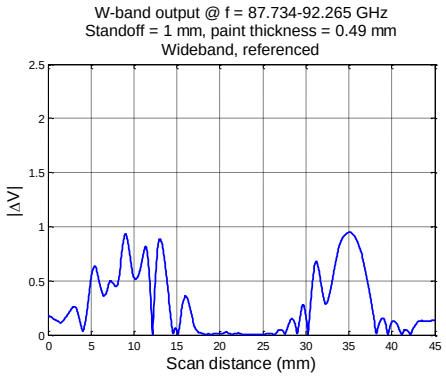

Figure 4.57. Referenced W-band wideband probe output signals at standoff distance of 1 mm, and paint thickness of 0.49 mm.

The measured and simulated data (with a 1.27 mm-long crack) at the four common frequencies (listed in Appendix G) are compared. The comparisons are shown in Figures 4.58 through 4.61. The results presented are referenced wideband data. As before, both the measurement and simulation results are referenced to the case of a clean surface. Note that the figures are not in the same scales.

These figures illustrate the comparison between ideal scan results and actual measurements. The simulation shows that the differential probe output is only non-zero when a crack is present, but this is difficult to achieve in measurements due to a potential non-uniform paint around the fastener heads (e.g., excess paint forms a clump over the fastener heads), which makes the behavior of the probe less straightforward to predict. It can also be observed that the magnitude of the output signal increases with respect to increase in paint thickness (except for when the layer is too thick, i.e., 0.51 mm), and it is likely due to the concentrated electric field bounded between paint and metal.

Figures 4.62 and 4.63 summarize the effect of paint thickness on W-band wideband differential probe output signal levels, at standoff distances of 0.5 and 1 mm. The signal levels presented in these figures are the peak values of the probe output signals when the probe is above the crack, in the region without fastener heads, and above the un-cracked fastener head. Both measurement and simulation results are presented.

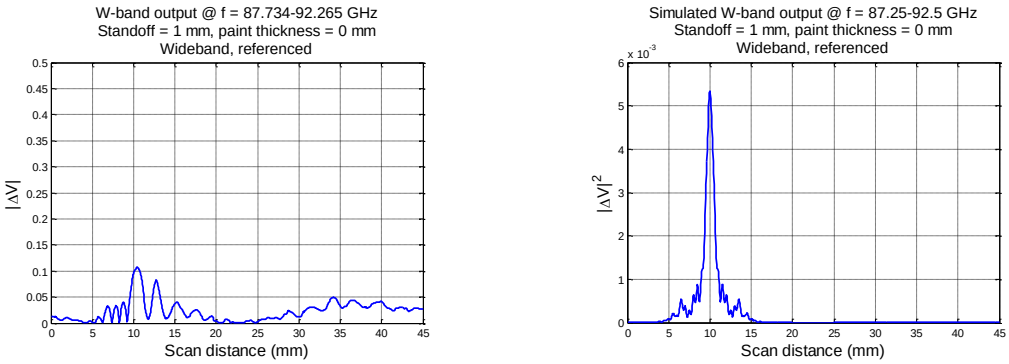

Figure 4.58. Measured (left) and simulated (right) W-band results of 1.27 mm-long crack, at standoff distance of 1 mm, and no paint.

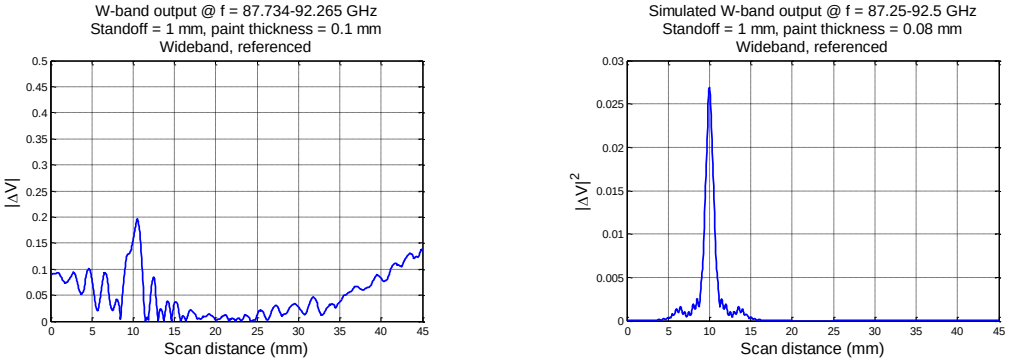

Figure 4.59. Measured (left) and simulated (right) W-band results of 1.27 mm-long crack, at standoff distance of 1 mm, and paint thickness of 0.1 mm (measurements) and 0.08 mm (simulations).

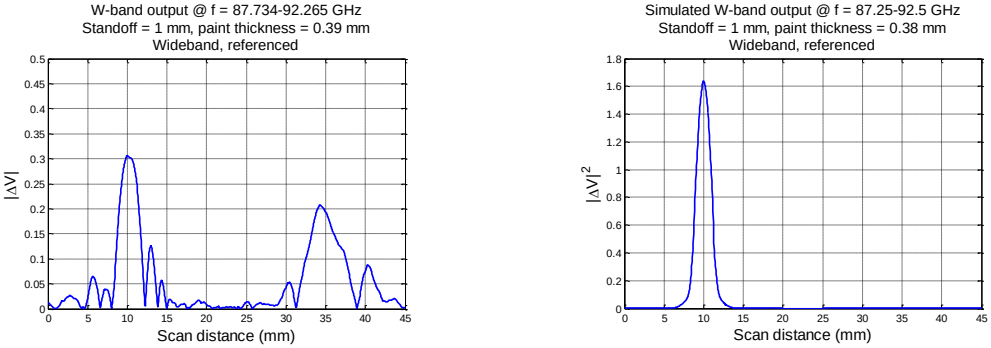

Figure 4.60. Measured (left) and simulated (right) W-band results of 1.27 mm-long crack, at standoff distance of 1 mm, and paint thickness of 0.39 mm (measurements) and 0.38 mm (simulations).

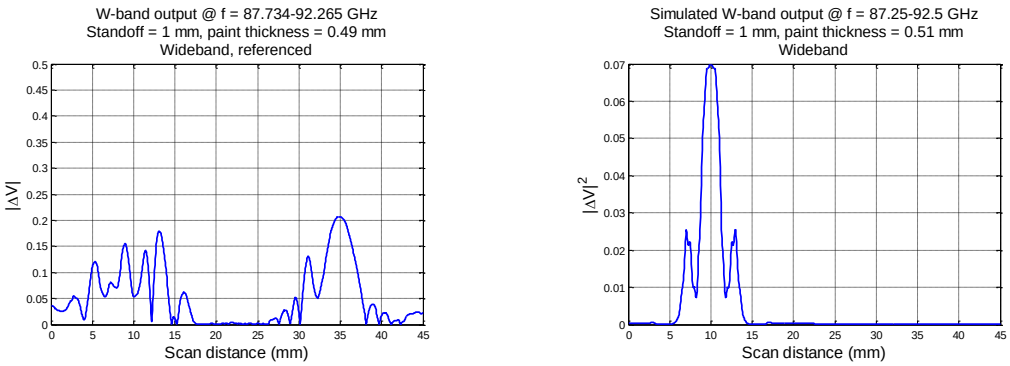

Figure 4.61. Measured (left) and simulated (right) W-band results of 1.27 mm-long crack, at standoff distance of 1 mm, and paint thickness of 0.49 mm (measurements) and 0.51 mm (simulations).

The simulated results demonstrate again that an ideal scan results in zero output when the probe is in the region without fastener heads (black curve), a non-zero output when the probe is near the crack (blue curve), and a much smaller output (close to zero) when the probe is above the un-cracked fastener head (red curve, not visible in Figure 4.63 (b)).

The results also suggest again that a thin layer of paint (thinner than ~0.1 mm) does not significantly affect the overall capability of the W-band probe on crack detection. But a layer of paint that is thicker than ~0.2 mm (more likely to be non-uniform) results in an imperfectly canceled scattered signals and false indications of cracks that are as large as the actual crack signals in magnitude.

To better illustrate the effect of paint thickness on the W-band wideband differential probe crack output signal level with the selected measured and simulated data (at the four common frequencies), the percentages of decreases in the probe output signal levels versus paint thicknesses are investigated. To do this, the signals with respect to the different combination of paint thicknesses and standoff distances are normalized to the largest (in magnitude) value among them. The normalized results provide a one-to-one comparison between the measured and simulated data (e.g., comparison in the amount of signal reduction under the same condition), as shown in Figures 4.64 and 4.65. These results confirm the conclusions previously made.

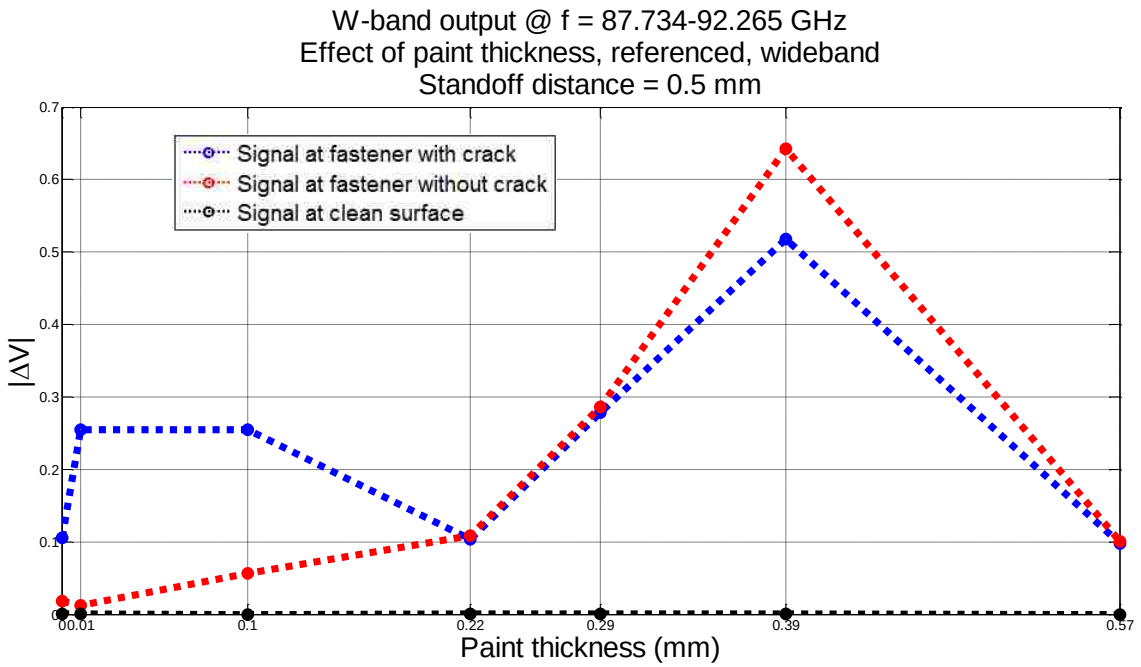

(a) Measurement results

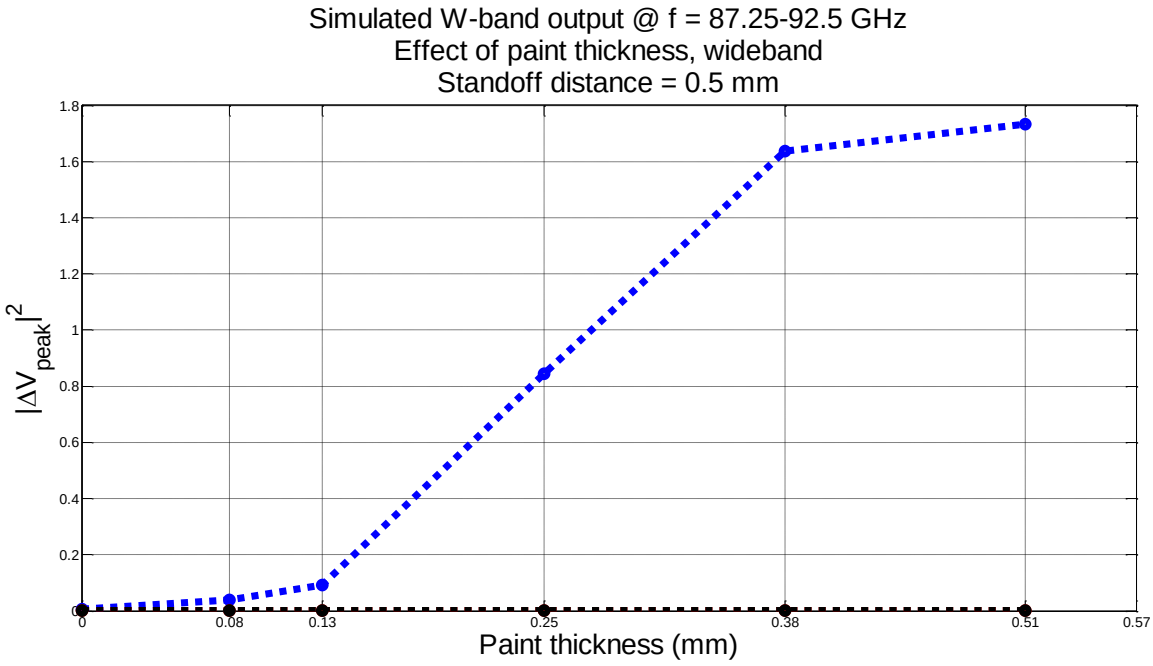

(b) Simulation results

Figure 4.62. Investigation on effect of paint thickness with W-band differential probe. Presented are: (a) measurement and (b) simulation results, at standoff distance of 0.5 mm.

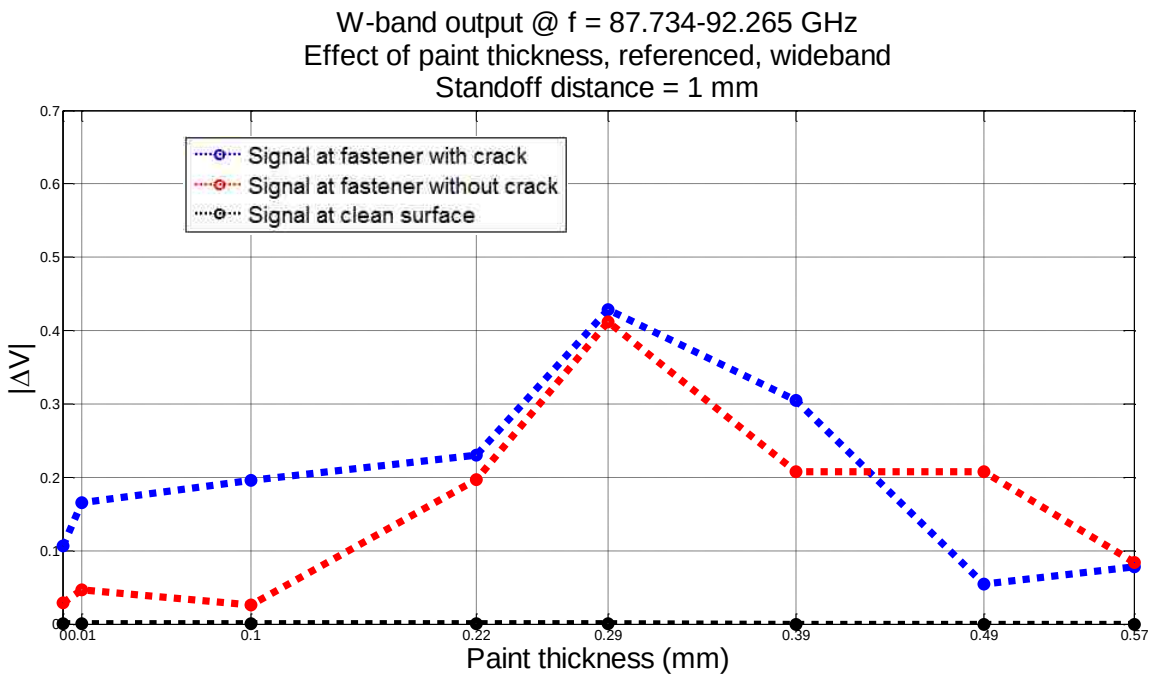

(a) Measurement results

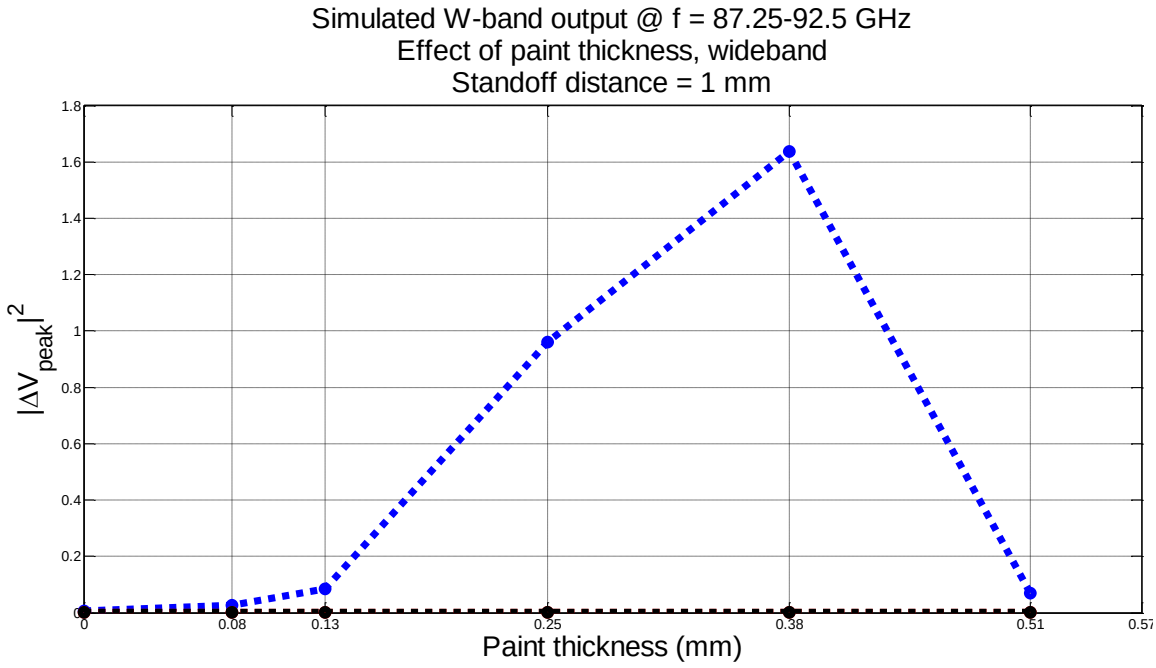

(b) Simulation results

Figure 4.63. Investigation on effect of paint thickness with W-band differential probe. Presented are: (a) measurement and (b) simulation results, at standoff distance of 1 mm.

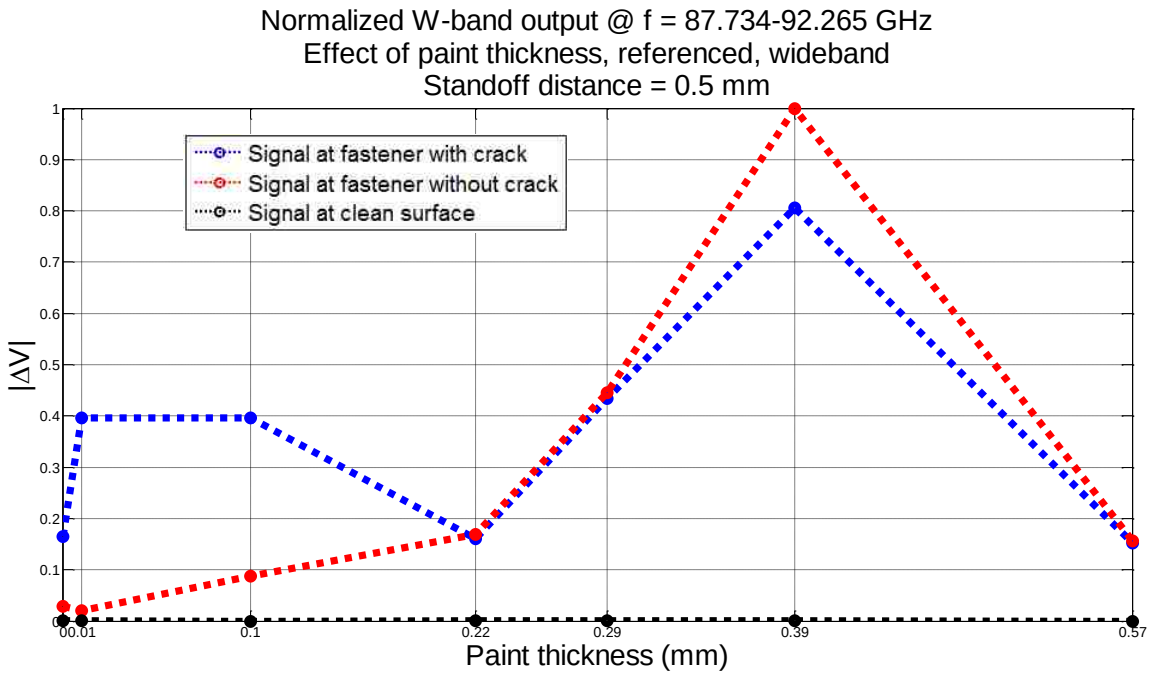

(a) Measurement results

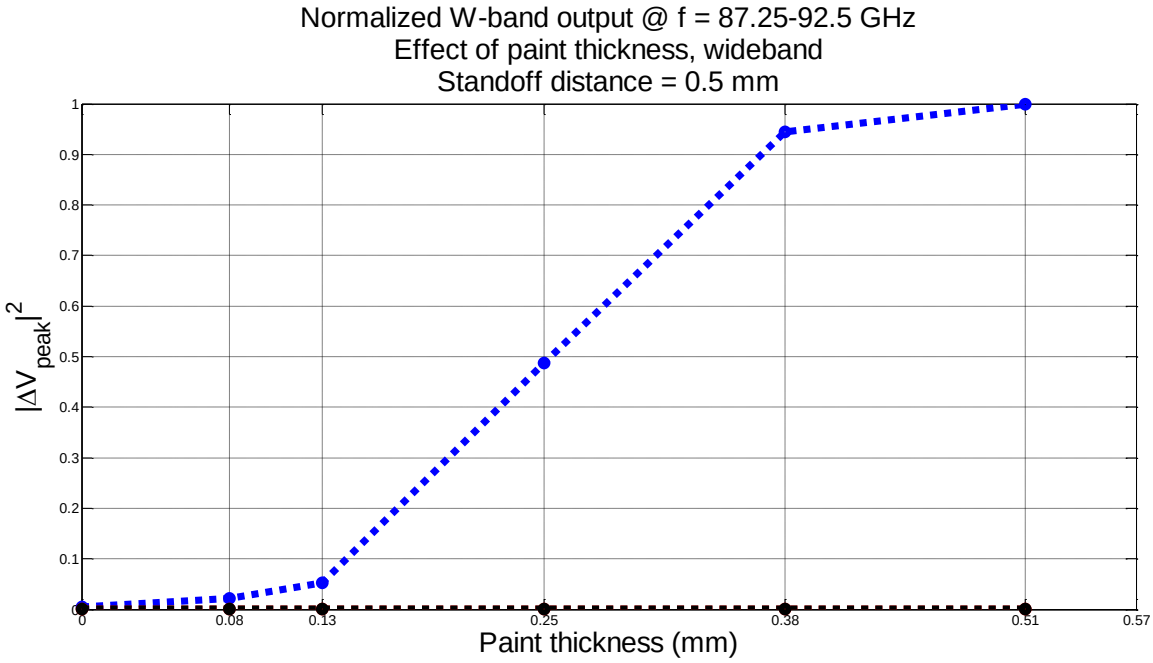

(b) Simulation results

Figure 4.64. Normalized W-band results on effect of paint thickness. Presented are: (a) measurement and (b) simulation results, at standoff distance of 0.5 mm.

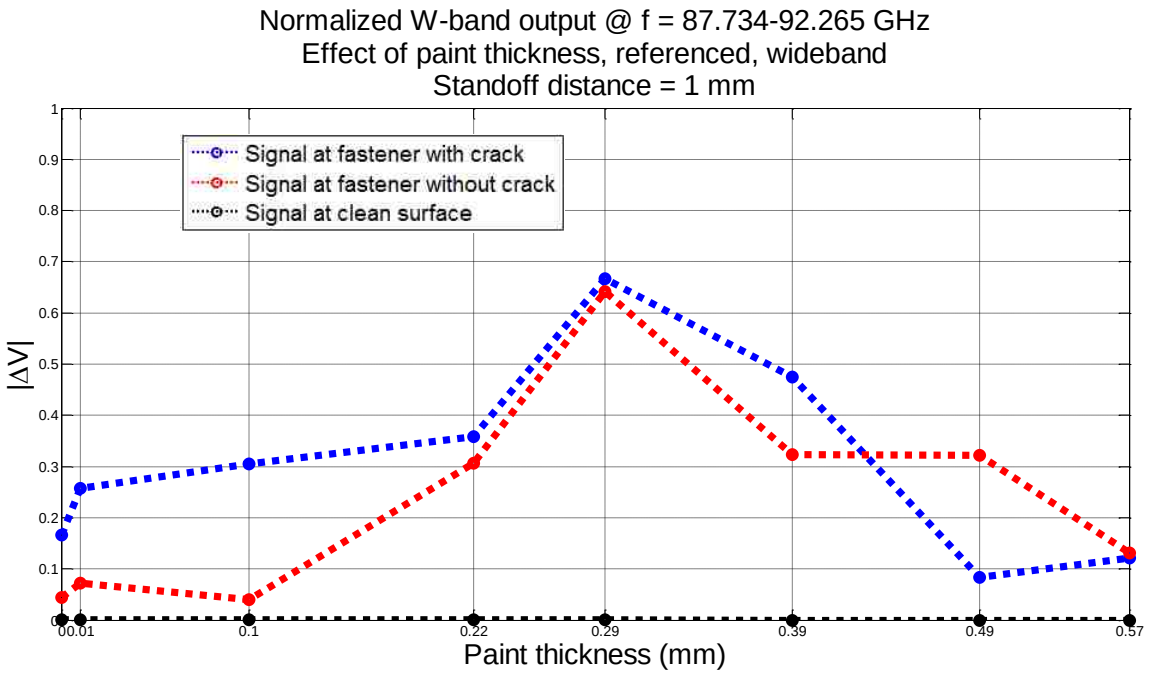

(a) Measurement results

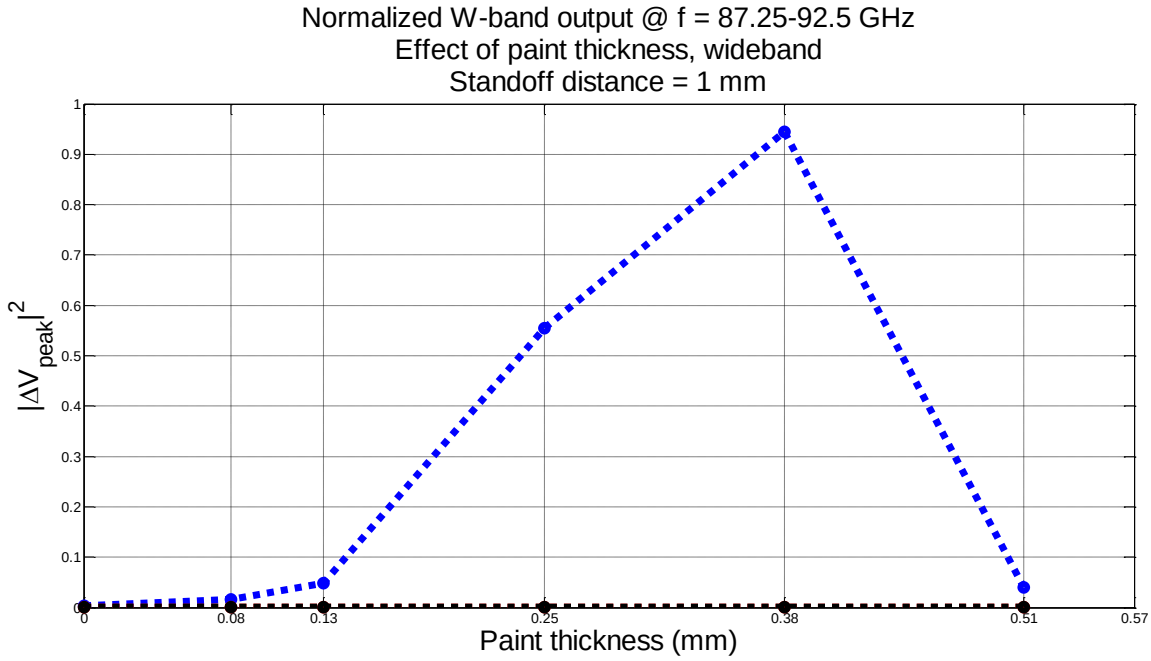

(b) Simulation results

Figure 4.65. Normalized W-band results on effect of paint thickness. Presented are: (a) measurement and (b) simulation results, at standoff distance of 1 mm.

4.4. EFFECT OF PROBE MISALIGNMENT

A probe misalignment represents a shift in the probe with respect to the location of fastener head. A negative probe misalignment is when the probe is shifted towards the crack, and a positive probe misalignment is when the probe is shifted away from the crack.

For the measurements, probe misalignments of ±1.27, ±0.635 and 0 mm were applied, along with standoff distances of 0.5 and 1 mm. The results from 1 mm standoff distance, and probe misalignments of ±1.27 and 0 mm are presented in the following figures, while the complete results (standoff distance of 0.5 mm and other probe misalignments) are provided in Appendix J. Figure 4.66 shows the relative position between the probe and the fastener head when probe misalignments of ±1.27 mm are applied.

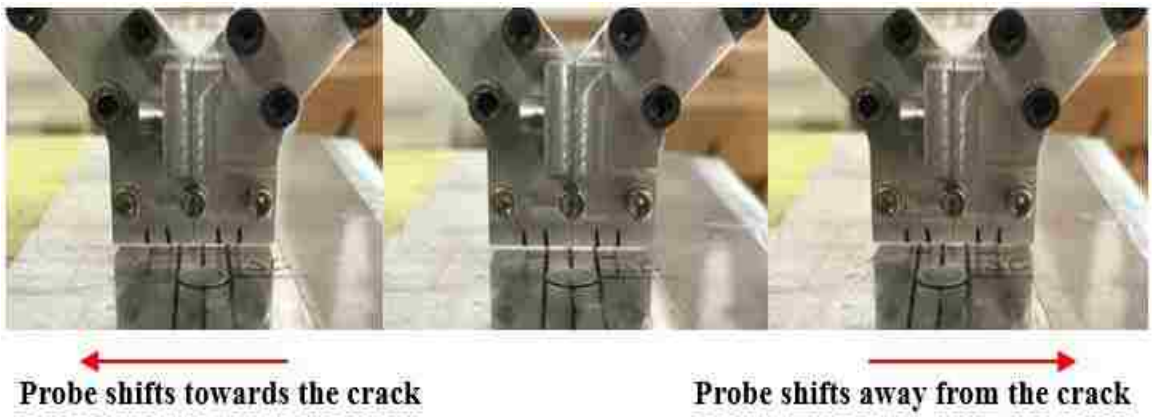

Figure 4.66. Probe misalignments of (from left to right): -1.27 mm, no misalignment, and +1.27 mm.

Similar to previous sections, only the wideband measurement results are evaluated. Figures 4.67 through 4.69 represent the W-band measurement results at standoff distance of 1 mm, and probe misalignments of -1.27, 0, and +1.27 mm, respectively.

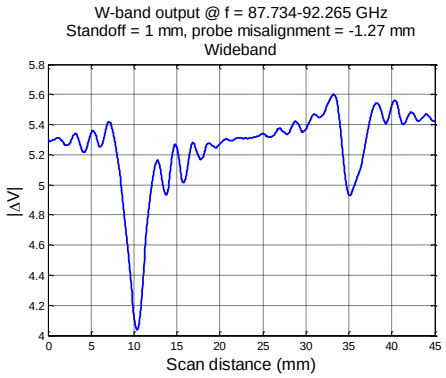

Figure 4.67. W-band wideband probe output signals at standoff distance of 1 mm, and probe misalignment of -1.27 mm.

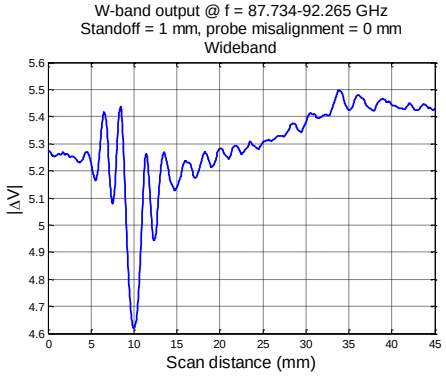

Figure 4.68. W-band wideband probe output signals at standoff distance of 1 mm, and no probe misalignment.

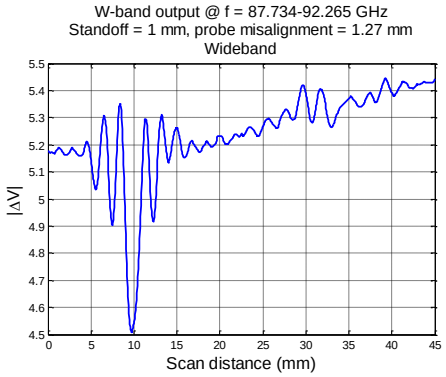

Figure 4.69. W-band wideband probe output signals at standoff distance of 1 mm, and probe misalignment of +1.27 mm.

The results suggest the similar observations as of previous measurements, as there are indications of crack near the 10 mm position, also, in the region without fastener heads the probe output signals are relatively consistent. In addition, when the probe is near the un-cracked fastener head, the resulted signal variations are weaker than ones from the cracked fastener head (except for when the probe is negatively misaligned). The variations in signals are better represented when the bias voltages are removed, as demonstrated in Figures 4.70 through 4.72.

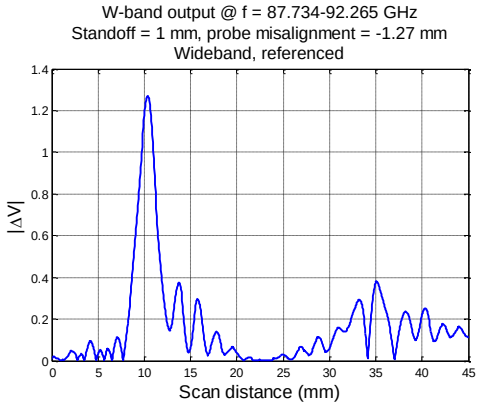

Figure 4.70. Referenced W-band wideband probe output signals at standoff distance of 1 mm, and probe misalignment of -1.27 mm.

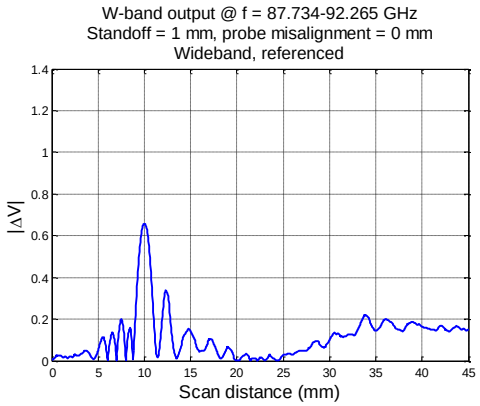

Figure 4.71. Referenced W-band wideband probe output signals at standoff distance of 1 mm, and no probe misalignment.

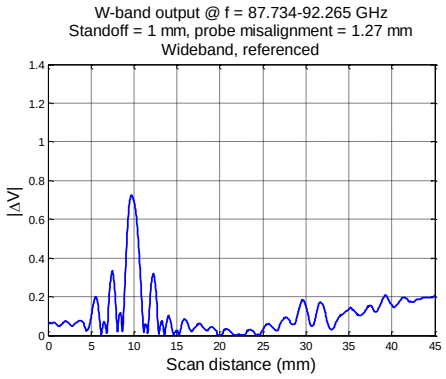

Figure 4.72. Referenced W-band wideband probe output signals at standoff distance of 1 mm, and probe misalignment of +1.27 mm.

Similar observations are found with the referenced data, where the probe output signal is composed of an indication of crack near the 10 mm position, and a relatively weaker response near the un-cracked fastener head.

The simulation results from Section 3.5 suggested that when the probe is negatively misaligned, the combination of additional scattered signals from the fastener head and crack results in a weaker peak signal at crack locations, and additional signal peaks near the edge of the fastener head. But this is not observed in Figure 4.70. Instead the crack signal level under negative misalignment surpasses the crack signal levels under positive or zero misalignment. This is likely due to that the additional scattered signals combine with the actual crack signals, resulting in a stronger probe output signal. In addition, under a negative probe misalignment of 1.27 mm, the amount of scattered signals from the crack (that is also 1.27 mm-long) may not be fully captured by the probe, as described in Figure 3.56.

The measured and simulated data (with a 1.27 mm-long crack) at the four common frequencies (listed in Appendix G) are compared. The comparisons are shown in Figures 4.73 through 4.75. The results presented are referenced wideband data. As before, both the measurement and simulation results are referenced to the case of a clean surface. Note that the figures may not be in the same scales.

These figures illustrate the comparison between ideal scan results and actual measurements. The simulation results at these frequencies show that the differential

probe output is non-zero when a crack is present, and nearly zero when a misalignment occurs (much less than the crack signals in magnitude), therefore, the contribution to probe output signals from probe misalignments (in either direction) is ideally negligible because the crack signals (at this specific crack length) dominate. Similar observations can be made on results at standoff distance of 0.5 mm provided in Appendix J. The two signal peaks near the actual crack location in Figure 4.73 are likely the consequences of edge effect from the probe flange.

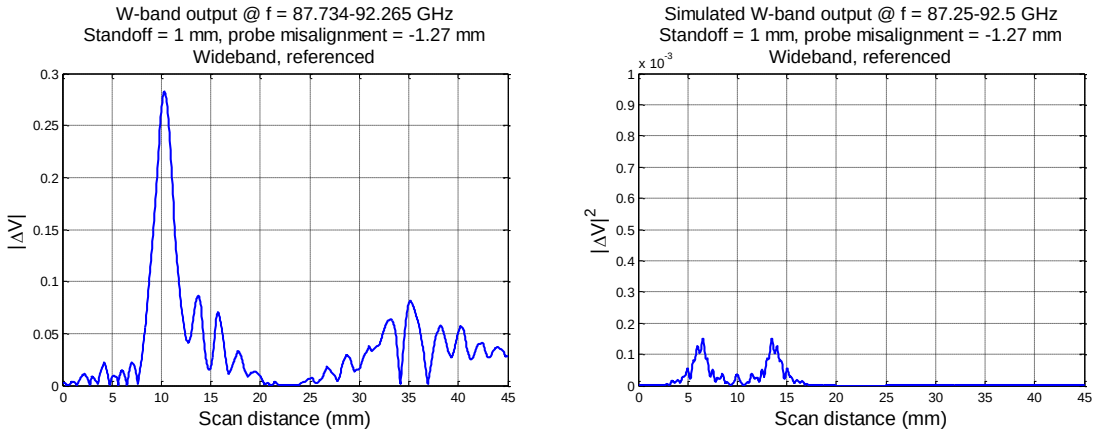

Figure 4.73. Measured (left) and simulated (right) W-band results of 1.27 mm-long crack, at standoff distance of 1 mm, and probe misalignment of -1.27 mm.

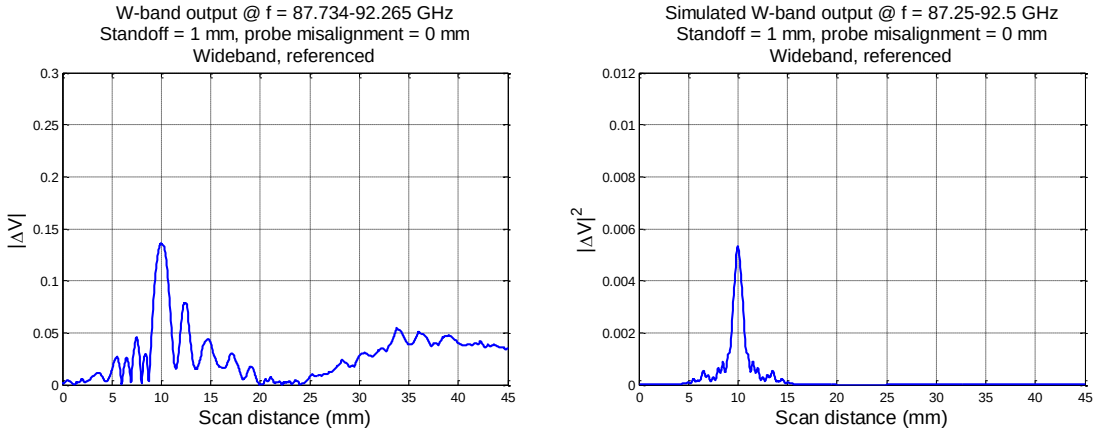

Figure 4.74. Measured (left) and simulated (right) W-band results of 1.27 mm-long crack, at standoff distance of 1 mm, and no probe misalignment.

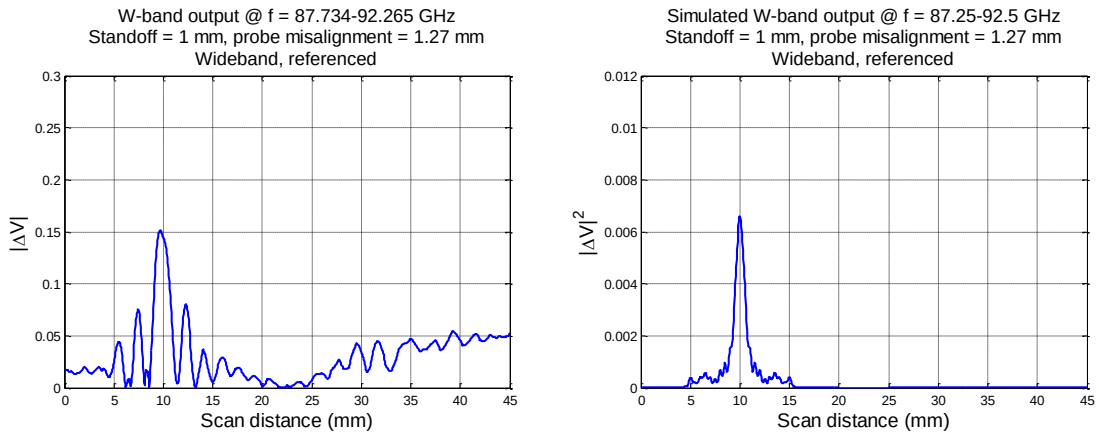

Figure 4.75. Measured (left) and simulated (right) W-band results of 1.27 mm-long crack, at standoff distance of 1 mm, and probe misalignment of +1.27 mm.

Figures 4.76 and 4.77 summarize the effect of probe misalignment on W-band wideband differential probe output signal levels, at standoff distances of 0.5 and 1 mm. The signal levels presented in these figures are the peak values of the probe output signals when the probe is above the crack, in the region without fastener heads, and above the un-cracked fastener head. Both measurement and simulation results are presented.

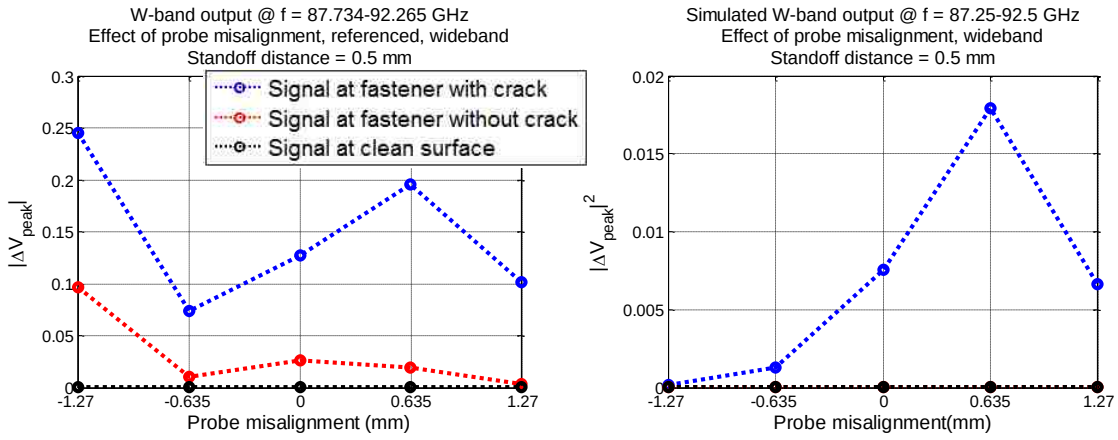

Figure 4.76. Investigation on effect of probe misalignment with W-band differential probe. Presented are measurement (left) and simulation results (right), at standoff distance of 0.5 mm.

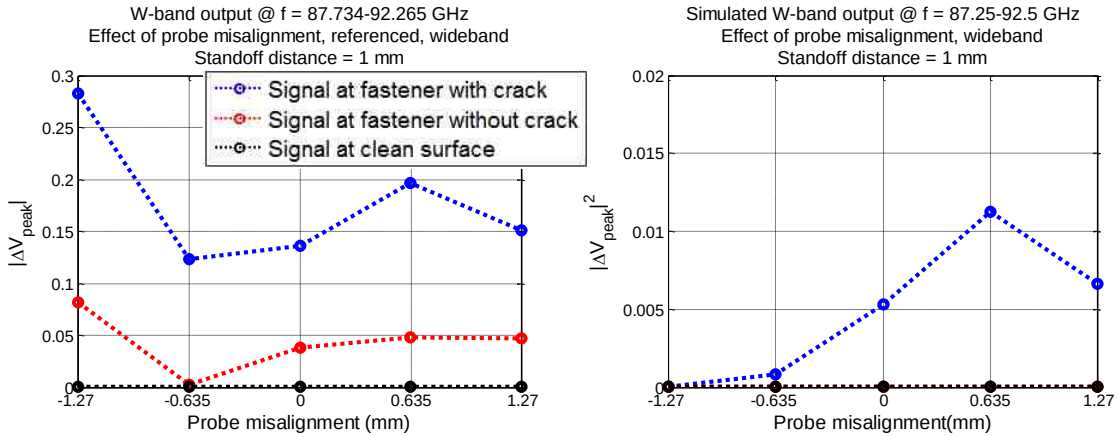

Figure 4.77. Investigation on effect of probe misalignment with W-band differential probe. Presented are measurement (left) and simulation results (right), at standoff distance of 1 mm.

The measurement results are in good agreements with the simulation results, except for the case when the probe misalignment of -1.27 mm is applied. This is likely due to what was stated before that the probe output signals at the crack location is the combination of the actual crack signals and the additional signal peaks due to the presence of a misalignment. The reasons for the non-zero probe output signals at un-cracked fastener head (in measurements) are previously stated.

To better illustrate the effect of probe misalignment on the W-band wideband differential probe crack output signal level with the selected measured and simulated data (at the four common frequencies), the percentages of decreases in the probe output signal levels versus probe misalignments are investigated. To do this, the signals with respect to the different combinations of probe misalignments and standoff distances are normalized to the largest (in magnitude) value among them. The normalized results provide a one-to-one comparison between the measured and simulated data (e.g., comparison in the amount of signal reduction under the same condition), as shown in Figures 4.78 and 4.79.

These normalized results demonstrate again that a negative probe misalignment results in higher amplitude of signal levels when scanned over the un-cracked fastener head, causing a potential false crack signal, and the effect becomes less significant if the probe is positively misaligned.

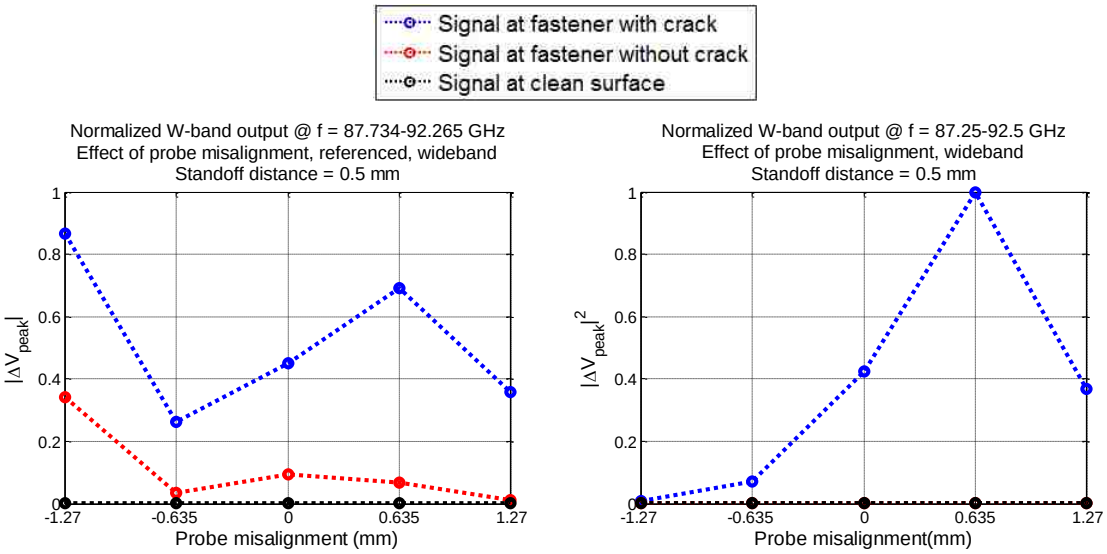

Figure 4.78. Normalized W-band results on effect of probe misalignment. Presented are measurement (left) and simulation results (right), at standoff distance of 0.5 mm.

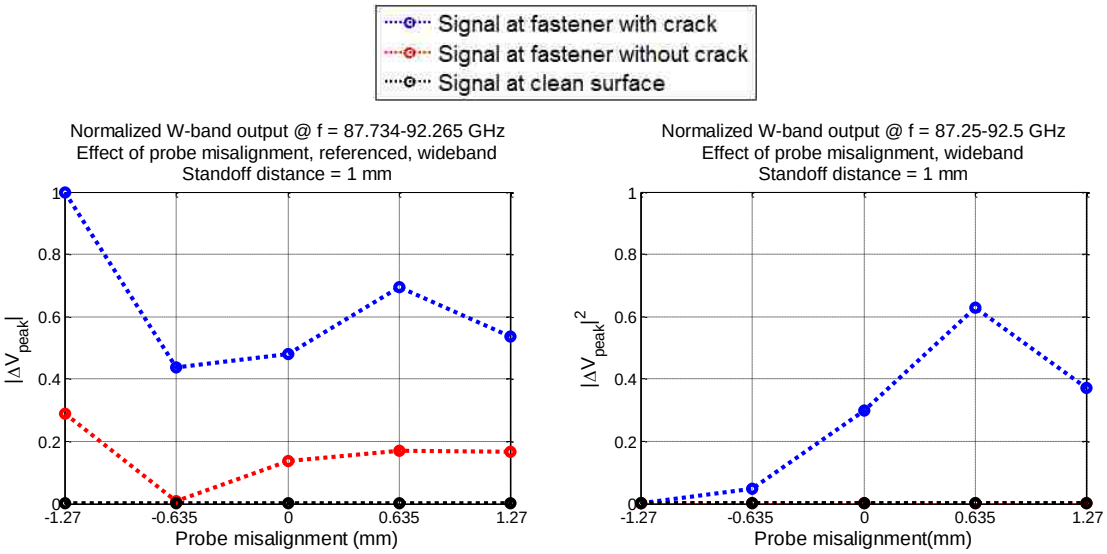

Figure 4.79. Normalized W-band results on effect of probe misalignment. Presented are measurement (left) and simulation results (right), at standoff distance of 1 mm.

4.5. EFFECT OF PROBE OFFSET

A probe offset represents a rotation of the probe with respect to the fastener axis, which causes one aperture to see the fastener head either earlier or later than the other

during a scan. A probe offset in the measurements is defined by the number of complete rotations (of the knob controlling angular movements, Figure 2.17), unlike simulations where the probe offset is defined by angle of rotation in degrees.

For the measurements, probe offsets of ±2, ±1 and 0 rotations were applied, along with standoff distances of 0.5 and 1 mm. The results from 1 mm standoff distance, and probe offsets of ±2 and 0 rotations are presented in the following figures, while the complete results (standoff distance of 0.5 mm and other probe offsets) are provided in Appendix K. Figure 4.80 shows the relative position between the probe and sample surface when probe offsets of ±2 rotations are applied. It is approximated that one complete rotation of the knob is ~2.5˚ of rotation, correspond to values applied in the simulations.

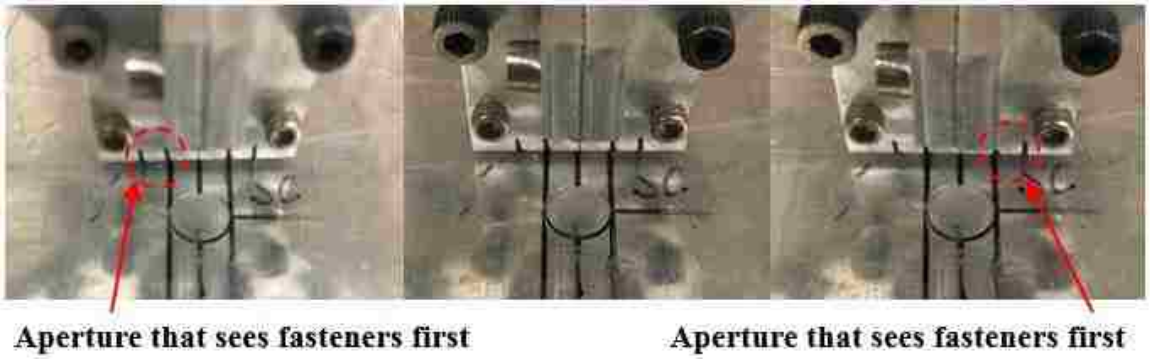

Figure 4.80. Probe offsets of (from left to right): -2 rotations, no rotation, and +2 rotations.

Similar to previous sections, only the wideband measurement results are evaluated. Figures 4.81 through 4.83 represent the W-band measurement results at standoff distance of 1 mm, and probe offset of -2, 0, and +2 rotations, respectively.

The results suggest the similar observations as of previous measurements, as there are indications of crack near the 10 mm position, also, in the region without fastener head the probe output signals are relatively consistent. In addition, when the probe is near the un-cracked fastener head, the resulted signal variations are weaker than the ones from the

cracked fastener head. The variations in signals are better represented when the bias voltages are removed, as demonstrated in Figures 4.84 through 4.86.

Similar observations are found with the referenced data, where the probe output signal is composed of an indication of crack near the 10 mm position, and a relatively weaker response near the un-cracked fastener head.

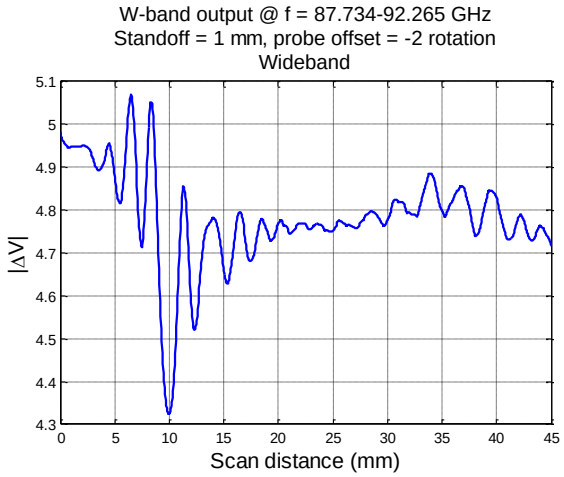

Figure 4.81. W-band wideband probe output signals at standoff distance of 1 mm, and probe offset of -2 rotations.

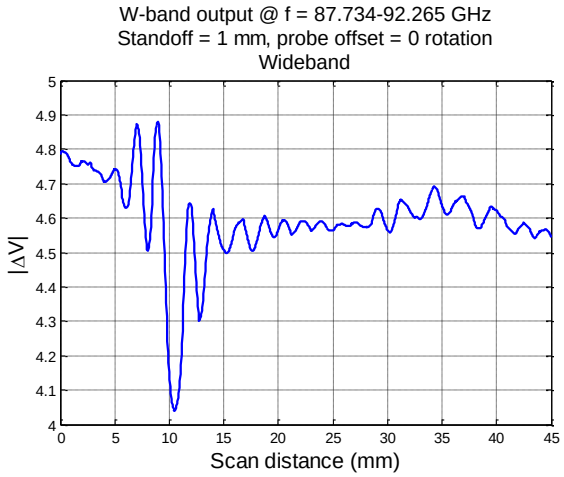

Figure 4.82. W-band wideband probe output signals at standoff distance of 1 mm, and no probe offset.

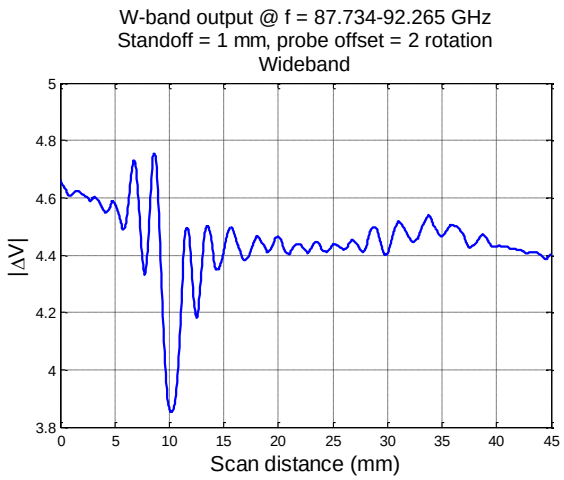

Figure 4.83. W-band wideband probe output signals at standoff distance of 1 mm, and probe offset of +2 rotations.

Similar to other positioning of the probe, this rotation can lead to undesired consequences where the scattered signals from the fastener heads cannot be completely removed as a result of the non-symmetrical configuration of the structure. The results are showing that a probe offset does not significantly affect the overall capability of the differential on crack detection, which confirms the conclusion made on the simulation results in Section 3.6.

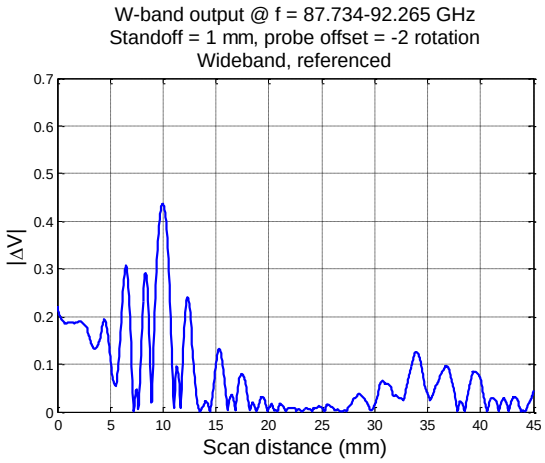

Figure 4.84. Referenced W-band wideband probe output signals at standoff distance of 1 mm, and probe offset of -2 rotations.

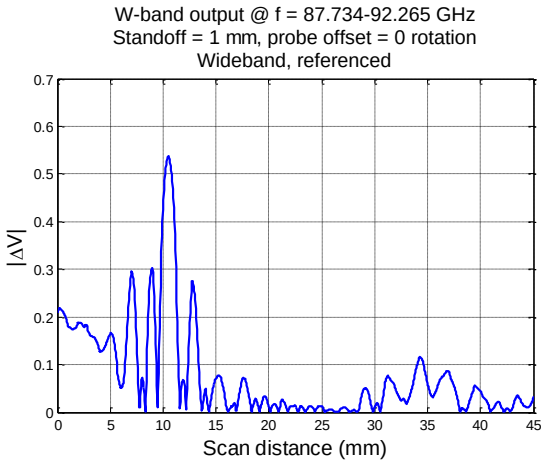

Figure 4.85. Referenced W-band wideband probe output signals at standoff distance of 1 mm, and no probe offset.

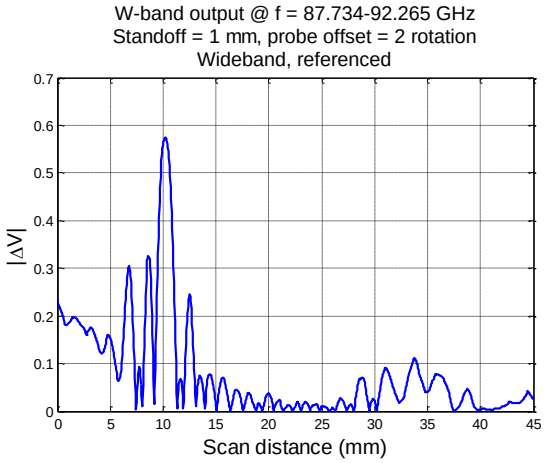

Figure 4.86. Referenced W-band wideband probe output signals at standoff distance of 1 mm, and probe offset of +2 rotations.

The measured and simulated data (with a 1.27 mm-long crack) at the four common frequencies (listed in Appendix G) are compared. The comparisons are shown in Figures 4.87 through 4.89. The results presented are referenced wideband data. As before, both the measurement and simulation results are referenced to the case of a clean surface.

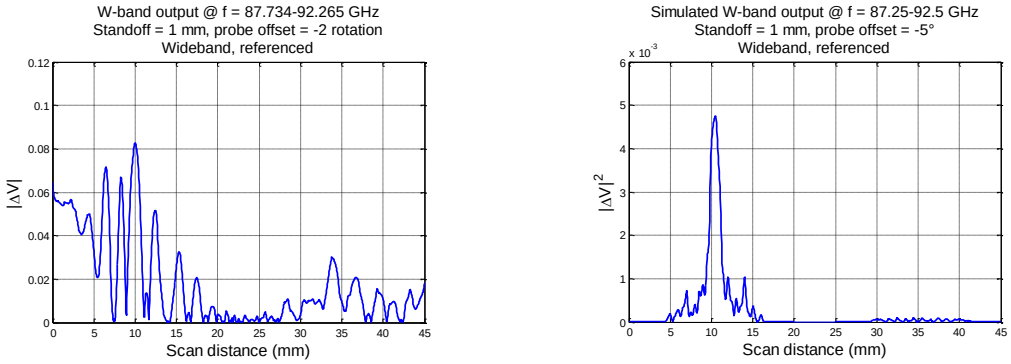

Figure 4.87. Measured (left) and simulated (right) W-band results of 1.27 mm-long crack, at standoff distance of 1 mm, and probe offset of -2 rotations (measurements) and -5˚ (simulations).

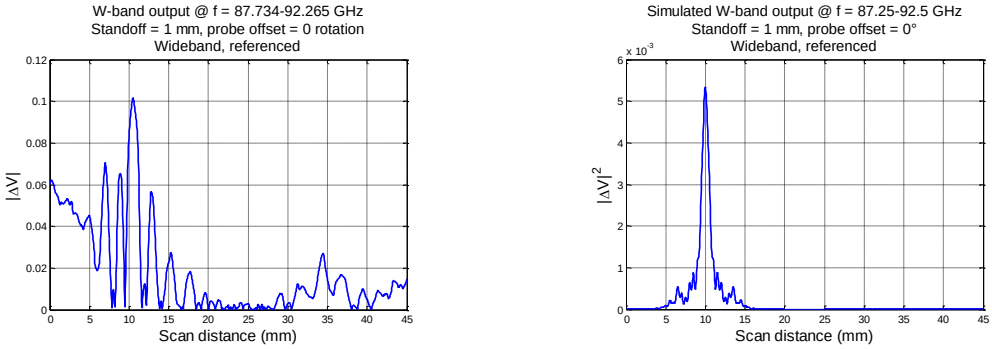

Figure 4.88. Measured (left) and simulated (right) W-band results of 1.27 mm-long crack, at standoff distance of 1 mm, and no probe offset.

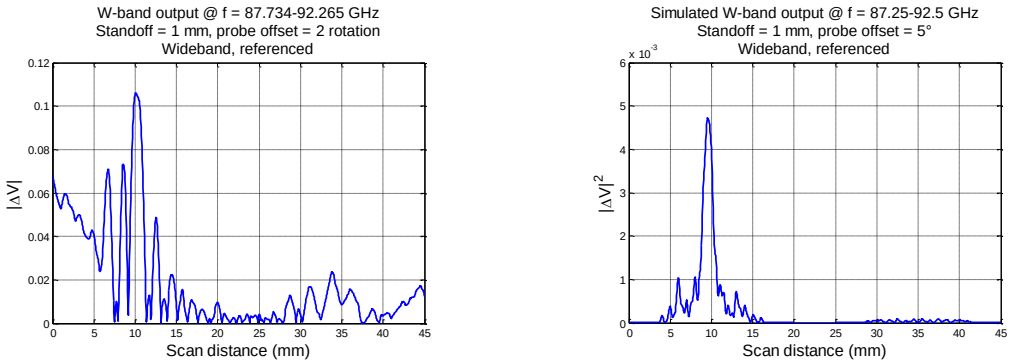

Figure 4.89. Measured (left) and simulated (right) W-band results of 1.27 mm-long crack, at standoff distance of 1 mm, and probe offset of +2 rotations (measurements) and +5˚ (simulations).

These figures illustrate the comparison between ideal scan results and actual measurements. The simulation shows that the differential probe output is not significantly affected by probe rotations, therefore, the contribution to probe output signals from probe offsets is ideally negligible, while it only affects the locations of the peak signals, and some detections appear on the un-cracked fastener head.

The strong signals (in measurements) at the 0 – 5 mm region are likely the consequences of measurement errors. Similar observations can be made on results at standoff distance of 0.5 mm provided in Appendix K.

Figures 4.90 and 4.91 summarize the effect of probe offset on W-band wideband differential probe output signal levels, at standoff distances of 0.5 and 1 mm. The signal levels presented in these figures are the peak values of the probe output signals when the probe is above the crack, in the region without fastener heads, and above the un-cracked fastener head. Both measurement and simulation results are presented.

The measurement results are in good agreements with the simulation results at both standoff distances, where the probe offset does not have a significant effect on the crack output signal levels. To better illustrate the effect of probe offset on the W-band wideband differential probe crack output signal level with the selected measured and simulated data (at the four common frequencies), the percentages of decreases in the probe output signal levels versus probe offsets are investigated.

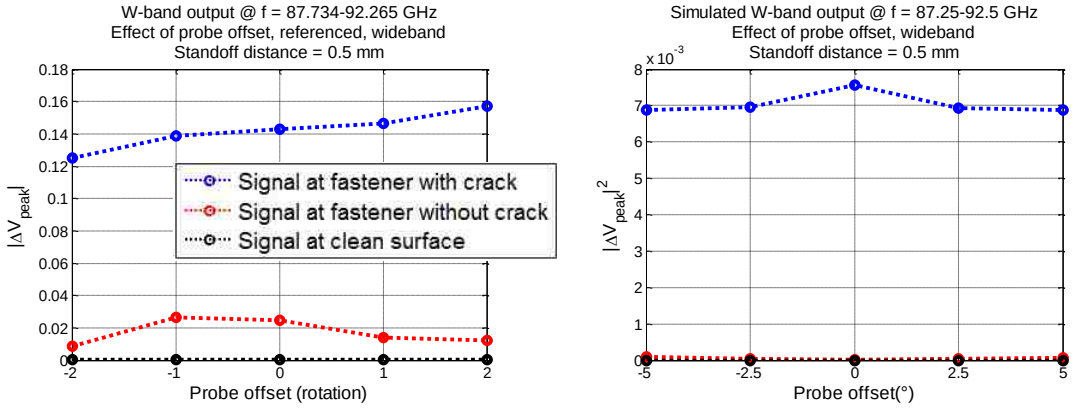

Figure 4.90. Investigation on effect of probe offset with W-band differential probe. Presented are measurement (left) and simulation results (right), at standoff distance of 0.5 mm.

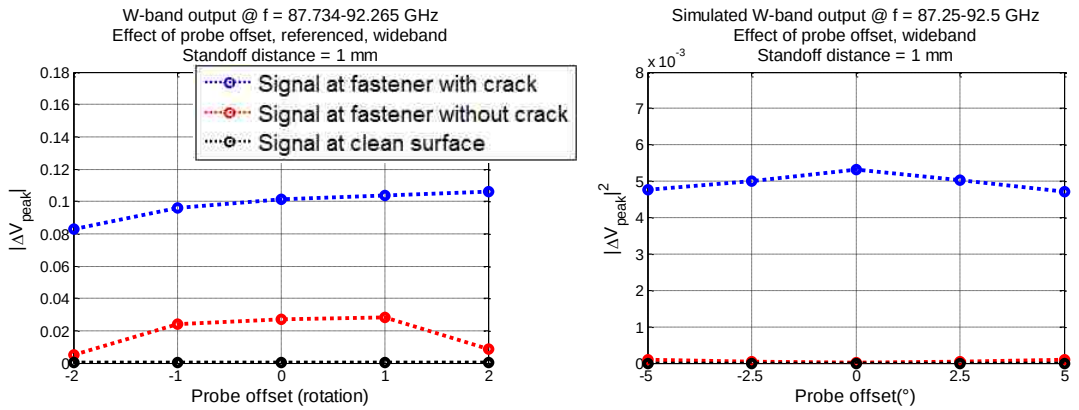

Figure 4.91. Investigation on effect of probe offset with W-band differential probe. Presented are measurement (left) and simulation results (right), at standoff distance of 1 mm.

To do this, the signals with respect to the different combinations of probe offsets and standoff distances are normalized to the largest (in magnitude) value among them. The normalized results provide a one-to-one comparison between the measured and simulated data (e.g., comparison in the amount of signal reduction under the same condition), as shown in Figures 4.92 and 4.93. The results suggest the same observations as the previous results.

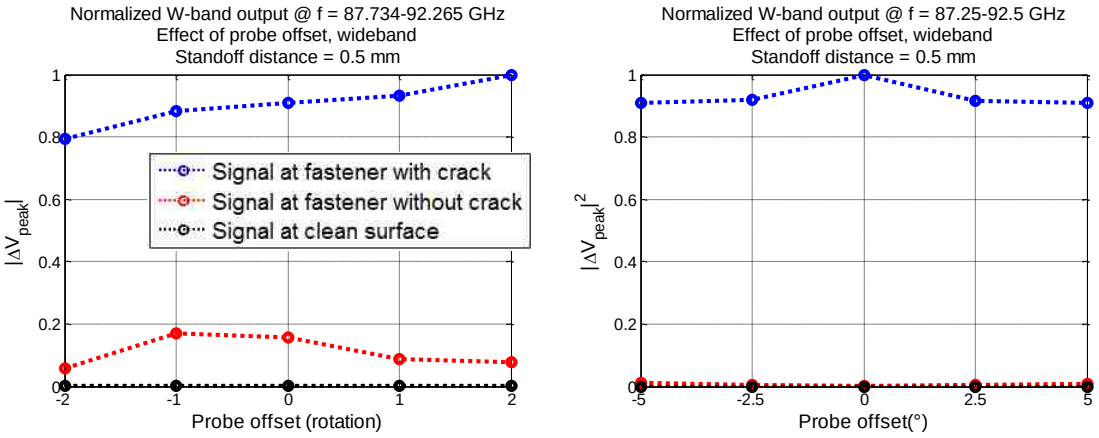

Figure 4.92. Normalized W-band results on effect of probe offset. Presented are measurement (left) and simulation results (right), at standoff distance of 0.5 mm.

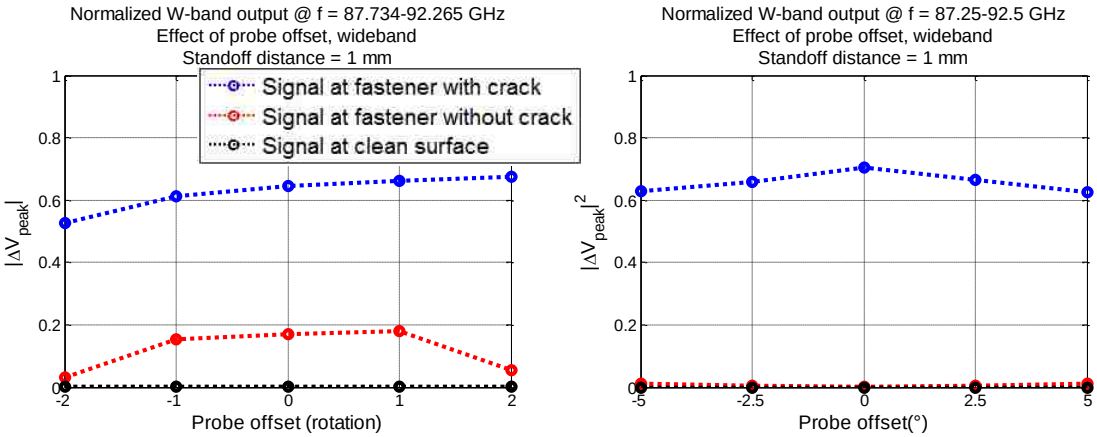

Figure 4.93. Normalized W-band results on effect of probe offset. Presented are measurement (left) and simulation results (right), at standoff distance of 1 mm.

4.6. SUMMARY

In this section, the simulation results on effects of various positing of the differential probe and variations of sample surfaces were verified through measurements. Most of the measurement results are in good agreements with the simulation results, except for some cases where the supposed control variable of the measurement varies (e.g., non-uniform paint thickness, potentially unequal standoff distances between the two probe apertures due to a non-flat surface, etc.). It is found through both the measurement and simulation results that the parameters considered (standoff distance, aperture offset, etc.) contribute to the differential probe output signals as follows:

- Standoff distance: A small standoff distance (0.25 mm) results in a strong probe output signal in the region of un-cracked fastener (in measurements), which is potentially a false indication of crack. However, a higher standoff distance reduces the significances of these issues. Overall, the crack signal level reduces with respect to increase in standoff distance.
- Aperture offset: both the measurement and simulation results have the same trends in crack output signal levels as a function of varying aperture offsets. At a lower standoff distance (0.5 mm), a negative aperture offset on the probe results in a higher probe output signal level, and reduces with respect to increase in aperture offset (from negative to positive), due to varying amount

of unwanted scattered signals from the fastener. The effects are minimized by increasing the standoff distance.

- Probe misalignment: the measurement and simulation results are in good agreements except for the case when the probe misalignment of -1.27 mm is applied (in which the scattered signals from the crack are likely not captured in full). This is probably because of the probe output signal at the crack location is the combination of the actual crack signals and the additional signal peaks due to the presence of a misalignment. A negative probe misalignment is also shown to have a higher amplitude of signal levels when scanned over the un-cracked fastener, causing a potential false crack signal, and the effect becomes less significant if the probe is positively misaligned (as the un-eliminated scattered signals from the fastener head is collected through the same probe aperture collecting the scattered signals from the crack).
- Probe offset: both the measurement and simulation results suggest that the contribution to probe output signals from probe offsets is ideally negligible, while it only affects the locations of the peak signals.
- Paint thickness: it is shown through measurement that a potential non-uniform paint around the fastener makes the behavior of the probe less straightforward to predict. It is found that a thin layer of paint (< ~0.1 mm) does not significantly affect the overall capability of the differential probe on crack detection. But a thick layer of paint (> ~0.2 mm, which is more likely to be non-uniform) results in an imperfectly canceled scattered signals and false indications of cracks that are as large as the actual crack signals in magnitude.

Future measurements will be conducted on samples with cracks (at varying lengths) to verify the effect of crack length on W-band differential probe output signals, if needed.

5. SYNTHETIC APERTURE PROCESSING

In the previous sections, it was observed that a misalignment between the probe and SUT often contributes to imperfectly canceled scattered signals from a fastener head, which could potentially affect the overall probe output signals. This can lead to false indications or distortions to the actual crack signals. Since in measurements a misalignment could not be completely avoided, this section investigates the efficacy of using wideband millimeter-wave synthetic aperture processing on enhancing the crack detection capabilities of a W-band and V-band differential probe.

Synthetic aperture processing, or synthetic aperture radar (SAR) technique, is a form of radar signal processing derived from microwave holography methods that leads to high image/signal resolution [32]. The benefit of SAR is that it helps to reconstruct a focused image of a target by utilizing the phase and amplitude information of the signals recorded over the target. SAR imaging technique has been applied in many fields such as radar imaging, remote sensing, security, NDT, and more [32]-[37].

In this investigation, SAR contributes to compensating for the standoff distance by coherently summing the wideband signals, which effectively focus the energy to the correct distance away from the aperture. Also, when a scan is completed, a crack (if present) will be seen by the probe from multiple positions along the scan path as the SUT is raster scanned, after the data are combined in SAR. Consequently, the resulting probe output signals are expected to have higher resolution (i.e., effectively a finer step size in the scan). The purpose of SAR is to reduce the potential signal distortions or false indications by averaging reflected data over many frequencies.

The results provided in the following sections are to compare the similarity between the measurement and simulation results. Therefore, only the summation of selected single-frequency results (as previously mentioned) are considered. To obtain an optimal SAR image, additional frequencies in a wider range may be desired as the target is effectively seen from more positions along the scan path. Therefore, the results presented in this section may not reflect the true benefits of SAR.

In the investigation, SAR (hereon referred to as SAR "filter") is applied to both the simulated and measured data to investigate the efficacy of SAR in enhancing crack

detection on effect of standoff distance (Section 5.1), aperture offset (Section 5.2), paint thickness (Section 5.3), probe misalignment (Section 5.4) and probe offset (Section 5.5).

5.1. EFFICACY OF SAR FILTER ON EFFECT OF STANDOFF DISTANCE

SAR filter is applied to both the measured and simulated data (presented in Section 4.1) to investigate the effect of standoff distance (from 0.25 mm to 1 mm) at W-band and V-band frequencies. Both data represent the scan results for a 1.27 mm-long crack, at the four common W-band frequencies and three common V-band frequencies (shown in Appendix G). Section 5.1.1 represents the W-band results, while Section 5.1.2 represents the V-band results.

5.1.1. W-band Wideband Response. Figures 5.1 through 5.4 represent the comparison between SAR-focused measurement and simulation results at W-band frequencies, with varying standoff distances between 0.25 and 1 mm. Both the original data and the SAR-focused data are provided.

In the previous sections, it was found that a small standoff distance (0.25 mm) results in a strong probe output signal (potential false indication) above the un-cracked fastener head (in measurements, Figure 5.1), due to possible imperfect alignments between the probe and the SUT.

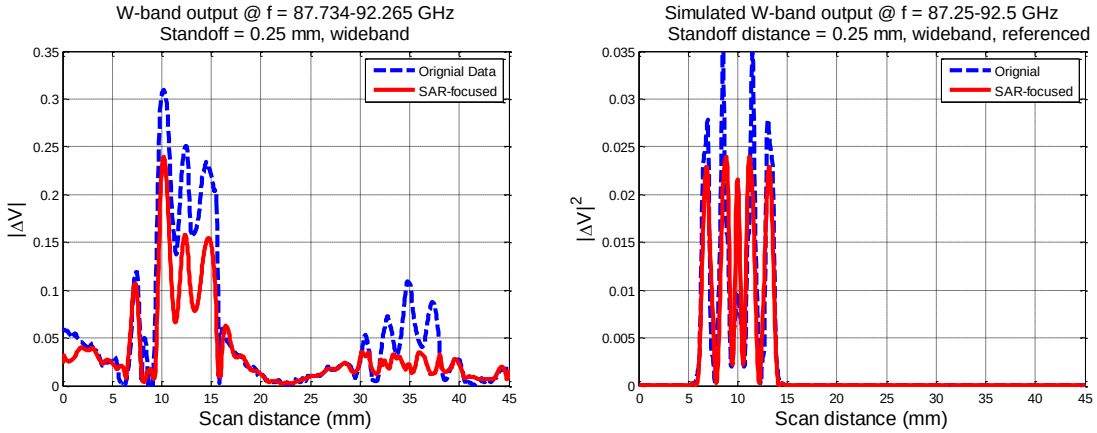

Figure 5.1. SAR-focused W-band results of 1.27 mm-long crack, as in measurement (left) and simulation (right), at standoff distance of 0.25 mm.

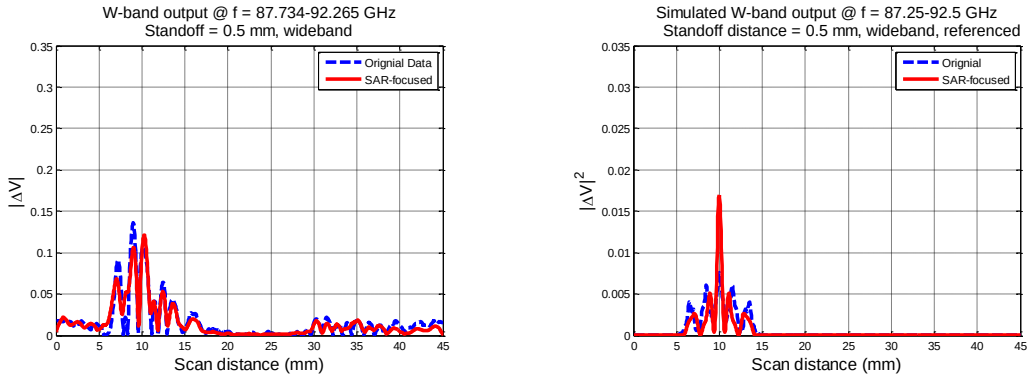

Figure 5.2. SAR-focused W-band results of 1.27 mm-long crack, as in measurement (left) and simulation (right), at standoff distance of 0.5 mm.

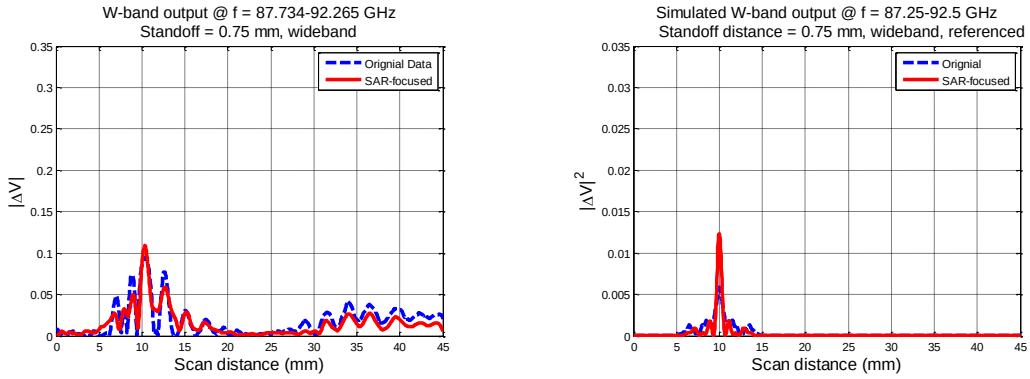

Figure 5.3. SAR-focused W-band results of 1.27 mm-long crack, as in measurement (left) and simulation (right), at standoff distance of 0.75 mm.

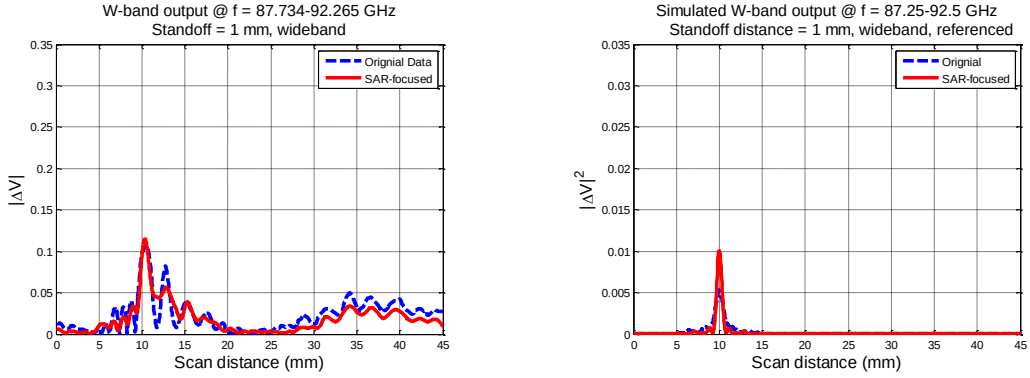

Figure 5.4. SAR-focused W-band results of 1.27 mm-long crack, as in measurement (left) and simulation (right), at standoff distance of 1 mm.

Such small distance between the aperture and SUT has also resulted in "sidelobe" (combination of scattered signals from both the fastener head and crack) that are comparable in magnitude to the actual crack signal, providing a more complex result for evaluation purposes. These issues become less significant with an increasing standoff distance, as the effect of misalignment reduces with respect to increase in travel distance of the transmitted signal.

Similar trends can be observed from Figures 5.1 through 5.4, as they suggest that the SAR filter contributes to smoothing the probe output signals (reducing the magnitude of "sidelobe", and magnitude of potential false indications), and providing an enhanced detection of cracks by focusing the energy to the crack location.

Shown in Figures 5.5 and 5.6 are comparisons of data before and after SAR filter are applied to the measurement (Figure 5.5) and simulation results (Figure 5.6). The signal levels presented in these figures are the peak values of the probe output signals when the probe is above the crack, in the region without fastener heads, and above the un-cracked fastener head.

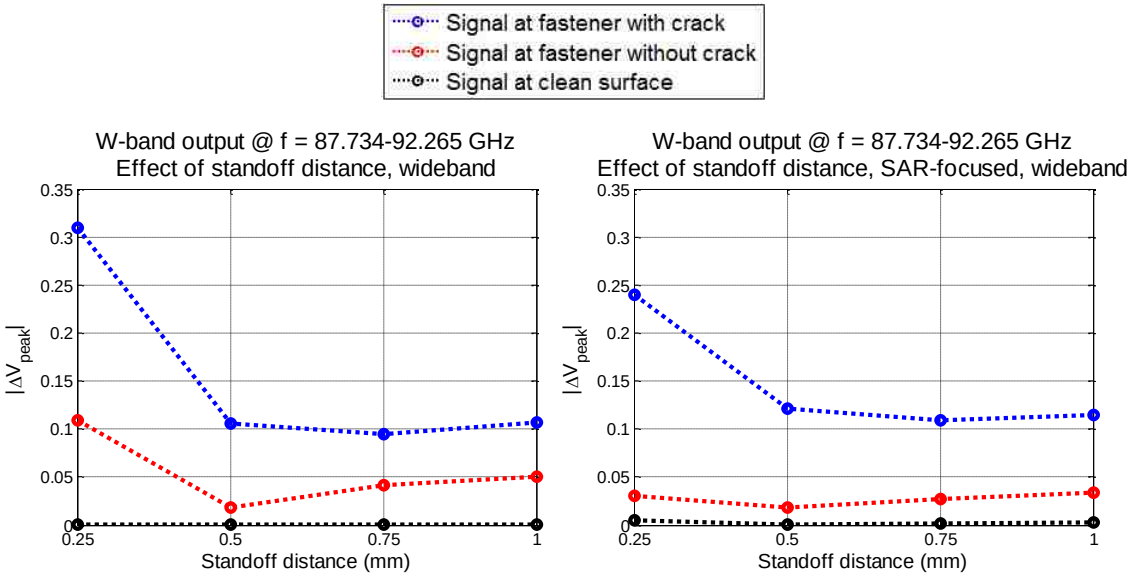

Figure 5.5. Comparison of measurement results with W-band differential probe, as in original (left) and SAR-focused (right), on effect of standoff distance.

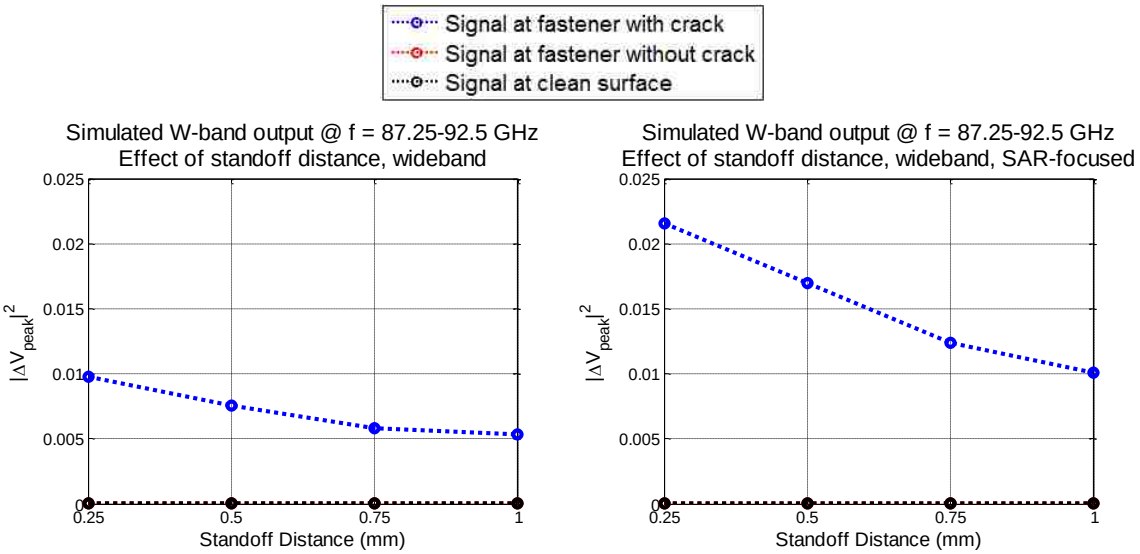

Figure 5.6. Comparison of simulation results with W-band differential probe, as in original (left) and SAR-focused (right), on effect of standoff distance.

Both figures suggest that the introduction of SAR contributes to enhancing the crack signals and reducing the magnitudes of probe output signals over the un-cracked fastener head (in measurements). The decreasing trend between the crack signals with respect to increase in standoff distance can still be observed. Overall, without the presence of potential misalignment (especially in the case of 0.25 mm standoff distance), SAR filter is demonstrated to be effective in providing enhanced detection in W-band fastener head crack scanning.

To compare the outcome of SAR filter in both measurements and simulations, the normalized probe output signal levels versus standoff distances are investigated. The normalized results provide a one-to-one comparison between the measured and simulated data (e.g., comparison in the amount of signal enhancement/reduction under the same condition). To do this, the signals with respect to different standoff distances are normalized to the largest (in magnitude) value among them. The results are presented in Figure 5.7.

The normalized results show a similar trend between both measurement and simulation, including the decreasing slope (over the entire range of standoff distance) in the crack output signal levels. The non-zero output signals over the un-cracked fastener

head region in measurements are likely due to measurement uncertainties (inconsistent standoff distance throughout the scan, surface unevenness, etc.).

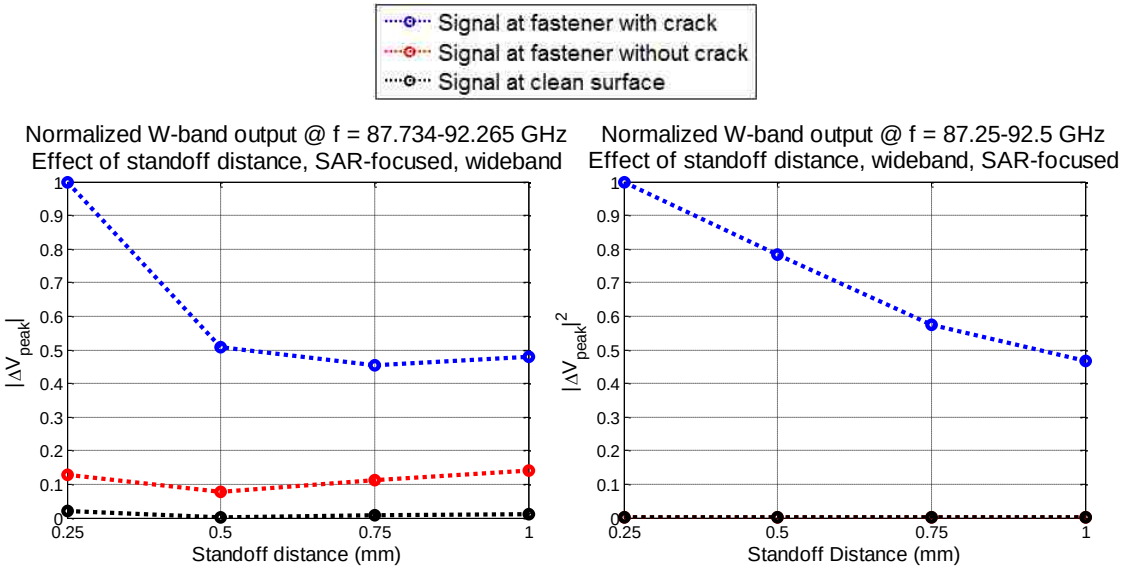

Figure 5.7. Normalized SAR-focused W-band results on effect of standoff distance. Presented are measurement (left) and simulation results (right).

5.1.2. V-band Wideband Response. Figures 5.8 through 5.11 represent the comparison between SAR-focused measurement and simulation results at V-band frequencies, with varying standoff distances between 0.25 and 1 mm. Both the original data and the SAR-focused data are provided.

Similar to W-band, the V-band results also suggest that the SAR filter contributes to smoothing the probe output signals, (reducing the magnitude of "sidelobe", and potential false indications), and providing an enhanced detection of cracks. However, since SAR is more generally used for measurements at higher standoff distance (or electrically far), its enhancing capability is limited due to longer wavelengths at V-band frequencies in comparison to W-band frequencies (same standoff distance appears electrically shorter at V-band), as observed from the figures below.

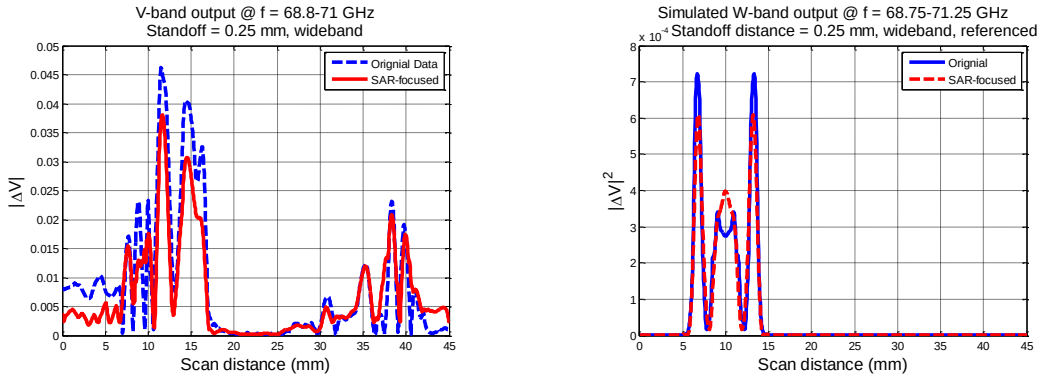

Figure 5.8. SAR-focused V-band results of 1.27 mm-long crack, as in measurement (left) and simulation (right), at standoff distance of 0.25 mm.

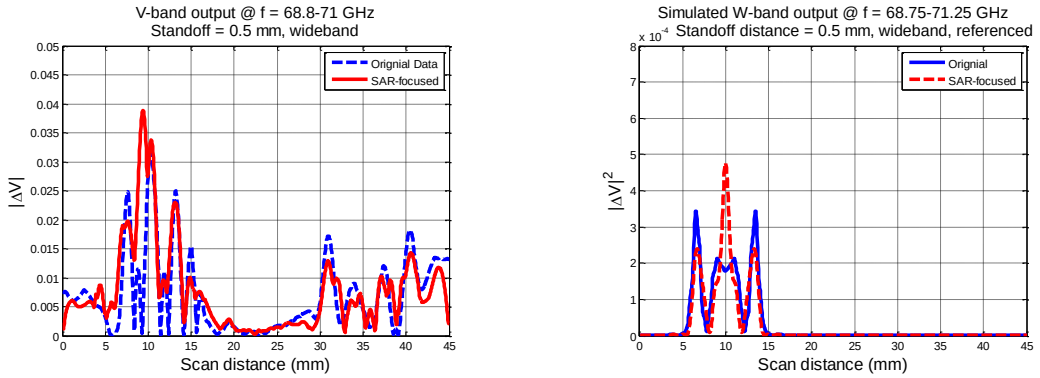

Figure 5.9. SAR-focused V-band results of 1.27 mm-long crack, as in measurement (left) and simulation (right), at standoff distance of 0.5 mm.

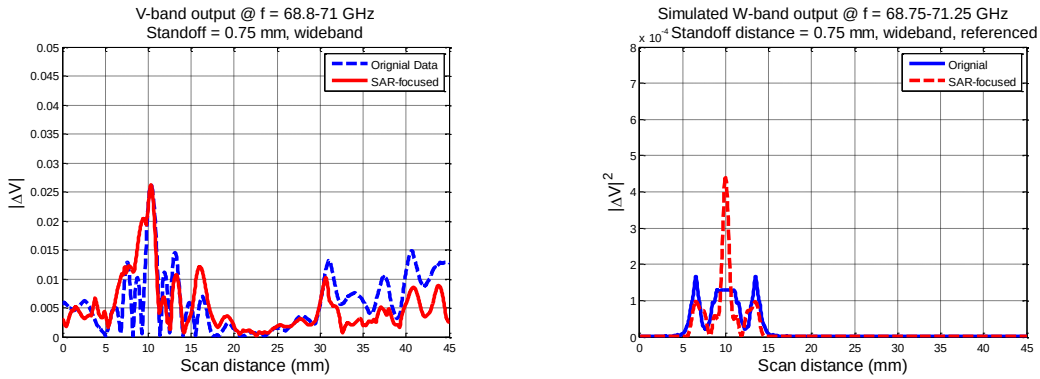

Figure 5.10. SAR-focused V-band results of 1.27 mm-long crack, as in measurement (left) and simulation (right), at standoff distance of 0.75 mm.

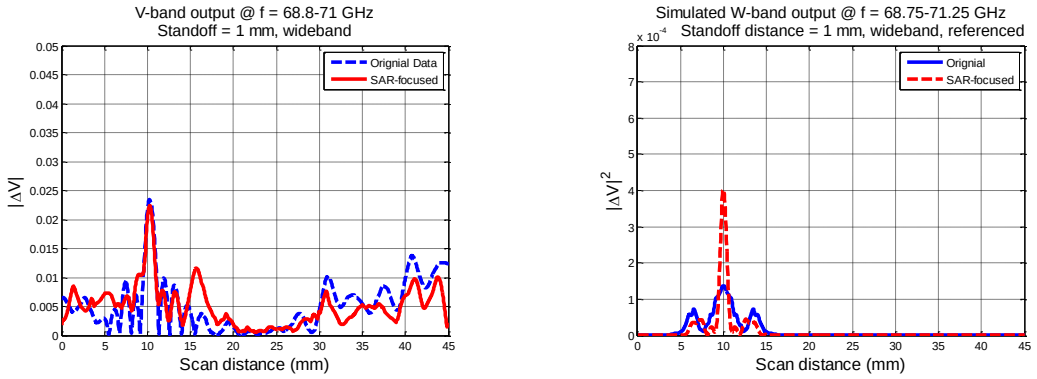

Figure 5.11. SAR-focused V-band results of 1.27 mm-long crack, as in measurement (left) and simulation (right), at standoff distance of 1 mm.

Shown in Figures 5.12 and 5.13 are comparisons of data before and after SAR filter are applied to the measurement (Figure 5.12) and simulation results (Figure 5.13). The signal levels presented in these figures are the peak values of the probe output signals when the probe is above the crack, in the region without fastener heads, and above the un-cracked fastener head.

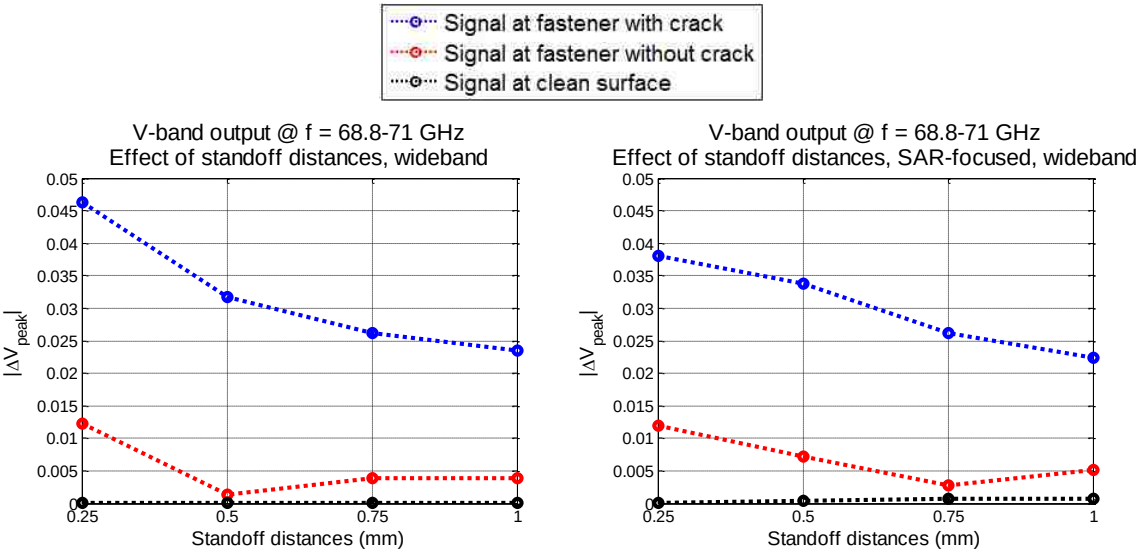

Figure 5.12. Comparison of measurement results with V-band differential probe, as in original (left) and SAR-focused (right), on effect of standoff distance.

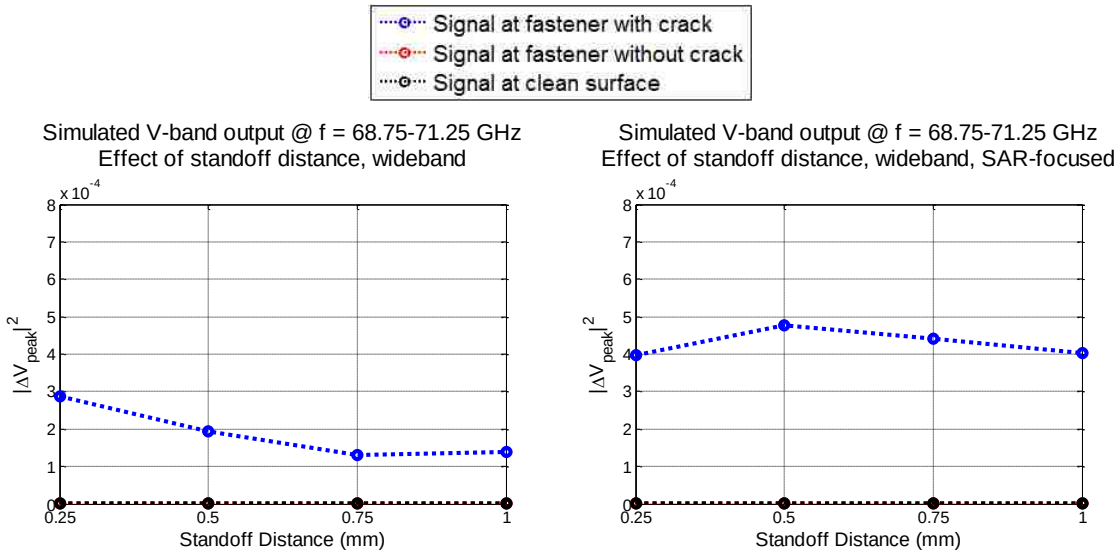

Figure 5.13. Comparison of simulation results with W-band differential probe, as in original (left) and SAR-focused (right), on effect of standoff distance.

The simulation results suggest that the introduction of SAR filter contributes to enhancing the crack signals for all standoff distances applied, but the enhancement is limited at 0.25 mm standoff distance likely due to close-up operation. While in measurements, the enhancements are limited across the entire range of standoff distance, for reasons previously stated.

To compare the outcome of SAR filter in both measurements and simulations, the normalized probe output signal levels versus standoff distances are investigated. The normalized results provide a one-to-one comparison between the measured and simulated data. To do this, the signals with respect to different standoff distances are normalized to the largest (in magnitude) value among them. The results are presented in Figure 5.14.

The normalized results show a similar trend between the measurement and simulation results, as the crack signal levels decrease with respect to increase in standoff distance, except for the case of 0.25 mm standoff distance, potentially due to the uncertainties in measurements (e.g., surface unevenness).

Overall, the W-band results demonstrate a more promising results than V-band on fastener head crack detection. This may be because the dimensions of the fastener head and cracks are more proportional to the wavelengths (and aperture dimensions) of the W-

band frequencies than V-band frequencies, which means W-band frequencies are much more sensitive to target of this nature.

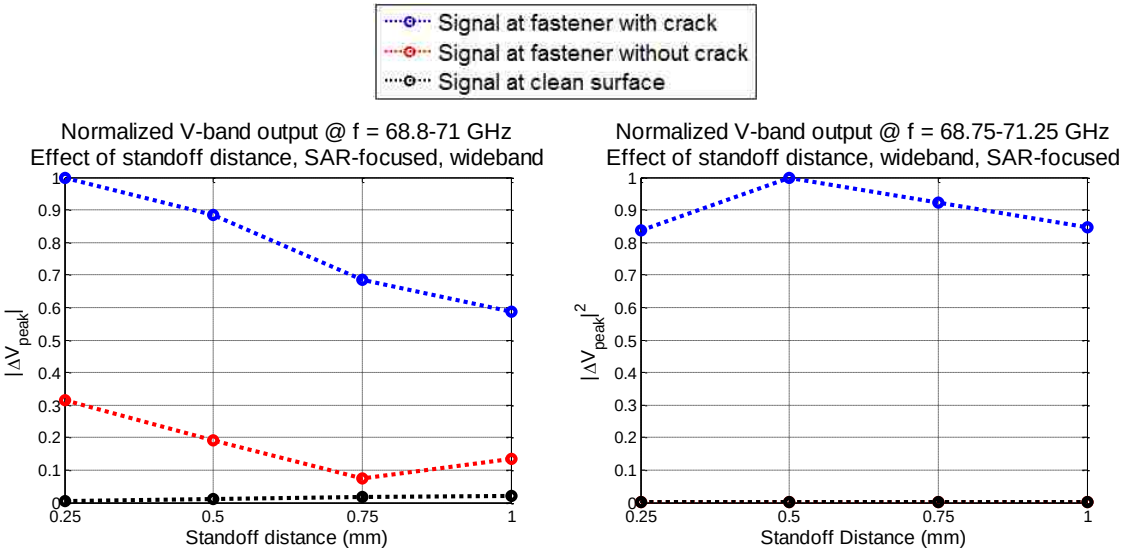

Figure 5.14. Normalized SAR-focused V-band results on effect of standoff distance. Presented are measurement (left) and simulation results (right).

5.2. EFFICACY OF SAR FILTER ON EFFECT OF APERTURE OFFSET

SAR filter is applied to both the measured and simulated data (presented in Section 4.2) to investigate the effect of aperture offset at W-band frequencies. Both data represent the scan results for a 1.27 mm-long crack, at the four common W-band frequencies (shown in Appendix G). The aperture offsets represent a tilt in the differential probe with respect to the sample surface. A negative aperture offset is when the probe aperture is closer to the crack, and a positive aperture offset is when the probe is further away from the crack (Figure 3.17 and 3.18).

Figures 5.15 through 5.17 represent the comparison between SAR-focused measurement and simulation results at W-band frequencies with a standoff distance of 1 mm, and aperture offsets of ±2 rotations (measurements)/±0.25 mm (simulations) and zero. It is approximated that one complete rotation of the knob (controlling aperture offset) is equivalent to 0.1 mm of offset. Therefore, an aperture offset of -2 rotations is

approximately equal to -0.2 mm of offset. The complete comparison results (standoff distance of 0.5 mm and other aperture offsets) are provided in Appendix L.

Similar to the previous sections, these results also suggest that the SAR filter contributes to smoothing the probe output signals (lower magnitudes of "sidelobe" and probe output signals over the un-cracked fastener head region, etc.) and providing an enhanced detection of cracks.

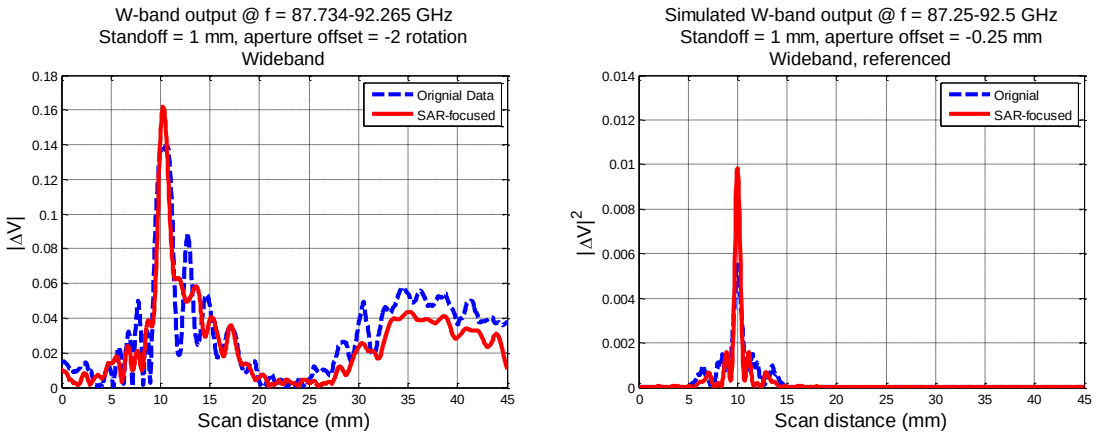

Figure 5.15. SAR-focused W-band results of 1.27 mm-long crack, as in measurement (left) and simulation (right), at standoff distance of 1 mm, and aperture offset of -2 rotations (measurements) and -0.25 mm (simulations).

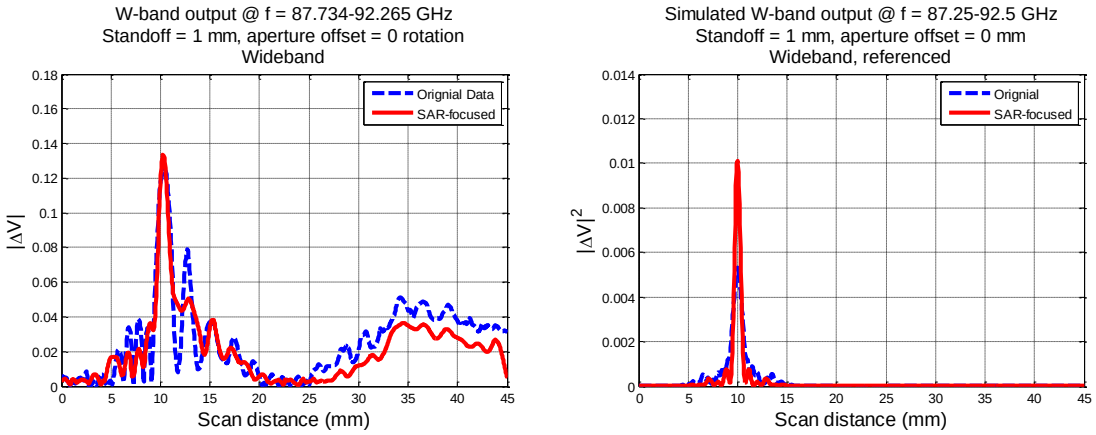

Figure 5.16. SAR-focused W-band results of 1.27 mm-long crack, as in measurement (left) and simulation (right), at standoff distance of 1 mm, and no aperture offset.

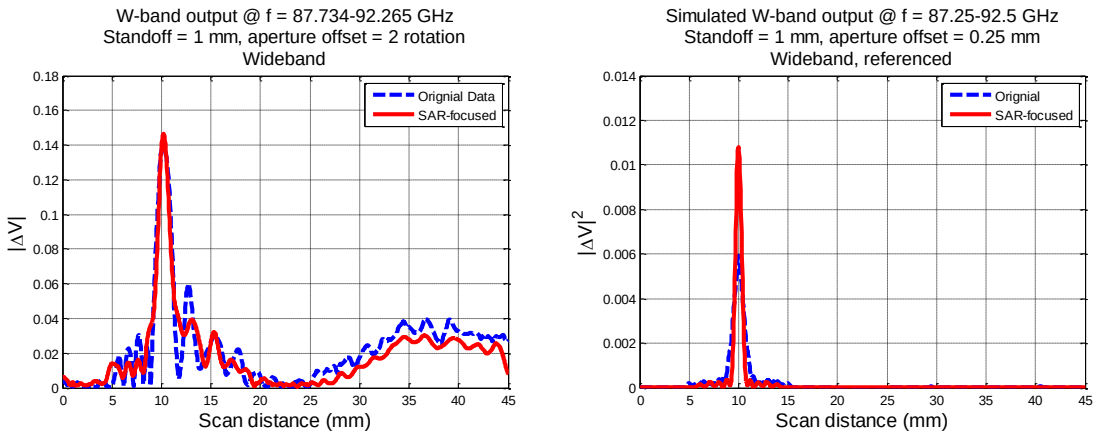

Figure 5.17. SAR-focused W-band results of 1.27 mm-long crack, as in measurement (left) and simulation (right), at standoff distance of 1 mm, and aperture offset of +2 rotations (measurements) and +0.25 mm (simulations).

In the previous sections, aperture offsets are determined to have minimal effect on the W-band probe output while at a high standoff distance (1 mm). The consequences of aperture offsets are the DC bias (consequences of the unequal distances between the two probe apertures and SUT) in the signals, which is removed during the implementation of SAR filter. These figures confirm the observations as the probe output signals are similar across the range of aperture offsets applied with a 1 mm standoff distance.

Shown in Figures 5.18 through 5.21 are comparisons of data before and after SAR filter are applied to the measurement (Figures 5.18 and 5.19) and simulation results (Figures 5.20 and 5.21), at both standoff distances (0.5 and 1 mm). The signal levels presented in these figures are the peak values of the probe output signals when the probe is above the crack, in the region without fastener heads, and above the un-cracked fastener head. These figures clearly suggest that the introduction of SAR filter contributes to enhancing the crack signals, as well as reducing the magnitudes of unwanted signals (signals over un-cracked fastener head). It can again be noticed at a higher standoff distance (1 mm), an aperture offset does not have a significant effect on the probe output signals. However, with a small standoff distance (0.5 mm), the crack output signal level decreases with respect to increase in aperture offset (from negative to positive). This can

be expected as a higher standoff distance reduces the effect the unwanted scattered signals caused by the offset.

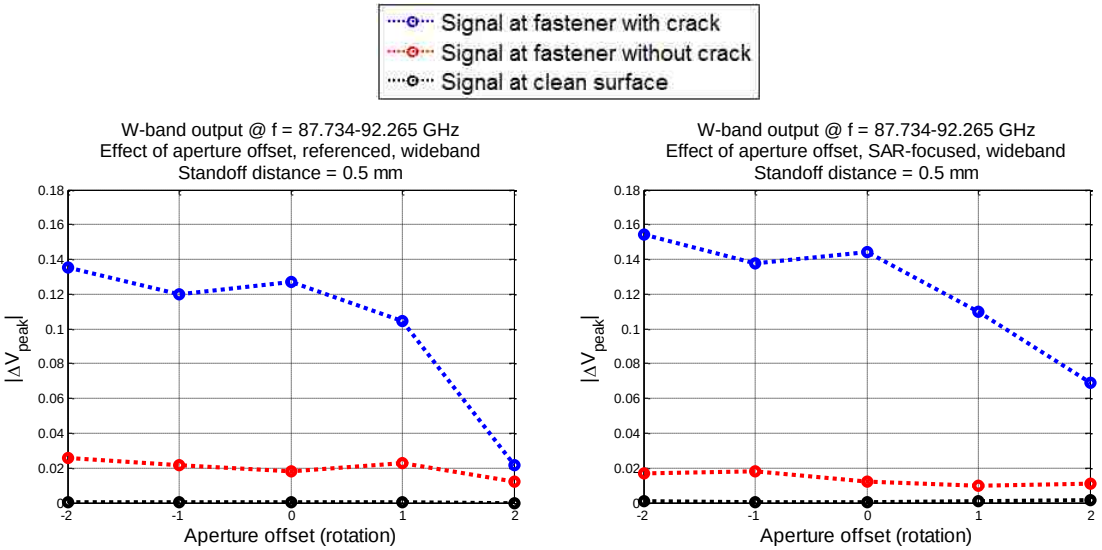

Figure 5.18. Comparison of measurement results with W-band differential probe, as in original (left) and SAR-focused (right), on effect of aperture offset, at standoff distance of 0.5 mm.

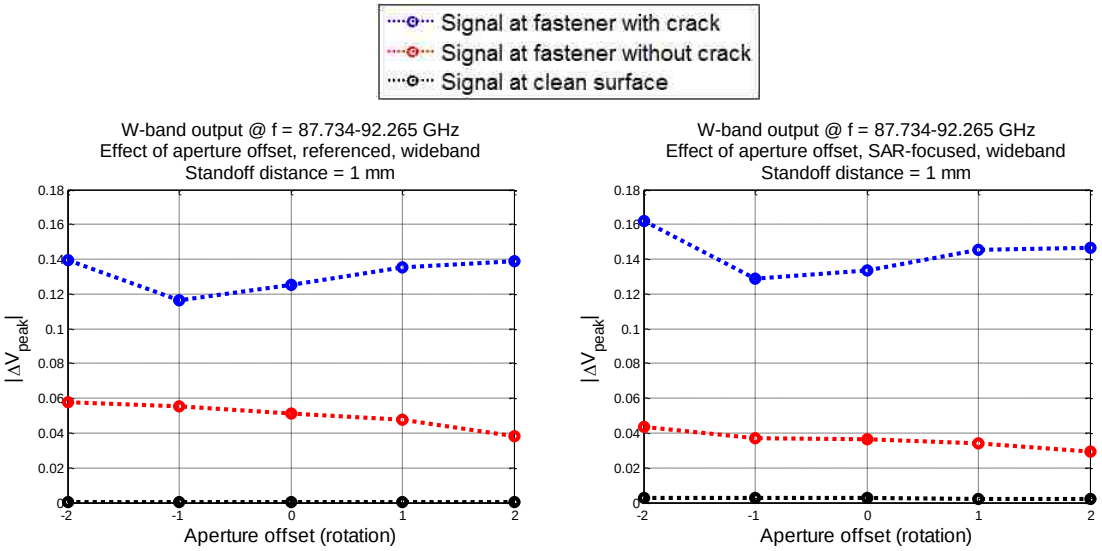

Figure 5.19. Comparison of measurement results with W-band differential probe, as in original (left) and SAR-focused (right), on effect of aperture offset, at standoff distance of 1 mm.

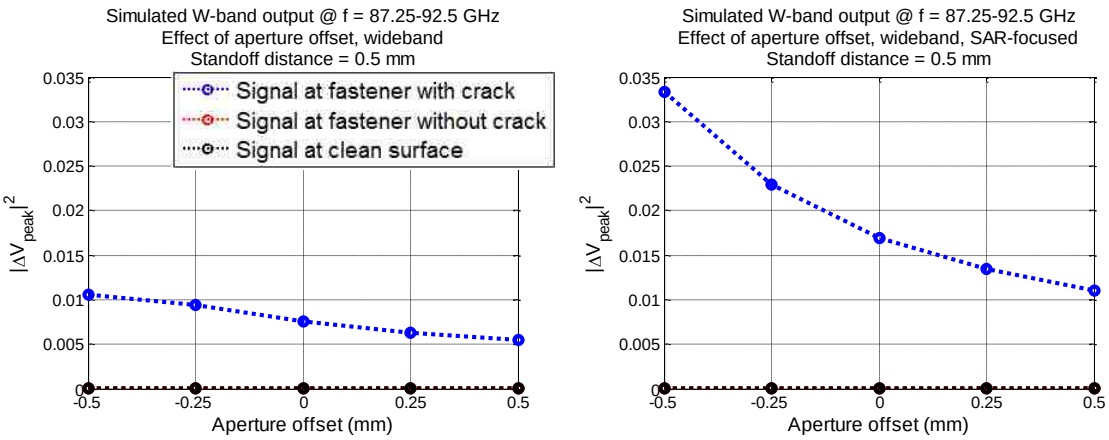

Figure 5.20. Comparison of simulation results with W-band differential probe, as in original (left) and SAR-focused (right), on effect of aperture offset, at standoff distance of 0.5 mm.

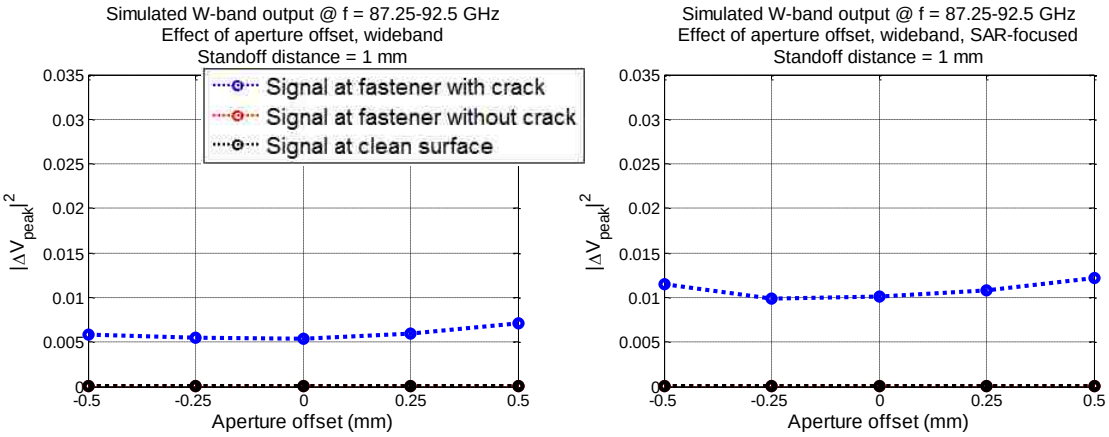

Figure 5.21. Comparison of simulation results with W-band differential probe, as in original (left) and SAR-focused (right), on effect of aperture offset, at standoff distance of 1 mm.

To compare the outcome of SAR filter in both measurements and simulations, the normalized probe output signal levels versus aperture offsets are investigated. The normalized results provide a one-to-one comparison between the measured and simulated data. To do this, the signals with respect to the different combination of aperture offsets and standoff distances are normalized to the largest (in magnitude) value among them.

The results are presented in Figures 5.22 and 5.23, for standoff distances of 0.5 and 1 mm, respectively.

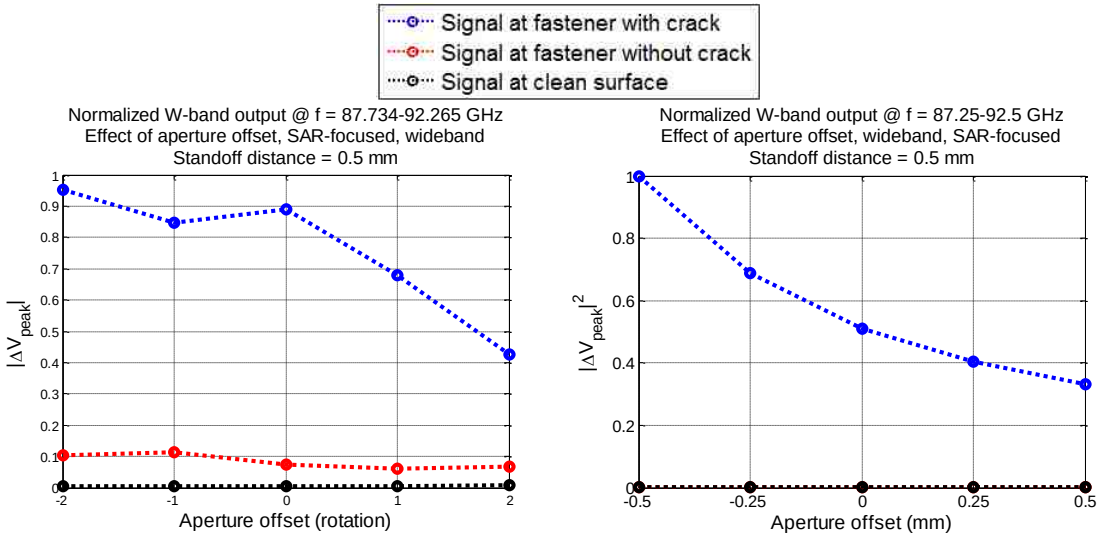

Figure 5.22. Normalized SAR-focused W-band results on effect of aperture offset. Presented are measurement (left) and simulation results (right), at standoff distance of 0.5 mm.

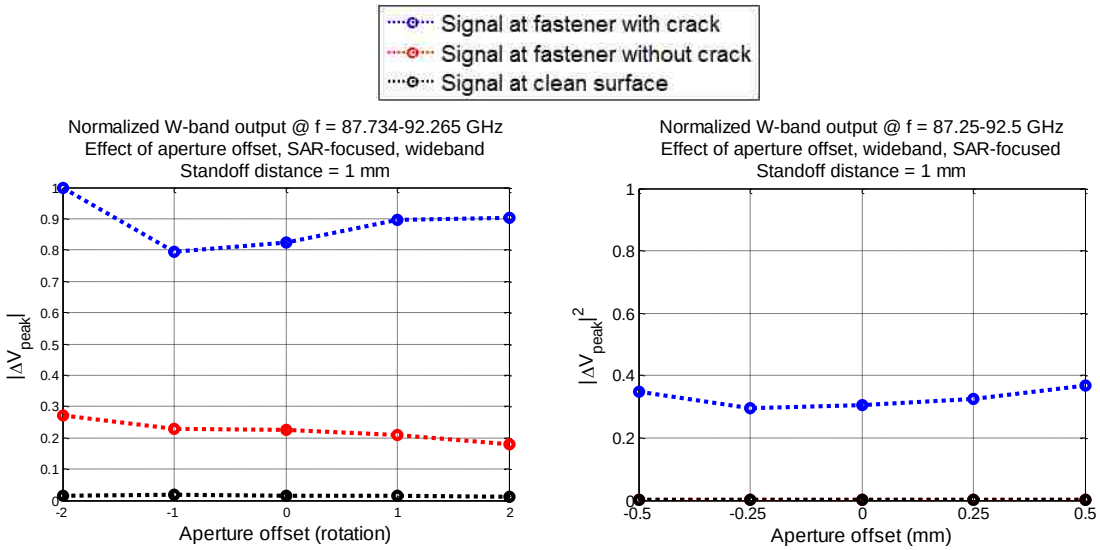

Figure 5.23. Normalized SAR-focused W-band results on effect of aperture offset. Presented are measurement (left) and simulation results (right), at standoff distance of 1 mm.

The normalized results show a similar trend between the measurements and simulations. Though the SAR filter does not contribute to resolving the consequences of a decreasing crack output signal level at lower standoff distance, it still provides an overall enhancement of the results. The results also suggest that it may be desired for the measurements to be completed with higher standoff distance between the probe and SUT.

5.3. EFFICACY OF SAR FILTER ON EFFECT OF PAINT THICKNESS

SAR filter is applied to both the measured and simulated data (presented in Section 4.3) to investigate the effect of paint thickness at W-band frequencies. Both data represent the scan results for a 1.27 mm-long crack, at the four common W-band frequencies (shown in Appendix G). The presence of paint acts as a dielectric layer between the probe and sample surface. Therefore, the electrical distance between the probe and the sample surface increases. The paint layer also causes internal reflections between itself and SUT, making the signal behavior more difficult to predict while altering the resonance properties of the crack.

Figures 5.24 through 5.27 represent the comparison between SAR-focused measurement and simulation results at W-band frequencies with a standoff distance of 1 mm, and a layer of paint with thicknesses of 0, ~0.1 mm (a thin layer), ~0.4 and ~0.5 mm (a thick layer). The complete comparison results (standoff distance of 0.5 mm and other paint thicknesses) are provided in Appendix M. Note that the figures may not be in the same scales.

In these figures, the simulation results suggest that the SAR filter contributes to reducing the magnitudes of unwanted signals and enhancing the detection. However, SAR filter appears to be less effective on the measurement results, as the magnitudes crack signals also reduce with the unwanted signals over the un-cracked fastener head (potentially due to measurement uncertainty and non-uniform paint layer). In these measurements, the signals travel through two layers: air (standoff distance) and paints. The standoff distance is adjusted manually (therefore slight uncertainties may occur), and the paint layer may not be uniformly spread, resulting in a non-flat surface. These uncertainties may lead to incorrectly calculated focusing distance and inaccurate SAR results.

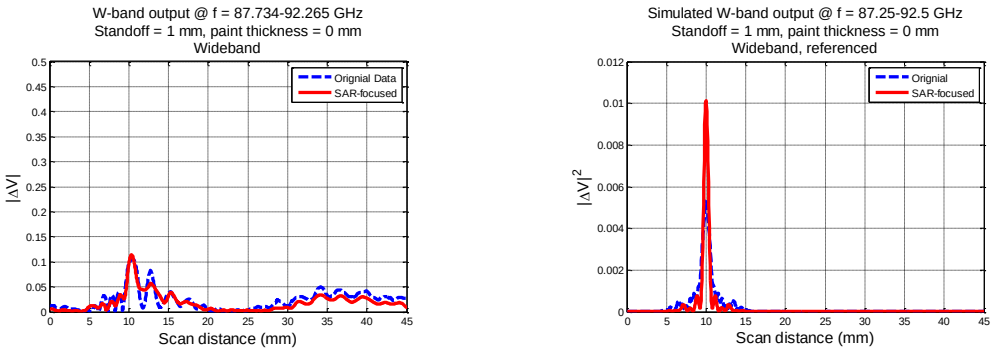

Figure 5.24. SAR-focused W-band results of 1.27 mm-long crack, as in measurement (left) and simulation (right), at standoff distance of 1 mm, and no paint.

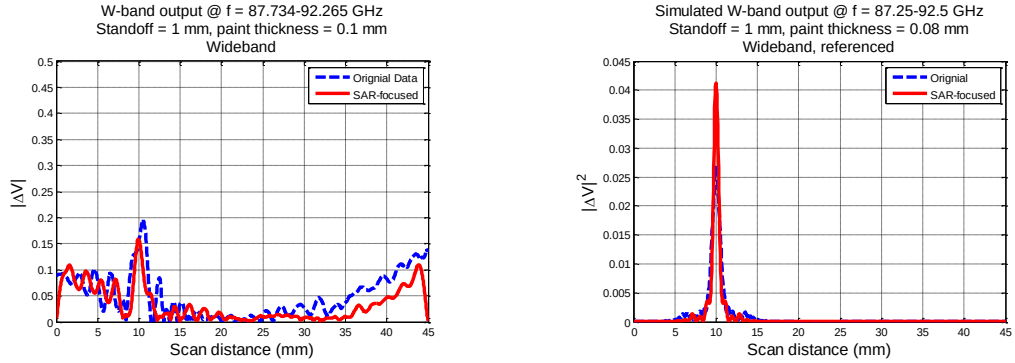

Figure 5.25. SAR-focused W-band results of 1.27 mm-long crack, as in measurement (left) and simulation (right), at standoff distance of 1 mm, and paint thickness of 0.1 mm (measurements) and 0.08 mm (simulations).

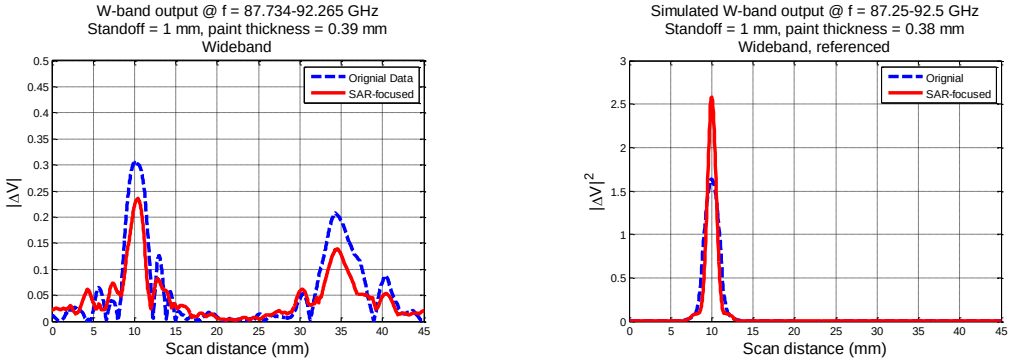

Figure 5.26. SAR-focused W-band results of 1.27 mm-long crack, as in measurement (left) and simulation (right), at standoff distance of 1 mm, and paint thickness of 0.39 mm (measurements) and 0.38 mm (simulations).

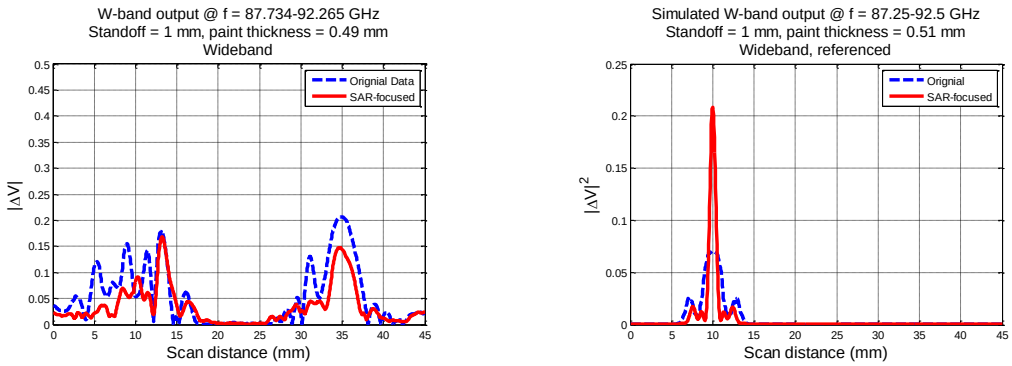

Figure 5.27. SAR-focused W-band results of 1.27 mm-long crack, as in measurement (left) and simulation (right), at standoff distance of 1 mm, and paint thickness of 0.49 mm (measurements) and 0.51 mm (simulations).

In the previous sections, it was found that a thin layer of paint (~0.1 to 0.4 mm) contributes to enhancing the signals, and a thick layer of paint (> 0.4 mm) makes the probe output signals less straightforward to predict (in measurements) due to a higher chance of paint clumps forming around the fastener head, and crack filling with paint. The similar observations can be found in Figures 5.24 through 5.27 (after SAR filter is applied), and as well as on results at standoff distance of 0.5 mm provided in Appendix M.

Shown in Figures 5.28 through 5.31 are comparisons of data before and after SAR filter are applied to the measurement (Figures 5.28 and 5.29) and simulation results (Figures 5.30 and 5.31), at both standoff distances (0.5 and 1 mm). The signal levels presented in these figures are the peak values of the probe output signals when the probe is above the crack, in the region without fastener heads, and above the un-cracked fastener head.

These figures also suggest that SAR filter does not effectively enhance the crack detections in measurements, in comparison to the enhancement on simulation results for reasons previously mentioned. In addition, there is a possibility that the crack inspected is filled with paint material, making the crack appear electrically bigger, and therefore stronger detections.

To compare the outcome of SAR filter in both measurements and simulations, the normalized probe output signal levels versus paint thicknesses are investigated. The normalized results provide a one-to-one comparison between the measured and simulated data. To do this, the signals with respect to the different combination of paint thicknesses and standoff distances are normalized to the largest (in magnitude) value among them. The results are presented in Figures 5.32 and 5.33, for standoff distances of 0.5 and 1 mm, respectively.

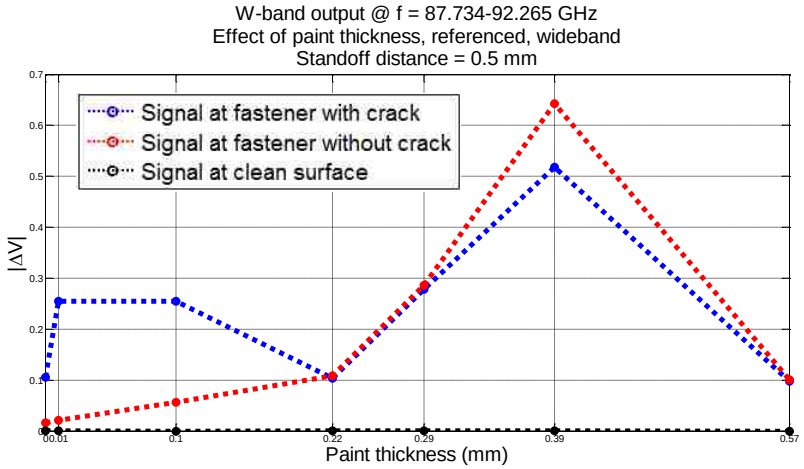

(a) Original measurement results

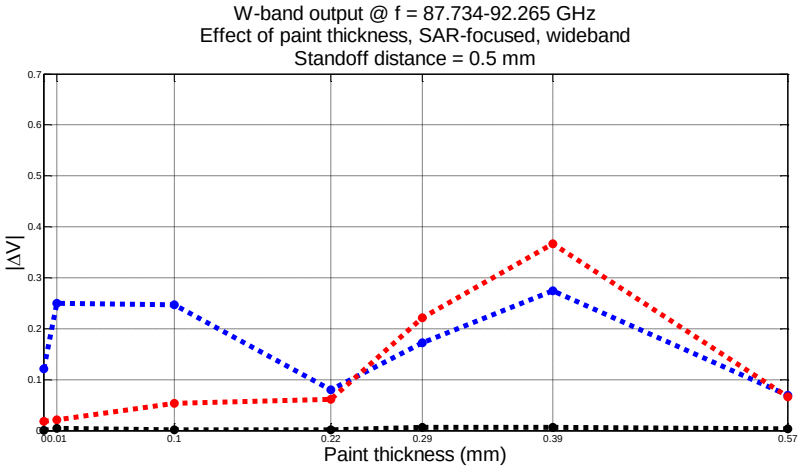

(b) SAR-focused measurement results

Figure 5.28. Comparison of measurement results with W-band differential probe, as in original (left) and SAR-focused (right), on effect of paint thickness, at standoff distance of 0.5 mm.

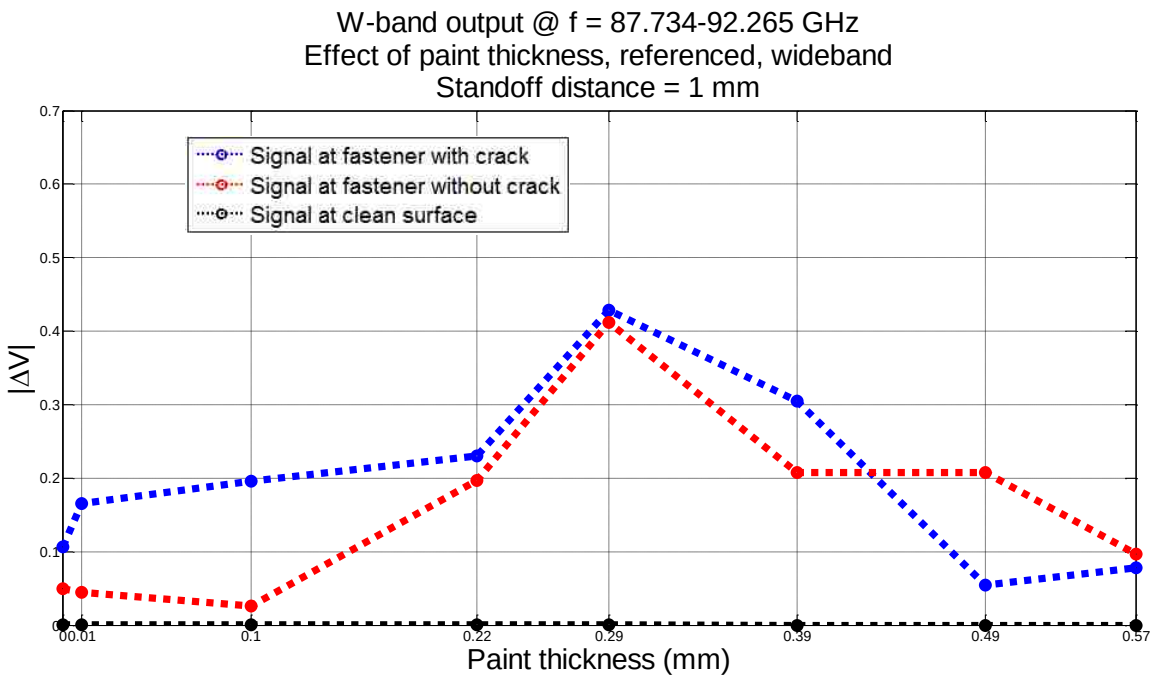

(a) Original measurement results

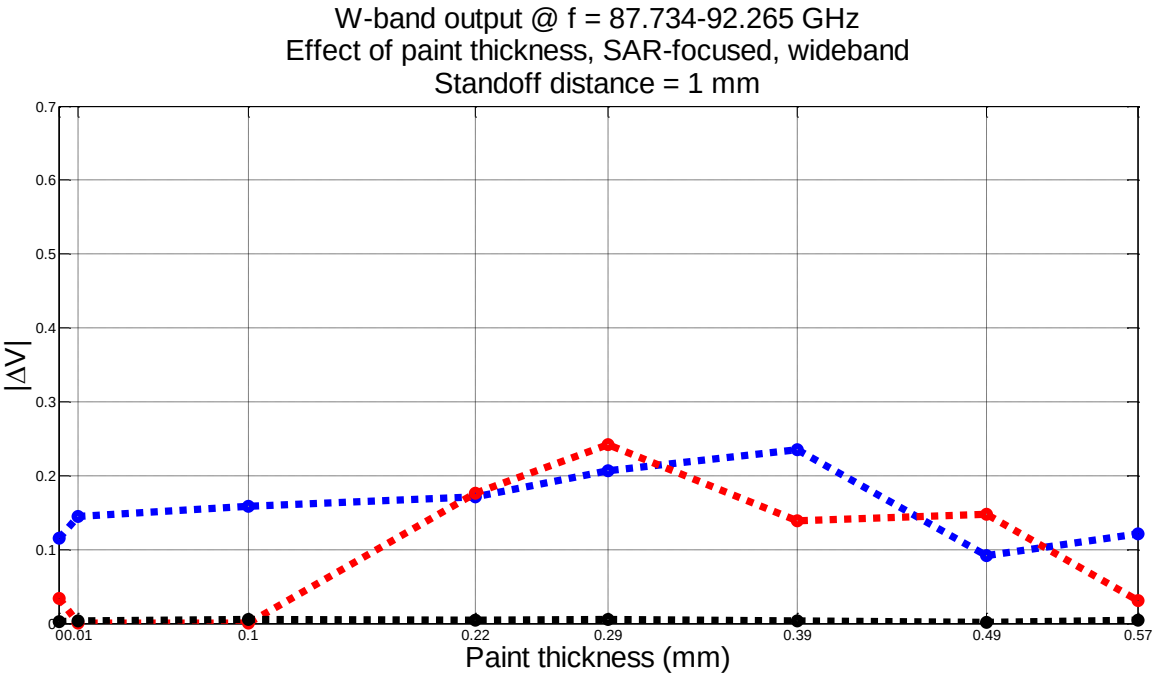

(b) SAR-focused measurement results

Figure 5.29. Comparison of measurement results with W-band differential probe, as in original (left) and SAR-focused (right), on effect of paint thickness, at standoff distance of 1 mm.

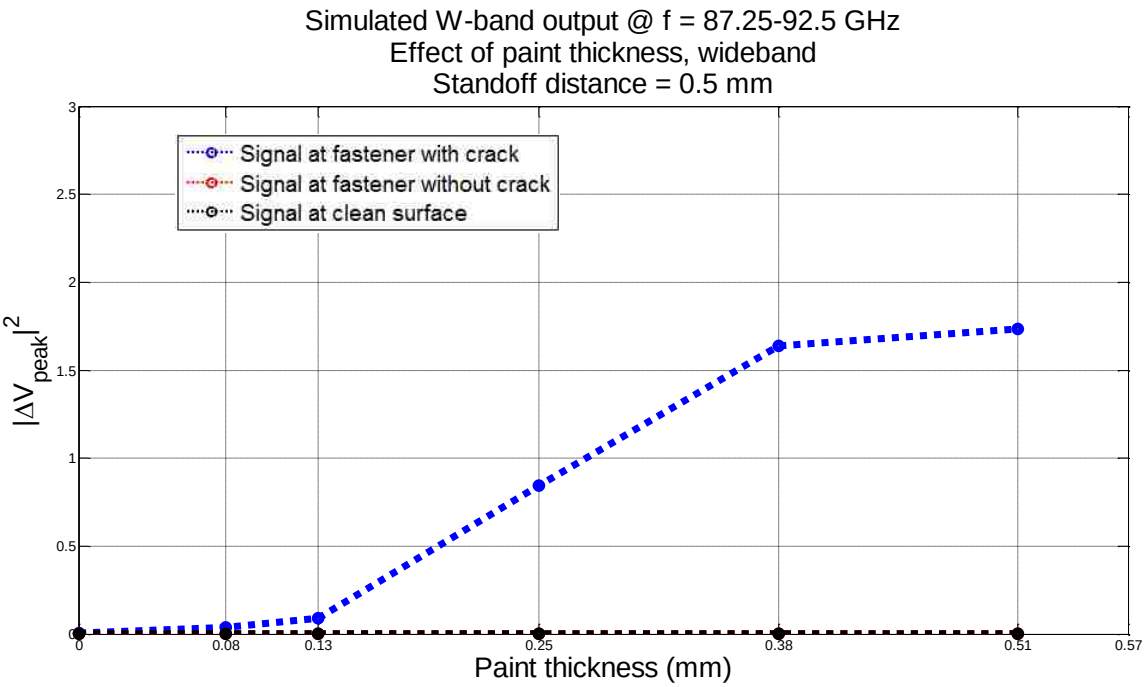

(a) Original simulation results

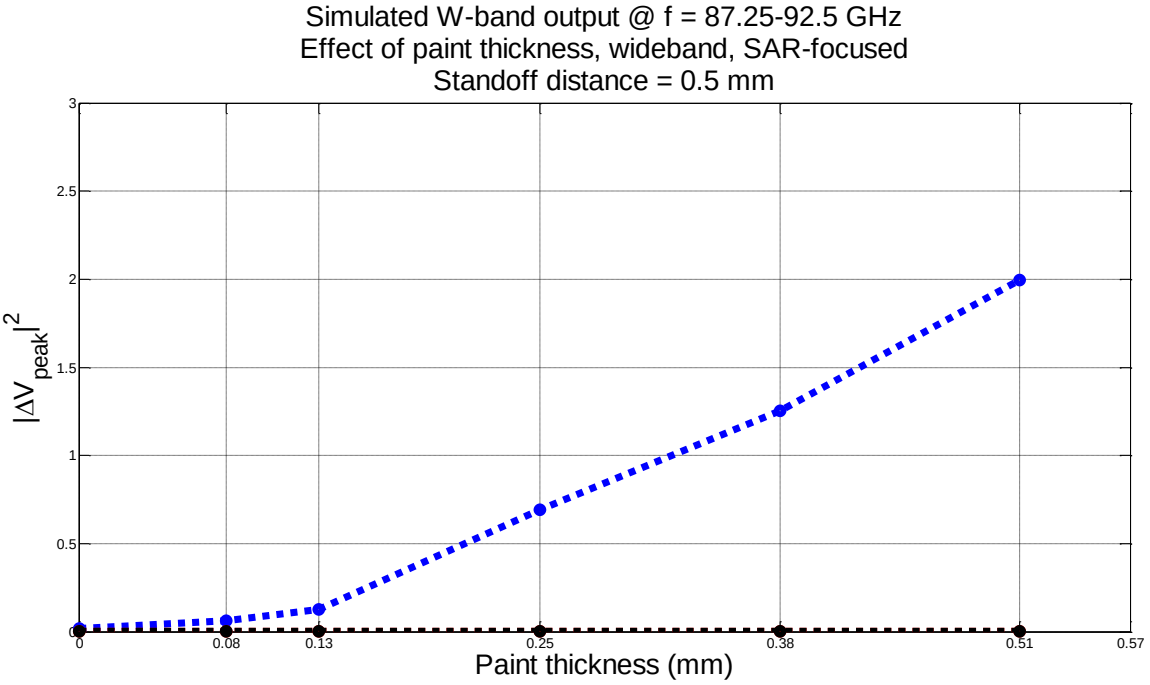

(b) SAR-focused simulation results

Figure 5.30. Comparison of simulation results with W-band differential probe, as in original (left) and SAR-focused (right), on effect of paint thickness, at standoff distance of 0.5 mm.

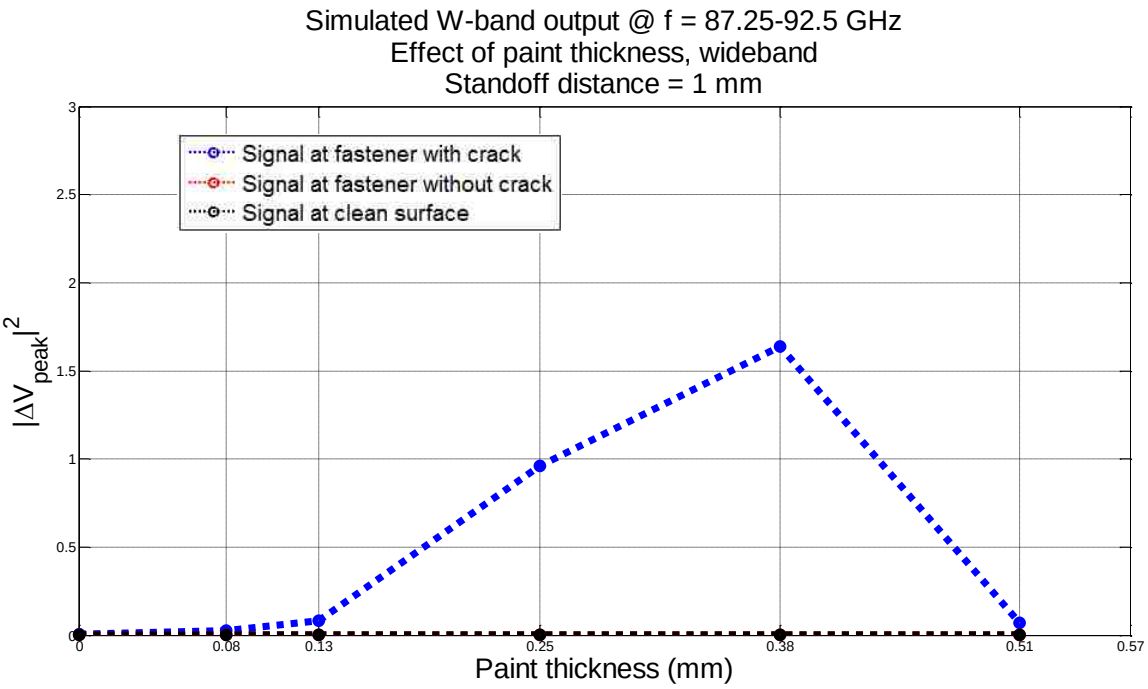

(a) Original simulation results

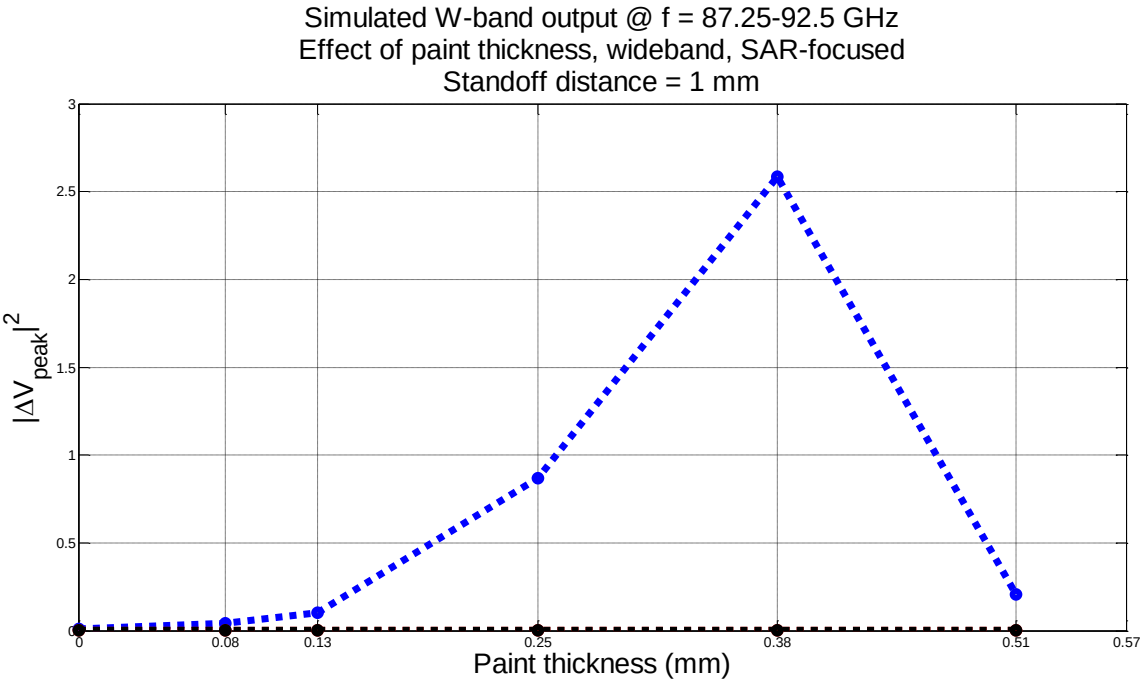

(b) SAR-focused simulation results

Figure 5.31. Comparison of simulation results with W-band differential probe, as in original (left) and SAR-focused (right), on effect of paint thickness, at standoff distance of 1 mm.

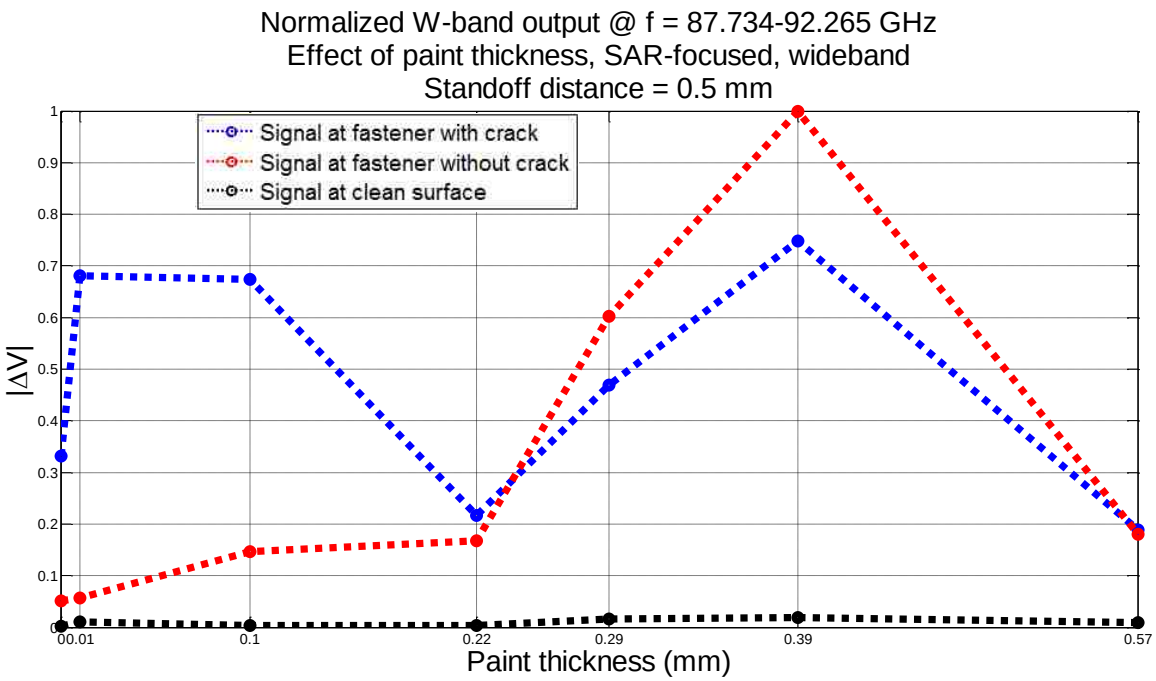

(a) SAR-focused measurement results

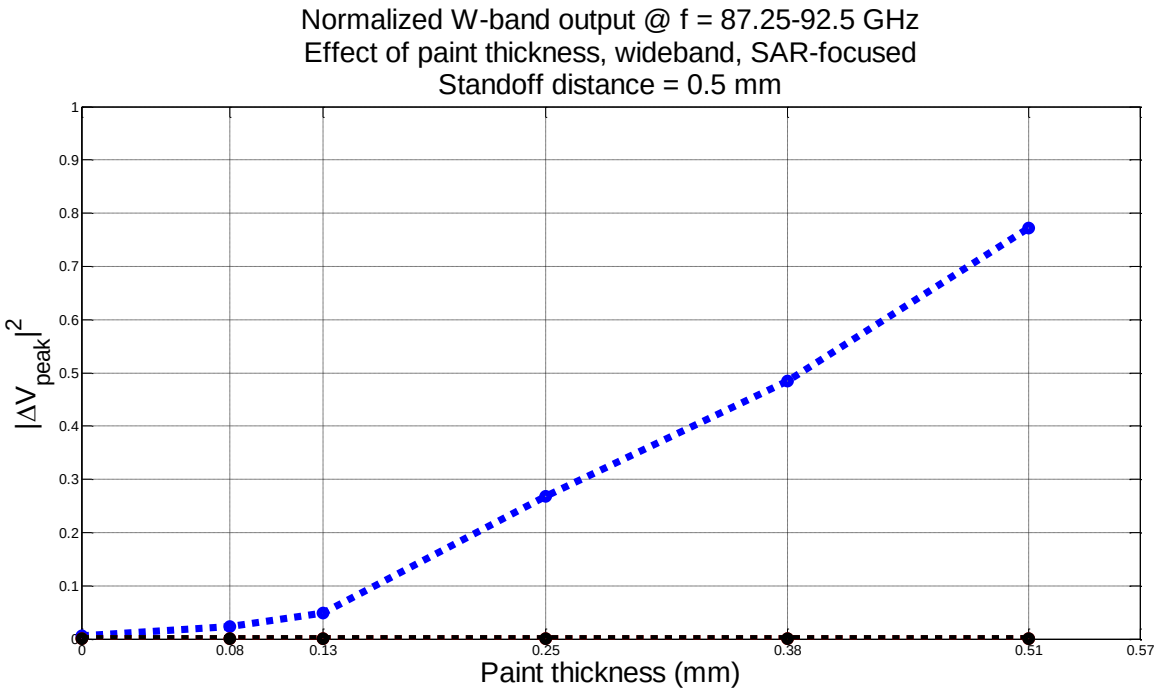

(b) SAR-focused simulation results

Figure 5.32. Normalized SAR-focused W-band results on effect of paint thickness. Presented are measurement (left) and simulation results (right), at standoff distance of 0.5 mm.

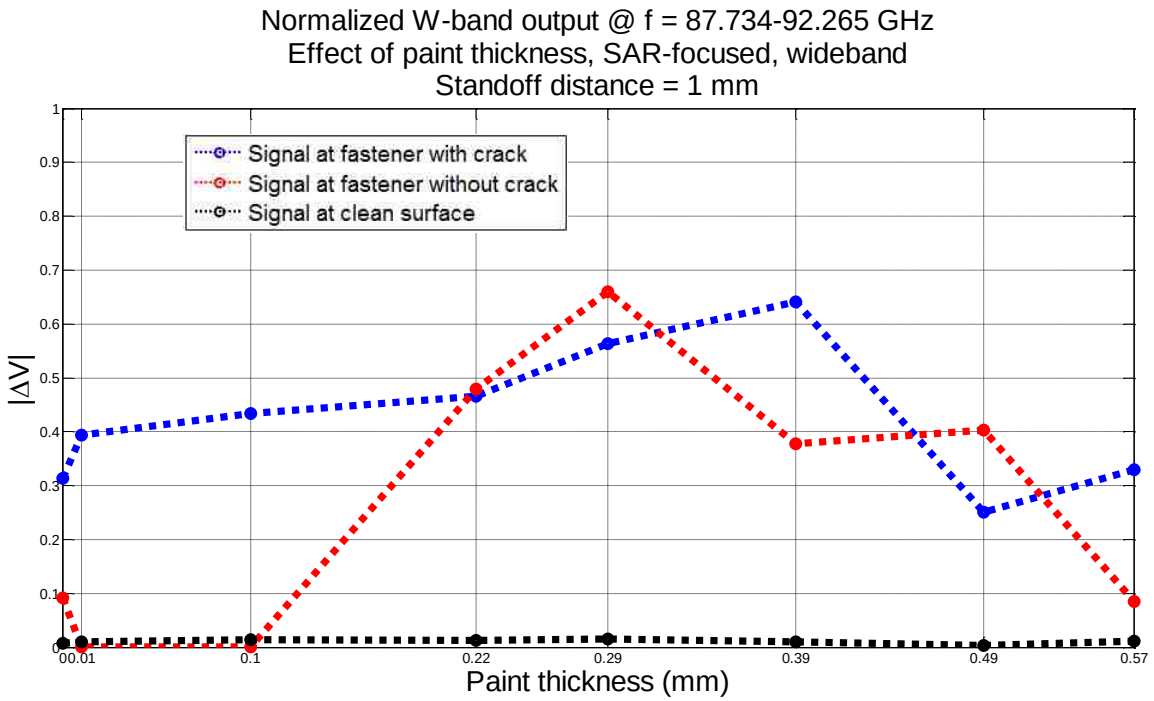

(a) SAR-focused measurement results

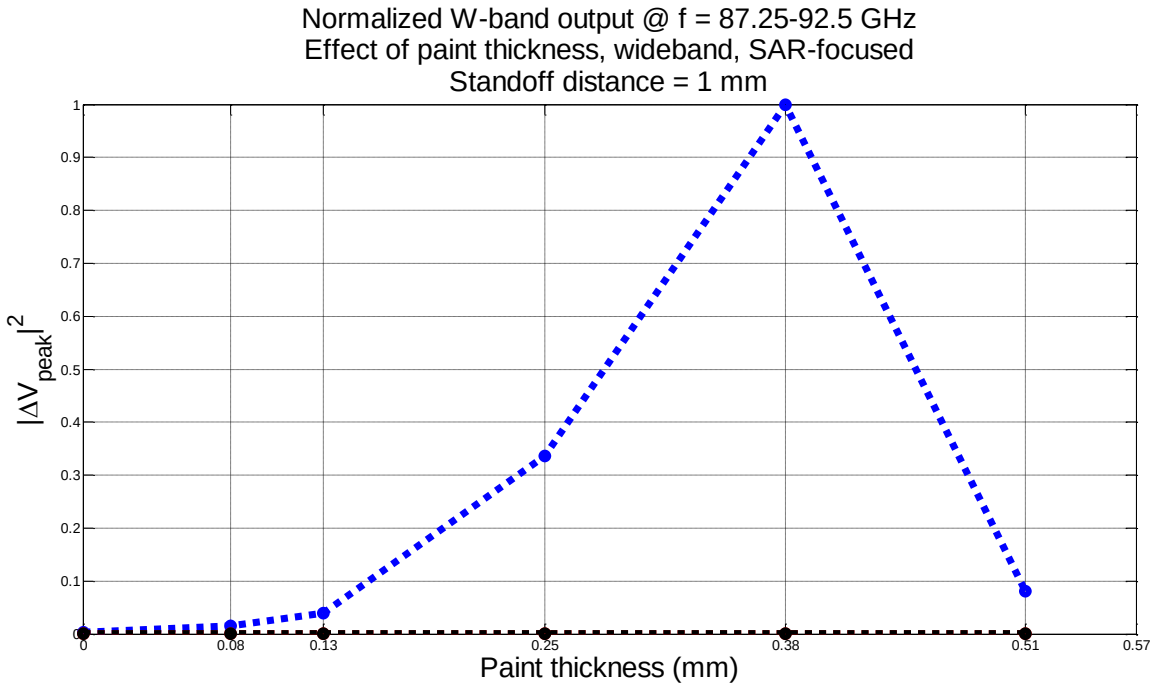

(b) SAR-focused simulation results

Figure 5.33. Normalized SAR-focused W-band results on effect of paint thickness. Presented are measurement (left) and simulation results (right), at standoff distance of 1 mm.

While no similar trends can be observed between the measurement and simulation results, it can be concluded that SAR filter may not be very efficient when there exists many measurement uncertainties such as: inaccurately measured standoff distance (when measured on a curved surface) or paint thickness, partially-filled or completely-filled cracks (that changes the resonance properties of cracks), and non-uniform paint, making the probe output signals unpredictable. A more in-depth analysis of non-uniform paint will be conducted and presented in Section 6.

5.4. EFFICACY OF SAR FILTER ON EFFECT OF PROBE MISALIGNMENT

SAR filter is applied to both the measured and simulated data (presented in Section 4.4) to investigate the effect of probe misalignment at W-band frequencies. Both data represent the scan results for a 1.27 mm-long crack, at the four common W-band frequencies (shown in Appendix G). A probe misalignment represents a shift in the probe with respect to the location of the fastener head. A negative probe misalignment is when the probe is shifted towards the crack, and a positive probe misalignment is when the probe is shifted away from the crack (Figure 3.48).

Figures 5.34 through 5.36 represent the comparison between SAR-focused measurement and simulation results at W-band frequencies with a standoff distance of 1 mm, and probe misalignments of ±1.27 and 0 mm. The complete comparison results (standoff distance of 0.5 mm and other probe misalignments) are provided in Appendix N. Note that the figures may not be in the same scales.

The results suggest that the contribution of SAR filter regarding to probe misalignments is the reduction of "sidelobe" around the crack locations, as demonstrated in both measurement and simulation results. It was observed in the previous results that, without a crack, a probe misalignment at either direction does not significantly affect the probe output signals as the unwanted signals (probe output signals between 30 – 40 mm positions) are well below the crack signals. However, with the presence of a crack and negative probe misalignment, the combined scattered signals from the crack and the fastener head edge results in the "sidelobe" around the crack location, and can potentially mask the actual crack signals. In this application, SAR filter contributes to reproduce the crack signals at the actual location while reducing the magnitudes of the "sidelobe".

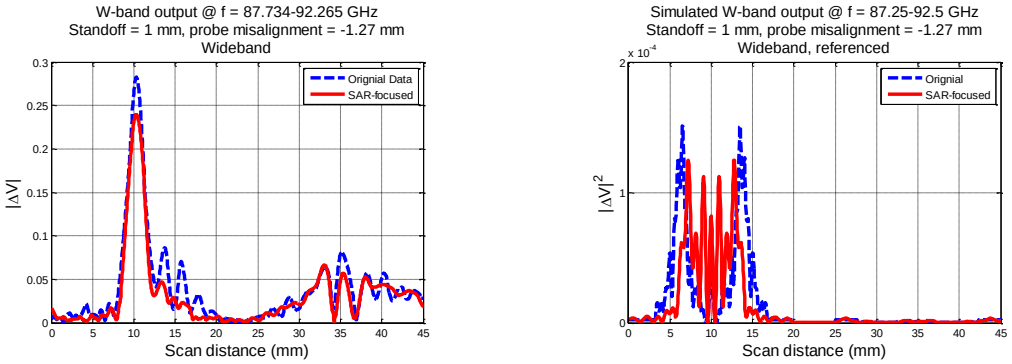

Figure 5.34. SAR-focused W-band results of 1.27 mm-long crack, as in measurement (left) and simulation (right), at standoff distance of 1 mm, and probe misalignment of -1.27 mm.

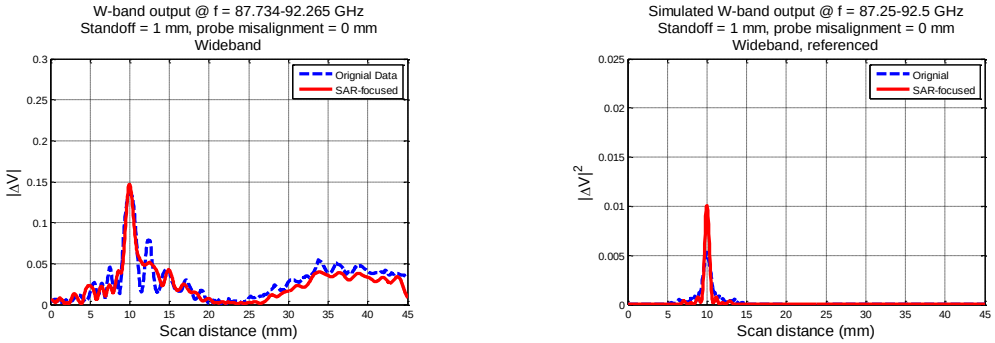

Figure 5.35. SAR-focused W-band results of 1.27 mm-long crack, as in measurement (left) and simulation (right), at standoff distance of 1 mm, and no probe misalignment.

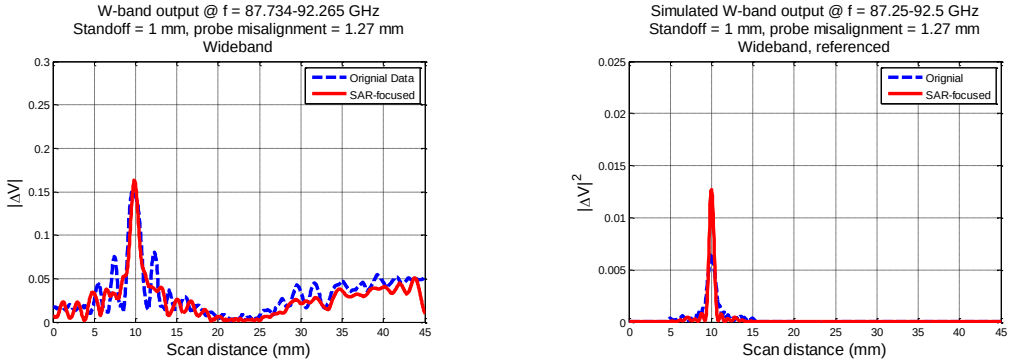

Figure 5.36. SAR-focused W-band results of 1.27 mm-long crack, as in measurement (left) and simulation (right), at standoff distance of 1 mm, and probe misalignment of +1.27 mm.

Similar observations can be made on results at 0.5 mm standoff distance provided in Appendix N.

Shown in Figures 5.37 through 5.40 are comparisons of data before and after SAR filter are applied to the measurement (Figures 5.37 and 5.38) and simulation results (Figures 5.39 and 5.40), at both standoff distances (0.5 and 1 mm). The signal levels presented in these figures are the peak values of the probe output signals when the probe is above the crack, in the region without fastener heads, and above the un-cracked fastener head.

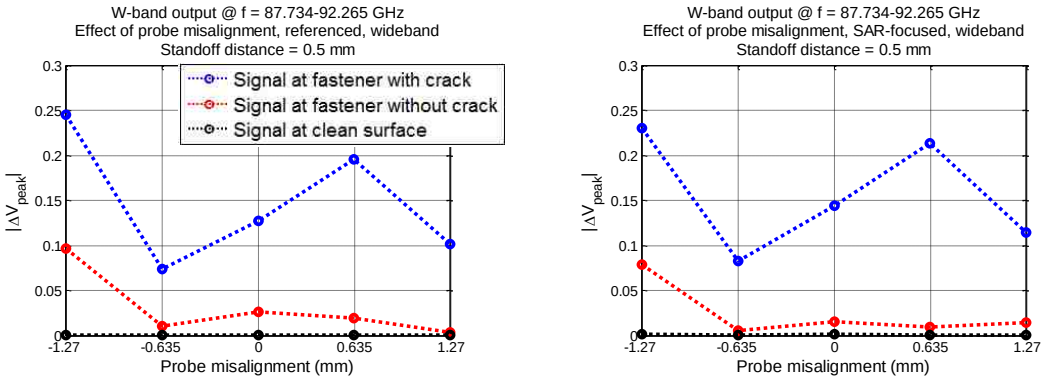

Figure 5.37. Comparison of measurement results with W-band differential probe, as in original (left) and SAR-focused (right), on effect of probe misalignment, at standoff distance of 0.5 mm.

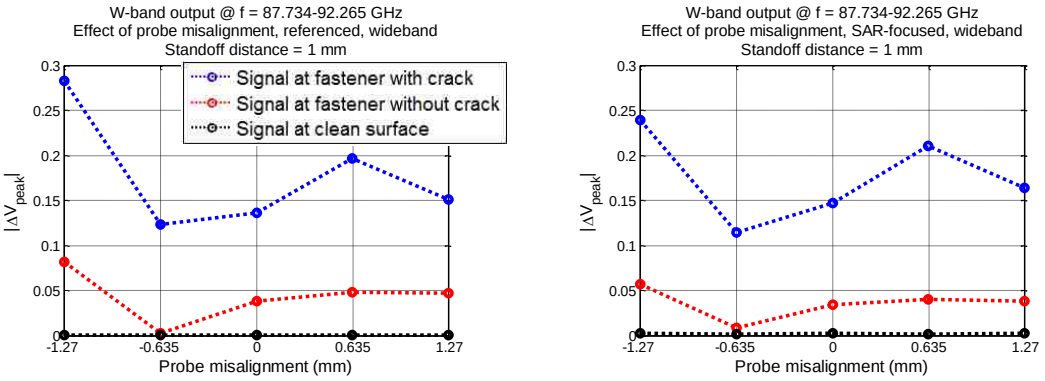

Figure 5.38. Comparison of measurement results with W-band differential probe, as in original (left) and SAR-focused (right), on effect of probe misalignment, at standoff distance of 1 mm.

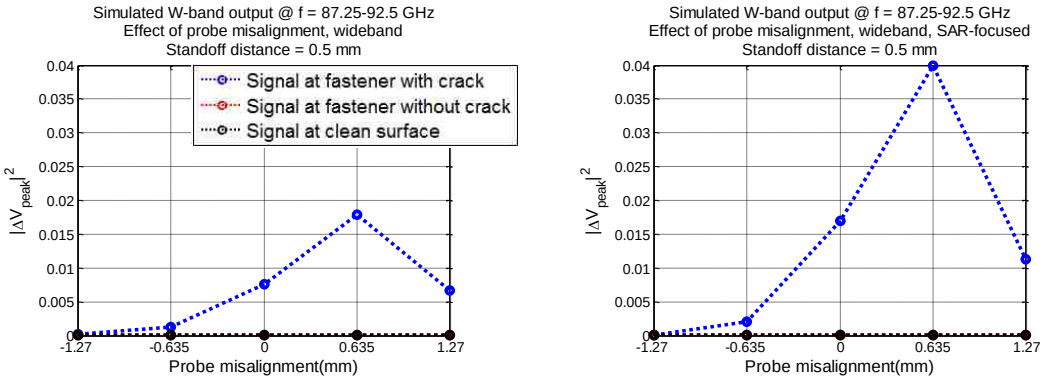

Figure 5.39. Comparison of simulation results with W-band differential probe, as in original (left) and SAR-focused (right), on effect of aperture offset, at standoff distance of 0.5 mm.

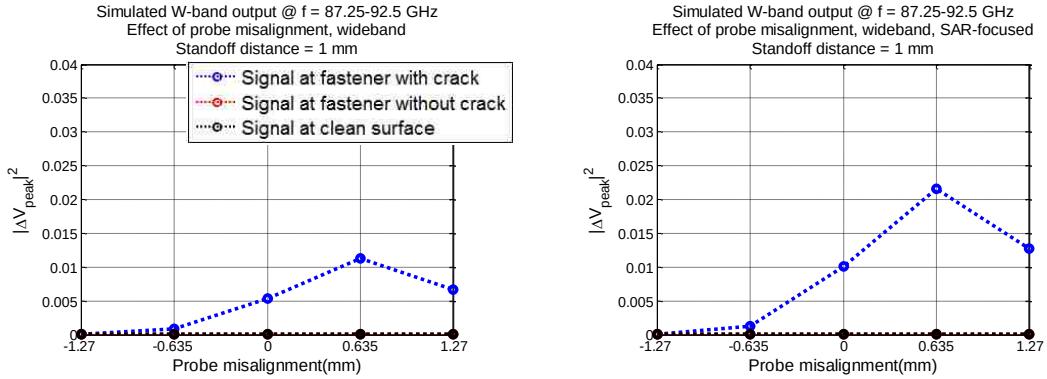

Figure 5.40. Comparison of simulation results with W-band differential probe, as in original (left) and SAR-focused (right), on effect of aperture offset, at standoff distance of 1 mm.

These figures also suggest that SAR contributes slightly towards enhancing the crack signals. The notable difference between the measurement and simulation results is the probe output signal when the probe is negatively misaligned by 1.27 mm, which is potentially the combination of the crack signals and the additional signal peaks.

To compare the outcome of SAR filter in both measurements and simulations, the normalized probe output signal levels versus probe misalignments are investigated. The normalized results provide a one-to-one comparison between the measured and simulated

data. To do this, the signals with respect to the different combination of probe misalignments and standoff distances are normalized to the largest (in magnitude) value among them. The results are presented in Figures 5.41 and 5.42, for standoff distances of 0.5 and 1 mm, respectively.

The normalized results suggest a similar pattern between the measurement and simulation results, except for the case of -1.27 mm of probe misalignment. Overall, the introduction of SAR filter contributes to enhance the crack signals, and at the same time reduce the magnitudes of the unwanted "sidelobe".

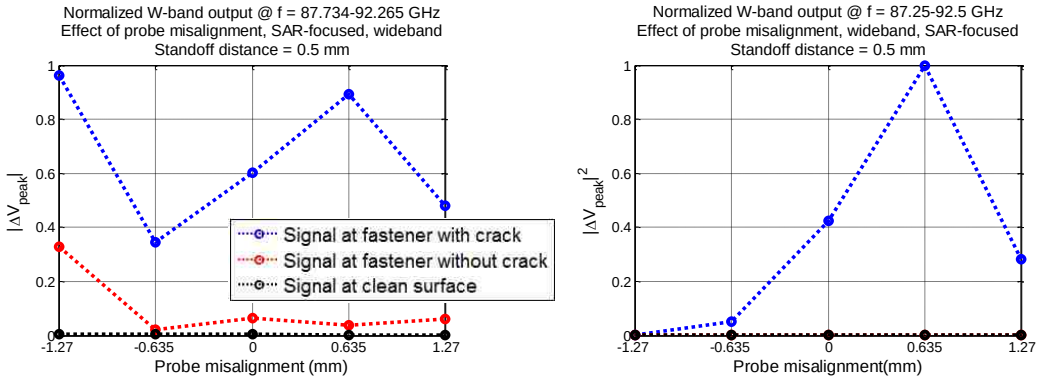

Figure 5.41. Normalized SAR-focused W-band results on effect of probe misalignment. Presented are measurement (left) and simulation results (right), at standoff distance of 0.5 mm.

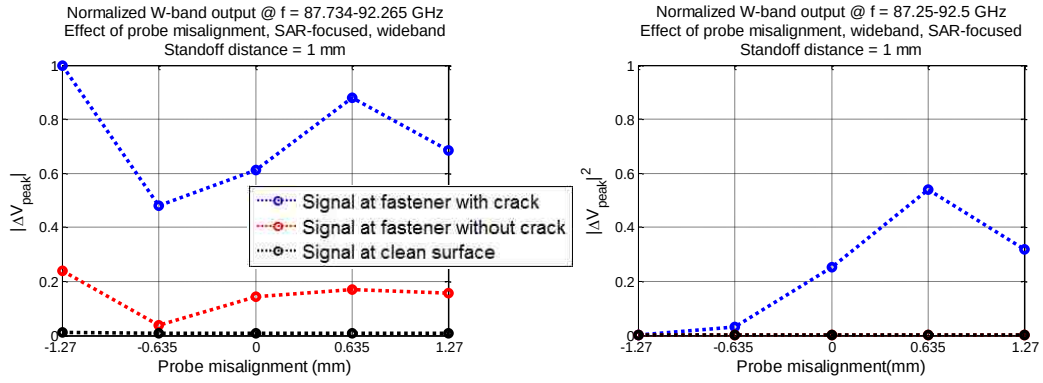

Figure 5.42. Normalized SAR-focused W-band results on effect of probe misalignment SAR-focused. Presented are measurement (left) and simulation results (right), at standoff distance of 1 mm.

5.5. EFFICACY OF SAR FILTER ON EFFECT OF PROBE OFFSET

SAR filter is applied to both the measured and simulated data (presented in Section 4.5) to investigate the effect of probe offset at W-band frequencies. Both data represent the scan results for a 1.27 mm-long crack, at the four common W-band frequencies (shown in Appendix G). A probe offset represents a rotation of the probe with respect to the fastener axis, which causes one aperture to see the fastener head either earlier or later than the other during a scan (Figure 3.59).

Figures 5.43 through 5.45 represent the comparison between SAR-focused measurement and simulation results at W-band frequencies with a standoff distance of 1 mm, and probe offsets of ±2 rotations (measurements)/ ±5° (simulations). The complete comparison results (standoff distance of 0.5 mm and other probe offsets) are provided in Appendix O.

Similar to the previous sections, these results also suggest that the SAR filter contributes to smoothing the probe output signal (lower "sidelobe" and weaker signals over the un-cracked fastener head) and producing enhanced crack signals in both measurements and simulations.

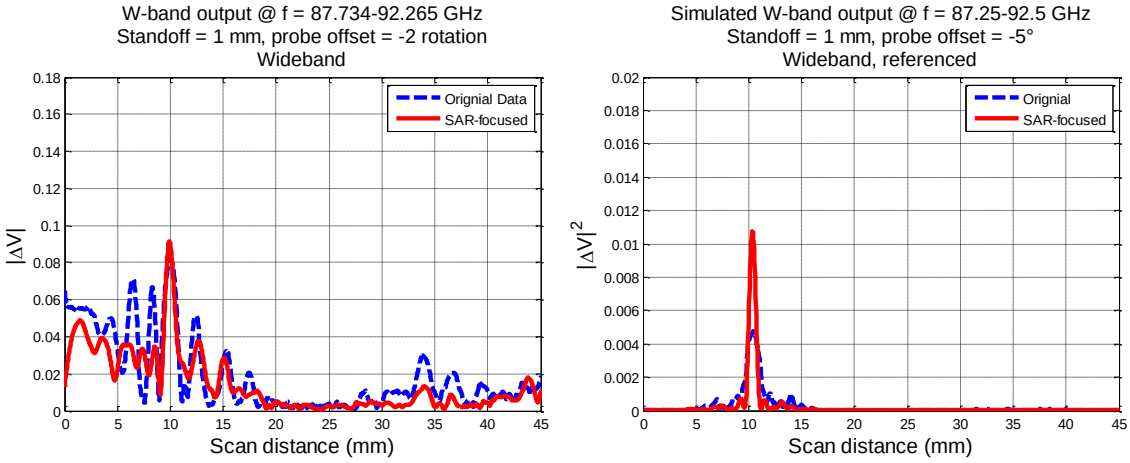

Figure 5.43. SAR-focused W-band results of 1.27 mm-long crack, as in measurement (left) and simulation (right), at standoff distance of 1 mm, and probe offset of -2 rotations (measurements) and -5˚ (simulations).

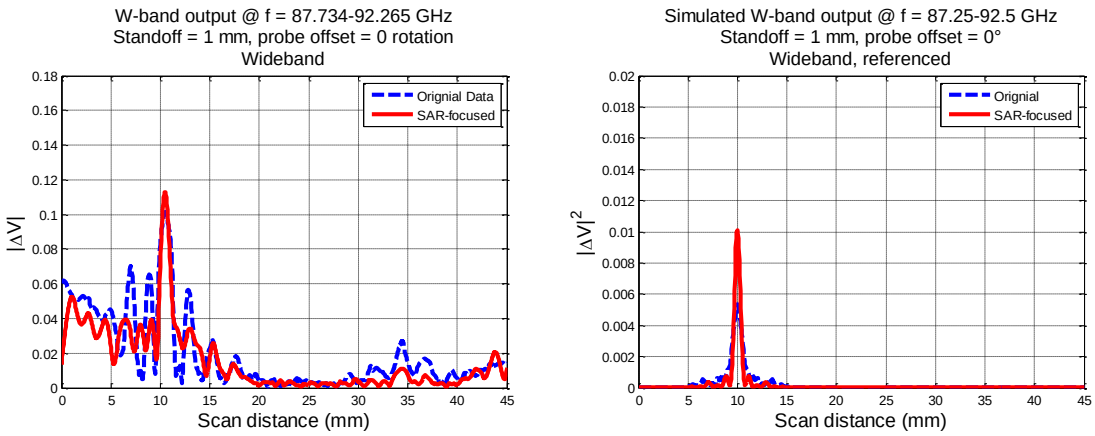

Figure 5.44. SAR-focused W-band results of 1.27 mm-long crack, as in measurement (left) and simulation (right), at standoff distance of 1 mm, and no probe offset.

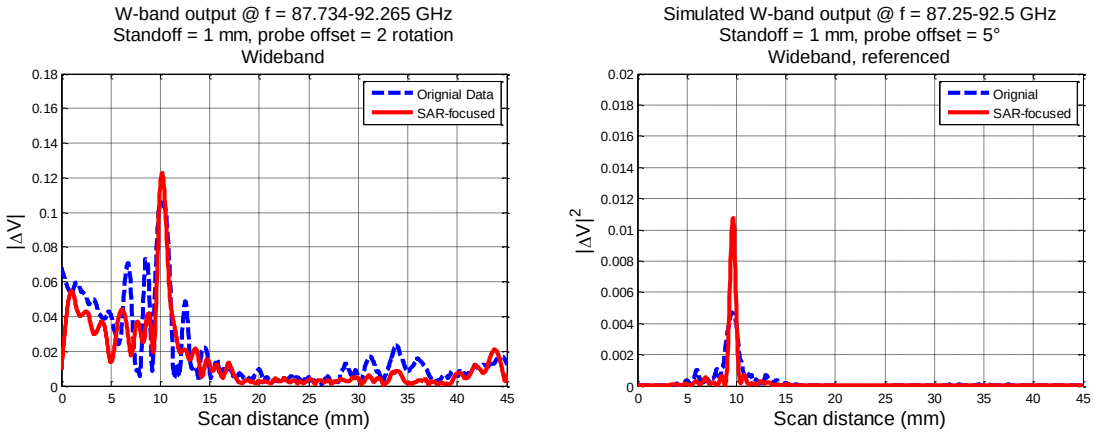

Figure 5.45. SAR-focused W-band results of 1.27 mm-long crack, as in measurement (left) and simulation (right), at standoff distance of 1 mm, and probe offset of +2 rotations (measurements) and +5˚ (simulations).

In the previous sections, probe offsets are determined to have insignificant effect on the W-band probe output. The only consequence is the location shift of the peak signal, as the relative location of the crack with respect to the probe changes. Therefore, the resulting outputs with different probe offsets are similar, as well as the corresponding SAR-focused results. Similar observations can be made on results at 0.5 mm standoff distance provided in Appendix O.

Shown in Figures 5.46 through 5.49 are comparisons of data before and after SAR filter are applied to the measurement (Figures 5.46 and 5.47) and simulation results (Figures 5.48 and 5.49), at both standoff distances (0.5 and 1 mm). The signal levels presented in these figures are the peak values of the probe output signals when the probe is above the crack, in the region without fastener heads, and above the un-cracked fastener head.

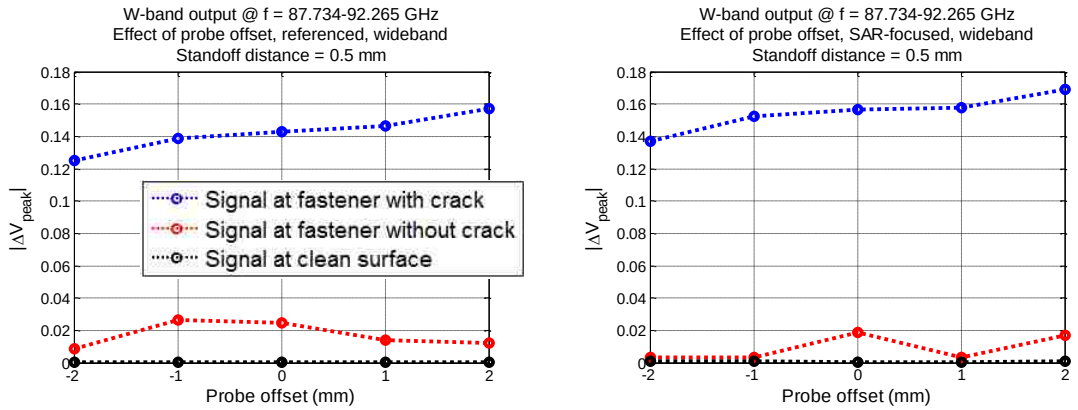

Figure 5.46. Comparison of measurement results with W-band differential probe, as in original (left) and SAR-focused (right), on effect of probe offset, at standoff distance of 0.5 mm.

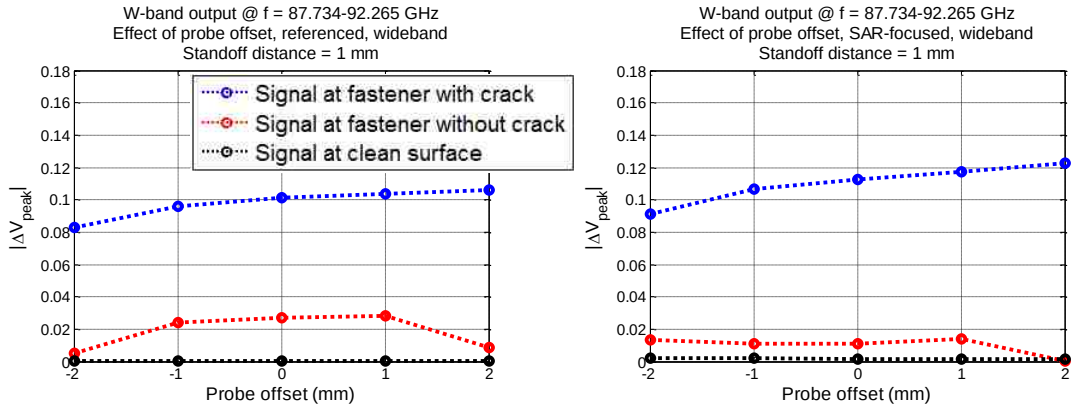

Figure 5.47. Comparison of measurement results with W-band differential probe, as in original (left) and SAR-focused (right), on effect of probe offset, at standoff distance of 1 mm.

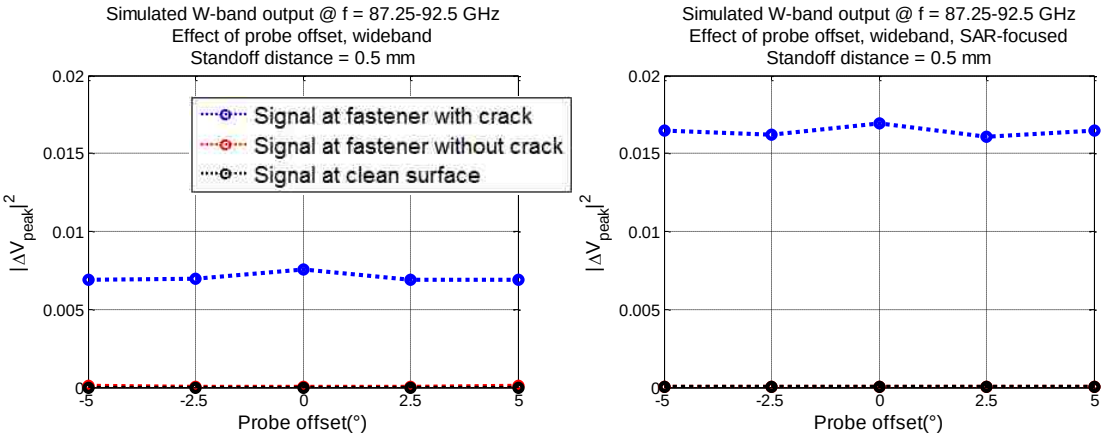

Figure 5.48. Comparison of simulation results with W-band differential probe, as in original (left) and SAR-focused (right), on effect of probe offset, at standoff distance of 0.5 mm.

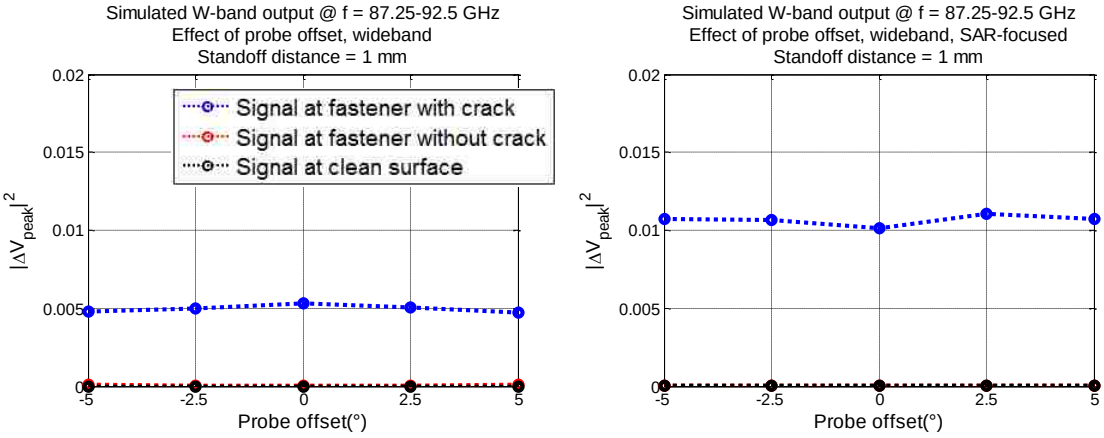

Figure 5.49. Comparison of simulation results with W-band differential probe, as in original (left) and SAR-focused (right), on effect of probe offset, at standoff distance of 1 mm.

These figures also suggest that the introduction of SAR contributes to enhancing the crack signals, while reducing the magnitude of unwanted "sidelobe" and probe output signals above the un-cracked fastener head, which are likely the results of imperfect scan setup.

To compare the outcome of SAR filter in both measurements and simulations, the normalized probe output signal levels versus probe offsets are investigated. The normalized results provide a one-to-one comparison between the measured and simulated data. To do this, the signals with respect to the different combination of probe offsets and standoff distances are normalized to the largest (in magnitude) value among them. The results are presented in Figures 5.50 and 5.51, for standoff distances of 0.5 and 1 mm, respectively.

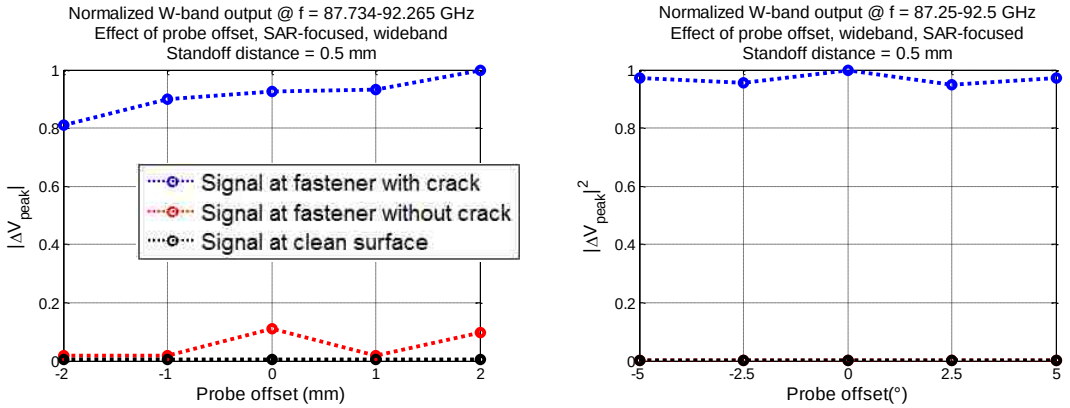

Figure 5.50. Normalized SAR-focused W-band results on effect of probe. Presented are measurement (left) and simulation results (right), at standoff distance of 0.5 mm.

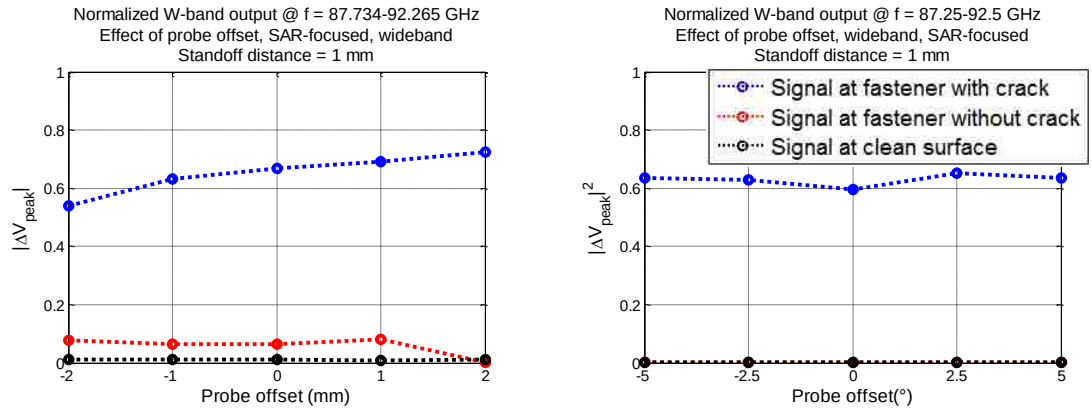

Figure 5.51. Normalized SAR-focused W-band results on effect of probe offset. Presented are measurement (left) and simulation results (right), at standoff distance of 1 mm.

The normalized results demonstrate a very similar trend between the measurement and simulation results, including the signal reduction (in magnitude) as a result of increasing standoff distance. Overall, the occurrence of a probe offset does not affect the ability of SAR on enhancing the probe output signals.

5.6. SUMMARY

In summary, the SAR filter implementation, for the most part, enhances the crack detections, but the enhancements could be limited with a more complex structure (e.g., paint layer) or signal response (e.g., combined scattered signals from both the fastener head and the crack result in sidelobe). The precise alignments between the probe and the SUT, as well as the conditions of the SUT (e.g. flatness) are also critical for the implementation of SAR filter, as observed from these results. For instance, since SAR filter requires a precise figure of the distance between the probe and the SUT, a non-flat surface will cause the standoff distance to vary throughout the scan, effectively reduce the capability of SAR filter.

It is also known that SAR filter is more generally used for measurements at higher standoff distance (far-field region), which is one of the reasons the V-band results have less of enhancements than W-band results after SAR filter is applied. But for the W-band measurements, since only the standoff distances of up to 1 mm are considered thus far, along with other limiting conditions (e.g., limited bandwidth), the results may not represent the true benefits of SAR filter on this application. Further investigations at higher standoff distance or source covering a wider range of frequency are desired to fully study the efficacy of SAR filter for this purpose, if needed.

6. EFFECT OF NON-UNIFORM PAINT ON W-BAND DIFFERENTIAL PROBE OUTPUT SIGNALS

In the earlier sections, it was observed (from measurements) that the presence of a non-uniform paint (often in the shape of a paint clump) can affect the probe output signals on fastener head crack scanning. This section presents the investigation (based on simulations only) on whether the presence of paint clumps (with various dimensions and at different locations) will create a distortion on crack signals or a false indication of cracks, as these effects are commonly observed in Section 4.3.

In this section, two simulation models with non-uniform paint are considered. The first model simulates the case when the excess paint forms a paint clump over the initiated crack (Figure 6.1), and the second model simulates when a paint clump is on the opposite side of the crack on the fastener head (Figure 6.2). Both simulation models consist of a uniform paint layer with a thickness of ~0.08 mm (0.003", not shown in both figures for a clearer view of paint clump locations with respect to fastener head and crack) and a paint clump with a fixed height (0.1 mm) and various radii. The reason for choosing the thin layer of paint in this investigation is it reflects more closely to what currently applies on real-world aircraft, as a thinner paint layer can reduce both the cost and weight of an aircraft [38].

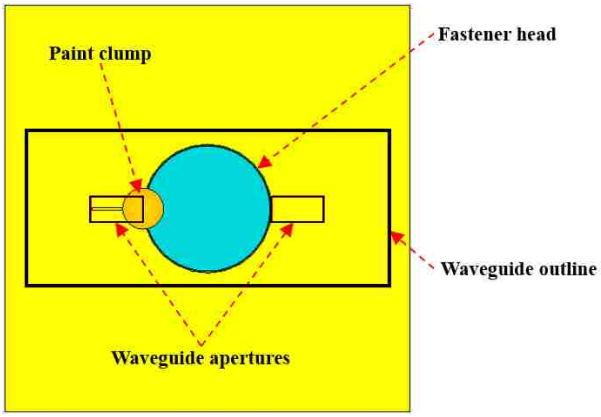

Figure 6.1. Simulation model showing the case when a paint clump forms over the initialized crack. Shown in the figure is a paint clump with a height of 0.1 mm and a radius of 1 mm.

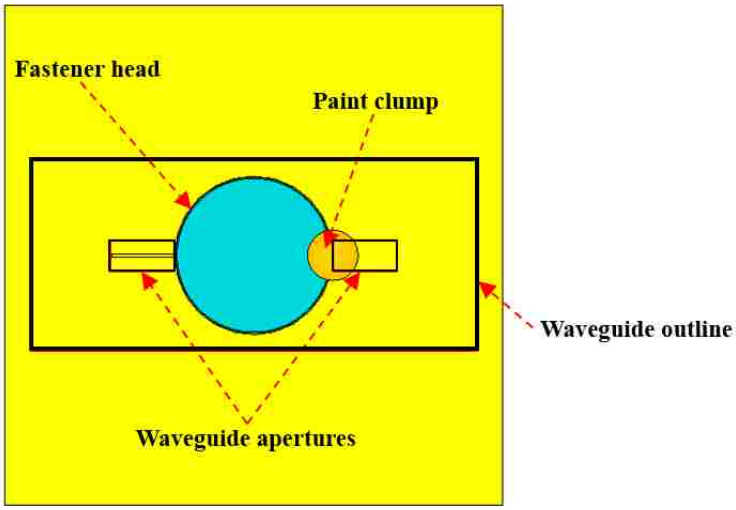

Figure 6.2. Simulation model showing the case when a paint clump forms on the opposite side of the crack on the fastener head. Shown in the figure is a paint clump with a height of 0.1 mm and a radius of 1 mm.

In the simulations, standoff distances of 0.5 and 1 mm were considered, along with crack lengths varying from 0 to 2.54 mm (0, 0.635, 1.27, 1.905, 2.54 mm). Twenty-one different frequencies equally spaced within the 75 – 110 GHz range for W-band probe were used in the simulations. The paint clump (illustrated in Figure 6.3) is in a shape of a hemisphere and have radii vary between 0 to 2 mm (and a fixed height of 0.1 mm). The paint clump in the simulation partially covers both the crack and the fastener head.

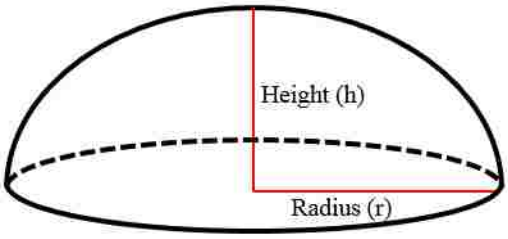

Figure 6.3. Schematic of a paint clump.

The investigation of the effect of paint clumps over the crack on W-band differential probe output signals is presented in Section 6.1, while the investigation of a paint clump on the opposite side of the crack on the fastener head is presented in Section 6.2.

6.1. EFFECT OF NON-UNIFORM PAINT ACCUMULATED OVER THE INITIALIZED CRACK

In the previous section, it was stated that the presence of paint acts as a dielectric layer between the probe and sample surface, increasing the electrical distance in between and making the cracks appearing electrically larger. The paint layer also causes additional internal reflections between itself and sample surface, making the signal behavior less straightforward to predict. Similar effects will take place with the presence of a paint clump, in addition, the internal reflections become more complex due to the non-flat boundaries.

6.1.1. Single-Frequency Response. Selected single-frequency results at a fixed standoff distance of 1 mm, and paint clump radii of 0, 1, and 2 mm are shown in Figures 6.4 through 6.6. The complete results (standoff distance of 0.5 mm and other paint clump radii) are provided in Appendix P.

Initially, cracks of different lengths can resonate at specific frequencies, for instance, the 1.905 mm-long crack resonates (have a relatively stronger signal response) at 75 GHz, and it was because that this specific crack length is approximately equal to the half-wavelength of this frequency (~2 mm). The 1.27 mm-long crack also resonates at 110 GHz (with half-wavelength of ~1.36 mm). Figures 6.4 through 6.6 suggest these resonances are affected by the presence of a paint clump, as a result of signal attenuation through the paint clump (with additional traveling distance of the signal and the internal reflections within the non-flat boundaries). In addition, cracks can be either fully- or partially covered by the paint clump, complexing the resonance properties of cracks.

The results for 0.5 mm standoff distance from Appendix P also show similar observations. To further understand the effect of non-uniform paint accumulated above the initialized crack, the wideband probe responses are also investigated.

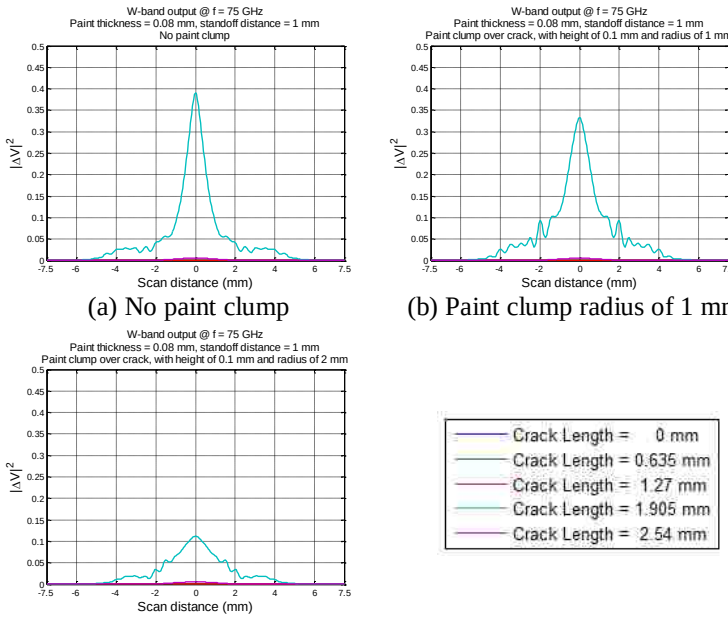

(a) No paint clump (b) Paint clump radius of 1 mm

(c) Paint clump radius of 2 mm

Figure 6.4. Simulated W-band differential probe output signals with various crack lengths, at a standoff distance of 1 mm, frequency of 75 GHz, and paint clump (located over crack) radii of (from (a) to (c)): 0, 1 and 2 mm.

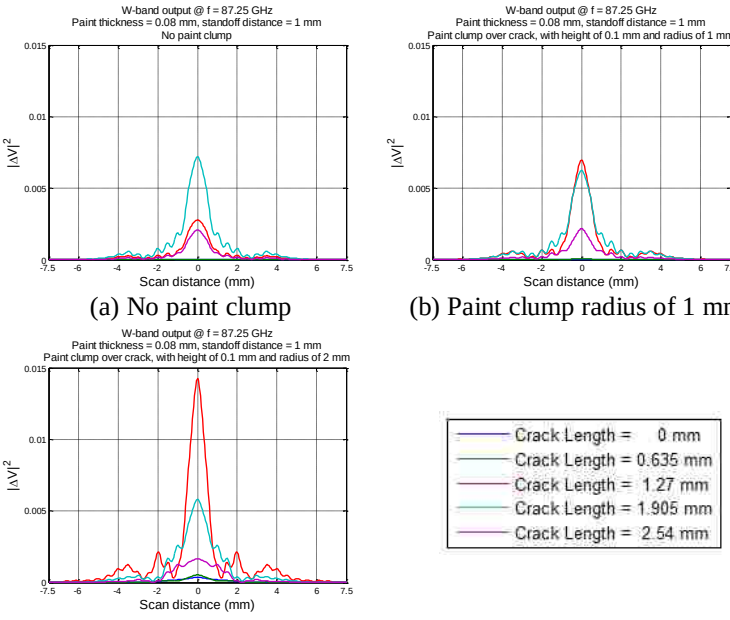

(a) No paint clump (b) Paint clump radius of 1 mm

(c) Paint clump radius of 2 mm

Figure 6.5. Simulated W-band differential probe output signals with various crack lengths, at a standoff distance of 1 mm, frequency of 87.25 GHz, and paint clump (located over crack) radii of (from (a) to (c)): 0, 1 and 2 mm.

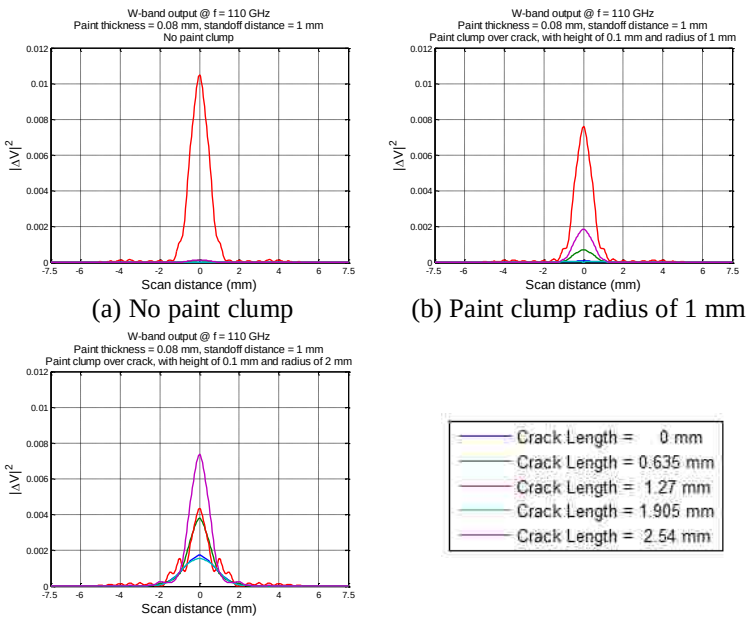

(a) No paint clump

(b) Paint clump radius of 1 mm

(c) Paint clump radius of 2 mm

Figure 6.6. Simulated W-band differential probe output signals with various crack lengths, at a standoff distance of 1 mm, frequency of 110 GHz, and paint clump (located over crack) radii of (from (a) to (c)): 0, 1 and 2 mm.

6.1.2. Wideband Response. The wideband responses of the W-band probe on fastener head crack scanning with 1 mm standoff distance and paint clump radii of 0, 1 and 2 mm are shown in Figure 6.7. The purpose of summing up all the single-frequency responses (total of twenty-one frequency points) across the bandwidth is that the frequency dependency of the probe output can be averaged (e.g., the 1.905 mm-long crack has a strong resonance at 75 GHz, but the resonance decreases across the bandwidth), and it also provides a clearer view on the applicability of W-band frequencies for fastener head crack detection, as previously mentioned.

The wideband results show that within the entire bandwidth of W-band, the resonances produced by the 1.905 mm-long crack decrease as the paint clump becomes larger, while for the cracks of other lengths, the detection signals are almost unaffected. However, no clear pattern of the correlations (besides the decreasing trend) between crack resonances and paint clump dimensions can be observed from the results,

additional simulations may be desired to fully study the effect of non-uniform paint, if needed.

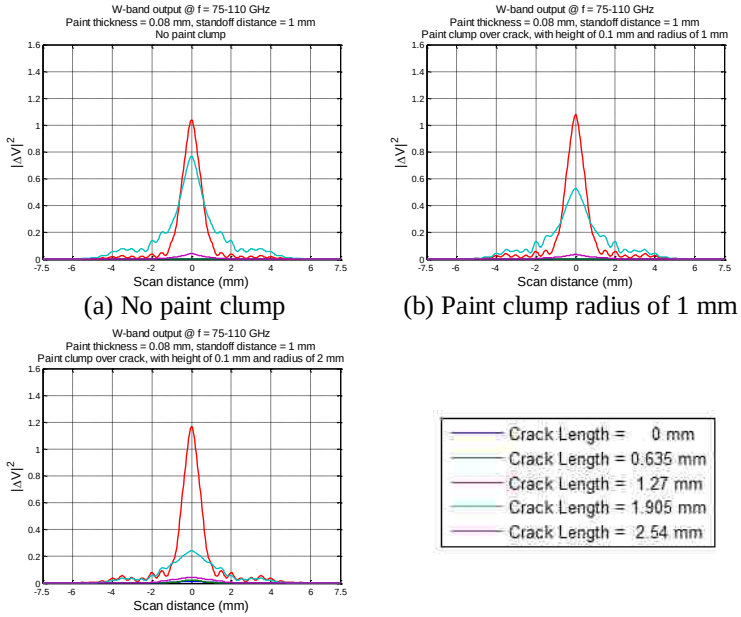

(a) No paint clump (b) Paint clump radius of 1 mm

(c) Paint clump radius of 2 mm

Figure 6.7. Simulated W-band wideband differential probe output signals with various crack lengths, at a standoff distance of 1 mm, and paint clump (located over crack) radii of (from (a) to (c)): 0, 1 and 2 mm.

Figures 6.8 and 6.9 summarize the effect of non-uniform paint on the W-band wideband differential probe crack output signal level, at standoff distances of 0.5 and 1 mm, respectively. The non-uniform paint here is in form of a paint clump and located over the initialized crack (Figure 6.1). The signal levels in these figures represent the crack responses when the probe is directly above the cracks. Both figures suggest that the presence of a paint clump over the initialized crack does not significantly influence the capabilities of W-band differential probe on fastener head crack scanning. Although the crack output signal levels of the 1.905 mm-long crack reduce with respect to increase in paint clump dimensions, the detection signals are still dominating as opposed to when there is no crack.

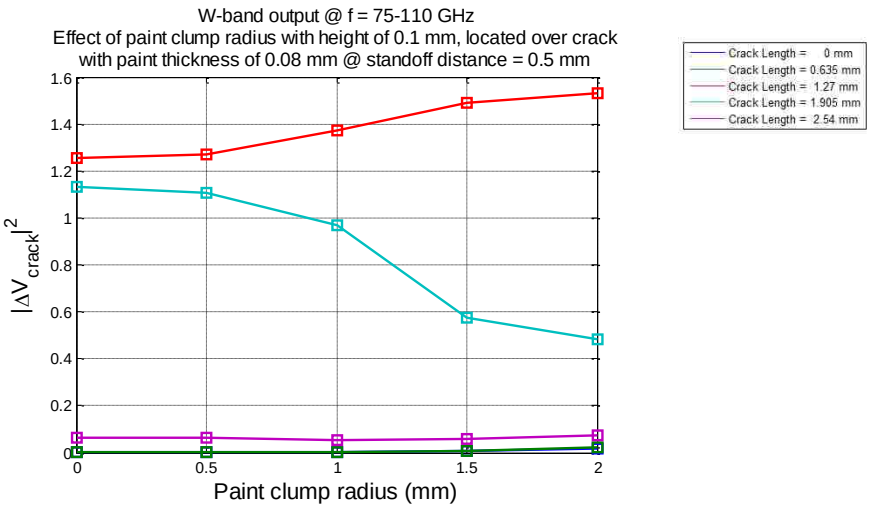

Figure 6.8. Effect of paint clump (located over crack) on the W-band wideband differential probe crack output signal level, at standoff distance of 0.5 mm.

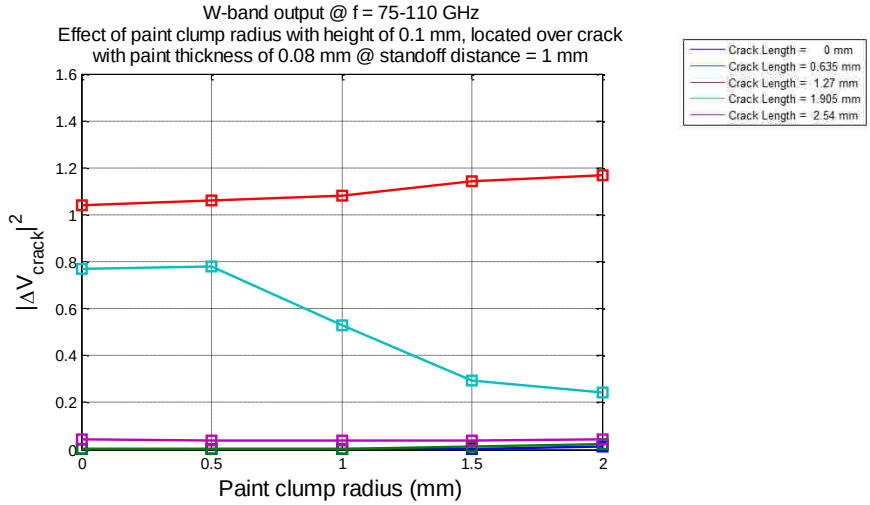

Figure 6.9. Effect of paint clump (located over crack) on the W-band wideband differential probe crack output signal level, at standoff distance of 1 mm.

However, the output signal levels of the un-cracked case are almost as strong as the crack output signal levels of the 0.635 mm-long crack. Therefore, a paint clump over the initialized crack can potentially result in a false indication suggesting that a small

crack exists, although in measurements, such small signals may be masked by system noises.

6.2. EFFECT OF NON-UNIFORM PAINT ACCUMULATED ON THE OPPOSITE SIDE OF CRACK ON THE FASTENER HEAD

An investigation similar to the one of Section 6.1 is presented here, but in this section, the paint clump is located on the opposite side of the crack on the fastener head (Figure 6.2). Paint clumps of this nature are also expected to affect the probe output signals such as causing a false indication of cracks.

6.2.1. Single-Frequency Response. Selected single-frequency results at a fixed standoff distance of 1 mm, and paint clump radii of 0, 1, and 2 mm are shown in Figures 6.10 through 6.12. The complete results (standoff distance of 0.5 mm and other paint clump radii) are provided in Appendix P.

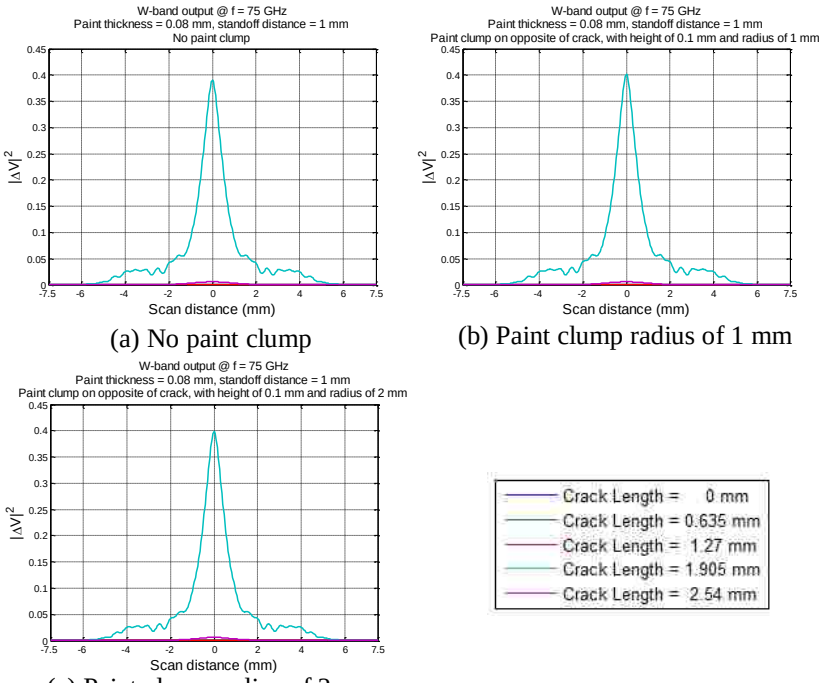

(a) No paint clump

(b) Paint clump radius of 1 mm

(c) Paint clump radius of 2 mm

Figure 6.10. Simulated W-band differential probe output signals with various crack lengths, at a standoff distance of 1 mm, frequency of 75 GHz, and paint clump (located on opposite side of fastener head) radii of (from (a) to (c)): 0, 1 and 2 mm.

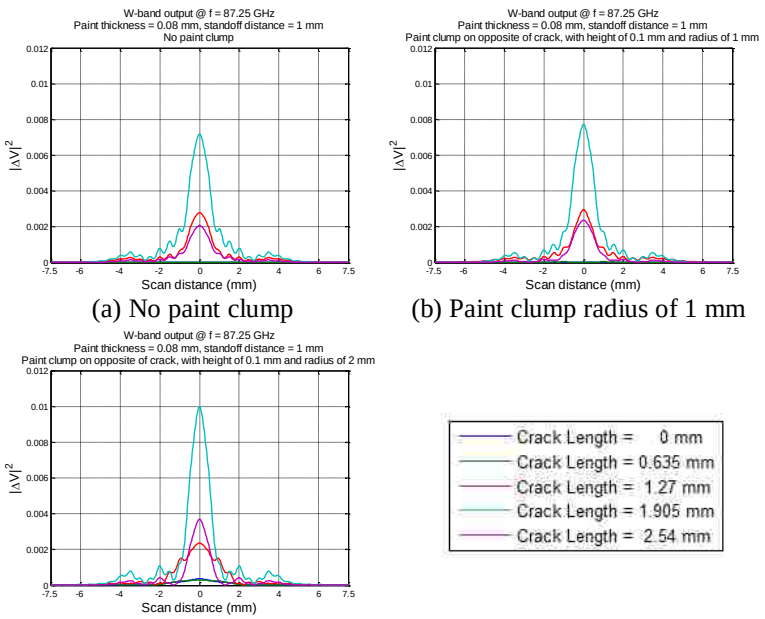

(a) No paint clump (b) Paint clump radius of 1 mm

(c) Paint clump radius of 2 mm

Figure 6.11. Simulated W-band differential probe output signals with various crack lengths, at a standoff distance of 1 mm, frequency of 87.25 GHz, and paint clump (located on opposite side of fastener head) radii of (from (a) to (c)): 0, 1 and 2 mm.

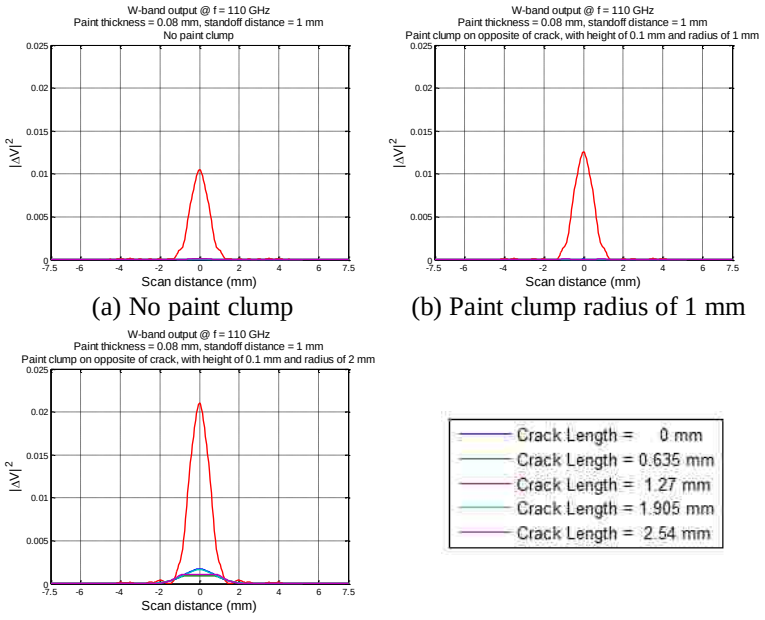

(a) No paint clump (b) Paint clump radius of 1 mm

(c) Paint clump radius of 2 mm

Figure 6.12. Simulated W-band differential probe output signals with various crack lengths, at a standoff distance of 1 mm, frequency of 110 GHz, and paint clump (located on opposite side of fastener head) radii of (from (a) to (c)): 0, 1 and 2 mm.

These single-frequency results suggest that the probe output signals are almost unaffected by the presence of paint clump (regardless of its dimensions). Similar to Section 6.1, the paint clump only produces a clear false indication that is comparable to crack signals from the 0.635 mm-long crack, but is well surpassed by crack signals from other cracks. It is also noticed that the crack signals are instead enhanced in many cases. This is most likely the result of a reduction in the magnitude of scattered signals (due to increasing overall paint thickness and complex internal reflections that contribute to signal attenuation) received by the probe aperture, effectively enhance the differential signals. The results for 0.5 mm standoff distance from Appendix P also show similar observations. To further understand the effect of non-uniform paint accumulated on the opposite of the crack, the wideband probe responses are also investigated.

6.2.2. Wideband Response. Shown in Figure 6.13 are the wideband responses of the W-band probe on fastener head crack scanning with 1 mm standoff distance and paint clump radii of 0, 1 and 2 mm.

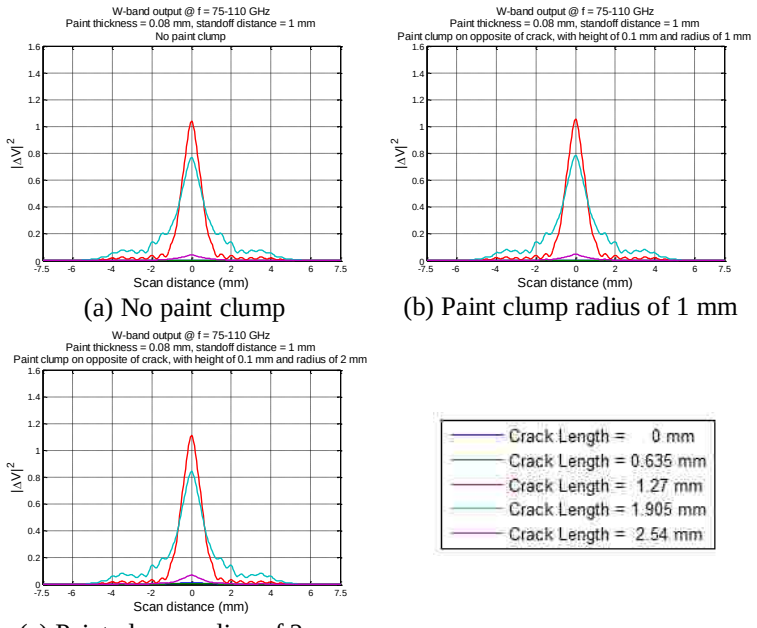

Figure 6.13. Simulated W-band wideband differential probe output signals with various crack lengths, at a standoff distance of 1 mm, and paint clump (located on opposite side of crack) radii of (from (a) to (c)): 0, 1 and 2 mm.

Similar to the single-frequency results, the paint clump over on the opposite side of the fastener head does not significantly affect the overall capabilities of W-band differential probe on fastener head scanning, and while the crack output signals are nearly unaffected, they are slightly enhanced for reasons previously mentioned.

Figures 6.14 and 6.15 summarize the effect of non-uniform paint on the W-band wideband differential probe crack output signal level, at standoff distances of 0.5 and 1 mm, respectively. The non-uniform paint here is in form of a paint clump and located on the opposite of the fastener head and crack (Figure 6.2). The signal levels in these figures represent the crack responses when the probe is directly above the cracks.

Both figures verify the observations from the previous results (single-frequency and wideband responses), that the presence of a paint clump does not result in a strong probe output signals that are enough to be recognized as a detection of a larger crack, and the detection signals from larger cracks (with length greater than 0.635 mm) are almost unaffected. The results suggest that if such paint clump exists on a measurement setup, its effect may be small or negligible.

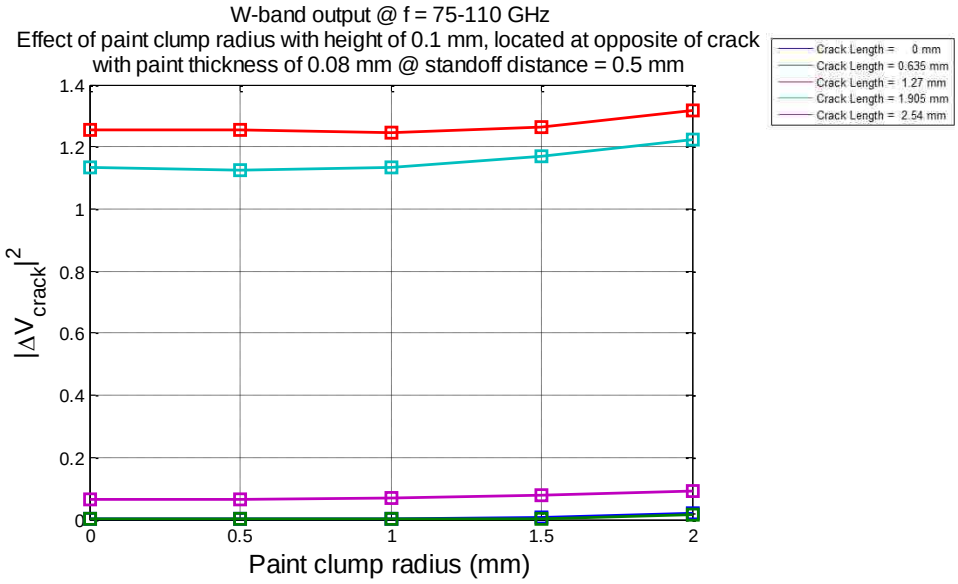

Figure 6.14. Effect of paint clump (located on opposite side of fastener head) on the W-band wideband differential probe crack output signal level, at standoff distance of 0.5 mm.

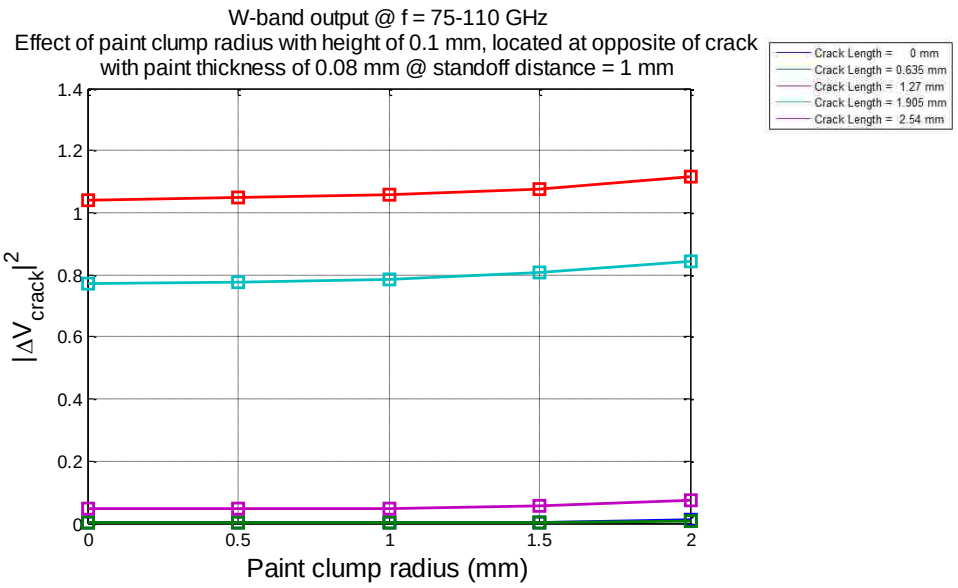

Figure 6.15. Effect of paint clump (located on opposite side of fastener head) on the W-band wideband differential probe crack output signal level, at standoff distance of 1 mm.

6.3. SUMMARY

This section presented the investigation on whether a paint clump formed by the excess paint on aircraft skin can affect the capabilities of W-band probe on detecting cracks. Two scenarios were considered in this section: the first was a paint clump partially or fully covering the crack, and the second was a paint clump on the other side of the crack. The results from both cases suggest that a paint clump does not significantly affect the crack detection capabilities at W-band, but some effects are still worth noting. For instance, a paint clump can result in probe output signal (at when there is no crack) that is comparable to signals produced by shorter cracks (e.g., 0.635 mm). Therefore, for fastener head measurements that are conducted on a paint-covered skin, it may be difficult to determine whether a small probe output signal is the result of a small crack (~0.635 mm long) or the consequence of non-uniform paint.

The simulation results presented in this section assume the paint clumps had a uniform shape (forming a hemisphere). But in reality, the clump may take on other shapes, and therefore additional simulations that are better representations of non-uniform paint clump shapes may be worth investigating, and post-processing on the data

(to distinguish the difference between probe output signals from small cracks and a paint clump) may become useful to fully understand the effect of non-uniform paint, if needed. It should also be mentioned that a paint clump with a radius of 2 mm is in general visible to naked eyes. Therefore, under the circumstances knowing that a paint clump (if exists) will likely not exceed certain dimensions, the effect of non-uniform paint may not be so critical.

7. CONCLUSION/FUTURE WORK

7.1. SUMMARY/CONCLUSION

In this thesis, a wideband millimeter-wave differential probe have been investigated as potential technique for crack detection on riveted structure. In Section 1, an overview of differential probe theory and design principles was provided. The design process, as well as the performance analysis of a W-band differential probe are provided in Section 2. The designed differential probe fulfills the design requirements and was employed for measurements of various kinds.

In Section 3, simulations were conducted to evaluate the effect of misalignments (of the differential probe) on the probe output signals, considerations are such as standoff distance, aperture offset, fastener head tilt, probe misalignment and probe offset. In addition, paint covering the SUT was also considered. Each of these considerations contribute to affecting the differential probe output signals in a different manner, such as creating a potential false indication of crack or distortion of the actual crack signal. In the section, both W-band and V-band frequencies are simulated to be suitable for crack detection on fastener heads. In addition, both frequency bands demonstrate the tendency to cause cracks of lengths approximately equal to the half-wavelengths to resonate (resulting in a relatively stronger probe output signals). However, as later observed from the measurements, the signal variations around the actual crack signals in the V-band results are much stronger than ones of W-band measurements due to the longer wavelengths of V-band frequencies (potentially enlarging the effect of misalignments), making W-band frequencies a more viable candidate on this application. In Section 3.1, simulations were conducted to investigate the effect of standoff distance on differential probe output signals, and it was observed that the probe output signals reduce with respect to increase in the standoff distance. But at the same time, a higher standoff distance can be intentionally applied to reduce the unwanted effects caused by other kinds of misalignments, as observed from other sections. In Section 3.2, a similar investigation was conducted with respect to aperture offset on the probe. An aperture offset was found to create a DC bias due to the unequal standoff distances between the two probe apertures, but the effect was not significant as it can be minimized through

post-processing on the probe output signals. In Section 3.3, the effect of fastener head tilt was studied. It was observed that a tilt in the fastener head significantly influence the probe output signals only if the edge of the fastener head is tilted to be below the crack, resulting in a probe that is more sensitive to the fastener head edges than to the crack, and potential false indications of cracks. In Section 3.4, an investigation on how paint materials interfere with the probe output signals was conducted. It was observed that a layer of paint introduces uncertainties to the probe output signals, not only the paint may not be uniformly spread onto the surface (creating variable standoff distance), but also the behaviors of the electric field near the aperture and the paint around it becomes difficult to predict. It was observed that the probe output signals were affected less only with a thin layer of paint. Future experiments may be conducted to fully understand the effect of paint on fastener head crack detection, if needed. In Section 3.5, the effect of a probe misalignment (shift) was investigated, and the results suggested that if the probe shifts towards the crack, the imperfectly canceled scattered signals from the fastener head is sufficiently strong that it may mask out the scattered signals from the crack, but not when the probe shifts away from the crack. Finally, in Section 3.6, the effect of rotation on the probe (probe offset) was investigated. From the results, it was concluded that a probe offset does not significantly interfere with the probe output signals, instead, a potential false information on the crack location may be given. These sections suggest that the W-band differential probe is suitable for fastener head crack detection under proper alignments.

In Section 4, the designed W-band probe, as well as the V-band probe were [29] used for measurements to verify the observations from Section 3. The measurements were conducted on the test panel, on which there are fastener heads with diameters of 6.35 mm and 1.27 mm-long cracks to the sides. Section 4 provides a one-to-one comparison between the measurement and simulation results on scanning such a crack. Most of the measurement results are in good agreements with the simulation results, except for some cases where the measurement uncertainties (e.g., non-uniform paint thickness, non-flat surface, etc.) cannot be avoided. In addition, when the probe misalignment of -1.27 mm is applied (the scattered signals from the crack are likely not captured in full, e.g., Figure 3.56), a strong signal (the combination of the actual crack

signals and the additional signal peaks due to the presence of the misalignment) is registered on the probe, resulting in a potential false indication. In the measurements, the most common non-ideal observations on the probe output signals were the presences of “sidelobe" either near the actual crack signals or over the un-cracked fastener head, providing false information about the presence or location of a crack. The "sidelobe" is the consequence of an imperfect measurement setup, for instance, the fastener head may not be completely aligned with the probe or the unequal standoff distance between the two probe apertures along the scan path as a result of uneven surfaces. In that case, the imperfectly canceled scattered signals from the fastener head interfere with the overall probe output signals.

In Section 5, synthetic aperture processing was applied to investigate the efficacy of applying such signal processing technique on enhancing the crack detections (by reducing the occurrence or significance of "sidelobe"). In this investigation, SAR acts as a filter that contributes to compensating for the standoff distance by coherently summing the wideband signals, which effectively focus the energy to the correct distance away from the probe aperture. It was observed from this investigation that SAR filter, for the most part, contributes to enhancing the crack detections, but the enhancements are limited with a more complex structure (e.g., non-uniform paint) or signal response (e.g., the "sidelobe"). In addition, SAR filter requires a precise figure of the distance between the probe and the SUT, and a non-flat surface (which will cause the standoff distance to vary throughout the scan) can effectively reduce the capability of SAR filter. Finally, SAR filter is more generally applied for measurements at higher standoff distance, but for the measurements, since only the standoff distances of up to 1 mm are considered, the results may not represent the true benefits of SAR filter on this application.

Lastly, in Section 6, an investigation was conducted to determine whether the presence of paint clumps (a type of non-uniform paint) will affect the overall probe output signals. In the section, two cases were evaluated. The first was a paint clump accumulated over the initialized crack (either partially or fully covering the crack, if present), and the second was a paint clump accumulated on the opposite side of the fastener head. Assuming that the paint layers are generally thin [38], the investigation showed that regardless of its location, and if the paint clump is not too large in

dimensions (e.g., a radius of 2 mm), the presence of a paint clump does not significantly affect the crack detection capabilities at W-band. But paint clumps of this size could be detected visually and removed before the inspection takes place, leaving the effect of paint clumps at the minimum.

7.2. FUTURE WORK

As a result of this investigation, the W-band differential probe have been shown to have great potential for crack detection on riveted structures. As such, in order to continue the development of this technique, the following future works are suggested:

- Throughout the investigations, it was often observed that an unintentional error in probe positioning can sometimes lead to a change ("sidelobe") in the probe responses. In the investigation, SAR filter was applied to reduce the effect of these unwanted signals, but the enhancements were limited with a complex structure or stronger "sidelobe". Therefore, another post-processing technique may be considered to achieve the same goal. The wavelet transform is an applicable candidate.
- It was observed from the investigations that at millimeter-wave frequencies, cracks of lengths that are approximately equal to the half-wavelengths (of the operating frequencies) result in a relative stronger probe output signals (resonance). However, since only a crack sample of 1.27 mm-long was provided, this observation cannot be verified experimentally. Measurements on cracks of other dimensions may be desired to fully understand the relationship between the frequency of operations and resonance properties of cracks.
- If the assumption stated above is true, it may be desired to obtain a wideband source which covers a wider range of frequency for inspection purposes. In this investigation, the V-band source covers frequencies from 68.8 – 71.3 GHz, and the W-band source covers frequencies from ~87.7 – ~92.3 GHz. Both sources can be considered limited in the available bandwidth, causing cracks of only few lengths to resonate. For instance, if the assumption is true, the 1.27 mm-long crack provided will result in the strongest probe output

signals at a frequency of operation around 118 GHz. In addition, the V-band and W-band sources will likely cause cracks of lengths around 2.15 mm and 1.67 mm to resonate, respectively. Although these sources can still be used to detect cracks of other lengths (as demonstrated in this investigation), a source with a wider bandwidth may serve as a better candidate on detecting surface-breaking cracks at the early stage. Also, a wider range of frequencies improve the capabilities of SAR filter as probe responses at more frequencies are averaged. However, wideband sources in these frequencies are usually very expensive, not to mention sources that have a large bandwidth.

- Lastly, it was observed from the investigations that a higher standoff distance can potentially reduce the effect of unwanted scattered signals on overall probe output signals. Therefore, a higher standoff distance can be intentionally applied in future measurements to minimize the unwanted effects. In addition, a higher standoff distance may also improve the enhancements of SAR filter.

APPENDIX A.
ADDITIONAL FIGURES OF SIMULATED RESULTS (EFFECT OF STANDOFF DISTANCE)

This appendix provides the complete simulated scan results (both selected single-frequency and wideband responses) for Section 3.1 – Effect of Standoff Distance. Figures 1 through 20 represent W-band results, and Figures 21 through 40 represent V-band results.

Figures 1 through 5 represent the simulated results at standoff distance of 0.25 mm. Among these figures, Figures 1 through 4 show the selected single-frequency responses and Figure 5 shows the wideband responses of the W-band differential probe. The results are provided in both linear and logarithmic scales.

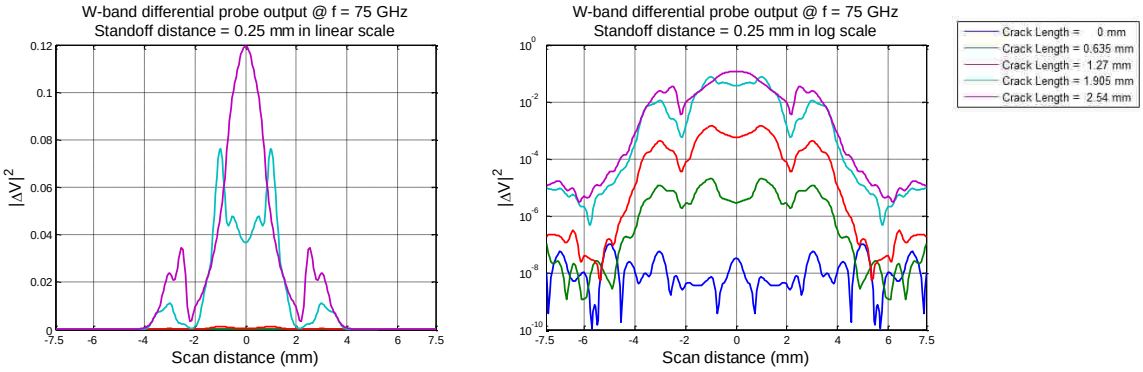

Figure 1. Simulated W-band differential probe output signals with various crack lengths, at a standoff distance of 0.25 mm and frequency of 75 GHz in linear scale (left), and in logarithmic scale (right).

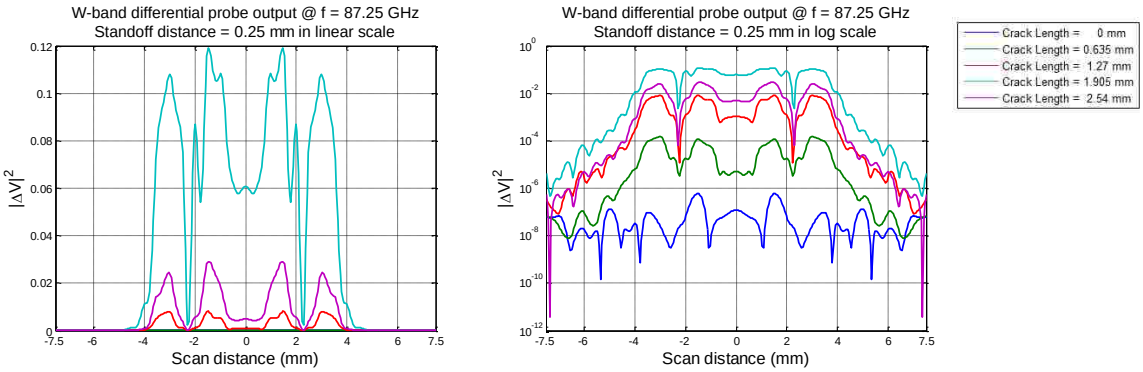

Figure 2. Simulated W-band differential probe output signals with various crack lengths, at a standoff distance of 0.25 mm and frequency of 87.25 GHz in linear scale (left), and in logarithmic scale (right).

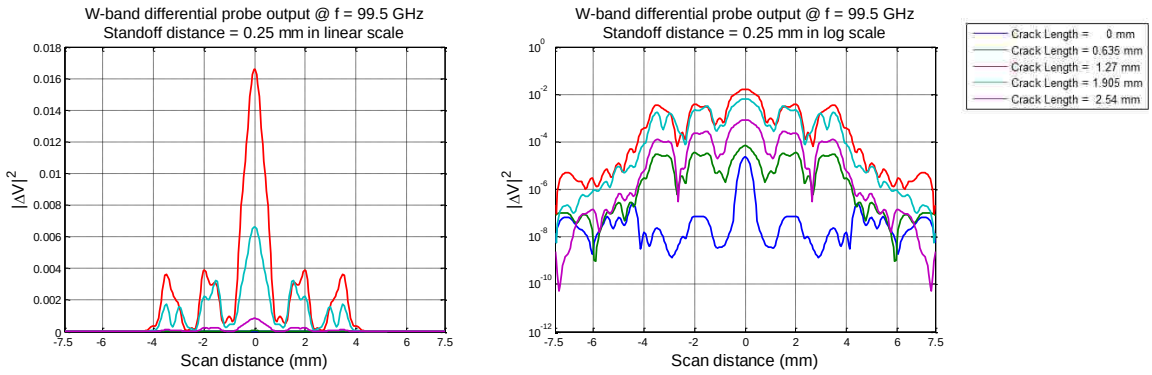

Figure 3. Simulated W-band differential probe output signals with various crack lengths, at a standoff distance of 0.25 mm and frequency of 99.5 GHz in linear scale (left), and in logarithmic scale (right).

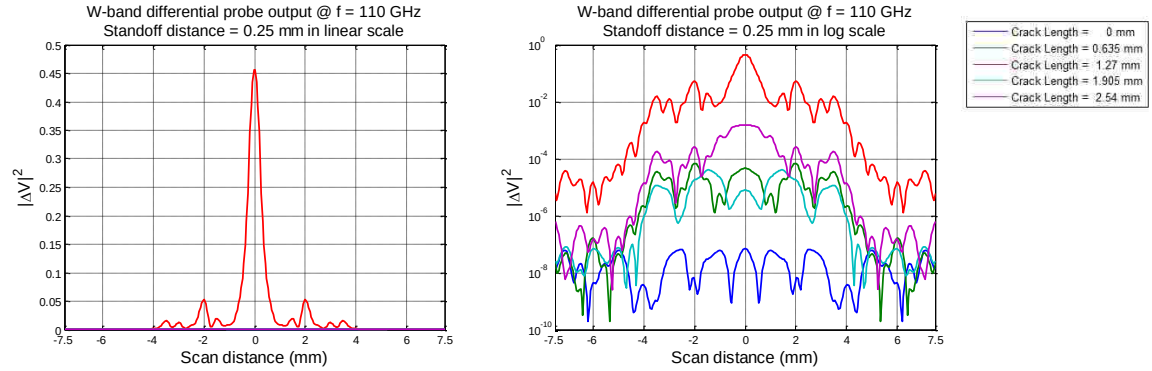

Figure 4. Simulated W-band differential probe output signals with various crack lengths, at a standoff distance of 0.25 mm and frequency of 110 GHz in linear scale (left), and in logarithmic scale (right).

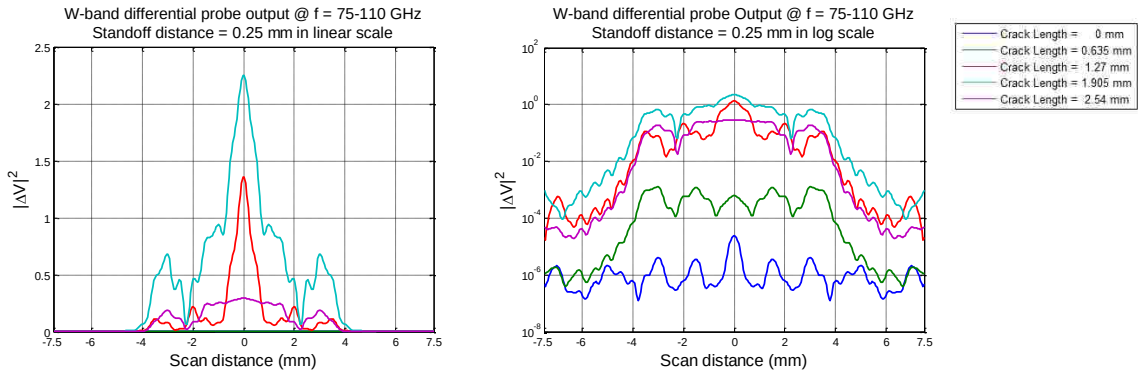

Figure 5. Simulated W-band wideband differential probe output signal with various crack lengths, at a standoff distance of 0.25 mm in linear scale (left), and in logarithmic scale (right).

Figures 6 through 10 represent the simulated results at standoff distance of 0.5 mm. Among these figures, Figures 6 through 9 show the selected single-frequency responses and Figure 10 shows the wideband responses of the W-band differential probe.

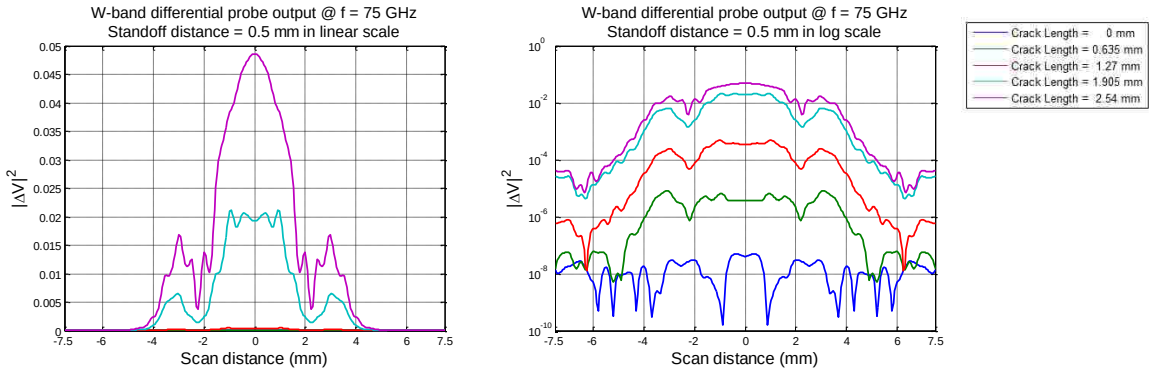

Figure 6. Simulated W-band differential probe output signals with various crack lengths, at a standoff distance of 0.5 mm and frequency of 75 GHz in linear scale (left), and in logarithmic scale (right).

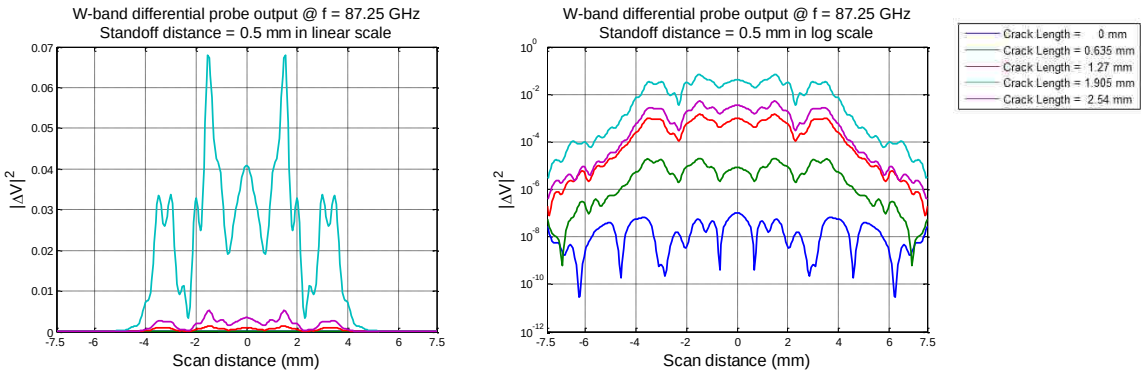

Figure 7. Simulated W-band differential probe output signals with various crack lengths, at a standoff distance of 0.5 mm and frequency of 87.25 GHz in linear scale (left), and in logarithmic scale (right).

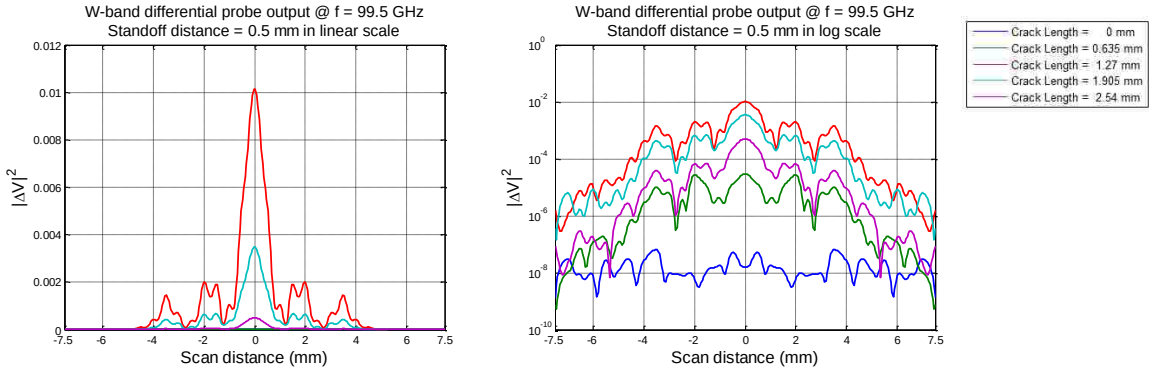

Figure 8. Simulated W-band differential probe output signals with various crack lengths, at a standoff distance of 0.5 mm and frequency of 99.5 GHz in linear scale (left), and in logarithmic scale (right).

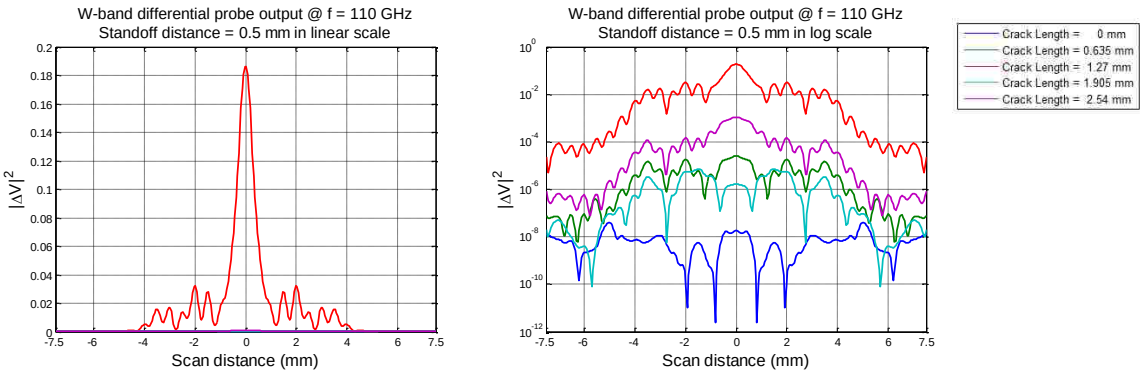

Figure 9. Simulated W-band differential probe output signals with various crack lengths, at a standoff distance of 0.5 mm and frequency of 110 GHz in linear scale (left), and in logarithmic scale (right).

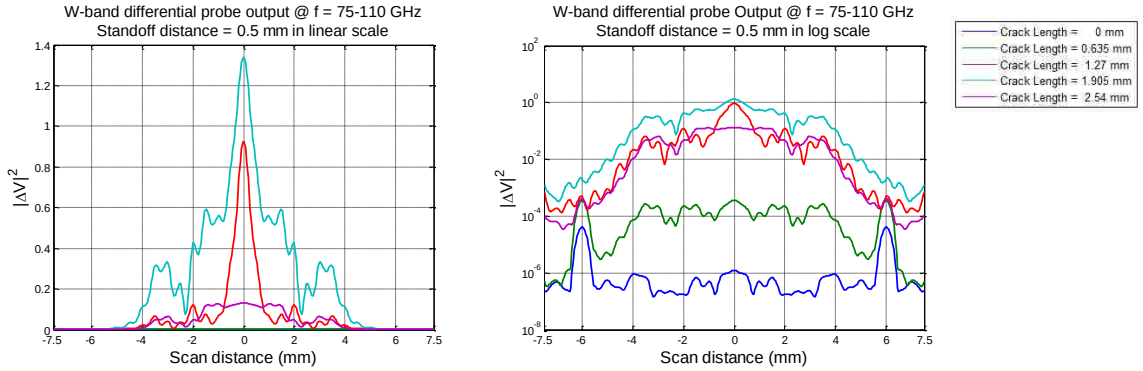

Figure 10. Simulated W-band wideband differential probe output signal with various crack lengths, at a standoff distance of 0.5 mm in linear scale (left), and in logarithmic scale (right).

Figures 11 through 15 represent the simulated results at standoff distance of 0.75 mm. Among these figures, Figures 11 through 14 show the selected single-frequency responses and Figure 15 shows the wideband responses of the W-band differential probe.

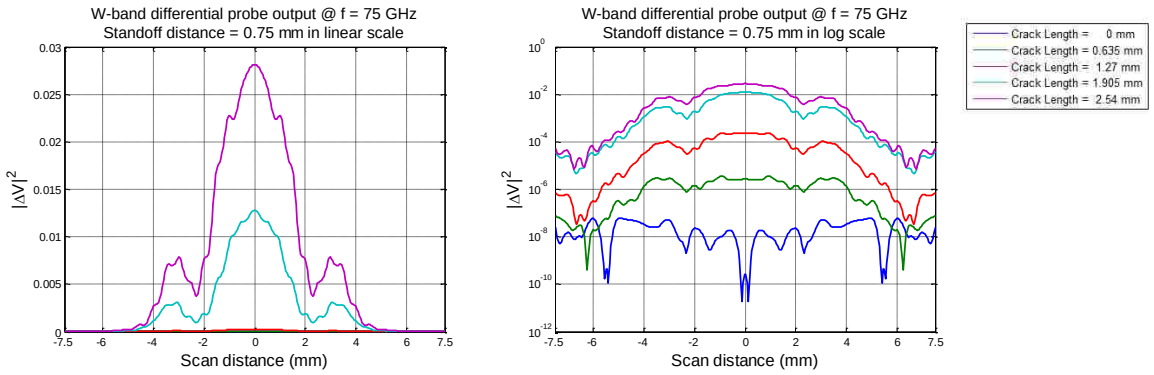

Figure 11. Simulated W-band differential probe output signals with various crack lengths, at a standoff distance of 0.75 mm and frequency of 75 GHz in linear scale (left), and in logarithmic scale (right).

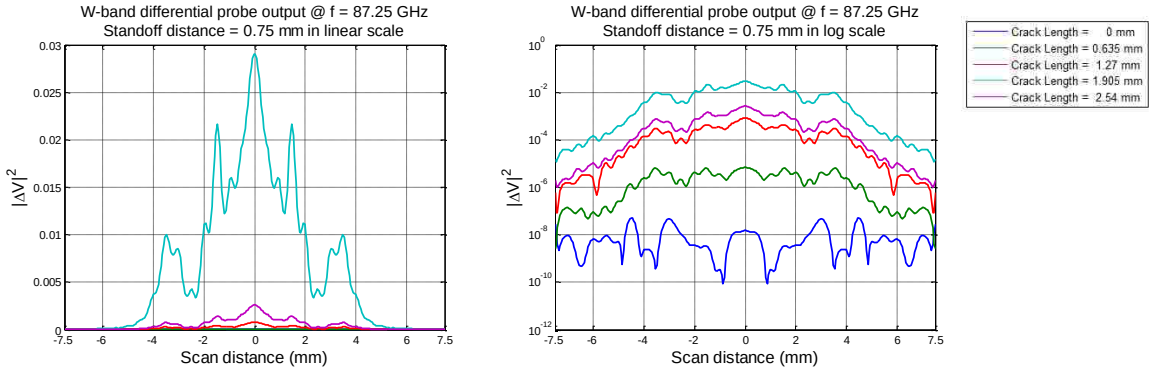

Figure 12. Simulated W-band differential probe output signals with various crack lengths, at a standoff distance of 0.75 mm and frequency of 87.25 GHz in linear scale (left), and in logarithmic scale (right).

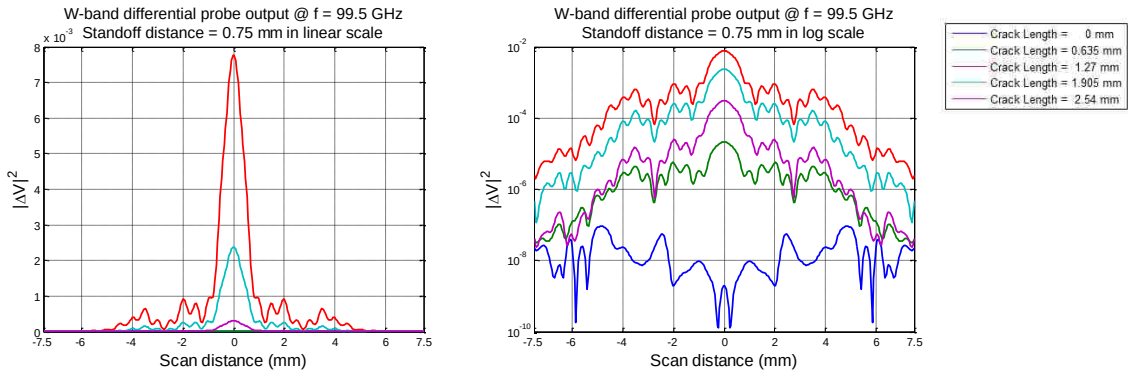

Figure 13. Simulated W-band differential probe output signals with various crack lengths, at a standoff distance of 0.75 mm and frequency of 99.5 GHz in linear scale (left), and in logarithmic scale (right).

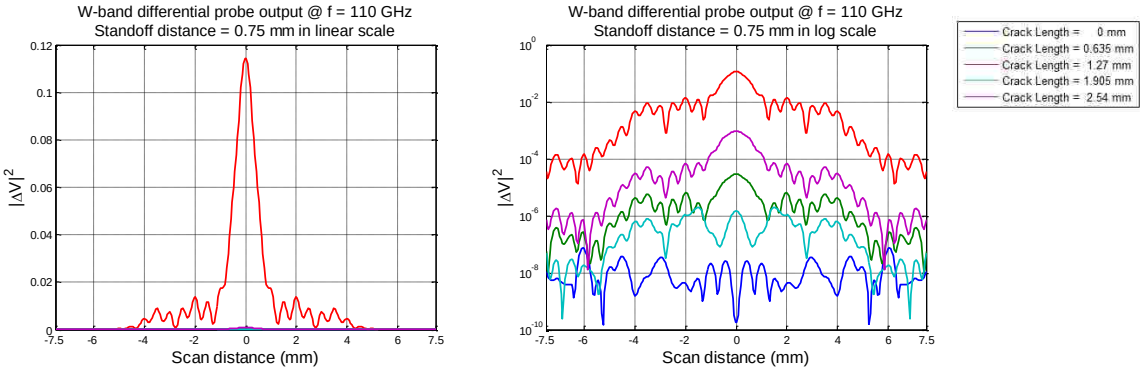

Figure 14. Simulated W-band differential probe output signals with various crack lengths, at a standoff distance of 0.75 mm and frequency of 110 GHz in linear scale (left), and in logarithmic scale (right).

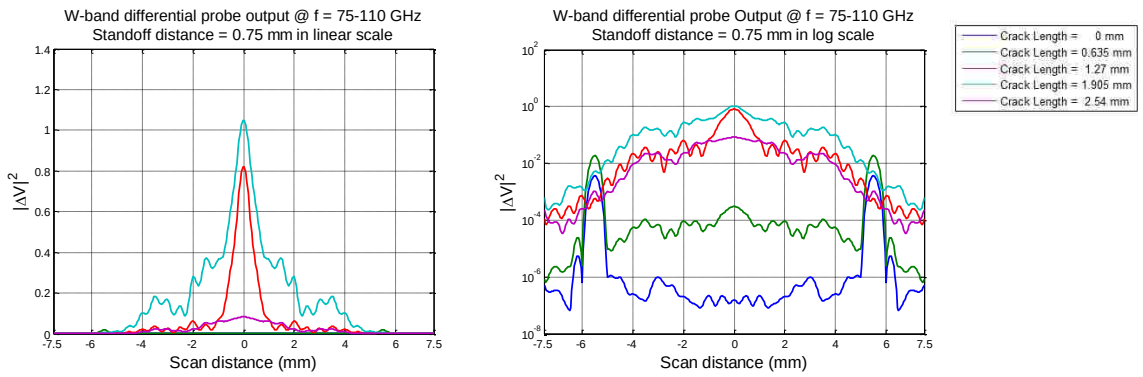

Figure 15. Simulated W-band wideband differential probe output signal with various crack lengths, at a standoff distance of 0.75 mm in linear scale (left), and in logarithmic scale (right).

Figures 16 through 20 represent the simulated results at standoff distance of 1 mm. Among these figures, Figures 16 through 19 show the selected single-frequency responses and Figure 20 shows the wideband responses of the W-band differential probe.

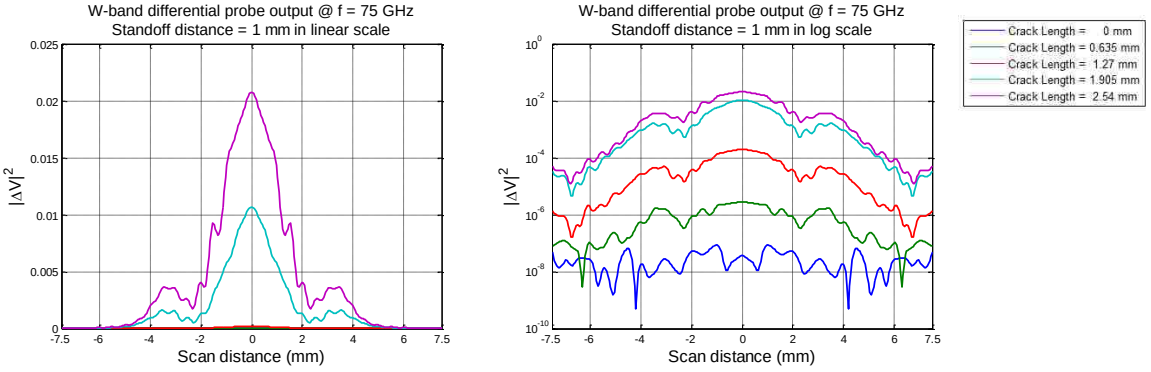

Figure 16. Simulated W-band differential probe output signals with various crack lengths, at a standoff distance of 1 mm and frequency of 75 GHz in linear scale (left), and in logarithmic scale (right).

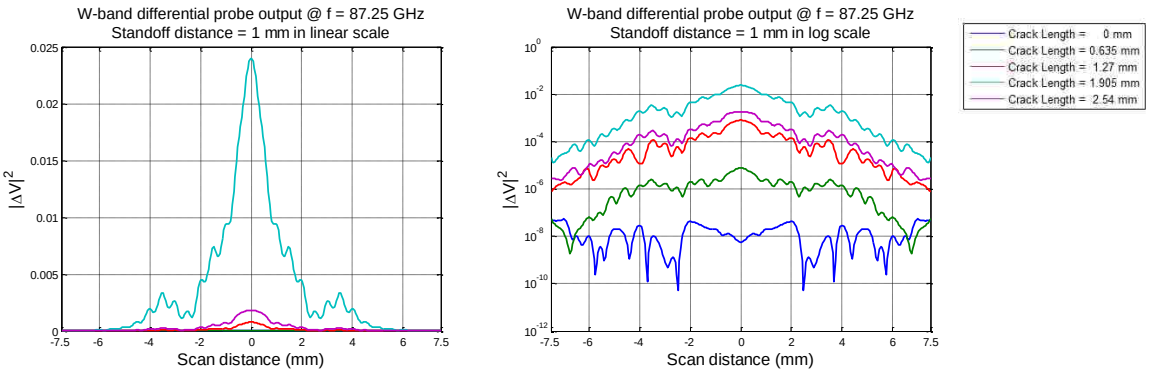

Figure 17. Simulated W-band differential probe output signals with various crack lengths, at a standoff distance of 1 mm and frequency of 87.25 GHz in linear scale (left), and in logarithmic scale (right).

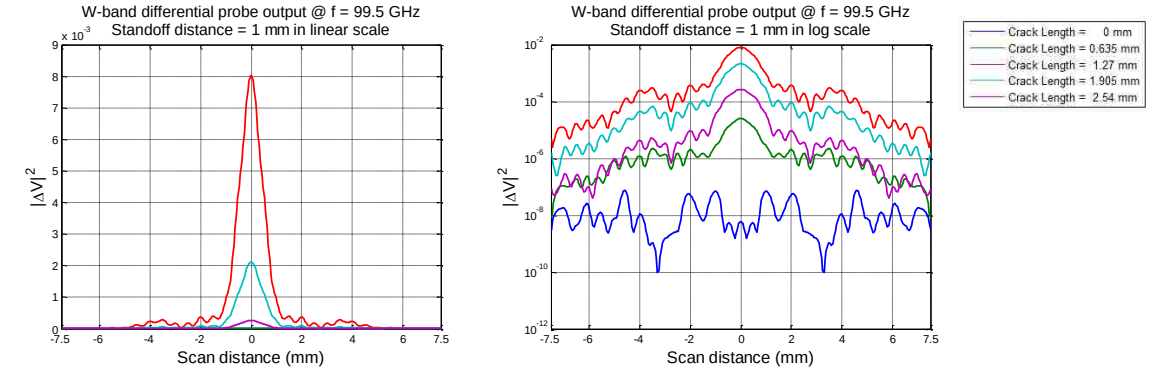

Figure 18. Simulated W-band differential probe output signals with various crack lengths, at a standoff distance of 1 mm and frequency of 99.5 GHz in linear scale (left), and in logarithmic scale (right).

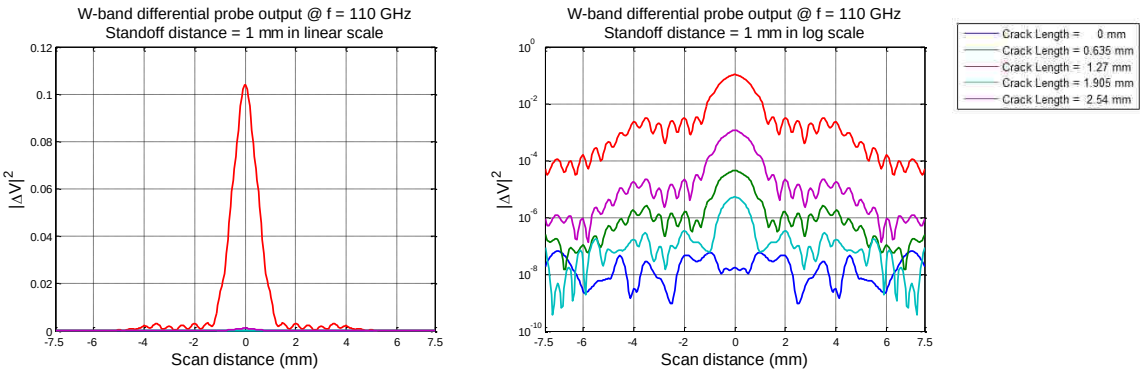

Figure 19. Simulated W-band differential probe output signals with various crack lengths, at a standoff distance of 1 mm and frequency of 110 GHz in linear scale (left), and in logarithmic scale (right).

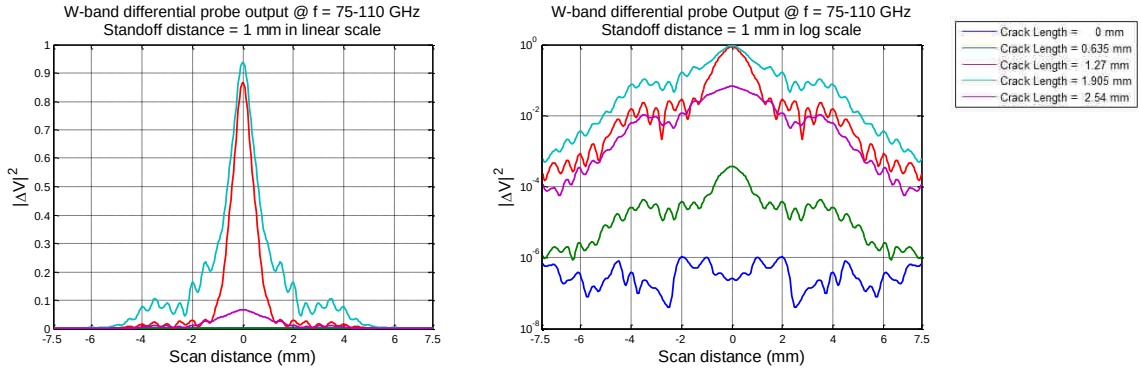

Figure 20. Simulated W-band wideband differential probe output signal with various crack lengths, at a standoff distance of 1 mm in linear scale (left), and in logarithmic scale (right).

The following results are V-band results. Figures 21 through 25 represent the simulated results at standoff distance of 0.25 mm. Among these figures, Figures 21 through 24 show the selected single-frequency responses and Figure 25 shows the wideband responses of the V-band differential probe. The results are provided in both linear and logarithmic scales.

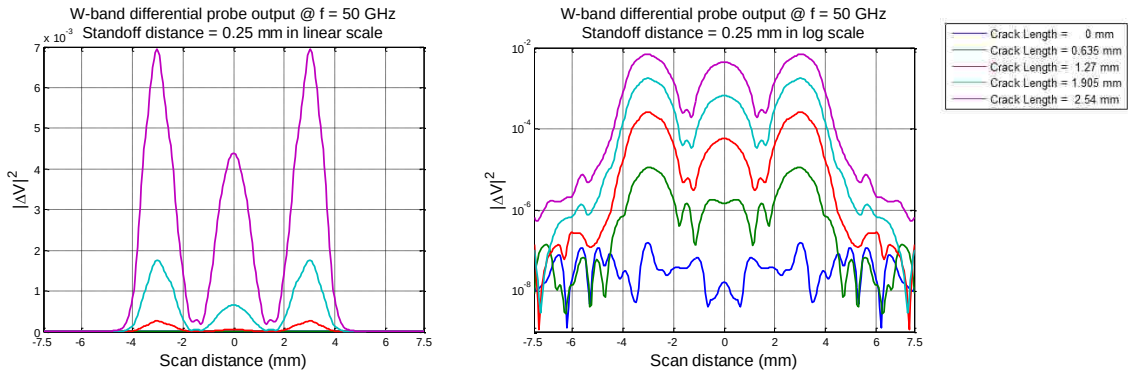

Figure 21. Simulated V-band differential probe output signals with various crack lengths, at a standoff distance of 0.25 mm and frequency of 50 GHz in linear scale (left), and in logarithmic scale (right).

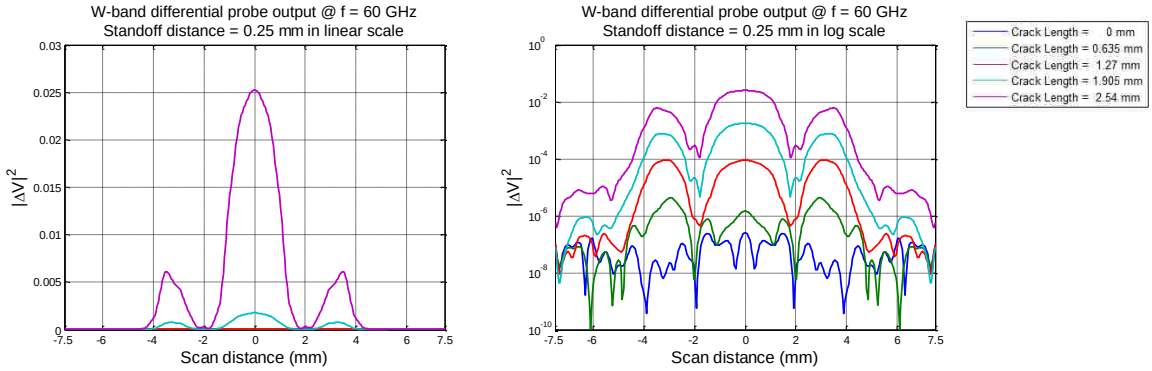

Figure 22. Simulated V-band differential probe output signals with various crack lengths, at a standoff distance of 0.25 mm and frequency of 60 GHz in linear scale (left), and in logarithmic scale (right).

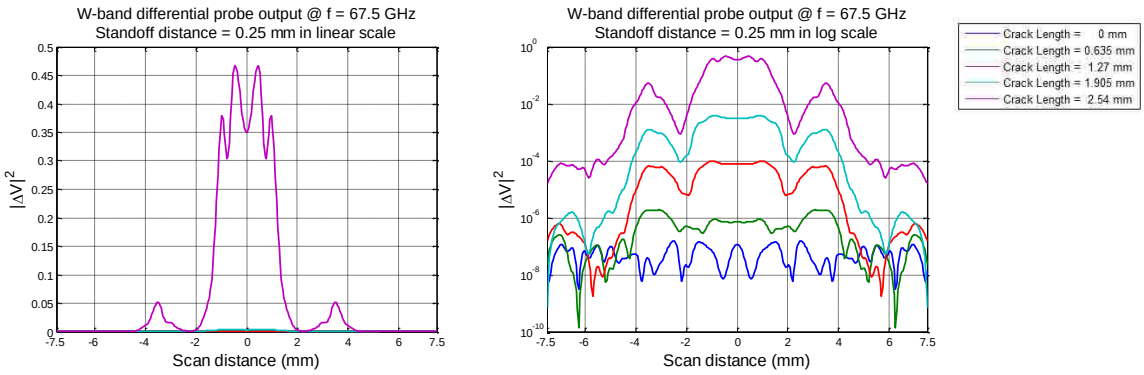

Figure 23. Simulated V-band differential probe output signals with various crack lengths, at a standoff distance of 0.25 mm and frequency of 67.5 GHz in linear scale (left), and in logarithmic scale (right).

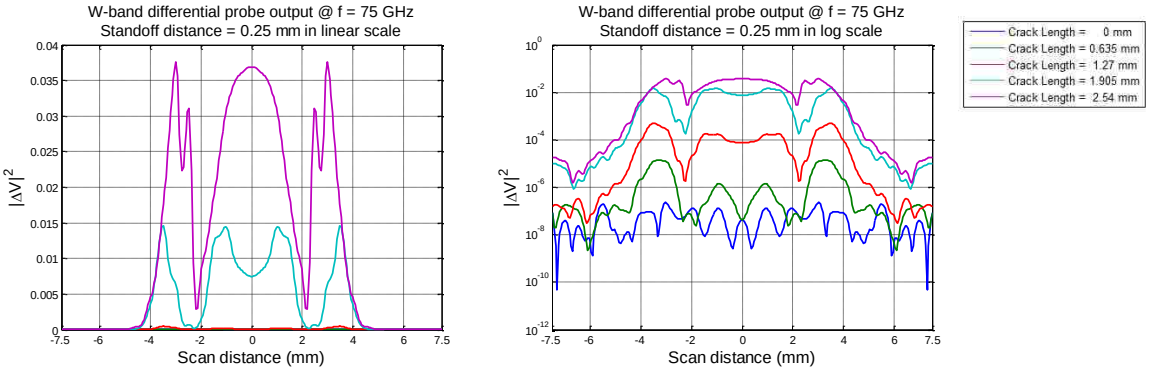

Figure 24. Simulated V-band differential probe output signals with various crack lengths, at a standoff distance of 0.25 mm and frequency of 75 GHz in linear scale (left), and in logarithmic scale (right).

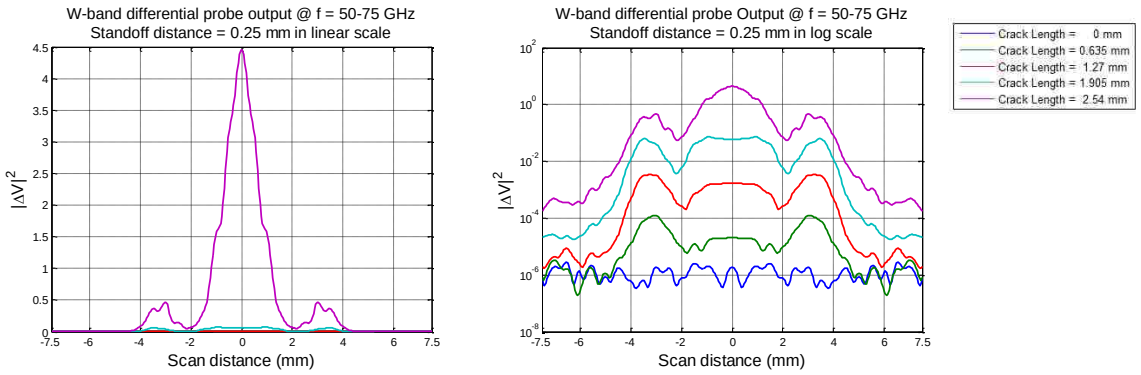

Figure 25. Simulated V-band wideband differential probe output signal with various crack lengths, at a standoff distance of 0.25 mm in linear scale (left), and in logarithmic scale (right).

Figures 26 through 30 represent the simulated results at standoff distance of 0.5 mm. Among these figures, Figures 26 through 29 show the selected single-frequency responses and Figure 30 shows the wideband responses of the V-band differential probe.

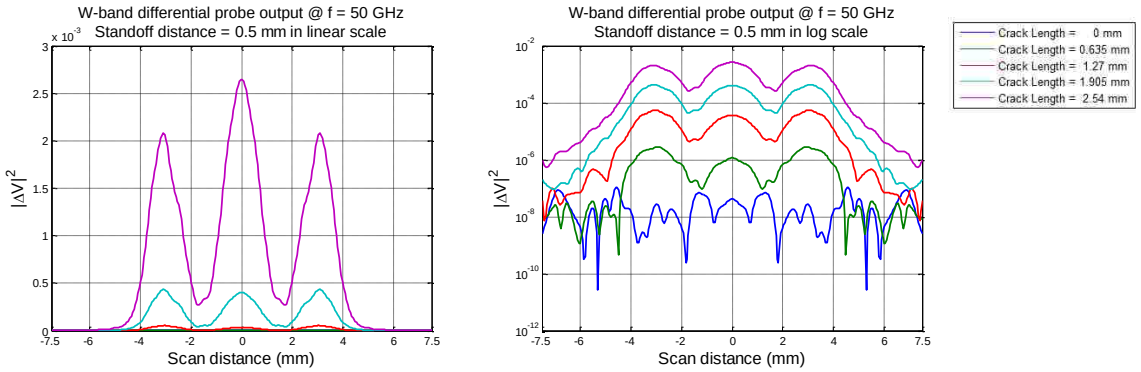

Figure 26. Simulated V-band differential probe output signals with various crack lengths, at a standoff distance of 0.5 mm and frequency of 50 GHz in linear scale (left), and in logarithmic scale (right).

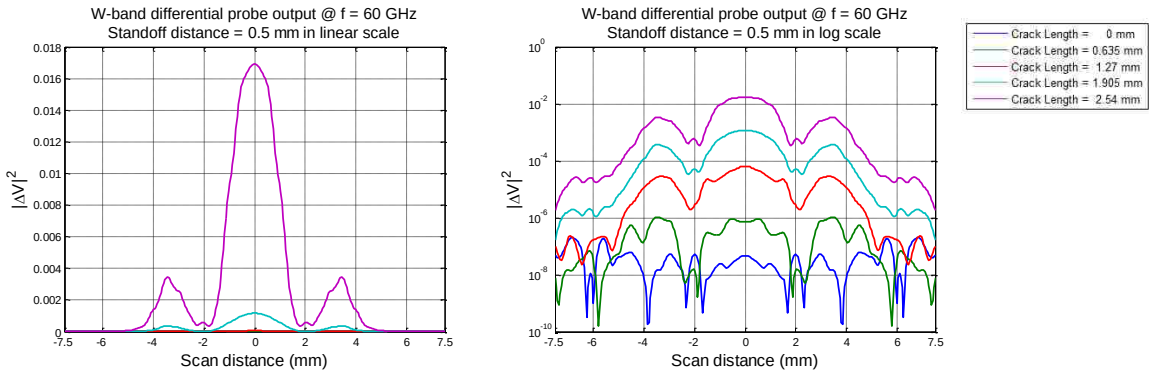

Figure 27. Simulated V-band differential probe output signals with various crack lengths, at a standoff distance of 0.5 mm and frequency of 60 GHz in linear scale (left), and in logarithmic scale (right).

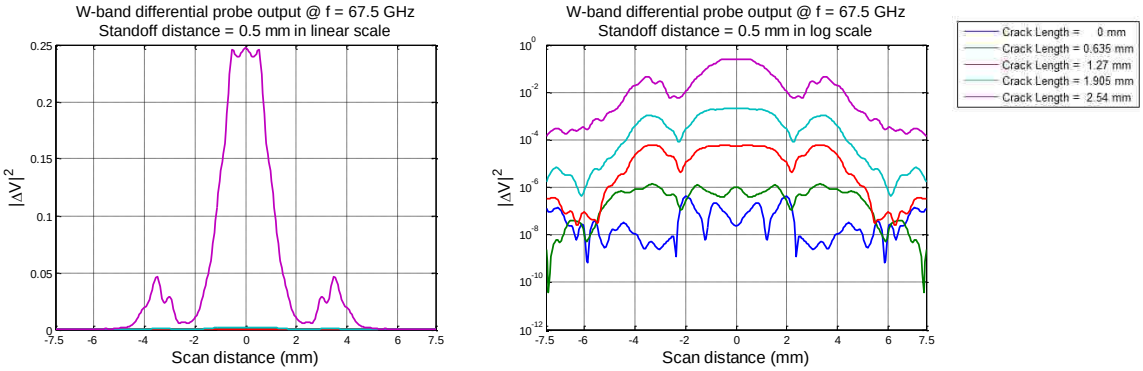

Figure 28. Simulated V-band differential probe output signals with various crack lengths, at a standoff distance of 0.5 mm and frequency of 67.5 GHz in linear scale (left), and in logarithmic scale (right).

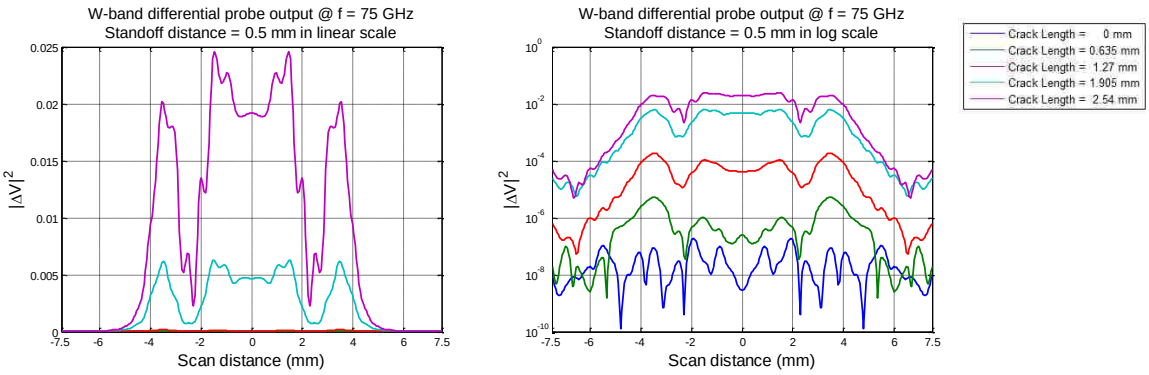

Figure 29. Simulated V-band differential probe output signals with various crack lengths, at a standoff distance of 0.5 mm and frequency of 75 GHz in linear scale (left), and in logarithmic scale (right).

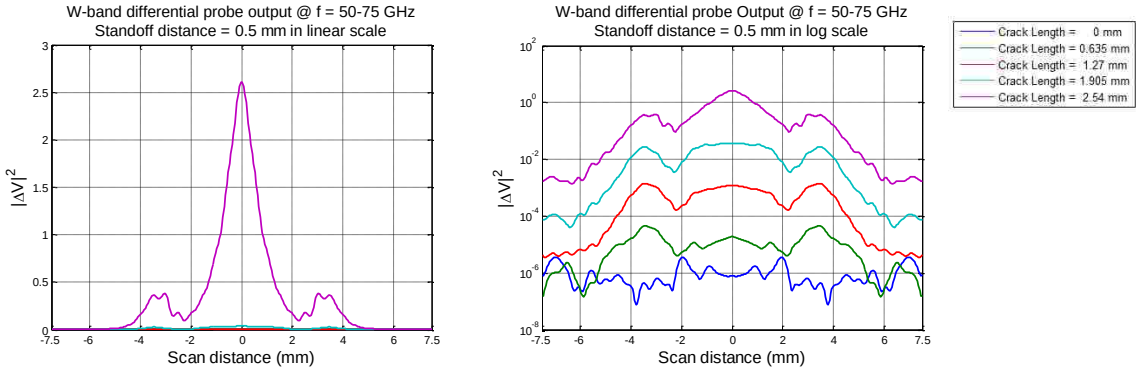

Figure 30. Simulated V-band wideband differential probe output signal with various crack lengths, at a standoff distance of 0.5 mm in linear scale (left), and in logarithmic scale (right).

Figures 31 through 35 represent the simulated results at standoff distance of 0.75 mm. Among these figures, Figures 31 through 34 show the selected single-frequency responses and Figure 35 shows the wideband responses of the V-band differential probe.

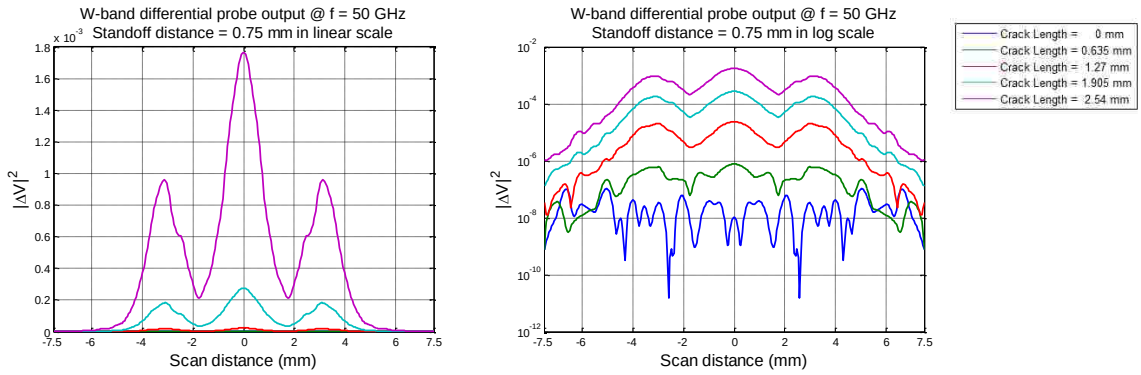

Figure 31. Simulated V-band differential probe output signals with various crack lengths, at a standoff distance of 0.75 mm and frequency of 50 GHz in linear scale (left), and in logarithmic scale (right).

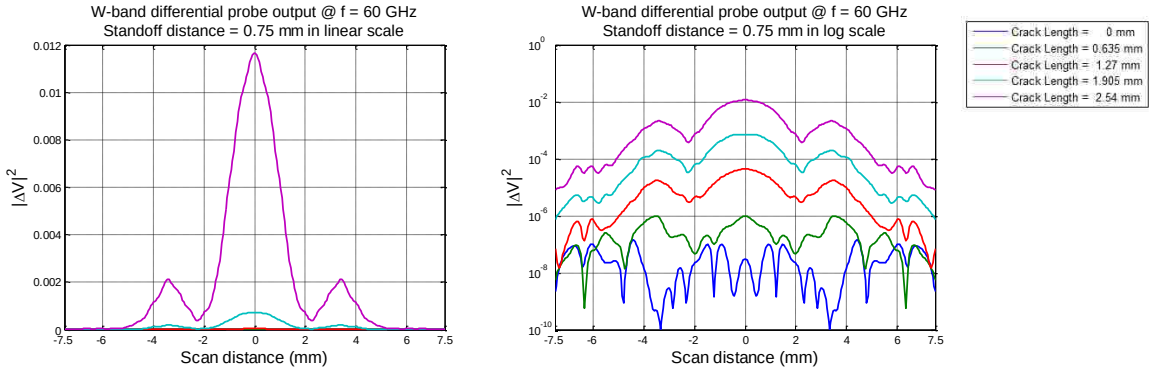

Figure 32. Simulated V-band differential probe output signals with various crack lengths, at a standoff distance of 0.75 mm and frequency of 60 GHz in linear scale (left), and in logarithmic scale (right).

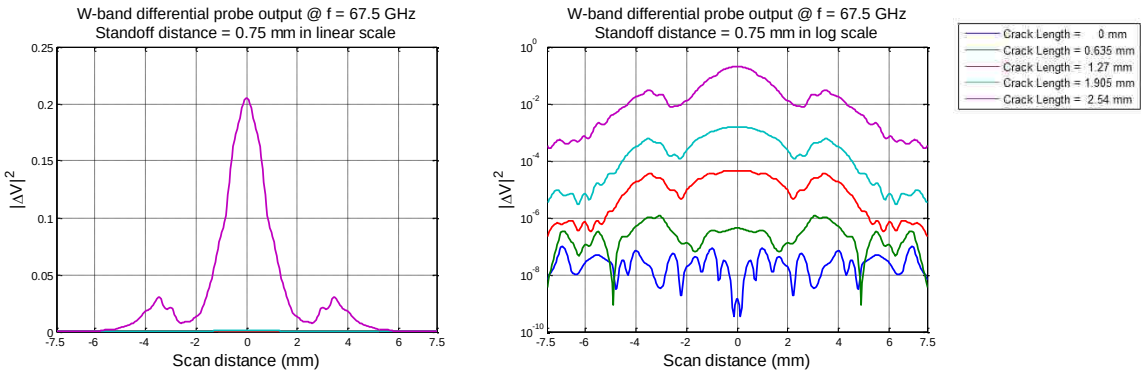

Figure 33. Simulated V-band differential probe output signals with various crack lengths, at a standoff distance of 0.75 mm and frequency of 67.5 GHz in linear scale (left), and in logarithmic scale (right).

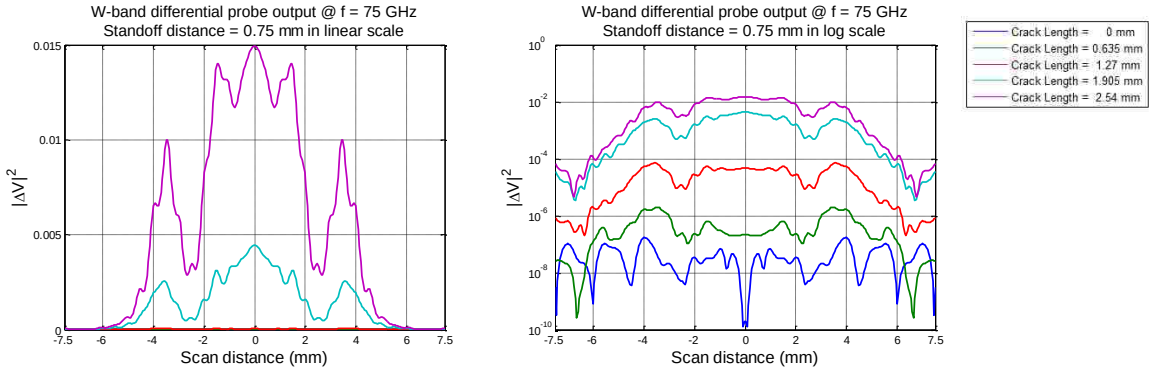

Figure 34. Simulated V-band differential probe output signals with various crack lengths, at a standoff distance of 0.75 mm and frequency of 75 GHz in linear scale (left), and in logarithmic scale (right).

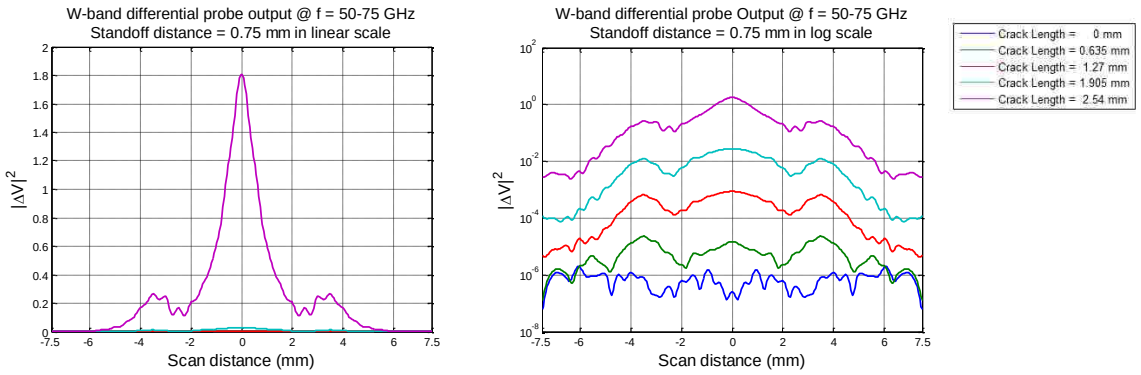

Figure 35. Simulated V-band wideband differential probe output signal with various crack lengths, at a standoff distance of 0.75 mm in linear scale (left), and in logarithmic scale (right).

Figures 36 through 40 represent the simulated results at standoff distance of 1 mm. Among these figures, Figures 36 through 39 show the selected single-frequency responses and Figure 40 shows the wideband responses of the V-band differential probe.

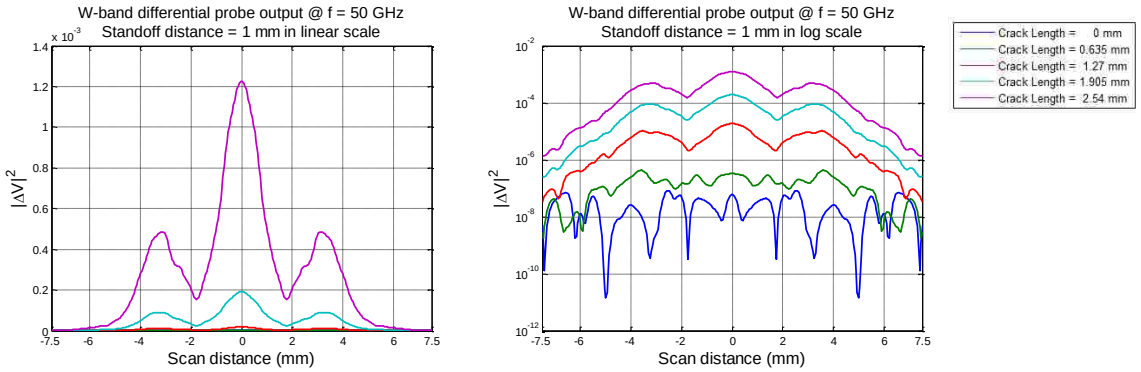

Figure 36. Simulated V-band differential probe output signals with various crack lengths, at a standoff distance of 1 mm and frequency of 50 GHz in linear scale (left), and in logarithmic scale (right).

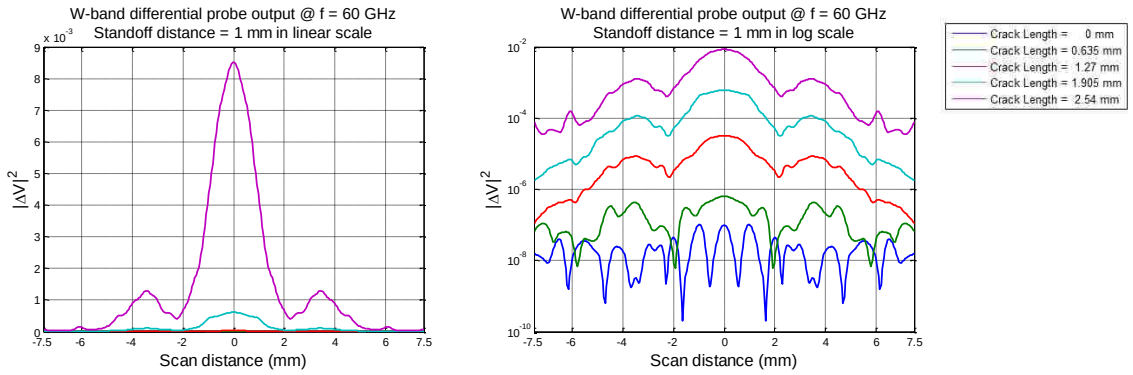

Figure 37. Simulated V-band differential probe output signals with various crack lengths, at a standoff distance of 1 mm and frequency of 60 GHz in linear scale (left), and in logarithmic scale (right).

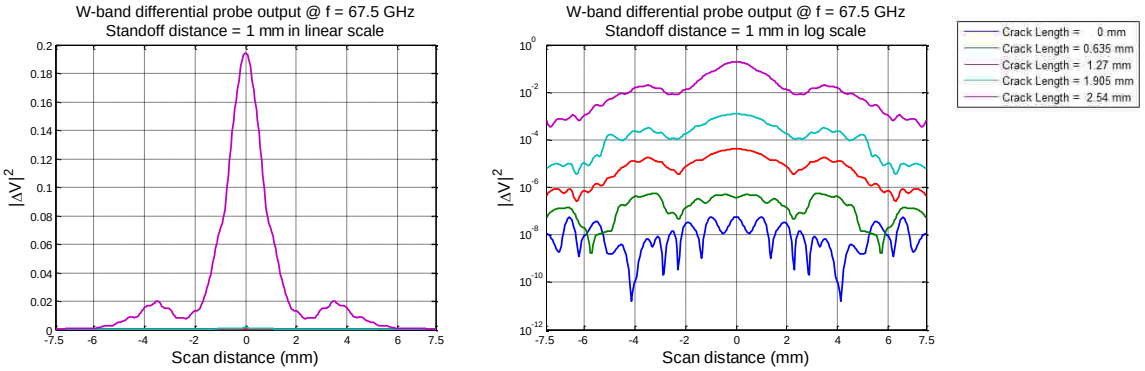

Figure 38. Simulated V-band differential probe output signals with various crack lengths, at a standoff distance of 1 mm and frequency of 67.5 GHz in linear scale (left), and in logarithmic scale (right).

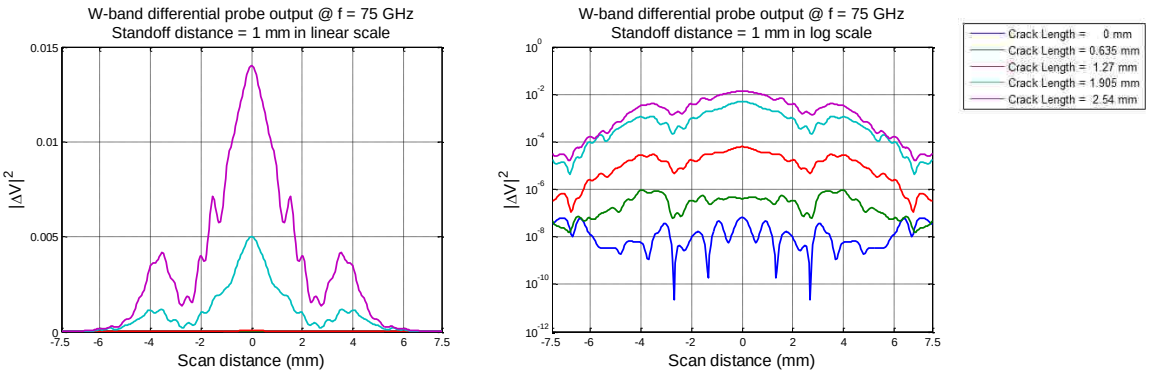

Figure 39. Simulated V-band differential probe output signals with various crack lengths, at a standoff distance of 1 mm and frequency of 75 GHz in linear scale (left), and in logarithmic scale (right).

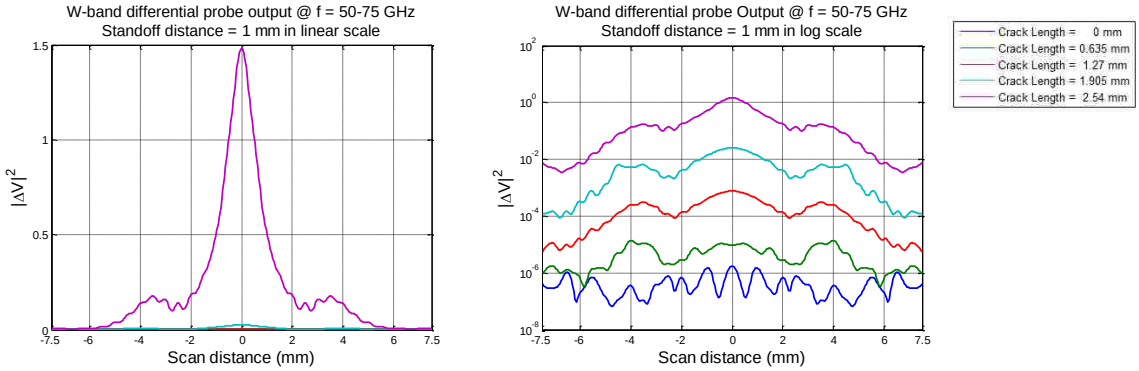

Figure 40. Simulated V-band wideband differential probe output signal with various crack lengths, at a standoff distance of 1 mm in linear scale (left), and in logarithmic scale (right).

APPENDIX B.
ADDITIONAL FIGURES OF SIMULATED RESULTS (EFFECT OF APERTURE OFFSET)

This appendix provides the complete simulated scan results (both selected single-frequency and wideband responses) for Section 3.2 – Effect of Aperture Offset.

Figures 1 through 4 represent the simulated results at standoff distance of 0.5 mm. Among these figures, Figures 1 through 3 show the selected single-frequency responses and Figure 4 shows the wideband responses of the W-band differential probe. The DC bias is removed from the responses (i.e., the responses are referenced to numerical floor). The results are provided in both linear and logarithmic scales.

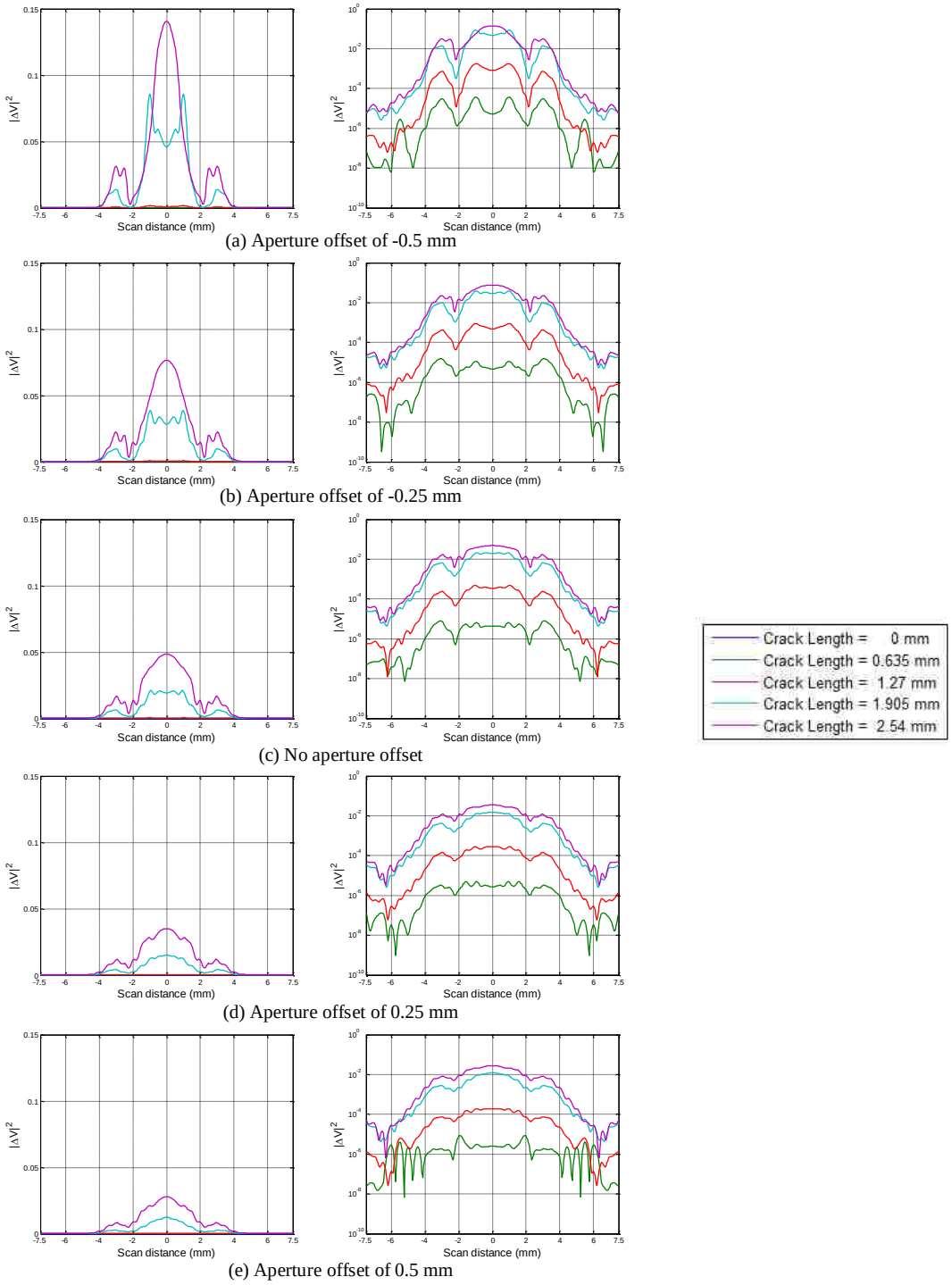

Figure 1. Simulated W-band results (referenced) with various crack lengths, at a standoff distance of 0.5 mm, frequency of 75 GHz, and aperture offset of (from (a) to (e)): -0.5, -0.25, 0, 0.25 and 0.5 mm, in linear (left) and logarithmic scales (right).

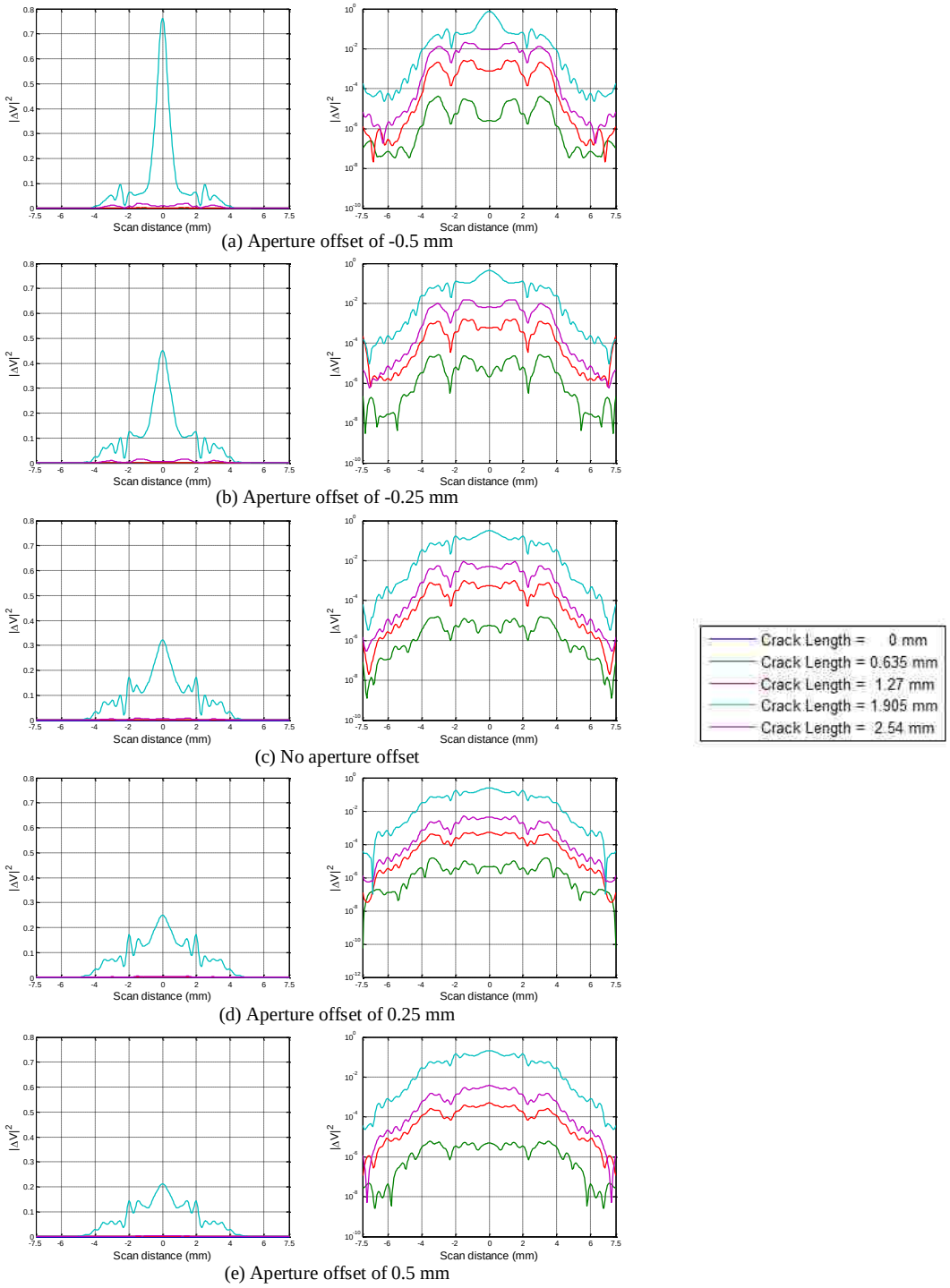

(a) Aperture offset of -0.5 mm

(b) Aperture offset of -0.25 mm

(c) No aperture offset

(d) Aperture offset of 0.25 mm

(e) Aperture offset of 0.5 mm

Figure 2. Simulated W-band results (referenced) with various crack lengths, at a standoff distance of 0.5 mm, frequency of 83.75 GHz, and aperture offset of (from (a) to (e)): -0.5, -0.25, 0, 0.25 and 0.5 mm, in linear (left) and logarithmic scales (right).

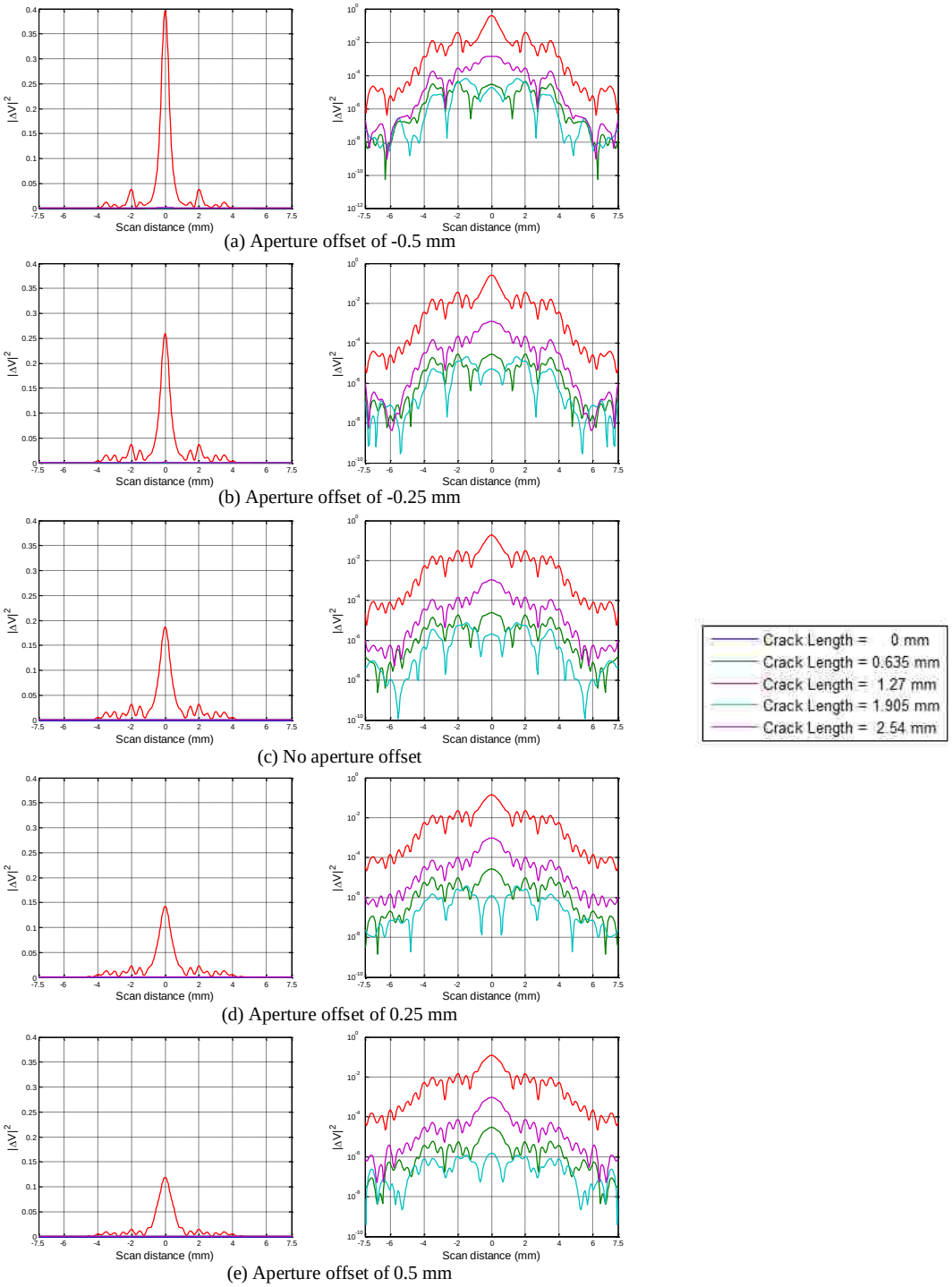

(a) Aperture offset of -0.5 mm

(b) Aperture offset of -0.25 mm

(c) No aperture offset

(d) Aperture offset of 0.25 mm

(e) Aperture offset of 0.5 mm

Figure 3. Simulated W-band results (referenced) with various crack lengths, at a standoff distance of 0.5 mm, frequency of 110 GHz, and aperture offset of (from (a) to (e)): -0.5, -0.25, 0, 0.25 and 0.5 mm, in linear (left) and logarithmic scales (right).

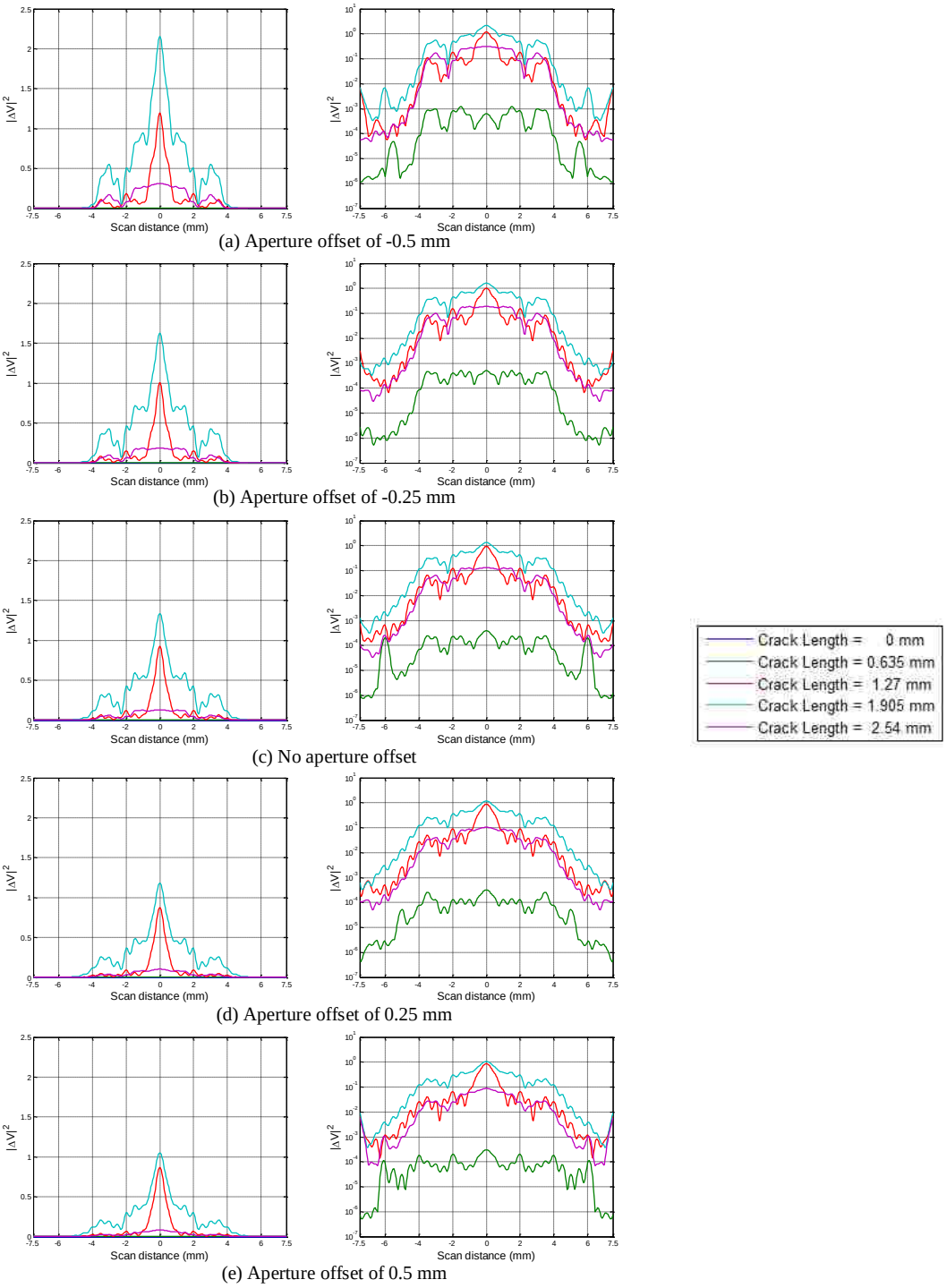

(a) Aperture offset of -0.5 mm

(b) Aperture offset of -0.25 mm

(c) No aperture offset

(d) Aperture offset of 0.25 mm

(e) Aperture offset of 0.5 mm

Figure 4. Simulated W-band wideband results (referenced) with various crack lengths, at a standoff distance of 0.5 mm, and aperture offset of (from (a) to (e)): -0.5, -0.25, 0, 0.25 and 0.5 mm, in linear (left) and logarithmic scales (right).

Figures 5 through 8 represent the simulated results at standoff distance of 1 mm. Among these figures, Figures 5 through 7 show the selected single-frequency responses and Figure 8 shows the wideband responses of the W-band differential probe. The DC bias is removed from the responses (i.e., the responses are referenced to numerical floor). The results are provided in both linear and logarithmic scales.

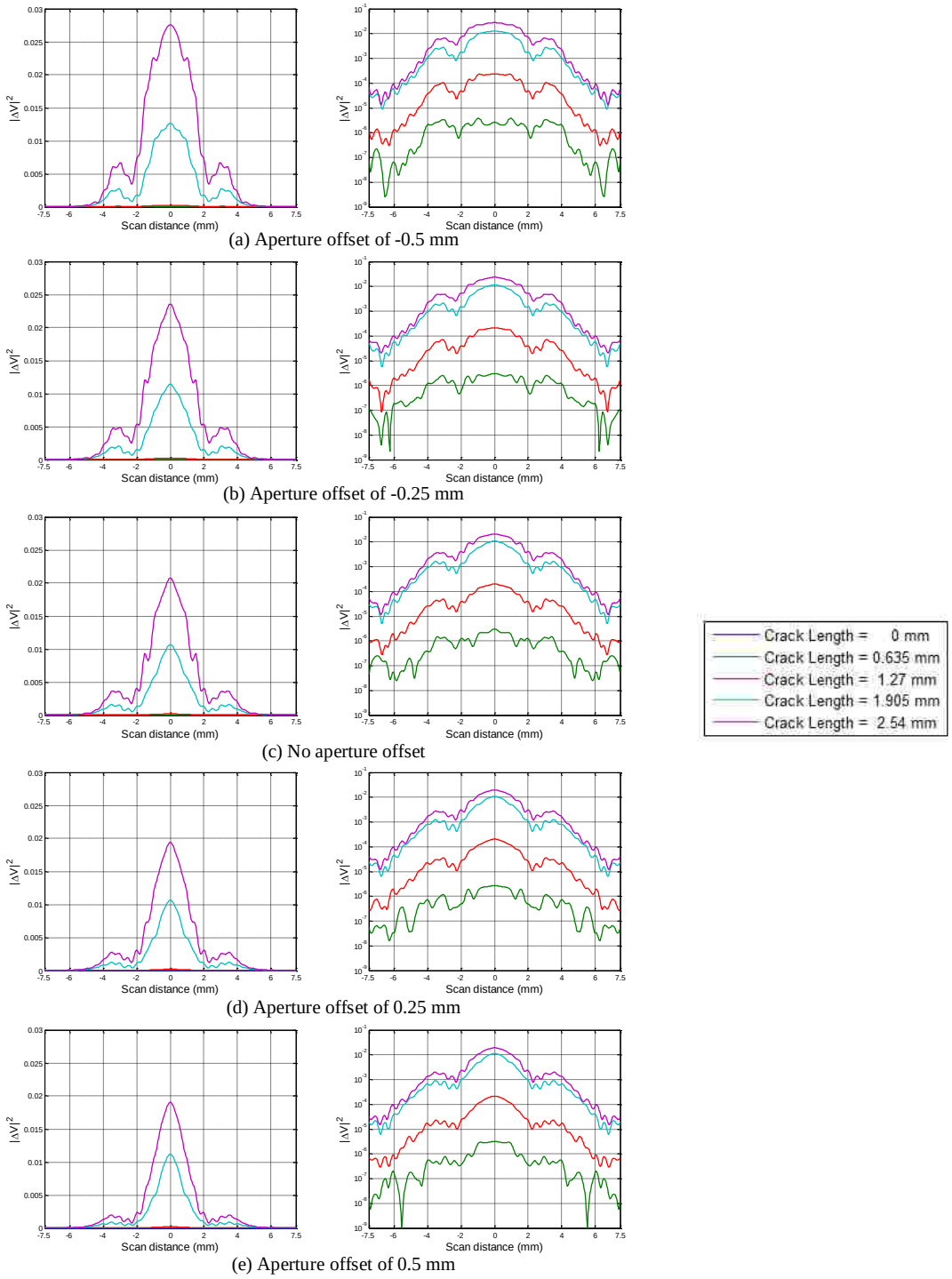

(a) Aperture offset of -0.5 mm

(b) Aperture offset of -0.25 mm

(c) No aperture offset

(d) Aperture offset of 0.25 mm

(e) Aperture offset of 0.5 mm

Figure 5. Simulated W-band results (referenced) with various crack lengths, at a standoff distance of 1 mm, frequency of 75 GHz, and aperture offset of (from (a) to (e)): -0.5, -0.25, 0, 0.25 and 0.5 mm, in linear (left) and logarithmic scales (right).

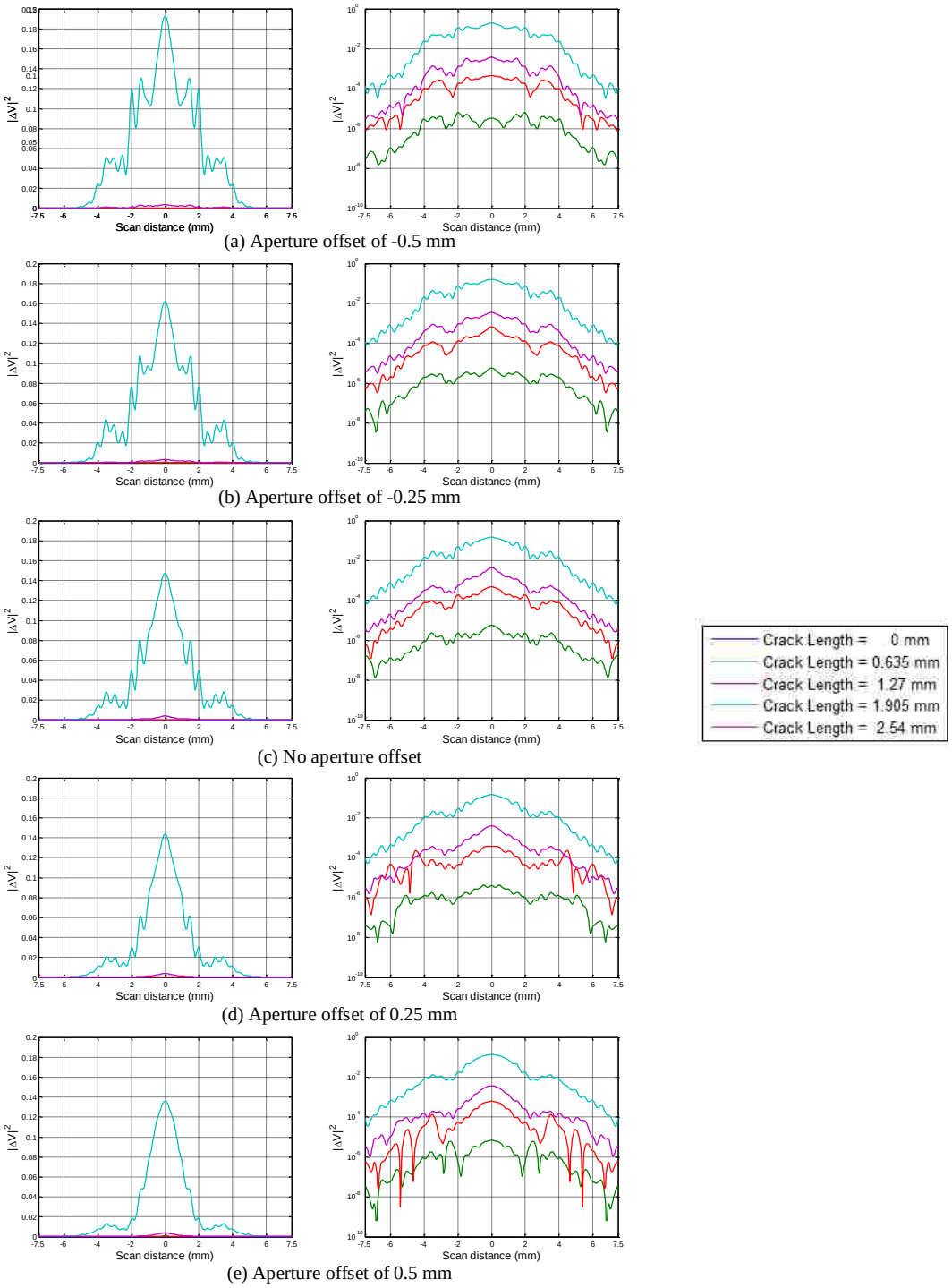

(a) Aperture offset of -0.5 mm

(b) Aperture offset of -0.25 mm

(c) No aperture offset

(d) Aperture offset of 0.25 mm

(e) Aperture offset of 0.5 mm

Figure 6. Simulated W-band results (referenced) with various crack lengths, at a standoff distance of 1 mm, frequency of 83.75 GHz, and aperture offset of (from (a) to (e)): -0.5, -0.25, 0, 0.25 and 0.5 mm, in linear (left) and logarithmic scales (right).

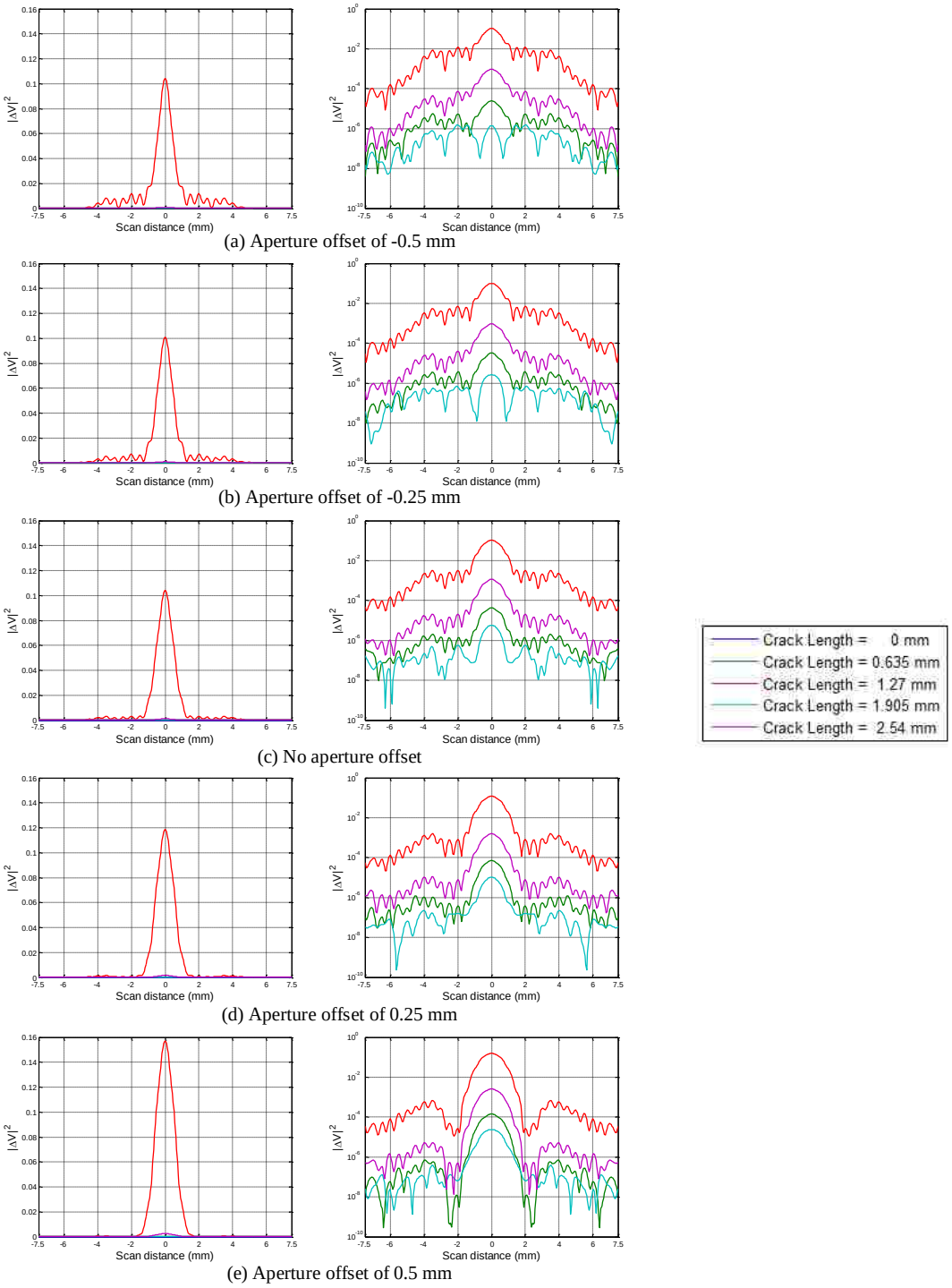

(a) Aperture offset of -0.5 mm

(b) Aperture offset of -0.25 mm

(c) No aperture offset

(d) Aperture offset of 0.25 mm

(e) Aperture offset of 0.5 mm

Figure 7. Simulated W-band results (referenced) with various crack lengths, at a standoff distance of 1 mm, frequency of 110 GHz, and aperture offset of (from (a) to (e)): -0.5, -0.25, 0, 0.25 and 0.5 mm, in linear (left) and logarithmic scales (right).

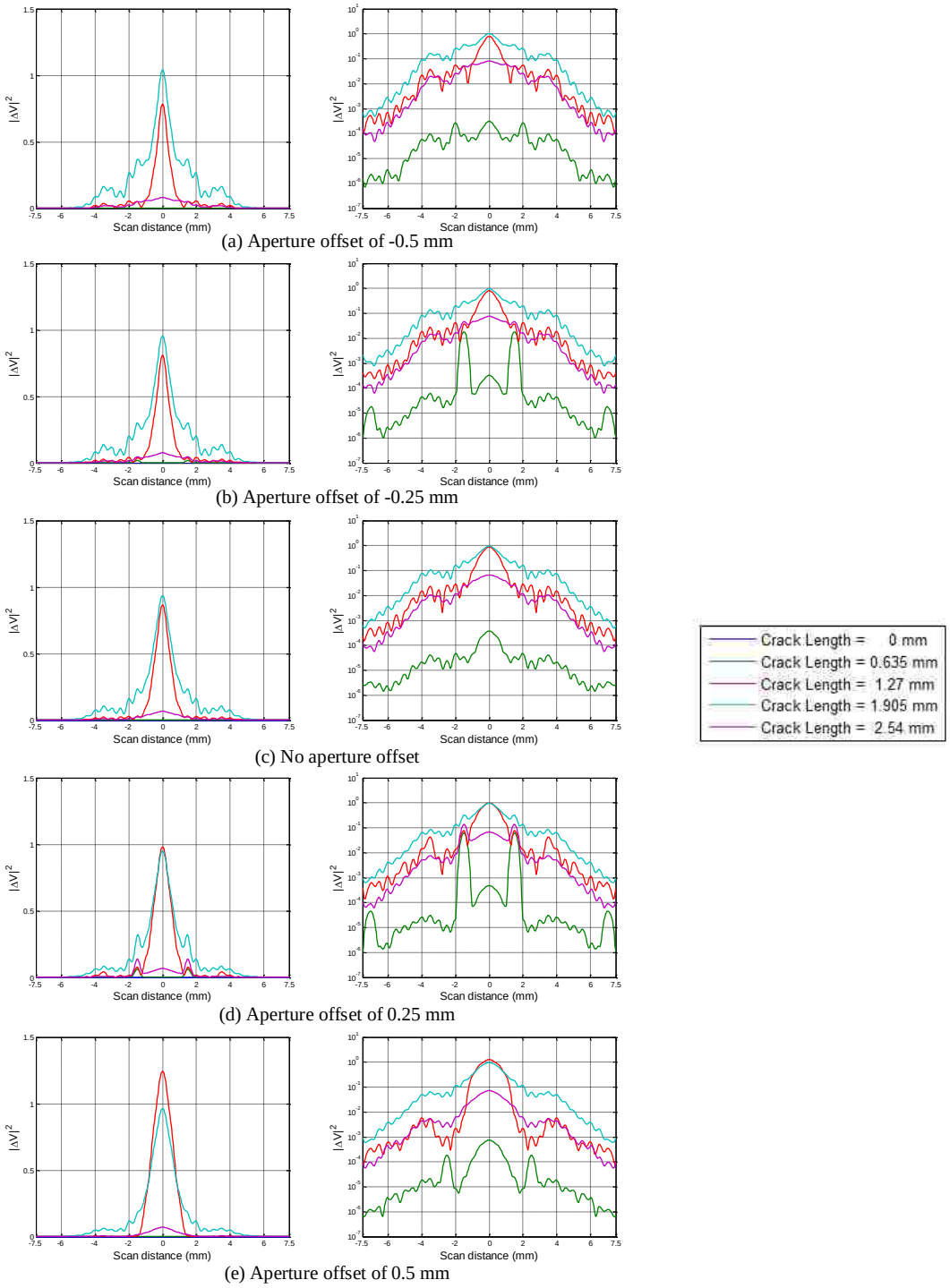

Figure 8. Simulated W-band wideband results (referenced) with various crack lengths, at a standoff distance of 1 mm, and aperture offset of (from (a) to (e)): -0.5, -0.25, 0, 0.25 and 0.5 mm, in linear (left) and logarithmic scales (right).

APPENDIX C.
ADDITIONAL FIGURES OF SIMULATED RESULTS (EFFECT OF FASTENER HEAD TILT)

This appendix provides the complete simulated scan results (both selected single-frequency and wideband responses) for Section 3.3 – Effect of Fastener Head Tilt.

Figures 1 through 4 represent the simulated results at standoff distance of 0.5 mm. Among these figures, Figures 1 through 3 show the selected single-frequency responses and Figure 4 shows the wideband responses of the W-band differential probe. The results are provided in both linear and logarithmic scales. Note the scales may not be the same for the sub-figures.

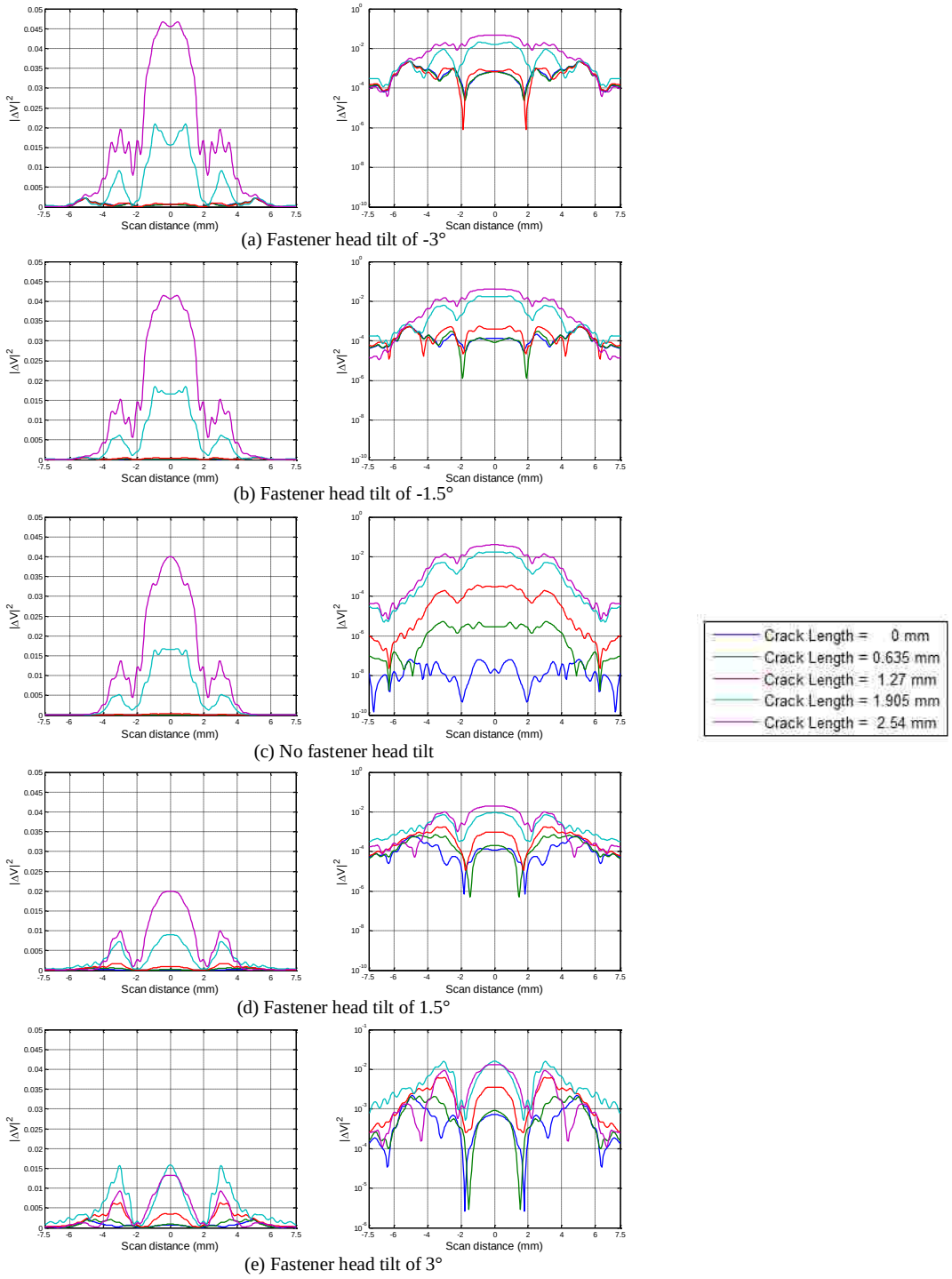

(a) Fastener head tilt of -3°

(b) Fastener head tilt of -1.5°

(c) No fastener head tilt

(d) Fastener head tilt of 1.5°

(e) Fastener head tilt of 3°

Figure 1. Simulated W-band results with various crack lengths, at a standoff distance of 0.5 mm, frequency of 75 GHz, and fastener head tilt of (from (a) to (e)): -3°, -1.5°, 0°, 1.5° and 3°, in linear (left) and logarithmic scales (right).

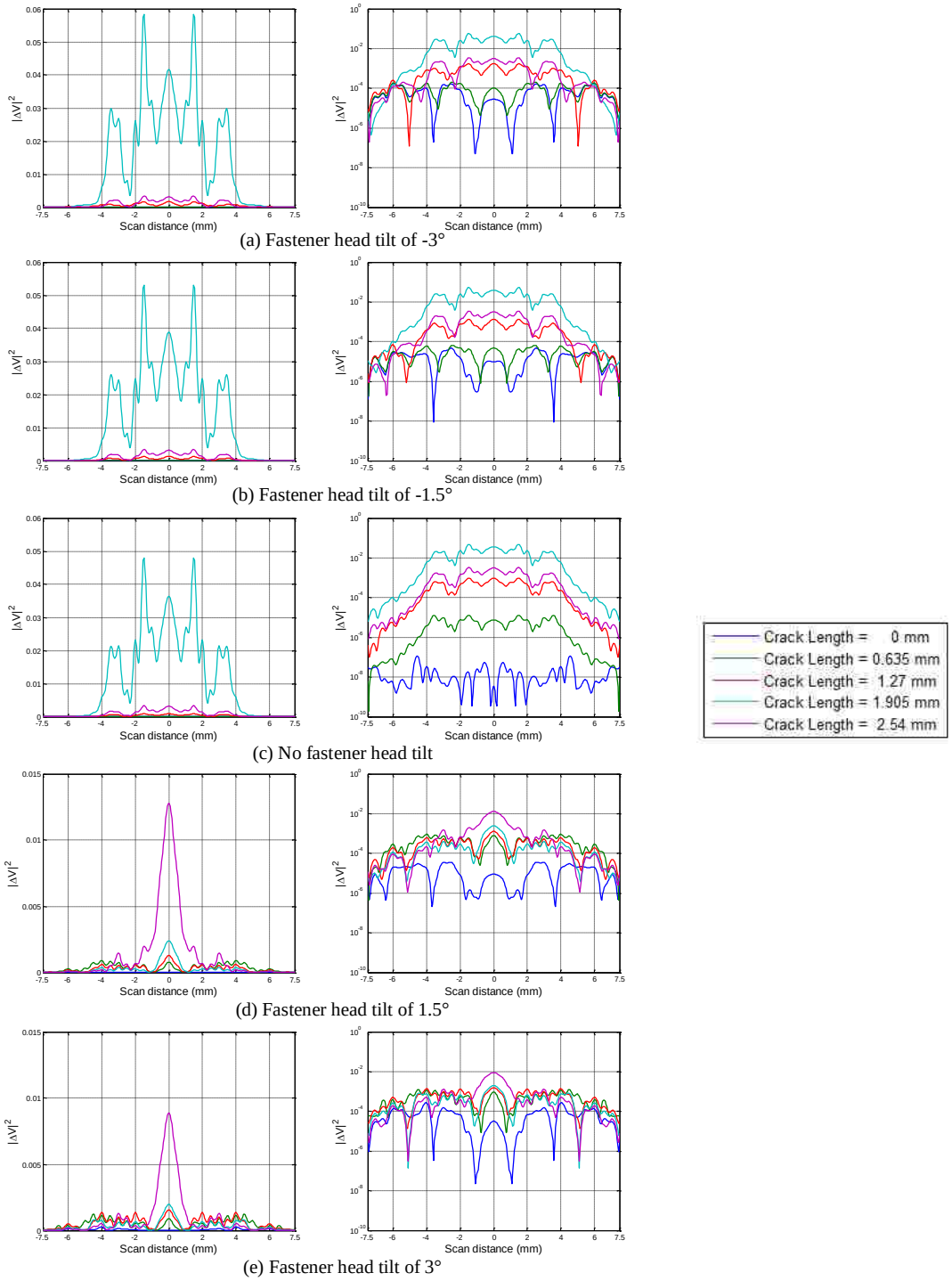

(a) Fastener head tilt of -3°

(b) Fastener head tilt of -1.5°

(c) No fastener head tilt

(d) Fastener head tilt of 1.5°

(e) Fastener head tilt of 3°

Figure 2. Simulated W-band results with various crack lengths, at a standoff distance of 0.5 mm, frequency of 87.25 GHz, and fastener head tilt of (from (a) to (e)): -3°, -1.5°, 0°, 1.5° and 3°, in linear (left) and logarithmic scales (right).

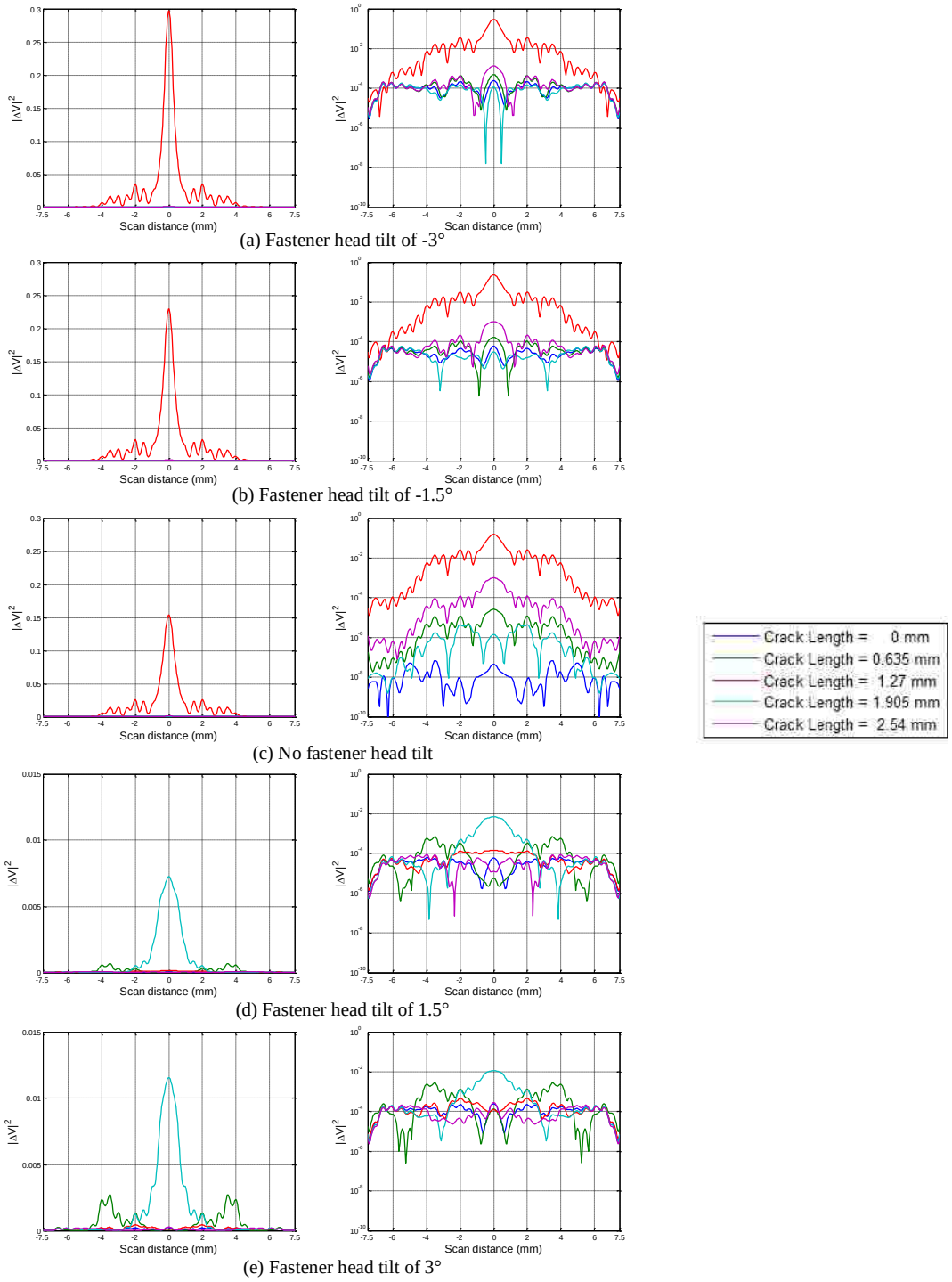

(a) Fastener head tilt of -3°

(b) Fastener head tilt of -1.5°

(c) No fastener head tilt

(d) Fastener head tilt of 1.5°

(e) Fastener head tilt of 3°

Figure 3. Simulated W-band results with various crack lengths, at a standoff distance of 0.5 mm, frequency of 110 GHz, and fastener head tilt of (from (a) to (e)): -3°, -1.5°, 0°, 1.5° and 3°, in linear (left) and logarithmic scales (right).

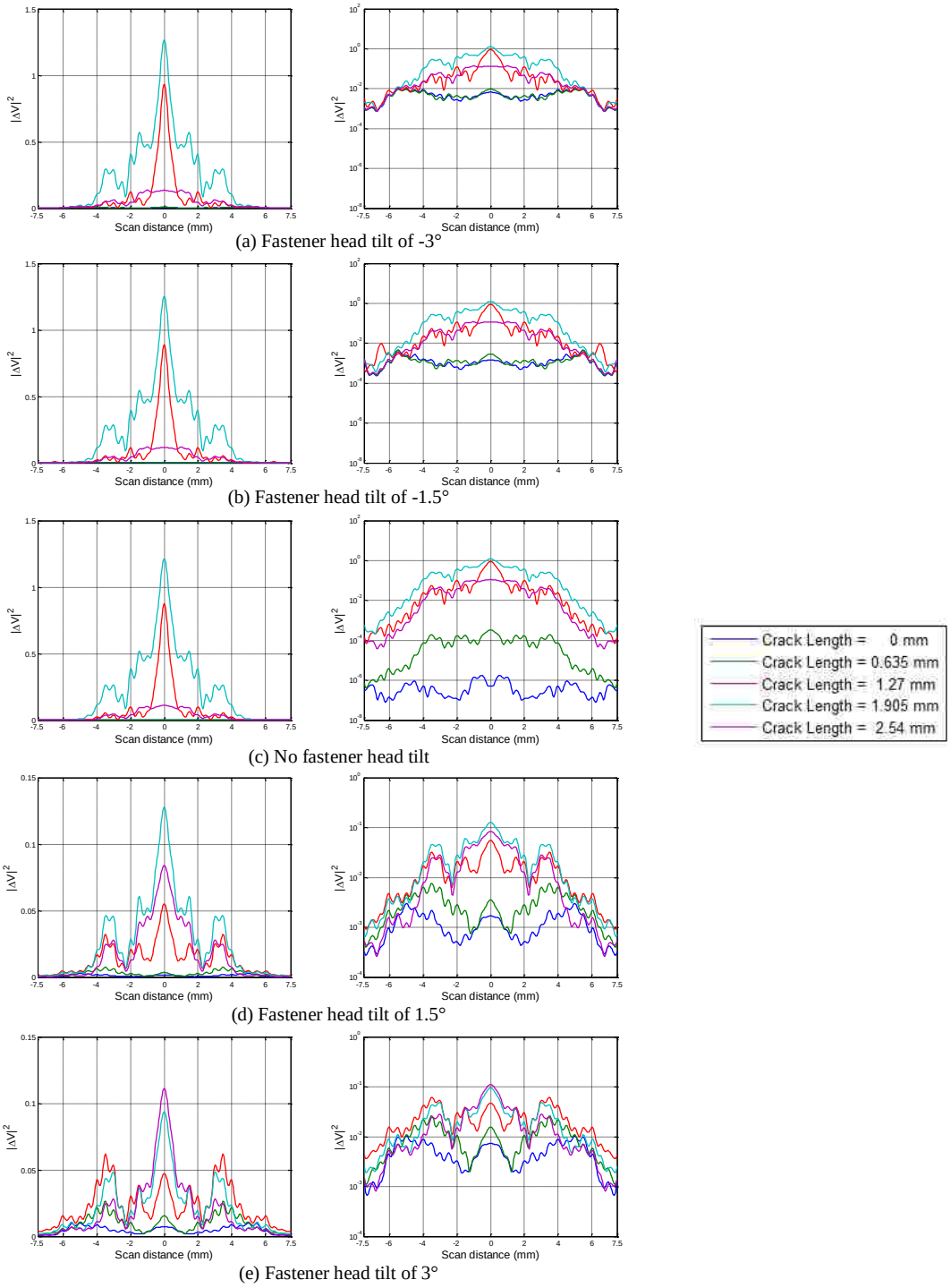

(a) Fastener head tilt of -3°

(b) Fastener head tilt of -1.5°

(c) No fastener head tilt

(d) Fastener head tilt of 1.5°

(e) Fastener head tilt of 3°

Figure 4. Simulated W-band wideband results with various crack lengths, at a standoff distance of 0.5 mm, and fastener head tilt of (from (a) to (e)): -3°, -1.5°, 0°, 1.5° and 3°, in linear (left) and logarithmic scales (right).

Figures 5 through 8 represent the simulated results at standoff distance of 1 mm. Among these figures, Figures 5 through 7 show the selected single-frequency responses and Figure 8 shows the wideband responses of the W-band differential probe. The results are provided in both linear and logarithmic scales. Note the scales may not be the same for the sub-figures.

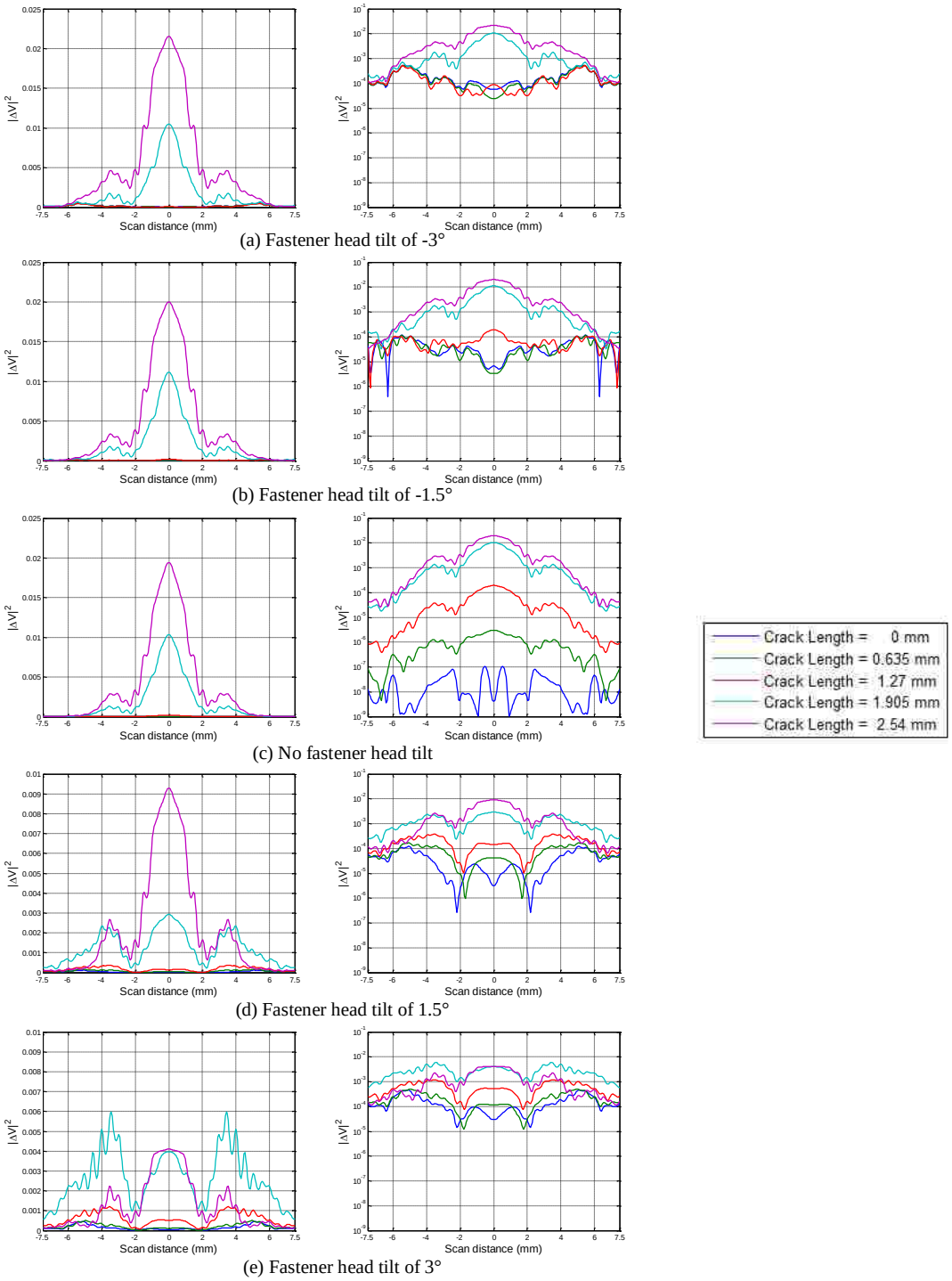

(a) Fastener head tilt of -3°

(b) Fastener head tilt of -1.5°

(c) No fastener head tilt

(d) Fastener head tilt of 1.5°

(e) Fastener head tilt of 3°

Figure 5. Simulated W-band results with various crack lengths, at a standoff distance of 1 mm, frequency of 75 GHz, and fastener head tilt of (from (a) to (e)): -3°, -1.5°, 0°, 1.5° and 3°, in linear (left) and logarithmic scales (right).

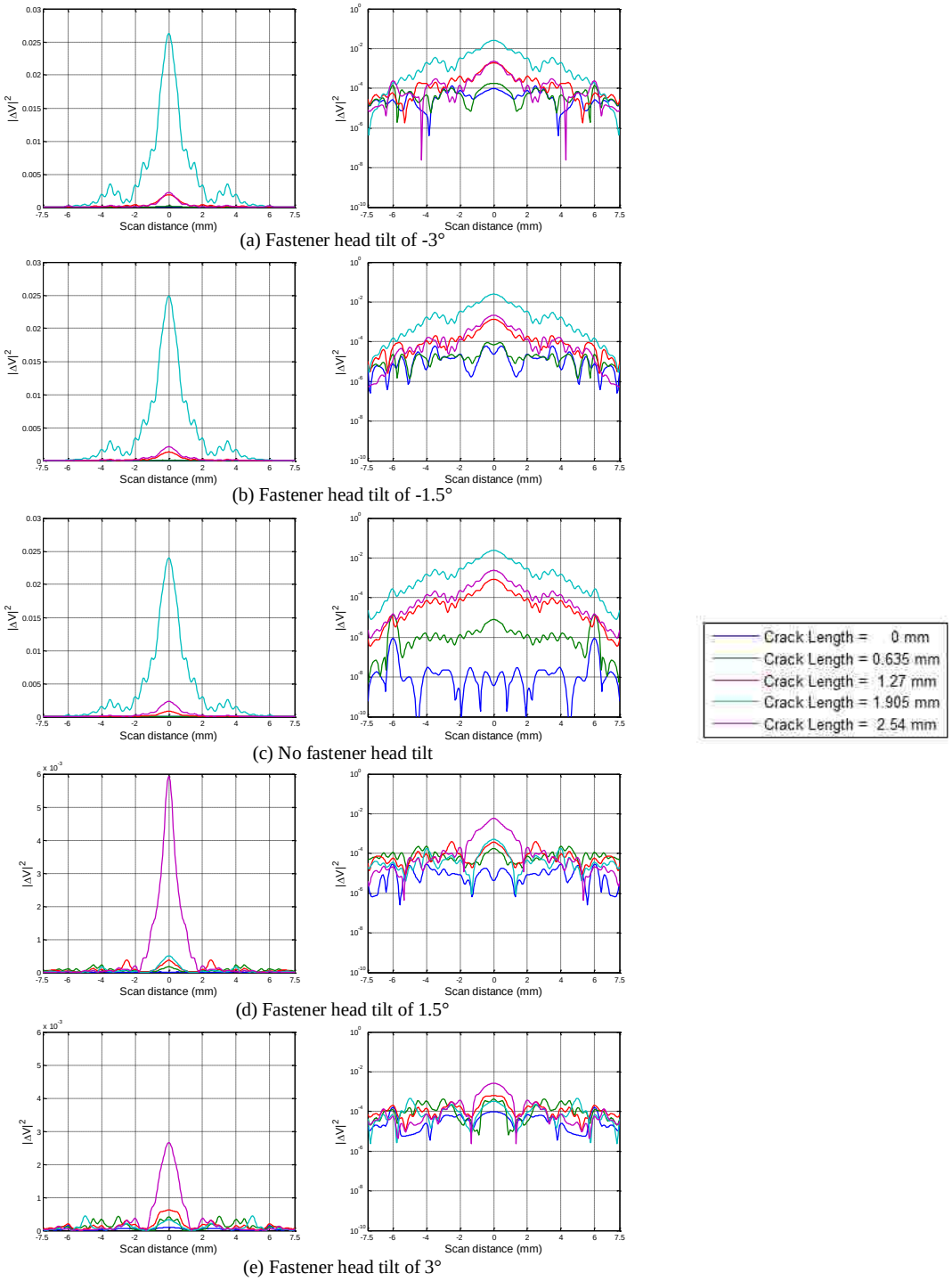

(a) Fastener head tilt of -3°

(b) Fastener head tilt of -1.5°

(c) No fastener head tilt

(d) Fastener head tilt of 1.5°

(e) Fastener head tilt of 3°

Figure 6. Simulated W-band results with various crack lengths, at a standoff distance of 1 mm, frequency of 87.25 GHz, and fastener head tilt of (from (a) to (e)): -3°, -1.5°, 0°, 1.5° and 3°, in linear (left) and logarithmic scales (right).

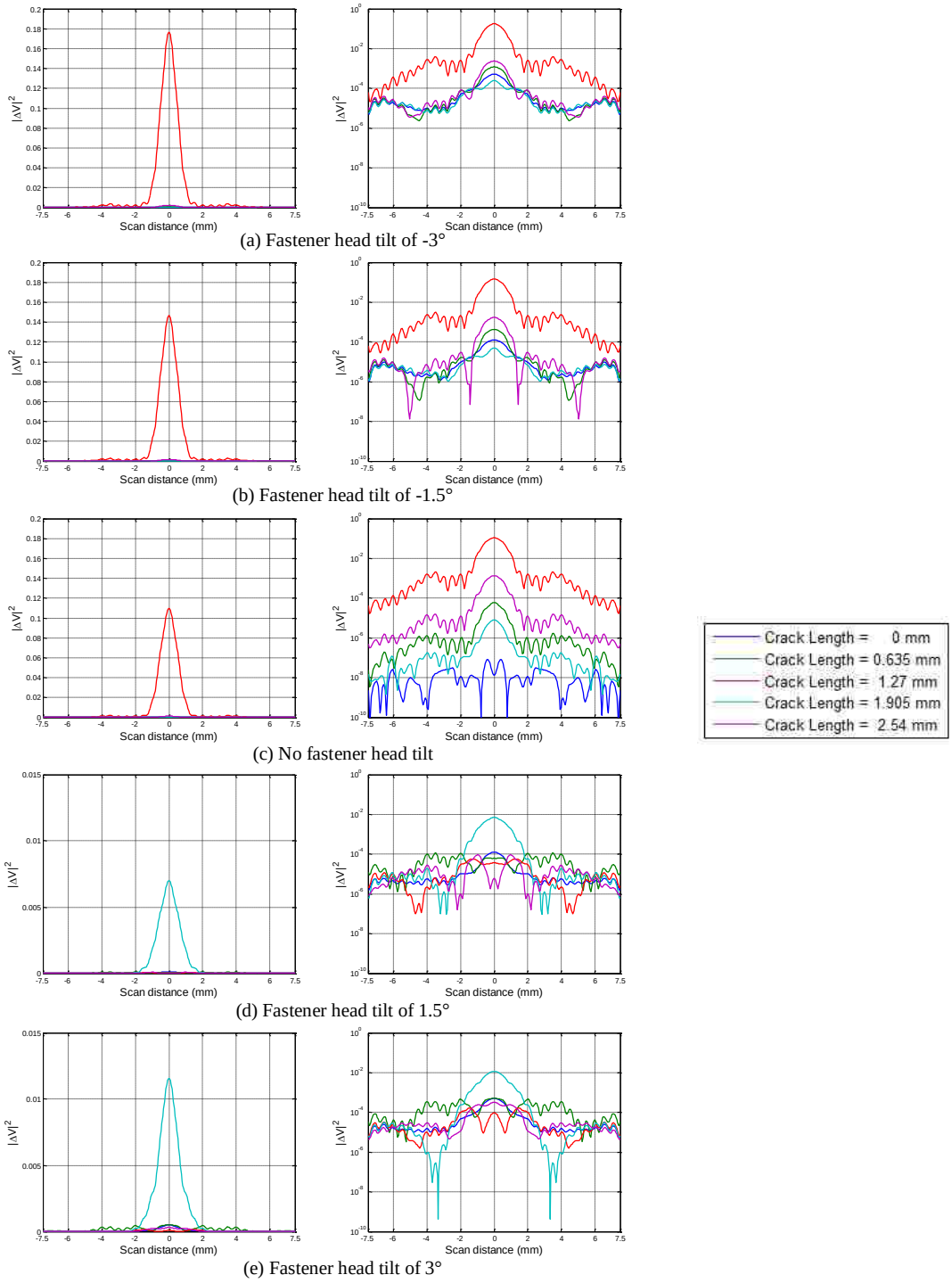

(a) Fastener head tilt of -3°

(b) Fastener head tilt of -1.5°

(c) No fastener head tilt

(d) Fastener head tilt of 1.5°

(e) Fastener head tilt of 3°

Figure 7. Simulated W-band results with various crack lengths, at a standoff distance of 1 mm, frequency of 110 GHz, and fastener head tilt of (from (a) to (e)): -3°, -1.5°, 0°, 1.5° and 3°, in linear (left) and logarithmic scales (right).

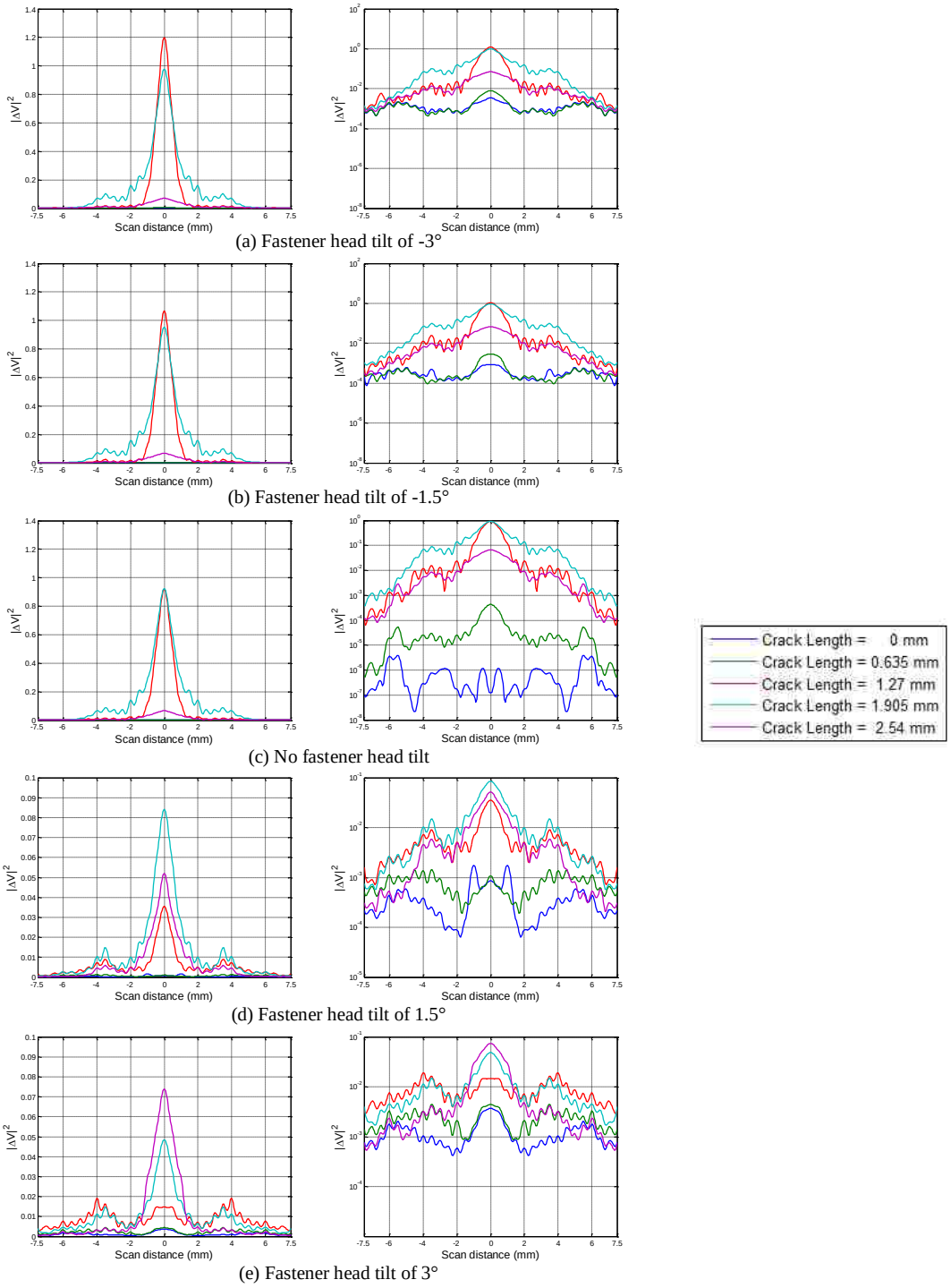

(a) Fastener head tilt of -3°

(b) Fastener head tilt of -1.5°

(c) No fastener head tilt

(d) Fastener head tilt of 1.5°

(e) Fastener head tilt of 3°

Figure 8. Simulated W-band wideband results with various crack lengths, at a standoff distance of 1 mm, and fastener head tilt of (from (a) to (e)): -3°, -1.5°, 0°, 1.5° and 3°, in linear (left) and logarithmic scales (right).

APPENDIX D.
ADDITIONAL FIGURES OF SIMULATED RESULTS (EFFECT OF PAINT THICKNESS)

This appendix provides the complete simulated scan results (both selected single-frequency and wideband responses) for Section 3.4 – Effect of Paint Thickness.

Figures 1 through 8 represent the simulated results at standoff distance of 0.5 mm. Among these figures, Figures 1 through 6 show the selected single-frequency responses (in both linear and logarithmic scales) and Figures 7 and 8 show the wideband responses of the W-band differential probe (in both linear and logarithmic scales). Note the scales may not be the same for the sub-figures.

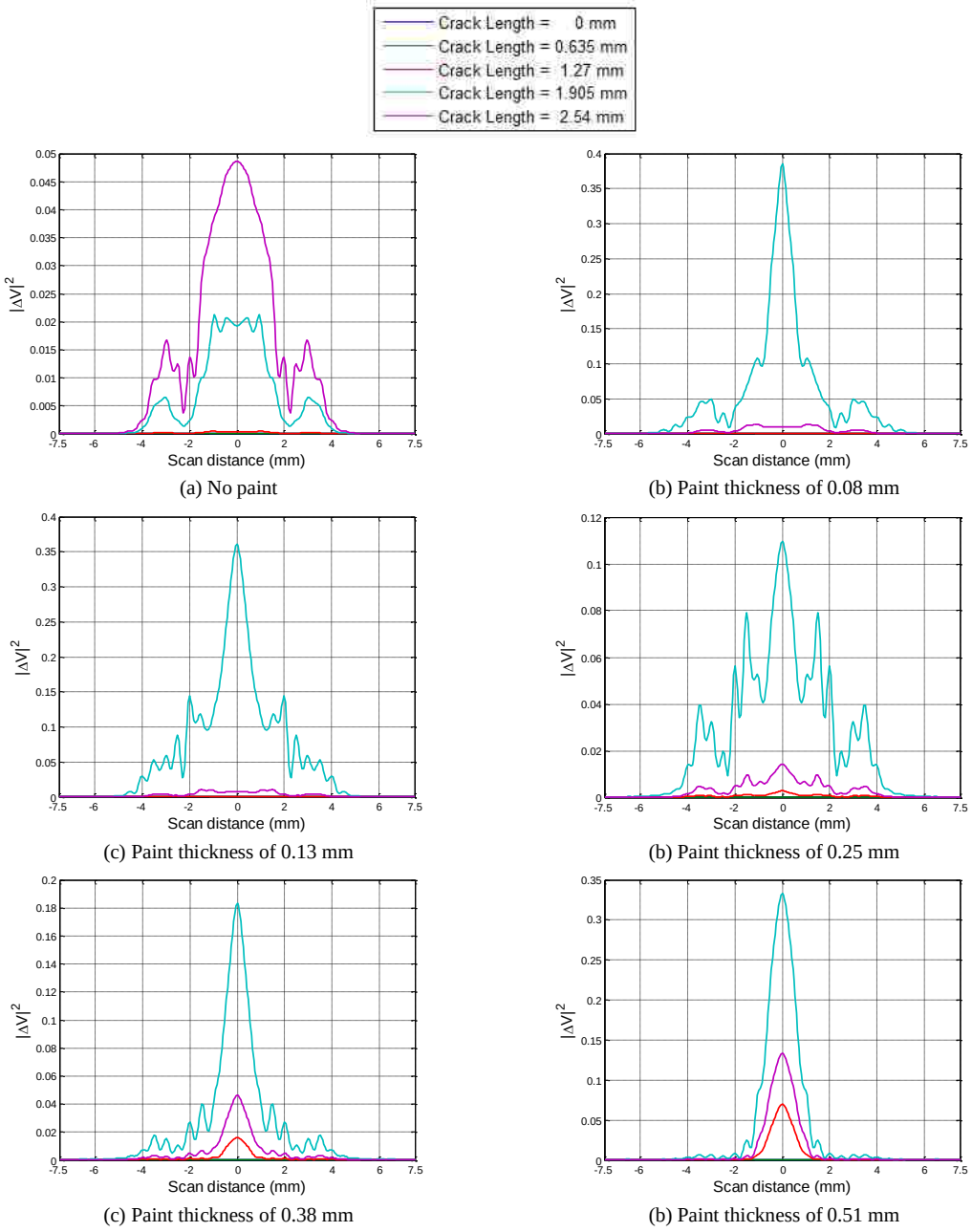

(a) No paint

(b) Paint thickness of 0.08 mm

(c) Paint thickness of 0.13 mm

(b) Paint thickness of 0.25 mm

(c) Paint thickness of 0.38 mm

(b) Paint thickness of 0.51 mm

Figure 1. Simulated W-band results with various crack lengths, at a standoff distance of 0.5 mm, frequency of 75 GHz, and paint thickness of (from (a) to (f)): 0, 0.08, 0.13, 0.25, 0.38, and 0.51 mm, in linear scales.

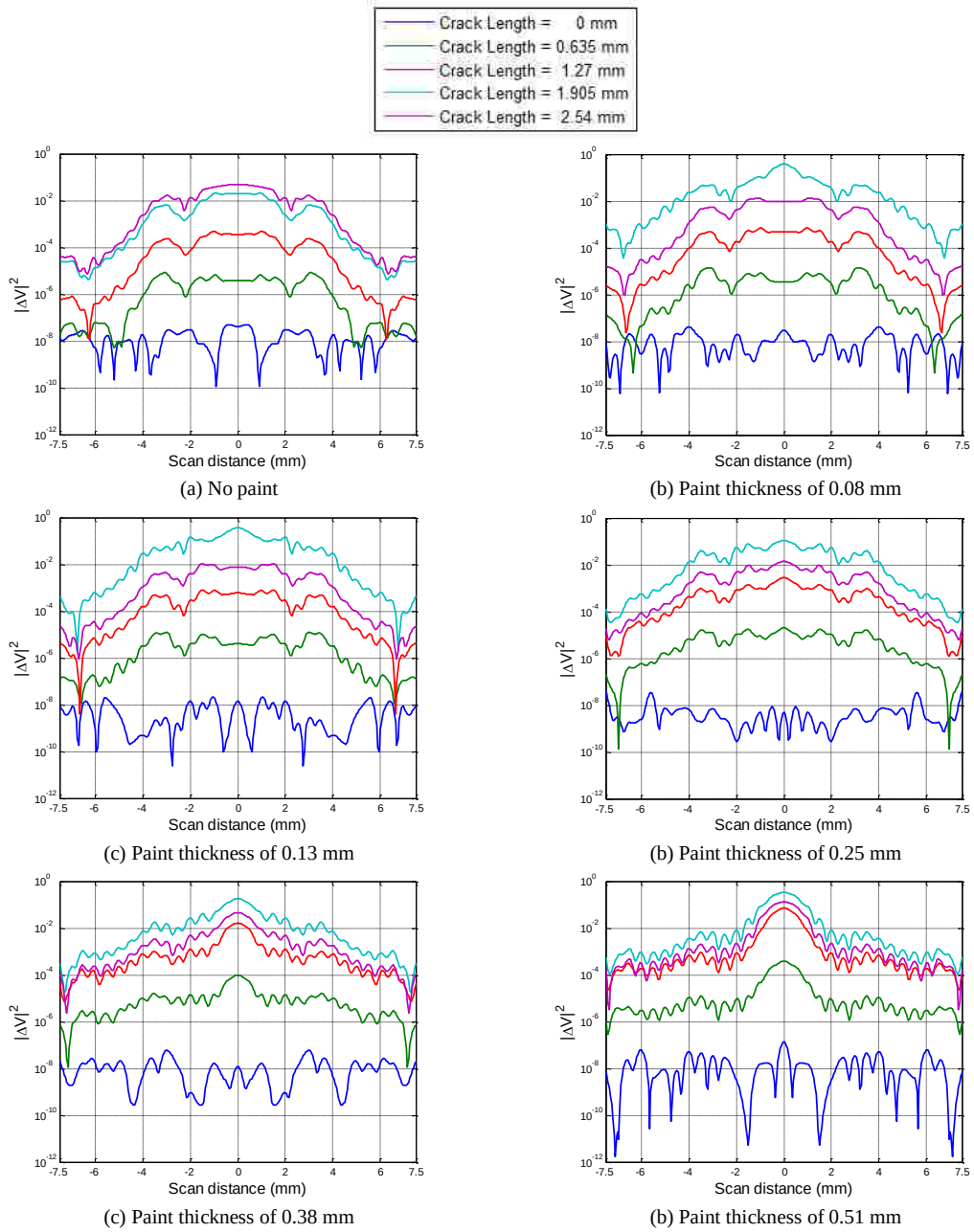

(a) No paint

(b) Paint thickness of 0.08 mm

(c) Paint thickness of 0.13 mm

(b) Paint thickness of 0.25 mm

(c) Paint thickness of 0.38 mm

(b) Paint thickness of 0.51 mm

Figure 2. Simulated W-band results with various crack lengths, at a standoff distance of 0.5 mm, frequency of 75 GHz, and paint thickness of (from (a) to (f)): 0, 0.08, 0.13, 0.25, 0.38, and 0.51 mm, in logarithmic scales.

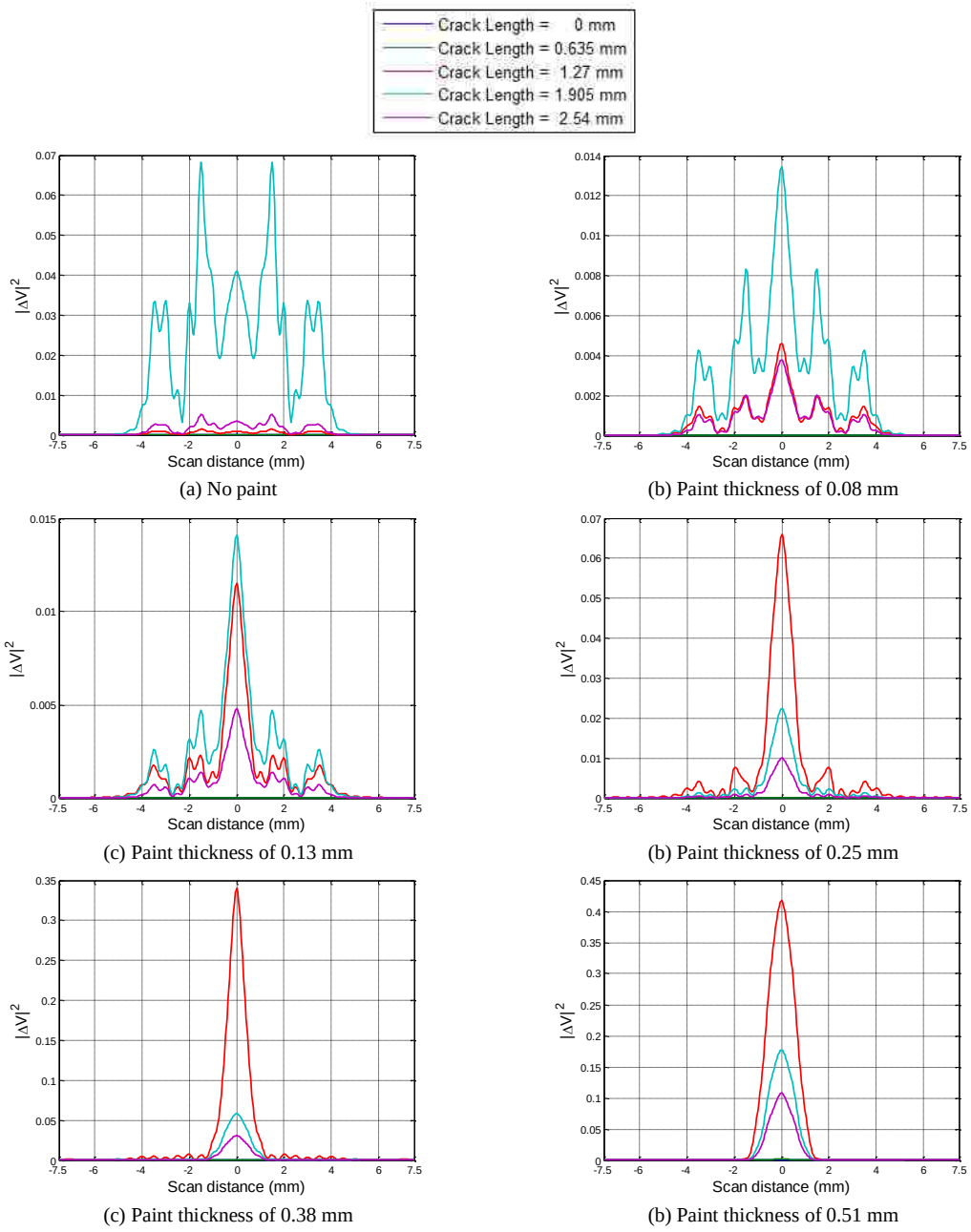

(a) No paint

(b) Paint thickness of 0.08 mm

(c) Paint thickness of 0.13 mm

(b) Paint thickness of 0.25 mm

(c) Paint thickness of 0.38 mm

(b) Paint thickness of 0.51 mm

Figure 3. Simulated W-band results with various crack lengths, at a standoff distance of 0.5 mm, frequency of 87.25 GHz, and paint thickness of (from (a) to (f)): 0, 0.08, 0.13, 0.25, 0.38, and 0.51 mm, in linear scales.

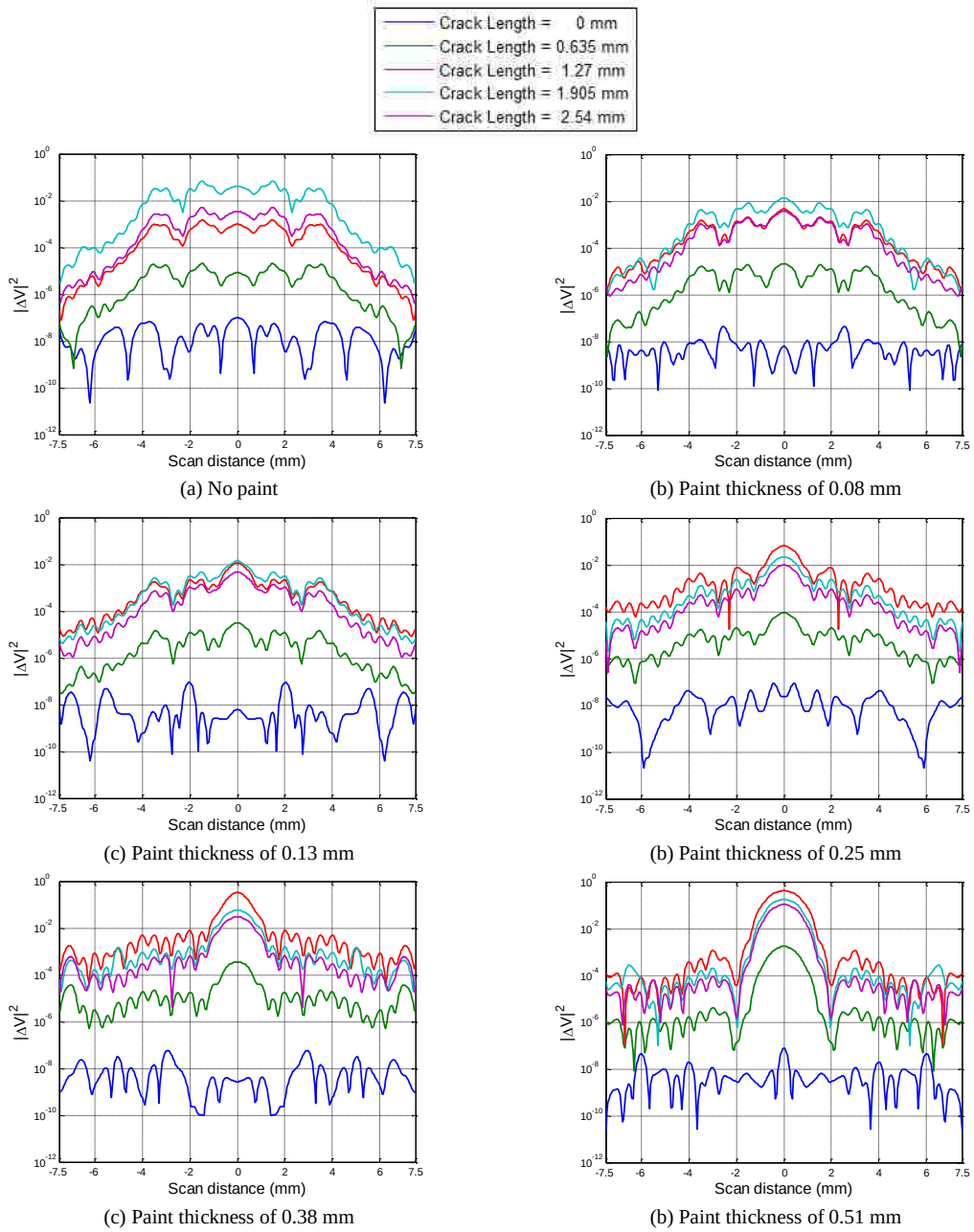

(a) No paint

(b) Paint thickness of 0.08 mm

(c) Paint thickness of 0.13 mm

(b) Paint thickness of 0.25 mm

(c) Paint thickness of 0.38 mm

(b) Paint thickness of 0.51 mm

Figure 4. Simulated W-band results with various crack lengths, at a standoff distance of 0.5 mm, frequency of 87.25 GHz, and paint thickness of (from (a) to (f)): 0, 0.08, 0.13, 0.25, 0.38, and 0.51 mm, in logarithmic scales.

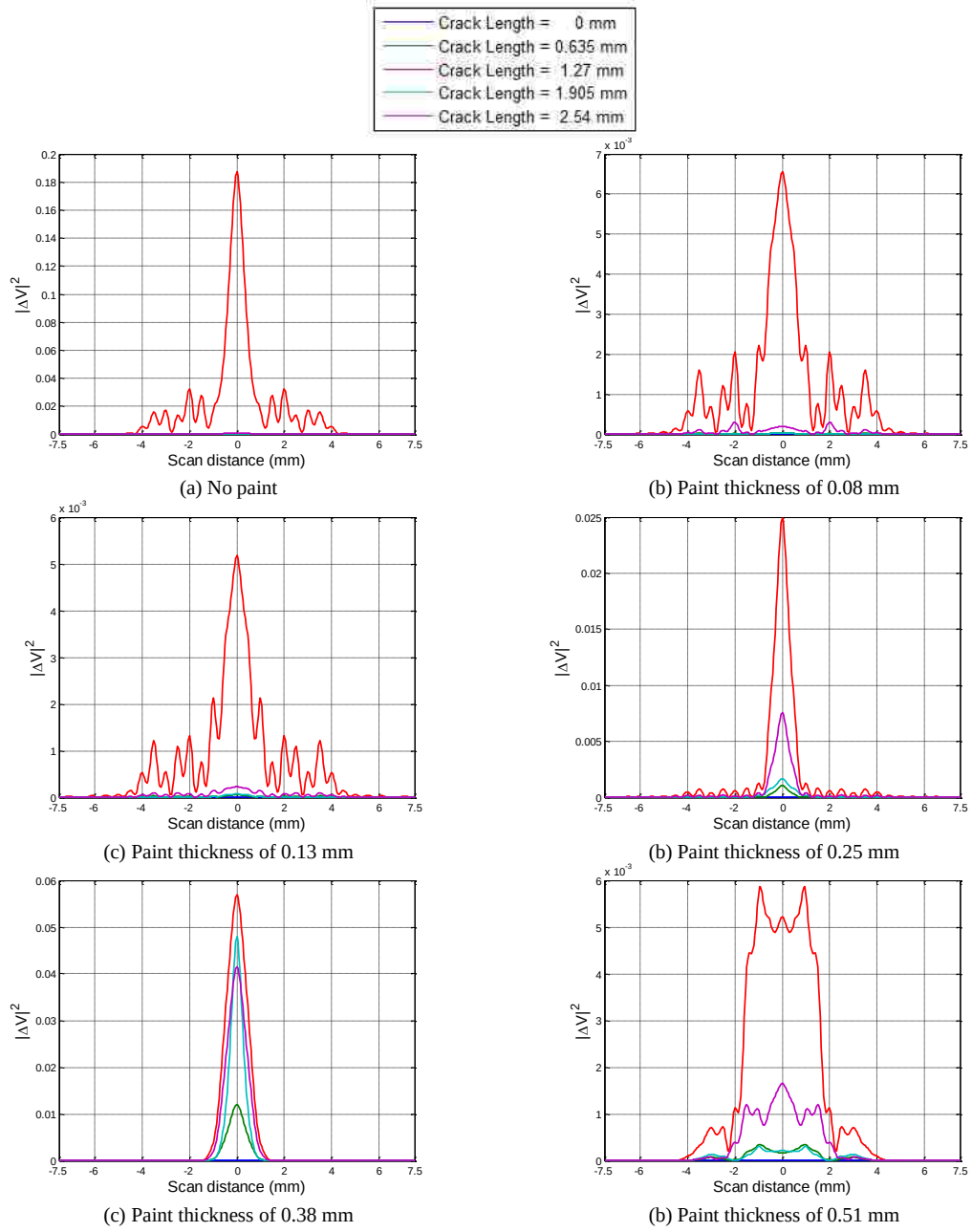

(a) No paint

(b) Paint thickness of 0.08 mm

(c) Paint thickness of 0.13 mm

(b) Paint thickness of 0.25 mm

(c) Paint thickness of 0.38 mm

(b) Paint thickness of 0.51 mm

Figure 5. Simulated W-band results with various crack lengths, at a standoff distance of 0.5 mm, frequency of 110 GHz, and paint thickness of (from (a) to (f)): 0, 0.08, 0.13, 0.25, 0.38, and 0.51 mm, in linear scales.

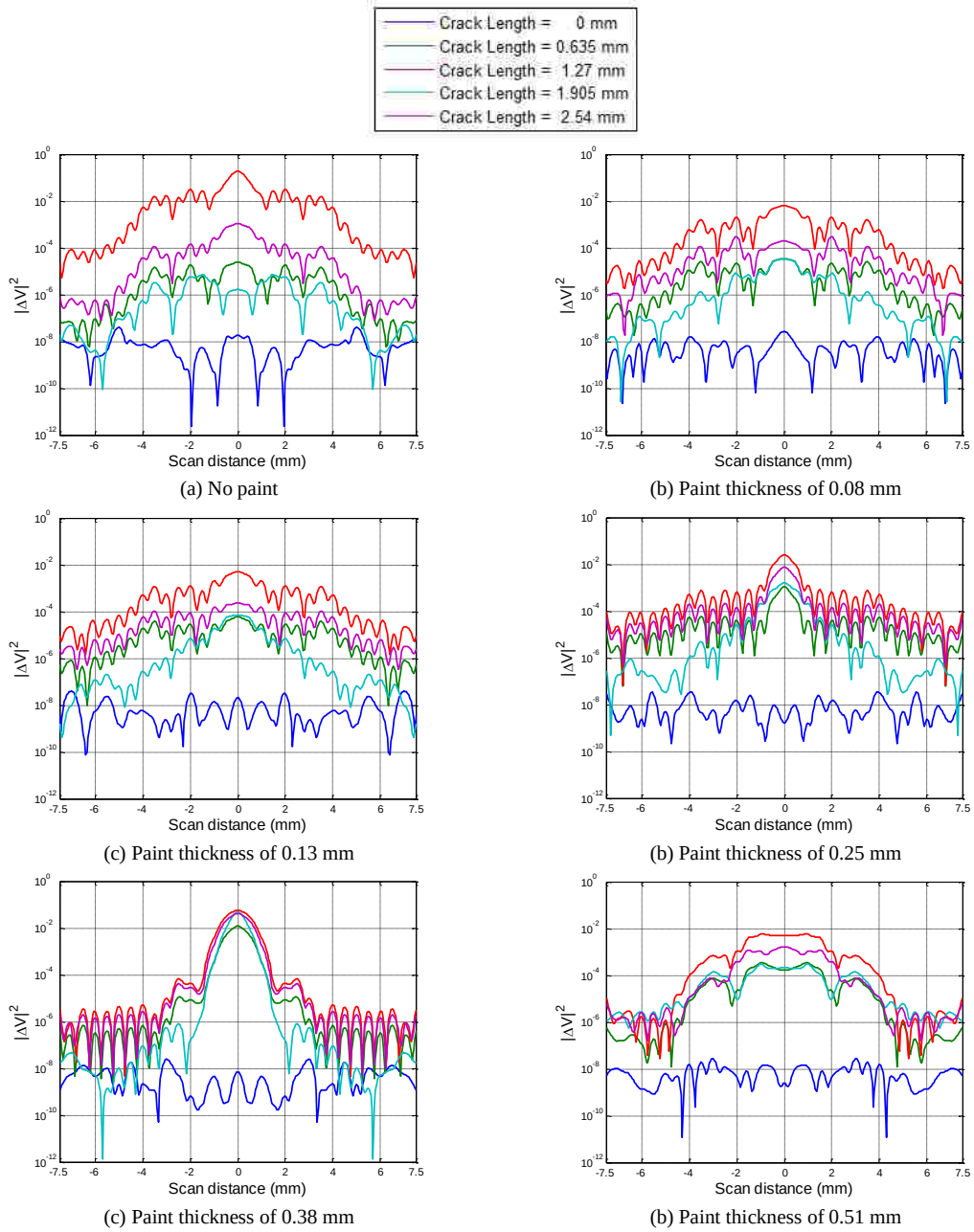

(a) No paint

(b) Paint thickness of 0.08 mm

(c) Paint thickness of 0.13 mm

(b) Paint thickness of 0.25 mm

(c) Paint thickness of 0.38 mm

(b) Paint thickness of 0.51 mm

Figure 6. Simulated W-band results with various crack lengths, at a standoff distance of 0.5 mm, frequency of 110 GHz, and paint thickness of (from (a) to (f)): 0, 0.08, 0.13, 0.25, 0.38, and 0.51 mm, in logarithmic scales.

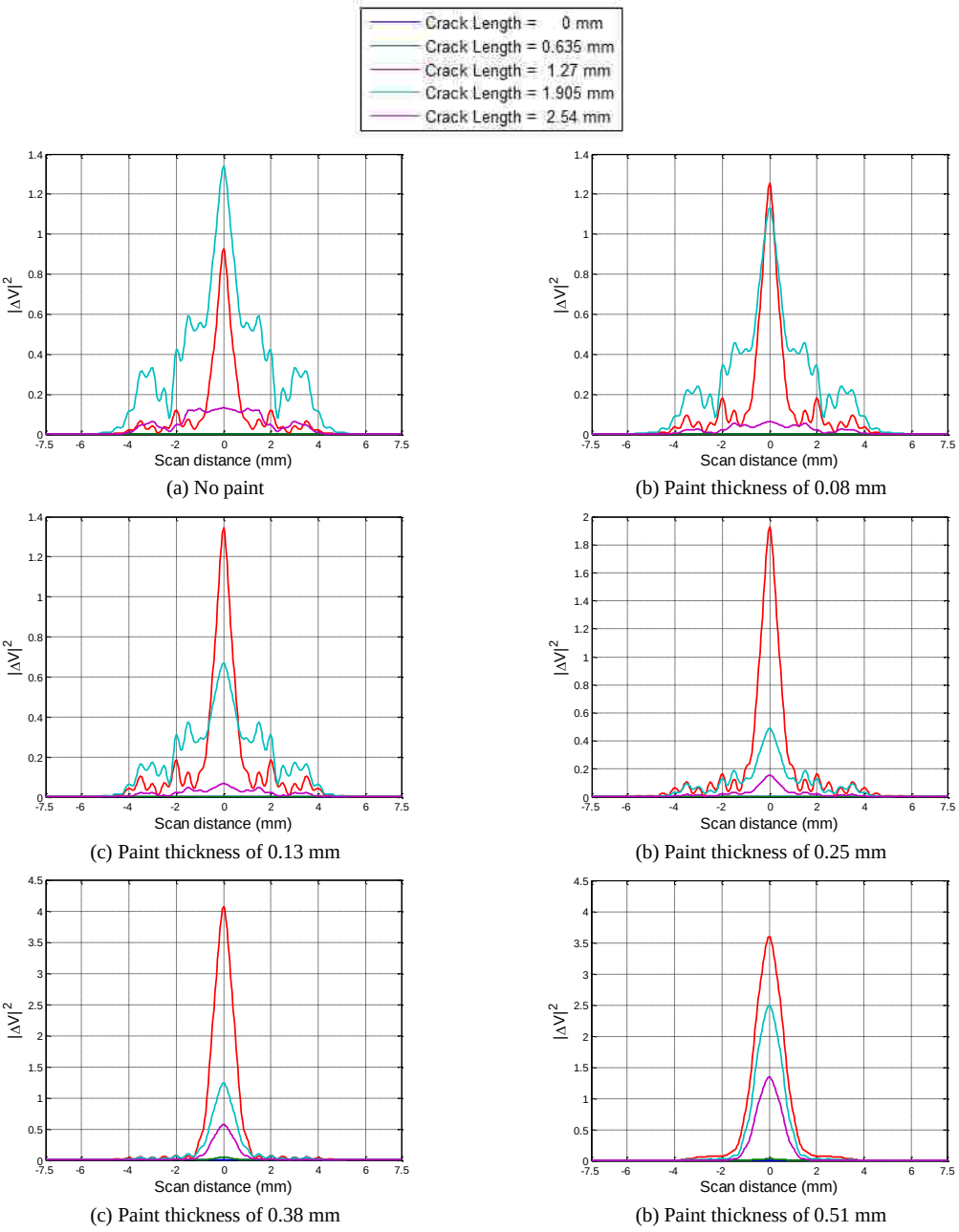

(a) No paint

(b) Paint thickness of 0.08 mm

(c) Paint thickness of 0.13 mm

(b) Paint thickness of 0.25 mm

(c) Paint thickness of 0.38 mm

(b) Paint thickness of 0.51 mm

Figure 7. Simulated W-band wideband results with various crack lengths, at a standoff distance of 0.5 mm, and paint thickness of (from (a) to (f)): 0, 0.08, 0.13, 0.25, 0.38, and 0.51 mm, in linear scales.

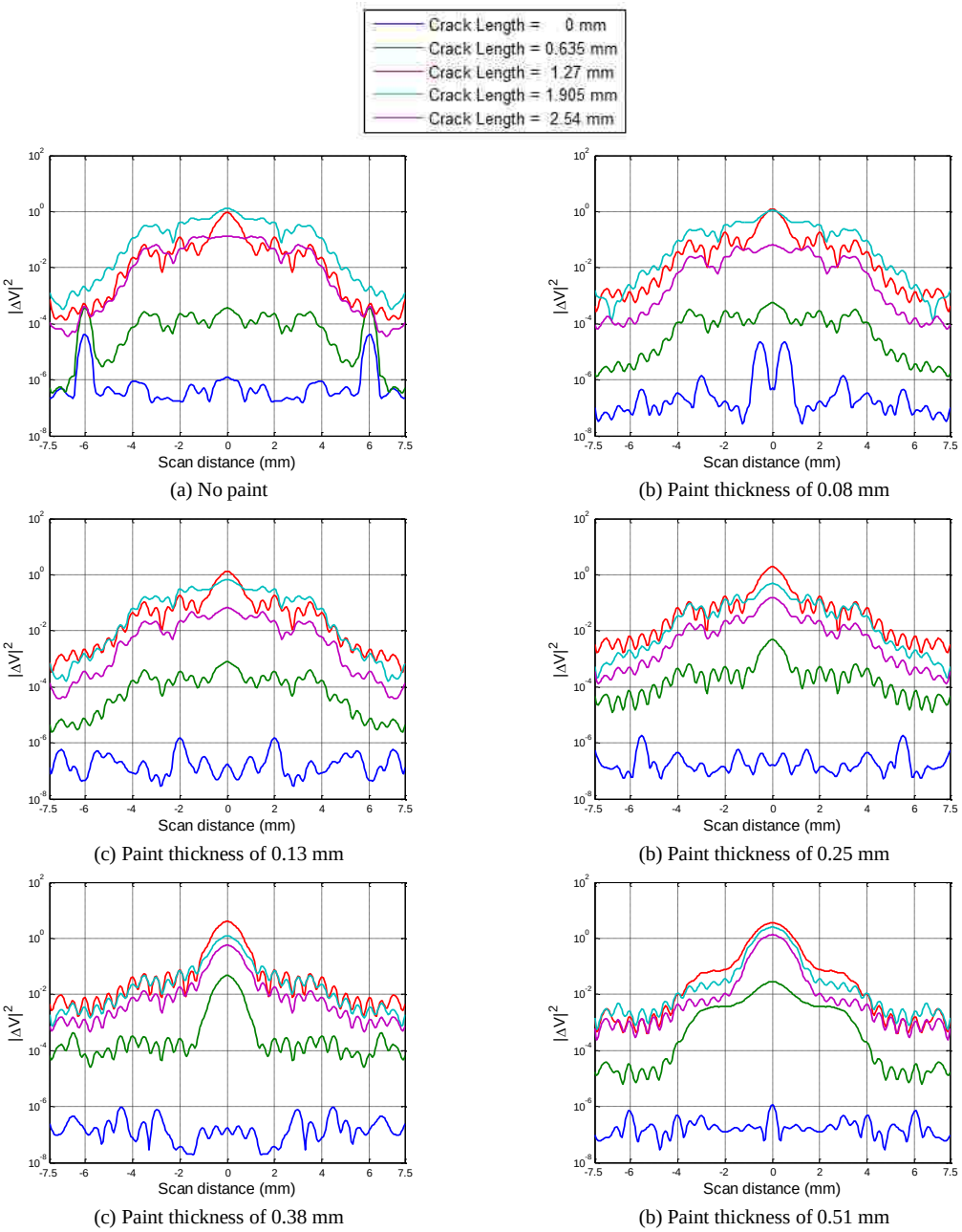

(a) No paint

(b) Paint thickness of 0.08 mm

(c) Paint thickness of 0.13 mm

(b) Paint thickness of 0.25 mm

(c) Paint thickness of 0.38 mm

(b) Paint thickness of 0.51 mm

Figure 8. Simulated W-band wideband results with various crack lengths, at a standoff distance of 0.5 mm, and paint thickness of (from (a) to (f)): 0, 0.08, 0.13, 0.25, 0.38, and 0.51 mm, in logarithmic scales.

Figures 9 through 16 represent the simulated results at standoff distance of 1 mm. Among these figures, Figures 9 through 14 show the selected single-frequency responses (in both linear and logarithmic scales) and Figures 15 and 16 show the wideband responses of the W-band differential probe (in both linear and logarithmic scales). Note the scales may not be the same for the sub-figures.

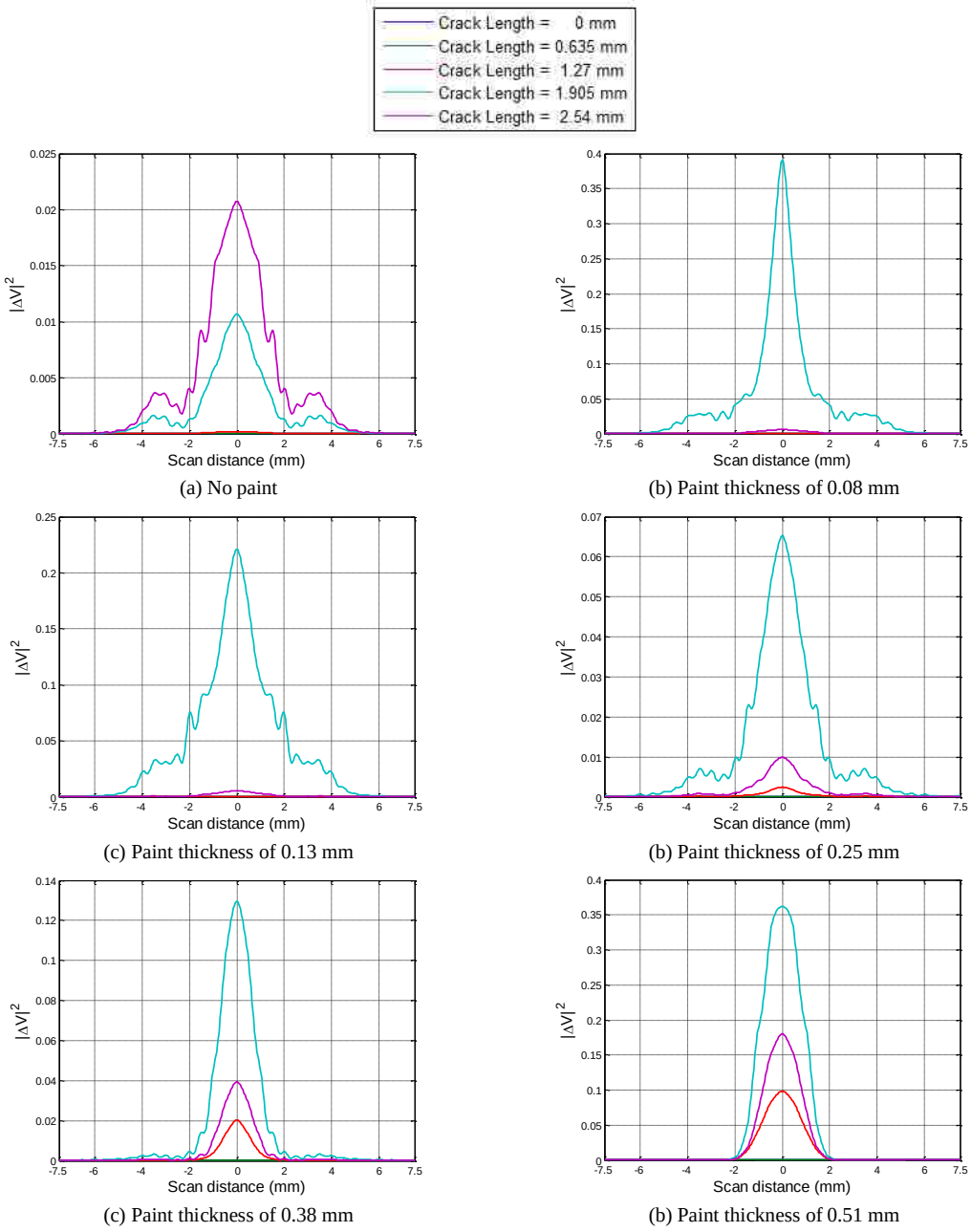

(a) No paint

(b) Paint thickness of 0.08 mm

(c) Paint thickness of 0.13 mm

(b) Paint thickness of 0.25 mm

(c) Paint thickness of 0.38 mm

(b) Paint thickness of 0.51 mm

Figure 9. Simulated W-band results with various crack lengths, at a standoff distance of 1 mm, frequency of 75 GHz, and paint thickness of (from (a) to (f)): 0, 0.08, 0.13, 0.25, 0.38, and 0.51 mm, in linear scales.

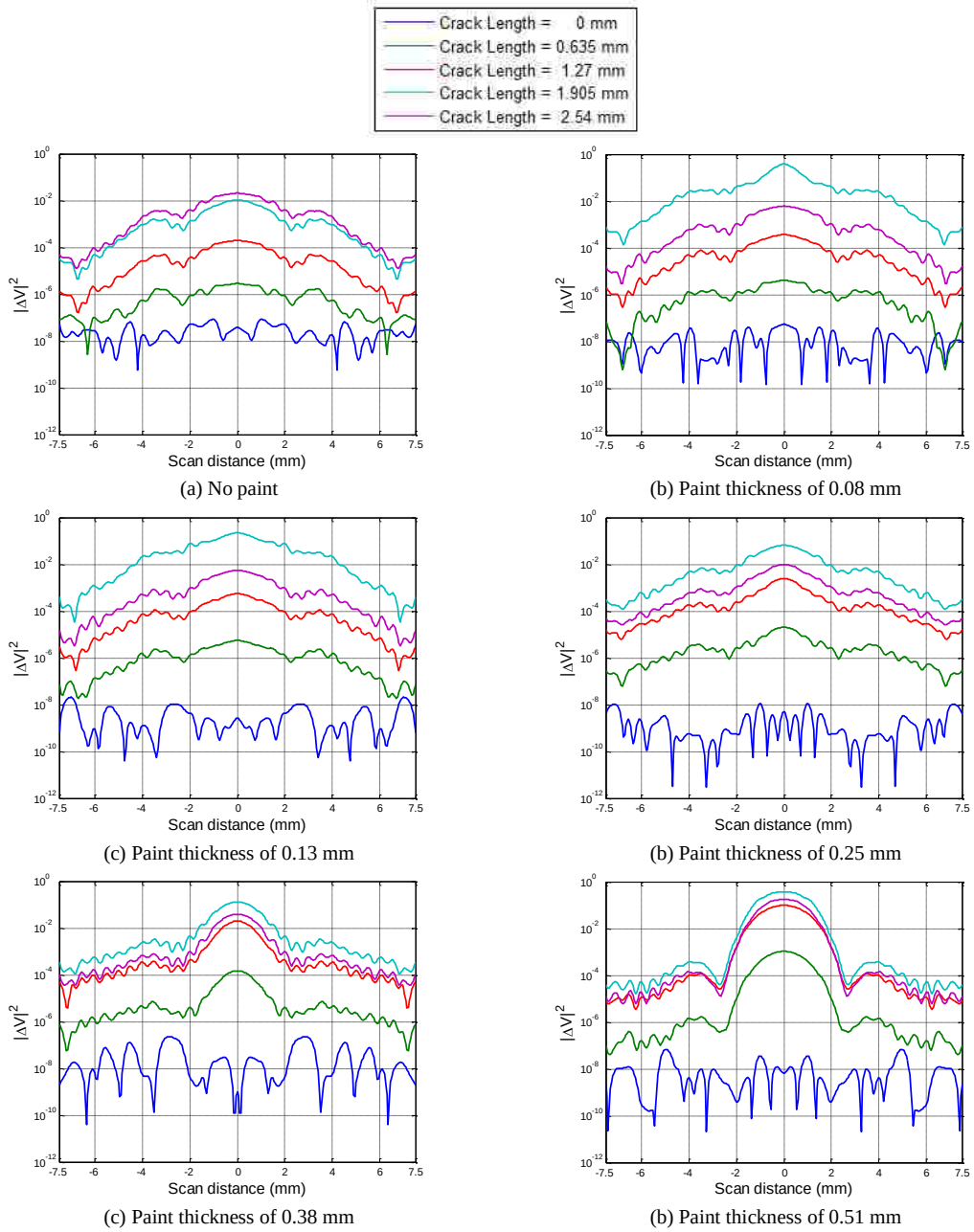

(a) No paint

(b) Paint thickness of 0.08 mm

(c) Paint thickness of 0.13 mm

(b) Paint thickness of 0.25 mm

(c) Paint thickness of 0.38 mm

(b) Paint thickness of 0.51 mm

Figure 10. Simulated W-band results with various crack lengths, at a standoff distance of 1 mm, frequency of 75 GHz, and paint thickness of (from (a) to (f)): 0, 0.08, 0.13, 0.25, 0.38, and 0.51 mm, in logarithmic scales.

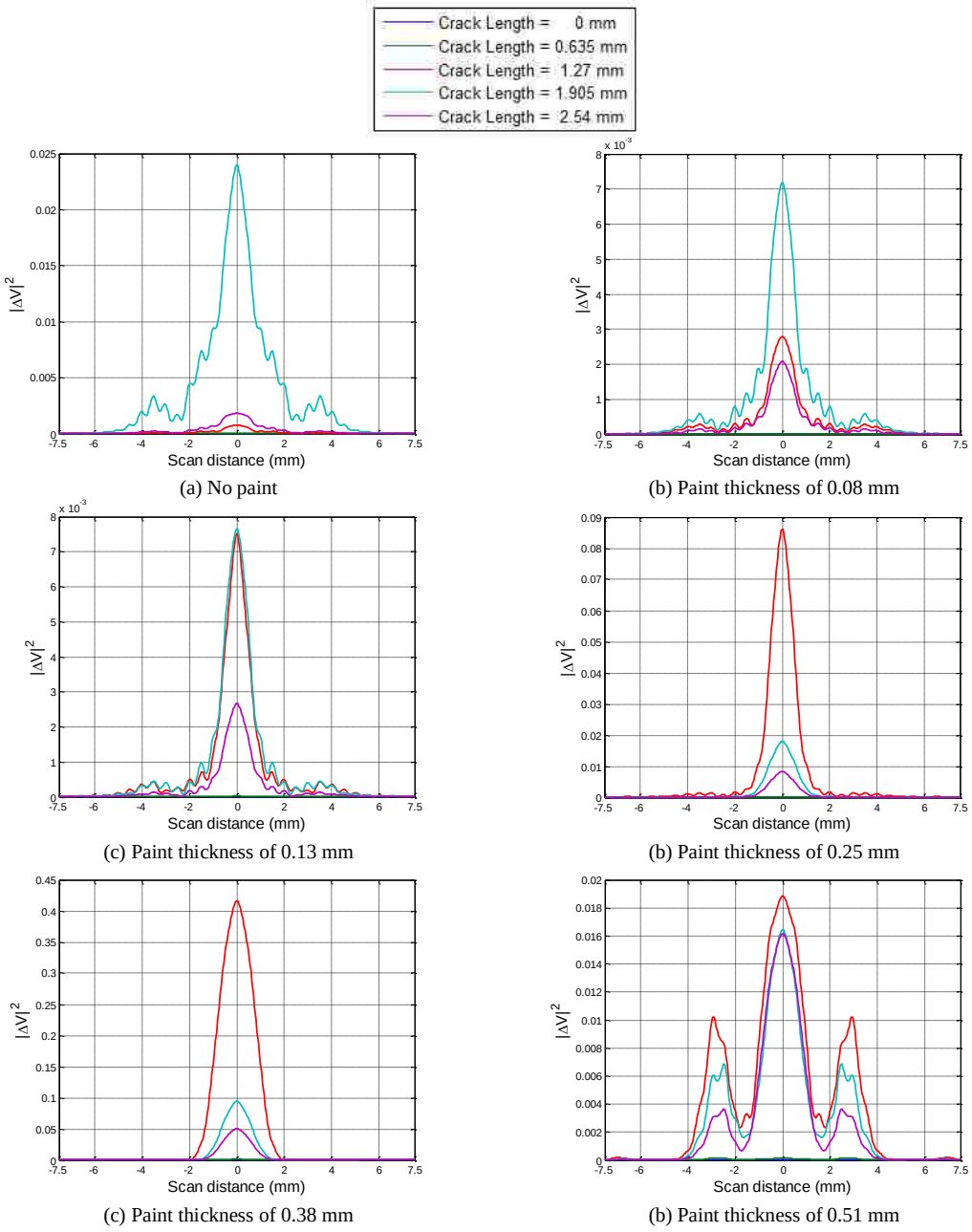

(a) No paint

(b) Paint thickness of 0.08 mm

(c) Paint thickness of 0.13 mm

(b) Paint thickness of 0.25 mm

(c) Paint thickness of 0.38 mm

(b) Paint thickness of 0.51 mm

Figure 11. Simulated W-band results with various crack lengths, at a standoff distance of 1 mm, frequency of 87.25 GHz, and paint thickness of (from (a) to (f)): 0, 0.08, 0.13, 0.25, 0.38, and 0.51 mm, in linear scales.

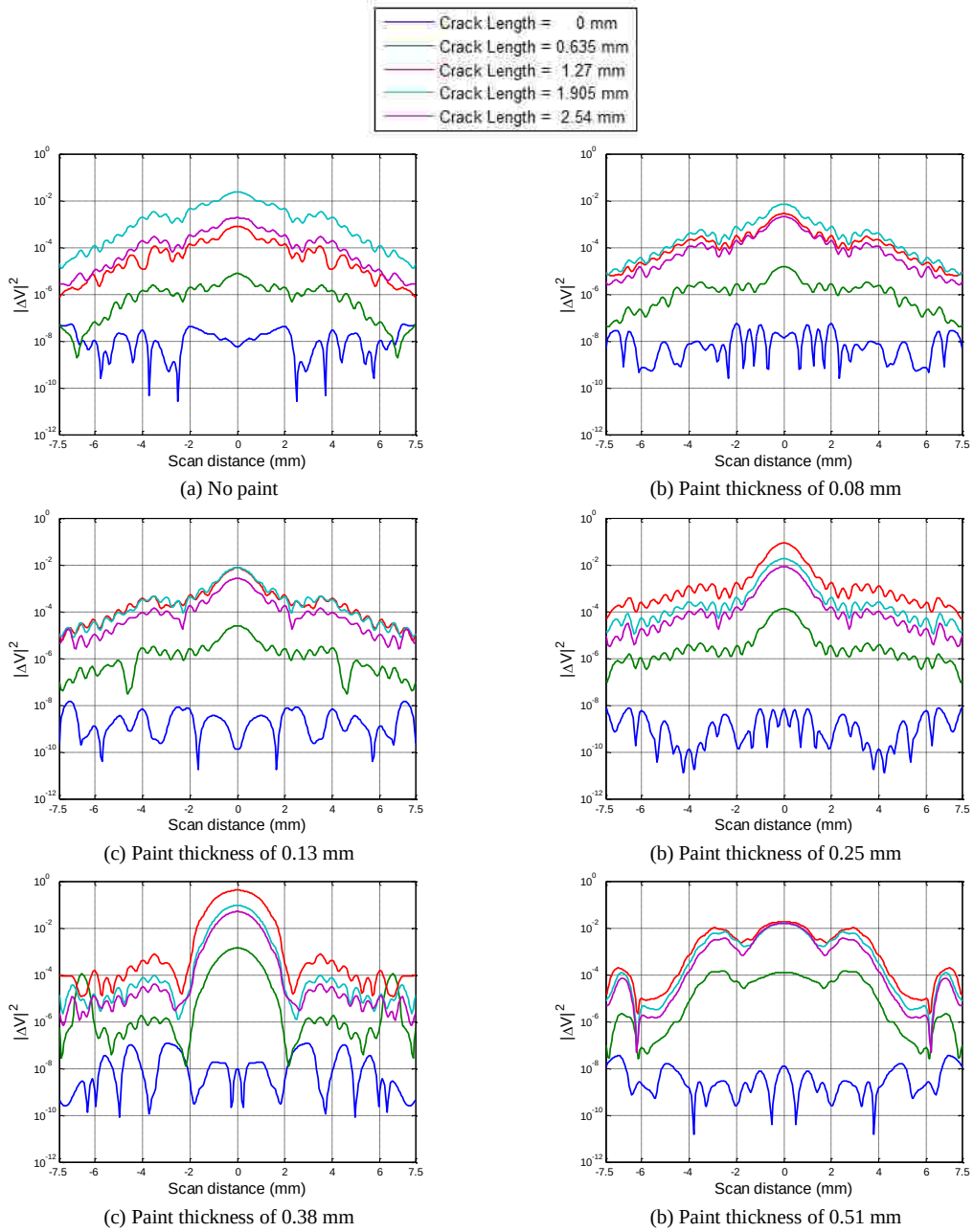

(a) No paint

(b) Paint thickness of 0.08 mm

(c) Paint thickness of 0.13 mm

(b) Paint thickness of 0.25 mm

(c) Paint thickness of 0.38 mm

(b) Paint thickness of 0.51 mm

Figure 12. Simulated W-band results with various crack lengths, at a standoff distance of 1 mm, frequency of 87.25 GHz, and paint thickness of (from (a) to (f)): 0, 0.08, 0.13, 0.25, 0.38, and 0.51 mm, in logarithmic scales.

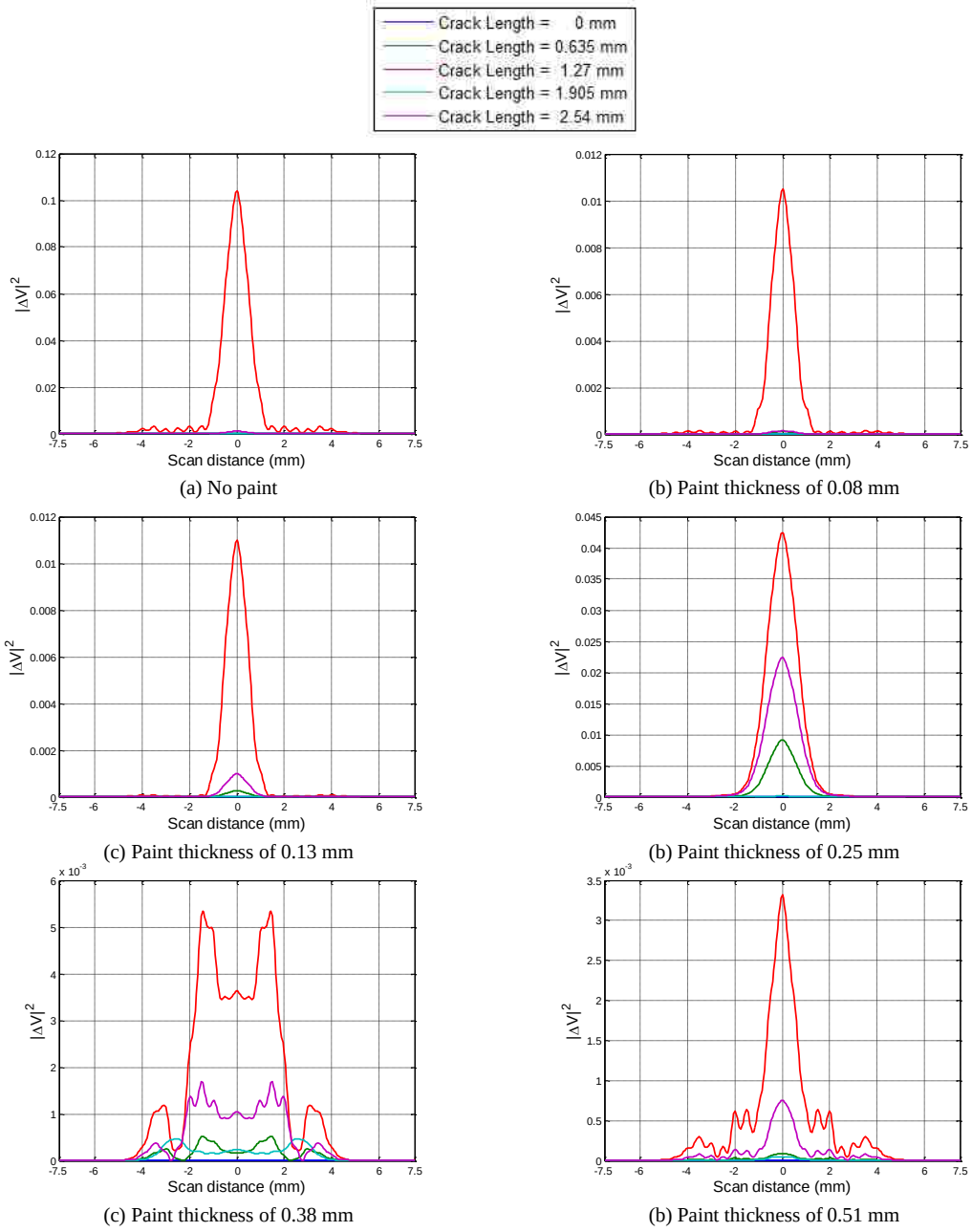

(a) No paint

(b) Paint thickness of 0.08 mm

(c) Paint thickness of 0.13 mm

(b) Paint thickness of 0.25 mm

(c) Paint thickness of 0.38 mm

(b) Paint thickness of 0.51 mm

Figure 13. Simulated W-band results with various crack lengths, at a standoff distance of 1 mm, frequency of 110 GHz, and paint thickness of (from (a) to (f)): 0, 0.08, 0.13, 0.25, 0.38, and 0.51 mm, in linear scales.

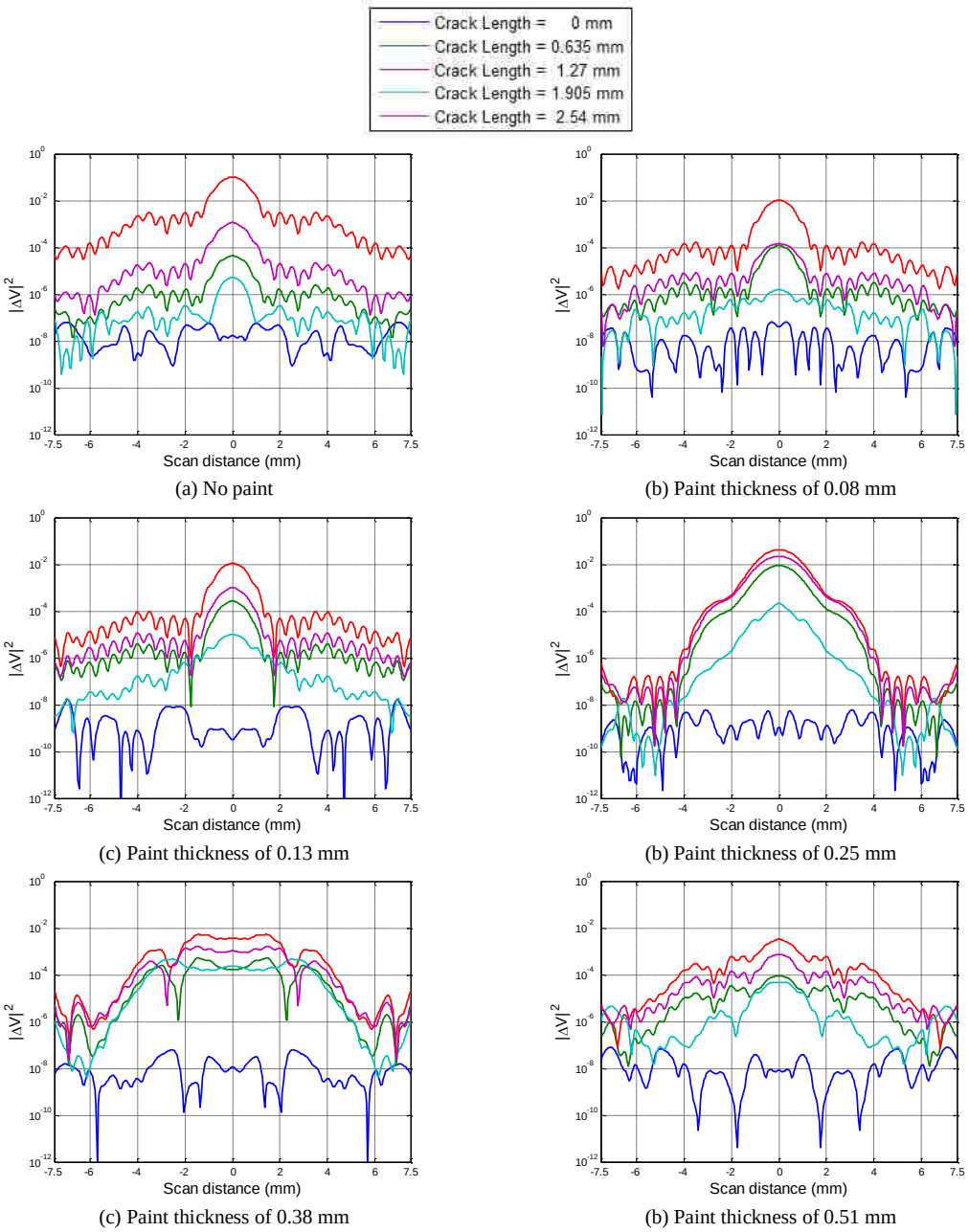

(a) No paint (b) Paint thickness of 0.08 mm

(c) Paint thickness of 0.13 mm (b) Paint thickness of 0.25 mm

(c) Paint thickness of 0.38 mm (b) Paint thickness of 0.51 mm

Figure 14. Simulated W-band results with various crack lengths, at a standoff distance of 1 mm, frequency of 110 GHz, and paint thickness of (from (a) to (f)): 0, 0.08, 0.13, 0.25, 0.38, and 0.51 mm, in logarithmic scales.

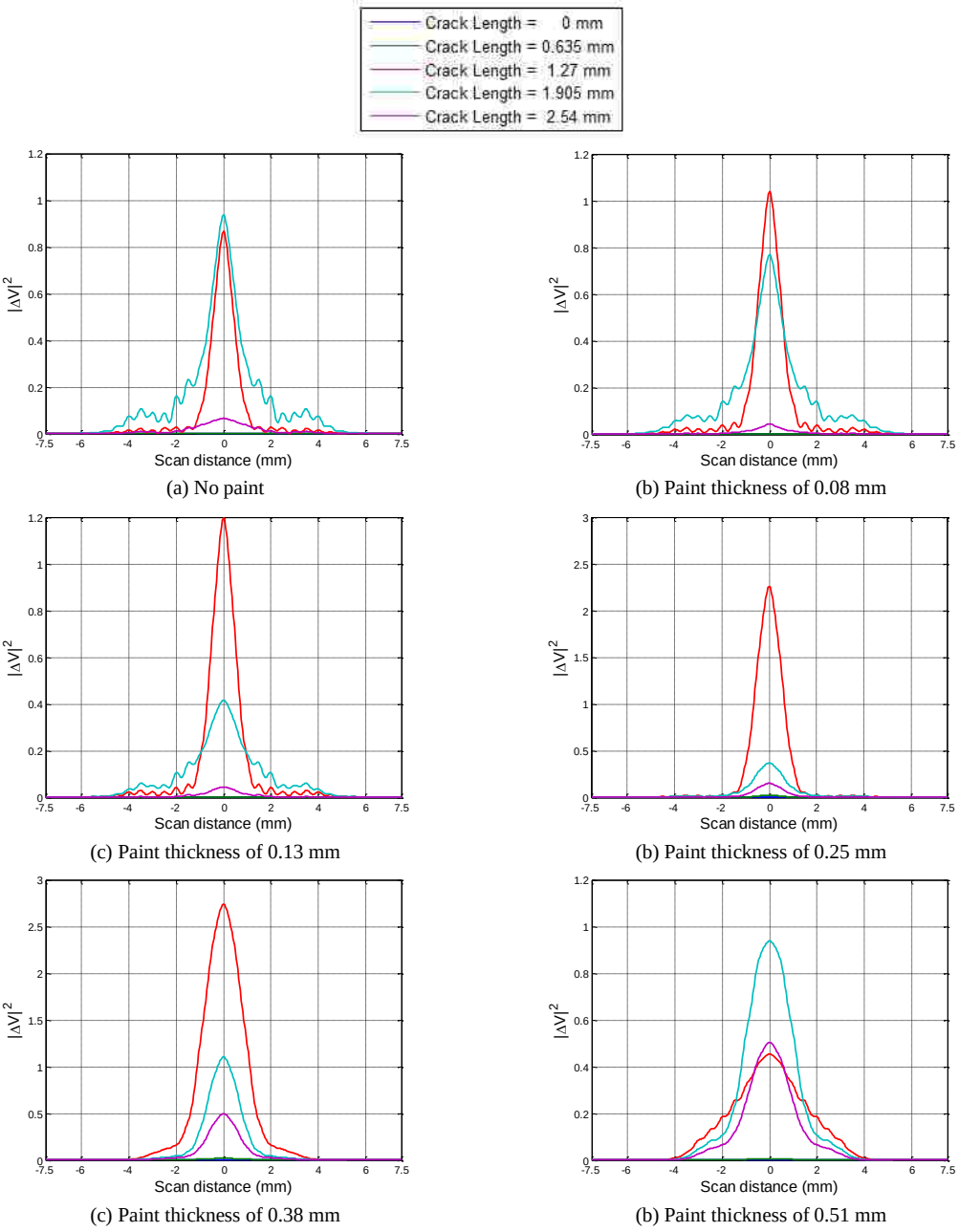

(a) No paint (b) Paint thickness of 0.08 mm

(c) Paint thickness of 0.13 mm (b) Paint thickness of 0.25 mm

(c) Paint thickness of 0.38 mm (b) Paint thickness of 0.51 mm

Figure 15. Simulated W-band wideband results with various crack lengths, at a standoff distance of 1 mm, and paint thickness of (from (a) to (f)): 0, 0.08, 0.13, 0.25, 0.38, and 0.51 mm, in linear scales.

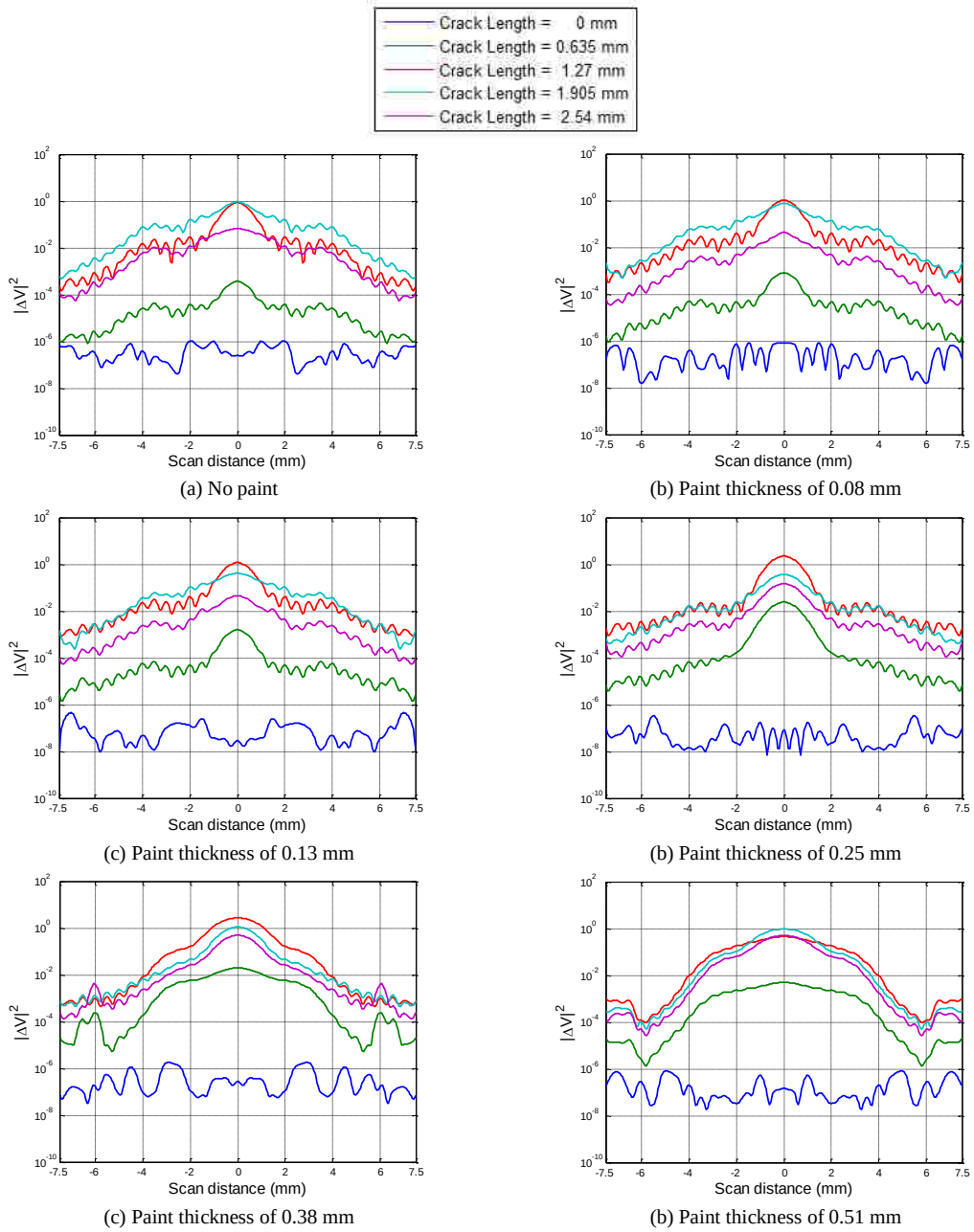

(a) No paint

(b) Paint thickness of 0.08 mm

(c) Paint thickness of 0.13 mm

(b) Paint thickness of 0.25 mm

(c) Paint thickness of 0.38 mm

(b) Paint thickness of 0.51 mm

Figure 16. Simulated W-band wideband results with various crack lengths, at a standoff distance of 1 mm, and paint thickness of (from (a) to (f)): 0, 0.08, 0.13, 0.25, 0.38, and 0.51 mm, in logarithmic scales.

APPENDIX E.

ADDITIONAL FIGURES OF SIMULATED RESULTS (EFFECT OF PROBE MISALIGNMENT)

This appendix provides the complete simulated scan results (both selected single-frequency and wideband responses) for Section 3.5 – Effect of Probe Misalignment.

Figures 1 through 5 represent the simulated results at standoff distance of 0.5 mm. Among these figures, Figures 1 through 4 show the selected single-frequency responses and Figure 5 shows the wideband responses of the W-band differential probe. The results are provided in both linear and logarithmic scales. Note the scales may not be the same for the sub-figures.

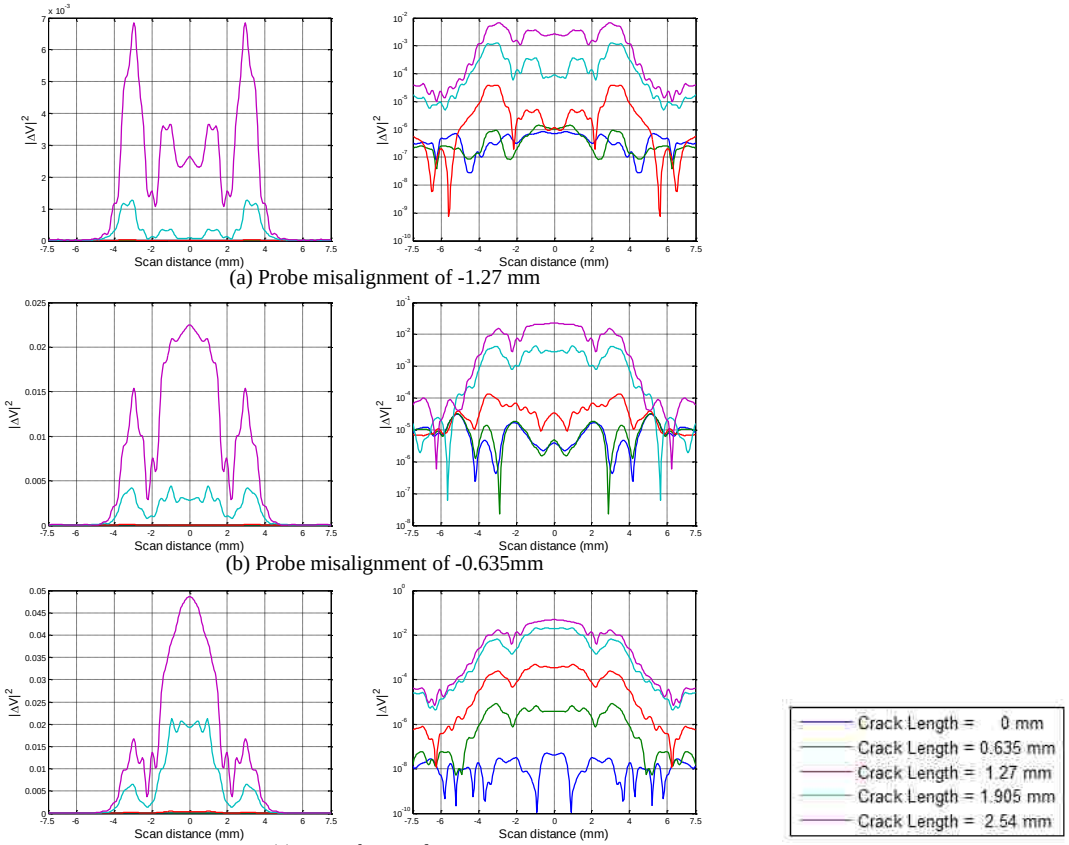

(a) Probe misalignment of -1.27 mm

(b) Probe misalignment of -0.635mm

(c) No probe misalignment

(d) Probe misalignment of 0.635mm

(e) Probe misalignment of 1.27 mm

Figure 1. Simulated W-band results with various crack lengths, at a standoff distance of 0.5 mm, frequency of 75 GHz, and probe misalignment of (from (a) to (e)): -1.27, -0.635, 0, 0.635 and 1.27 mm, in linear (left) and logarithmic scales (right).

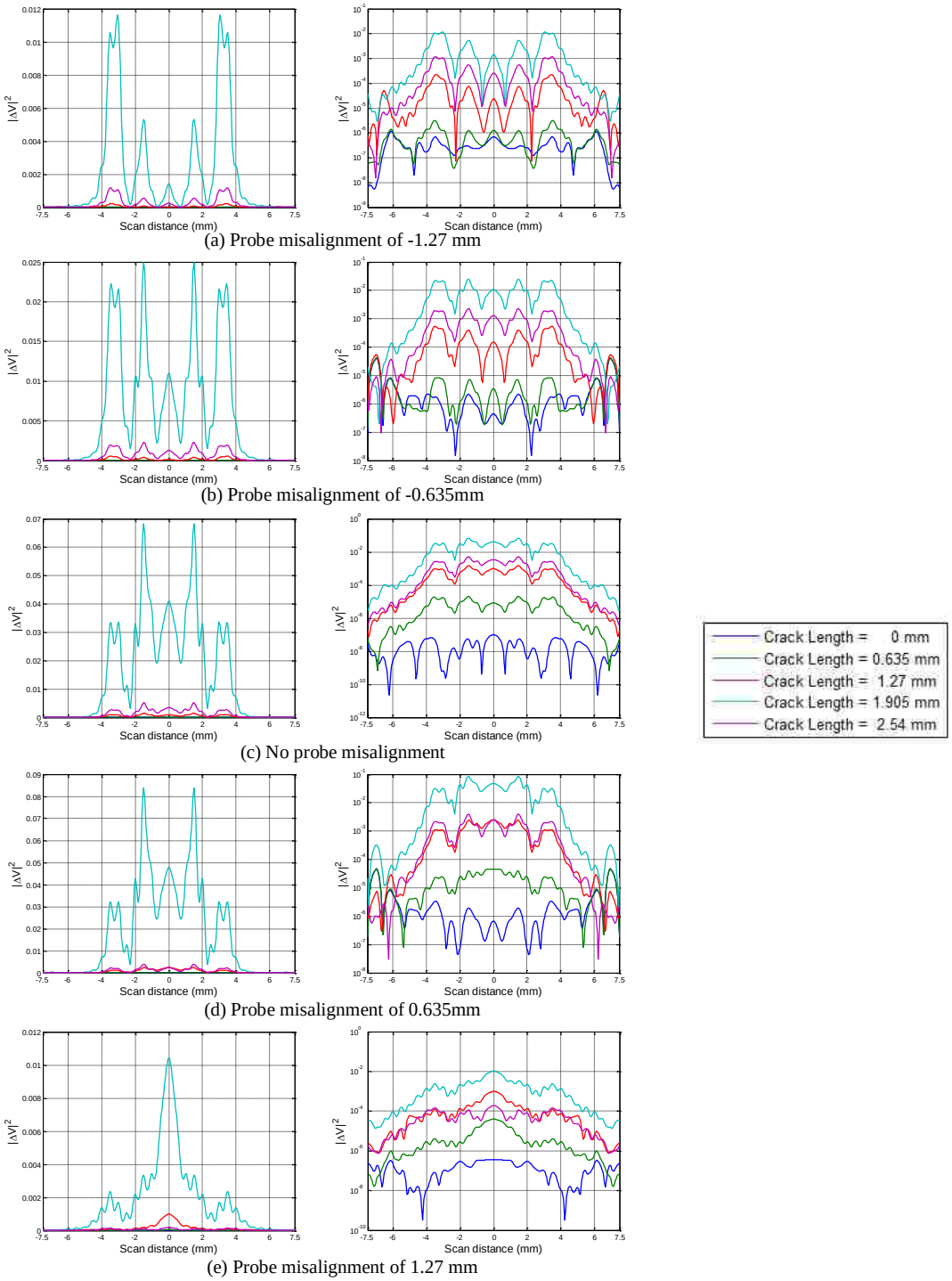

(a) Probe misalignment of -1.27 mm

(b) Probe misalignment of -0.635mm

(c) No probe misalignment

(d) Probe misalignment of 0.635mm

(e) Probe misalignment of 1.27 mm

Figure 2. Simulated W-band results with various crack lengths, at a standoff distance of 0.5 mm, frequency of 87.25 GHz, and probe misalignment of (from (a) to (e)): -1.27, -0.635, 0, 0.635 and 1.27 mm, in linear (left) and logarithmic scales (right).

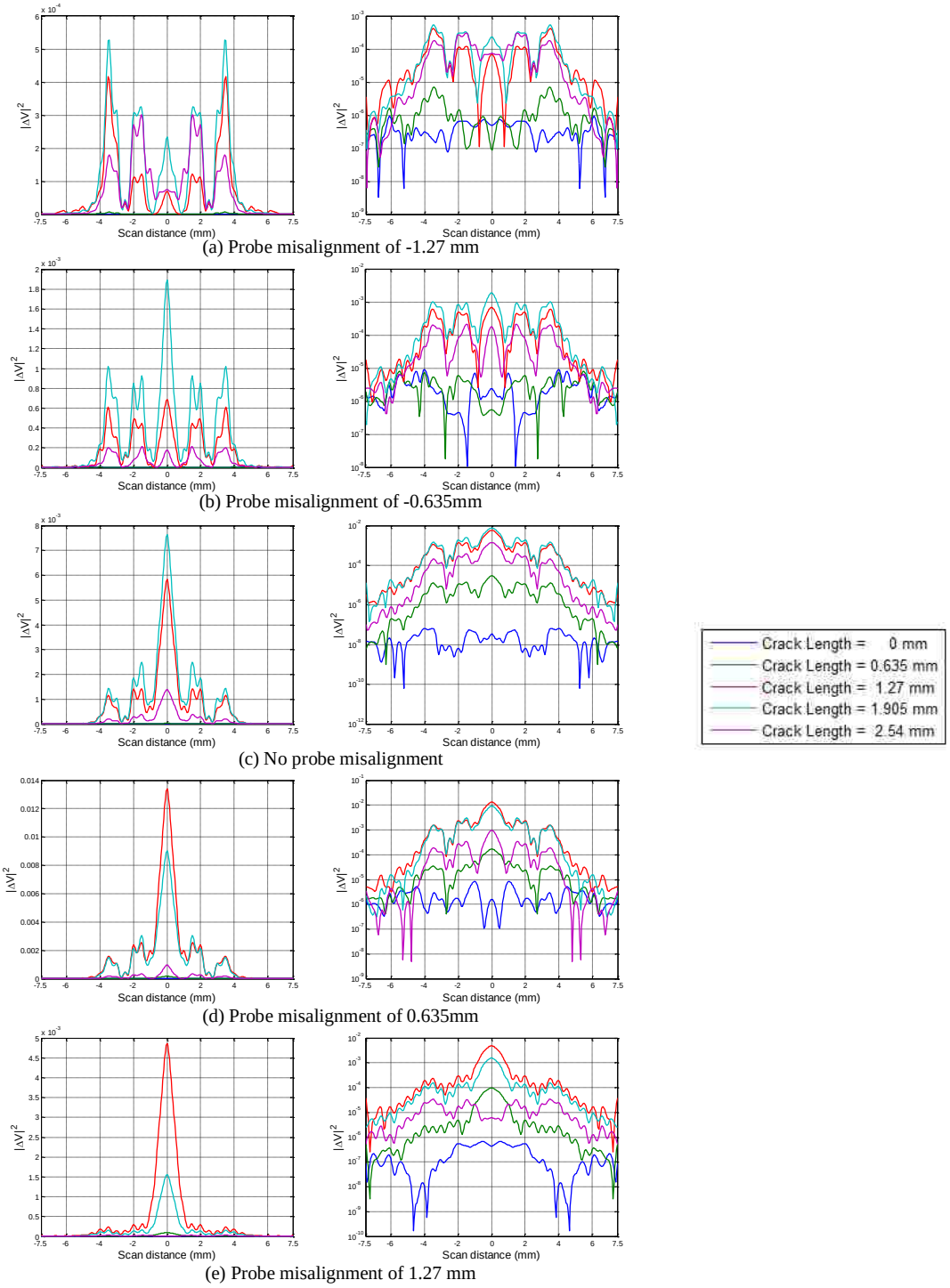

(a) Probe misalignment of -1.27 mm

(b) Probe misalignment of -0.635mm

(c) No probe misalignment

(d) Probe misalignment of 0.635mm

(e) Probe misalignment of 1.27 mm

Figure 3. Simulated W-band results with various crack lengths, at a standoff distance of 0.5 mm, frequency of 96 GHz, and probe misalignment of (from (a) to (e)): -1.27, -0.635, 0, 0.635 and 1.27 mm, in linear (left) and logarithmic scales (right).

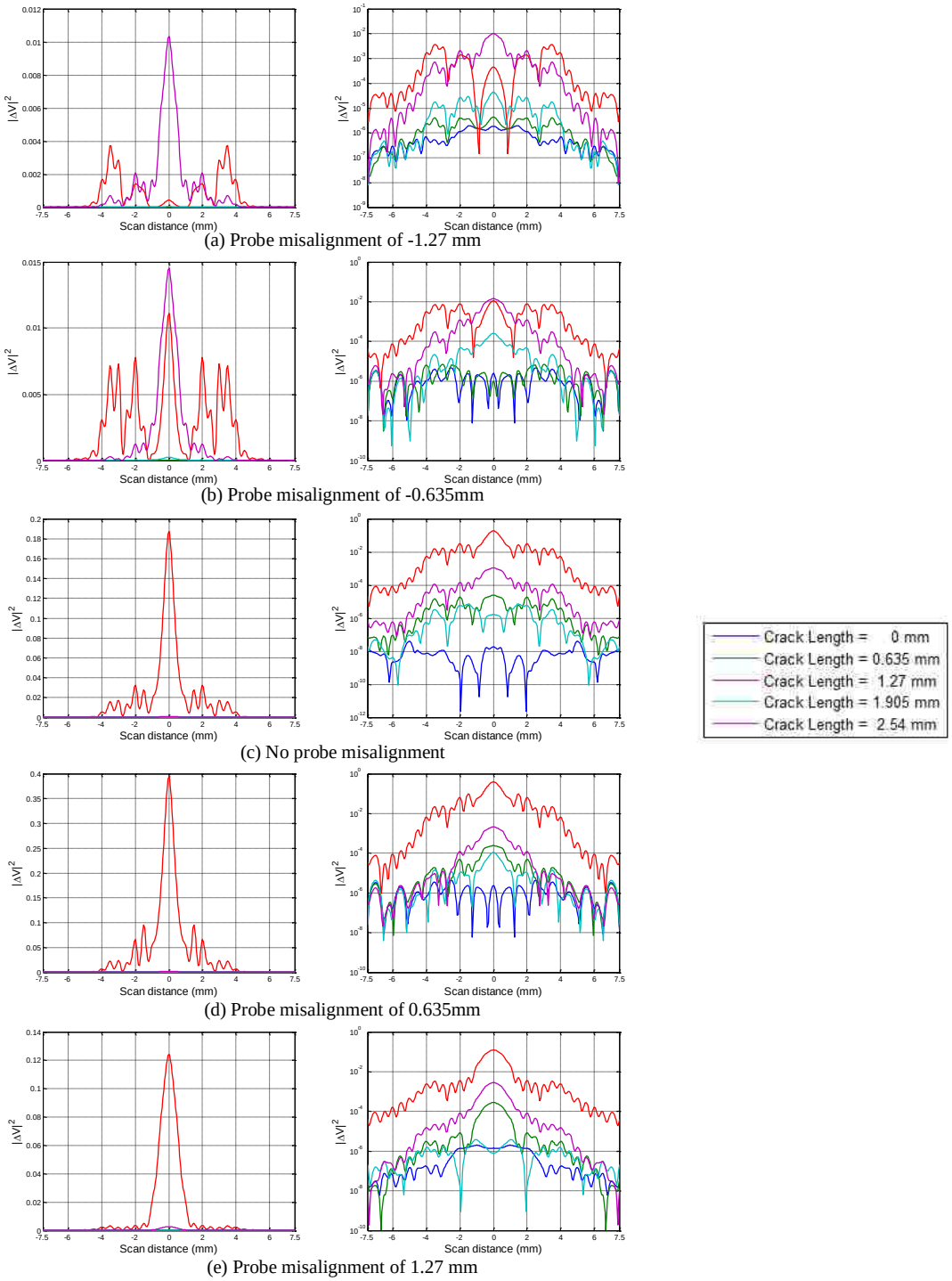

(a) Probe misalignment of -1.27 mm

(b) Probe misalignment of -0.635mm

(c) No probe misalignment

(d) Probe misalignment of 0.635mm

(e) Probe misalignment of 1.27 mm

Figure 4. Simulated W-band results with various crack lengths, at a standoff distance of 0.5 mm, frequency of 110 GHz, and probe misalignment of (from (a) to (e)): -1.27, -0.635, 0, 0.635 and 1.27 mm, in linear (left) and logarithmic scales (right).

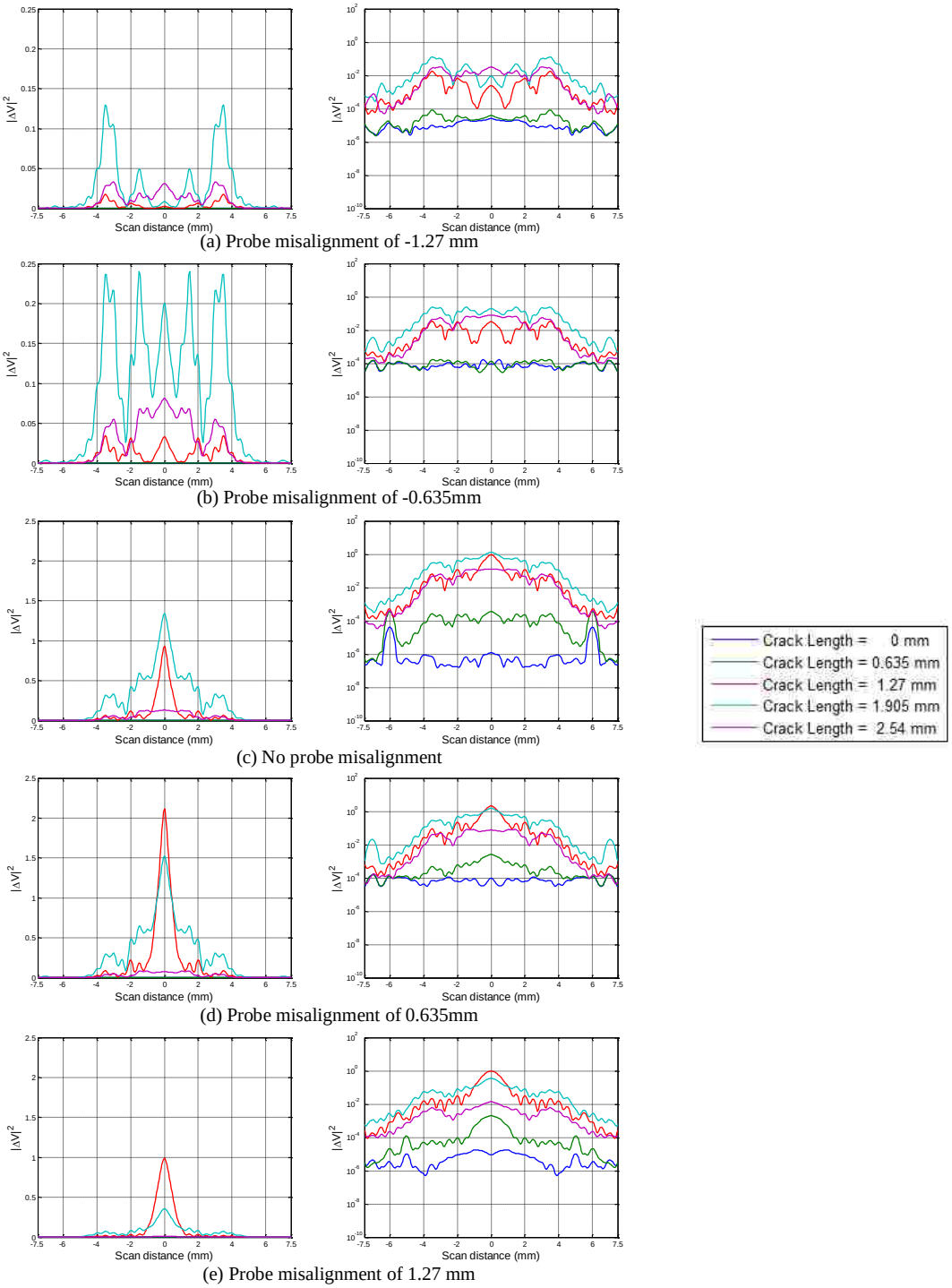

(a) Probe misalignment of -1.27 mm

(b) Probe misalignment of -0.635mm

(c) No probe misalignment

(d) Probe misalignment of 0.635mm

(e) Probe misalignment of 1.27 mm

Figure 5. Simulated W-band wideband results with various crack lengths, at a standoff distance of 0.5 mm, and probe misalignment of (from (a) to (e)): -1.27, -0.635, 0, 0.635 and 1.27 mm, in linear (left) and logarithmic scales (right).

Figures 6 through 10 represent the simulated results at standoff distance of 1 mm. Among these figures, Figures 6 through 9 show the selected single-frequency responses and Figure 10 shows the wideband responses of the W-band differential probe. The results are provided in both linear and logarithmic scales. Note the scales may not be the same for the sub-figures.

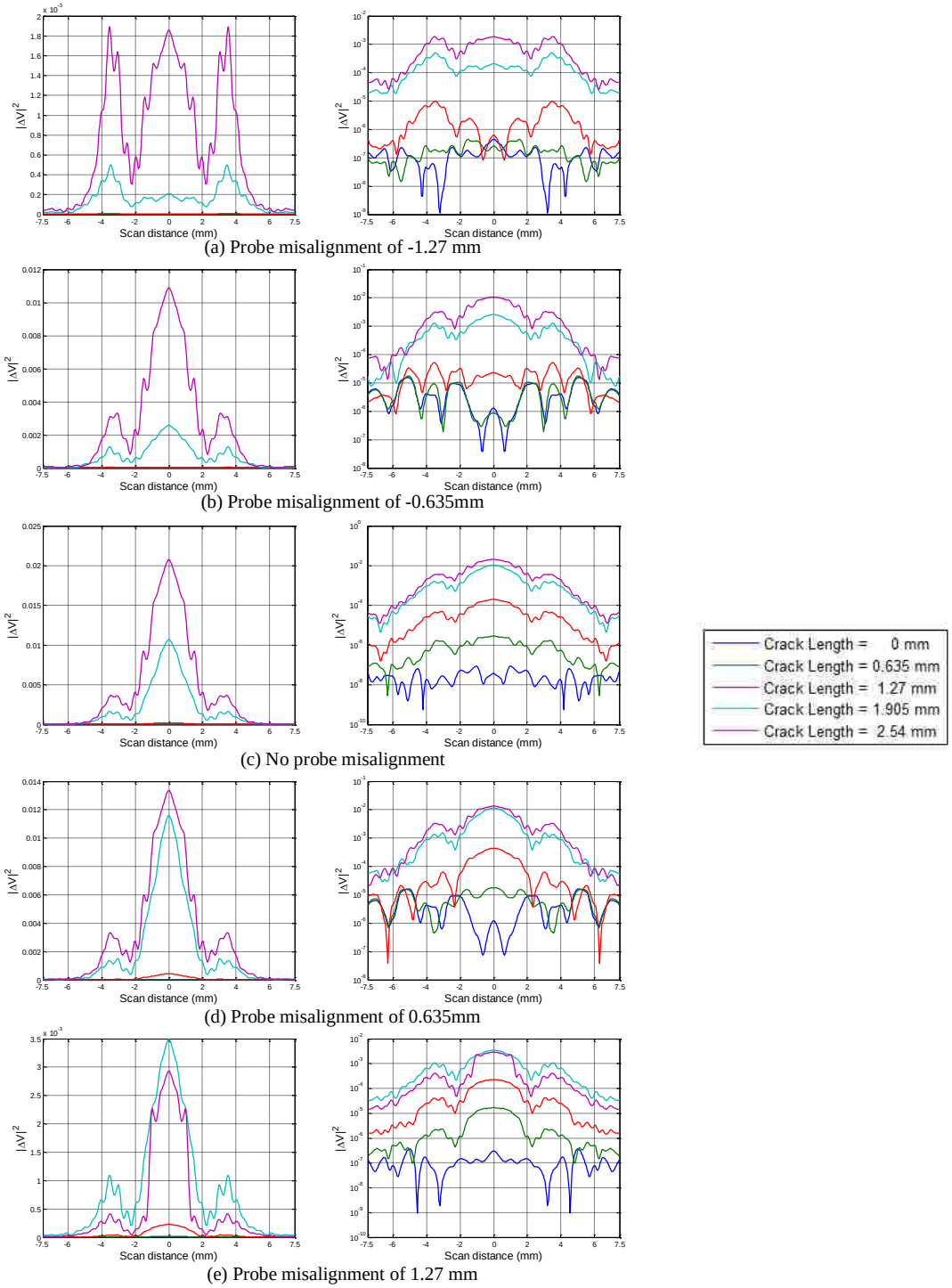

(a) Probe misalignment of -1.27 mm

(b) Probe misalignment of -0.635mm

(c) No probe misalignment

(d) Probe misalignment of 0.635mm

(e) Probe misalignment of 1.27 mm

Figure 6. Simulated W-band results with various crack lengths, at a standoff distance of 1 mm, frequency of 75 GHz, and probe misalignment of (from (a) to (e)): -1.27, -0.635, 0, 0.635 and 1.27 mm, in linear (left) and logarithmic scales (right).

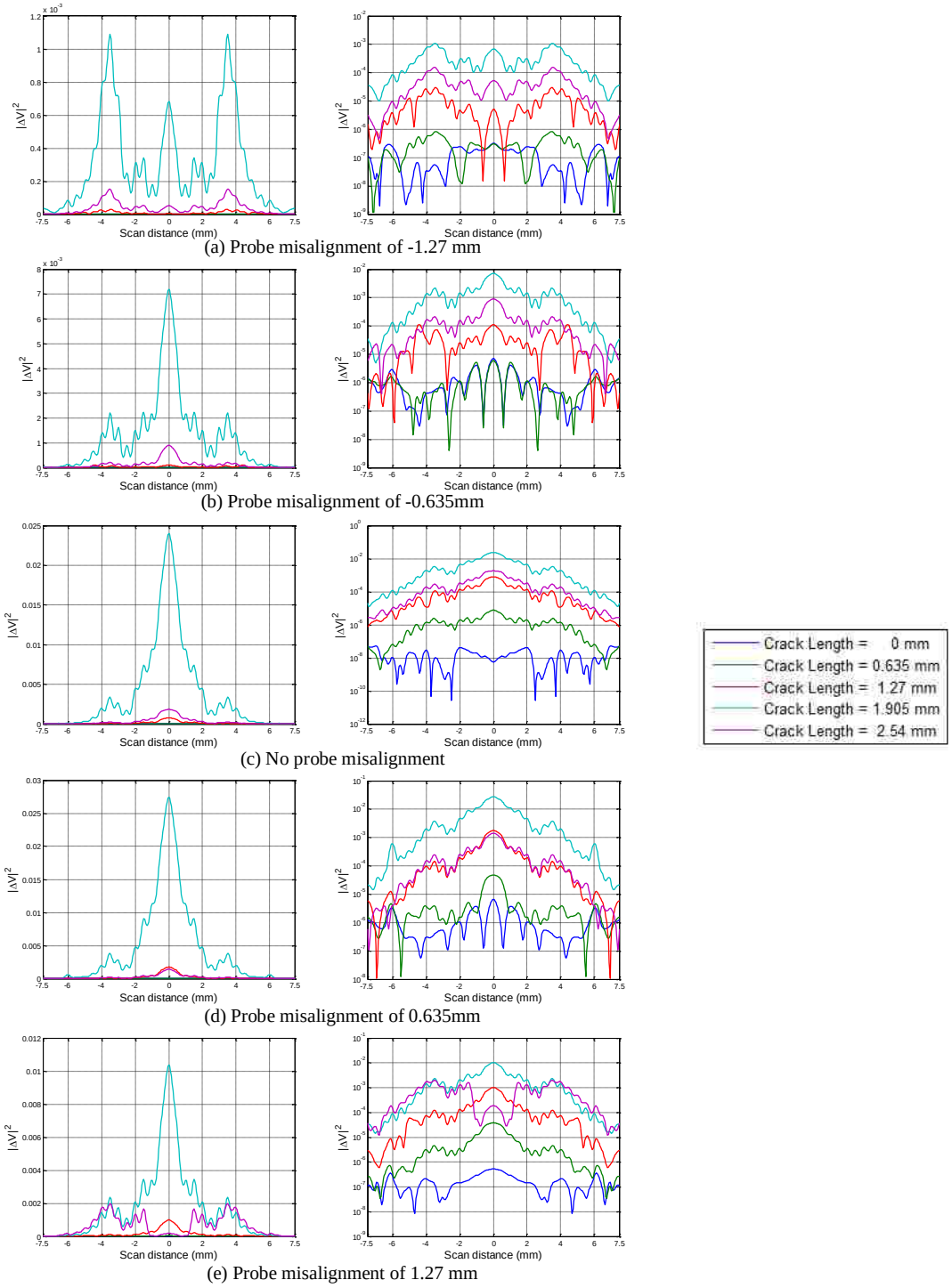

(a) Probe misalignment of -1.27 mm

(b) Probe misalignment of -0.635mm

(c) No probe misalignment

(d) Probe misalignment of 0.635mm

(e) Probe misalignment of 1.27 mm

Figure 7. Simulated W-band results with various crack lengths, at a standoff distance of 1 mm, frequency of 87.25 GHz, and probe misalignment of (from (a) to (e)): -1.27, -0.635, 0, 0.635 and 1.27 mm, in linear (left) and logarithmic scales (right).

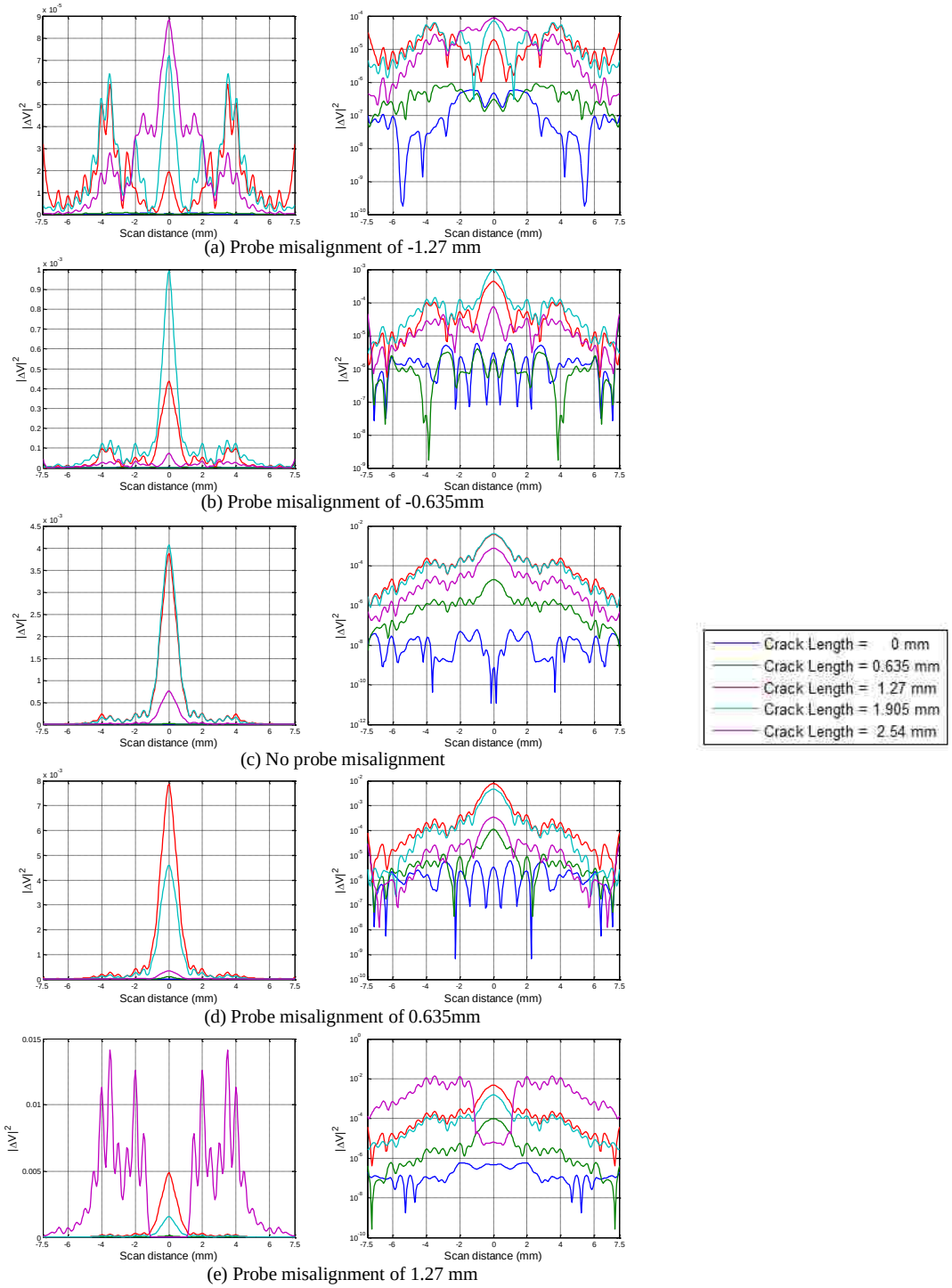

(a) Probe misalignment of -1.27 mm

(b) Probe misalignment of -0.635mm

(c) No probe misalignment

(d) Probe misalignment of 0.635mm

(e) Probe misalignment of 1.27 mm

Figure 8. Simulated W-band results with various crack lengths, at a standoff distance of 1 mm, frequency of 96 GHz, and probe misalignment of (from (a) to (e)): -1.27, -0.635, 0, 0.635 and 1.27 mm, in linear (left) and logarithmic scales (right).

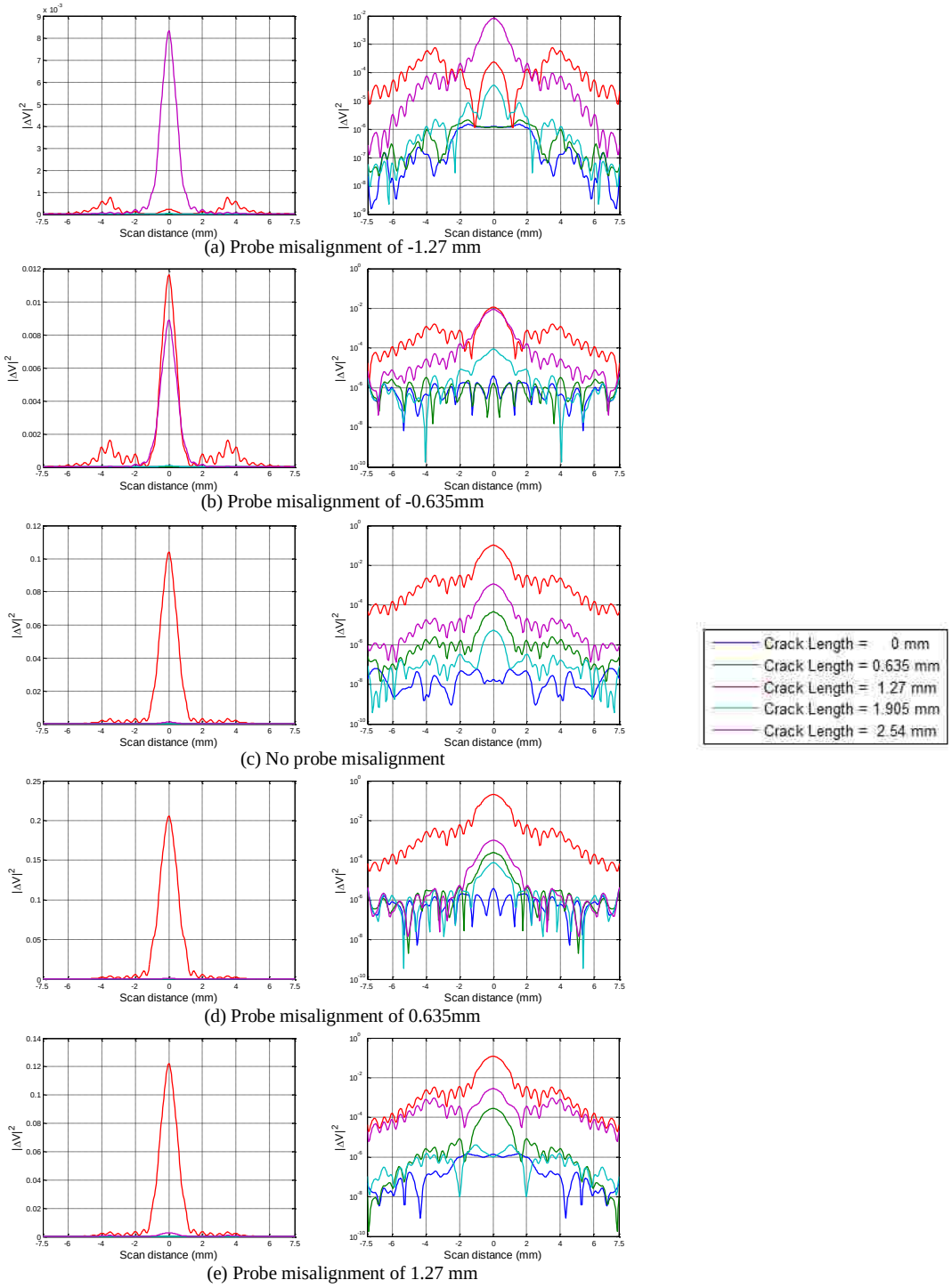

Figure 9. Simulated W-band results with various crack lengths, at a standoff distance of 1 mm, frequency of 110 GHz, and probe misalignment of (from (a) to (e)): -1.27, -0.635, 0, 0.635 and 1.27 mm, in linear (left) and logarithmic scales (right).

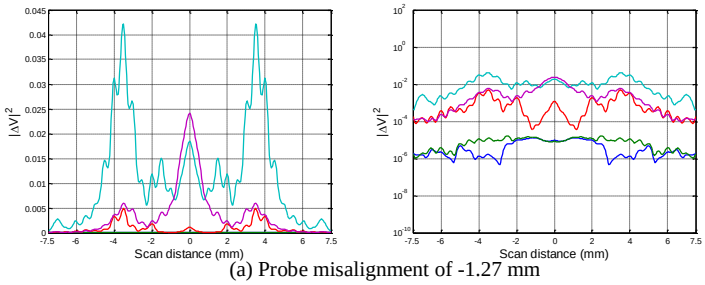

(a) Probe misalignment of -1.27 mm

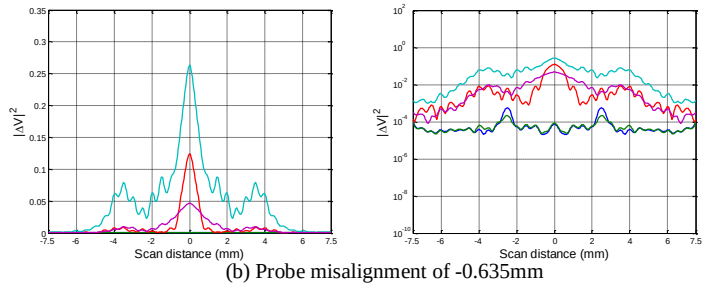

(b) Probe misalignment of -0.635mm

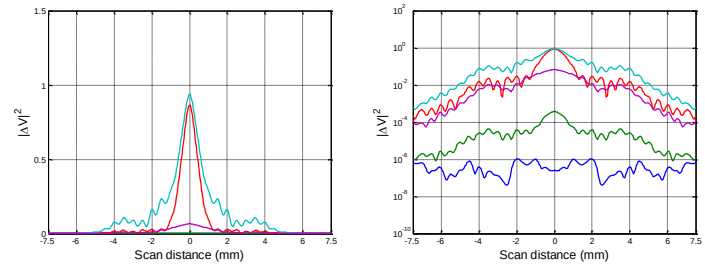

(c) No probe misalignment

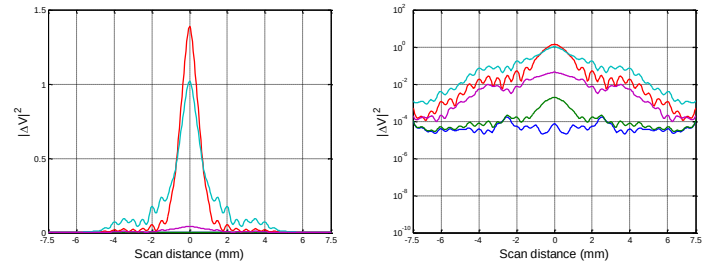

(d) Probe misalignment of 0.635mm

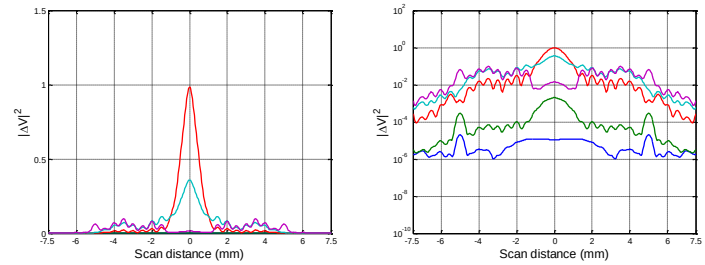

(e) Probe misalignment of 1.27 mm

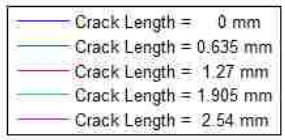

Figure 10. Simulated W-band wideband results with various crack lengths, at a standoff distance of 1 mm, and probe misalignment of (from (a) to (e)): -1.27, -0.635, 0, 0.635 and 1.27 mm, in linear (left) and logarithmic scales (right).

APPENDIX F.

ADDITIONAL FIGURES OF SIMULATED RESULTS (EFFECT OF PROBE OFFSET)

This appendix provides the complete simulated scan results (both selected single-frequency and wideband responses) for Section 3.6 – Effect of Probe Offset.

Figures 1 through 4 represent the simulated results at standoff distance of 0.5 mm. Among these figures, Figures 1 through 3 show the selected single-frequency responses and Figure 4 shows the wideband responses of the W-band differential probe. The results are provided in both linear and logarithmic scales.

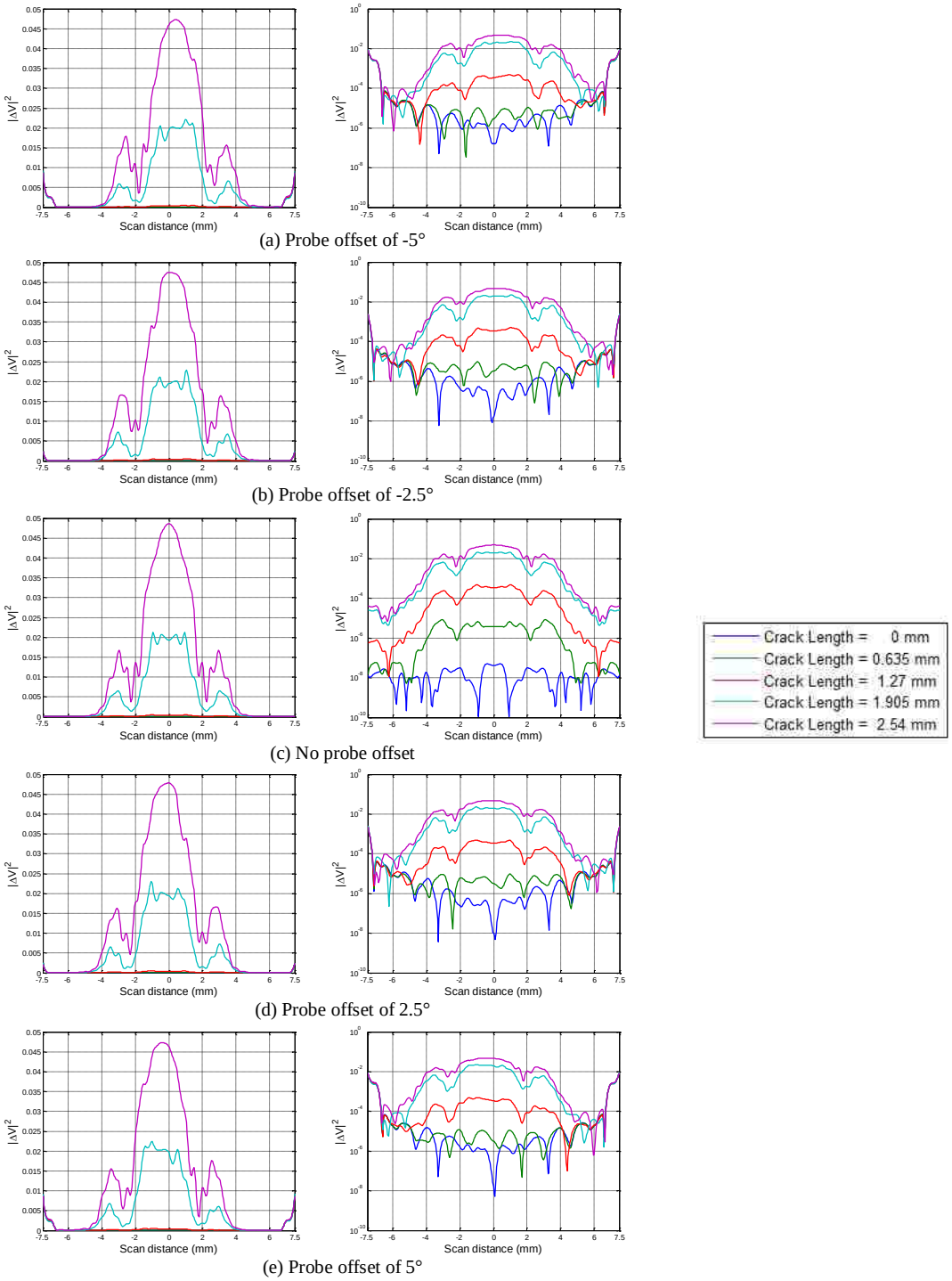

(a) Probe offset of -5°

(b) Probe offset of -2.5°

(c) No probe offset

(d) Probe offset of 2.5°

(e) Probe offset of 5°

Figure 1. Simulated W-band results with various crack lengths, at a standoff distance of 0.5 mm, frequency of 75 GHz, and probe offset of (from (a) to (e)): -5°, -2.5°, 0°, 2.5° and 5°, in linear (left) and logarithmic scales (right).

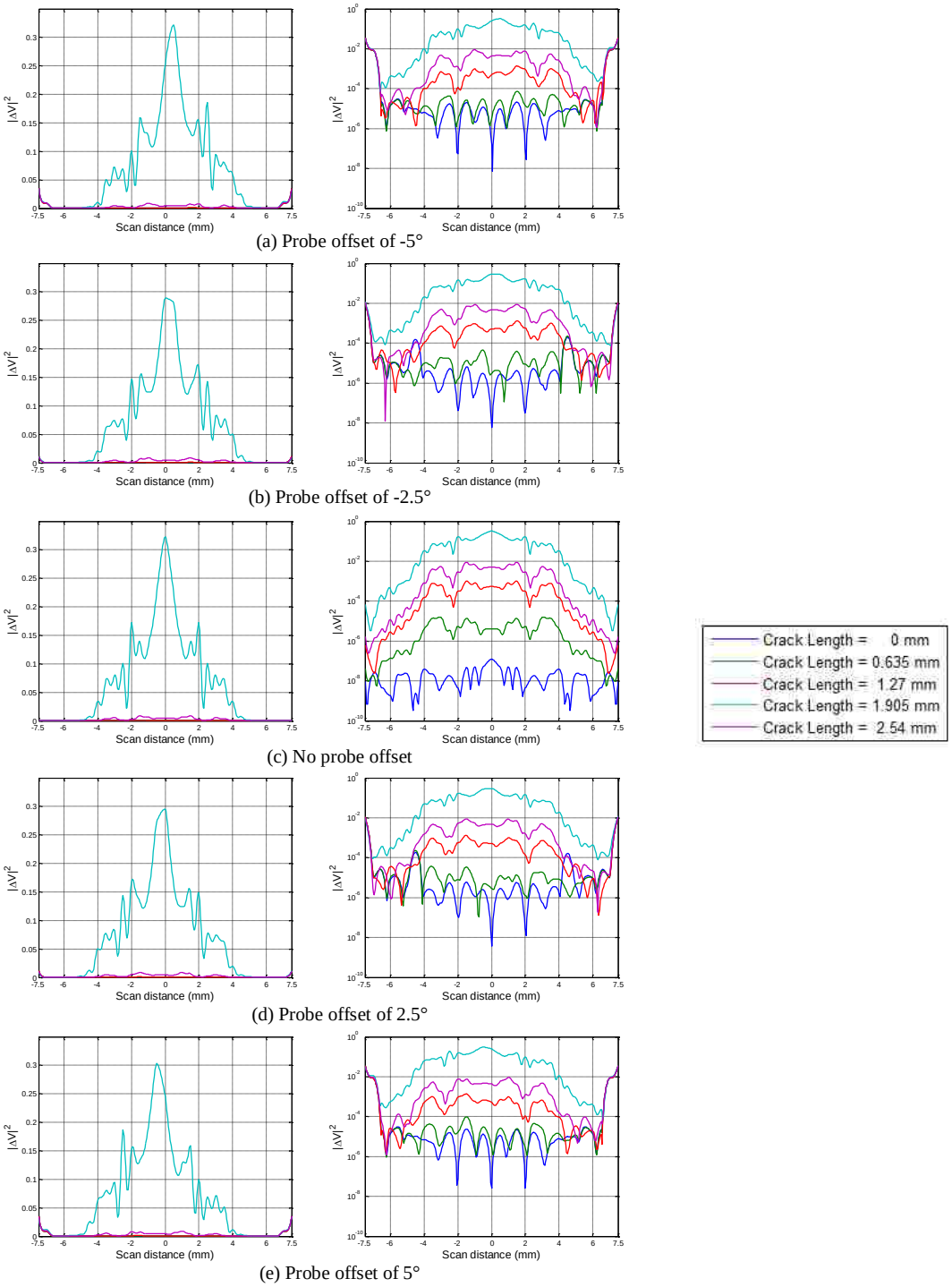

(a) Probe offset of -5°

(b) Probe offset of -2.5°

(c) No probe offset

(d) Probe offset of 2.5°

(e) Probe offset of 5°

Figure 2. Simulated W-band results with various crack lengths, at a standoff distance of 0.5 mm, frequency of 83.75 GHz, and probe offset of (from (a) to (e)): -5°, -2.5°, 0°, 2.5° and 5°, in linear (left) and logarithmic scales (right).

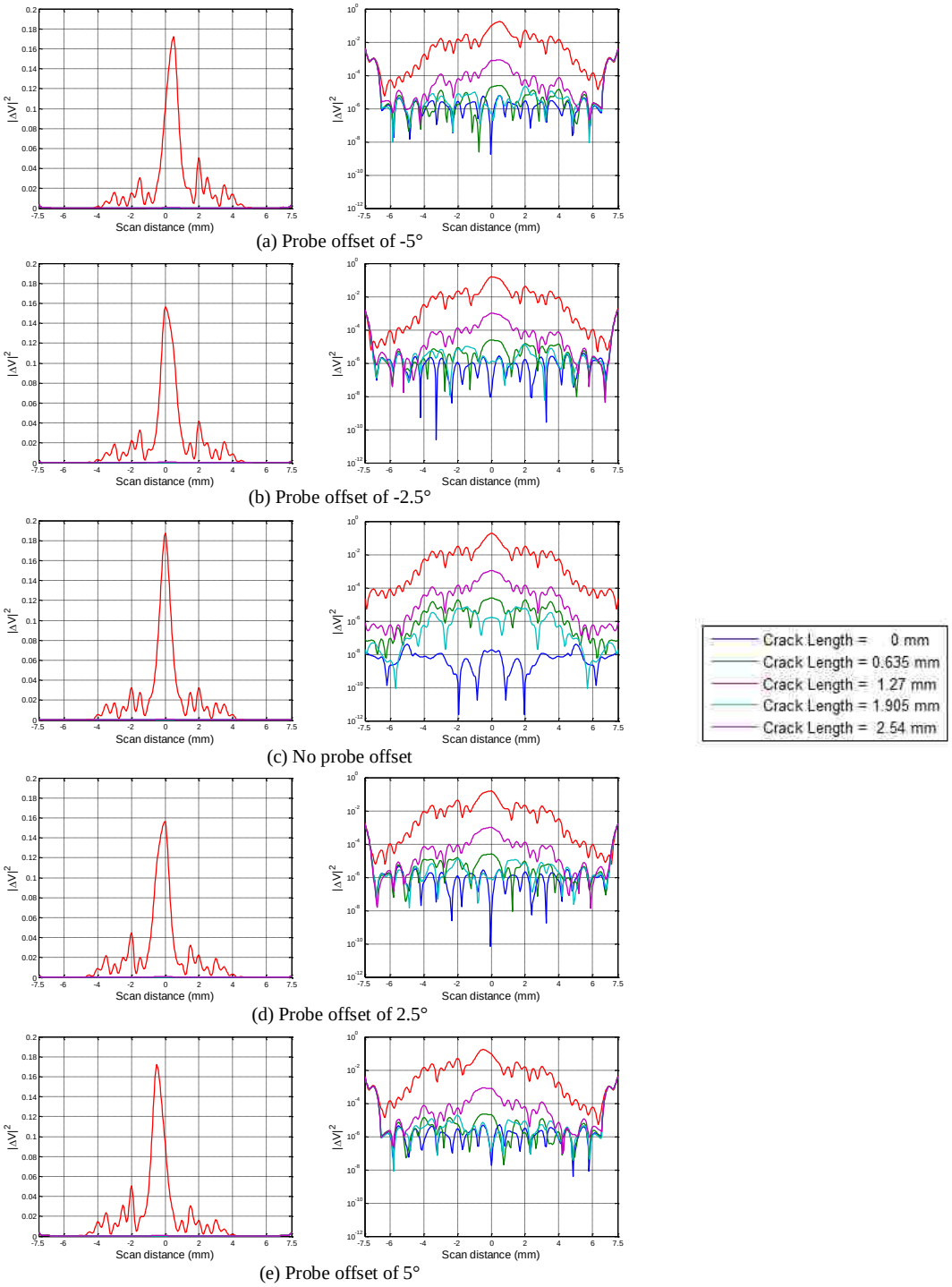

(a) Probe offset of -5°

(b) Probe offset of -2.5°

(c) No probe offset

(d) Probe offset of 2.5°

(e) Probe offset of 5°

Figure 3. Simulated W-band results with various crack lengths, at a standoff distance of 0.5 mm, frequency of 110 GHz, and probe offset of (from (a) to (e)): -5°, -2.5°, 0°, 2.5° and 5°, in linear (left) and logarithmic scales (right).

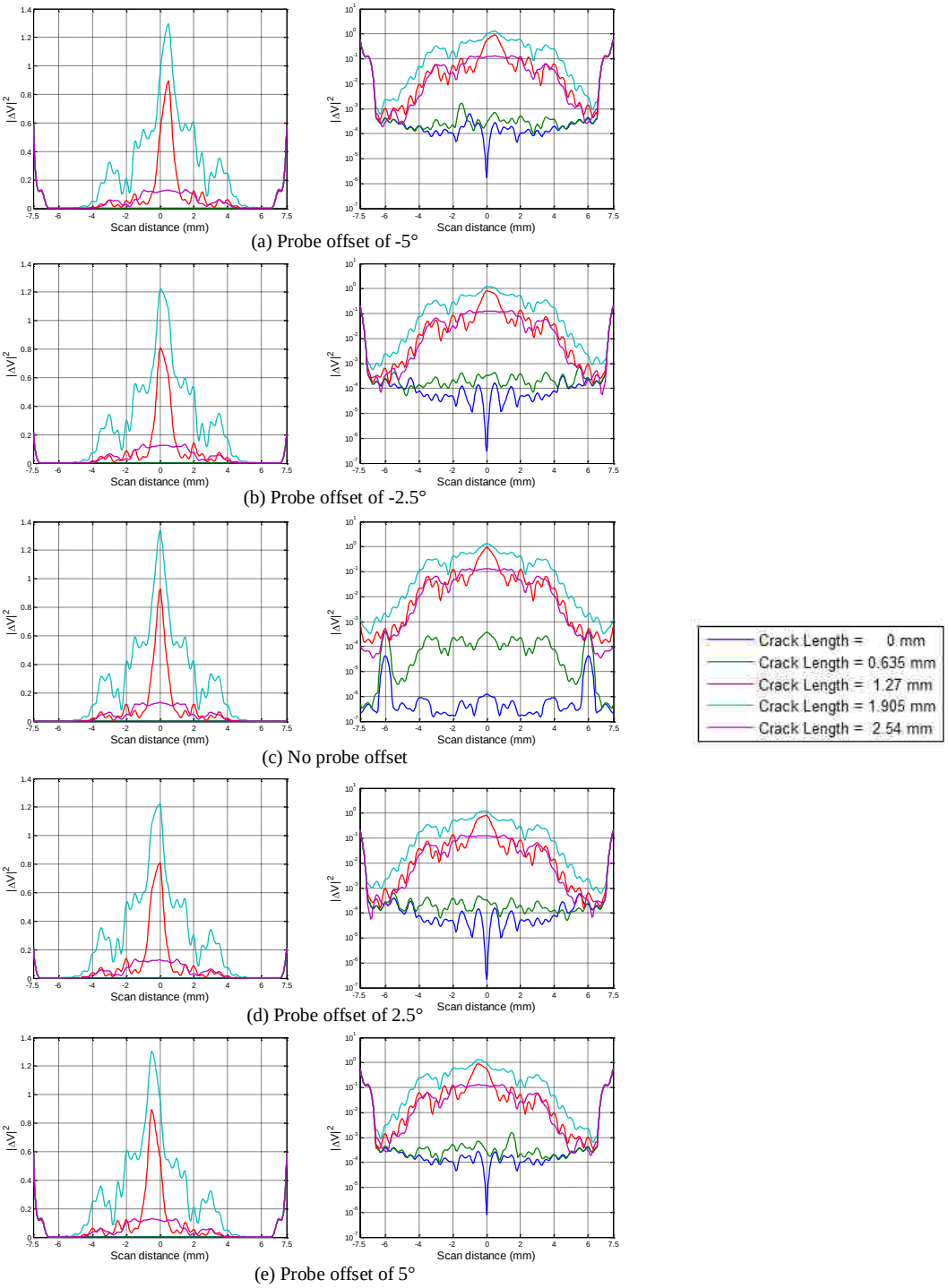

(a) Probe offset of -5°

(b) Probe offset of -2.5°

(c) No probe offset

(d) Probe offset of 2.5°

(e) Probe offset of 5°

Figure 4. Simulated W-band wideband results with various crack lengths, at a standoff distance of 0.5 mm, and probe offset of (from (a) to (e)): -5°, -2.5°, 0°, 2.5° and 5°, in linear (left) and logarithmic scales (right).

Figures 5 through 8 represent the simulated results at standoff distance of 1 mm. Among these figures, Figures 5 through 7 show the selected single-frequency responses and Figure 8 shows the wideband responses of the W-band differential probe. The results are provided in both linear and logarithmic scales.

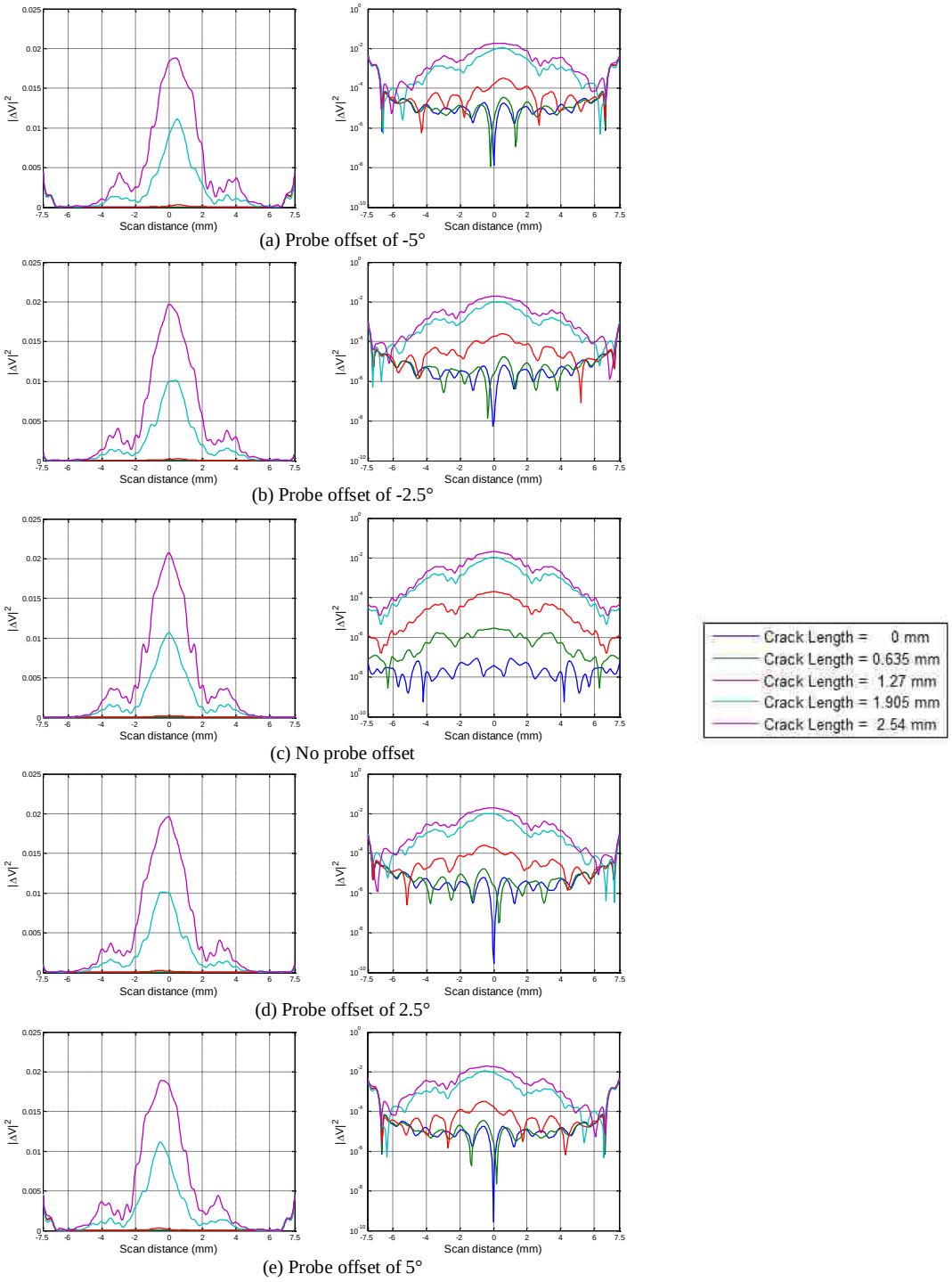

(a) Probe offset of -5°

(b) Probe offset of -2.5°

(c) No probe offset

(d) Probe offset of 2.5°

(e) Probe offset of 5°

Figure 5. Simulated W-band results with various crack lengths, at a standoff distance of 1 mm, frequency of 75 GHz, and probe offset of (from (a) to (e)): -5°, -2.5°, 0°, 2.5° and 5°, in linear (left) and logarithmic scales (right).

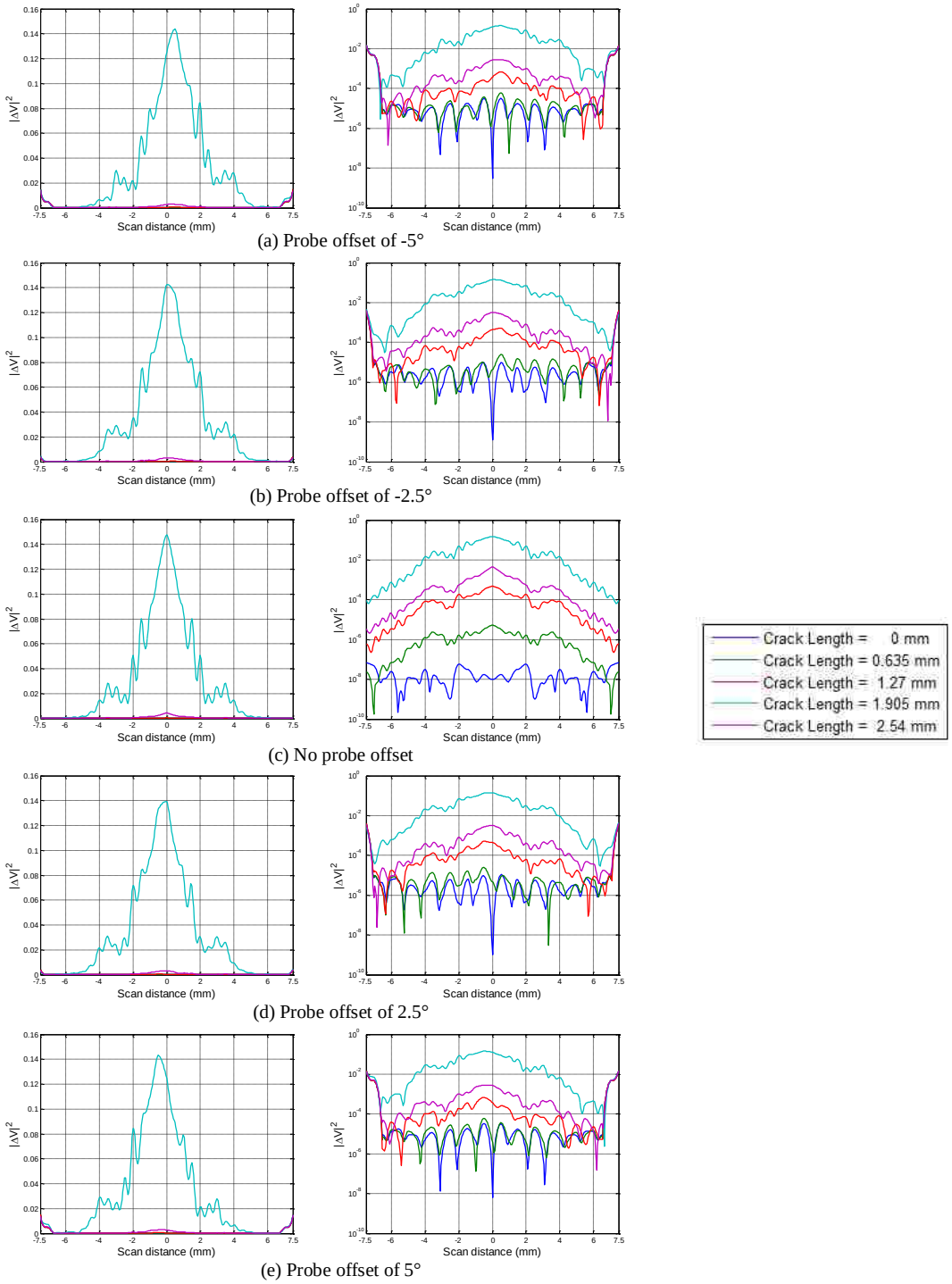

(a) Probe offset of -5°

(b) Probe offset of -2.5°

(c) No probe offset

(d) Probe offset of 2.5°

(e) Probe offset of 5°

Figure 6. Simulated W-band results with various crack lengths, at a standoff distance of 1 mm, frequency of 83.75 GHz, and probe offset of (from (a) to (e)): -5°, -2.5°, 0°, 2.5° and 5°, in linear (left) and logarithmic scales (right).

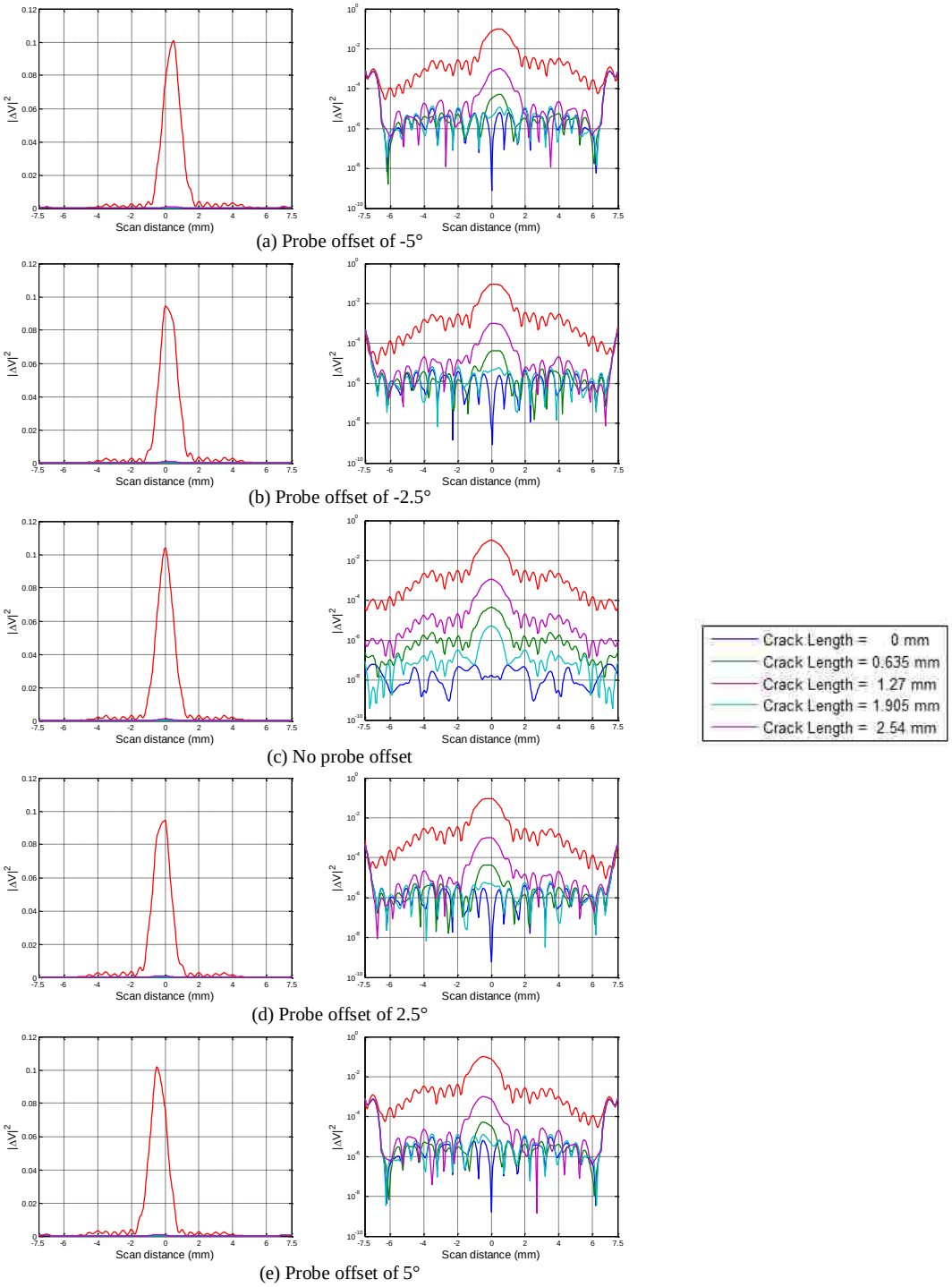

(a) Probe offset of -5°

(b) Probe offset of -2.5°

(c) No probe offset

(d) Probe offset of 2.5°

(e) Probe offset of 5°

Figure 7. Simulated W-band results with various crack lengths, at a standoff distance of 1 mm, frequency of 110 GHz, and probe offset of (from (a) to (e)): -5°, -2.5°, 0°, 2.5° and 5°, in linear (left) and logarithmic scales (right).

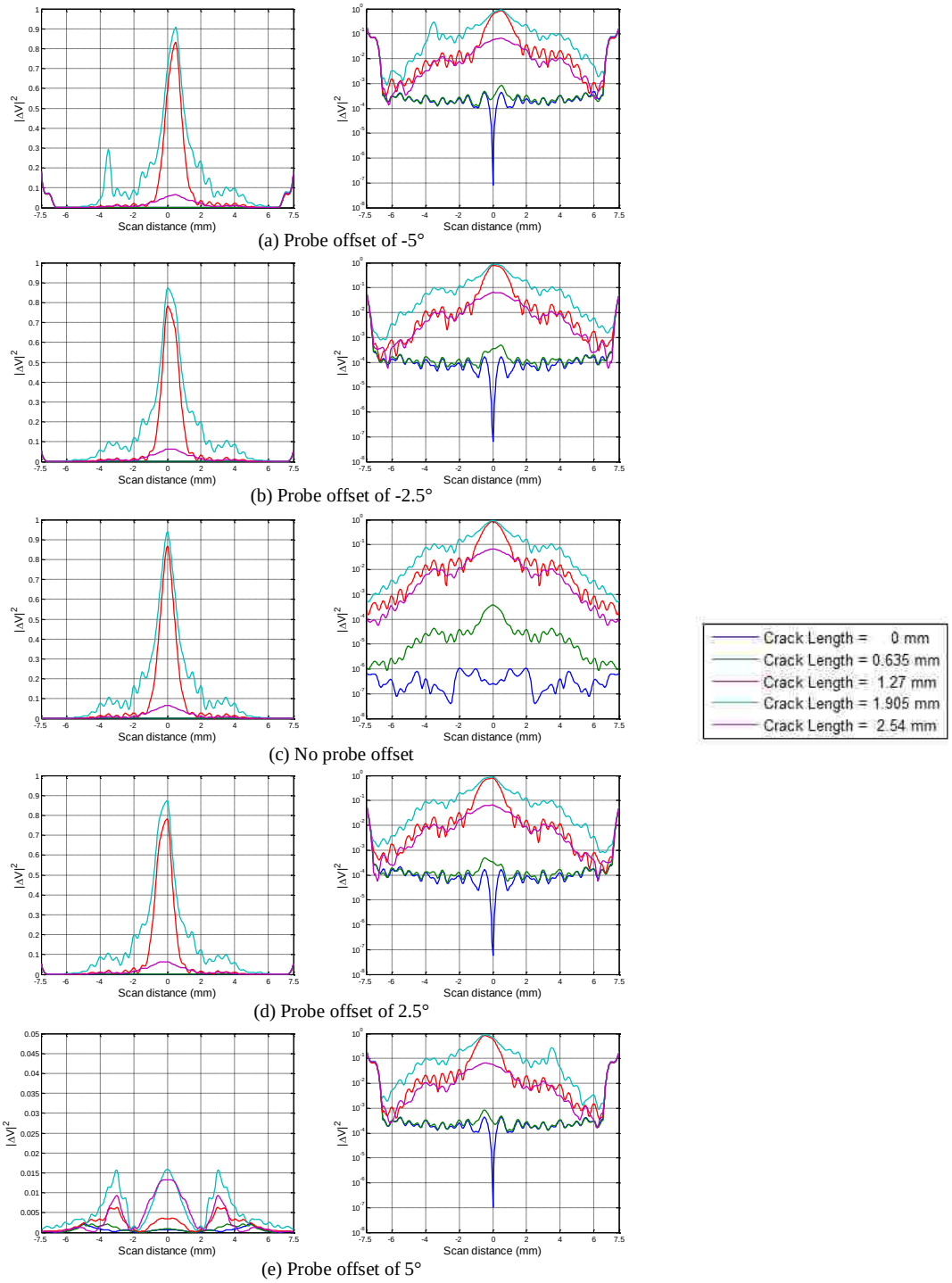

(a) Probe offset of -5°

(b) Probe offset of -2.5°

(c) No probe offset

(d) Probe offset of 2.5°

(e) Probe offset of 5°

Figure 8. Simulated W-band wideband results with various crack lengths, at a standoff distance of 1 mm, and probe offset of (from (a) to (e)): -5°, -2.5°, 0°, 2.5° and 5°, in linear (left) and logarithmic scales (right).

APPENDIX G.

FREQUENCIES OF OPERATION IN SIMULATIONS AND MEASUREMENTS

This appendix provides the comparison between frequencies of operation in both simulations and measurements, as shown in Table 1 (W-band) and Table 2 (V-band). The frequencies highlighted in red are the frequencies that are approximately the same for both cases.

Table 1. Comparison between simulated and measured W-band frequencies.

Simulated frequencies (GHz)	Measured frequencies (GHz)
75.00 (min)	87.7340 (min)
76.75	87.8680
78.50	88.0424
80.25	88.2765
82.00	88.5221
83.75	88.7443
85.50	88.9755
87.25	89.2482
89.00	89.5269
90.75	89.7746
92.50	90.0222
94.25	90.2890
96.00	90.5486
97.75	90.7912
99.50	91.0222
101.25	91.2397
103.00	91.4521
104.75	91.6738
106.50	91.8959
108.25	92.0927
110.00 (max)	92.2650 (max)

Table 2. Comparison between simulated and measured V-band frequencies.

Simulated frequencies (GHz)	Measured frequencies (GHz)
50.00 (min)	68.8 (min)
51.25	69.0
52.50	69.4
53.75	69.6
55.00	69.8
56.25	70.0
57.50	70.2
58.75	70.4
60.00	70.6
61.25	71.0
62.50	71.3 (max)
63.75	
65.00	
66.25	
67.50	
68.75	
70.00	
71.25	
72.50	
73.75	
110.00 (max)	

APPENDIX H.
ADDITIONAL FIGURES OF MEASUREMENT RESULTS (EFFECT OF APERTURE OFFSET)

This appendix provides the following results for Section 4.2 – Effect of Aperture Offset:

- wideband measurement results,
- referenced wideband measurement results,
- and comparisons between measurement and simulation results

Figures 1 through 5 represent the wideband measurement results at both standoff distances of 0.5 and 1 mm, while the referenced wideband data is shown in Figures 6 through 10. The comparisons between measurement and simulation results (at four common frequencies) are shown in Figures 11 through 17 (at standoff distance of 0.5 mm) and Figures 18 through 24 (at standoff distance of 1 mm).

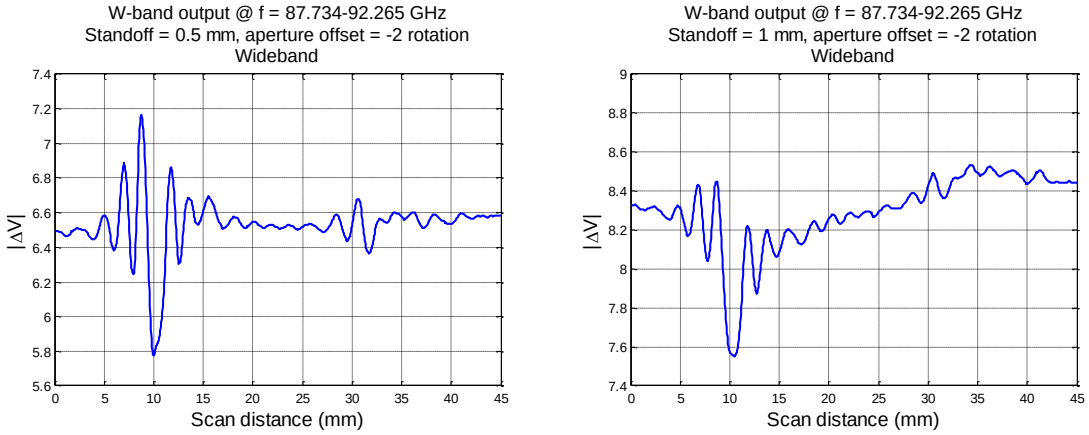

Figure 1. W-band wideband probe output signals at aperture offset of -2 rotations, and standoff distance of 0.5 mm (left) and 1 mm (right).

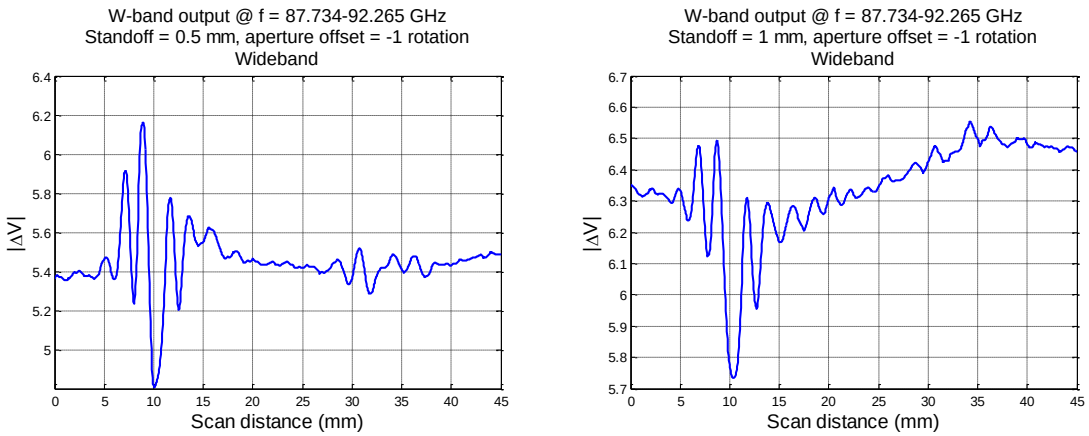

Figure 2. W-band wideband probe output signals at aperture offset of -1 rotation, and standoff distance of 0.5 mm (left) and 1 mm (right).

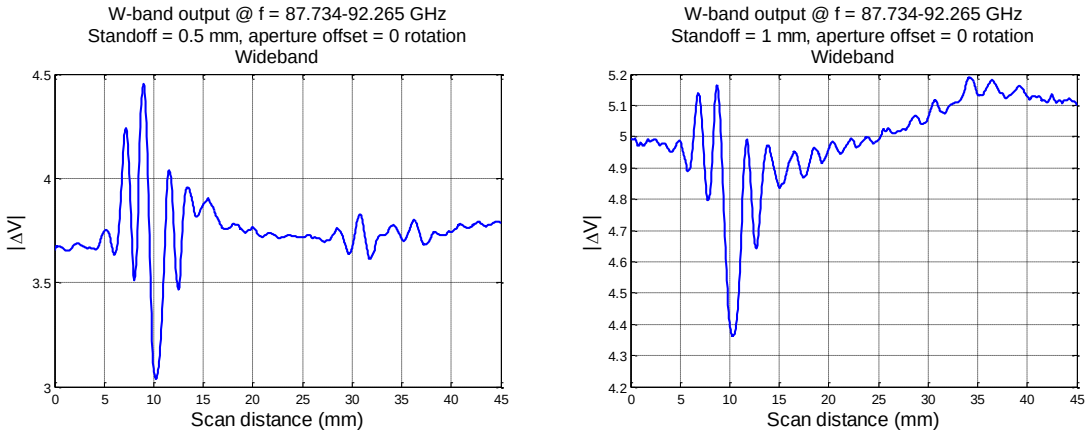

Figure 3. W-band wideband probe output signals at no aperture offset, and standoff distance of 0.5 mm (left) and 1 mm (right).

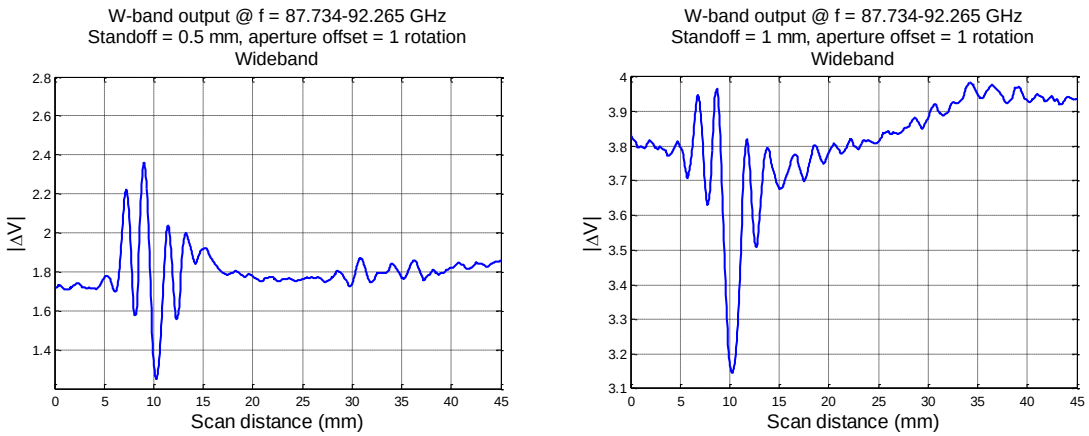

Figure 4. W-band wideband probe output signals at aperture offset of +1 rotation, and standoff distance of 0.5 mm (left) and 1 mm (right).

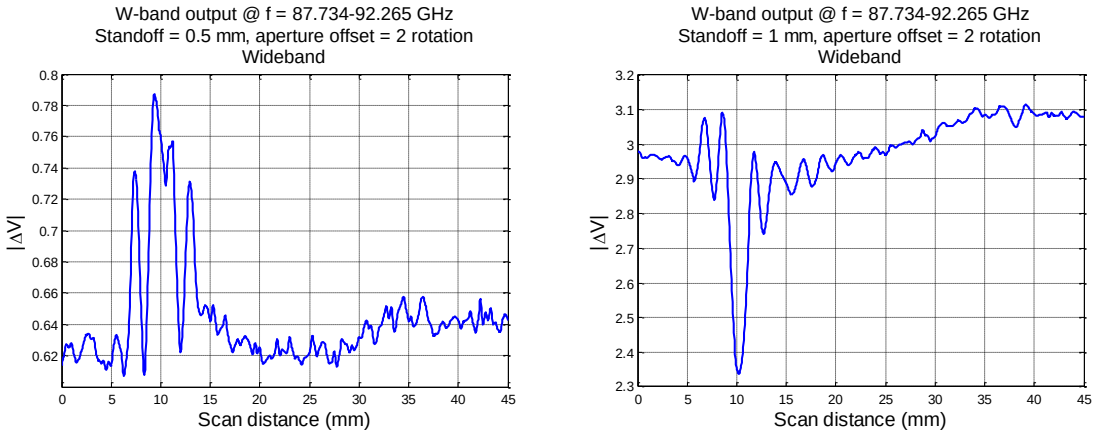

Figure 5. W-band wideband probe output signals at aperture offset of +2 rotations, and standoff distance of 0.5 mm (left) and 1 mm (right).

Figures 6 through 10 represent the referenced measurement results.

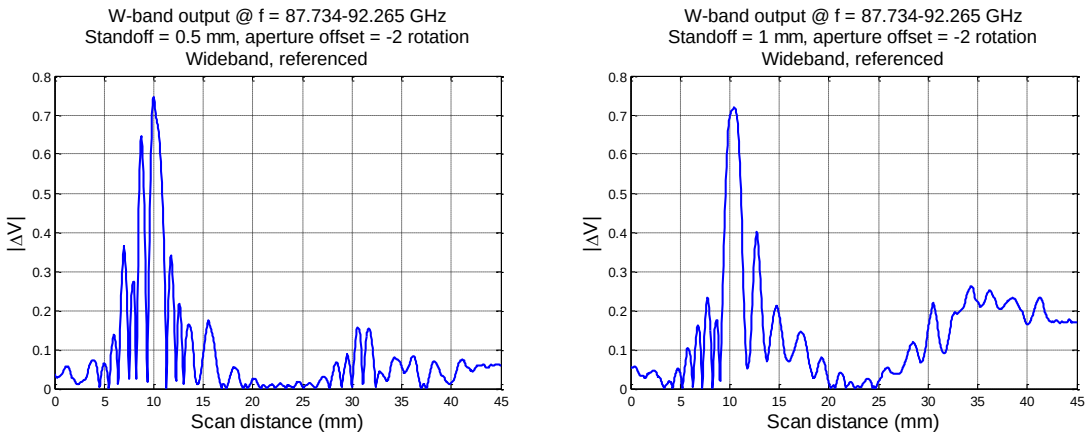

Figure 6. Referenced W-band wideband probe output signals at aperture offset of -2 rotations, and standoff distance of 0.5 mm (left) and 1 mm (right).

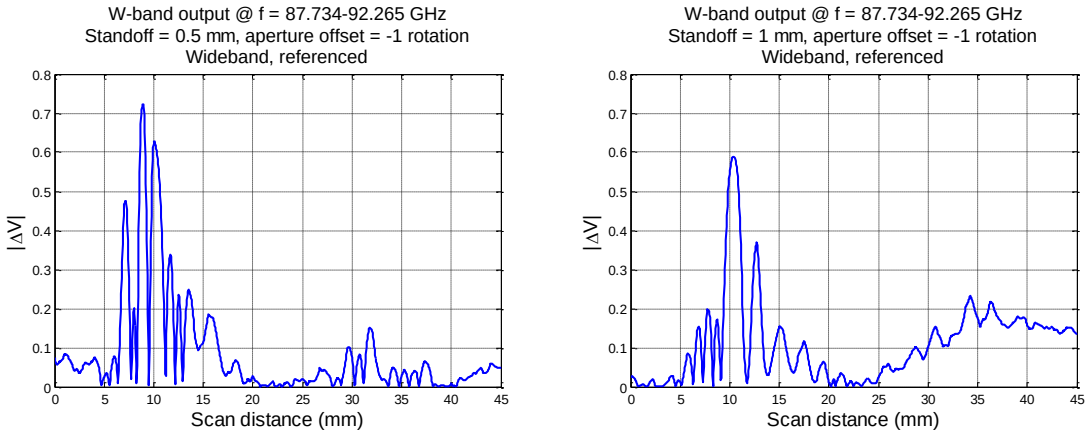

Figure 7. Referenced W-band wideband probe output signals at aperture offset of -1 rotation, and standoff distance of 0.5 mm (left) and 1 mm (right).

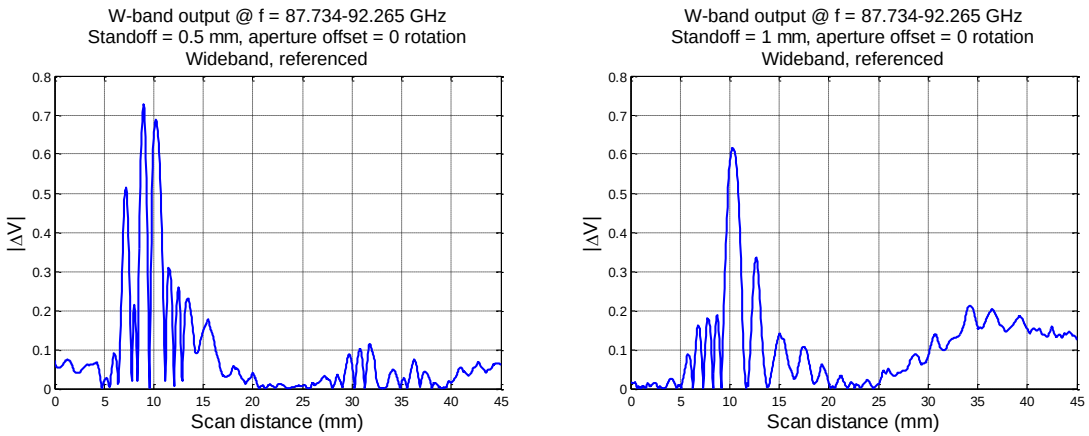

Figure 8. Referenced W-band wideband probe output signals at no aperture offset, and standoff distance of 0.5 mm (left) and 1 mm (right).

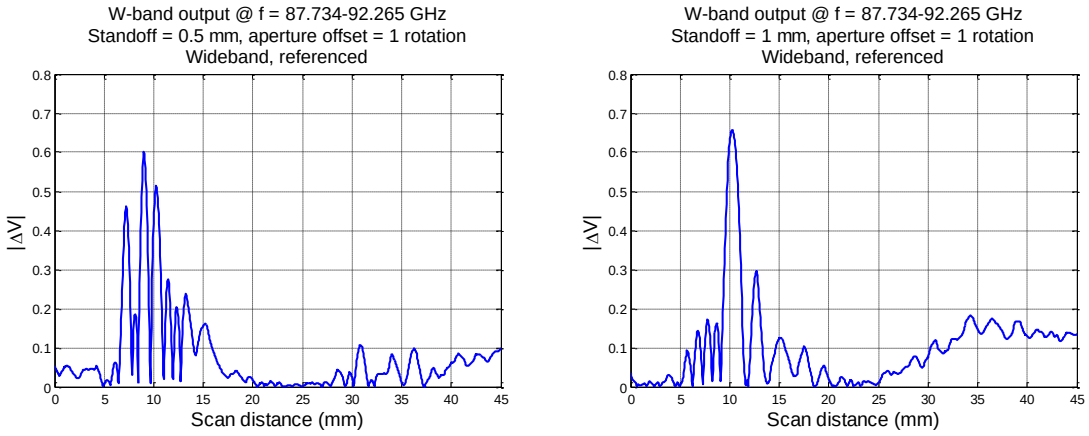

Figure 9. Referenced W-band wideband probe output signals at aperture offset of +1 rotation, and standoff distance of 0.5 mm (left) and 1 mm (right).

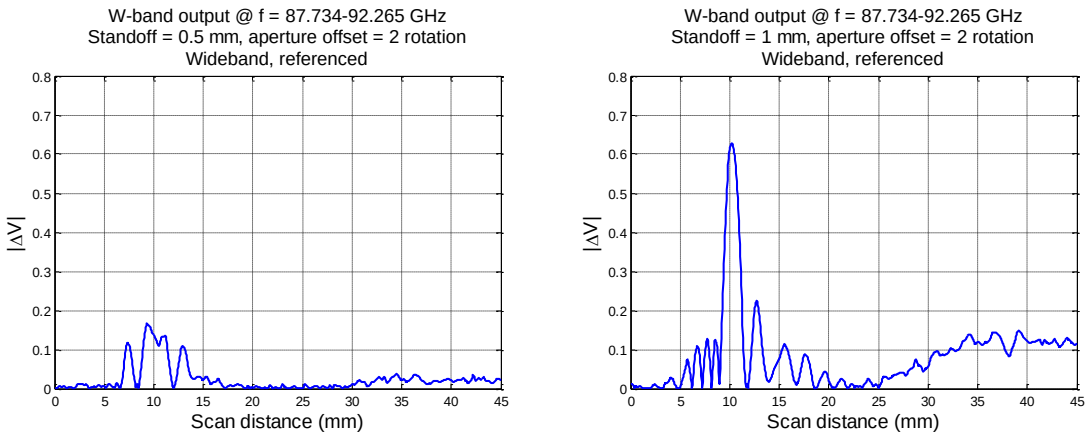

Figure 10. Referenced W-band wideband probe output signals at aperture offset of +2 rotations, and standoff distance of 0.5 mm (left) and 1 mm (right).

Figures 11 through 17 represent the comparisons between measurement and simulation results at standoff distance of 0.5 mm. Since a +2 and -2 rotation of aperture offset is approximately equal to +0.2 and -0.2 mm, respectively, these measurement results are compared to simulation results with aperture offset of ±0.25 mm.

Measurement results with aperture offsets of ±1 rotation (Figure 13 and 15), as well as simulation results with aperture offsets of ±0.5 mm (Figure 11 and 17) cannot be compared due to limited data available.

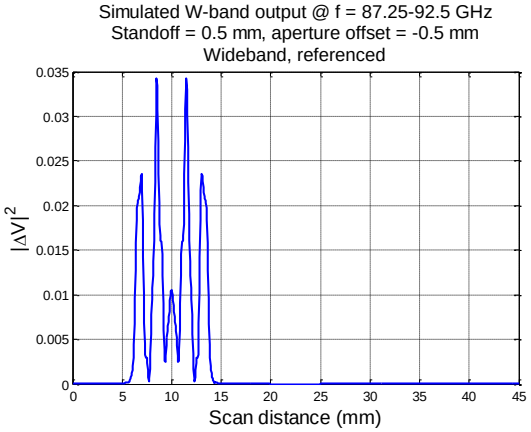

Figure 11. Simulated W-band results of 1.27 mm-long crack, at standoff distance of 0.5 mm, and aperture offset of -0.5 mm.

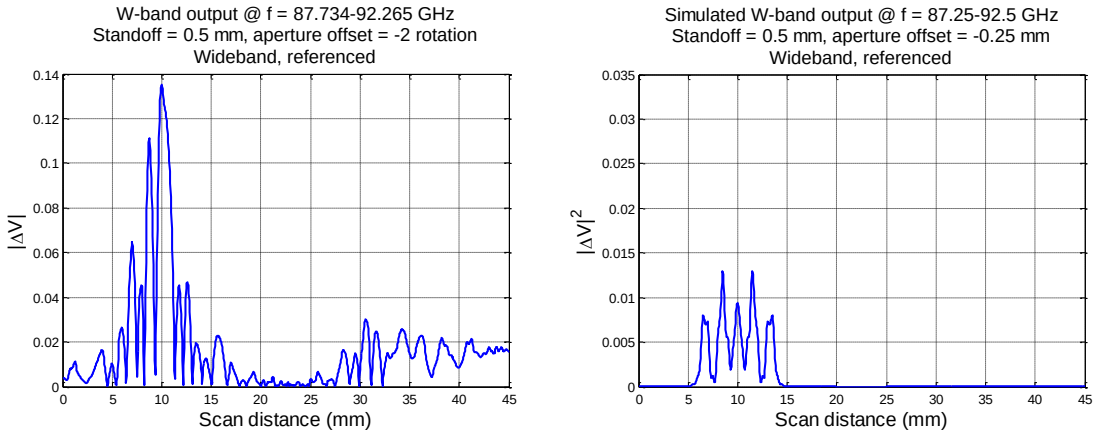

Figure 12. Measured (left) and simulated (right) W-band results of 1.27 mm-long crack, at standoff distance of 0.5 mm, and aperture offset of -2 rotations (measurements) and -0.25 mm (simulations).

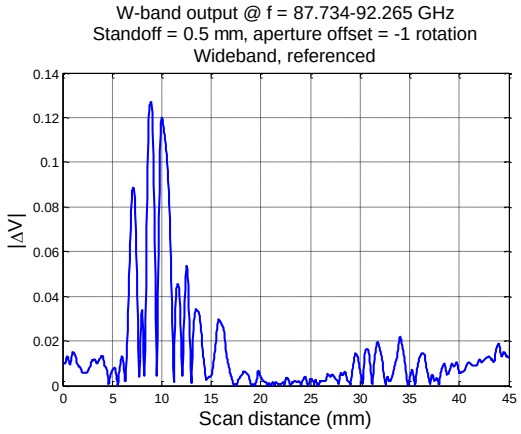

Figure 13. Measured W-band results of 1.27 mm-long crack, at standoff distance of 0.5 mm, and aperture offset of -1 rotation.

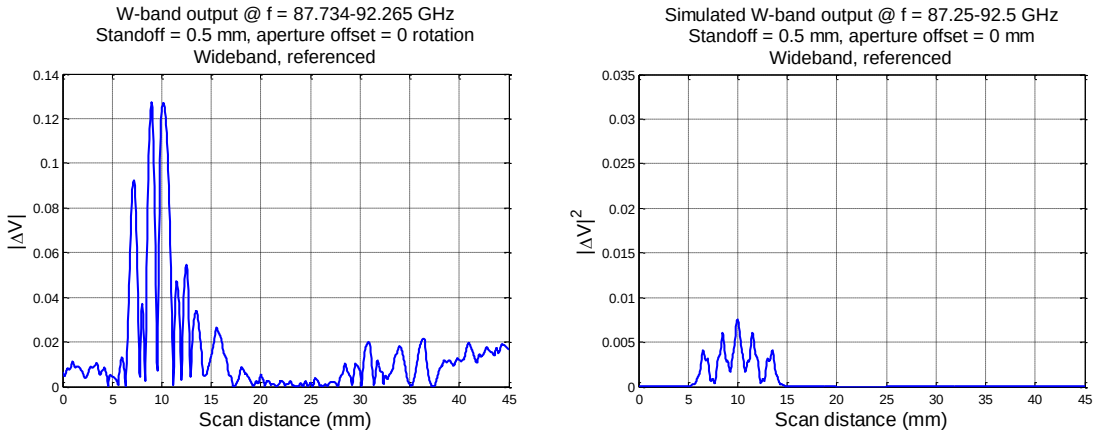

Figure 14. Measured (left) and simulated (right) W-band results of 1.27 mm-long crack, at standoff distance of 0.5 mm, and no aperture offset.

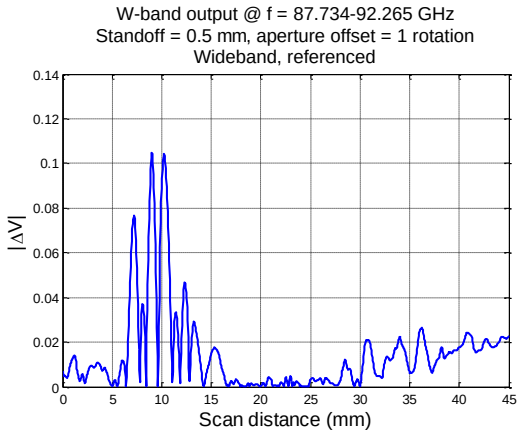

Figure 15. Measured W-band results of 1.27 mm-long crack, at standoff distance of 0.5 mm, and aperture offset of +1 rotation.

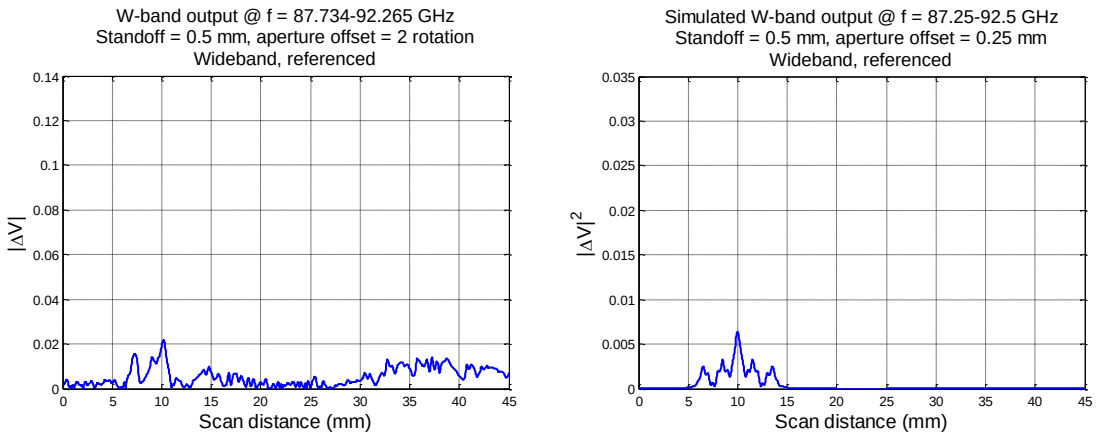

Figure 16. Measured (left) and simulated (right) W-band results of 1.27 mm-long crack, at standoff distance of 0.5 mm, and aperture offset of +2 rotations (measurements) and +0.25 mm (simulations).

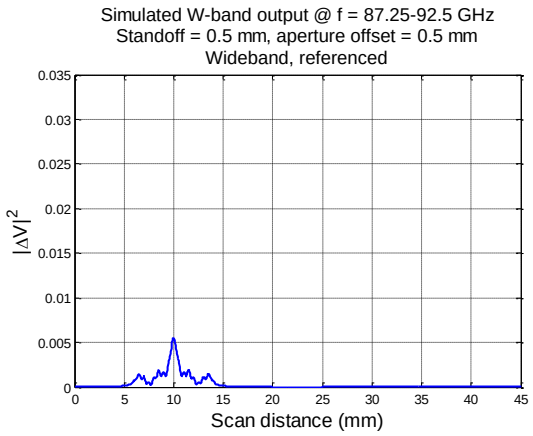

Figure 17. Simulated W-band results of 1.27 mm-long crack, at standoff distance of 0.5 mm, and aperture offset of +0.5 mm.

Figures 18 through 24 represent the comparisons between measurement and simulation results at standoff distance of 1 mm. Similar to results from 0.5 mm standoff distance, measurement results with aperture offsets of ±2 rotations are compared to simulation results with aperture offsets of ±0.2 mm.

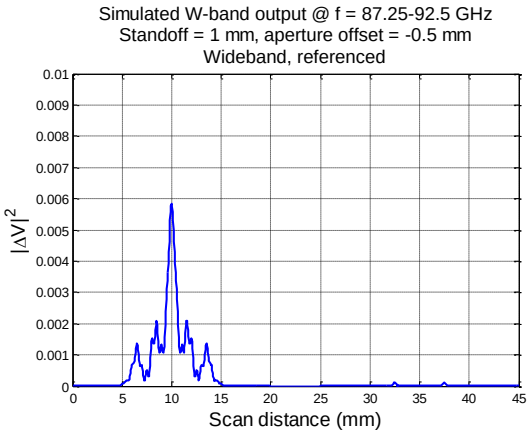

Figure 18. Simulated (right) W-band results of 1.27 mm-long crack, at standoff distance of 1 mm, and aperture offset of -0.5 mm.

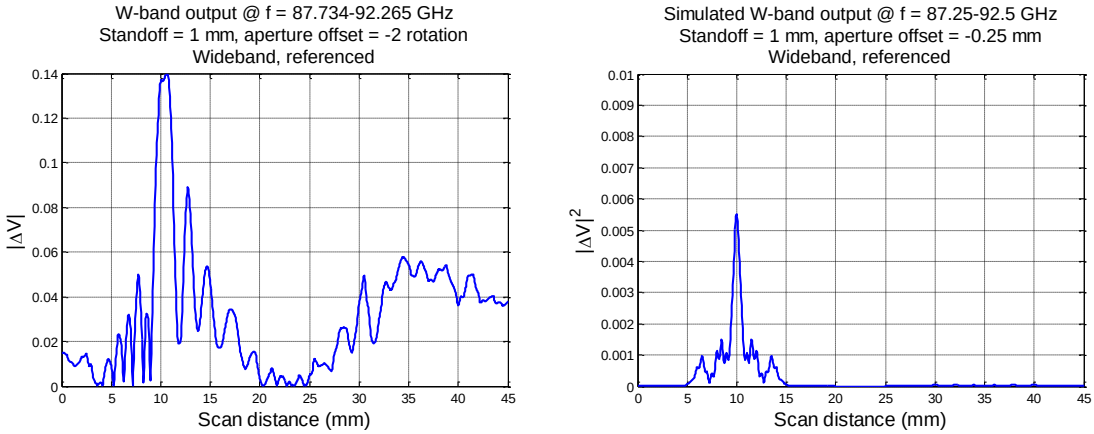

Figure 19. Measured (left) and simulated (right) W-band results of 1.27 mm-long crack, at standoff distance of 1 mm, and aperture offset of -2 rotations (measurements) and -0.25 mm (simulations).

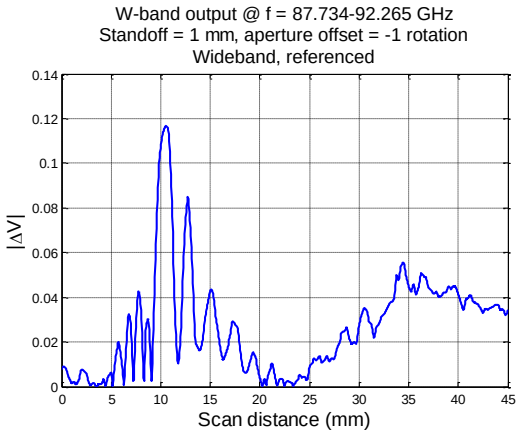

Figure 20. Measured W-band results of 1.27 mm-long crack, at standoff distance of 1 mm, and aperture offset of -1 rotation.

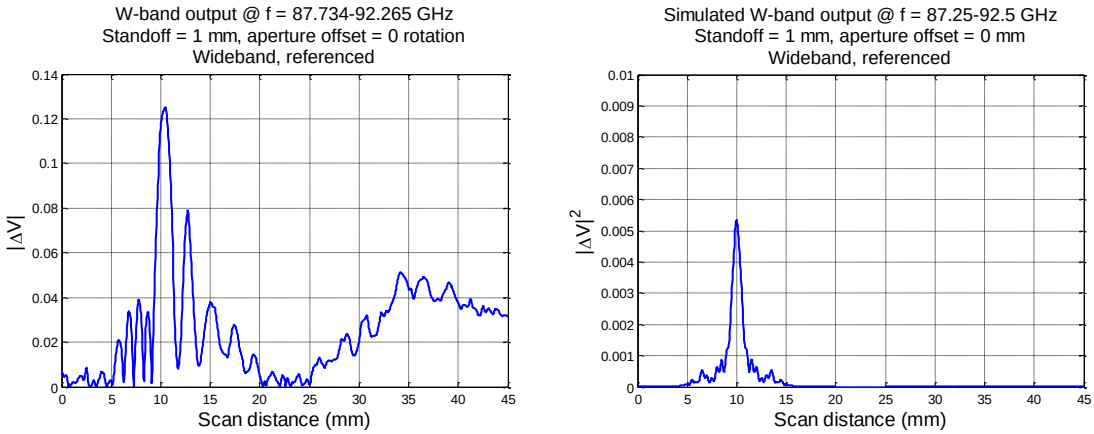

Figure 21. Measured (left) and simulated (right) W-band results of 1.27 mm-long crack, at standoff distance of 1 mm, and no aperture offset.

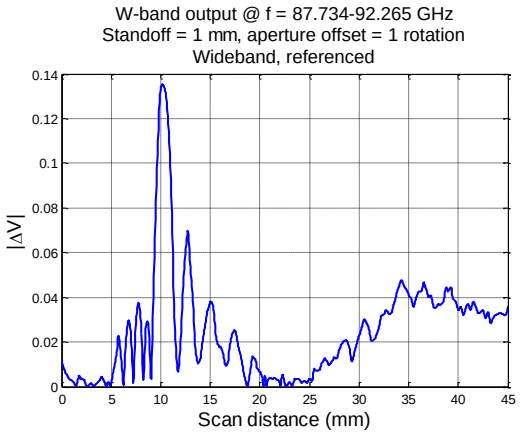

Figure 22. Measured W-band results of 1.27 mm-long crack, at standoff distance of 1 mm, and aperture offset of +1 rotation.

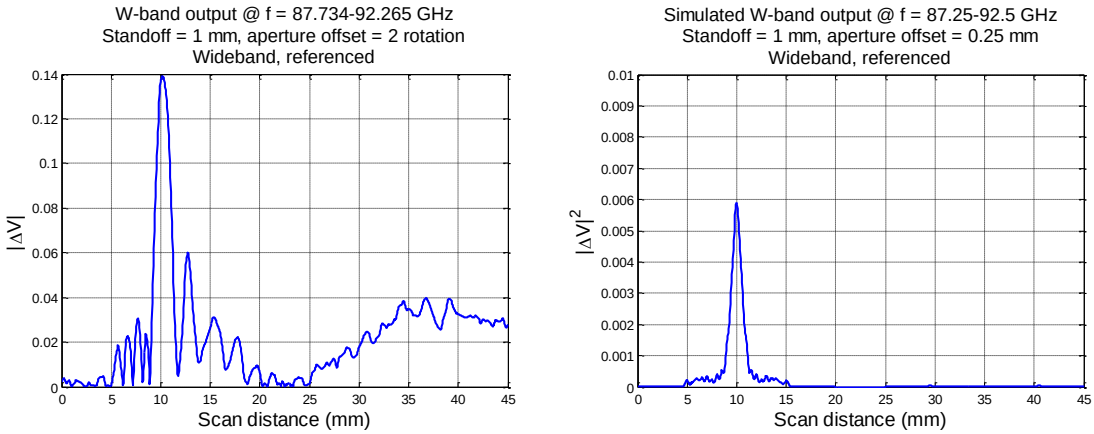

Figure 23. Measured (left) and simulated (right) W-band results of 1.27 mm-long crack, at standoff distance of 1 mm, and aperture offset of +2 rotation (measurements) and +0.25 mm (simulations).

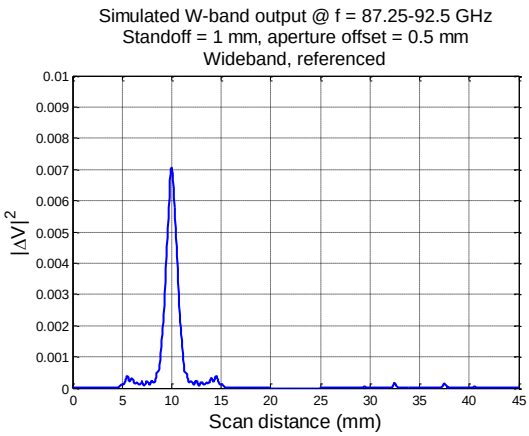

Figure 24. Simulated W-band results of 1.27 mm-long crack, at standoff distance of 1 mm, and aperture offset of +0.5 mm.

APPENDIX I.

ADDITIONAL FIGURES OF MEASUREMENT RESULTS (EFFECT OF PAINT THICKNESS)

This appendix provides the following results for Section 4.3 – Effect of Paint Thickness:

- wideband measurement results,
- referenced wideband measurement results,
- and comparisons between measurement and simulation results

Figures 1 through 8 represent the wideband measurement results at both standoff distances of 0.5 and 1 mm (measurement cannot be completed on the 0.49 mm-thick paint at a 0.5 mm standoff distance, therefore, only the results for 1 mm standoff distance are presented), while the referenced wideband data is shown in Figures 9 through 16. The comparisons between measurement and simulation results (at four common frequencies) are shown in Figures 17 through 24 (at standoff distance of 0.5 mm) and Figures 25 through 33 (at standoff distance of 1 mm).

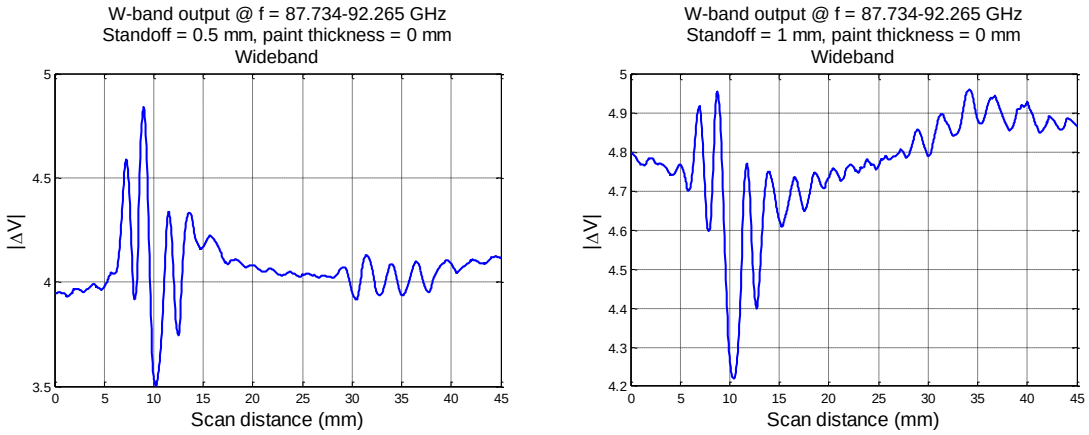

Figure 1. W-band wideband probe output signals at no paint, and standoff distance of 0.5 mm (left) and 1 mm (right).

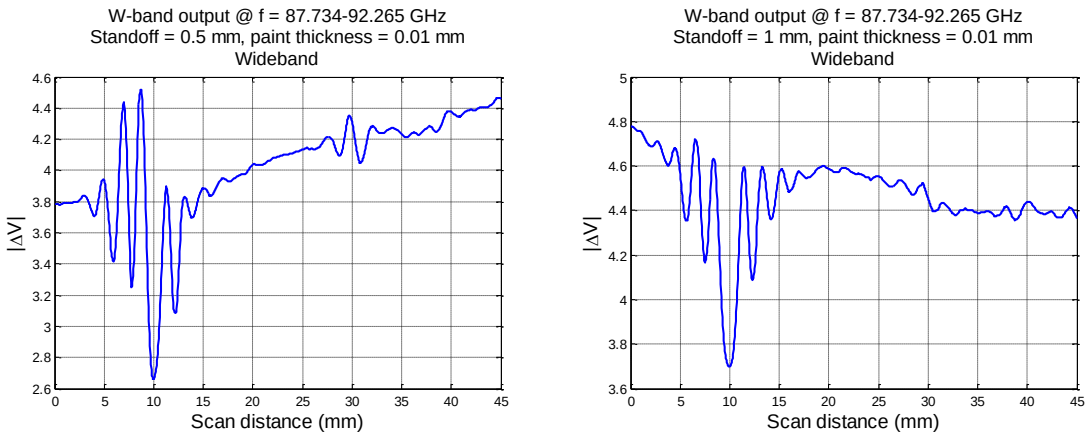

Figure 2. W-band wideband probe output signals at paint thickness of 0.01 mm, and standoff distance of 0.5 mm (left) and 1 mm (right).

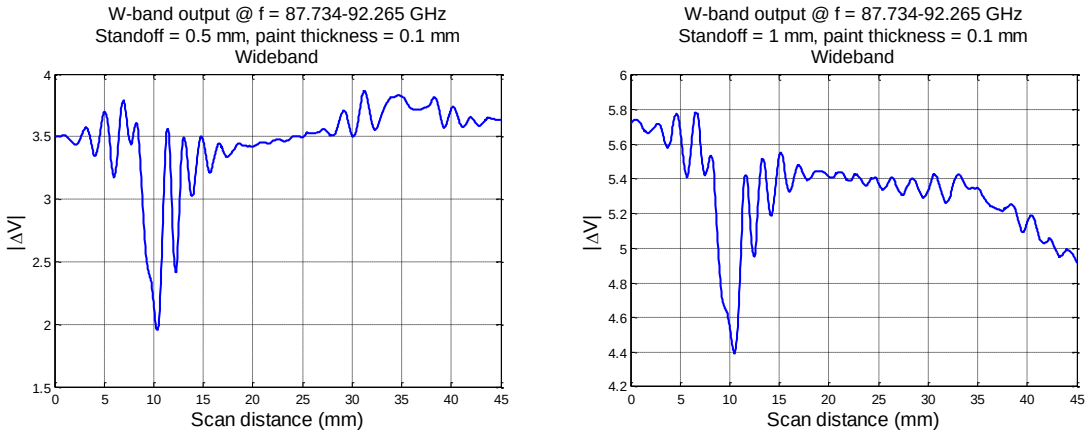

Figure 3. W-band wideband probe output signals at paint thickness of 0.1 mm, and standoff distance of 0.5 mm (left) and 1 mm (right).

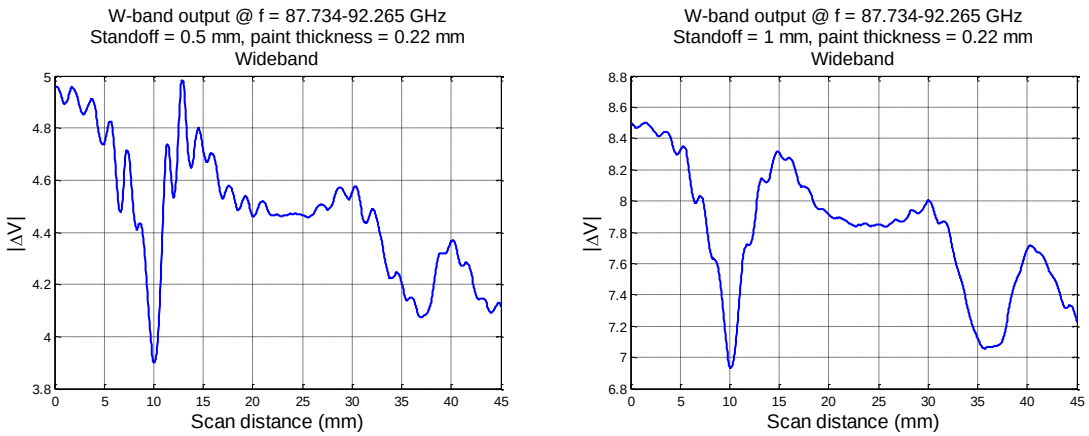

Figure 4. W-band wideband probe output signals at paint thickness of 0.22 mm, and standoff distance of 0.5 mm (left) and 1 mm (right).

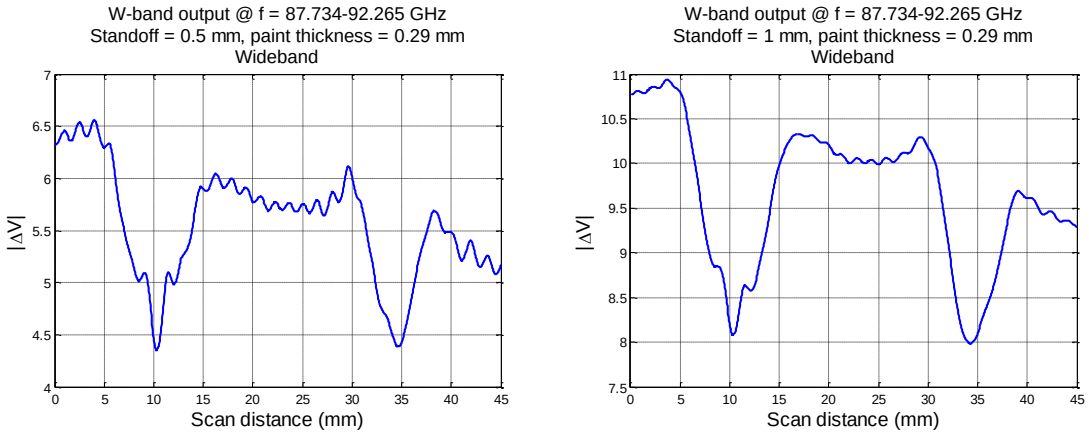

Figure 5. W-band wideband probe output signals at paint thickness of 0.29 mm, and standoff distance of 0.5 mm (left) and 1 mm (right).

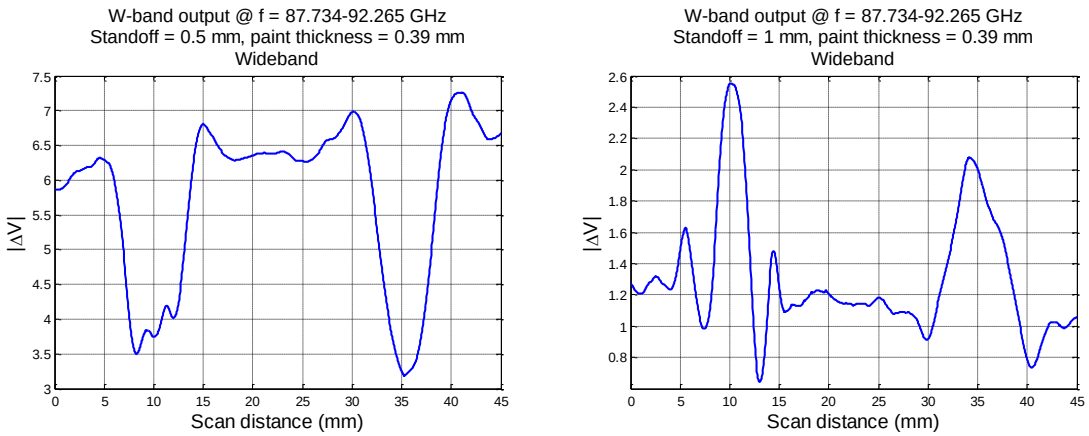

Figure 6. W-band wideband probe output signals at paint thickness of 0.39 mm, and standoff distance of 0.5 mm (left) and 1 mm (right).

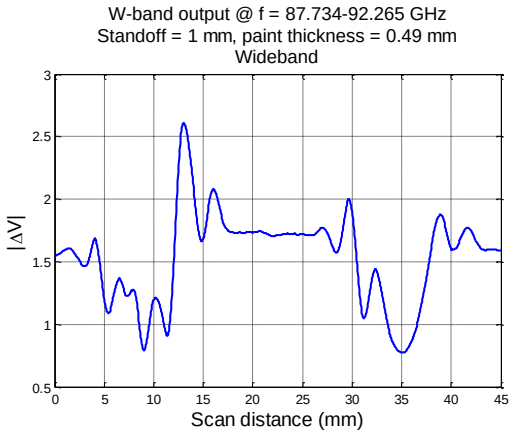

Figure 7. W-band wideband probe output signals at paint thickness of 0.49 mm, and standoff distance of 1 mm.

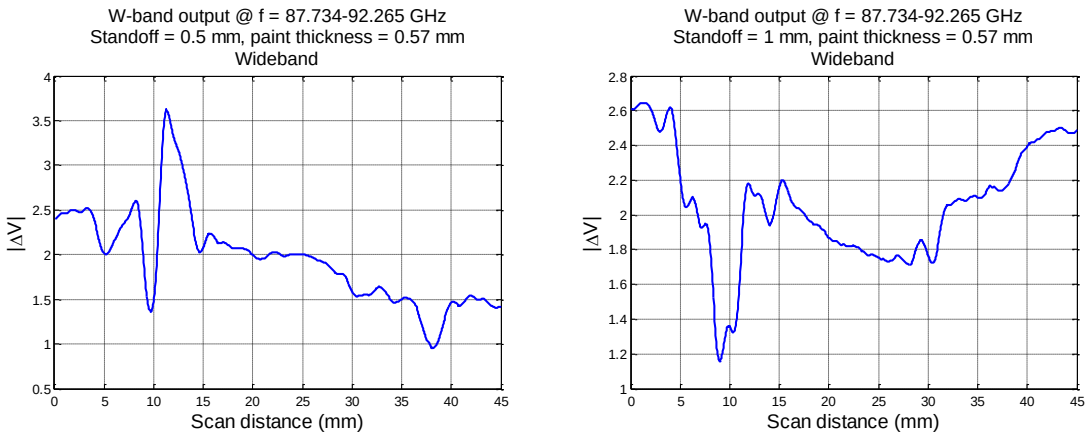

Figure 8. W-band wideband probe output signals at paint thickness of 0.57 mm, and standoff distance of 0.5 mm (left) and 1 mm (right).

Figures 9 through 16 represent the referenced measurement results.

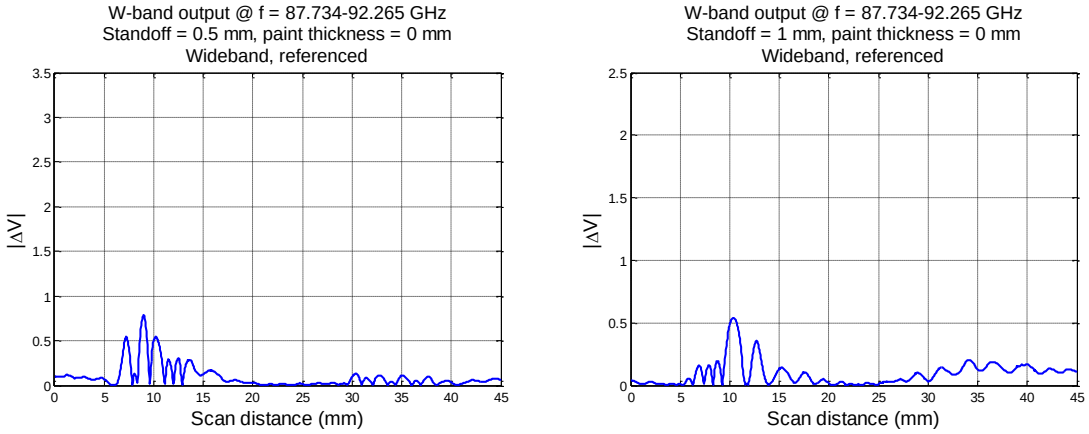

Figure 9. Referenced W-band wideband probe output signals at no paint, and standoff distance of 0.5 mm (left) and 1 mm (right).

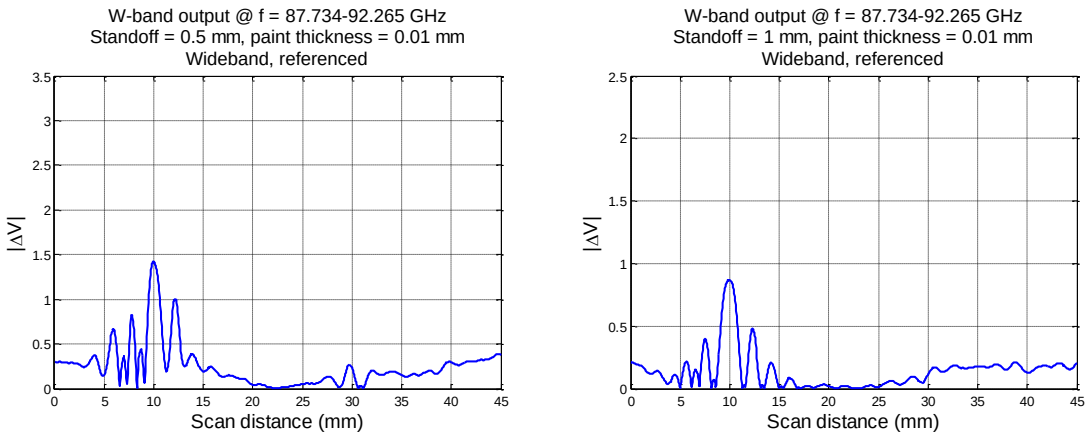

Figure 10. Referenced W-band wideband probe output signals at paint thickness of 0.01 mm, and standoff distance of 0.5 mm (left) and 1 mm (right).

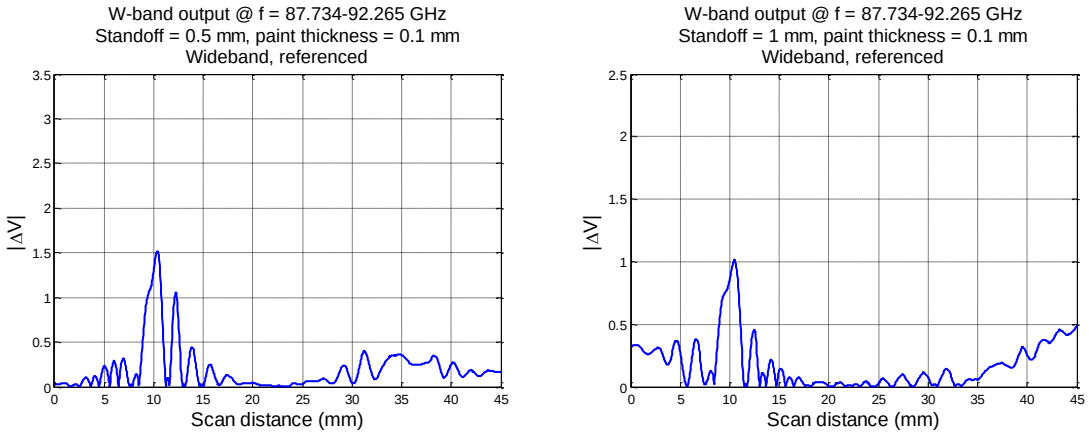

Figure 11. Referenced W-band wideband probe output signals at paint thickness of 0.1 mm, and standoff distance of 0.5 mm (left) and 1 mm (right).

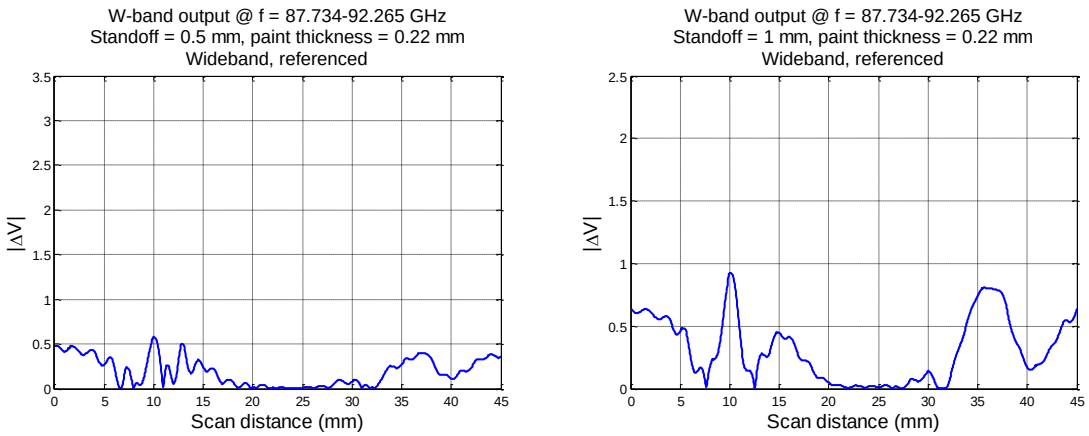

Figure 12. Referenced W-band wideband probe output signals at paint thickness of 0.22 mm, and standoff distance of 0.5 mm (left) and 1 mm (right).

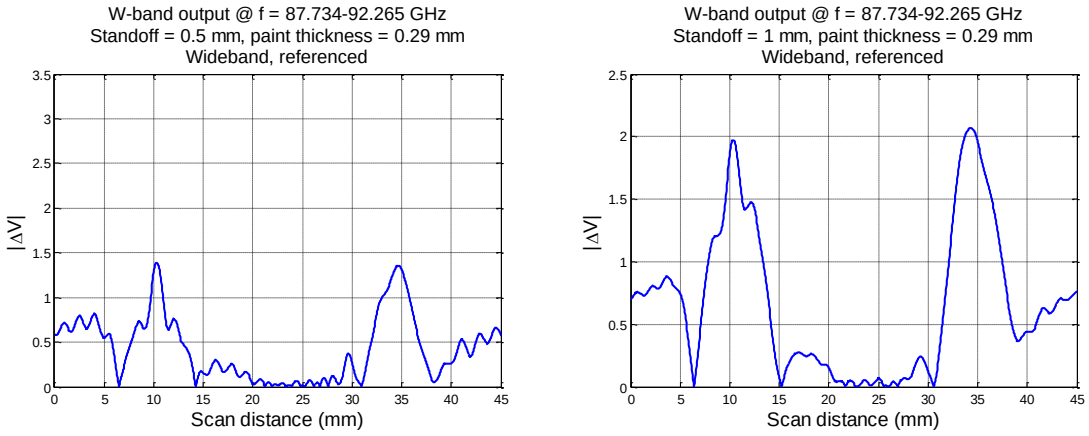

Figure 13. Referenced W-band wideband probe output signals at paint thickness of 0.29 mm, and standoff distance of 0.5 mm (left) and 1 mm (right).

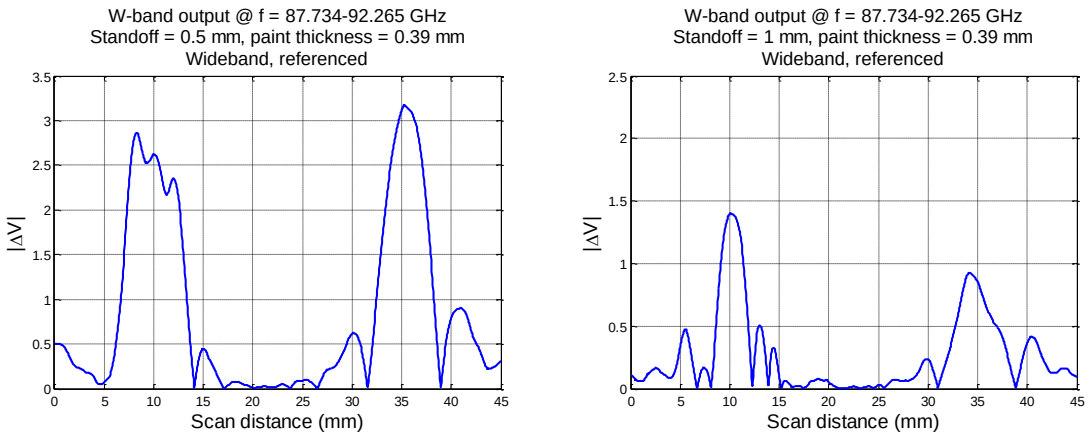

Figure 14. Referenced W-band wideband probe output signals at paint thickness of 0.39 mm, and standoff distance of 0.5 mm (left) and 1 mm (right).

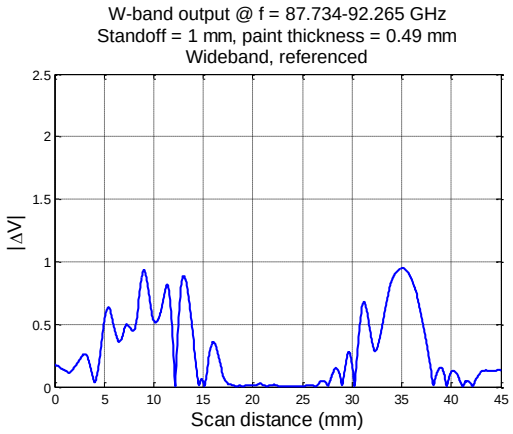

Figure 15. Referenced W-band wideband probe output signals at paint thickness of 0.49 mm, and standoff distance of 0.5 mm (left) and 1 mm (right).

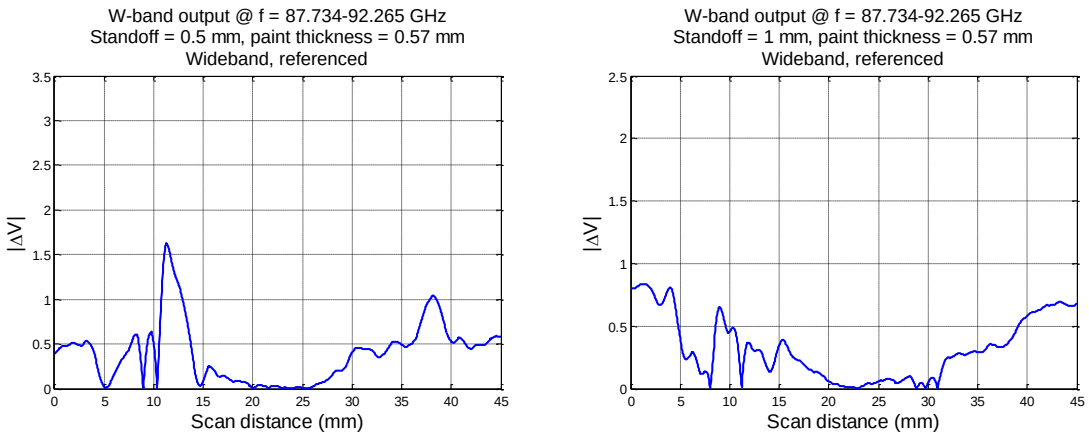

Figure 16. Referenced W-band wideband probe output signals at paint thickness of 0.57 mm, and standoff distance of 0.5 mm (left) and 1 mm (right).

Figures 17 through 24 represent the comparisons between measurement and simulation results at standoff distance of 0.5 mm. Measurement results with paint thicknesses of 0.01 (Figure 18) and 0.29 mm (Figure 22), and simulation results with paint thickness of 0.13 mm (Figure 20) cannot be compared due to limited data available. Note the figures may not be in the same scale.

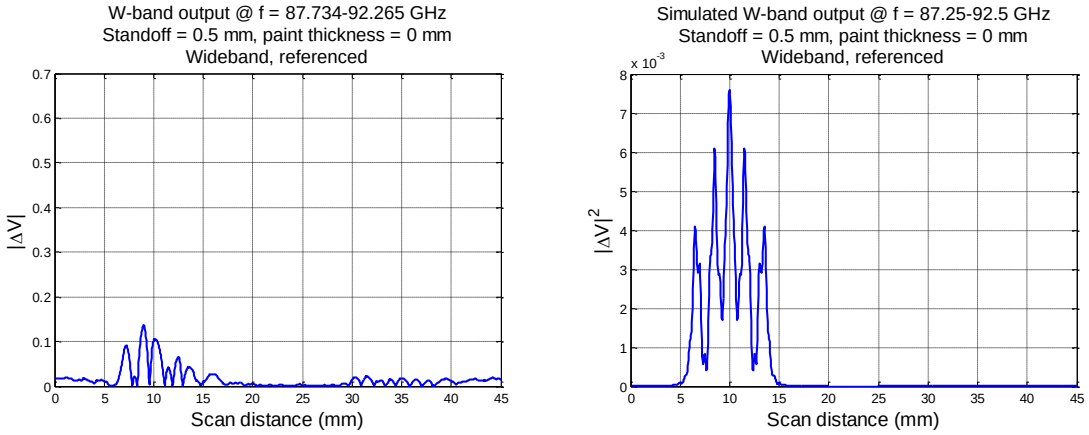

Figure 17. Measured (left) and simulated (right) W-band results of 1.27 mm-long crack, at standoff distance of 0.5 mm, and no paint.

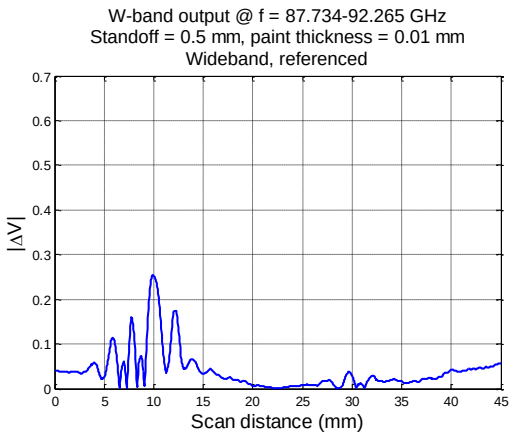

Figure 18. Measured W-band results of 1.27 mm-long crack, at standoff distance of 0.5 mm, and paint thickness of 0.01 mm.

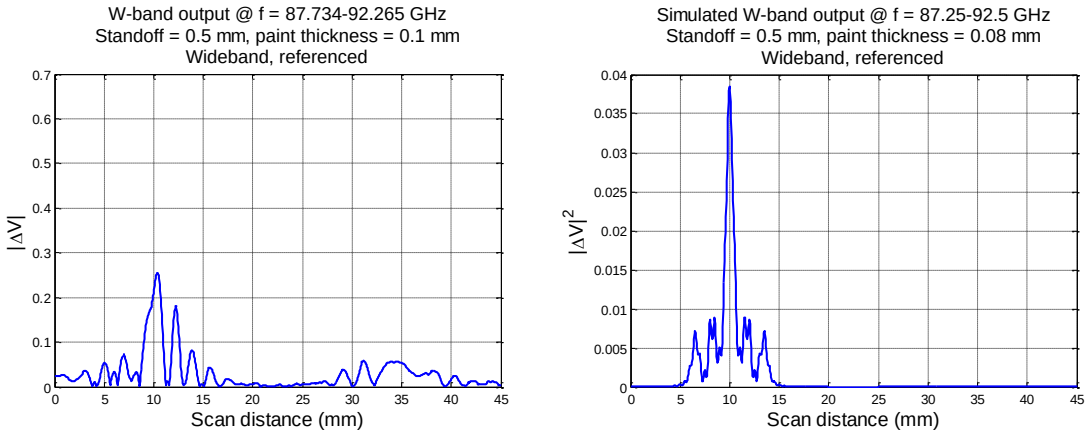

Figure 19. Measured (left) and simulated (right) W-band results of 1.27 mm-long crack, at standoff distance of 0.5 mm, and paint thickness of 0.1 mm (measurements) and 0.08 mm (simulations).

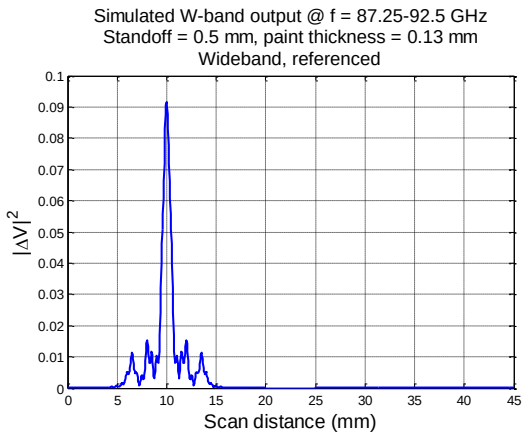

Figure 20. Simulated W-band results of 1.27 mm-long crack, at standoff distance of 0.5 mm, and paint thickness of 0.13 mm.

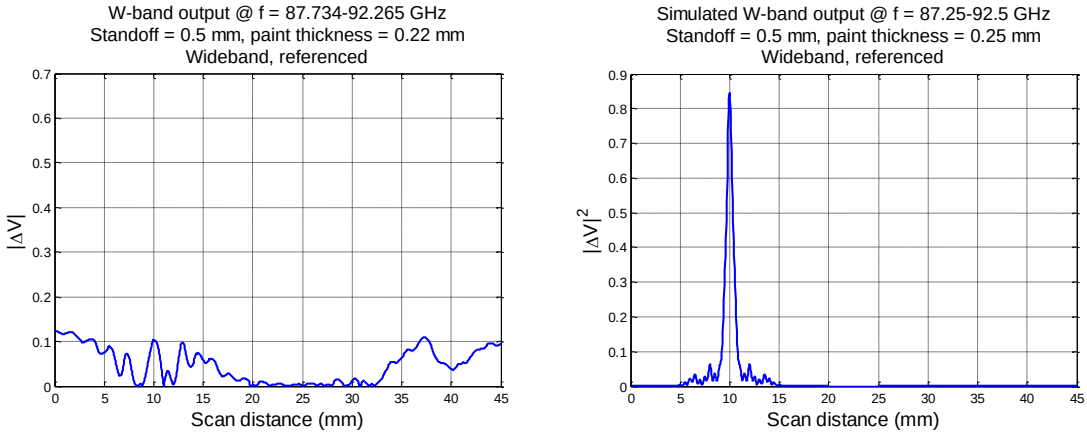

Figure 21. Measured (left) and simulated (right) W-band results of 1.27 mm-long crack, at standoff distance of 0.5 mm, and paint thickness of 0.22 mm (measurements) and 0.25 mm (simulations).

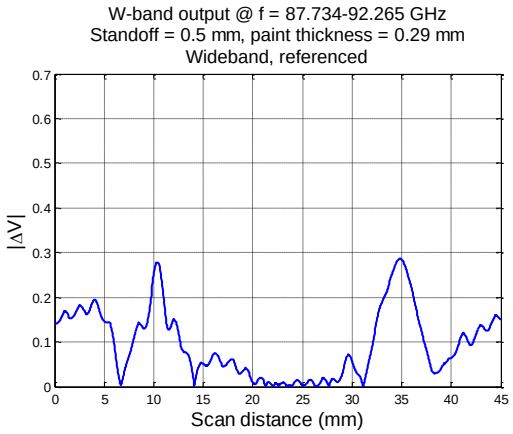

Figure 22. Measured W-band results of 1.27 mm-long crack, at standoff distance of 0.5 mm, and paint thickness of 0.29 mm.

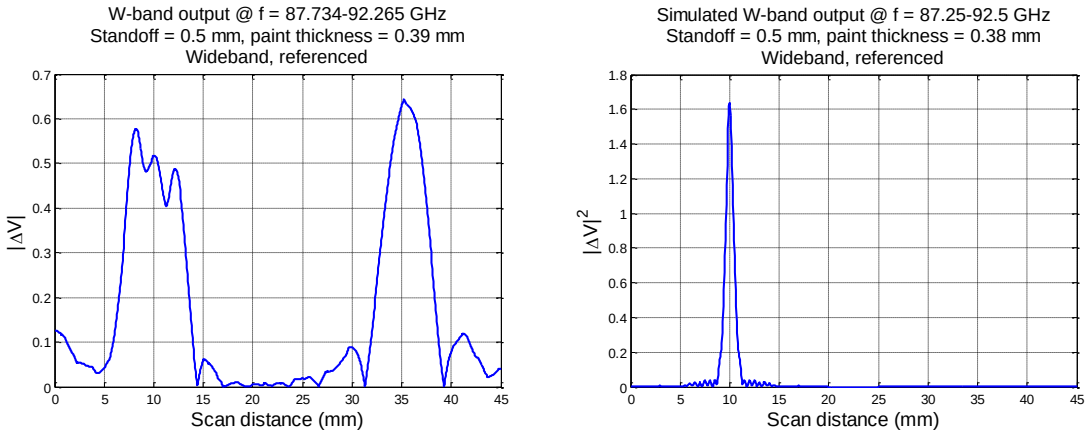

Figure 23. Measured (left) and simulated (right) W-band results of 1.27 mm-long crack, at standoff distance of 0.5 mm, and paint thickness of 0.38 mm (measurements) and 0.39 mm (simulations).

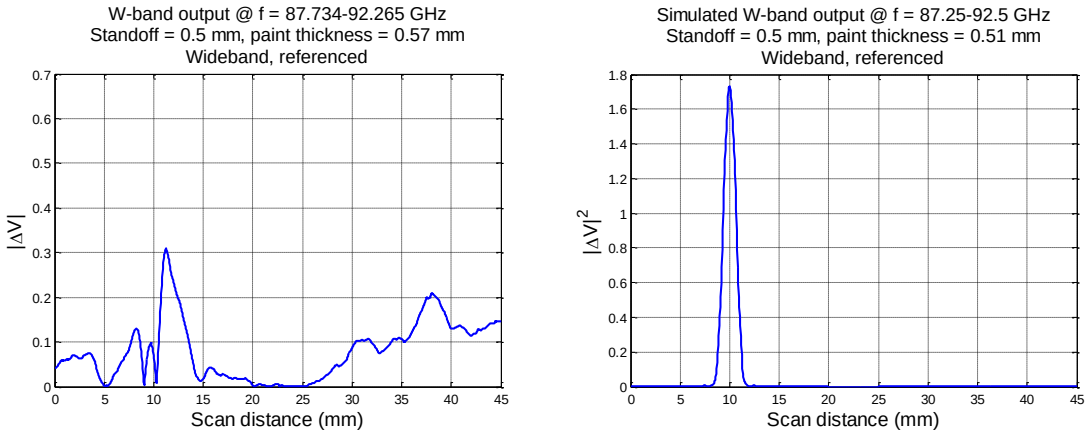

Figure 24. Measured (left) and simulated (right) W-band results of 1.27 mm-long crack, at standoff distance of 0.5 mm, and paint thickness of 0.57 mm (measurements) and 0.51 mm (simulations).

Figures 25 through 33 represent the comparisons between measurement and simulation results at standoff distance of 1 mm. Similar to results from 0.5 mm standoff distance, measurement results with paint thicknesses of 0.01 (Figure 26), 0.29 (Figure 30), and 0.57 mm (Figure 33), and simulation results with paint thickness of 0.13 mm (Figure 28) cannot be compared due to limited data available. Note the figures may not be in the same scale.

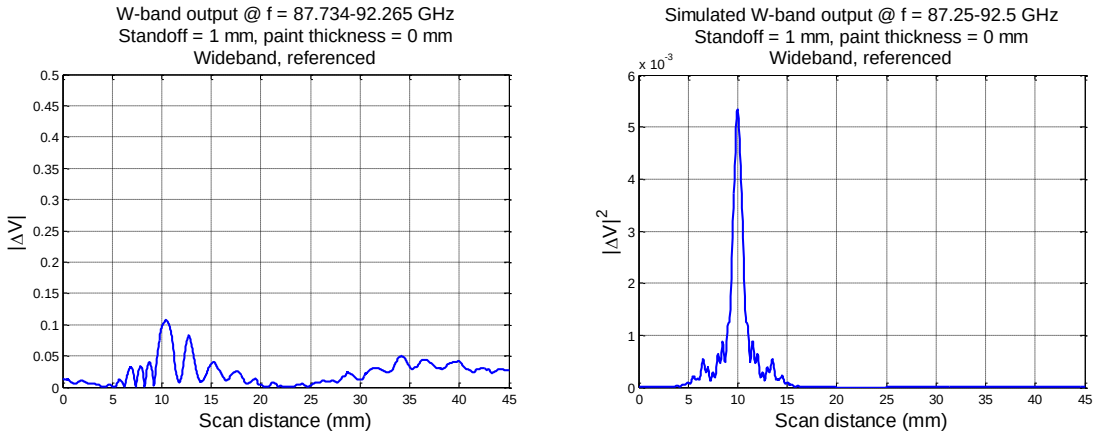

Figure 25. Measured (left) and simulated (right) W-band results of 1.27 mm-long crack, at standoff distance of 1 mm, and no paint.

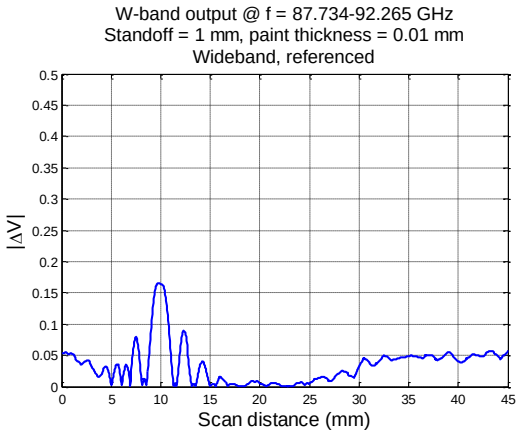

Figure 26. Measured W-band results of 1.27 mm-long crack, at standoff distance of 1 mm, and paint thickness of 0.01 mm.

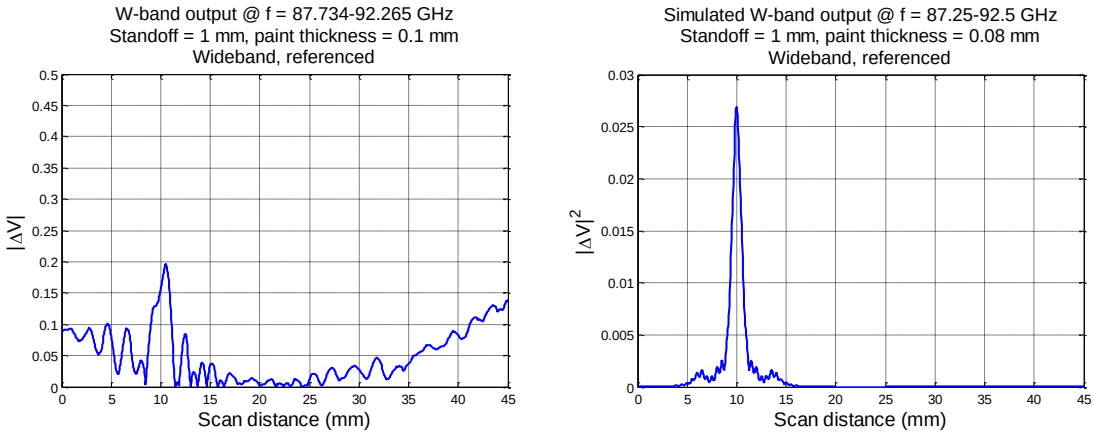

Figure 27. Measured (left) and simulated (right) W-band results of 1.27 mm-long crack, at standoff distance of 1 mm, and paint thickness of 0.1 mm (measurements) and 0.08 mm (simulations).

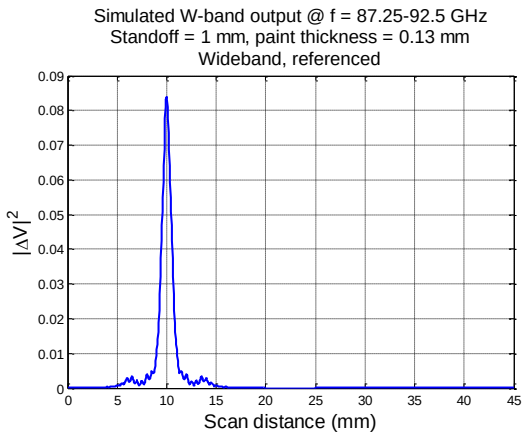

Figure 28. Simulated W-band results of 1.27 mm-long crack, at standoff distance of 1 mm, and paint thickness of 0.13 mm.

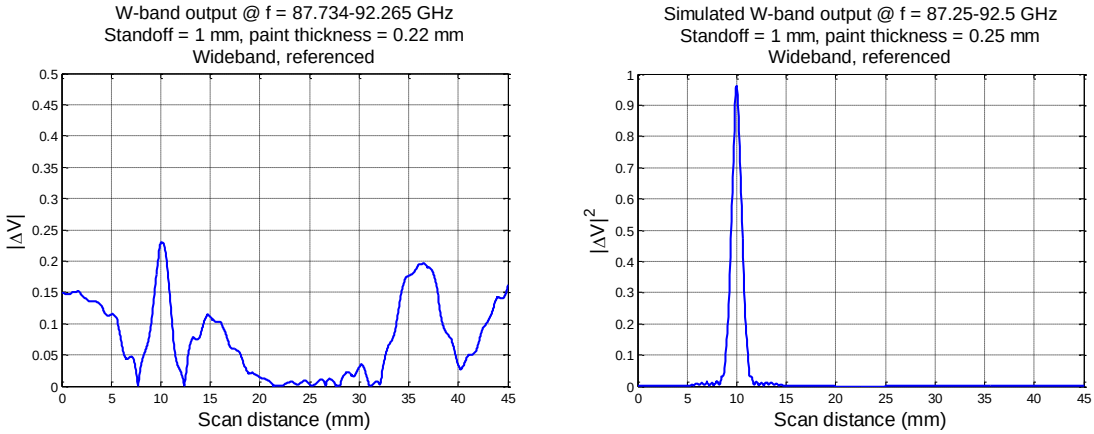

Figure 29. Measured (left) and simulated (right) W-band results of 1.27 mm-long crack, at standoff distance of 1 mm, and paint thickness of 0.22 mm (measurements) and 0.25 mm (simulations).

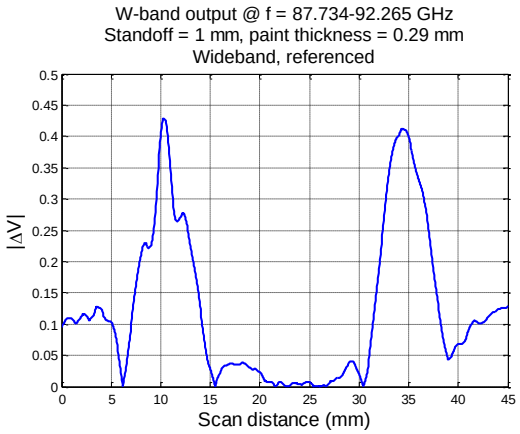

Figure 30. Measured W-band results of 1.27 mm-long crack, at standoff distance of 1 mm, and paint thickness of 0.29 mm.

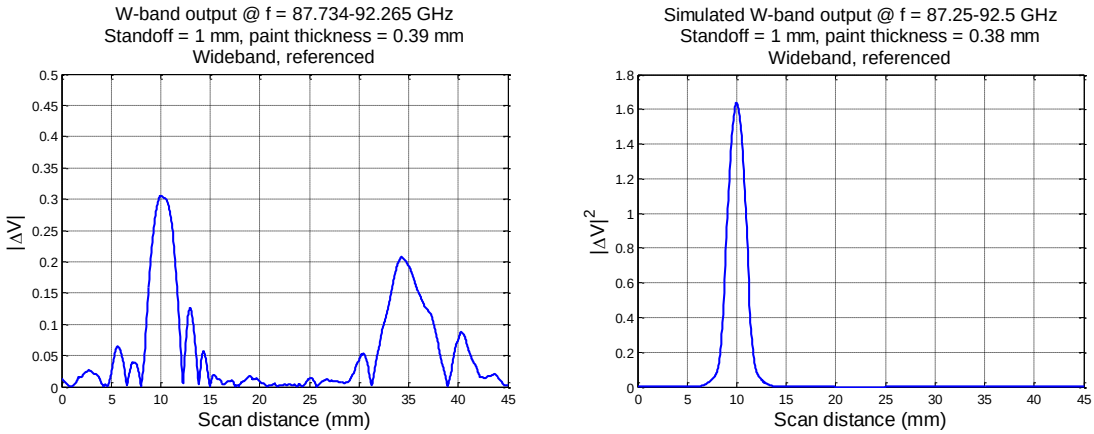

Figure 31. Measured (left) and simulated (right) W-band results of 1.27 mm-long crack, at standoff distance of 1 mm, and paint thickness of 0.39 mm (measurements) and 0.38 mm (simulations).

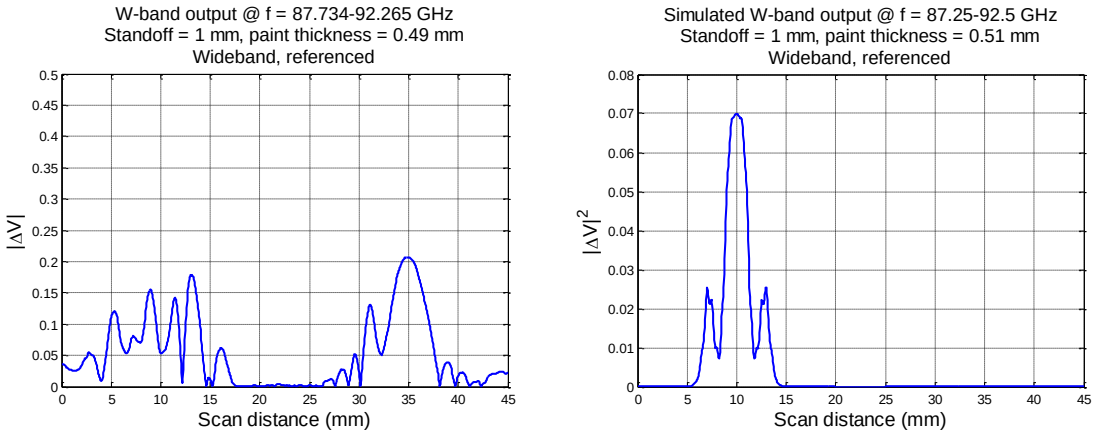

Figure 32. Measured (left) and simulated (right) W-band results of 1.27 mm-long crack, at standoff distance of 1 mm, and paint thickness of 0.49 mm (measurements) and 0.51 mm (simulations).

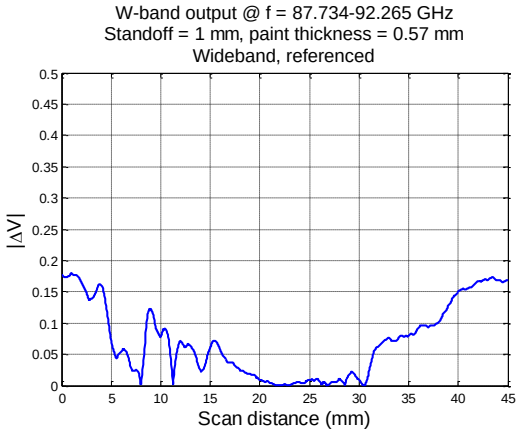

Figure 33. Measured W-band results of 1.27 mm-long crack, at standoff distance of 1 mm, and paint thickness of 0.57 mm.

APPENDIX J.

ADDITIONAL FIGURES OF MEASUREMENT RESULTS (EFFECT OF PROBE MISALIGNMENT)

This appendix provides the following results for Section 4.4 – Effect of Probe Misalignment:

- wideband measurement results,
- referenced wideband measurement results,
- and comparisons between measurement and simulation results

Figures 1 through 5 represent the wideband measurement results at both standoff distances of 0.5 and 1 mm, while the referenced wideband data is shown in Figures 6 through 10. The comparisons between measurement and simulation results (at four common frequencies) are shown in Figures 11 through 15 (at standoff distance of 0.5 mm) and Figures 16 through 20 (at standoff distance of 1 mm).

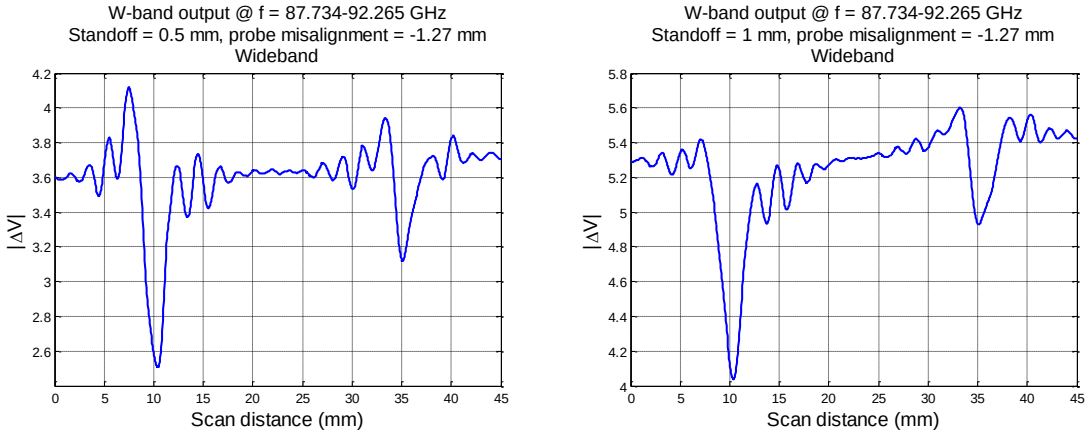

Figure 1. W-band wideband probe output signals at probe misalignment of -1.27 mm, and standoff distance of 0.5 mm (left) and 1 mm (right).

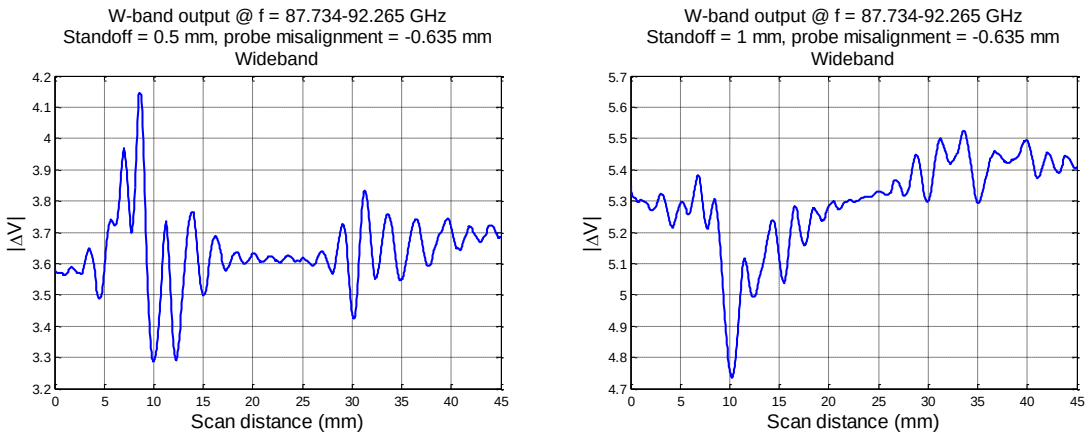

Figure 2. W-band wideband probe output signals at probe misalignment of -0.635 mm, and standoff distance of 0.5 mm (left) and 1 mm (right).

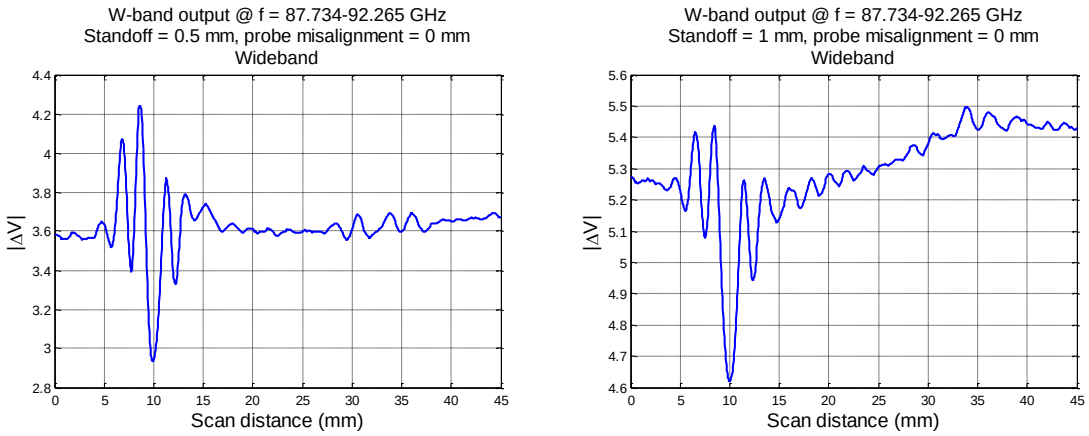

Figure 3. W-band wideband probe output signals at no probe misalignment, and standoff distance of 0.5 mm (left) and 1 mm (right).

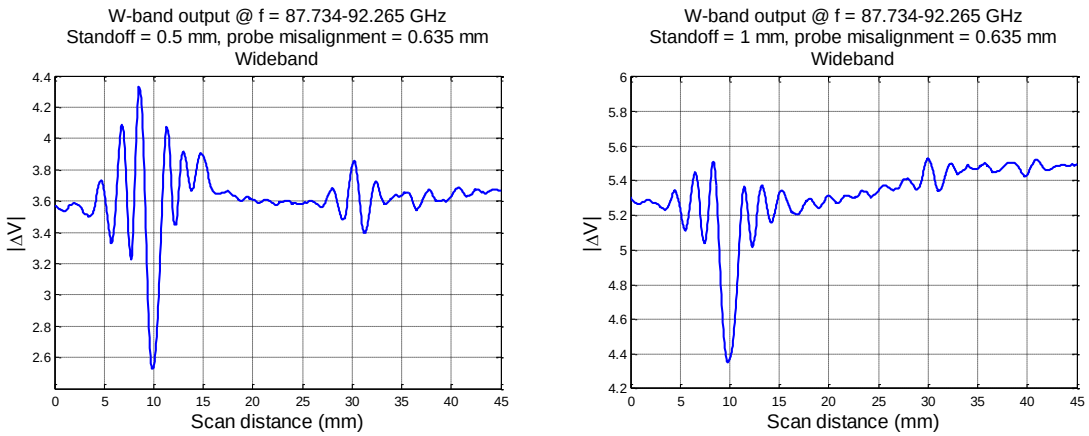

Figure 4. W-band wideband probe output signals at probe misalignment of +0.635 mm, and standoff distance of 0.5 mm (left) and 1 mm (right).

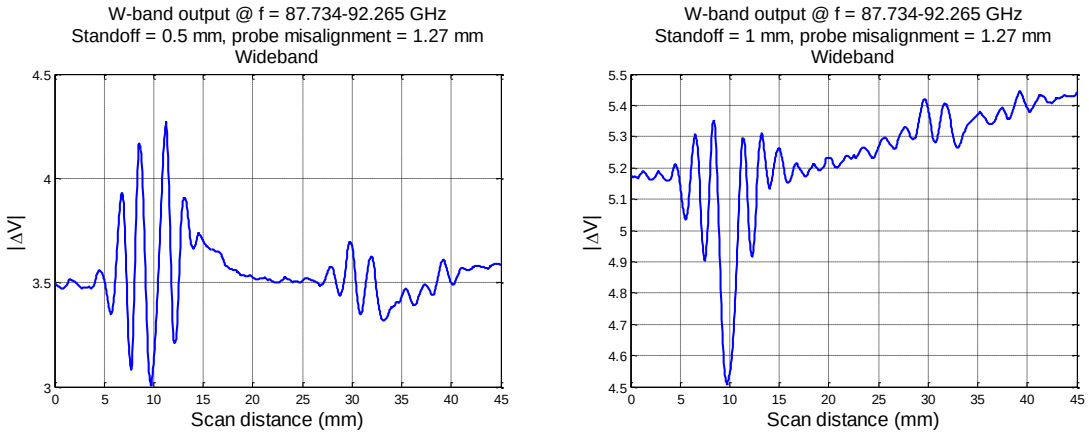

Figure 5. W-band wideband probe output signals at probe misalignment of +1.27 mm, and standoff distance of 0.5 mm (left) and 1 mm (right).

Figures 6 through 10 represent the referenced measurement results.

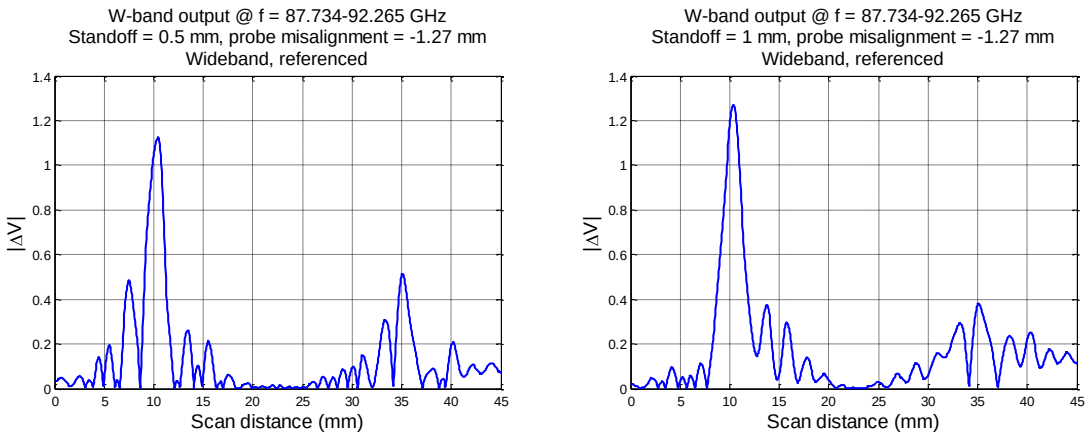

Figure 6. Referenced W-band wideband probe output signals at probe misalignment of -1.27 mm, and standoff distance of 0.5 mm (left) and 1 mm (right).

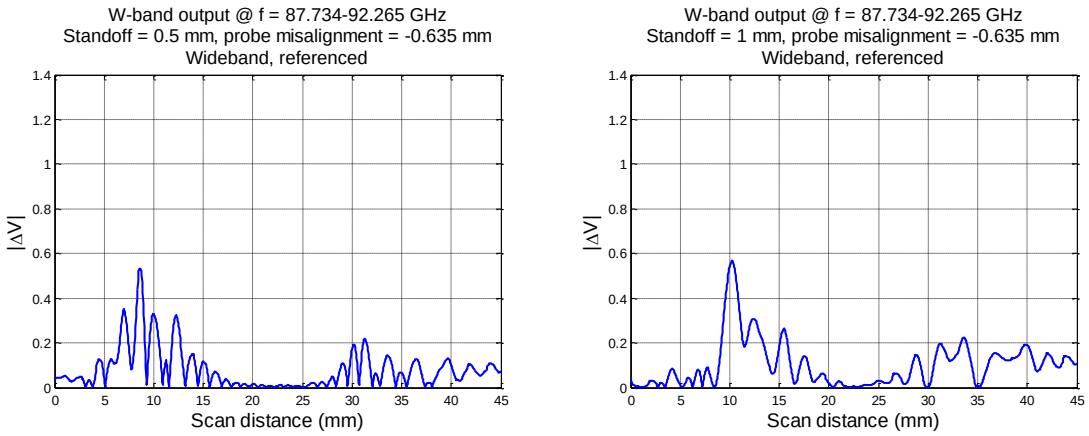

Figure 7. Referenced W-band wideband probe output signals at probe misalignment of -0.635 mm, and standoff distance of 0.5 mm (left) and 1 mm (right).

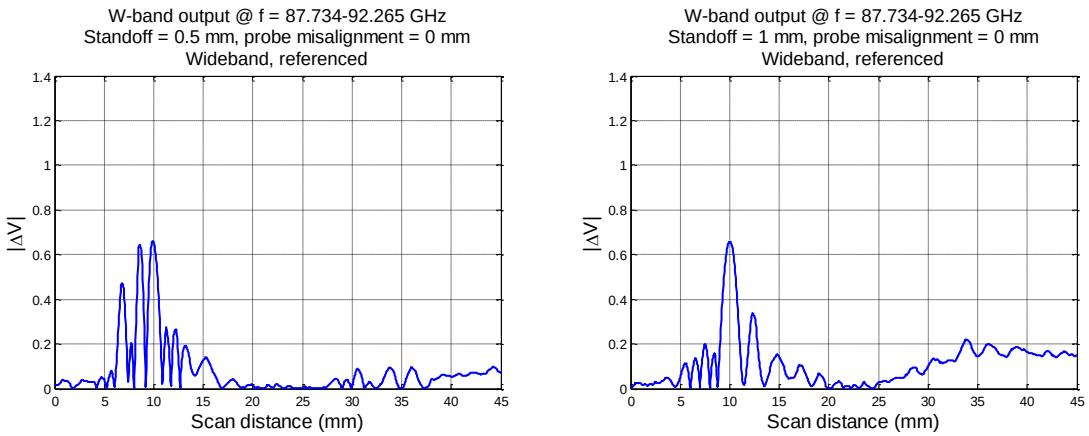

Figure 8. Referenced W-band wideband probe output signals at no probe, and standoff distance of 0.5 mm (left) and 1 mm (right).

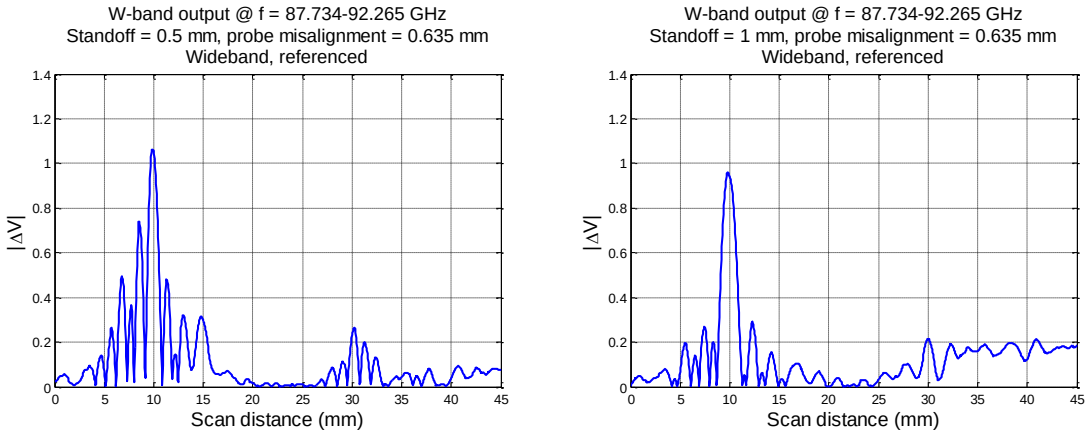

Figure 9. Referenced W-band wideband probe output signals at probe misalignment of +0.635 mm, and standoff distance of 0.5 mm (left) and 1 mm (right).

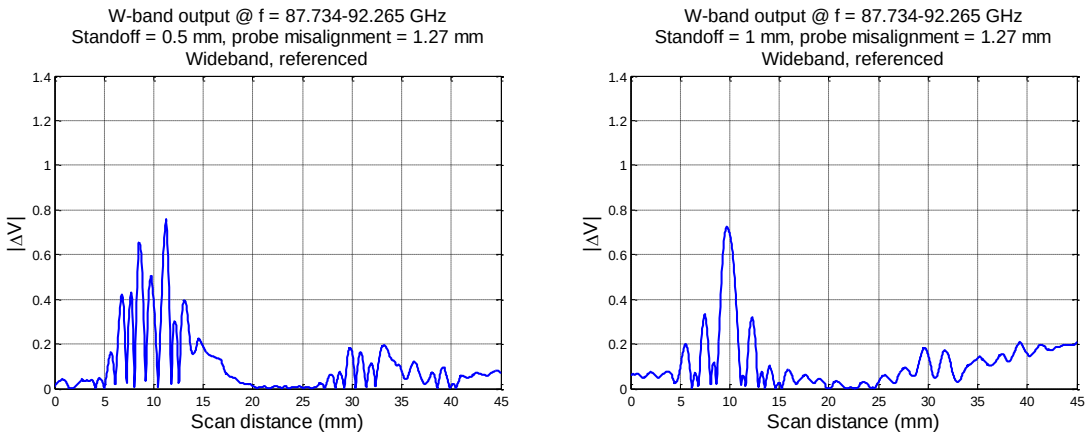

Figure 10. Referenced W-band wideband probe output signals at probe misalignment of +1.27 mm, and standoff distance of 0.5 mm (left) and 1 mm (right).

Figures 11 through 15 represent the comparisons between measurement and simulation results at standoff distance of 0.5 mm. Note the figures may not be in the same scale.

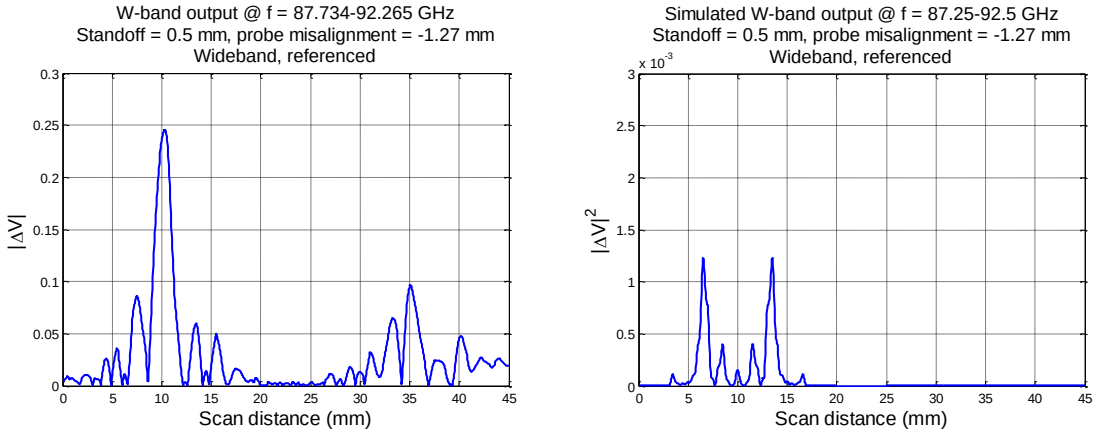

Figure 11. Measured (left) and simulated (right) W-band results of 1.27 mm-long crack, at standoff distance of 0.5 mm, and probe misalignment of -1.27 mm.

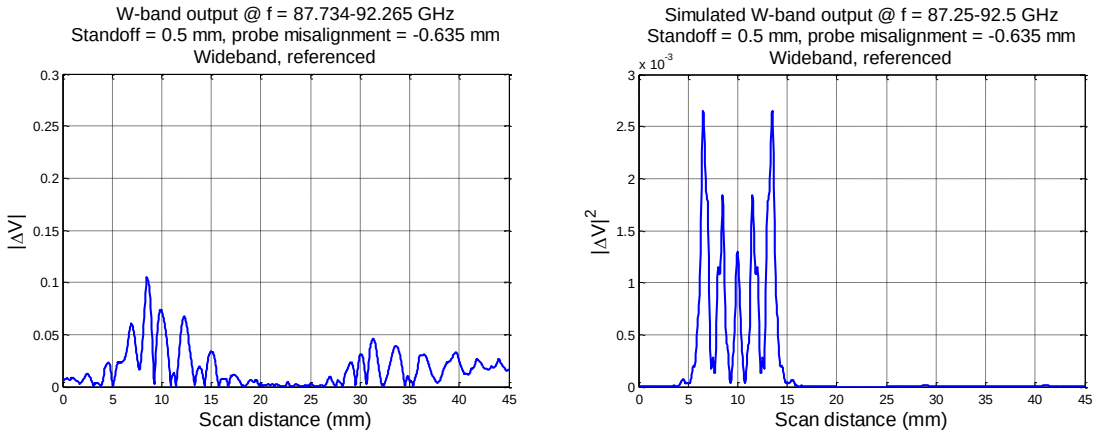

Figure 12. Measured (left) and simulated (right) W-band results of 1.27 mm-long crack, at standoff distance of 0.5 mm, and probe misalignment of -0.635 mm.

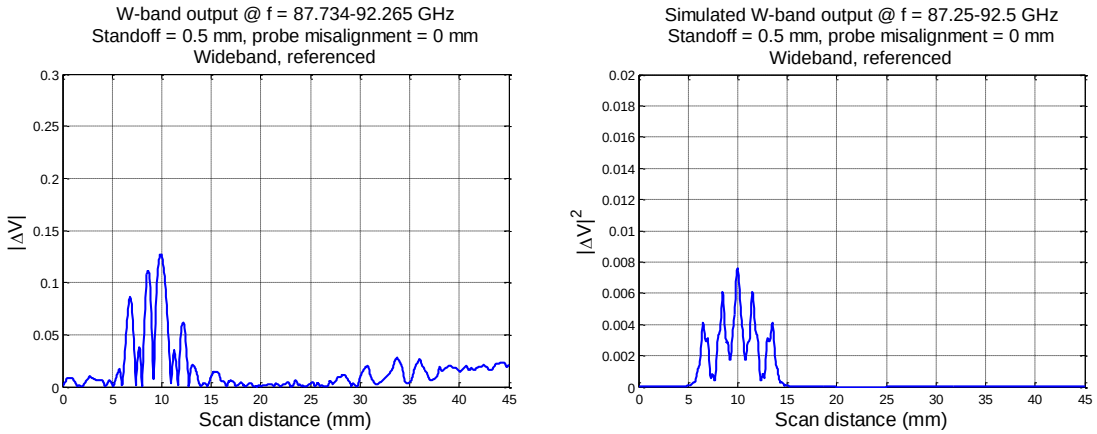

Figure 13. Measured (left) and simulated (right) W-band results of 1.27 mm-long crack, at standoff distance of 0.5 mm, and no probe misalignment.

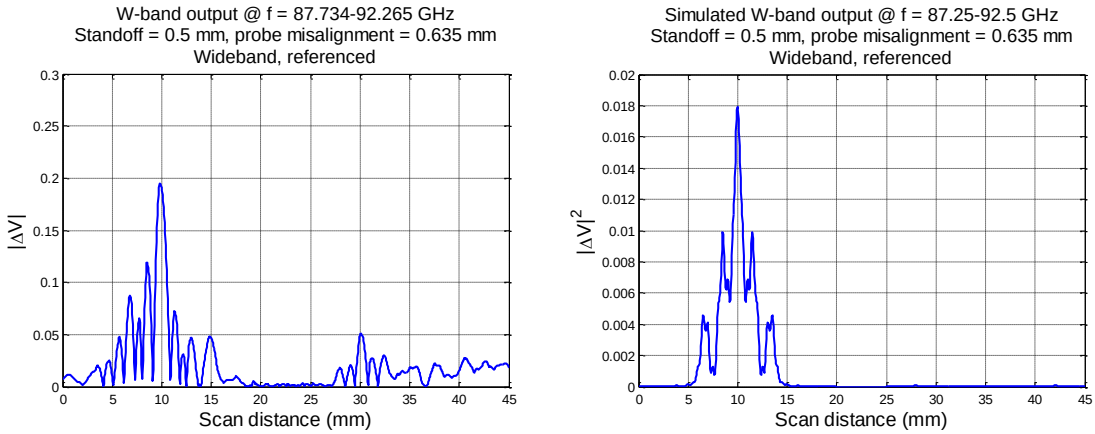

Figure 14. Measured (left) and simulated (right) W-band results of 1.27 mm-long crack, at standoff distance of 0.5 mm, and probe misalignment of +0.635 mm.

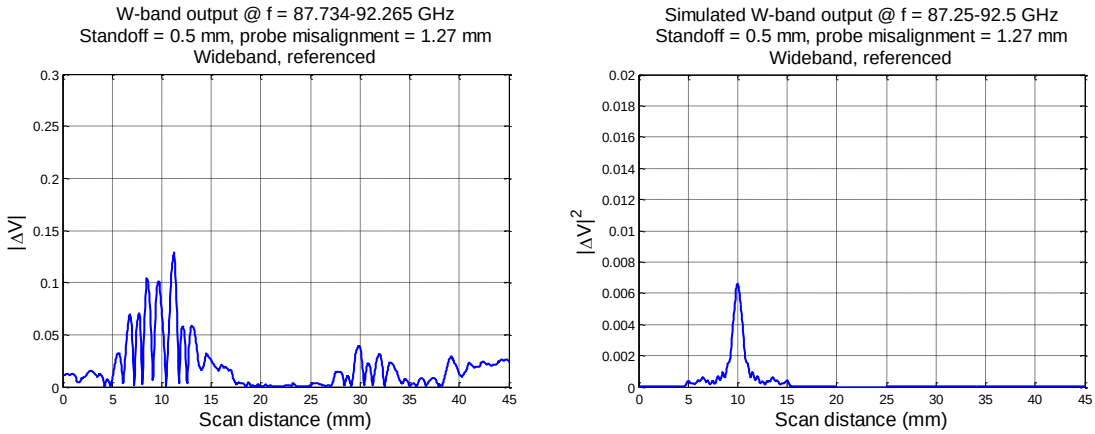

Figure 15. Measured (left) and simulated (right) W-band results of 1.27 mm-long crack, at standoff distance of 0.5 mm, and probe misalignment of +1.27 mm.

Figures 16 through 20 represent the comparisons between measurement and simulation results at standoff distance of 1 mm. Note the figures may not be in the same scale.

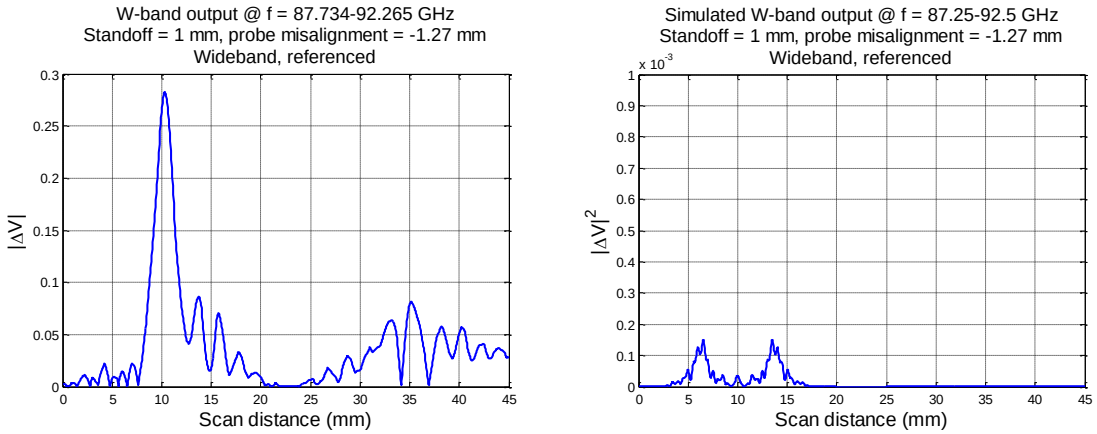

Figure 16. Measured (left) and simulated (right) W-band results of 1.27 mm-long crack, at standoff distance of 1 mm, and probe misalignment of -1.27 mm.

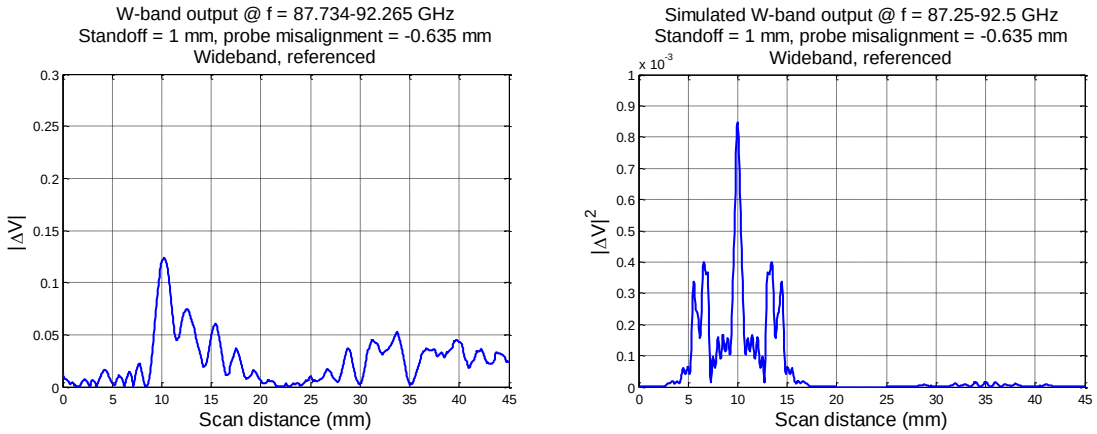

Figure 17. Measured (left) and simulated (right) W-band results of 1.27 mm-long crack, at standoff distance of 1 mm, and probe misalignment of -0.635 mm.

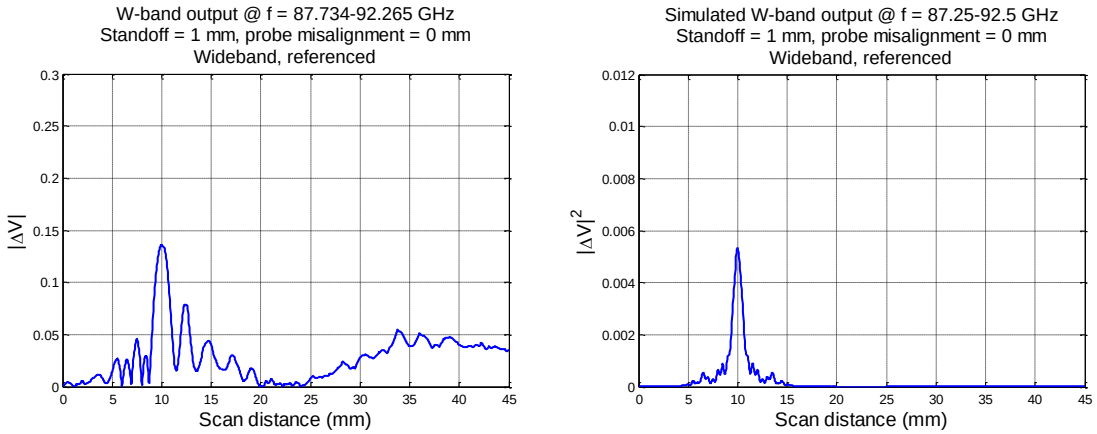

Figure 18. Measured (left) and simulated (right) W-band results of 1.27 mm-long crack, at standoff distance of 1 mm, and no probe misalignment.

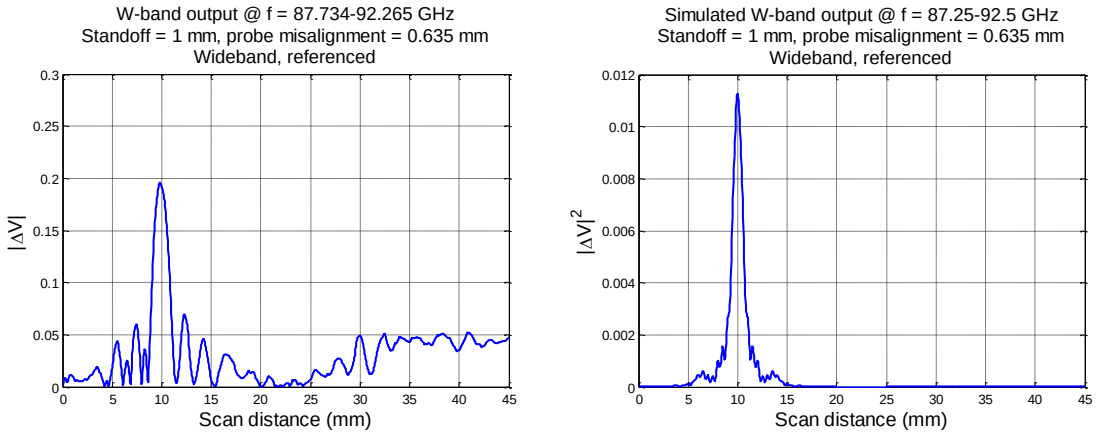

Figure 19. Measured (left) and simulated (right) W-band results of 1.27 mm-long crack, at standoff distance of 1 mm, and probe misalignment of +0.635 mm.

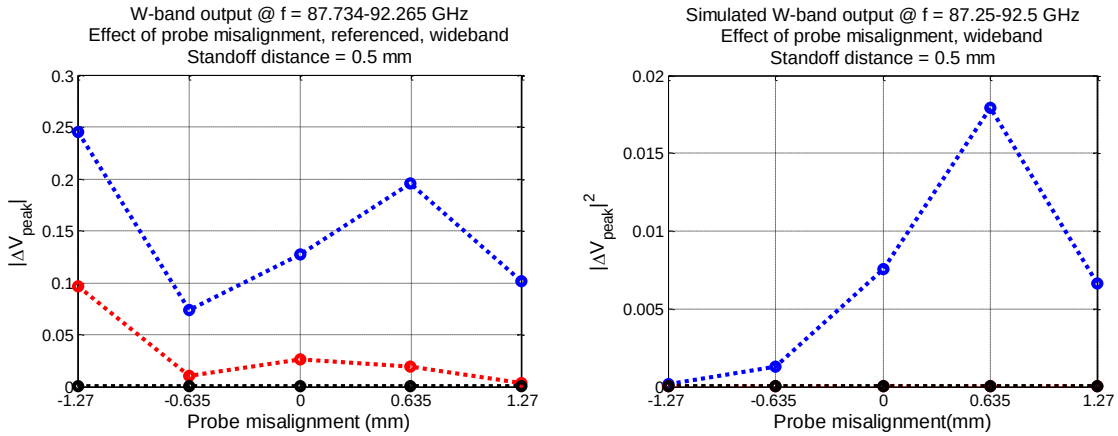

Figure 20. Measured (left) and simulated (right) W-band results of 1.27 mm-long crack, at standoff distance of 1 mm, and probe misalignment of +1.27 mm.

APPENDIX K.

ADDITIONAL FIGURES OF MEASUREMENT RESULTS (EFFECT OF PROBE OFFSET)

This appendix provides the following results for Section 4.5 – Effect of Probe Offset:

- wideband measurement results,
- referenced wideband measurement results,
- and comparisons between measurement and simulation results

Figures 1 through 5 represent the wideband measurement results at both standoff distances of 0.5 and 1 mm, while the referenced wideband data is shown in Figures 6 through 10. The comparisons between measurement and simulation results (at four common frequencies) are shown in Figures 11 through 15 (at standoff distance of 0.5 mm) and Figures 16 through 20 (at standoff distance of 1 mm).

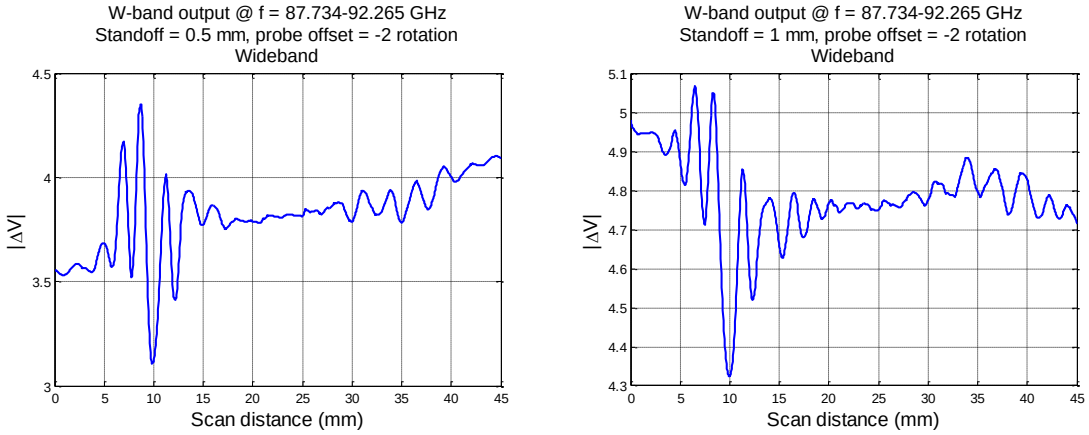

Figure 1. W-band wideband probe output signals at probe offset of -2 rotations, and standoff distance of 0.5 mm (left) and 1 mm (right).

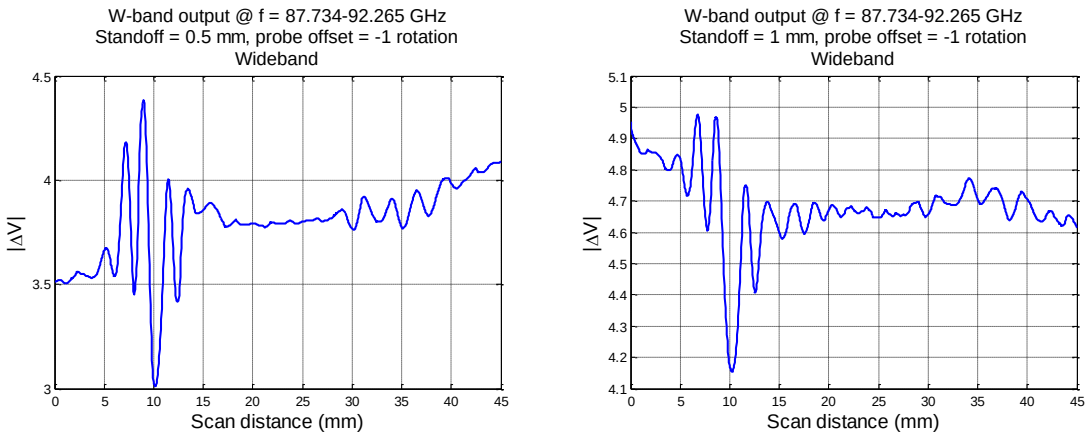

Figure 2. W-band wideband probe output signals at probe offset of -1 rotation, and standoff distance of 0.5 mm (left) and 1 mm (right).

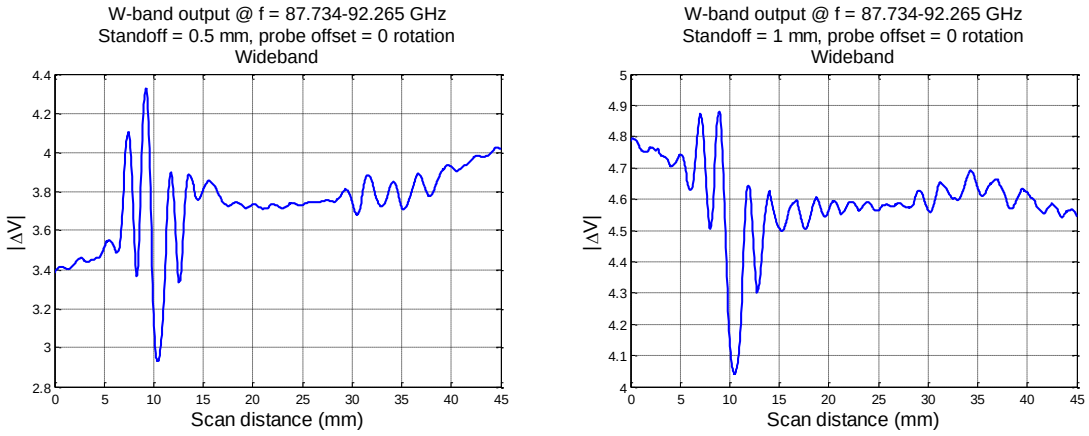

Figure 3. W-band wideband probe output signals at no probe offset, and standoff distance of 0.5 mm (left) and 1 mm (right).

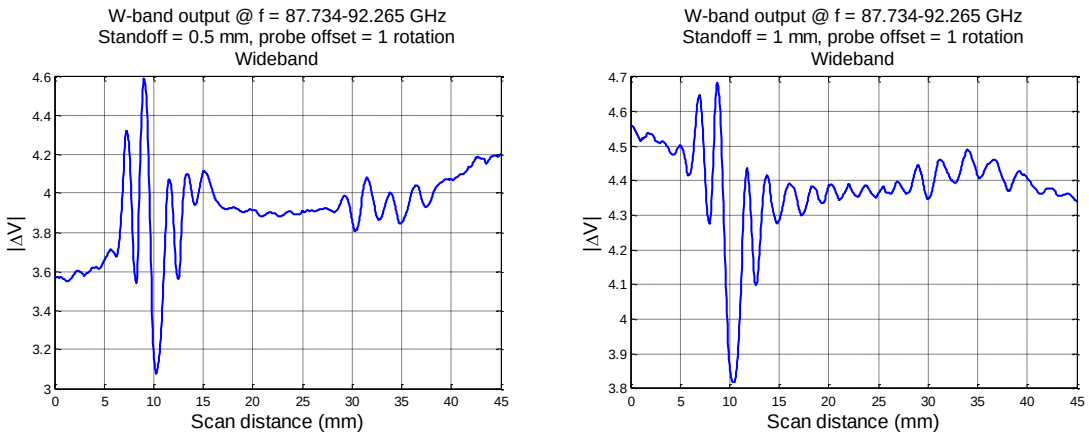

Figure 4. W-band wideband probe output signals at probe offset of +1 rotation, and standoff distance of 0.5 mm (left) and 1 mm (right).

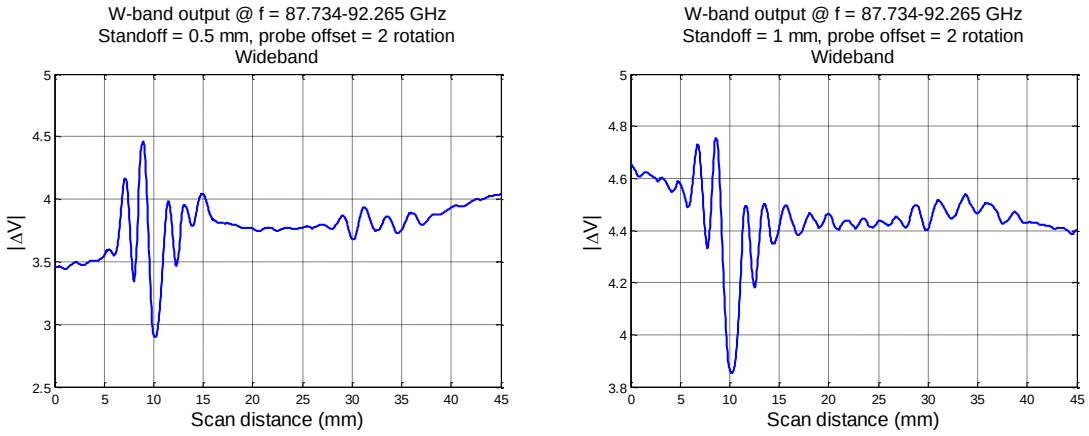

Figure 5. W-band wideband probe output signals at probe offset of +2 rotations, and standoff distance of 0.5 mm (left) and 1 mm (right).

Figures 6 through 10 represent the referenced measurement results.

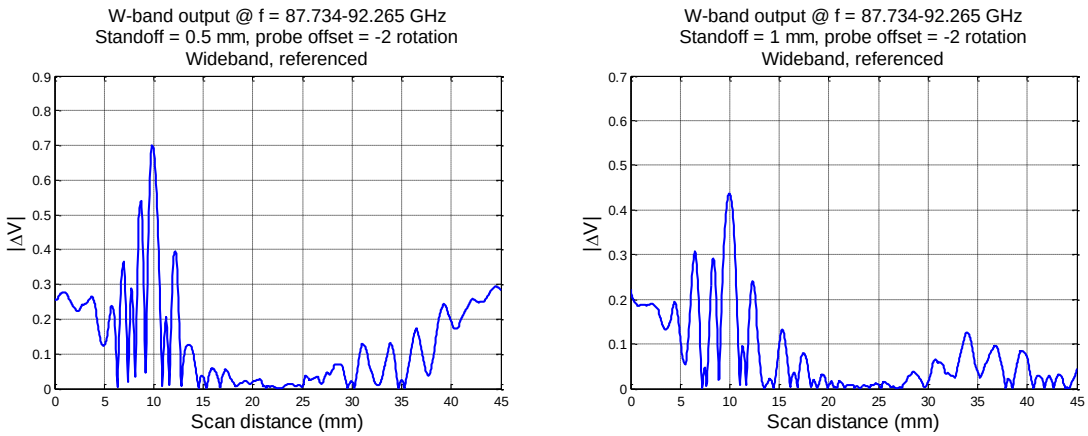

Figure 6. Referenced W-band wideband probe output signals at probe offset of -2 rotations, and standoff distance of 0.5 mm (left) and 1 mm (right).

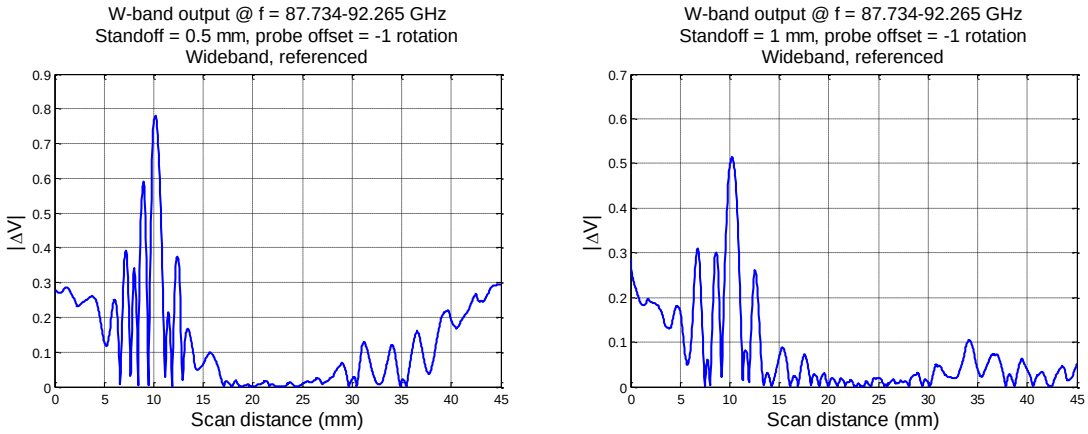

Figure 7. Referenced W-band wideband probe output signals at probe offset of -1 rotation, and standoff distance of 0.5 mm (left) and 1 mm (right).

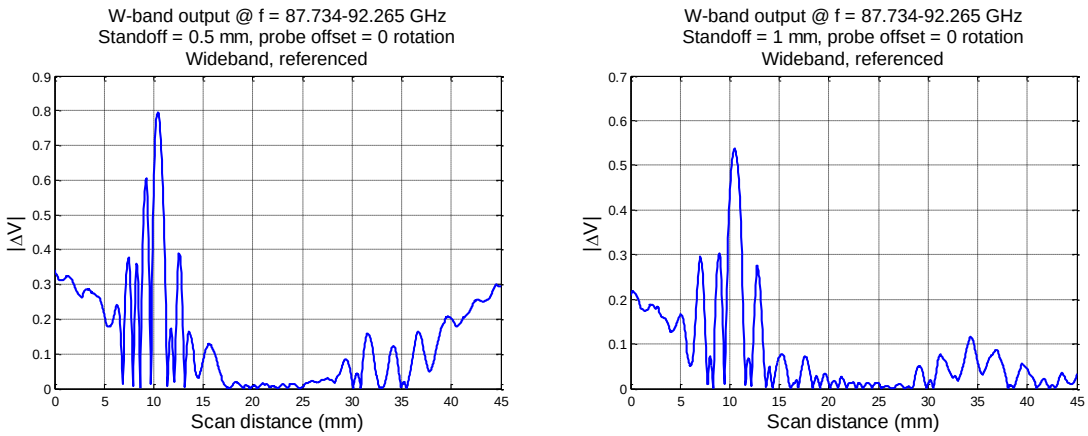

Figure 8. Referenced W-band wideband probe output signals at no probe offset, and standoff distance of 0.5 mm (left) and 1 mm (right).

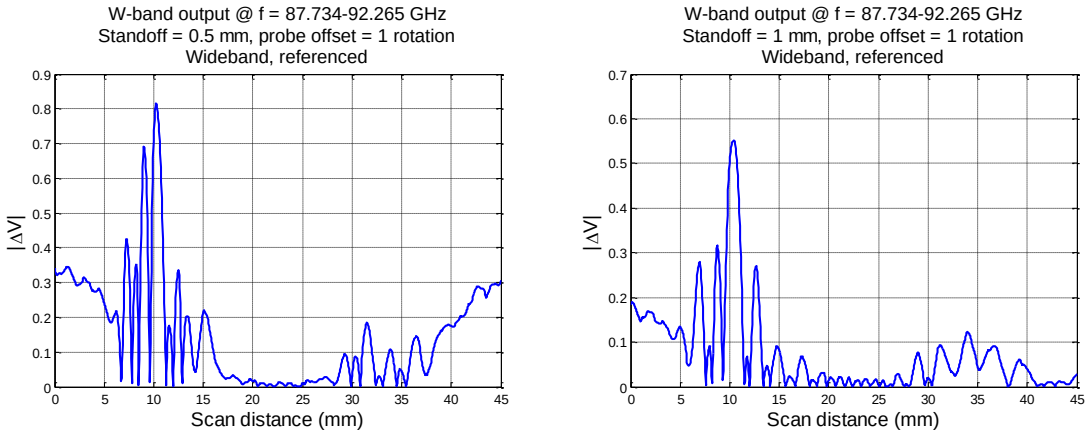

Figure 9. Referenced W-band wideband probe output signals at probe offset of +1 rotation, and standoff distance of 0.5 mm (left) and 1 mm (right).

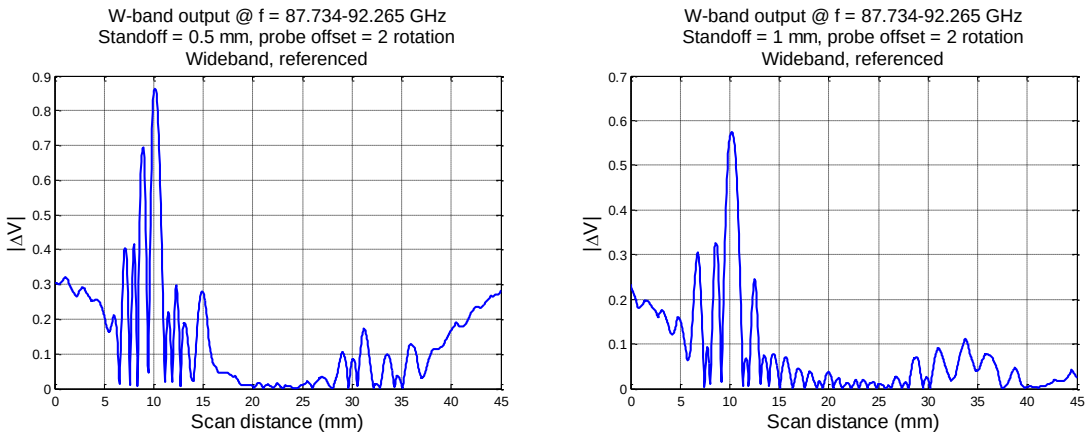

Figure 10. Referenced W-band wideband probe output signals at probe offset of +2 rotations, and standoff distance of 0.5 mm (left) and 1 mm (right).

Figures 11 through 15 represent the comparisons between measurement and simulation results at standoff distance of 0.5 mm.

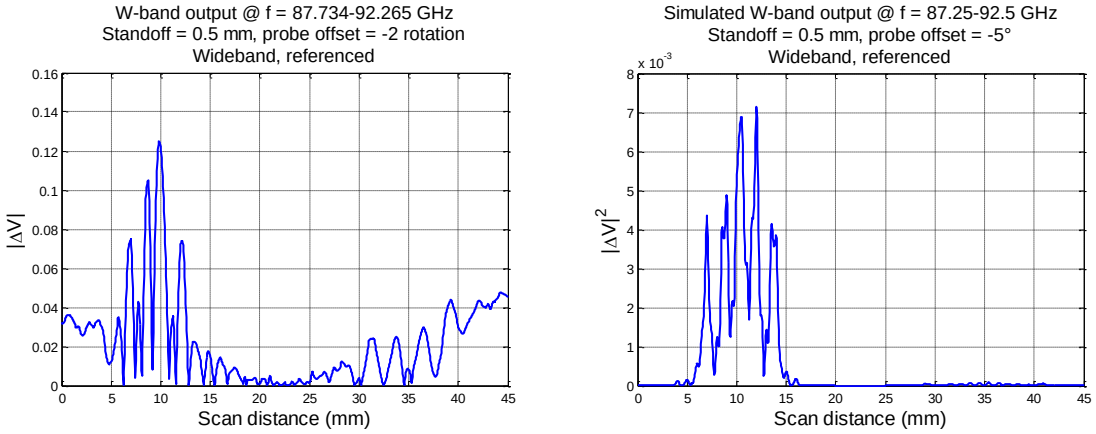

Figure 11. Measured (left) and simulated (right) W-band results of 1.27 mm-long crack, at standoff distance of 0.5 mm, and probe offset of -2 rotations (measurements) and -5° (simulations).

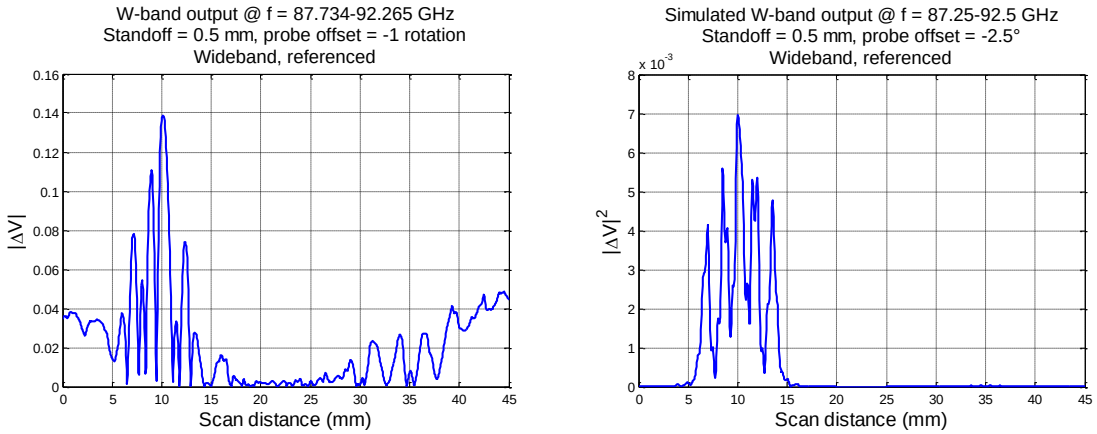

Figure 12. Measured (left) and simulated (right) W-band results of 1.27 mm-long crack, at standoff distance of 0.5 mm, and probe offset of -1 rotation (measurements) and -2.5° (simulations).

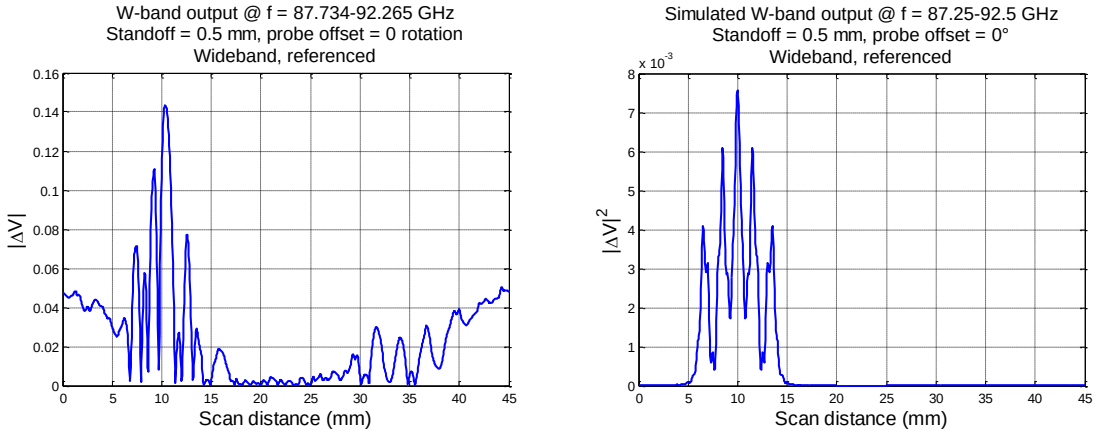

Figure 13. Measured (left) and simulated (right) W-band results of 1.27 mm-long crack, at standoff distance of 0.5 mm, and no probe offset.

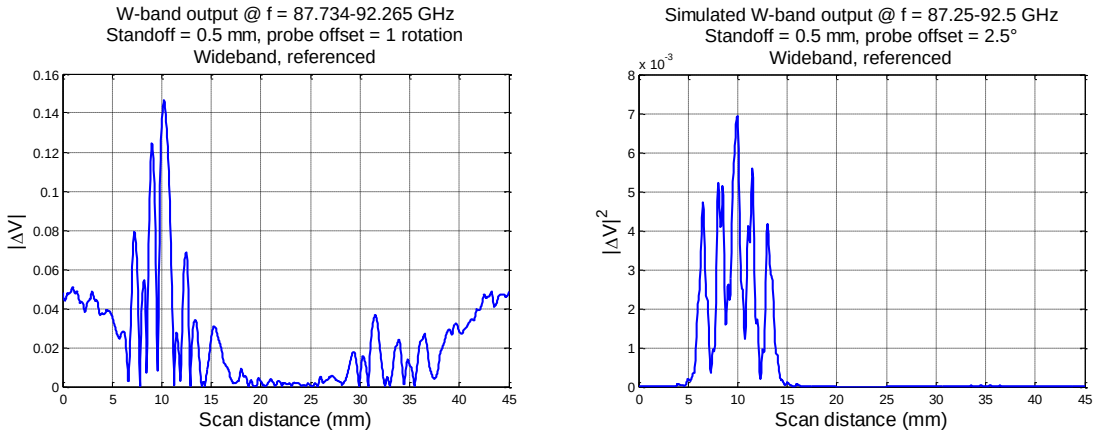

Figure 14. Measured (left) and simulated (right) W-band results of 1.27 mm-long crack, at standoff distance of 0.5 mm, and probe offset of +1 rotation (measurements) and +2.5° (simulations).

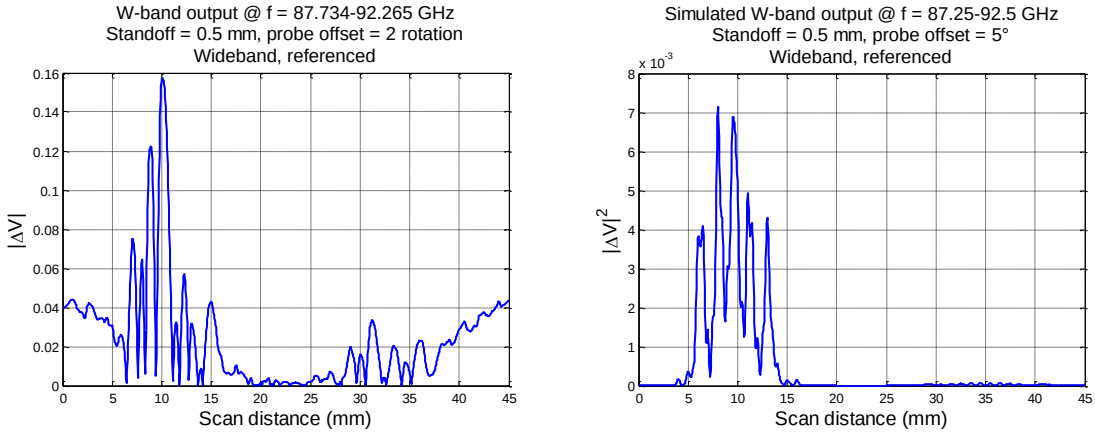

Figure 15. Measured (left) and simulated (right) W-band results of 1.27 mm-long crack, at standoff distance of 0.5 mm, and probe offset of +2 rotations (measurements) and +5° (simulations).

Figures 16 through 20 represent the comparisons between measurement and simulation results at standoff distance of 1 mm.

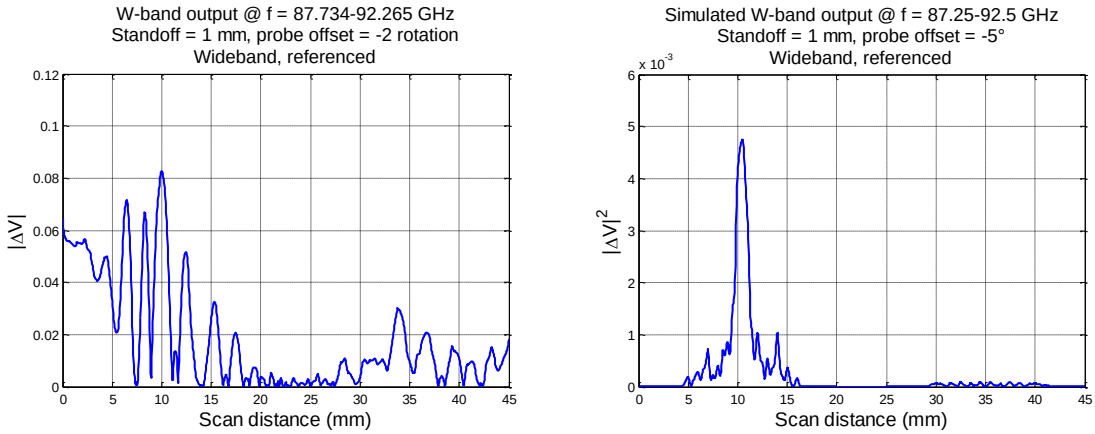

Figure 16. Measured (left) and simulated (right) W-band results of 1.27 mm-long crack, at standoff distance of 1 mm, and probe offset of -2 rotations (measurements) and -5° (simulations).

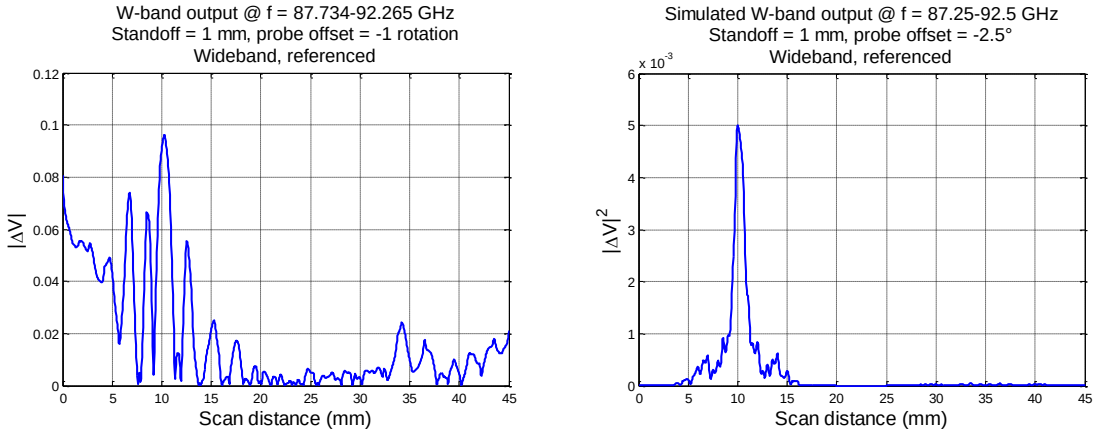

Figure 17. Measured (left) and simulated (right) W-band results of 1.27 mm-long crack, at standoff distance of 1 mm, and probe offset of -1 rotation (measurements) and -2.5° (simulations).

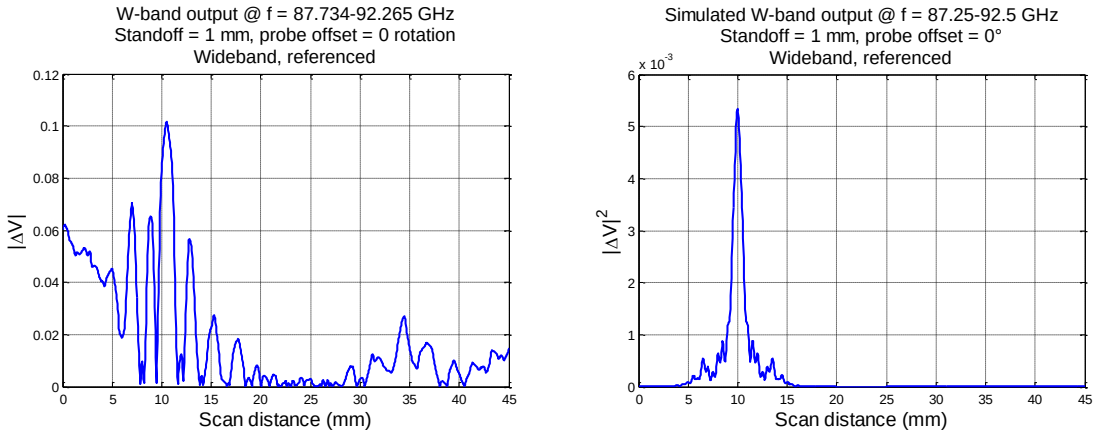

Figure 18. Measured (left) and simulated (right) W-band results of 1.27 mm-long crack, at standoff distance of 1 mm, and no probe offset.

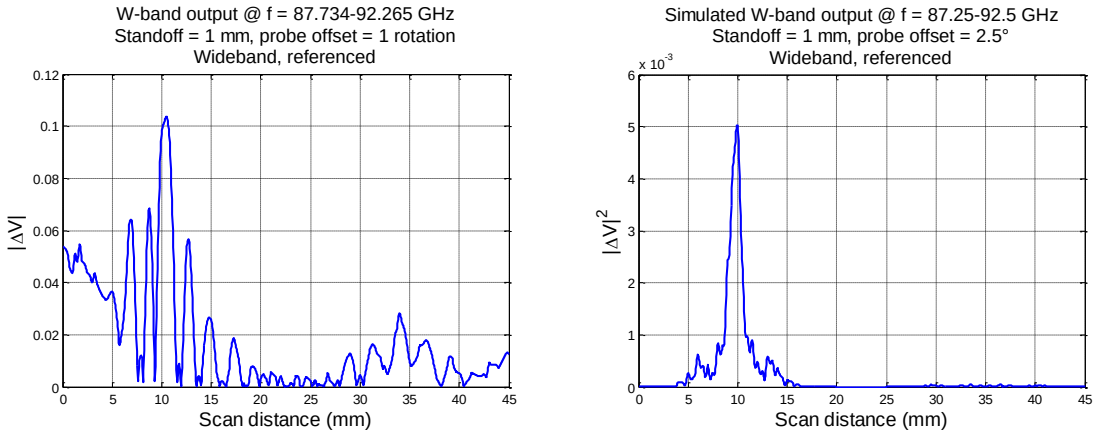

Figure 19. Measured (left) and simulated (right) W-band results of 1.27 mm-long crack, at standoff distance of 1 mm, and probe offset of +1 rotation (measurements) and +2.5° (simulations).

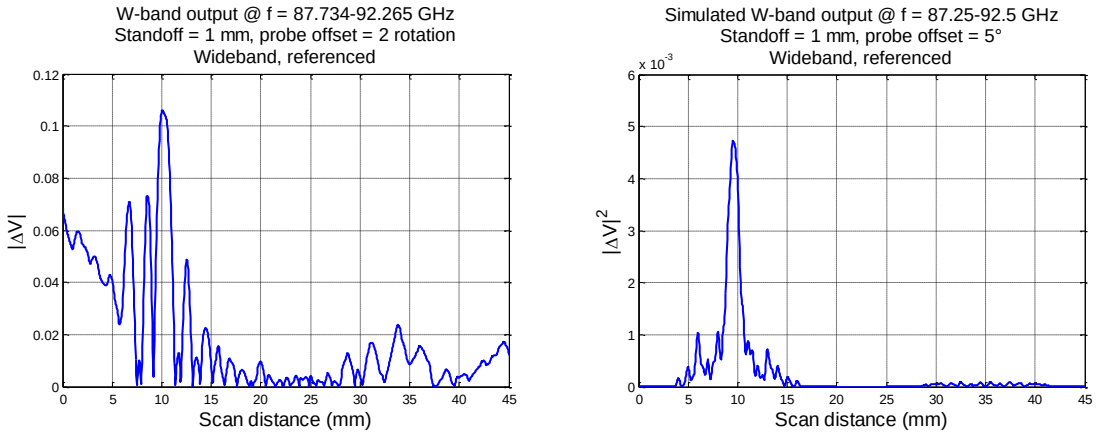

Figure 20. Measured (left) and simulated (right) W-band results of 1.27 mm-long crack, at standoff distance of 1 mm, and probe offset of +2 rotations (measurements) and +5° (simulations).

APPENDIX L.
ADDITIONAL FIGURES OF SAR FILTER ON SIMULATION AND MEASUREMENT RESULTS (EFFECT OF APERTURE OFFSET)

This appendix provides the complete comparisons between SAR-focused measurement and simulation results for Section 5.2 – Synthetic Aperture Processing on Effect of Aperture Offset.

Figures 1 through 7 represent the comparisons (at four common frequencies) between measurement and simulation results (after SAR is applied) at 0.5 mm standoff distance, while Figures 8 through 14 represent the results at 1 mm standoff distance. Since a +2 or -2 rotation of aperture offset is approximately equal to +0.2 or -0.2 mm, these measurement results are compared to simulation results with aperture offset of ±0.25 mm. Measurement results with aperture offsets of ±1 rotation (Figures 3 and 5), as well as simulation results with aperture offsets of ±0.5 mm (Figures 1 and 7) cannot be compared due to limited data available.

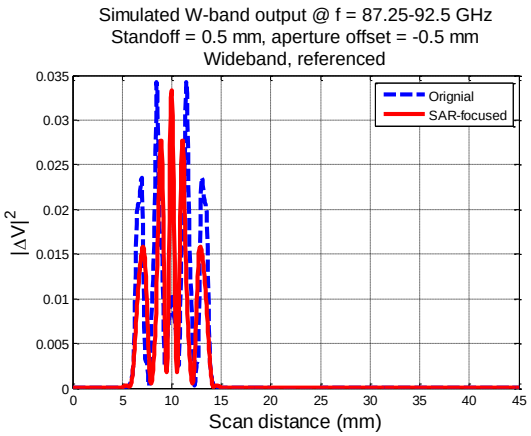

Figure 1. SAR-focused W-band results of 1.27 mm-long crack, as in simulation, at standoff distance of 0.5 mm, and aperture offset of -0.5 mm.

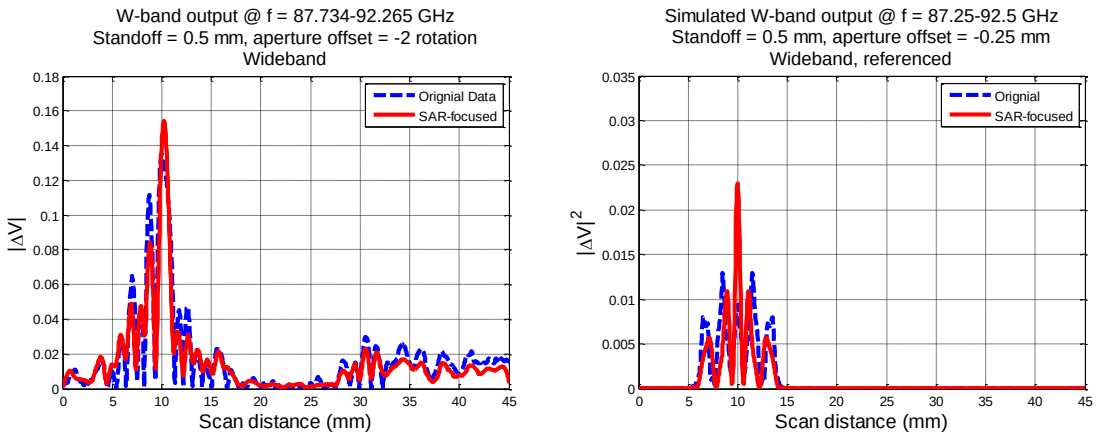

Figure 2. SAR-focused W-band results of 1.27 mm-long crack, as in measurement (left) and simulation (right), at standoff distance of 0.5 mm, and aperture offset of -2 rotations (measurements) and -0.25 mm (simulations).

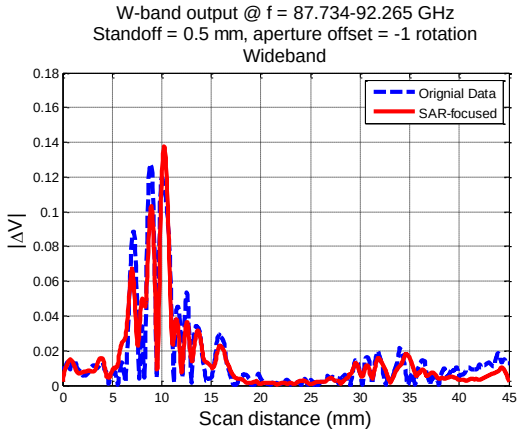

Figure 3. SAR-focused W-band results of 1.27 mm-long crack, as in measurement, at standoff distance of 0.5 mm, and aperture offset of -1 rotation.

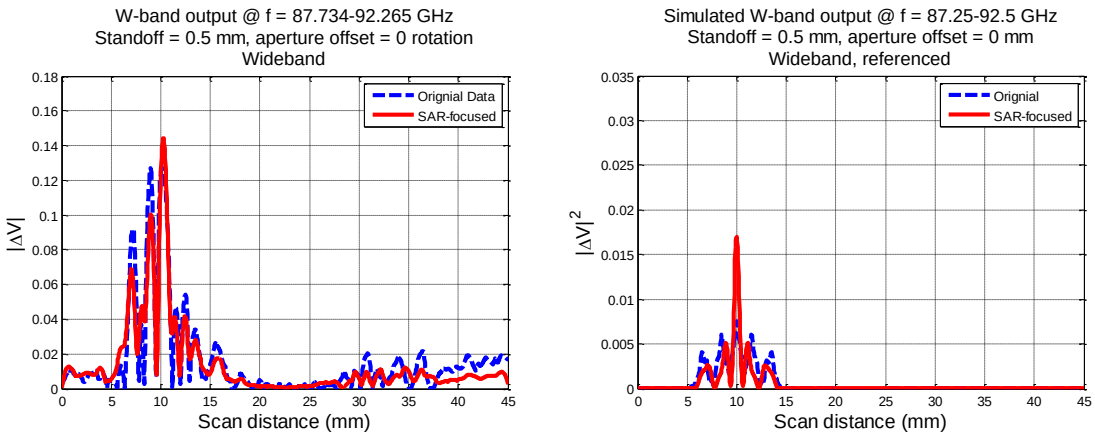

Figure 4. SAR-focused W-band results of 1.27 mm-long crack, as in measurement (left) and simulation (right), at standoff distance of 0.5 mm, and no aperture offset.

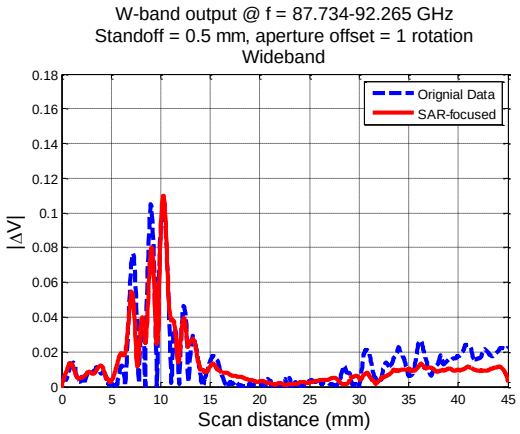

Figure 5. SAR-focused W-band results of 1.27 mm-long crack, as in measurement, at standoff distance of 0.5 mm, and aperture offset of +1 rotation.

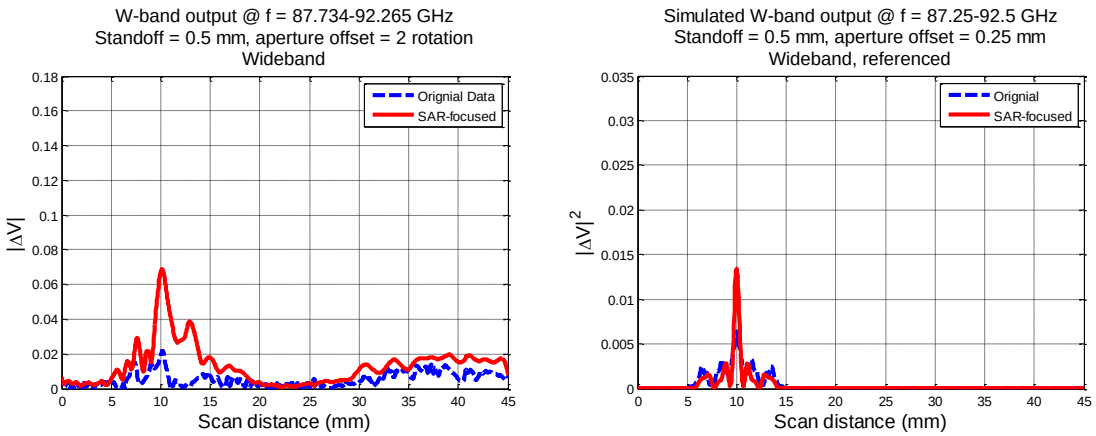

Figure 6. SAR-focused W-band results of 1.27 mm-long crack, as in measurement (left) and simulation (right), at standoff distance of 0.5 mm, and aperture offset of +2 rotations (measurements) and +0.25 mm (simulations).

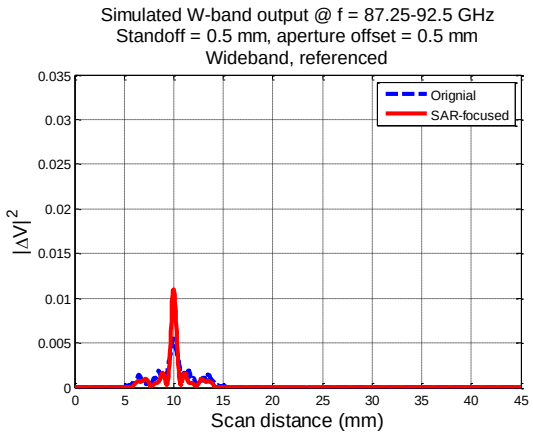

Figure 7. SAR-focused W-band results of 1.27 mm-long crack, as in simulation, at standoff distance of 0.5 mm, and aperture offset of +0.5 mm.

Figures 8 through 14 represent the comparisons between measurement and simulation results (after SAR is applied) at standoff distance of 1 mm. Similar to results from 0.5 mm standoff distance, measurement results with aperture offsets of ±2 rotations are compared to simulation results with aperture offsets of ±0.2 mm. Measurement results with aperture offsets of ±1 rotation (Figures 10 and 12), as well as simulation results with

aperture offsets of ±0.5 mm (Figures 8 and 14) cannot be compared due to limited data available.

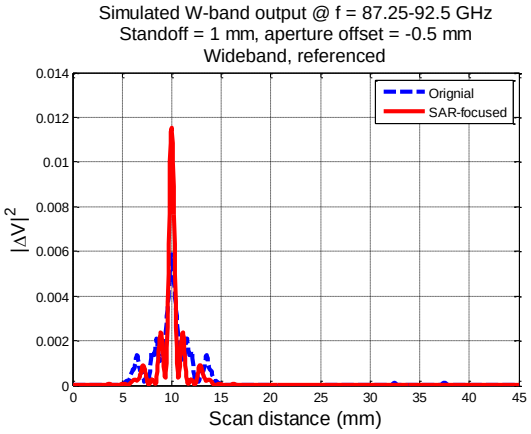

Figure 8. SAR-focused W-band results of 1.27 mm-long crack, as in simulation, at standoff distance of 1 mm, and aperture offset of -0.5 mm.

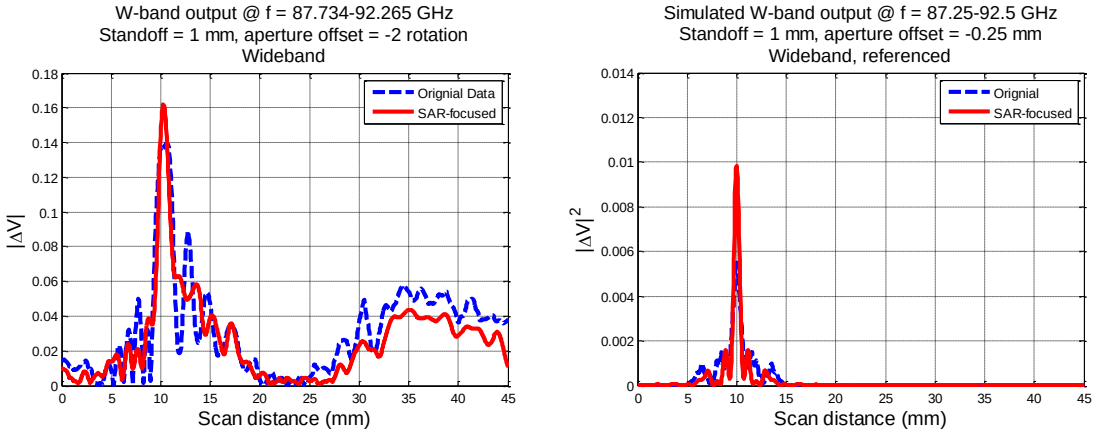

Figure 9. SAR-focused W-band results of 1.27 mm-long crack, as in measurement (left) and simulation (right), at standoff distance of 1 mm, and aperture offset of -2 rotations (measurements) and -0.25 mm (simulations).

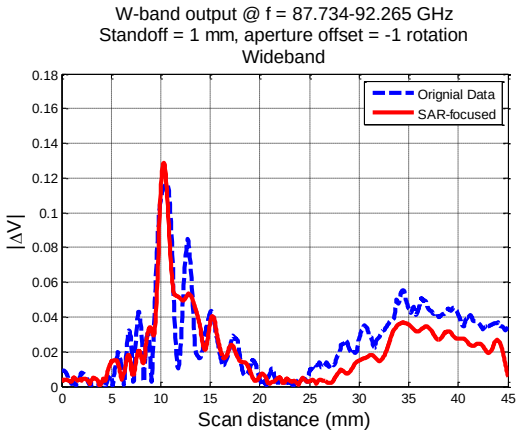

Figure 10. SAR-focused W-band results of 1.27 mm-long crack, as in measurement, at standoff distance of 1 mm, and aperture offset of -1 rotation.

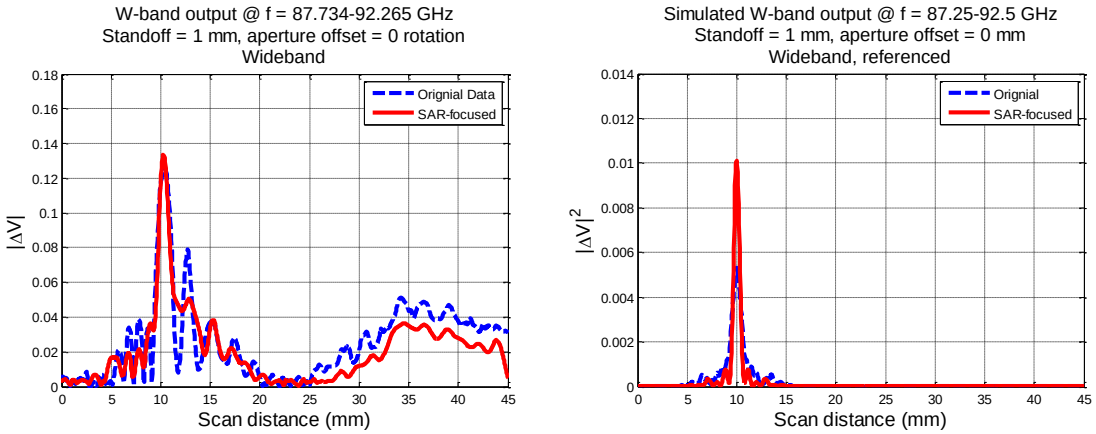

Figure 11. SAR-focused W-band results of 1.27 mm-long crack, as in measurement (left) and simulation (right), at standoff distance of 1 mm, and no aperture offset.

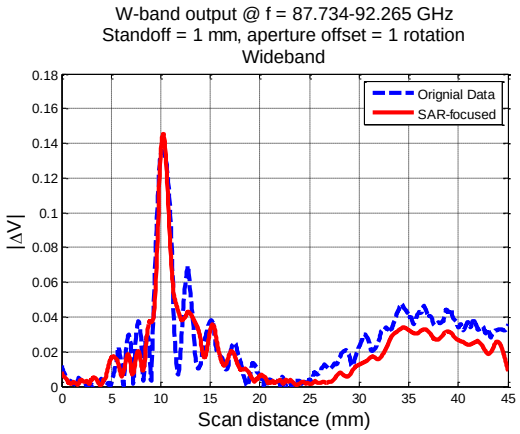

Figure 12. SAR-focused W-band results of 1.27 mm-long crack, as in measurement, at standoff distance of 1 mm, and aperture offset of +1 rotation.

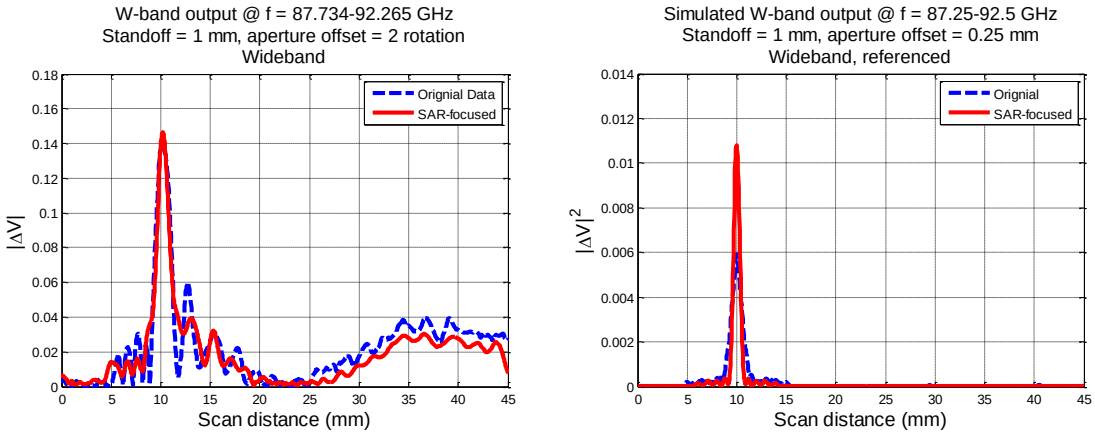

Figure 13. SAR-focused W-band results of 1.27 mm-long crack, as in measurement (left) and simulation (right), at standoff distance of 1mm, and aperture offset of +2 rotations (measurements) and +0.25 mm (simulations).

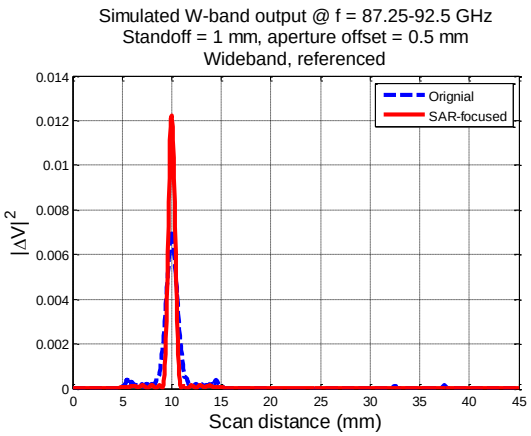

Figure 14. SAR-focused W-band results of 1.27 mm-long crack, as in simulation, at standoff distance of 1 mm, and aperture offset of +0.5 mm.

APPENDIX M.
ADDITIONAL FIGURES OF SAR FILTER ON SIMULATION AND MEASUREMENT RESULTS (EFFECT OF PAINT THICKNESS)

This appendix provides the complete comparisons between SAR-focused measurement and simulation results for Section 5.3 – Synthetic Aperture Processing on Effect of Paint Thickness.

Figures 1 through 8 represent the comparisons (at four common frequencies) between measurement and simulation results (after SAR is applied) at 0.5 mm standoff distance, while Figures 9 through 17 represent the results at 1 mm standoff distance. Measurement results with paint thicknesses of 0.01 (Figure 2) and 0.29 mm (Figure 6), and simulation results with paint thickness of 0.13 mm (Figure 4) cannot be compared to due limited data available. Note the figures may not be in the same scale.

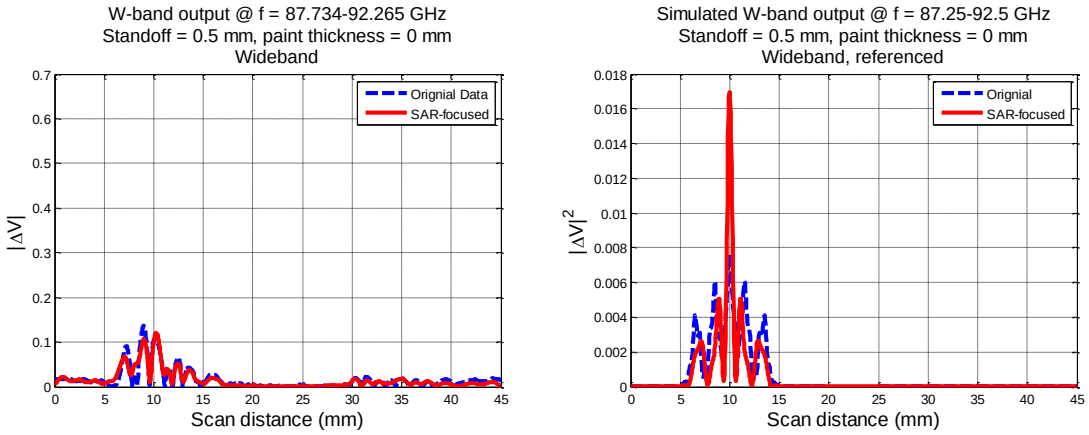

Figure 1. SAR-focused W-band results of 1.27 mm-long crack, as in measurement (left) and simulation (right), at standoff distance of 0.5 mm, and no paint.

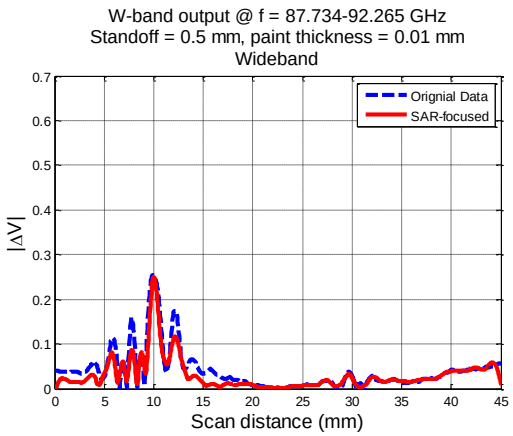

Figure 2. SAR-focused W-band results of 1.27 mm-long crack, as in measurement, at standoff distance of 0.5 mm, and paint thickness of 0.01 mm.

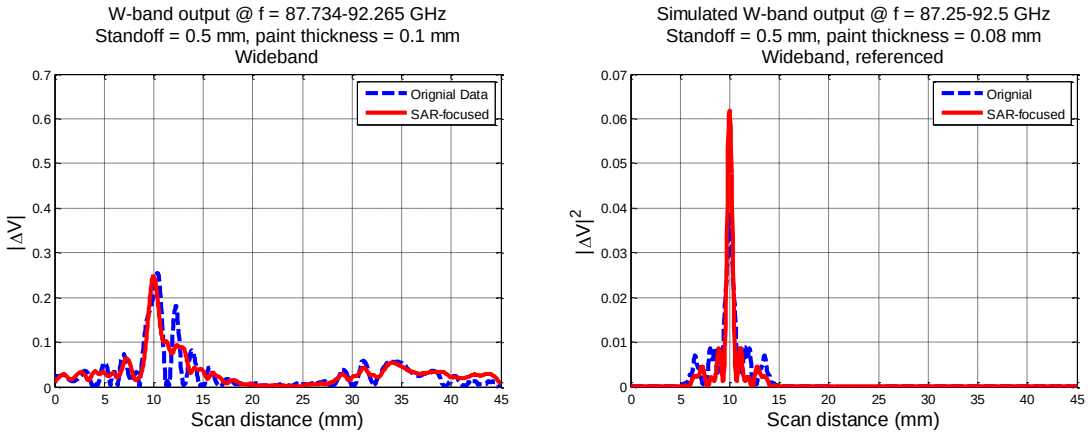

Figure 3. SAR-focused W-band results of 1.27 mm-long crack, as in measurement (left) and simulation (right), at standoff distance of 0.5 mm, and paint thickness of 0.1 mm (measurements) and 0.08 mm (simulations).

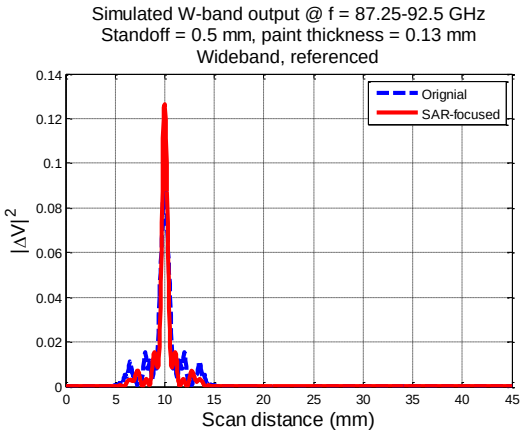

Figure 4. SAR-focused W-band results of 1.27 mm-long crack, as in simulation, at standoff distance of 0.5 mm, and paint thickness of 0.13 mm.

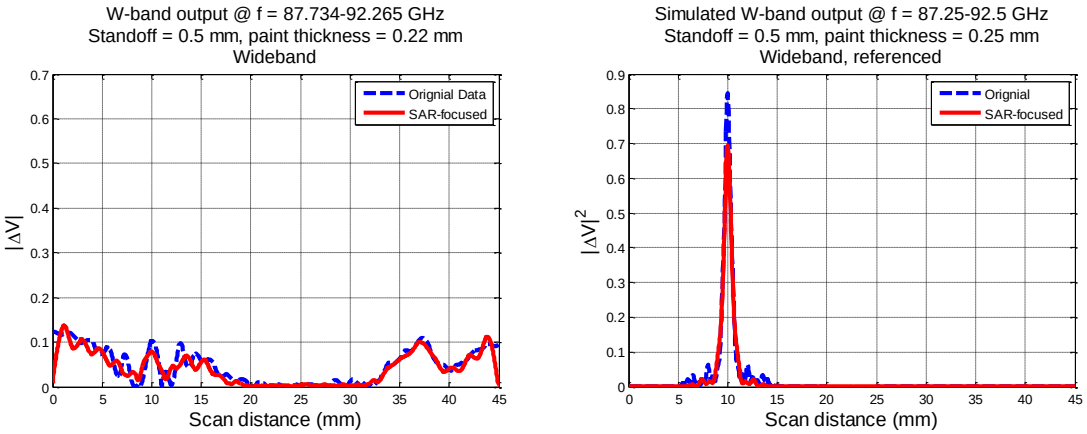

Figure 5. SAR-focused W-band results of 1.27 mm-long crack, as in measurement (left) and simulation (right), at standoff distance of 0.5 mm, and paint thickness of 0.22 mm (measurements) and 0.25 mm (simulations).

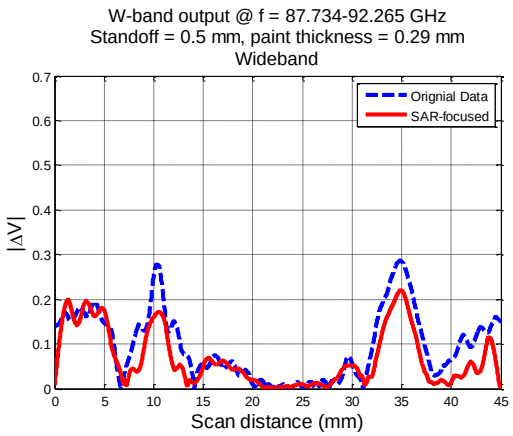

Figure 6. SAR-focused W-band results of 1.27 mm-long crack, as in measurement, at standoff distance of 0.5 mm, and paint thickness of 0.29 mm.

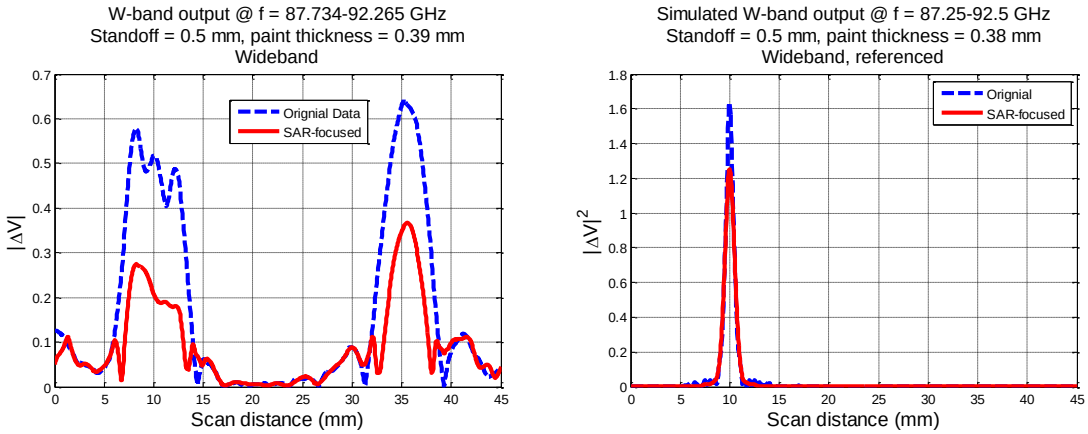

Figure 7. SAR-focused W-band results of 1.27 mm-long crack, as in measurement (left) and simulation (right), at standoff distance of 0.5 mm, and paint thickness of 0.38 mm (measurements) and 0.39 mm (simulations).

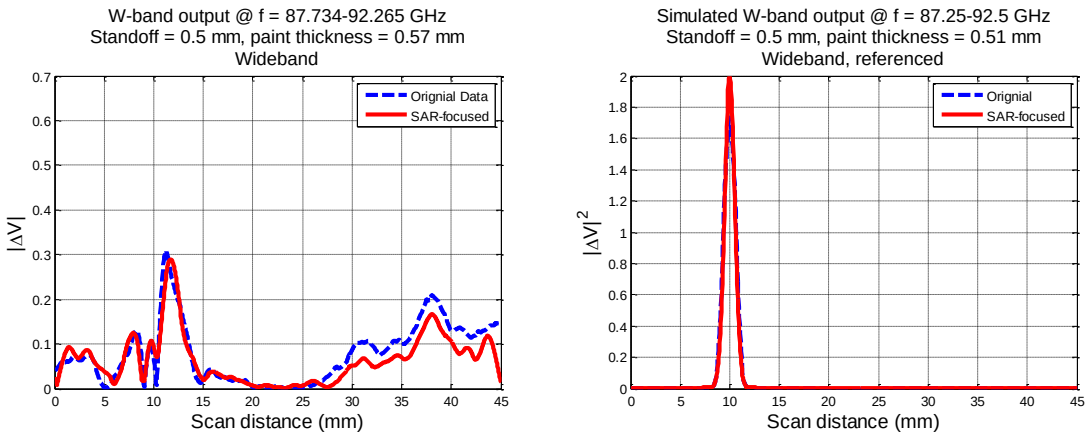

Figure 8. SAR-focused W-band results of 1.27 mm-long crack, as in measurement (left) and simulation (right), at standoff distance of 0.5 mm, and paint thickness of 0.57 mm (measurements) and 0.51 mm (simulations).

Figures 9 through 17 represent the comparisons between measurement and simulation results at standoff distance of 1 mm. Similar to results from 0.5 mm standoff distance, measurement results with paint thicknesses of 0.01 (Figure 10), 0.29 (Figure 14), and 0.57 mm (Figure 17), and simulation results with paint thickness of 0.13 mm (Figure 12) cannot be compared to due limited data available. Note the figures may not be in the same scale.

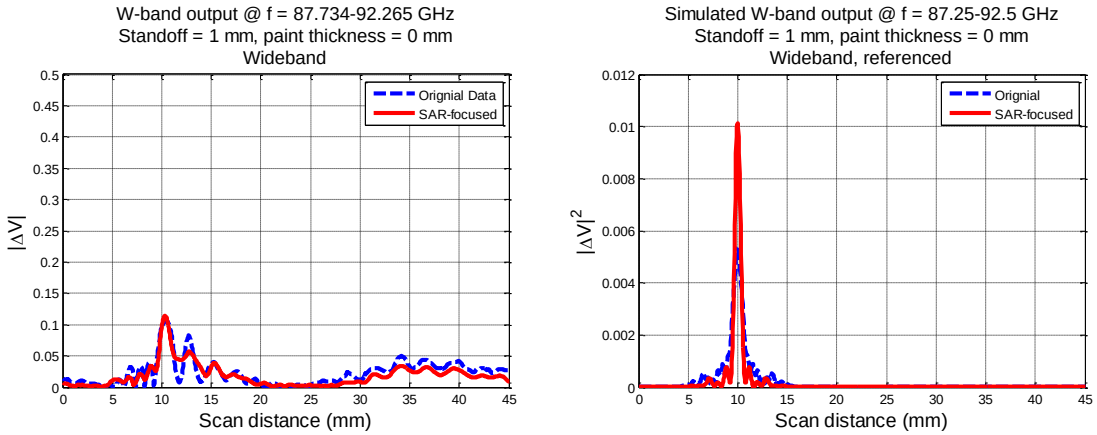

Figure 9. SAR-focused W-band results of 1.27 mm-long crack, as in measurement (left) and simulation (right), at standoff distance of 1 mm, and no paint.

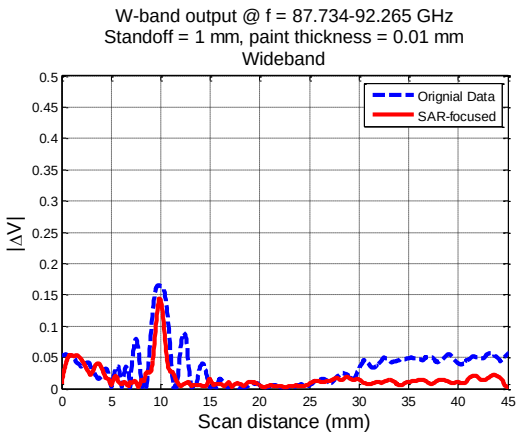

Figure 10. SAR-focused W-band results of 1.27 mm-long crack, as in measurement, at standoff distance of 1 mm, and paint thickness of 0.01 mm.

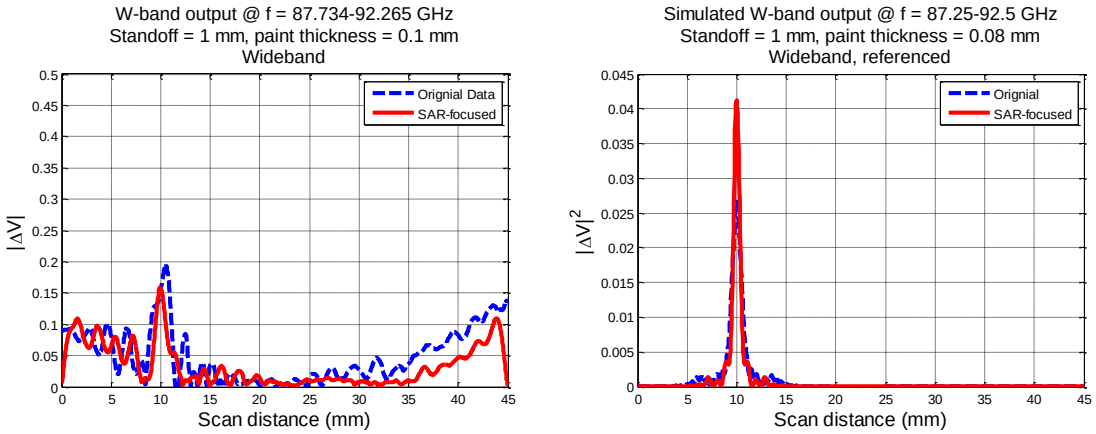

Figure 11. SAR-focused W-band results of 1.27 mm-long crack, as in measurement (left) and simulation (right), at standoff distance of 1 mm, and paint thickness of 0.1 mm (measurements) and 0.08 mm (simulations).

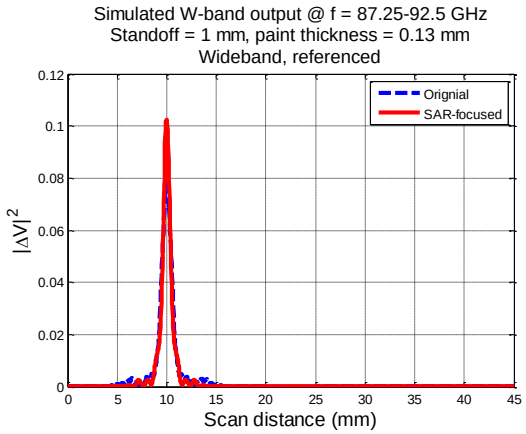

Figure 12. SAR-focused W-band results of 1.27 mm-long crack, as in simulation, at standoff distance of 1 mm, and paint thickness of 0.13 mm.

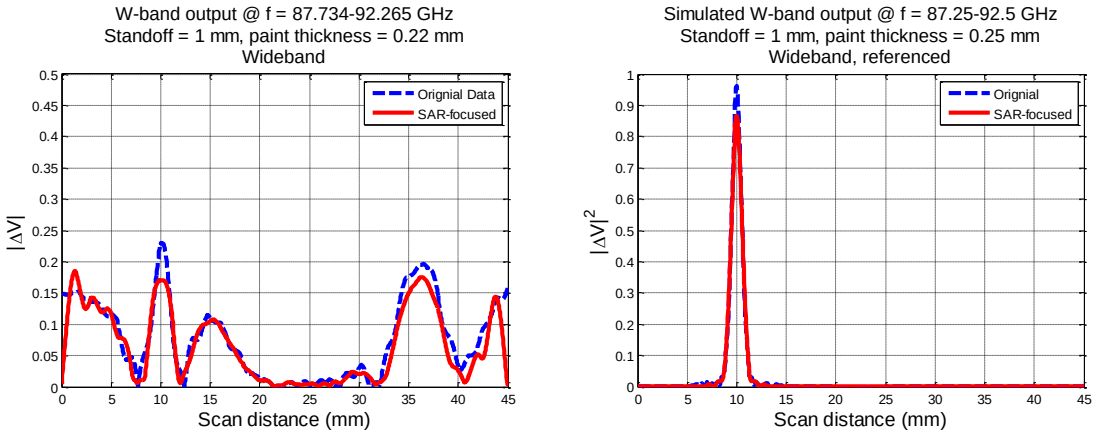

Figure 13. SAR-focused W-band results of 1.27 mm-long crack, as in measurement (left) and simulation (right), at standoff distance of 1 mm, and paint thickness of 0.22 mm (measurements) and 0.25 mm (simulations).

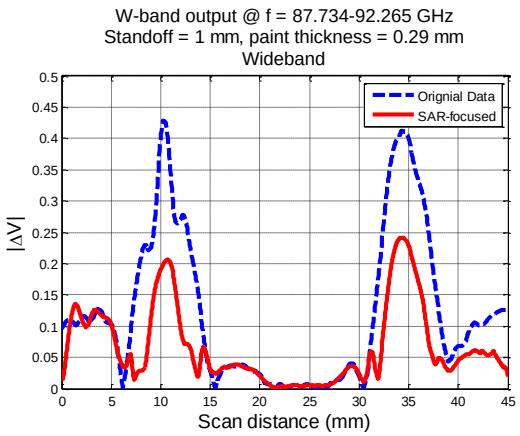

Figure 14. SAR-focused W-band results of 1.27 mm-long crack, as in measurement, at standoff distance of 1 mm, and paint thickness of 0.29 mm.

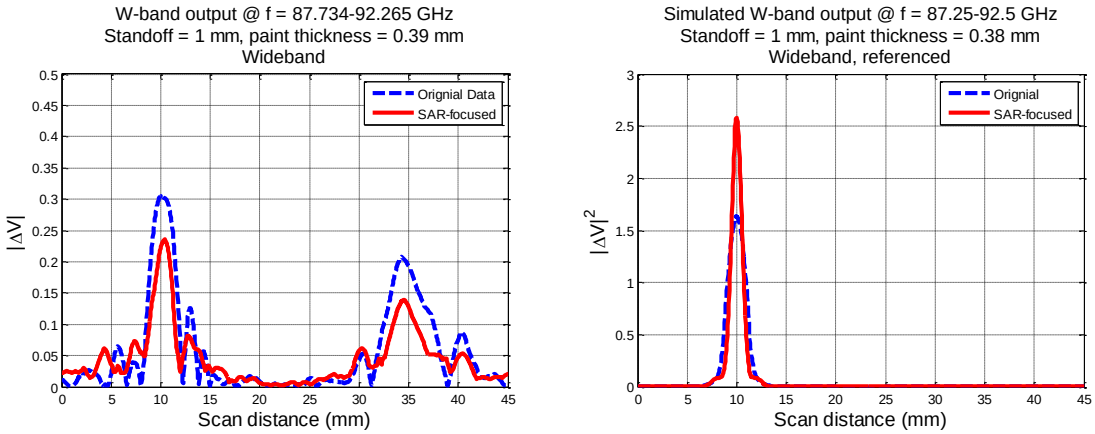

Figure 15. SAR-focused W-band results of 1.27 mm-long crack, as in measurement (left) and simulation (right), at standoff distance of 1 mm, and paint thickness of 0.39 mm (measurements) and 0.38 mm (simulations).

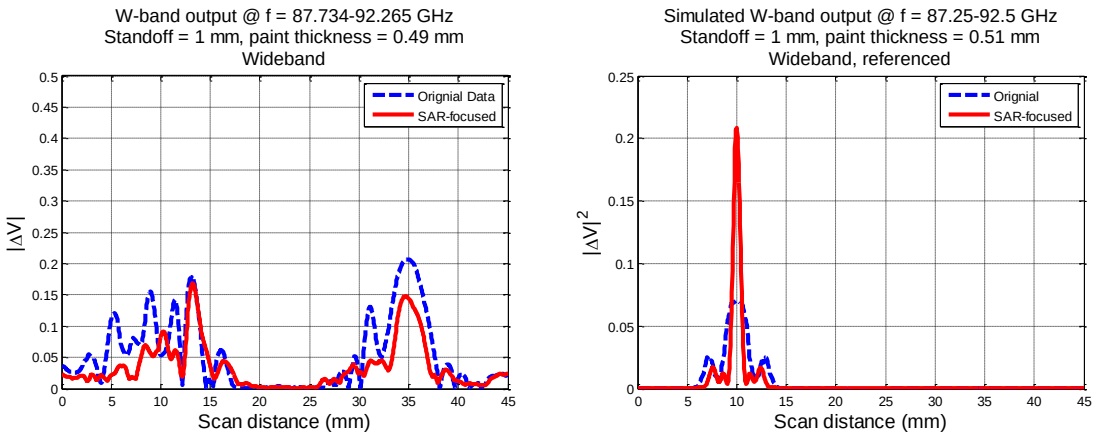

Figure 16. SAR-focused W-band results of 1.27 mm-long crack, as in measurement (left) and simulation (right), at standoff distance of 1 mm, and paint thickness of 0.49 mm (measurements) and 0.51 mm (simulations).

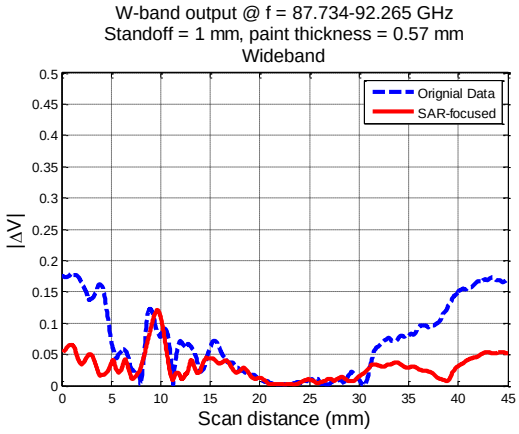

Figure 17. SAR-focused W-band results of 1.27 mm-long crack, as in measurement, at standoff distance of 1 mm, and paint thickness of 0.57 mm.

APPENDIX N.
ADDITIONAL FIGURES OF SAR FILTER ON SIMULATION AND MEASUREMENT RESULTS (EFFECT OF PROBE MISALIGNMENT)

This appendix provides the complete comparisons between SAR-focused measurement and simulation results for Section 5.4 – Synthetic Aperture Processing on Effect of Probe Misalignment.

Figures 1 through 5 represent the comparisons (at four common frequencies) between measurement and simulation results (after SAR is applied) at 0.5 mm standoff distance, while Figures 6 through 10 represent the results at 1 mm standoff distance. Note the figures may not be in the same scale.

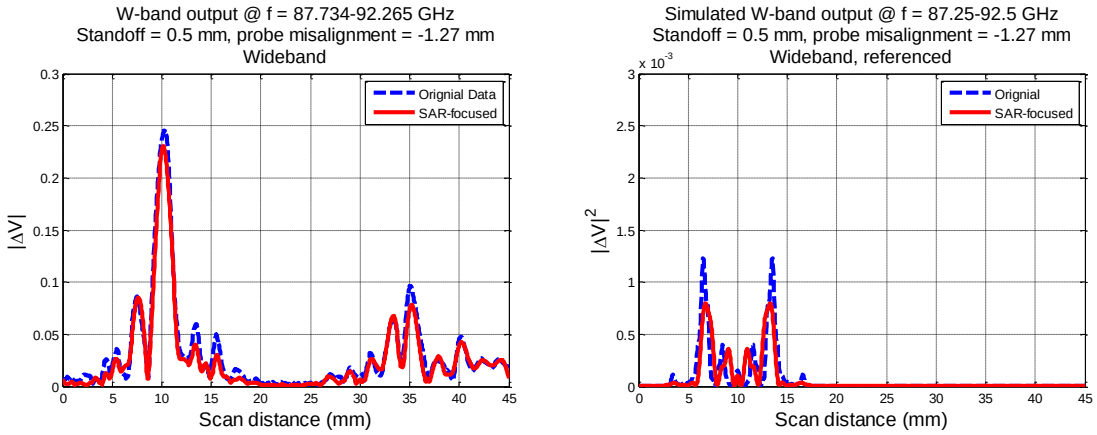

Figure 1. SAR-focused W-band results of 1.27 mm-long crack, as in measurement (left) and simulation (right), at standoff distance of 0.5 mm, and probe misalignment of -1.27 mm.

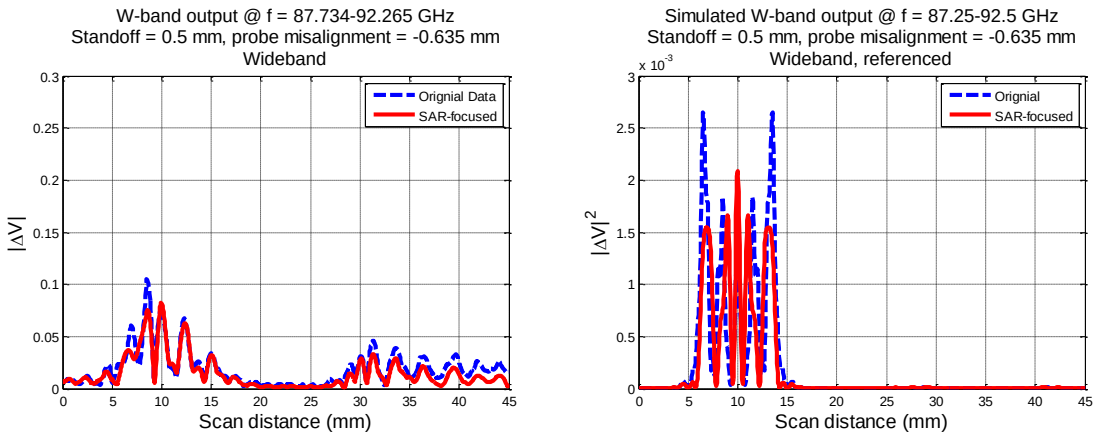

Figure 2. SAR-focused W-band results of 1.27 mm-long crack, as in measurement (left) and simulation (right), at standoff distance of 0.5 mm, and probe misalignment of -0.635 mm.

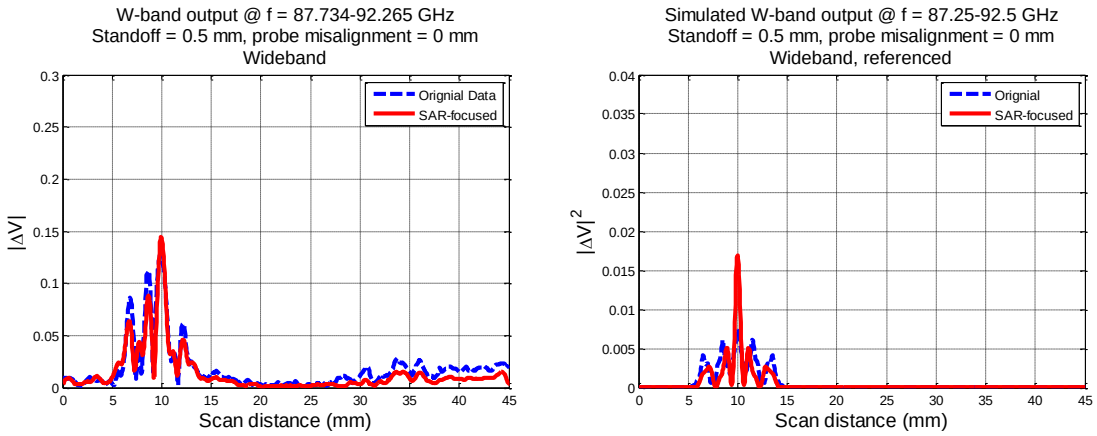

Figure 3. SAR-focused W-band results of 1.27 mm-long crack, as in measurement (left) and simulation (right), at standoff distance of 0.5 mm, and no probe misalignment.

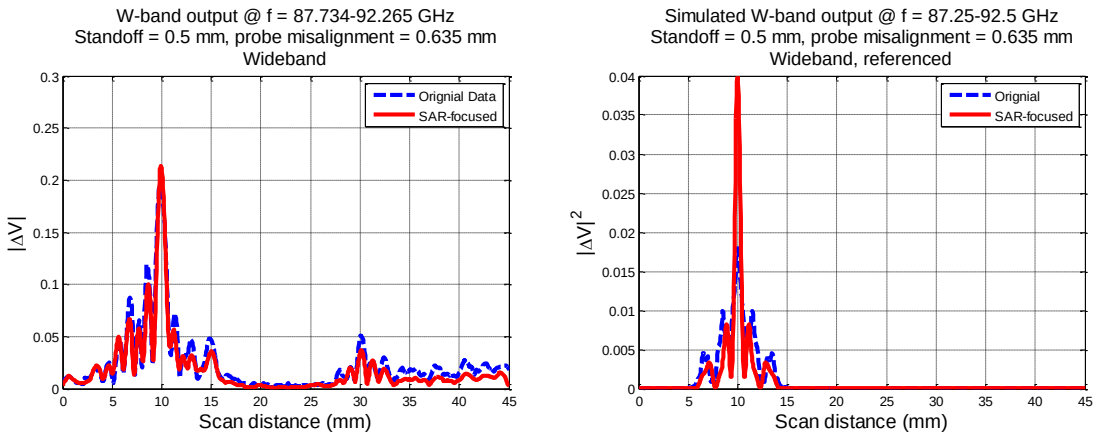

Figure 4. SAR-focused W-band results of 1.27 mm-long crack, as in measurement (left) and simulation (right), at standoff distance of 0.5 mm, and probe misalignment of +0.635 mm.

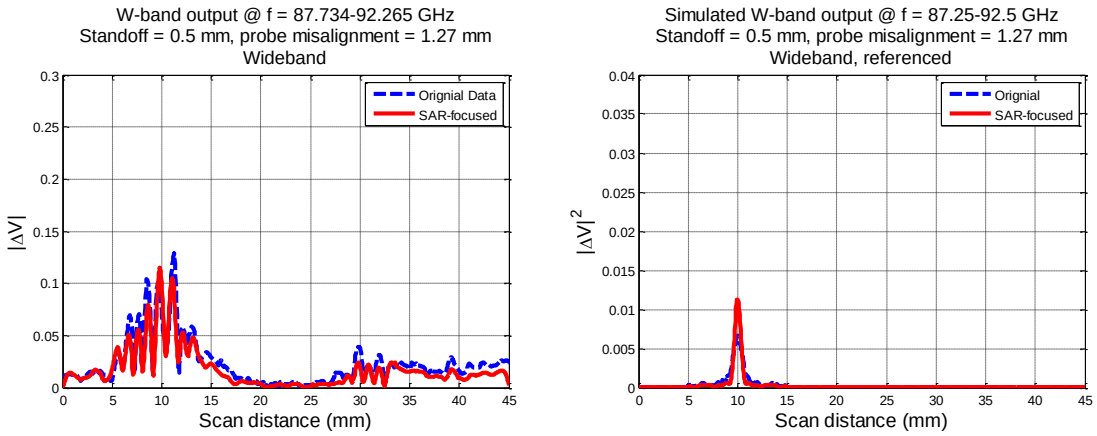

Figure 5. SAR-focused W-band results of 1.27 mm-long crack, as in measurement (left) and simulation (right), at standoff distance of 0.5 mm, and probe misalignment of +1.27 mm.

Figures 6 through 10 represent the comparisons between measurement and simulation results at standoff distance of 1 mm. Note the figures may not be in the same scale.

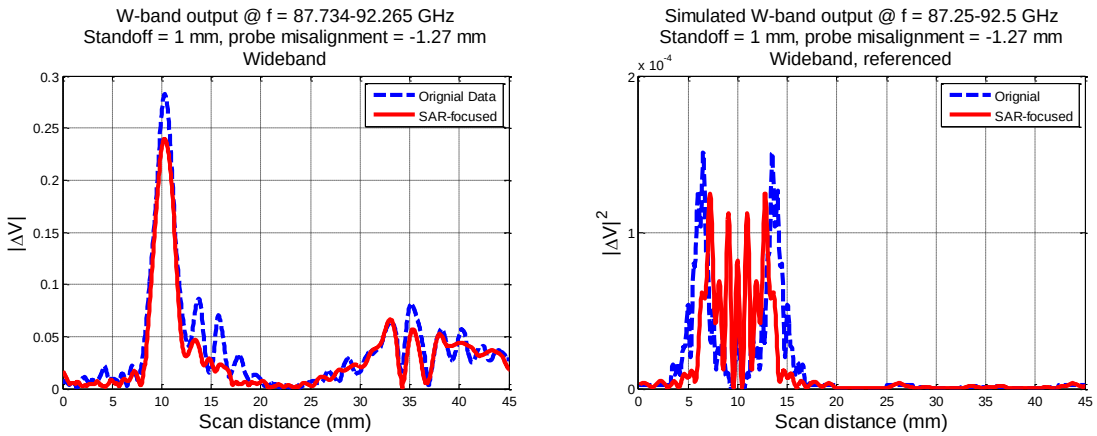

Figure 6. SAR-focused W-band results of 1.27 mm-long crack, as in measurement (left) and simulation (right), at standoff distance of 1 mm, and probe misalignment of -1.27 mm.

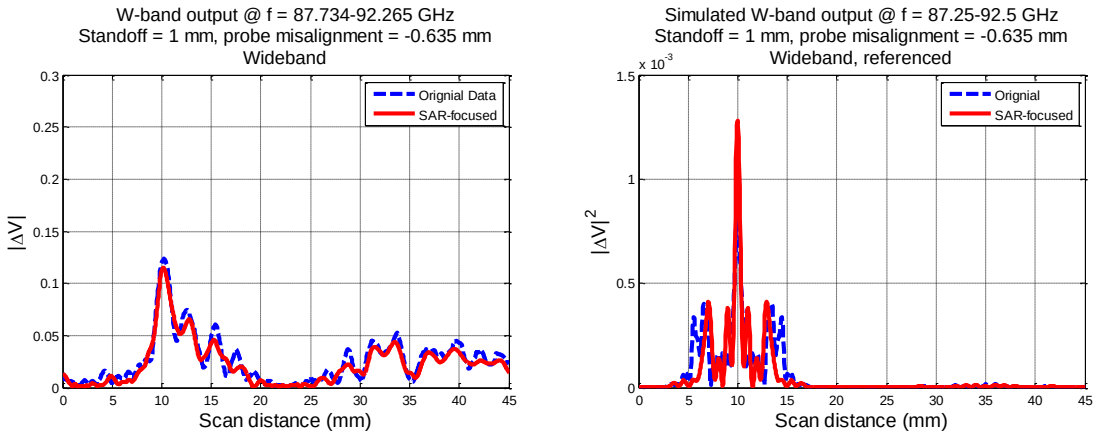

Figure 7. SAR-focused W-band results of 1.27 mm-long crack, as in measurement (left) and simulation (right), at standoff distance of 1 mm, and probe misalignment of -0.635 mm.

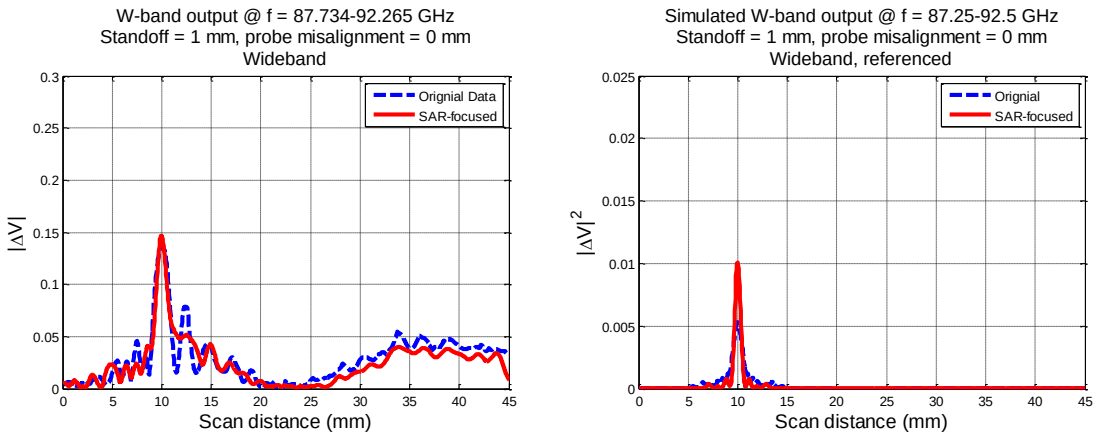

Figure 8. SAR-focused W-band results of 1.27 mm-long crack, as in measurement (left) and simulation (right), at standoff distance of 1 mm, and no probe misalignment.

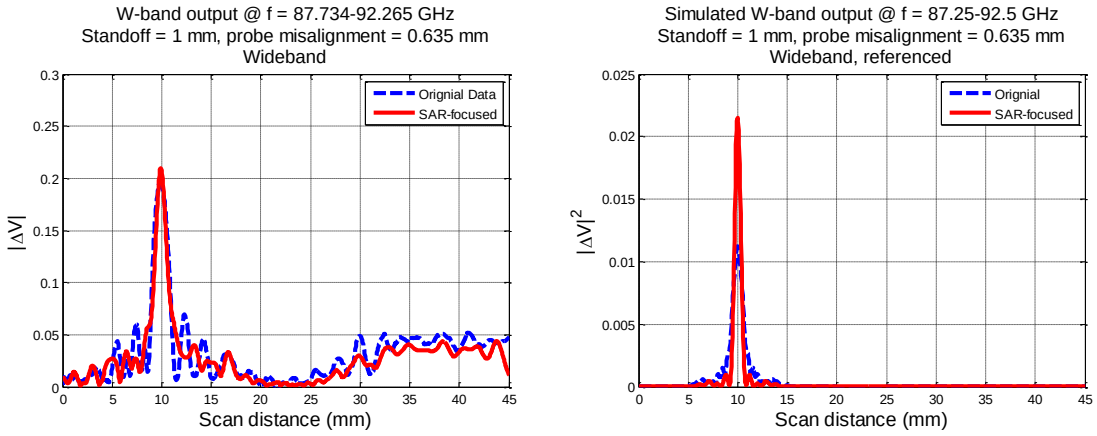

Figure 9. SAR-focused W-band results of 1.27 mm-long crack, as in measurement (left) and simulation (right), at standoff distance of 1 mm, and probe misalignment of +0.635 mm.

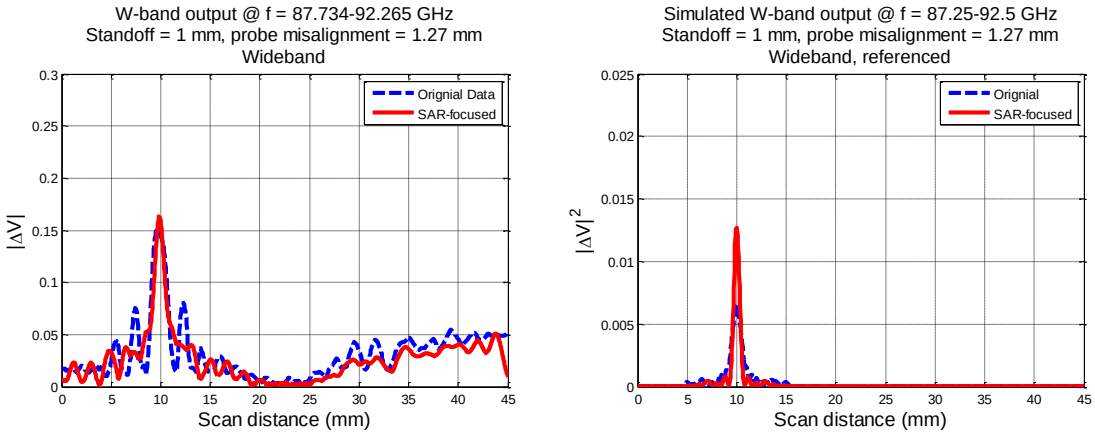

Figure 10. SAR-focused W-band results of 1.27 mm-long crack, as in measurement (left) and simulation (right), at standoff distance of 1 mm, and probe misalignment of +1.27 mm.

APPENDIX O.
ADDITIONAL FIGURES OF SAR FILTER ON SIMULATION AND MEASUREMENT RESULTS (EFFECT OF PROBE OFFSET)

This appendix provides the complete comparisons between SAR-focused measurement and simulation results for Section 5.5 – Synthetic Aperture Processing on Effect of Probe Offset.

Figures 1 through 5 represent the comparisons (at four common frequencies) between measurement and simulation results (after SAR is applied) at 0.5 mm standoff distance, while Figures 6 through 10 represent the results at 1 mm standoff distance.

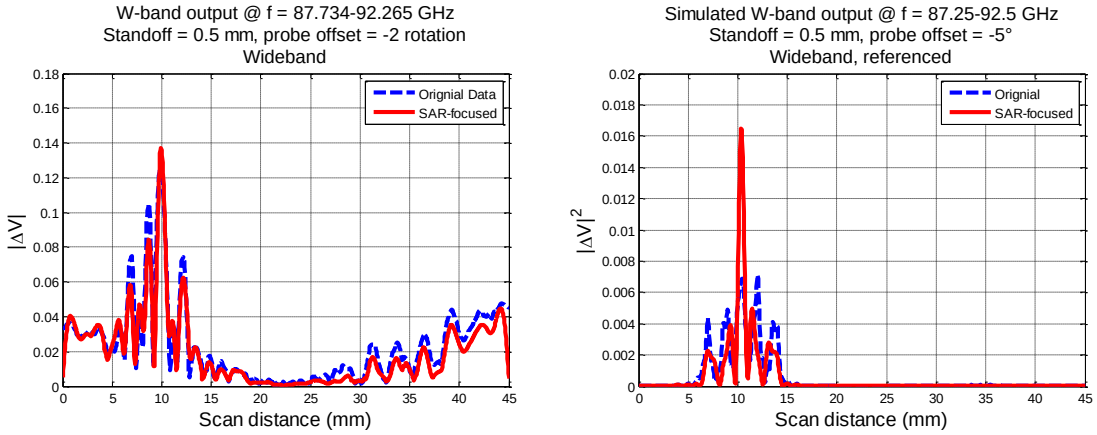

Figure 1. SAR-focused W-band results of 1.27 mm-long crack, as in measurement (left) and simulation (right), at standoff distance of 0.5 mm, and probe offset of -2 rotations (measurements) and -5° (simulations).

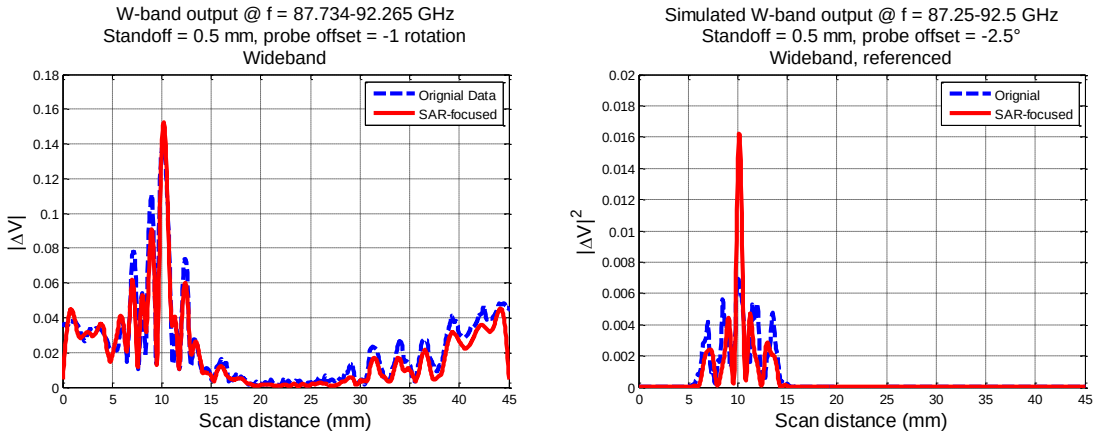

Figure 2. SAR-focused W-band results of 1.27 mm-long crack, as in measurement (left) and simulation (right), at standoff distance of 0.5 mm, and probe offset of -1 rotation (measurements) and -2.5° (simulations).

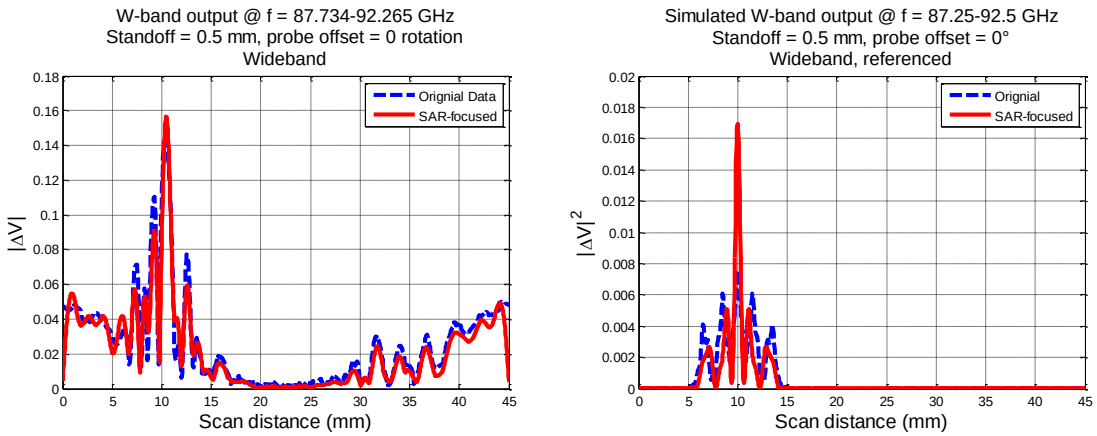

Figure 3. SAR-focused W-band results of 1.27 mm-long crack, as in measurement (left) and simulation (right), at standoff distance of 0.5 mm, and no probe offset.

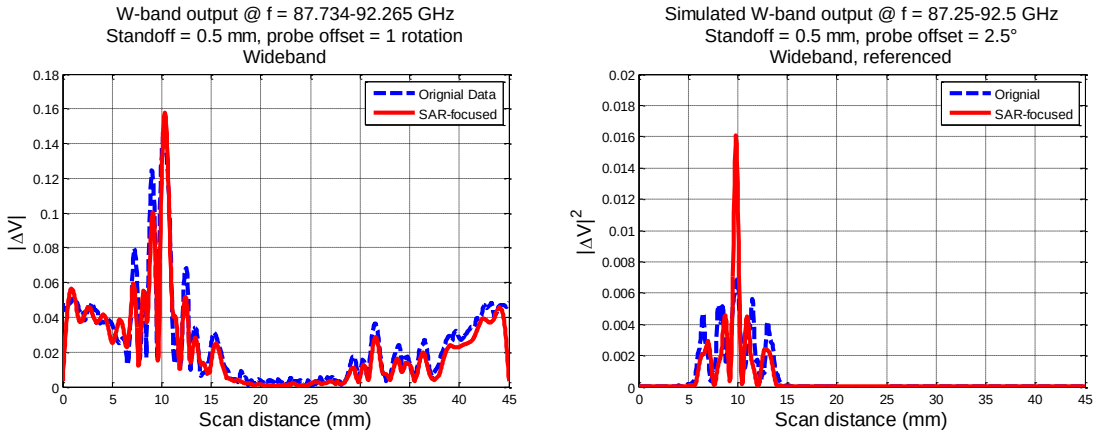

Figure 4. SAR-focused W-band results of 1.27 mm-long crack, as in measurement (left) and simulation (right), at standoff distance of 0.5 mm, and probe offset of +1 rotation (measurements) and +2.5° (simulations).

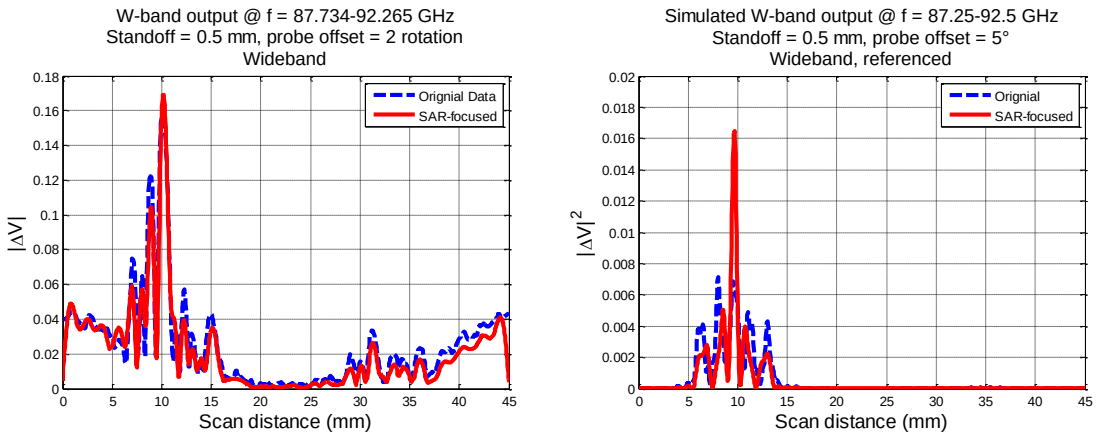

Figure 5. SAR-focused W-band results of 1.27 mm-long crack, as in measurement (left) and simulation (right), at standoff distance of 0.5 mm, and probe offset of +2 rotations (measurements) and +5° (simulations).

Figures 6 through 10 represent the comparisons between measurement and simulation results at standoff distance of 1 mm.

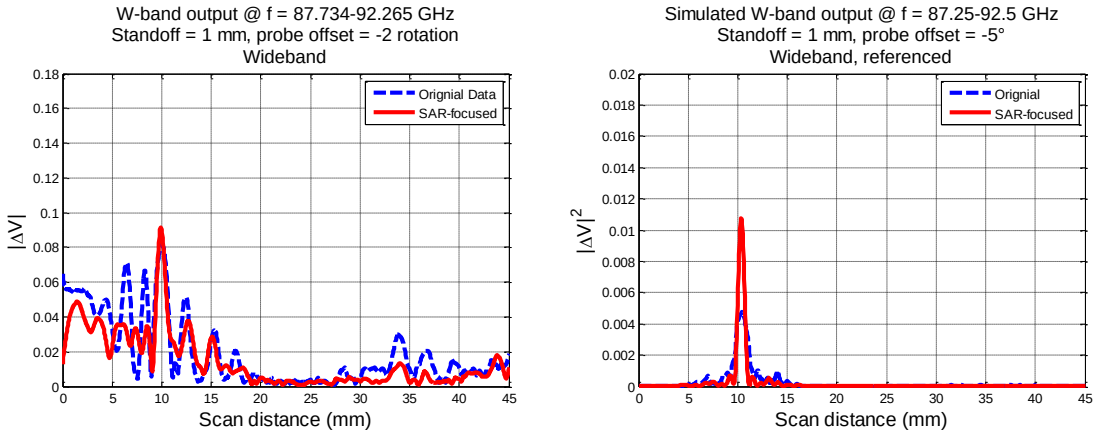

Figure 6. SAR-focused W-band results of 1.27 mm-long crack, as in measurement (left) and simulation (right), at standoff distance of 1 mm, and probe offset of -2 rotations (measurements) and -5° (simulations).

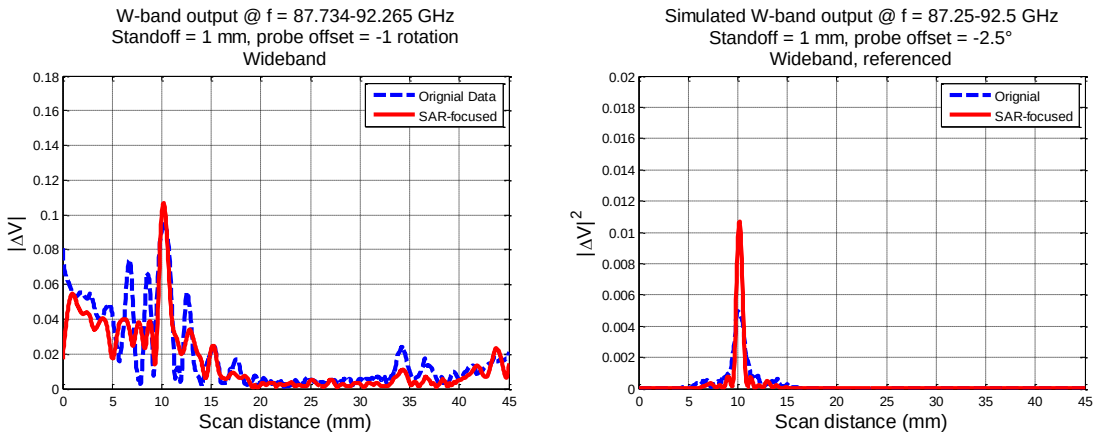

Figure 7. SAR-focused W-band results of 1.27 mm-long crack, as in measurement (left) and simulation (right), at standoff distance of 1 mm, and probe offset of -1 rotation (measurements) and -2.5° (simulations).

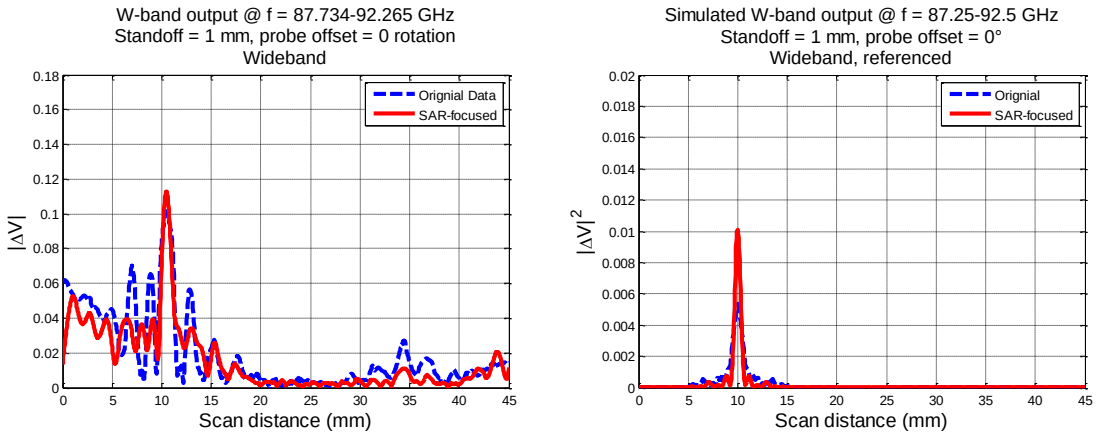

Figure 8. SAR-focused W-band results of 1.27 mm-long crack, as in measurement (left) and simulation (right), at standoff distance of 1 mm, and no probe offset.

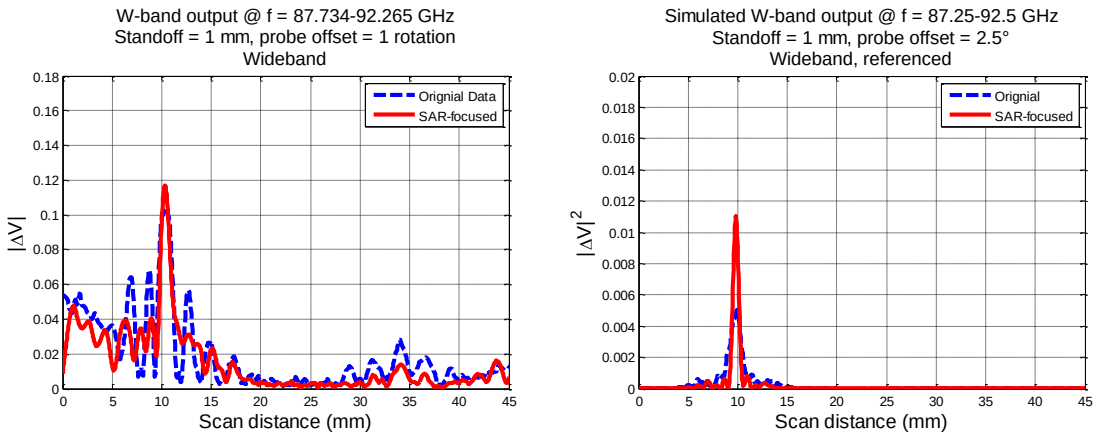

Figure 9. SAR-focused W-band results of 1.27 mm-long crack, as in measurement (left) and simulation (right), at standoff distance of 1 mm, and probe offset of +1 rotation (measurements) and +2.5° (simulations).

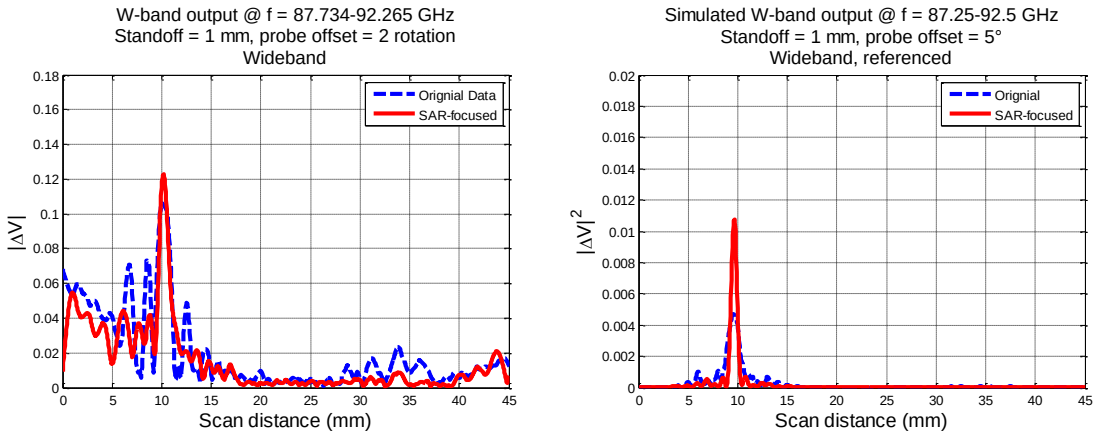

Figure 10. SAR-focused W-band results of 1.27 mm-long crack, as in measurement (left) and simulation (right), at standoff distance of 1 mm, and probe offset of +2 rotations (measurements) and +5° (simulations).

APPENDIX P.

ADDITIONAL FIGURES OF SIMULATED RESULTS (EFFECT OF NON-UNIFORM PAINT)

This appendix provides the complete simulated scan results (both selected single-frequency and wideband responses) for Section 6.1 – Effect of non-uniform paint accumulated over crack (from Figures 1 through 8) and Section 6.2 – Effect of non-uniform paint accumulated on the opposite side of crack (from Figures 9 through 16).

Figures 1 through 4 represent the simulated results at standoff distance of 0.5 mm, while the paint clump is located over the initiated crack. Among these figures, Figures 1 through 3 show the selected single-frequency responses and Figure 4 shows the wideband responses of the W-band differential probe. The results are provided in both linear and logarithmic scales.

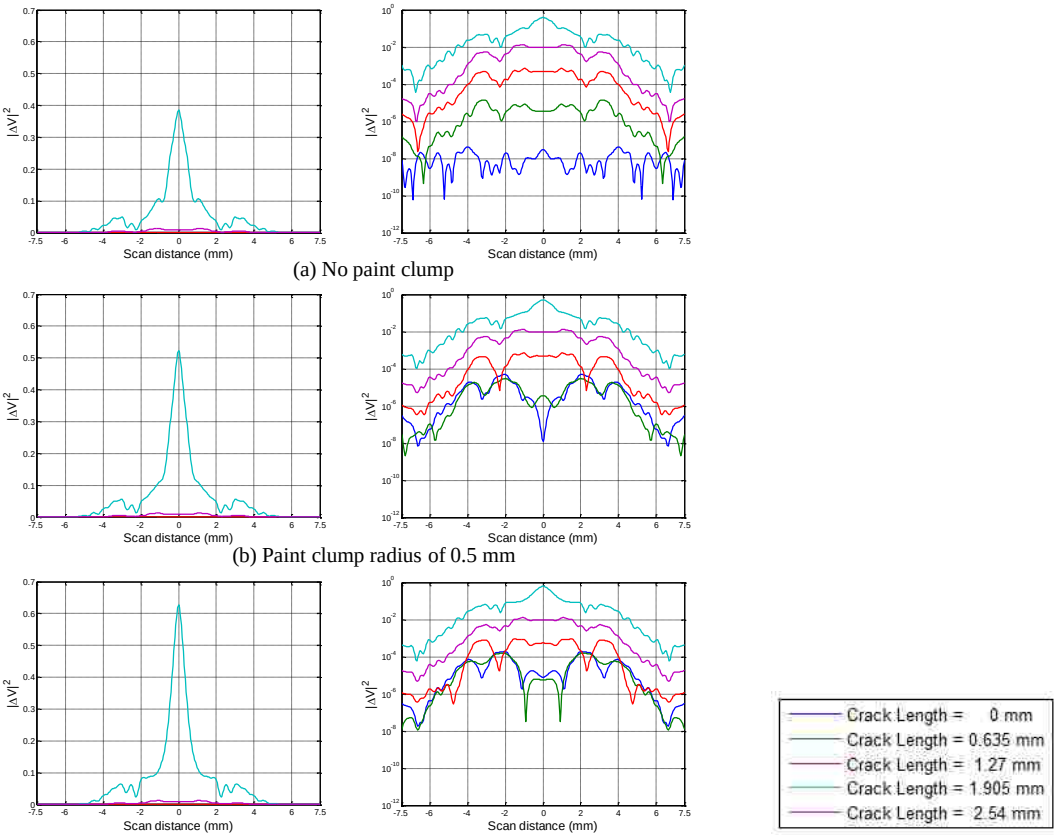

(a) No paint clump

(b) Paint clump radius of 0.5 mm

(c) Paint clump radius of 1 mm

(d) Paint clump radius of 1.5 mm

(e) Paint clump radius of 2 mm

Figure 1. Simulated W-band results with various crack lengths, at a standoff distance of 0.5 mm, frequency of 75 GHz, and paint clump (located over crack) radii of (from (a) to (e)): 0, 0.5, 1, 1.5, and 2 mm, in linear (left) and logarithmic scales (right).

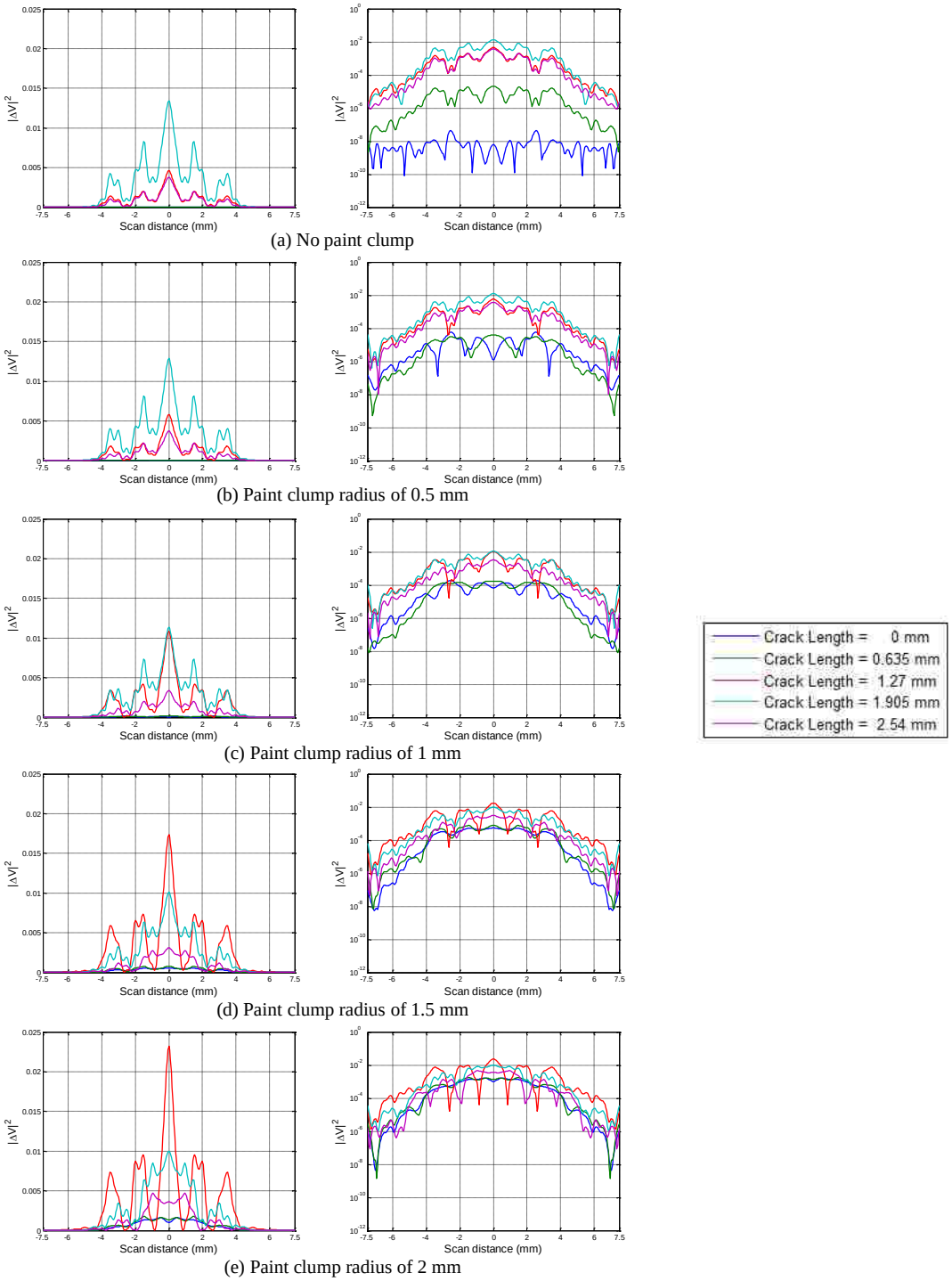

(a) No paint clump

(b) Paint clump radius of 0.5 mm

(c) Paint clump radius of 1 mm

(d) Paint clump radius of 1.5 mm

(e) Paint clump radius of 2 mm

Figure 2. Simulated W-band results with various crack lengths, at a standoff distance of 0.5 mm, frequency of 87.25 GHz, and paint clump (located over crack) radii of (from (a) to (e)): 0, 0.5, 1, 1.5, and 2 mm, in linear (left) and logarithmic scales (right).

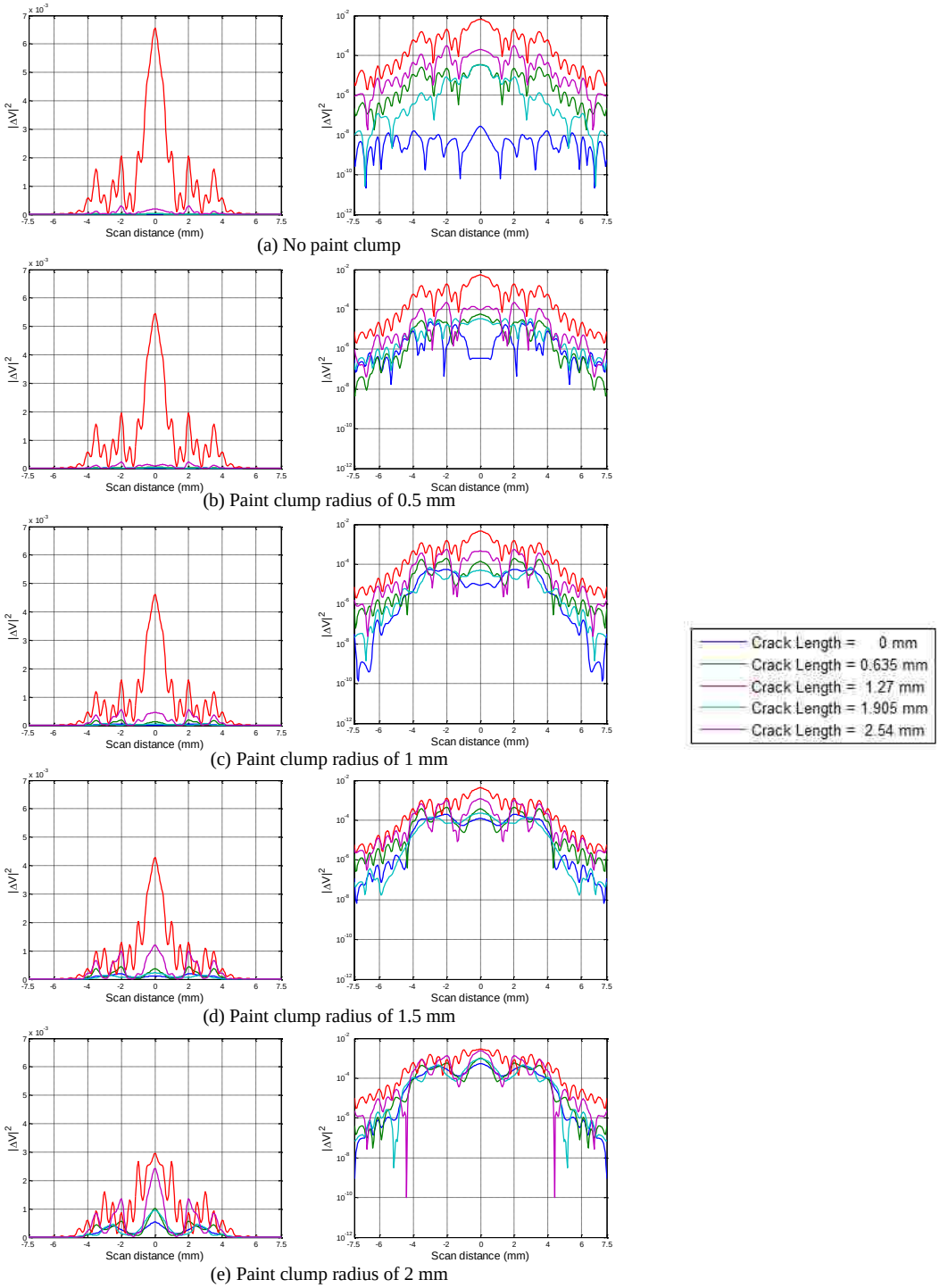

Figure 3. Simulated W-band results with various crack lengths, at a standoff distance of 0.5 mm, frequency of 110 GHz, and paint clump (located over crack) radii of (from (a) to (e)): 0, 0.5, 1, 1.5, and 2 mm, in linear (left) and logarithmic scales (right).

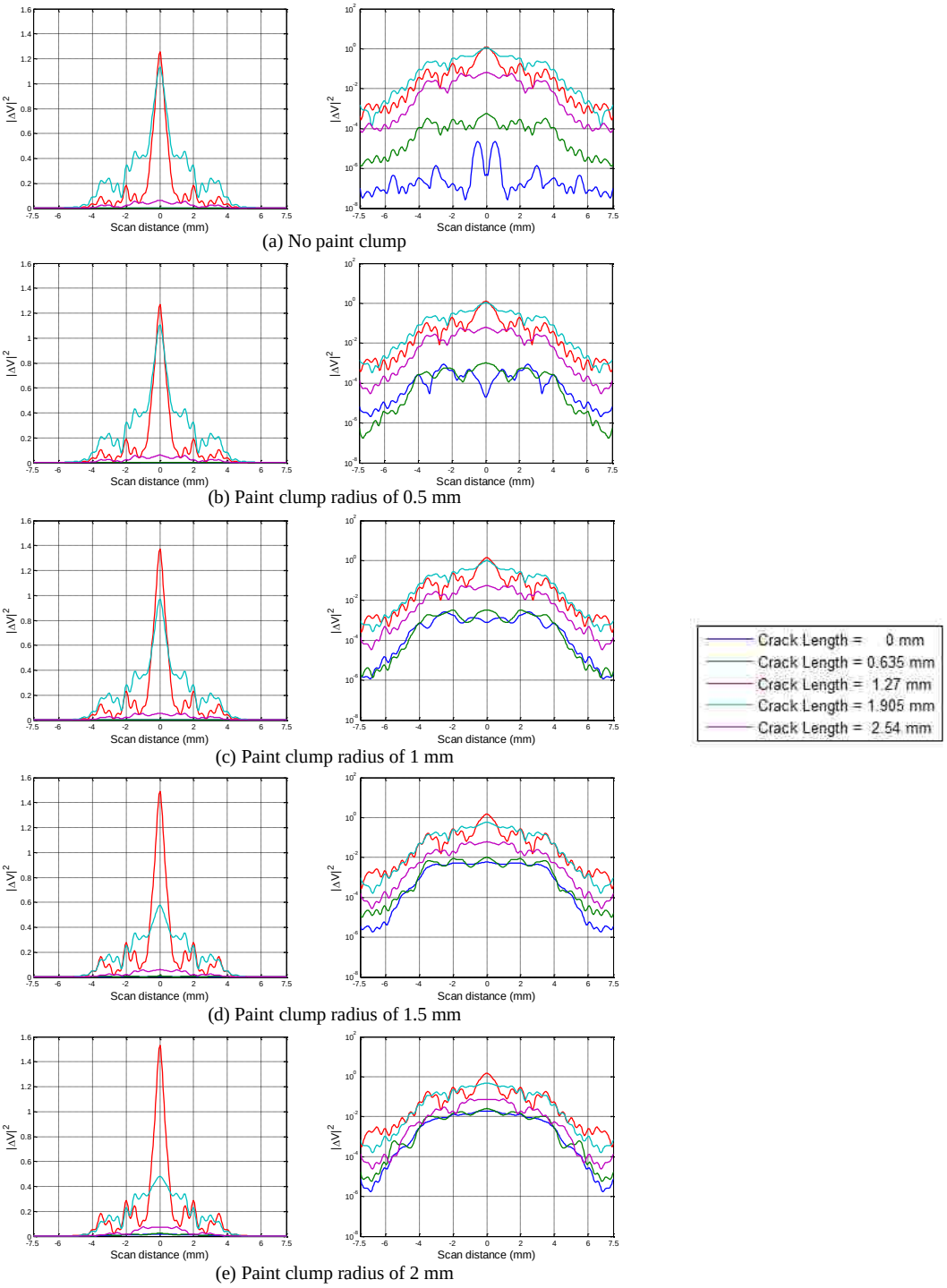

(a) No paint clump

(b) Paint clump radius of 0.5 mm

(c) Paint clump radius of 1 mm

(d) Paint clump radius of 1.5 mm

(e) Paint clump radius of 2 mm

Figure 4. Simulated W-band wideband results with various crack lengths, at a standoff distance of 0.5 mm, and paint clump (located over crack) radii of (from (a) to (e)): 0, 0.5, 1, 1.5, and 2 mm, in linear (left) and logarithmic scales (right).

Figures 5 through 8 represent the simulated results at standoff distance of 1 mm, while the paint clump is located over the initiated crack. Among these figures, Figures 5 through 7 show the selected single-frequency responses and Figure 8 shows the wideband responses of the W-band differential probe. The results are provided in both linear and logarithmic scales.

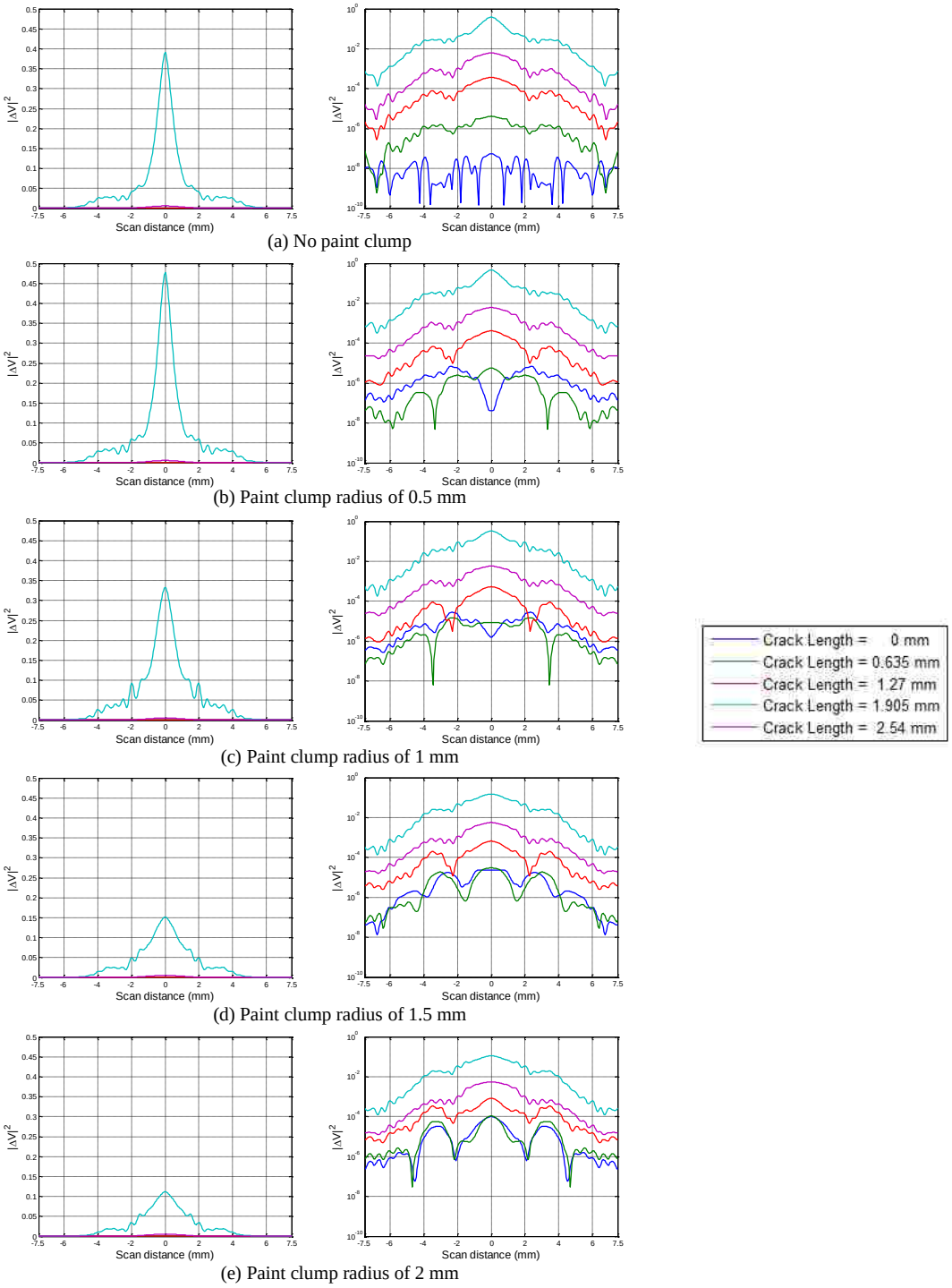

(a) No paint clump

(b) Paint clump radius of 0.5 mm

(c) Paint clump radius of 1 mm

(d) Paint clump radius of 1.5 mm

(e) Paint clump radius of 2 mm

Figure 5. Simulated W-band results with various crack lengths, at a standoff distance of 1 mm, frequency of 75 GHz, and paint clump (located over crack) radii of (from (a) to (e)): 0, 0.5, 1, 1.5, and 2 mm, in linear (left) and logarithmic scales (right).

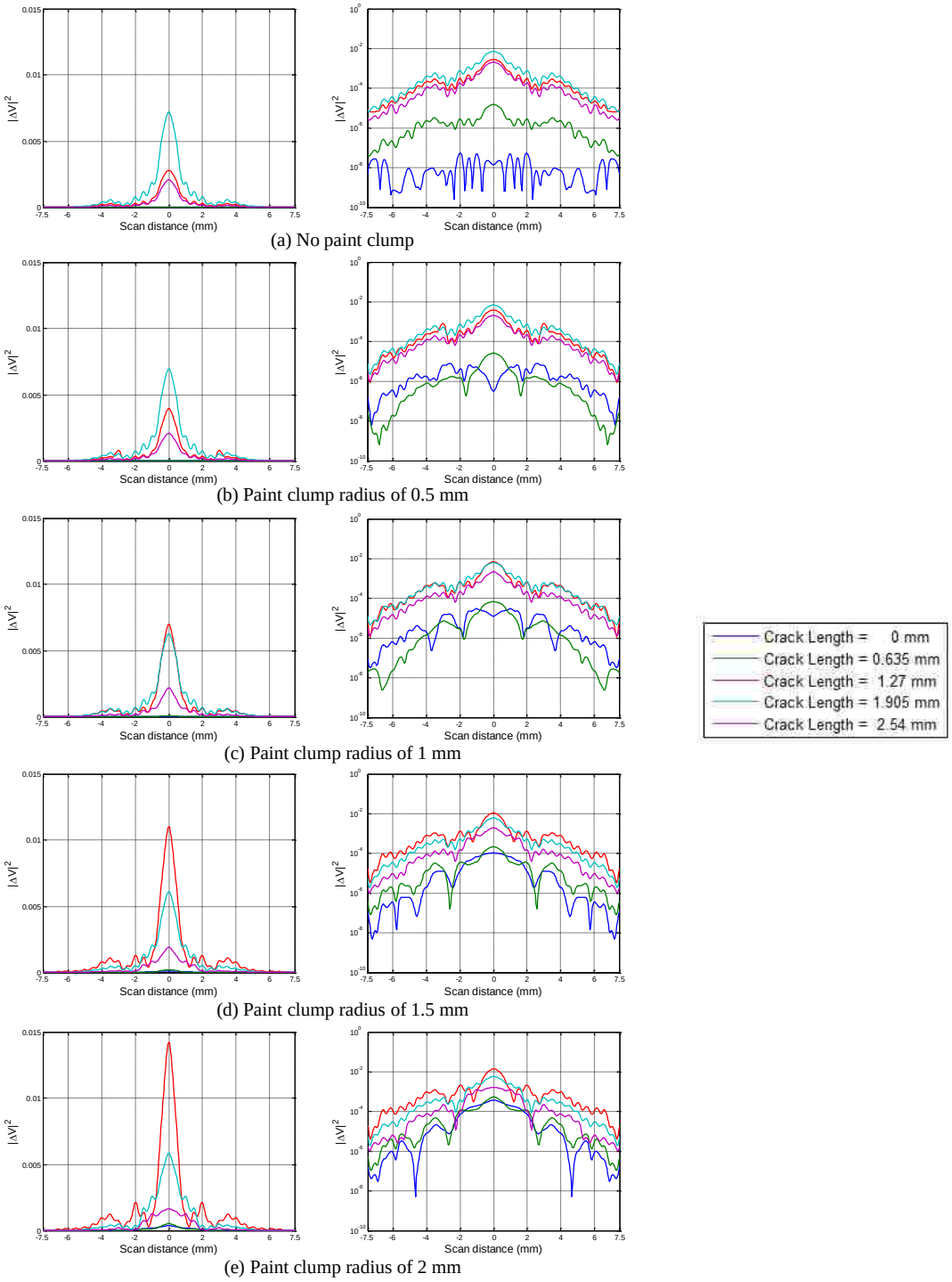

(a) No paint clump

(b) Paint clump radius of 0.5 mm

(c) Paint clump radius of 1 mm

(d) Paint clump radius of 1.5 mm

(e) Paint clump radius of 2 mm

Figure 6. Simulated W-band results with various crack lengths, at a standoff distance of 1 mm, frequency of 87.25 GHz, and paint clump (located over crack) radii of (from (a) to (e)): 0, 0.5, 1, 1.5, and 2 mm, in linear (left) and logarithmic scales (right).

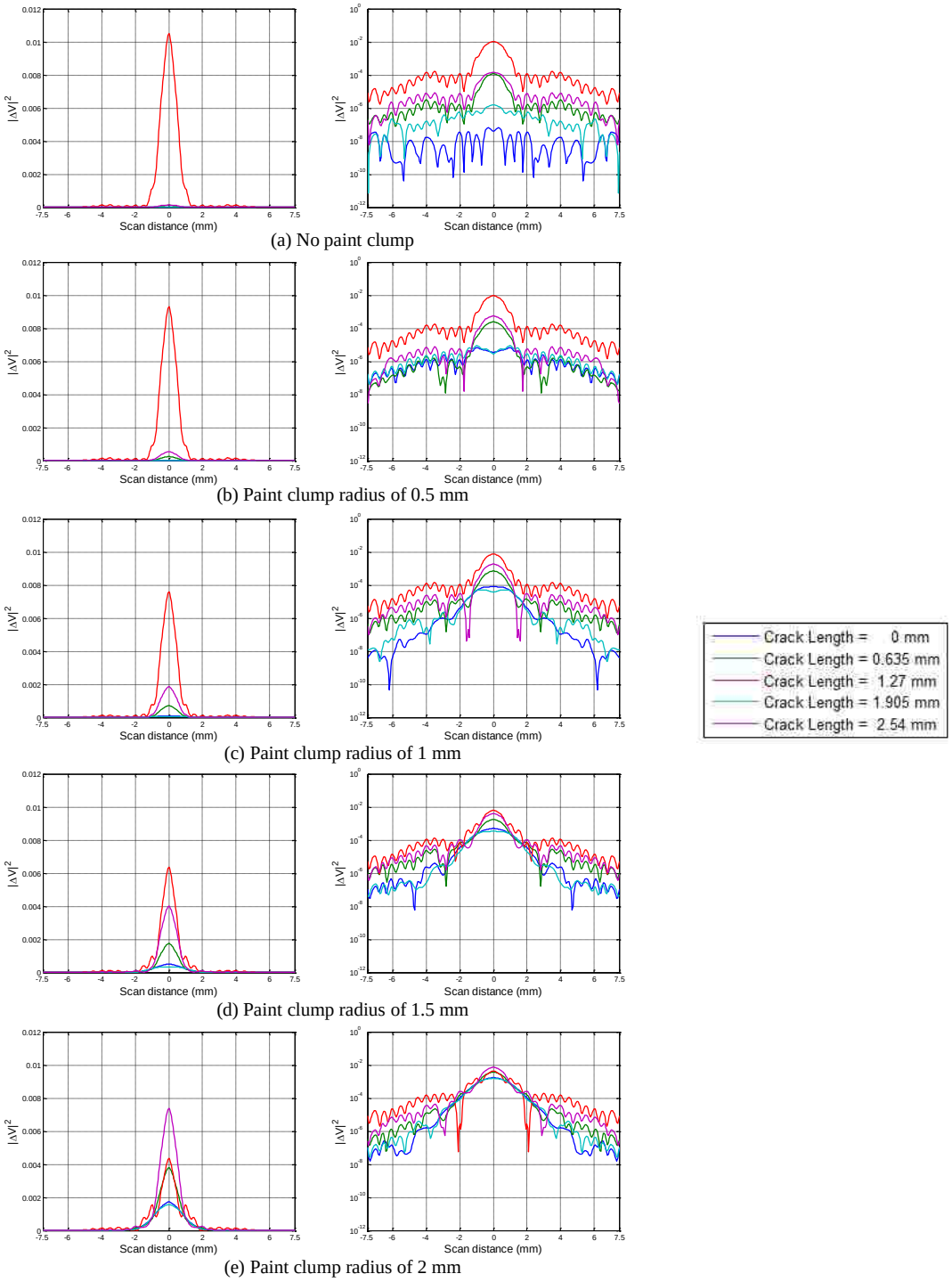

(a) No paint clump

(b) Paint clump radius of 0.5 mm

(c) Paint clump radius of 1 mm

(d) Paint clump radius of 1.5 mm

(e) Paint clump radius of 2 mm

Figure 7. Simulated W-band results with various crack lengths, at a standoff distance of 1 mm, frequency of 110 GHz, and paint clump (located over crack) radii of (from (a) to (e)): 0, 0.5, 1, 1.5, and 2 mm, in linear (left) and logarithmic scales (right).

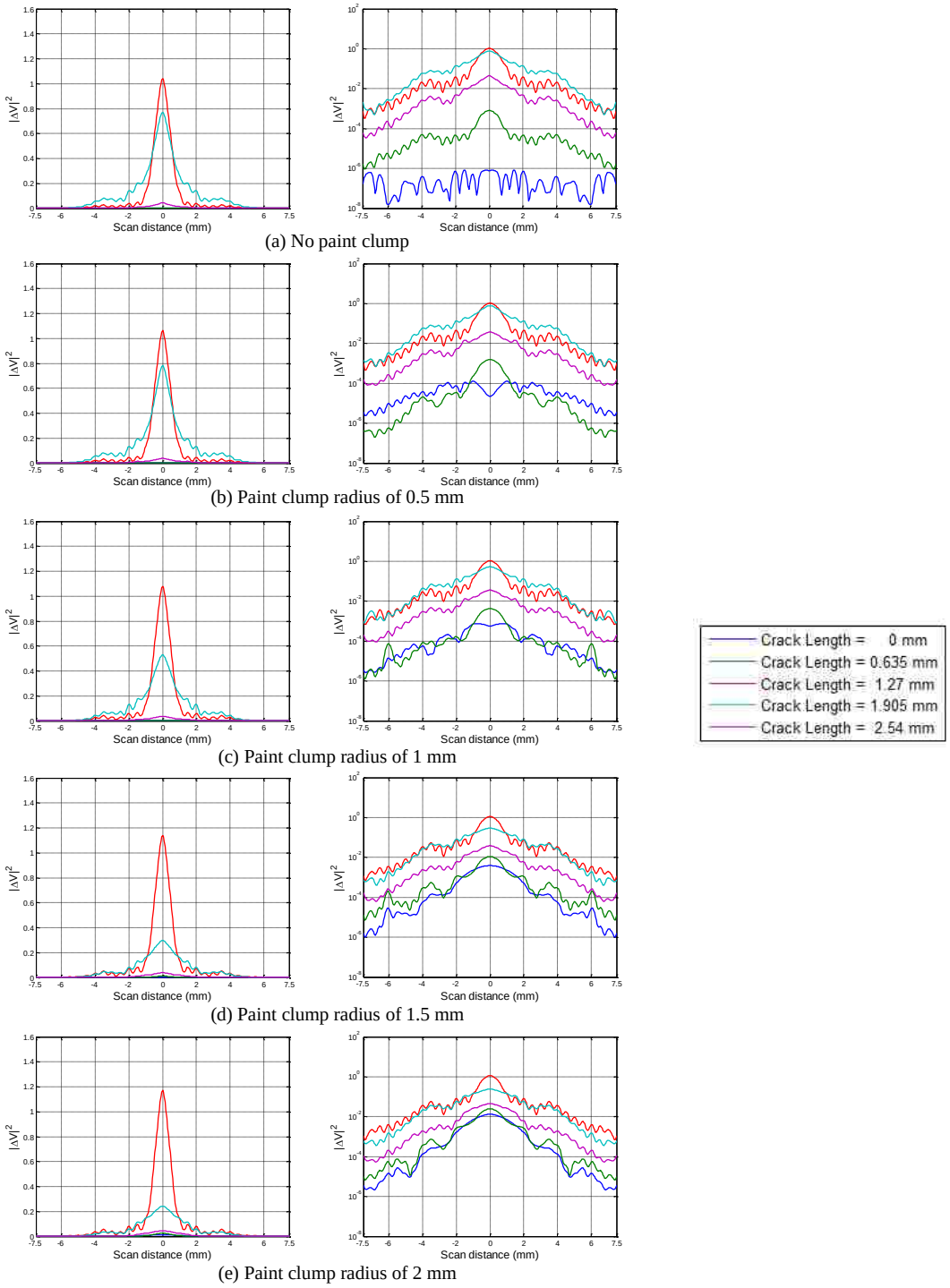

(a) No paint clump

(b) Paint clump radius of 0.5 mm

(c) Paint clump radius of 1 mm

(d) Paint clump radius of 1.5 mm

(e) Paint clump radius of 2 mm

Figure 8. Simulated W-band wideband results with various crack lengths, at a standoff distance of 1 mm, and paint clump (located over crack) radii of (from (a) to (e)): 0, 0.5, 1, 1.5, and 2 mm, in linear (left) and logarithmic scales (right).

Figures 9 through 12 represent the simulated results at standoff distance of 0.5 mm, while the paint clump is located on the opposite side of crack. Among these figures, Figures 9 through 11 show the selected single-frequency responses and Figure 12 shows the wideband responses of the W-band differential probe. The results are provided in both linear and logarithmic scales.

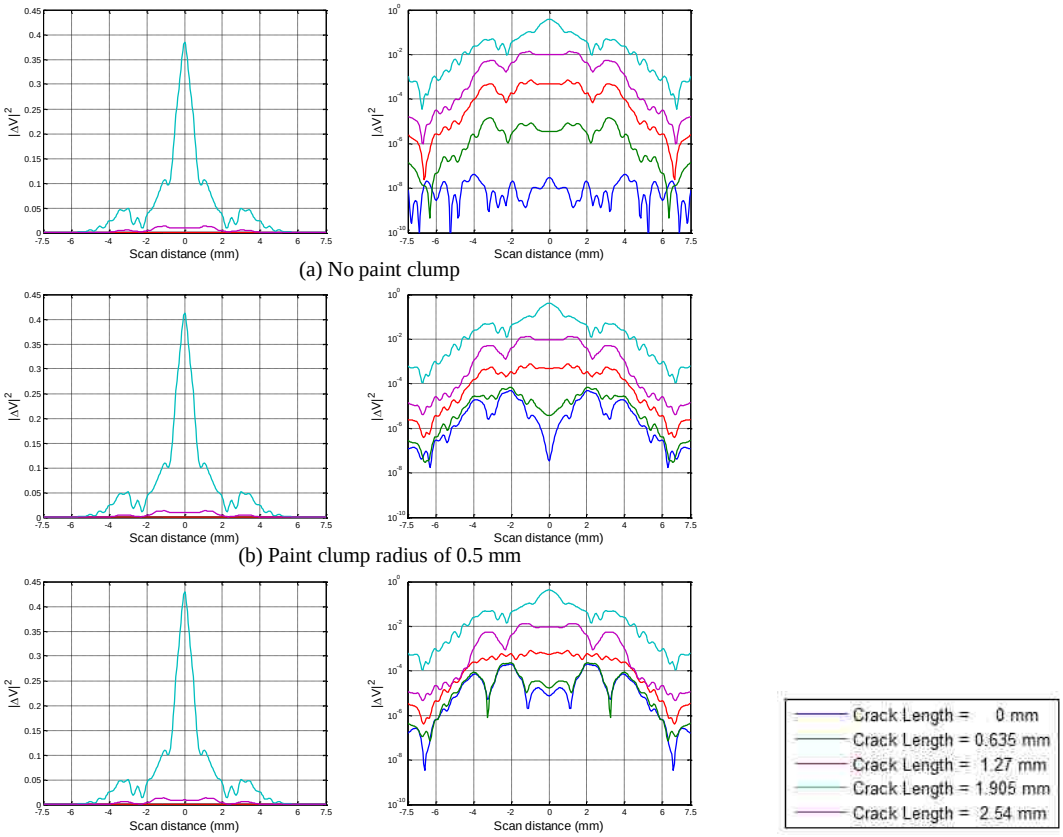

(a) No paint clump

(b) Paint clump radius of 0.5 mm

(c) Paint clump radius of 1 mm

(d) Paint clump radius of 1.5 mm

(e) Paint clump radius of 2 mm

Figure 9. Simulated W-band results with various crack lengths, at a standoff distance of 0.5 mm, frequency of 75 GHz, and paint clump (located on opposite side of crack) radii of (from (a) to (e)): 0, 0.5, 1, 1.5, and 2 mm, in linear (left) and logarithmic scales (right).

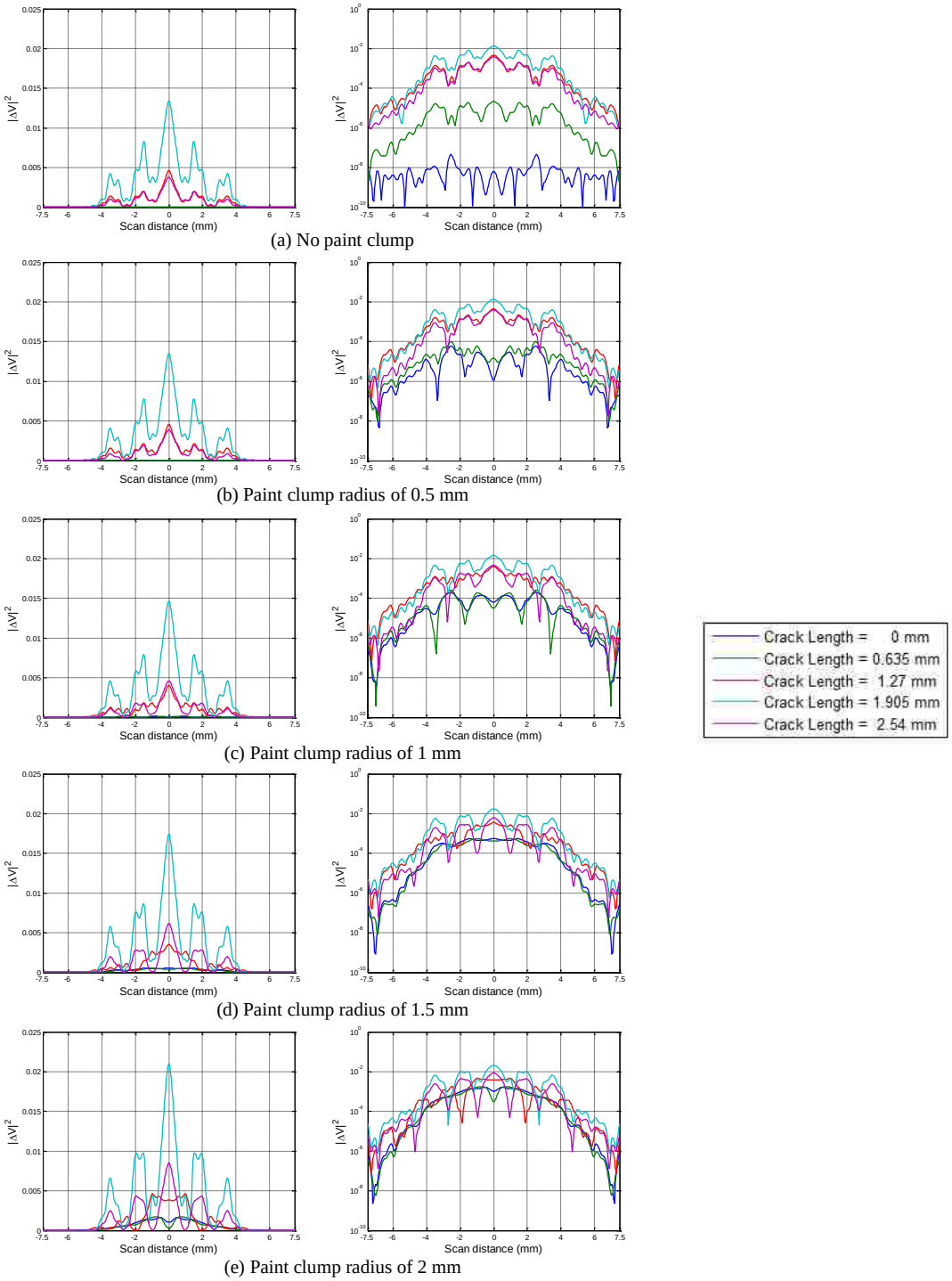

(a) No paint clump

(b) Paint clump radius of 0.5 mm

(c) Paint clump radius of 1 mm

(d) Paint clump radius of 1.5 mm

(e) Paint clump radius of 2 mm

Figure 10. Simulated W-band results with various crack lengths, at a standoff distance of 0.5 mm, frequency of 87.25 GHz, and paint clump (located on opposite side of crack) radii of (from (a) to (e)): 0, 0.5, 1, 1.5, and 2 mm, in linear (left) and logarithmic scales (right).

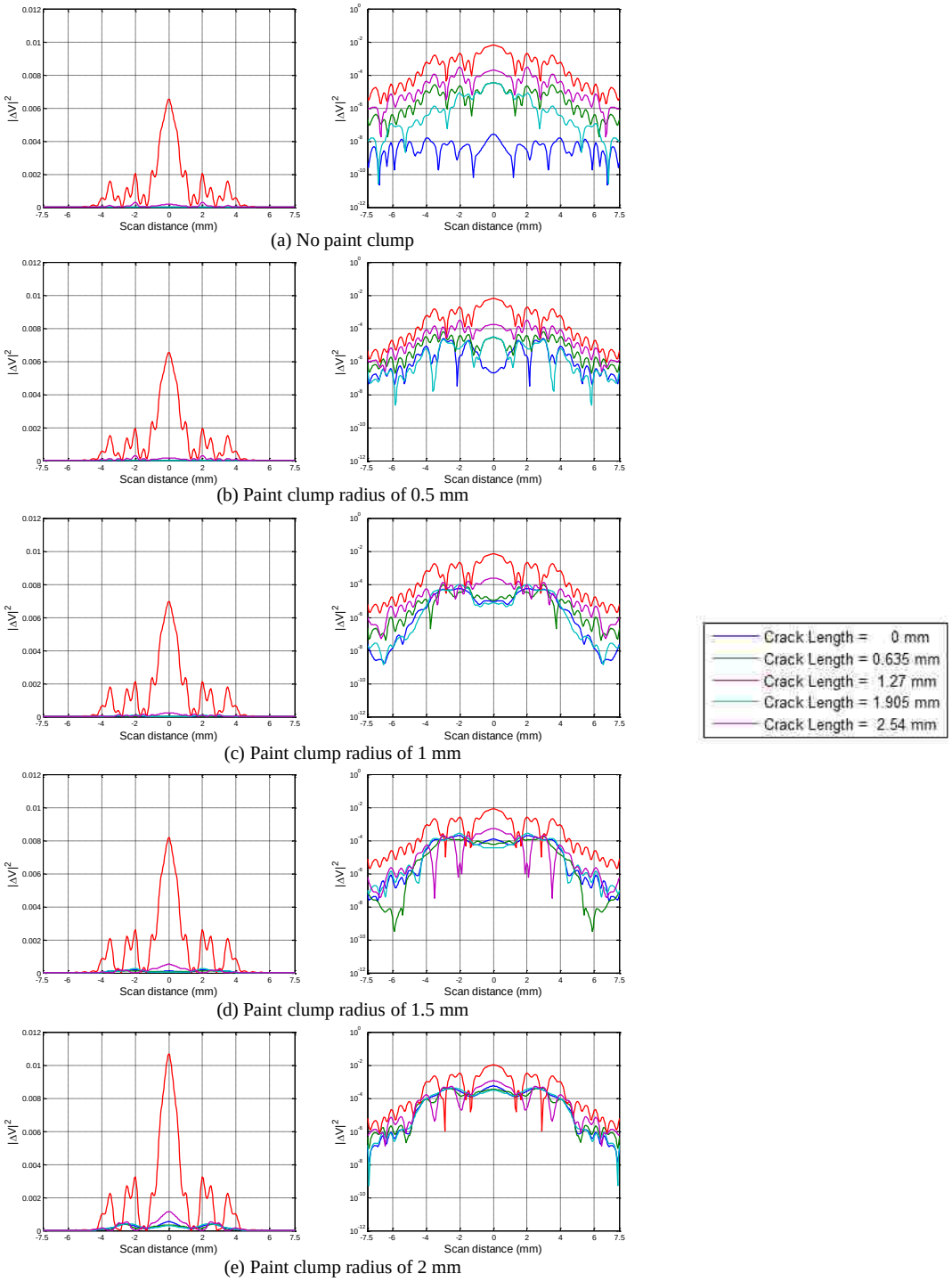

(a) No paint clump

(b) Paint clump radius of 0.5 mm

(c) Paint clump radius of 1 mm

(d) Paint clump radius of 1.5 mm

(e) Paint clump radius of 2 mm

Figure 11. Simulated W-band results with various crack lengths, at a standoff distance of 0.5 mm, frequency of 110 GHz, and paint clump (located on opposite side of crack) radii of (from (a) to (e)): 0, 0.5, 1, 1.5, and 2 mm, in linear (left) and logarithmic scales (right).

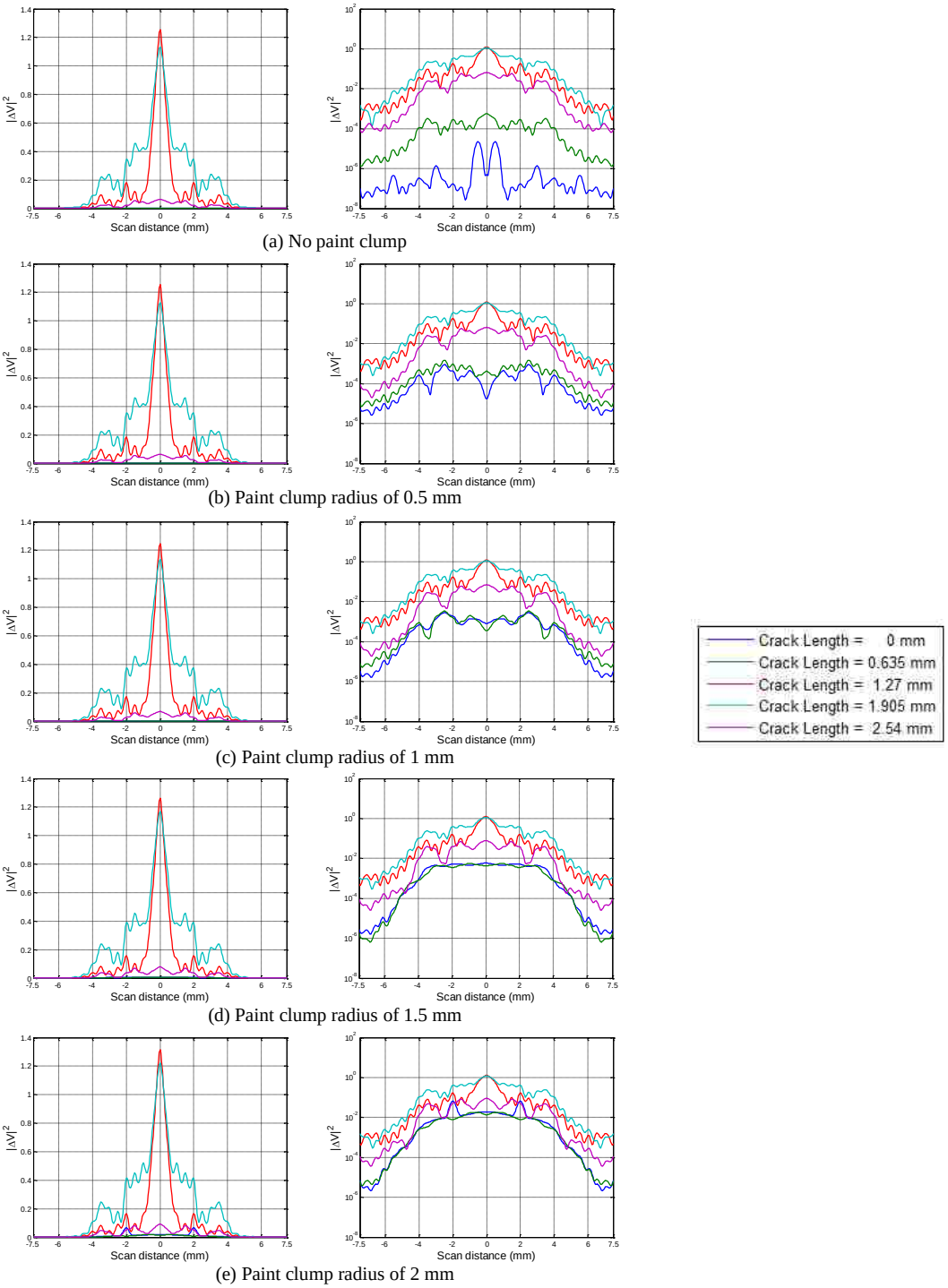

(a) No paint clump

(b) Paint clump radius of 0.5 mm

(c) Paint clump radius of 1 mm

(d) Paint clump radius of 1.5 mm

(e) Paint clump radius of 2 mm

Figure 12. Simulated W-band wideband results with various crack lengths, at a standoff distance of 0.5 mm, and paint clump (located on opposite side of crack) radii of (from (a) to (e)): 0, 0.5, 1, 1.5, and 2 mm, in linear (left) and logarithmic scales (right).

Figures 13 through 16 represent the simulated results at standoff distance of 1 mm, while the paint clump is located on the opposite side of crack. Among these figures, Figures 13 through 15 show the selected single-frequency responses and Figure 16 shows the wideband responses of the W-band differential probe. The results are provided in both linear and logarithmic scales.

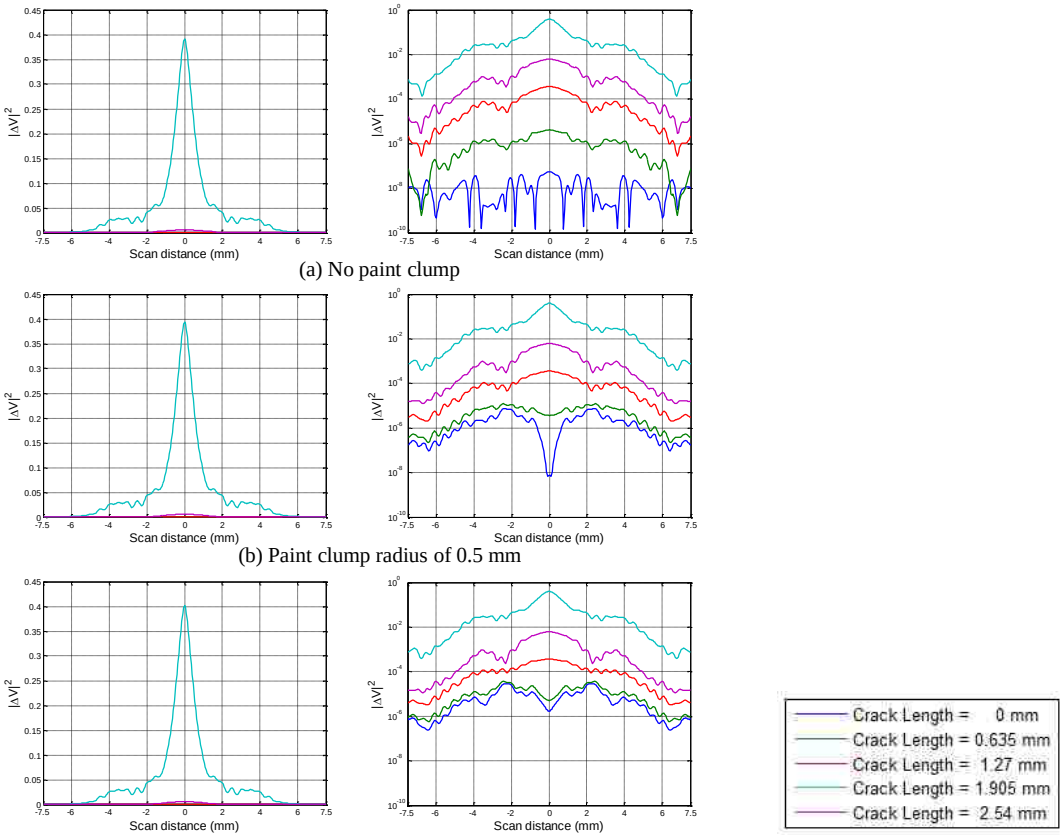

(a) No paint clump

(b) Paint clump radius of 0.5 mm

(c) Paint clump radius of 1 mm

(d) Paint clump radius of 1.5 mm

(e) Paint clump radius of 2 mm

Figure 13. Simulated W-band results with various crack lengths, at a standoff distance of 1 mm, frequency of 75 GHz, and paint clump (located on opposite side of crack) radii of (from (a) to (e)): 0, 0.5, 1, 1.5, and 2 mm, in linear (left) and logarithmic scales (right).

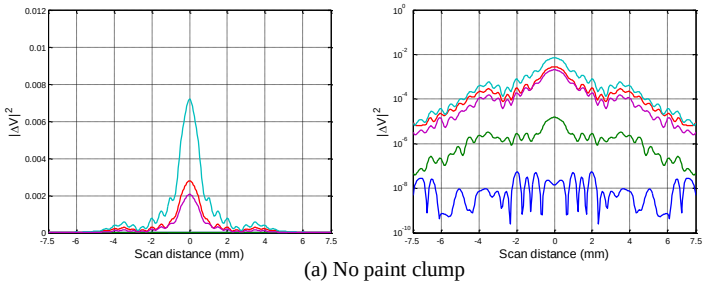

(a) No paint clump

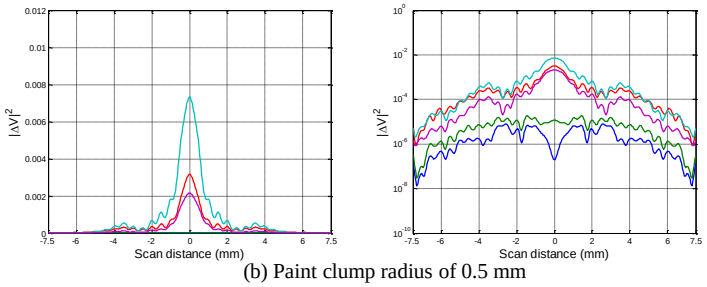

(b) Paint clump radius of 0.5 mm

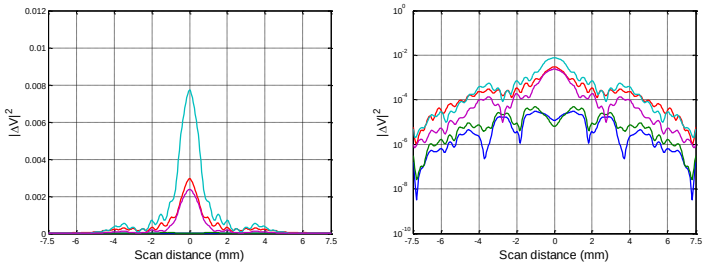

(c) Paint clump radius of 1 mm

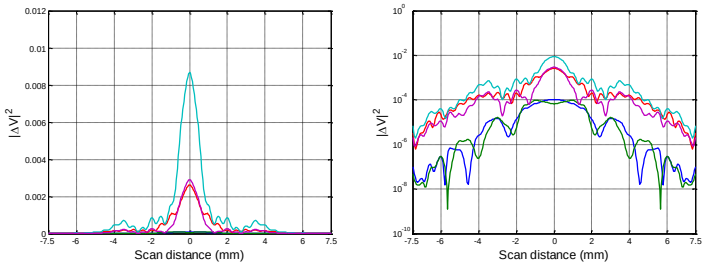

(d) Paint clump radius of 1.5 mm

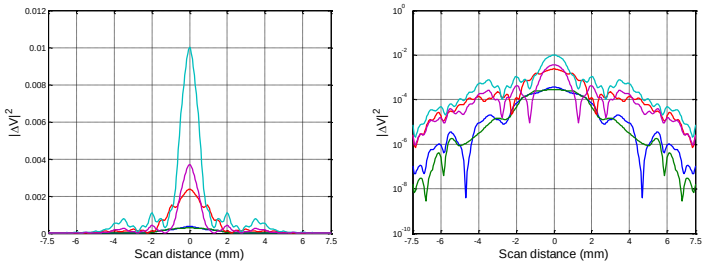

(e) Paint clump radius of 2 mm

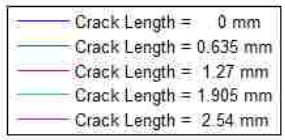

Figure 14. Simulated W-band results with various crack lengths, at a standoff distance of 1 mm, frequency of 87.25 GHz, and paint clump (located on opposite side of crack) radii of (from (a) to (e)): 0, 0.5, 1, 1.5, and 2 mm, in linear (left) and logarithmic scales (right).

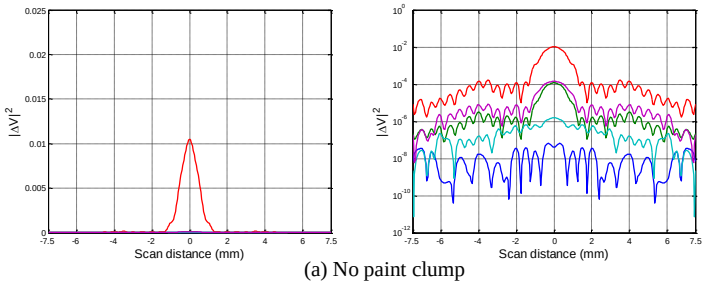

(a) No paint clump

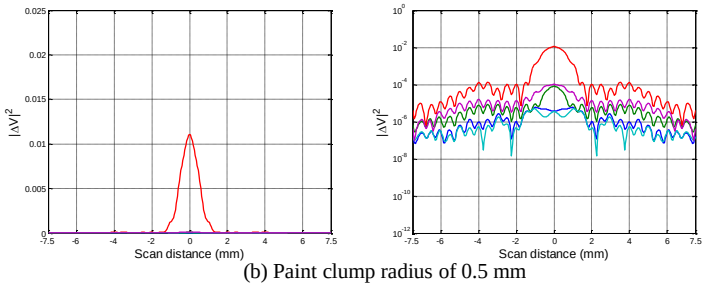

(b) Paint clump radius of 0.5 mm

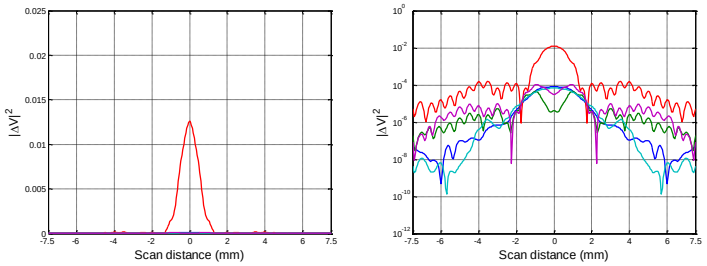

(c) Paint clump radius of 1 mm

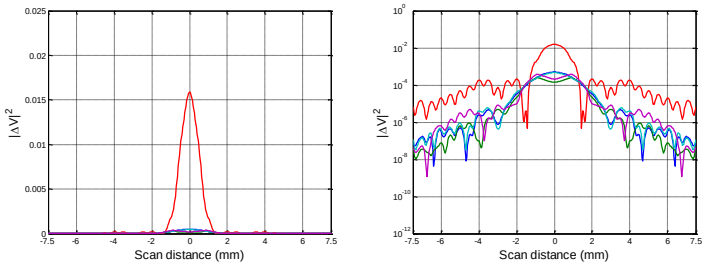

(d) Paint clump radius of 1.5 mm

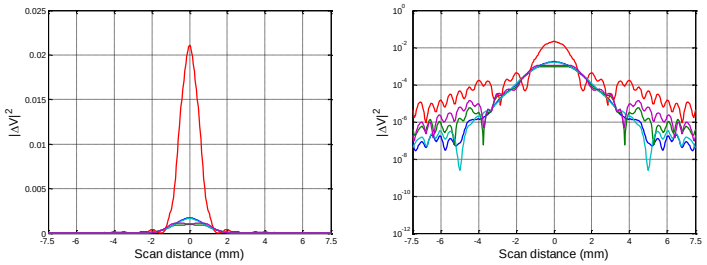

(e) Paint clump radius of 2 mm

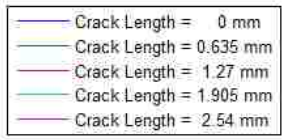

Figure 15. Simulated W-band results with various crack lengths, at a standoff distance of 1 mm, frequency of 110 GHz, and paint clump (located on opposite side of crack) radii of (from (a) to (e)): 0, 0.5, 1, 1.5, and 2 mm, in linear (left) and logarithmic scales (right).

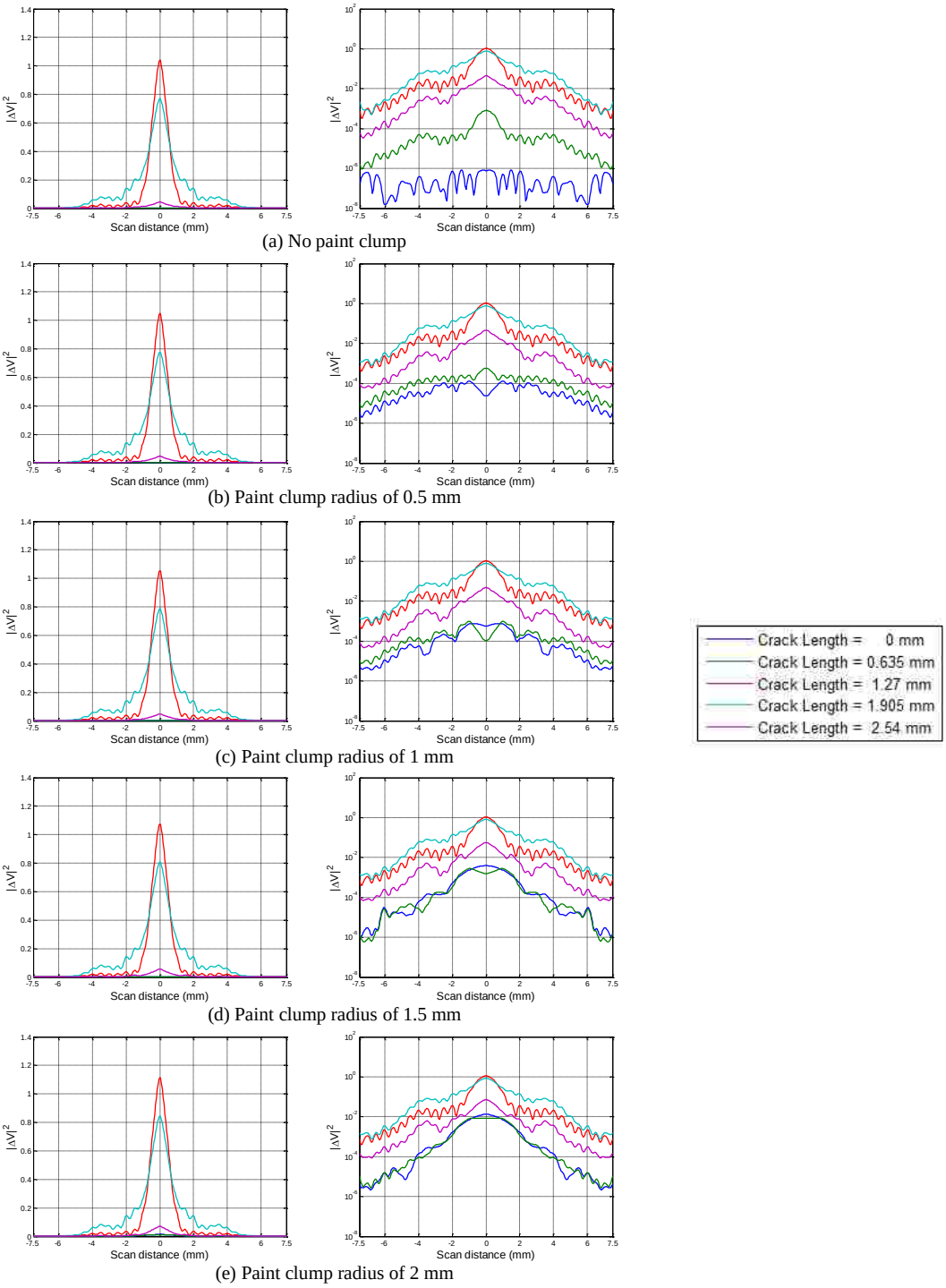

(a) No paint clump

(b) Paint clump radius of 0.5 mm

(c) Paint clump radius of 1 mm

(d) Paint clump radius of 1.5 mm

(e) Paint clump radius of 2 mm

Figure 16. Simulated W-band wideband results with various crack lengths, at a standoff distance of 1 mm, and paint clump (located on opposite side of crack) radii of (from (a) to (e)): 0, 0.5, 1, 1.5, and 2 mm, in linear (left) and logarithmic scales (right).

BIBLIOGRAPHY

[1] A. W. Hoggard and S. R. Johnson. (2012) Understanding the new widespread fatigue damage rule. *AERO magazine*.

[2] United States Government, "Aircraft accident report, Aloha Airlines flight 243, Boeing 737-100, N73711, near Maui, Hawaii, April 28, 1998," National Transportation Safety Board,, Washington D.C. 1989.

[3] National Research Council and Committee on Aging of U. S. Air Force Aircraft, *Aging of U.S. Air Force aircraft: final report*. Washington, D.C.: National Academy Press, 1997.

[4] P. J. Shull, *Nondestructive evaluation: theory, techniques, and applications*: CRC press, 2002.

[5] R. Zoughi, *Microwave non-destructive testing and evaluation principles* vol. 4: Springer Science & Business Media, 2012.

[6] N. V. Nair, V. R. Melapudi, H. R. Jimenez, X. Liu, Y. Deng, Z. Zeng, *et al.*, "A GMR-based eddy current system for NDE of aircraft structures," *IEEE Transactions on Magnetics,* vol. 42, pp. 3312-3314, 2006.

[7] G. Yang, A. Tamburrino, L. Udpa, S. S. Udpa, Z. Zeng, Y. Deng, *et al.*, "Pulsed eddy-current based giant magnetoresistive system for the inspection of aircraft structures," *IEEE Transactions on Magnetics,* vol. 46, pp. 910-917, 2010.

[8] Z. Zeng, Y. Deng, X. Liu, L. Udpa, S. S. Udpa, B. E. C. Koltenbah, *et al.*, "EC-GMR data analysis for inspection of multilayer airframe structures," *IEEE Transactions on Magnetics,* vol. 47, pp. 4745-4752, 2011.

[9] P. Y. Joubert and Y. L. Diraison, "Pulsed eddy current imager for the enhanced non destructive evaluation of aeronautical riveted assemblies," in *IEEE SENSORS 2014 Proceedings*, 2014, pp. 1188-1191.

[10] G. Yang, G. Dib, L. Udpa, A. Tamburrino, and S. S. Udpa, "Rotating field EC-GMR sensor for crack detection at fastener site in layered structures," *IEEE Sensors Journal,* vol. 15, pp. 463-470, 2015.

[11] S. P. Kelly, R. Farlow, and G. Hayward, "Applications of through-air ultrasound for rapid NDE scanning in the aerospace industry," *IEEE Transactions on Ultrasonics, Ferroelectrics, and Frequency Control,* vol. 43, pp. 581-591, 1996.

[12] J. Sanz, M. Ferre, A. Espada, M. C. Narocki, and J. F. Pardo, "Robotized inspection system of the external aircraft fuselage based on ultrasound," in *Intelligent Robots and Systems (IROS), 2010 IEEE/RSJ International Conference on*, 2010, pp. 2612-2617.

[13] S. Ross, M. Lusk, and W. Lord, "A comparison of millimeter wave and eddy current detection of surface breaking defects in conducting materials," in *Review of Progress in Quantitative Nondestructive Evaluation*, ed: Springer, 1995, pp. 629-636.

[14] D. M. Pozar, *Microwave Engineering, 4th Edition*: Wiley, 2011.

[15] R. Zoughi and S. Kharkovsky, "Microwave and millimetre wave sensors for crack detection," *Fatigue & Fracture of Engineering Materials & Structures,* vol. 31, pp. 695-713, 2008.

[16] S. Kharkovsky, A. McClanahan, R. Zoughi, and D. D. Palmer, "Microwave dielectric-loaded rectangular waveguide resonator for depth evaluation of shallow flaws in metals," *IEEE Transactions on Instrumentation and Measurement,* vol. 60, pp. 3923-3930, 2011.

[17] S. Kharkovsky, M. T. Ghasr, and R. Zoughi, "Near-field millimeter-wave imaging of exposed and covered fatigue cracks," *IEEE Transactions on Instrumentation and Measurement,* vol. 58, pp. 2367-2370, 2009.

[18] A. McClanahan, S. Kharkovsky, A. R. Maxon, R. Zoughi, and D. D. Palmer, "Depth evaluation of shallow surface cracks in metals using rectangular waveguides at millimeter-wave frequencies," *IEEE Transactions on Instrumentation and Measurement,* vol. 59, pp. 1693-1704, 2010.

[19] F. Mazlumi, S. H. H. Sadeghi, and R. Moini, "Interaction of rectangular open-ended waveguides with surface tilted long cracks in metals," *IEEE Transactions on Instrumentation and Measurement,* vol. 55, pp. 2191-2197, 2006.

[20] R. Zoughi, S. I. Ganchev, and C. Huber, "Measurement parameter optimization for surface crack detection in metals using an open-ended waveguide probe," in *Instrumentation and Measurement Technology Conference, 1996. IMTC-96. Conference Proceedings. Quality Measurements: The Indispensable Bridge between Theory and Reality., IEEE*, 1996, pp. 1391-1394 vol.2.

[21] C. Huber, H. Abiri, S. I. Ganchev, and R. Zoughi, "Analysis of the crack characteristic signal using a generalized scattering matrix representation," *IEEE Transactions on Microwave Theory and Techniques,* vol. 45, pp. 477-484, 1997.

[22] A. M. Albishi, M. S. Boybay, and O. M. Ramahi, "Complementary split-ring resonator for crack detection in metallic surfaces," *IEEE Microwave and Wireless Components Letters,* vol. 22, pp. 330-332, 2012.

[23] N. Qaddoumi, E. Ranu, J. D. McColskey, R. Mirshahi, and R. Zoughi, "Microwave detection of stress-induced fatigue cracks in steel and potential for crack opening determination," *Journal of Research in Nondestructive Evaluation,* vol. 12, pp. 87-103, 2000.

[24] C. Yeh and R. Zoughi, "A novel microwave method for detection of long surface cracks in metals," *IEEE Transactions on Instrumentation and Measurement,* vol. 43, pp. 719-725, 1994.

[25] K. M. Donnell, A. McClanahan, and R. Zoughi, "On the crack characteristic signal from an open-ended coaxial probe," *IEEE Transactions on Instrumentation and Measurement,* vol. 63, pp. 1877-1879, 2014.

[26] M. T. Ghasr, B. Carroll, S. Kharkovsky, R. Austin, and R. Zoughi, "Millimeter-wave differential probe for nondestructive detection of corrosion precursor pitting," *IEEE Transactions on Instrumentation and Measurement,* vol. 55, pp. 1620-1627, 2006.

[27] M. T. Ghasr, S. Kharkovsky, R. Zoughi, and R. Austin, "Comparison of near-field millimeter-wave probes for detecting corrosion precursor pitting under paint," *IEEE Transactions on Instrumentation and Measurement,* vol. 54, pp. 1497-1504, 2005.

[28] M. T. Ghasr, "Detection and size evaluation of corrosion precursor pitting using near-field microwave and millimeter wave nondestructive testing methods," M.S. in Electrical Engineering Thesis, Electrical and Computer Engineering, University of Missouri--Rolla, 2004.

[29] M. T. Ghasr, S. Hatfield, and R. Zoughi, "Design and performance analysis of a millimeter wave differential probe for fastener crack detection: final report," The Boeing Company, 2012.

[30] M. T. Ghasr, R. Zoughi, and G. Steffes, "Estimation of corrosion thickness under paint using a simple millimeter wave probe," in *3rd International Conference on Electromagnetic Near-Field Characterization & Imaging (ICONIC 2007)*, 2007, pp. 83-88.

[31] CST Microwave Studio®. *Computer Simulation Technology*. Available: http://www.cst.com

[32] D. M. Sheen, D. L. McMakin, and T. E. Hall, "Three-dimensional millimeter-wave imaging for concealed weapon detection," *IEEE Transactions on Microwave Theory and Techniques,* vol. 49, pp. 1581-1592, 2001.

[33] I. G. Cumming and F. H. Wong, "Digital processing of synthetic aperture radar data," *Artech house,* vol. 1, p. 3, 2005.

[34] J. M. Lopez-Sanchez and J. Fortuny-Guasch, "3-D radar imaging using range migration techniques," *IEEE Transactions on Antennas and Propagation,* vol. 48, pp. 728-737, 2000.

[35] P. A. Rosen, S. Hensley, I. R. Joughin, F. K. Li, S. N. Madsen, E. Rodriguez, *et al.*, "Synthetic aperture radar interferometry," *Proceedings of the IEEE,* vol. 88, pp. 333-382, 2000.

[36] P. Berardino, G. Fornaro, R. Lanari, and E. Sansosti, "A new algorithm for surface deformation monitoring based on small baseline differential SAR interferograms," *IEEE Transactions on Geoscience and Remote Sensing,* vol. 40, pp. 2375-2383, 2002.

[37] A. Ferretti, C. Prati, and F. Rocca, "Permanent scatterers in SAR interferometry," *IEEE Transactions on Geoscience and Remote Sensing*, vol. 39, pp. 8-20, 2001.

[38] D. Hansen. (1999) Painting versus polishing. *AERO magazine*. Available: http://www.boeing.com/commercial/aeromagazine/aero_05/fo/fo01/index.html

VITA

Kuang-Ping Ying was born in Tainan, Taiwan (R.O.C). He finished middle school in Taiwan in 2007 before moving to the U.S. and attended Central High School in Springfield, MO. After graduating from high school, he attended the Missouri University of Science and Technology in 2011, where he received his Bachelor of Science degree in Electrical Engineering as well as a Minor in Mathematics in the Fall of 2015. He subsequently started his master's program, also in Electrical Engineering and at Missouri S&T. He received his Master of Science degree in July 2017.

In the summer of 2013, Kuang joined the Applied Microwave Nondestructive Testing Laboratory (*amntl)* as an undergraduate research assistant, and continued to become a graduate research assistant in 2015, with research interests included microwave and millimeter-wave imaging, microwave material characterization, and surface crack detection techniques. During this time, he also worked as a lab tutor for the Digital Systems Design lab course. In addition, he was a member of Eta Kappa Nu, Tau Beta Pi and IEEE while at Missouri S&T.